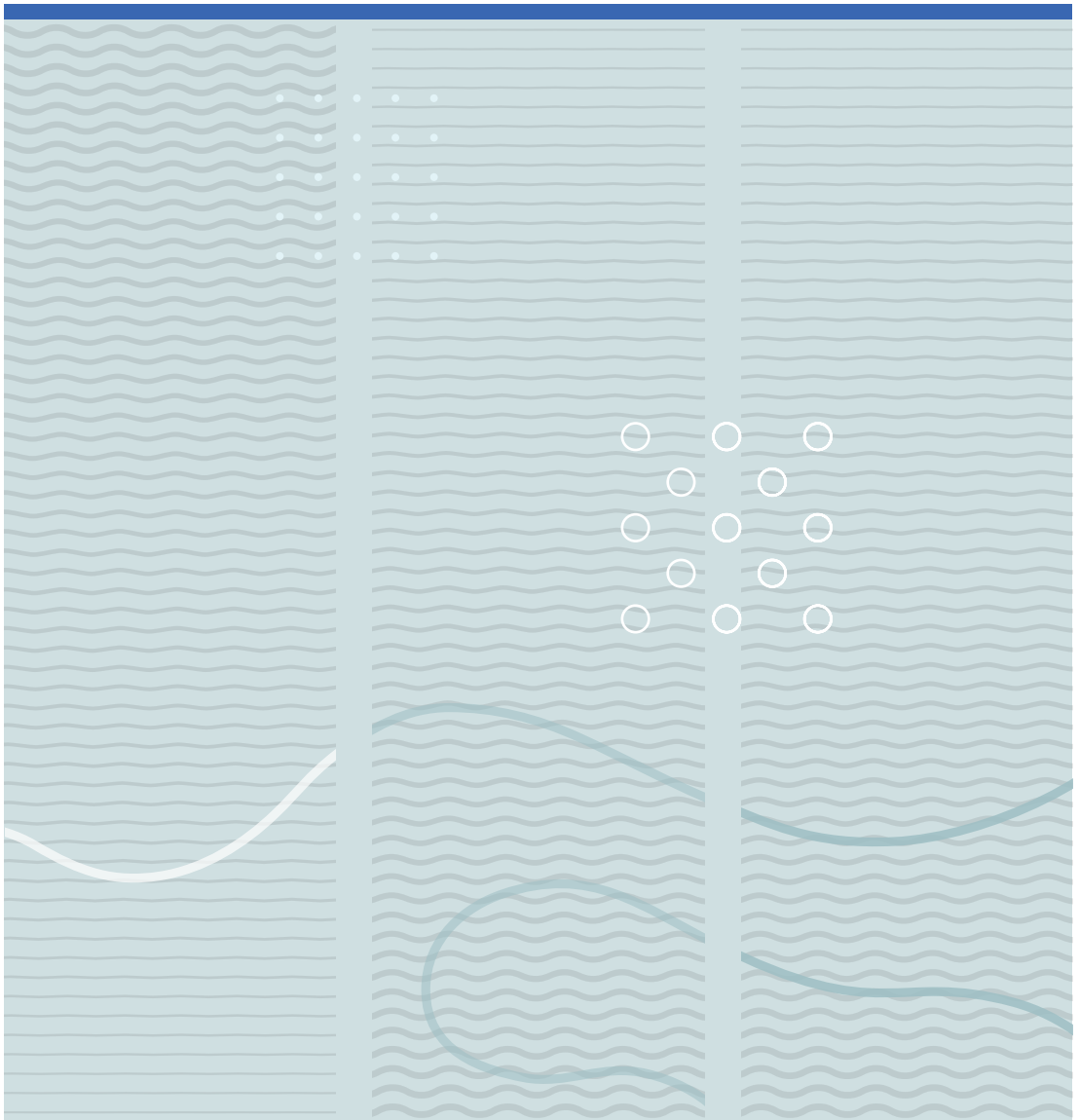


Janitha Bandara

Simulation and parameter optimization of fluidized-bed and biomass gasification





Janitha Bandara

**Electrical and Electronic Engineering
Department of Electrical and Electronic Engineering
University of Northumbria, Newcastle upon Tyne
United Kingdom**

A PhD dissertation in
Process, Energy and Automation Engineering

© 2021 Janitha Bandara
Faculty of Technology, Natural Sciences and Maritime Studies
University of South-Eastern Norway
Porsgrunn, 2021

Doctoral dissertations at the University of South-Eastern Norway no .92

ISSN: 2535-5244 (print)

ISSN: 2535-5252 (online)

ISBN: 978-82-7206-590-3 (print)

ISBN: 978-82-7206-591-0 (online)



This publication is, except otherwise stated, licenced under Creative Commons. You may copy and redistribute the material in any medium or format. You must give appropriate credit provide a link to the license, and indicate if changes were made.

<http://creativecommons.org/licenses/by-nc-sa/4.0/deed.en>

Print: University of South-Eastern Norway

I dedicate this to,

My beloved parents...

All the teachers from primary school...

My loving family...

Preface

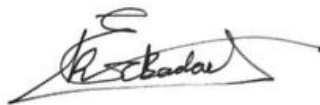
This dissertation is submitted as a partial fulfillment for the completion of the degree of philosophy doctor (PhD) at University of Southeastern Norway (USN). The research studies were carried out between October 2016 and December 2020 with the funding support of Norwegian Research Council.

Achieving a PhD is a lifetime dream. A rare dream for many. It is not an easy task as a piece of cake either and, it is not a journey paddling alone, but with backing up of many resource personals. Therefore, I take this opportunity to mention those who supported for the successful completing of my PhD research.

In first hand, I would like to express my profound gratitude to principal supervisor, Professor Marianne Eikeland and co-supervisors, Professor Britt Moldestad and Professor Henrik Nielsen. If not their excellent guidance and technical support, I would rarely cross the hurdles encountered along the journey. I am mindful to mention the immense support from associate Professor Rajan Thapa as well. There are many other supporting personal including Chameera (Barracuda VR), Amila (Barracuda VR, SolidWorks), Øyvind Johansen (experimental rig construction), Aleksander (IT division), Hiromi (sharing computer resources), Rajan Jaiswal & Sumudu (experimental support), Nora (GC), Ali, Nastaran, Masih and Sharfuddin who spent their valuable time on behalf of helping for my research work.

I should also mention Professor Ajith de Alwis at University of Moratuwa, Sri Lanka who always encouraged and inspired me in building up my academic career. Finally, I would like to give my earnest thanks to all of my teachers from University of Southeastern Norway, University of Moratuwa, Pinnawala National School and St. Mary's College.

Unless the immense love and courage from my family I would never succeed in achieving my life goals. Therefore, finally yet importantly, I owe a great debt of gratitude to my late mother, father, wife and my two princess daughters.



Janitha Bandara (Porsgrunn, Norway / 31 December 2020)

Summary

This thesis gives an insight to experimental studies and computational particle fluid dynamic (CPFD) simulations of fluidized bed and fluidized bed gasification reactors. CPFD models were validated against experimental data and used in subsequent parametric studies. The deviation of simulation results were discussed with possible uncertainties related to both the experiments and the CPFD model setup. Bubbling fluidized bed cold-rig, circulating fluidized bed cold-rig and bubbling fluidized bed gasification reactor were used for the experimental studies. Barracuda VR® 17.3.0 commercial CFD platform was used for the simulations.

Understanding of minimum fluidization velocity (MFV) is the prime importance of any fluidized bed study. Sand particles were sieved in 8 different narrow size ranges from 200 μm to 1180 μm and the MFVs were calculated by plotting experimentally measured bed pressure drop data against superficial gas velocity. The change of MFV was not exactly linear over tested particle sizes and instead, different size groups showed linear relationships separately. A cold-rig of circulating fluidized bed (CFB) with a riser, cyclone and a loopseal was constructed at USN to reinforce the CPFD model validation. Contribution of the standpipe aeration in controlling the rate of particle circulation was slightly over 60%, whereas bottom aeration was necessary to put the loopseal in operation.

As the gasification reactor was equipped with electrically heated walls, the experiments were designed at lower equivalence ratios (ER) between 0.1-0.16. At lower ER, char particles accumulated in the reactor and the ER was needed to increase up to 0.16 for a steady char concentration at 800°C. Gasification of grass pellets was not successful due to clinker formation and low carbon conversion. Wood chips and wood pellets showed reasonable results and the temperature was needed to maintain around 800°C for an efficient carbon conversion above 70%.

CPFD simulation with Wen-Yu-Ergun blended construction, as the fluid drag model, could predict the MFV with a 3.5% error for 200-255 μm particles. The calculated bed expansion at minimum fluidization was lower in CPFD simulation than experiments. Optimization of the particle modeling parameters was necessary for CPFD simulation of the CFB cold-reactor to achieve the rate of particle circulation observed during the experiments. The pressure constant of the particle stress model was the most affecting parameter followed by particle-wall momentum retention coefficients. The particle hydrodynamics at the loopseal, especially the bubble formation at the standpipe, and core annulus structure in the riser were illustrated using CPFD simulation graphical data. The optimized model parameters were reviewed with follow up simulations for the CFB geometry at USN. The results confirmed the reproducibility of optimized parameters.

The predicted gas composition of H₂, CO and CH₄ from the CPFD simulation for air-blown gasification of biomass in bubbling fluidized bed showed a close match with the experiments. However, the predicted composition of CO₂ was higher than the experiments while lower for N₂. Local temperature at the biomass feeding point is, however, possible to drop sharply due to endothermic moisture evaporation and pyrolysis reactions, which will in turn cause fluctuating pyrolysis composition. Therefore, high prediction of CO₂ with simultaneous low prediction of N₂, could be due to the under-prediction of tar generation during the pyrolysis step.

Keywords: Bioenergy, Gasification, Fluidized bed, CPFD simulation

A journey towards a sustainable world

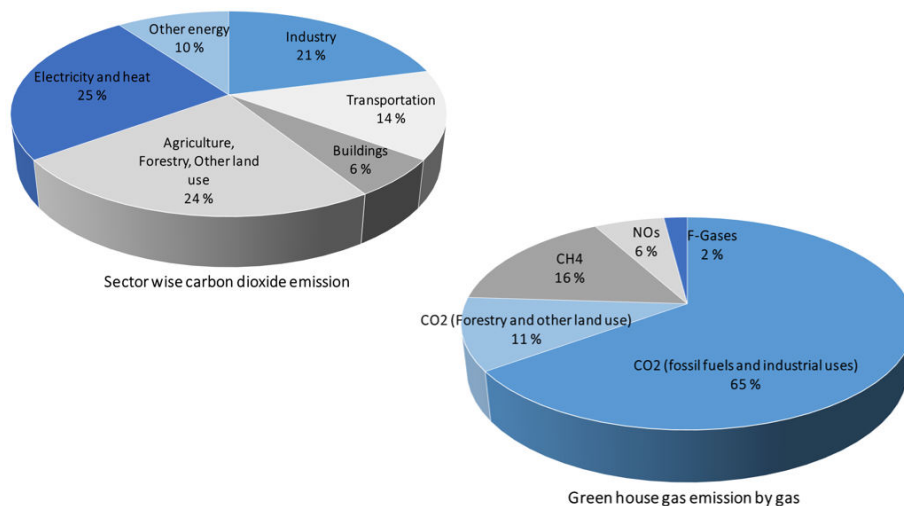
“I do not wish to seem overdramatic, but I can only conclude from the information that is available to me as secretary general, that the members of the United Nations have perhaps ten years left in which to subordinate their ancient quarrels and launch a global partnership to curb the arms race, to improve the human environment, to diffuse the population explosion, and to supply the required momentum to development efforts. If such as global partnership is not forged within the next decade, then I very much fear that the problems I have mentioned will have reach such staggering proportions that they will be beyond our capacity to control”

U Thant, 1969 – Secretary General to United Nations

The book “Limits to Growth” published in 1972 [1] foresaw the upcoming issues on planet earth. Later in well-known Brundtland report, the requirement of sustainable development was brought forward, which is also called “Our Common Future” published in 1987. Addressing the social, economic and environmental issues to find integrated solutions is the core of the sustainable development principal. Subsequent to the United Nations Conference on the Human Environment (1972) in Stockholm, Sweden, the global environment owned a permanent position in universal agendas [2]. Consequently, a number of environmental agreements were established such as Geneva Convention on long-range transboundary air pollution (1979), Helsinki agreement on reducing Sulphur dioxide emission (1985), Basel Convention on substances depleting Ozone layer (1988), which are directly linked to global air quality [3]. United Nations Framework Convention on Climate Change (UNFCCC) was formulated at the UN conference on environment and development in 1992, Rio de Janeiro. The conference is also renowned as the “Earth Summit” and the report “Agenda 21” was published with concluding remarks. Intergovernmental Panel on Climate Change (IPCC) was formed by collective contribution of world meteorological organization and UN Environment Program in 1988 in order to organize all the scientific findings and strengthen the climate policy development. The delegates were gathered for a second time in 1997 in New York to review the progress of Agenda 21. The conference is recognized as UN General Assembly Special Session (UNGASS) on top. Gradually over this period, the environmental concerns were greatly synchronized with “Green House Gas emissions” attached to climate change. As a progressive development, the famous “Kyoto Protocol” was adopted in 1997 during the third Conference of Parties (COP3) under UNFCCC. The underline goal was to reduce the GHG emission with the baseline of 1990 levels

where two commitment periods were highlighted from 2008 to 2012 and 2013 to 2020. The millennium development goals (MDGs) were brought forward by UN in 2000 to combat critical social and environmental issues where “ensure environmental sustainability” was one wing out of eight goals. In 2002, the world Summit on Sustainable Development (WSSD) was held in Johannesburg as a progressive event of the Stockholm Conference and the Rio Conference. The Kyoto protocol was ratified to meet the increasing climate concerns. Millennium development goals were extended to include 17 components during UN sustainable development summit in 2015 where “climate action” and “affordable and clean energy” are two wings. As a continuation to this successive discussion since 1972, the renowned “Paris Agreement” was launched with great expectations to limit the average global temperature increment below 2°C compared to pre-industrial level [4].

In midst of many other localized pollution measures, the greenhouse gas (GHG) emission emerged as a global concern, because the climate change is believed to be concretely linked with anthropogenic emissions. Carbon dioxide (CO₂) accounts for three fourth of the GHG emissions originated mainly from fuel combustion. Methane (CH₄) and nitrous oxide (N₂O) are the other main GHGs. Fluorinated gases, which is now being banned, have a higher global warming potential (GWP) compared to CO₂, CH₄ and N₂O. Non-energy related emissions are process emissions (i.e. cement manufacturing), deforestation/land use change, livestock and agriculture, release of soil carbon due to excessive topsoil plowing, organic land filling and permafrost. The emission of N₂O is primarily a result of agriculture. Apart from agriculture, CH₄ is released in large quantities during extraction and processing of petroleum products [5]. The greenhouse gas emission breakdown as per sector and gas type are illustrated in following figure.



Greenhouse gas emission by sector and by gas[5]

According to the statistics, emission of GHGs are mainly linked to different aspects of energy production and usage, which is approximately 90% of the total. By December 2019, coal is the largest contributor of CO₂ among different fuels while in country wise, China leads in front. However, until 1950s, over 80% of the CO₂ emissions were released from USA and Europe. The current global temperature rise is 0.7°C compared to the base line of 1960-1991 and 1.1°C compared to pre-industrial years [6, 7]. The atmospheric CO₂ concentration was recorded as high as 414 ppm in March 2020. Therefore, it is crucial the reshaping of energy profile to achieve the climate goals.

“This is the first time a global generation of children will grow up in a world made far more dangerous and uncertain as a result of a changing climate and degraded environment”

- UNICEF

Contents

Preface	v
Summary.....	vii
A journey towards a sustainable world.....	ix
List of Tables	xv
List of Figures.....	xvi
1 Introduction	1
1.1 Background	2
1.2 The problem statement	4
1.3 Research objectives.....	4
1.4 Thesis outline	5
1.5 List of Publications	5
2 Literature Studies	9
2.1 Bioenergy resources	10
2.2 Biomass to energy conversion.....	12
2.3 Biomass gasification	14
2.4 Modeling of biomass gasification.....	19
2.4.1 CFD modeling.....	20
2.4.2 The MP PIC method	22
2.4.3 The CFPD construction	24
2.4.4 Previous CFPD studies	29
2.5 Conclusion-literature.....	31
3 Experimental and CFD Methods.....	33
3.1 Experimental Studies	33
3.1.1 Minimum fluidization studies	34
3.1.2 Experimental studies of air gasification in bubbling fluidized bed	37
3.2 CFD simulation studies	38
3.2.1 Bubbling fluidized bed simulations.....	38
3.2.2 Circulating fluidized bed analysis	39
3.2.3 Steam Gasification in bubbling fluidized bed	40

3.2.4	Air Gasification in Bubbling fluidized bed.....	41
4	Results.....	45
4.1	Experimental analysis of minimum fluidization velocity	45
4.2	CPFD simulations for estimating MFV.....	47
4.3	Circulating Fluidized bed - Experiment.....	51
4.4	CPFD simulation of circulating fluidized bed	54
4.4.1	Revalidation of the CPFD particle-modeling parameters	57
4.4.2	Effect of the particle inventory for particle circulation	58
4.5	Bubbling fluidized bed gasification	60
4.6	CPFD simulation of bubbling fluidized bed gasification.....	62
4.7	Summary.....	65
5	Conclusion.....	69
	References	71
	Annexure A.....	83
	Annexure B.....	115

List of Tables

Table 1: Properties of biomass different biomass feedstock	11
Table 2: Principle reactions considered during modeling [61, 62]	19
Table 3: Particle modeling parameter.....	26
Table 4: Particle properties and modeling parameters used in simulation	43
Table 5: Chemical kinetics	44
Table 6: Gasification performance indicators for wood chips.....	62

List of Figures

Figure 1: The world energy profile and modern renewable energy profile [11].....	2
Figure 2: Overview of various bioenergy resources redrawn from [27]	10
Figure 3: Biomass to energy conversion routes –redrawn from [51]	14
Figure 4: Distinguished steps in biomass gasification process	15
Figure 5: Fixed bed gasification reactors – Downdraft (left) and Updraft (right)...	15
Figure 6: Fluidized bed gasification reactors – Bubbling fluidized bed (left) and dual reactor circulation fluidized bed (right)	16
Figure 7: Designing concerns of dual reactor circulating fluidized bed gasification	17
Figure 8: Experimental test rig for evaluate MFV with airflow controller and pressure transducers connected via LabVIEW program.....	34
Figure 9: Calculating procedure of minimum fluidization velocity.....	35
Figure 10: Circulating fluidized bed experimental rig. The dimensions are in mm and inner pipe diameters are mentioned.....	36
Figure 11: Bubbling fluidized bed gasifier and auxiliary equipment at USN.....	37
Figure 12: CPFDF geometry for calculating MFV (a) grid, (b) boundary conditions and (c) transient data points for pressure.....	38
Figure 13: Computational grid, boundary conditions and initial particle filling of CFB simulation setup.....	39
Figure 14: Computational domain use in loopseal analysis	40
Figure 15: Dual reactor CFB gasification	41
Figure 16: Computational domain and boundary conditions used in steam gasification in a bubbling fluidized bed.....	41
Figure 17: Replacement of circular section with square section	42
Figure 18: Simulation setup (A) initial particle filling (B, C) boundary conditions (D) flux plane (E) transient data points	43
Figure 19: Pressure gradient vs superficial velocity plots for estimating the MFV for 200-255 μm (a) and 1000-1180 μm (b) sized particles	46
Figure 20: Change of minimum fluidization velocity as a function of particle size.	46
Figure 21: Comparison of experimental data and CPFDF simulation results of MFV for different Ergun coefficients (200-250 μm).....	48

Figure 22: Sensitivity of MFV for different particle size distributions (Paper A)	50
Figure 23: Particle accumulation at riser-to-cyclone connector and flow hindrance across loopseal overflow during experiments	51
Figure 24: PCA plots for 850-1000 μm particle size (Factor-1 represent the FR3 and Factor-2 is for FR2).....	52
Figure 25: The relationships between particle circulation vs standpipe bed height, and particle circulation vs loopseal aeration for 1000-1180 μm particles.....	53
Figure 26: The relationships of particle circulation vs standpipe bed height and particle circulation vs loopseal aeration for 850-1000 μm particles.....	54
Figure 27: Effect of the pressure constant in particle stress model for the rate of particle circulation. Different colors represent different constants from 2.5 to 5...55	55
Figure 28: Effect of the loopseal aeration for the rate of particle circulation (P1 and P2 refer to loopseal recycle pipe and standpipe respectively).....	55
Figure 29: Particle speed over the CFB and sectional views at different heights in the riser (left) and particle vertical velocity (right)	56
Figure 30: Flux planes used for the calculation of residence time and cumulative flow across flux planes.	57
Figure 31: CFB model re-validation. Boundary conditions and particle hydrodynamics.....	58
Figure 32: Rate of particle circulation as a function of particle inventory	59
Figure 33: The change of particle circulation against particle inventory and visualization of particle hydrodynamics	59
Figure 34: Pressure over the CFB system for different particle inventories.	60
Figure 35: Composition of producer gas with ER and temperature for wood chips.	61
Figure 36: Variation of the temperature along the reactor height.....	63
Figure 37: Distribution of the gaseous components across the reactor	64
Figure 38: comparison of gas composition from simulation against experiments for wood pellets at 750°C and 0.125 ER	65

1 Introduction

The availability of abandoned energy reshaped the ancient human civilization into the modern living. The strong correlation between energy consumption and economic development has been confirmed by many researchers [8]. Fuel wood, animal power and human muscle power have been the key components in the energy mix until 1850s. Ever since, the energy profile was dramatically changed with the appearance of coal and especially, with the outset of cheap petroleum, about a 100 years later in 1940s [9]. Successive development of energy generation and conversion boosted the world's production, which backed the feeding of multiplying population and the improving life comfort. The energy trilemma index, which is a cooperative paradigm of energy security, energy equity and environmental sustainability, is therefore the core strength for a smooth functioning economy. However, the energy trilemma is not completely balanced in many geographical regions [10]. As illustrated in Figure 1, approximately 80% of the world energy production is derived using fossil fuel resources of coal, petroleum and natural gas in 2016 [11]. The narrow geographical distribution of fossil resources greatly effects on many countries either as a shortage of supply or volatility of the market price. Consequently, the oil crisis in 1970s forced many countries to reshape their energy flows. In long term, it is uncertain the years left before we run out of fossil reserves. With the uneven distribution of wealth between countries and even societies, the energy equity is also largely challenged. Above all, the environmental damage (i.e. global warming) caused by excessive emissions of greenhouse gases (GHG) set a common goal of reducing the consumption of fossil fuels. A reduction of energy usage per capita can be mainly expected by cut down the wastage where in contrast, the total energy consumption is piling up annually due to the population growth, increasing life comfort and rapid industrialization of developing countries. Increasing energy efficiency and carbon capture & storage are two other tools identified in reducing total emissions to the atmosphere. Fuel switching, such as shifting from coal fired power generation to nuclear power, has also been suggested. Nevertheless, a number of countries proceed to phase out the nuclear power generation due to the high risks involved. In particular, shifting towards renewable energy sources is the mostly discussed and endeavored element in the quest for emission reduction. Notwithstanding the added capacity from renewable energy systems, its global share has been continued to anchor around 17% between 2000-2017 [12].

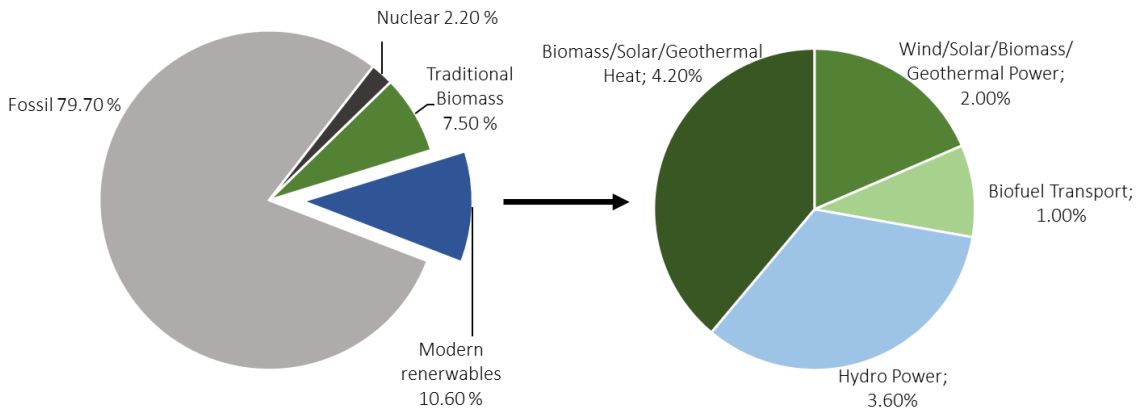


Figure 1: The world energy profile and modern renewable energy profile [11]

1.1 Background

Biomass is the only renewable energy (RE) source with the dispatchable characteristic and hydrocarbon origin, which can deliver the full spectrum of fossil-based products. By 2050, nearly 90% of the world population is expected to reside in economically developing regions where 90% of their rural economies rely on biomass as the primary energy source [8, 13]. The public involvement is higher in bioenergy business, which creates more employments compared to other RE. Beyond the target emission reduction and diversifying energy mix, upgrading of arable land for energy crops improves the ecological environment and the biodiversity. Due to the aforementioned facts, biomass has been identified as a high potential energy source to the future in all geographical regions [14]. The exergy of bioenergy is naturally positive unless the forestlands are distorted, since forests are large sinks trapping carbon in both trees and soil [15, 16].

The European Union (EU) has set up their own emission reduction and renewable energy targets for 2020 and 2030 [17]. The 2020 target relies on 20% reduction of GHG emissions, 20% share of RE in the national energy mix with 10% renewables in the transport sector and 20% increase in energy efficiency. According to the 2030 targets, the respective values are supposed to improve as 40%, 32% and 32.5%. In the long term, Europe has high hopes to be a carbon neutral territory by 2050. Bioenergy contribution in the RE profile is 60% in the EU countries. Of that, 74.6% comes from heating applications, 13.4% from electricity generations and the rest of 12% from liquid biofuels [17]. The average use of liquid biofuels in EU countries is slightly below 5%. In the Norwegian context, 98% of the electricity is generated using hydropower. The principal format of bioenergy development is, therefore, in the field of liquid biofuels and heating. Brazil and United States are the world leading

producers of ethanol as liquid biofuel, which is derived from sugar cane and corn respectively. Germany is the pioneer producer of biodiesel derived from rapeseed and used cooking oil [18]. Pumping of food grade feedstock for the synthesis of biofuel and consequent rise of food price is a long debated topic, which resulted in growing interest for second-generation biofuels from lignocellulosic fraction and third generation from algae. Declining of paper and pulp production in Norway resulted in growing forest stock that can be used in energy production [19, 20].

Lignocellulosic biomass has different origins. Dedicated energy crops, forest residues, agricultural residues, processing residues of agriculture products and wastes. Hydrolysis and fermentation of solid biomass to produce bioethanol is still in the development stage, whereas high moist biomass feedstock such as manure and municipal solid waste (MSW) is used by biogas production. Combustion is the mostly established biomass-to-energy conversion method used in low efficient cook stoves to large-scale boilers and combined heat and power (CHP). However, synchronizing with the European and Norwegian prospects, synthesis of liquid biofuels is the prime importance.

Pyrolysis is one possible biomass-to-energy conversion method, in which the biomass is heated under oxygen free environment. The process can be biased to produce more liquid oils with reduced gaseous and solid fraction by adjusting the operating conditions. The liquid product is a complex mixture of oxygenated compounds that needs extensive post processing in upgrading it to meet with the standards of fossil fuels. The gasification process, in contrast, converts solid biomass into a gaseous mixture of carbon monoxide (CO), hydrogen (H₂), carbon dioxide (CO₂), methane (CH₄), light hydrocarbons (propane, butane etc.) and heavier tars using heat and one or a mixture of gasifying agents of air, oxygen and steam. Gasification has several benefits over pyrolysis including the versatility of produced gas and high carbon conversion.

Fluidized bed reactors are more favorable in large-scale biomass gasification units compared to fixed bed designs. Entrained flow gasifiers are operated at elevated temperatures and the particle size should be in sum-millimeter range due to low residence time. Air gasification in bubbling fluidized bed (BFB) and steam gasification in dual reactor circulating fluidized bed (DCFB) gasification are the mostly discussed reactor types. The nitrogen dilution in BFB gasification can easily be eliminated using DCFB, which can be the best choice for syngas utilization in downstream processing into fuels and chemicals. The syngas is more versatile as it can be used in various processes such as internal combustion engines, turbines, Fisher Tropsch synthesis of liquid biofuels, fermentation and solid oxide fuel cells.

1.2 The problem statement

Fluidized bed gasification reactors require simultaneous optimization of particle hydrodynamics such as rate of particle circulation in DCFB and operational conditions such as temperature, equivalence ratio etc.

Biomass particles are difficult to fluidize due to low density, large size and irregularity in shape. Therefore a second particle phase, which is called as bed material, is used to assist the fluidization. In general, hydrodynamics of the bed material approximately represent the overall reactor hydrodynamics and consequently, it affects the overall reactor performances. Therefore, a detailed study of bed material behavior in bubbling and circulating fluidized bed reactors in cold conditions is worthwhile.

The chemical and physical properties of biomass, fluidization conditions and operational parameters such as temperature, pressure etc. can be varied between each BFB gasification reactor. Any publications does not count on all the possible variables and gives a universal picture of biomass gasification. Therefore, each experimental analysis is important where new concepts are born and possible improvements are identified.

A complete system optimization of a fluidized bed gasifier is challenging to achieve with experiments alone. Computational fluid dynamic (CFD) modeling and simulation has emerged as a useful tool in system upscaling and optimization. Multiphase flow modeling and simulation is comparatively complex and time consuming compared to single-phase fluid flows. Computational particle fluid dynamics (CPFD) is a novel development compared to Eulerian-Eulerian (EE) and Eulerian-Lagrangian (EL) approaches, which is built on “multiphase particle in cell” (MP PIC) theory. CPFD simulation with reaction kinetics in a DCBF is time consuming. Therefore, optimization of the particle hydrodynamics before integrating the reaction kinetics is productive. CFD model validation against experiments is an essential step, especially in multiphase systems, because of the errors and uncertainties originated from model simplification, approximation techniques and empirical models.

1.3 Research objectives

The research was planned with simultaneous experimental and identical CPFD simulations studies.

- Experimental studies in bubbling fluidized bed cold rig to understand the minimum fluidization velocity.
- Construct a cold circulating fluidized bed (CFB) reactor to investigate the particle circulation.

- Parametric study of air-blown gasification reactor using different biomass feedstock of wood chips, wood pellets and grass pellets.
- Validate a CPFD hydrodynamic model using bubbling and CFB experimental data.
- Parametric study of CFB using developed model and extend it to DCFB reactor system
- Validate a CPFD gasification model using experimental data of air-blown gasification reactor
- CPFD analysis of steam gasification reactor and char combustion reactor separately

1.4 Thesis outline

The thesis is a collection of five chapters and an annexure with 9 published or submitted papers. Chapter 1 gives a basic insight to the research background, problem statement and objectives. A comprehensive literature review is presented in the Chapter 2 discussing the particulars of bioenergy, biomass gasification, CFD simulation of multiphase flows and computational particle fluid dynamic studies.

In Chapter 3, the experimental and CPFD method are discussed. The construction of CFB and guidelines for the operation of bubbling gasification reactor are included in detail. In related with the CPFD model set up, the grid configuration, boundary conditions, particle modeling parameters and chemical kinetics used are mentioned. Chapter 4 includes the experimental findings and CFD simulation results for both non-reactive and reactive systems. The chapter further discuss the data trends, deviations of CPFD results and uncertainties. To the end of the thesis in Chapter 5, conclusions for the research project are briefed along with future works. In the Annexure, published, accepted and submitted scientific articles are lined up.

1.5 List of Publications

Paper A

“Analyzing the effects of particle density, size, size distribution and shape for minimum fluidization velocity with Eulerian-Lagrangian CFD simulation”

Conference: Proceedings of the 58th Conference on Simulation and Modelling (SIMS 58), September 25 – 27, 2017, Reykjavik, Iceland. PP 60-65

DOI: 0.3384/ecp1713860

Paper B

“Sensitivity Analysis and Effect of Simulation parameters of CPFD Simulation in Fluidized Beds”

Conference: Proceedings of the 59th Conference on Simulation and Modelling (SIMS 59), 26-28 September 2018, Oslo Metropolitan University, Norway. PP 334-341

DOI: 10.3384/ecp18153334

Paper C

“Circulating Fluidized Bed Reactors – Part 01: Analyzing the Effect of Particle Modelling Parameters in Computational Particle Fluid Dynamic (CPFD) Simulation with Experimental Validation”

Journal: Taylor and Francis, Particulate Science and Technology (2019)

DOI: 10.1080/02726351.2019.1697773

ISSN: 0272-6351 (Print) 1548-0046 (Online)

Paper D

“Analyzing the Effects of Geometrical and Particle Size Uncertainty in Circulating Fluidized Beds using CPFD Simulation”

Conference: Proceedings of the 60th SIMS Conference on Simulation and Modelling (SIMS 60), September 25 – 27, 2019, Västerås, Sweden. PP 182-189

DOI: 10.3384/ecp20170182

Paper E

“Loop seals in circulating fluidized beds – Review and parametric studies using CPFD”

Journal: Chemical Engineering Science, Volume 227, 14 December 2020, 115917

DOI: 10.1016/j.ces.2020.115917

Paper F

“Analysis of the Effect of Steam-to-Biomass Ratio in Fluidized Bed Gasification with Multiphase Particle-in-cell CFD Simulation”

Conference: Proceedings of the 58th Conference on Simulation and Modelling (SIMS 58), September 25 – 27, 2017, Reykjavik, Iceland. PP 54-59

DOI: 10.3384/ecp1713854

Paper G

“Analysing the effect of temperature for steam fluidized-bed gasification of biomass with MP-PIC simulation”

Journal: International Journal of Energy and Environment, 2018, Volume 9, Issue 6, PP 529-542

Paper H

“Air gasification of biomass in bubbling fluidized bed – short review and experimental studies”

Journal: Chemical Engineering Science (2020 – Submitted)

Paper I

“Experimental and Computational studies of circulating fluidized bed”

Journal: International Journal of Energy Production and Management, 2020, Volume 05, PP 302-313 16-18 June 2020 (online)

2 Literature Studies

Struggle for life is not a struggle for basic elements or energy, but a struggle for the availability of negative entropy in energy transfer from the hot sun to cold earth.

-Boltzmann, a physical chemistry scientist

Biomass counteracts this negative entropy via photosynthesis, which has been the key natural resource that blended with civilization, especially in pre-industrialization [21]. It serves people in different forms such as food, fodder, fibers, building and constructions, fuel, medicine and many more. According to the definition of McKendry, "Biomass is a term for all organic materials that stems from plants including trees, crops and algae" [22]. Other organic substances derived during the consumption of plant material along the entire food chain are also characterized as biomass. Alternatively, it can be referred to all material with biological origin, which did not undergo geological formation [23].

The main challenges of bioenergy development are resource and land conflicts against food supply, water and conservation of forestry and related biodiversity [24]. Instead of reduced emissions, deforestation for energy plantations with energy intensive feedstock processing can lead for increased emissions. Apart from the technical shortcomings, there are ethical aspects of forest clearing for energy crops, especially in Asian, African and Latin American regions. As an example, it can cut-off the daily supplies of herbal medicines, timber for housing etc. and cause water scarcity and pollution. In spite of all of these limitations, international energy agency (IEA) says that bioenergy is the fastest growing renewable energy source from 2018 to 2023 with estimated 30% growth [14].

The composition of biomass feedstock is varying depending on the species, soil, geographical distribution, weather etc. Household cooking needs wood to be mainly in reasonably dry conditions, whereas standardization of physical and chemical properties of the feedstock for modern technologies is even more demanding. Many processes including internal combustion engines, turbines and secondary fuel require normally solid biomass first to be converted into liquid or gaseous form. Efficient conversion of biomass is, therefore, crucial, which has been extensively studied and, still, a long way to go.

2.1 Bioenergy resources

According to Szczodrak and Fiedurek [25], annual world biomass production is approximately 2×10^{11} tons where only 10% of it remains potentially accessible. On the other hand, 90% of accessible fraction is composed with lignocellulosic material [21, 25]. Approximately 38% out of total biomass production originates in marine environment and almost all of it deposits in the seabed and turns in to fossils. The rest of 62% is terrestrial biomass that undergoes various processes such as food, fuel, pulp & paper, swan timber, chemicals etc. However, 75% of this terrestrial production grow, die and decay without any form of use, while only 25% is consumed by human activities [26].

Hoogwijk, et al. [27] worked on analysing the energy potential of biomass with the potential resources as stated in Figure 2. Energy crops in surplus agricultural lands was identified as the highest potential source with a maximum of 988 EJ/yr. As all the material inflows were concerned under different scenarios, the global bioenergy potential was in a broad range from 33 to 1135 EJ/yr. The observed variations were due to the varying considerations of future food demand, productivity of forestry and energy plantations, change of bio material inflow for non-energy usage and competing of surplus/degraded land between agriculture, energy crops and reforestation [28].

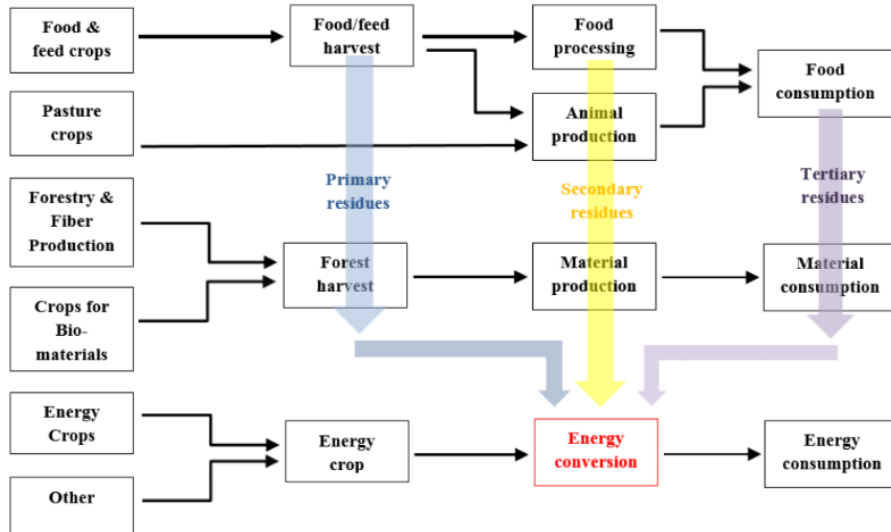


Figure 2: Overview of various bioenergy resources redrawn from [27]

In exception to the dedicated energy plantations, all other bioenergy feedstock are derived as residues in forestry and agricultural operations followed by industrial processing and end utilization. Primary residues are the leftovers at the field after harvesting that includes forestry logging residues (i.e. branches), residues from forest thinning and agricultural residues (i.e. straw). Secondary residues include by-products, refuse/residue from food processing facilities (i.e. husks, shells, sugarcane

bagasse and meat processing waste etc.), residue from sawn timber production (i.e. sawdust and bark) and pulp production (i.e. black liquor). The tertiary residues emerge from end utilization of value added products, which can be referred as waste (i.e. municipal solid waste, manure, demolished timber etc.) [27, 29]. However, economic viability of collecting and converting all these residues into useful energy is questionable due to the undesired feedstock characteristics (i.e. moisture, ash, contamination, low energy and bulk densities etc.), sustainability concerns (i.e. exergy or net CO₂ emission, nutrient removal from soil, standards of forestry cutting) and logistics (i.e. transportation and storage). Energy crops are identified as short rotation woody energy crops (i.e. willow and poplar), perennial grasses (i.e. switch grass and miscanthus), oil seeds (i.e. soybean, sunflower and rapeseed), sugar (i.e. sugarcane) and starch crops (i.e. corn) [30]. Algae [31] and other aquatic plants [32] (i.e. waterweeds) are also prospective bioenergy feedstock. The structural part of the plant including stem, bark, branches, roots etc. is known as lignocelluloses. The lignocellulosic fraction is composed with cellulose, hemicellulose and lignin. Extractives and mineral ash are the other minor components. The chemical characteristics of biomass are identified in many different ways such as elemental analysis, proximate analysis and chemical analysis. Table 1 includes properties of some selected biomass species.

Table 1: Properties of biomass different biomass feedstock

Species	Ultimate Analysis (%)				Proximate Analysis (%)				LHV/HHV* (MJ/kg)	Ref
	C	H	O	N	VM	FC	M	A		
Beech	48.1	5.9	45.	0.2	74.8	15.7	8.8	0.7	15	[33]
Pine	51.3	5.8	42.	0.1	78.1	14.7	6.3	0.5	17.4	[34]
pine	47.9	6.2	38.		79.7	12.7	7.5	0.1	17.6	[35]
Pine bark	55.5	5.6	37.	0.17	62.5	25.7	10.9	0.8	20	[36]
MSW	48	6.3	43.	1.39	79.8	20	17.6	0.2	14.4	[37]
Rice straw	35.6	4.63	58.	0.94	62.8	15.9	13.5	7.8		[38]
		Cellulose %		Hemicellulose		Lignin%		Extractives		
Almond shell		26		30		33		-		[39]
Hardwood		43		35		22				[40]
Switch grass		32		19.2		18.8		18.5		[41]

Notations: C-carbon, H-hydrogen, O-oxygen, N-nitrogen, VM-volatile matter, FC-fixed carbon, M-moisture, A-ash, LHV-lower heating value, HHV-higher heating value

The ash content of the woody material is less than 1% for most species. The ash content of grass feedstock is higher compared to wood, whereas the ash content in rice husks can reach over 20%. The heating value of biomass is also important,

which can be different between species mainly due the varying ash content and slightly with lignin and cellulosic fraction [22].

2.2 Biomass to energy conversion

In many developing countries in Southeast Asia, Africa and South America, biomass is the primary energy source in cooking and heating, which account for two third of the global bioenergy production. In certain countries such as Nepal, Bhutan and African region, the bioenergy contribution exceeds 80% of the country's total energy consumption [28, 42].

Combustion is the widely used method of biomass to energy conversion, which ranges from highly inefficient three-stone cooking stove to large scale biomass boilers such as suspension fired, fluidized bed and grate firing boilers [43]. Traditional cook stoves are highly inefficient and evaluated as a major cause for respiratory problems and pre-mature deaths. Co-firing of biomass with coal is another interesting and proven alternative, which is in practice. A proper consideration should be given for possible process interruptions due to the varying properties of biomass feedstock such as high moisture content, low carbon-to-oxygen ratio, high chlorine content, low ash melting temperature etc. [44]. To the bright side, the ability of using existing infrastructure with reduced emissions and efficiency improvement compared to stand alone biomass combustion, are the highlighted features of the co-firing technology [45].

In contrast to direct heat generation, fuel upgrading or conversion into secondary fuels or chemicals is the main future prospect of bioenergy systems. High moisture content, susceptibility for bio-degradation, low energy density and resistance for grinding are some major drawbacks of raw biomass [46]. Torrefaction is a controlled heating process with temperature up to 300°C in an oxygen free environment. Even if 30% of the initial weight is lost after the process, the energy loss is merely 10%. Consequently, the energy density and many of the aforementioned drawbacks are improved. The released gas is a combustible mixture that can be used for the process heat requirement [47]. Torrefaction has also been used as a pretreatment method for other thermal process of combustion, co-firing and gasification.

With the improving market for bio-ethanol and bio-diesel as automotive liquid fuels, the utilization of food grade feedstock such as sugar cane, corn and oil seeds for fuel synthesis was multiplied during last two decades. Brazil and USA are the leading bio-ethanol producers using sugar cane and corn respectively [48]. Biofuels derived from food grade feedstock are referred as first-generation biofuels. Bioethanol is produced by fermentation sugars followed by dehydration and distillation whereas the starch based process needs an additional hydrolysis step in the process

upstream. Bio-butanol over bio-ethanol has also been a research interest due to its higher energy density and better combustion performances in internal combustion engines. Vegetable oils such as soybean, sunflower, rapeseed etc. are the feedstock for first-generation biodiesel. The oil is extracted by mechanical means and processed with transesterification reactions [49]. Adjusting to the prolonged debate of using food grade feedstock for fuel synthesis, second-generation biofuels using lignocellulose fraction is a growing interest. Even though the second-generation biofuels are yet to enter to the commercial production, large number of research works are being conducted to identify the most efficient pathways. Hydrolysis of cellulosic and hemi-cellulosic fraction followed by fermentation and distillation is one of the possible pathways. The inherent slow nature of biochemical hydrolysis and low carbon conversion due to inert lignin fraction are the main disadvantages of this process. Maabjerg energy concept, Denmark and Borregaad ethanol from spruce, Norway are Nordic examples for prospecting quests for second generation bioethanol. Being a fast process and high carbon conversion, thermochemical pathways are preferred in many situations [49, 50]. Considerably dry feedstock is needed for the thermal conversion and however, can be counter weighted due to less demand for very fine particle size.

Gasification is the most versatile thermochemical process as the produced gas, which is known as either syngas or producer gas, can be directly used in IC engines, gas turbines and solid oxide fuel cells. Biomass gasifier integrated combined cycle (BIGCC) for heat and power is also identify as a better option. Or else, syngas can be used as a feedstock for second-generation liquid fuel or chemical synthesis. Biodiesel from Fisher-Tropsch conversion of syngas or methanol/ethanol via syngas fermentation are two possible processing methods [51-53].

Pyrolysis is another pronounced thermochemical process, which converts the solid biomass into oil using external heat. Char and gases are derived as by-products. The fractional composition between oil, char and gas can be biased by adjusting the particle size of biomass, heating rate, maximum temperature and the gas residence time. High oil production prefers smaller particles, medium temperature, high heating rate and low residence time. Produced oil is a viscous mixture of hundreds of complex organic compounds, which needs extensive downstream processing in upgrading to comply with the standard fuels. Biogas production is also a well-established process, which uses anaerobic digestion to breakdown the organic material into a methane rich gas mixture. Manure from animal farms and organic fraction of municipal solid waste (MSW) are the major feedstock.

Looking into the latest prospects, third-generation biofuels from algae is also showing a dramatic entrance to the bio-fuel picture [49]. Figure 3 briefs the energy

extraction from biomass where syngas from biomass gasification is the most versatile compared to the products from other processes.

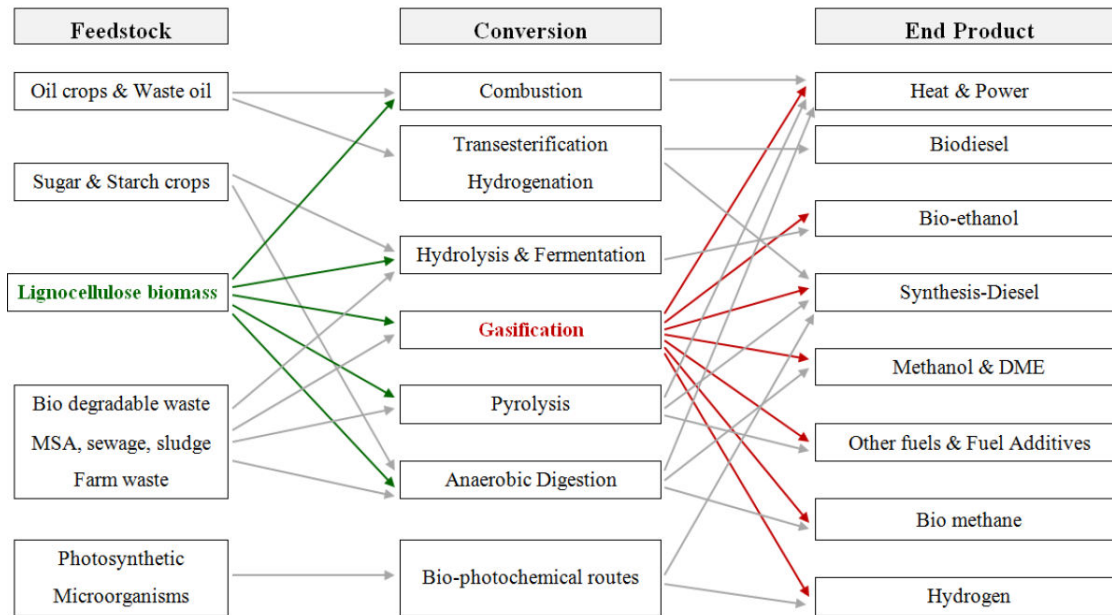


Figure 3: Biomass to energy conversion routes –redrawn from [51]

2.3 Biomass gasification

Gasification thermally converts the solid biomass into a gaseous mixture under a limited¹ oxygen environment. The overall process is endothermic. Carbon monoxide (CO), hydrogen (H₂), methane (CH₄), ethane (C₂H₆), carbon dioxide (CO₂), steam (H₂O) and condensable high molecular weight hydrocarbons (tar) are the principle product components, which is called as syngas [54]. If air is used instead of pure oxygen, the gaseous product is diluted with nitrogen, which is identified as producer gas. Gasification reactors can be classified depending on different features. Adhering to the inside biomass flow, it can be a fixed bed/moving bed, fluidized bed or an entrained flow reactor. Gasification can also be classified based on gasifying agent, which can be air, oxygen, steam or a mixture of these. In contrast to the pyrolysis, the main purpose of the gasifying agent is to achieve a complete carbon conversion. As the process enthalpy is concerned, the process can be either auto-thermal or allo-thermal where respectively, the heat is generated internally or supply externally [55]. Drying of biomass and pyrolysis are the initial conversion steps, whereas other hundreds of involved reactions are broadly grouped into combustion and gasification reactions as illustrated in Figure 4. The extent of gasification reactions decides the gas quality at the exit. The gas composition is sensitive towards the reactor type, gasifying agent, chemical properties of biomass, temperature,

¹ 6:1 to 6.5:1 stoichiometric air to fuel ratio is needed for the complete combustion of biomass. It is 1.5:1 to 1.8:1 for gasification

residence time and the internals such as catalysts. Fixed bed configurations are depicted in Figure 5 where Figure 6 illustrates the fluidized bed designing.

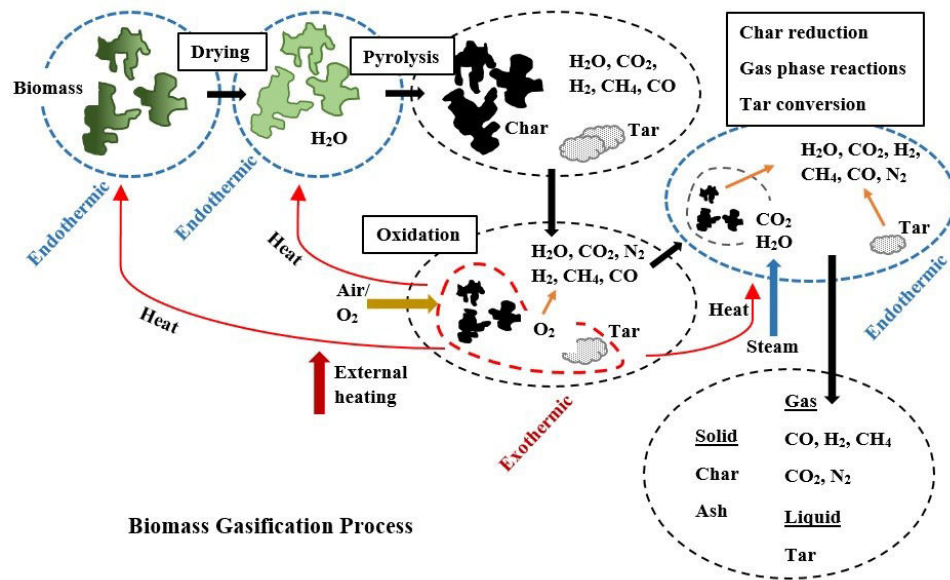


Figure 4: Distinguished steps in biomass gasification process

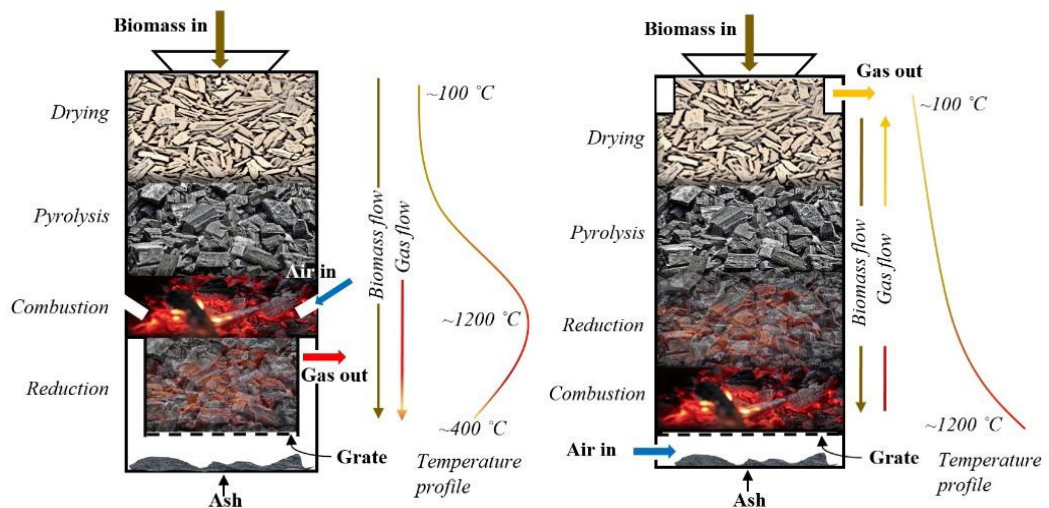


Figure 5: Fixed bed gasification reactors – Downdraft (left) and Updraft (right)

Different configurations have their own advantages and disadvantages, whereas the reactor selection is further decided by the end use of product gas. Product gas from the updraft fixed bed designing suffers from high tar content, while non-uniform radial temperature profile and local slagging problems make it difficult for the downdraft design to operate in large scale [56]. In fixed bed systems, biomass descends along the reactor in which the biomass particles can be large (i.e. small logs). However, the feedstock should be homogeneous in size and if not, channeling can cause gas bypass, especially in updraft reactors. The simple design of updraft

units attracts the small scale applications such as cooking stoves while the low tar content in downdraft units is a smart option to run small/medium scale IC engines or boilers.

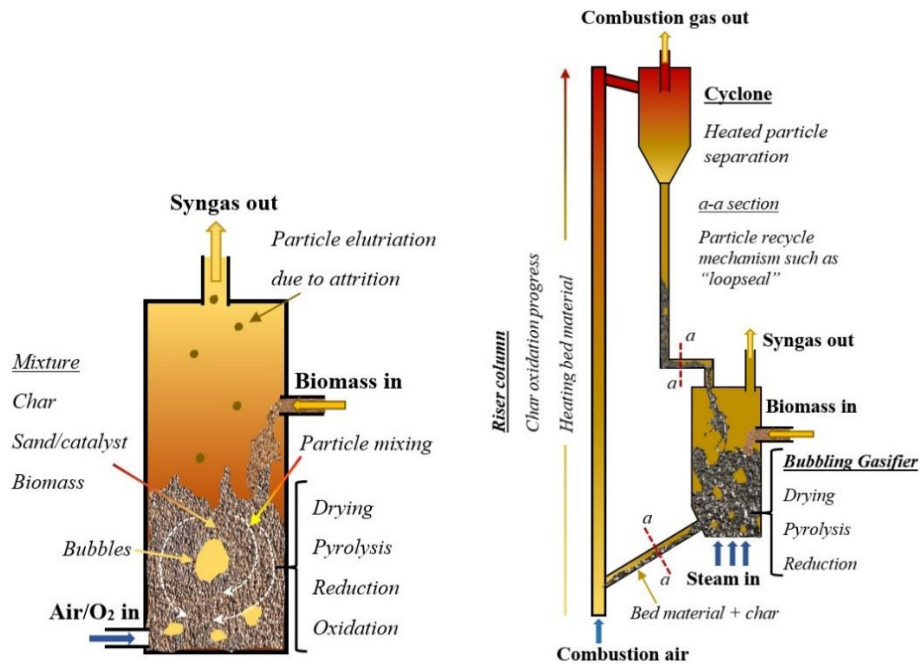


Figure 6: Fluidized bed gasification reactors – Bubbling fluidized bed (left) and dual reactor circulation fluidized bed (right)

Fluidized bed reactors are normally preferred in large-scale operation due to homogeneous conditions across the reactor volume resulting from intense mixing of internals. Bubbling fluidized bed is the simplest layout where the wood particles/chips/pellets are fed into a bubbling sand/catalysts (i.e. olivine, nickel catalysts etc.) bed at an elevated temperature. Integration of external heat is difficult in bubbling reactor and therefore in general, in situ char combustion provides the overall reaction enthalpy. The dual reactor circulating fluidized bed (DCFB) gasification overcomes the nitrogen dilution related to air-fed bubbling fluidized bed gasification by isolating the char combustion into a separate reactor. As illustrated in Figure 6, the primary reactor operates with steam as the fluidizing agent in which drying, pyrolysis and gasification reactions progress. The heat demand of involved endothermic reactions is supplied by the circulating bed material that are heated by the char combustion in the combustion reactor. In a typical design, the gasification reactor operates at bubbling regime while the combustion reactor at fast fluidization [57]. Elimination of nitrogen dilution and increased concentration of H_2 content enhance the gas quality. Moreover, the carbon-to-hydrogen ratio can be adjusted by manipulating the steam injection, which is crucial in downstream processing into chemicals such as Fischer-Tropsch

(FT) process. A detailed overview of designing concerns of the dual reactor circulating fluidized bed is given in Figure 7.

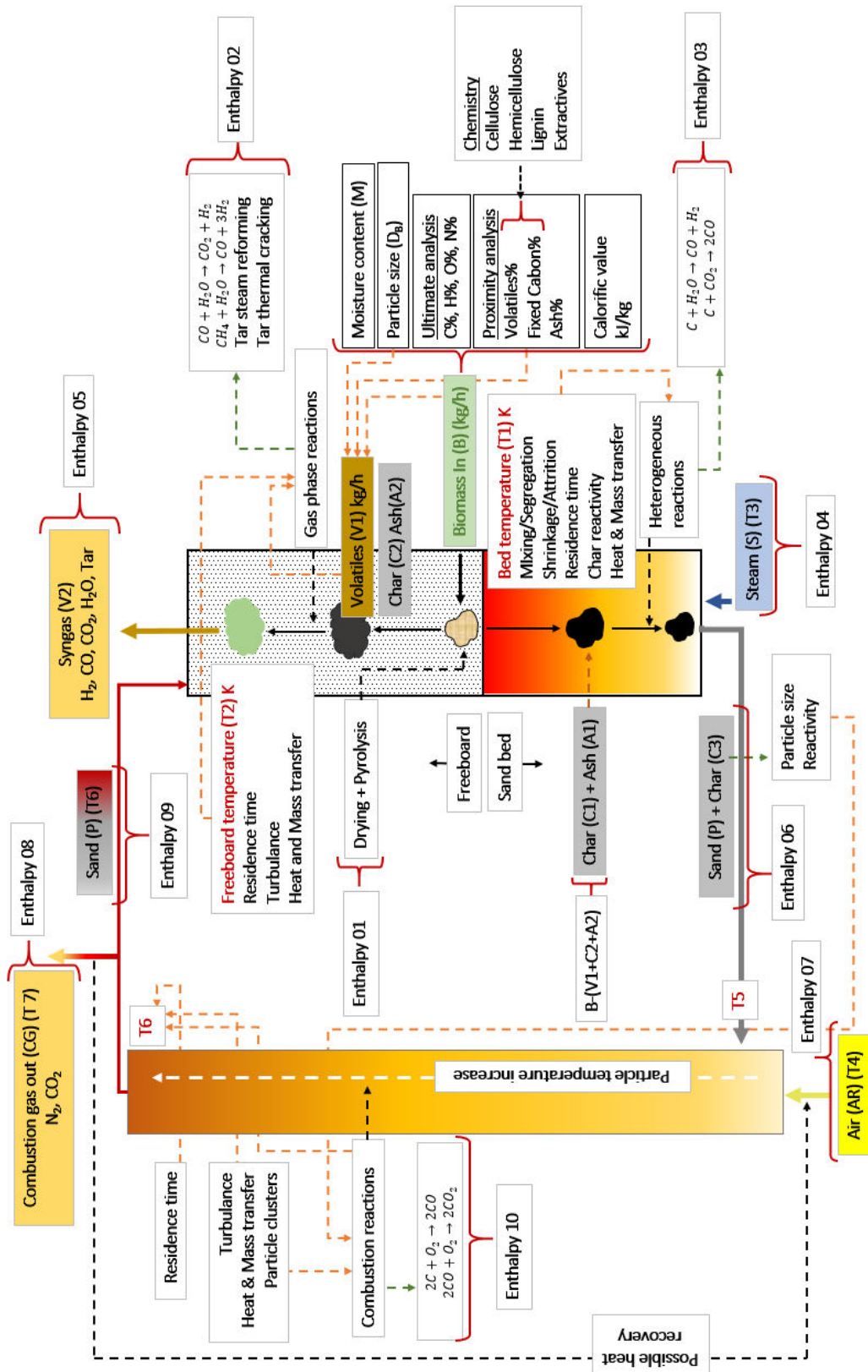


Figure 7: Designing concerns of dual reactor circulating fluidized bed gasification

Gas heating value for air-blown biomass gasification is approximately 4-7 MJ/Nm³, whereas 10-18 MJ/Nm³ for oxygen fed reactors and 14-18 MJ/Nm³ for steam gasification. H₂ and CO volumetric percentages of air-blown gasifier are 12-20% and 17-22%, whereas respective values for steam gasification are 38-56% and 17-32%. Steam-oxygen mixture maximize the CO production with 42-52% with 13-31% of H₂ [58-60].

Entrained flow reactors are operated at high temperatures above 1200°C, where the ash is collected as molten slag at the bottom of the reactor. Normally these are oxygen blown systems, which need small particle size in sub-millimeter range. Both oxygen and fuel particles are injected at the top and a co-current flow exists along the reactor. Due to the requirement of high reactor temperatures and narrow particle size, coal has been used in commercial scale reactors.

Fluidized bed gasification is the major concern in this study and therefore, authors exclude the detailed literature related to fixed bed and entrained flow gasification. A detailed literature review on bubbling fluidized bed gasification and gasification in general is included in Appendix (Paper I).

The utmost concern of the DCFB gasification is the enthalpy balance over the entire closed loop. That is the enthalpy generation by char combustion in the riser reactor and subsequent enthalpy gain by the particles should be sufficient to maintain the enthalpy demand in the steam gasification reactor (Figure 7). As illustrated in Figure 4, the pyrolysis and moisture evaporation are endothermic reactions. The pyrolysis temperature with particle size decides the fractional composition of char, tar and gases. Table 2 includes the major reactions involved in gasification process where there can be hundreds of minor reactions. The heterogeneous char reaction with CO₂ and H₂O are also endothermic, which decides the degree of char conversion before they migrate into the combustion reactor. The understanding of the particle hydrodynamics in bubbling bed and riser combustor is important during the designing stage. Particle for the bed material should be carefully selected to assist a healthy fluidization in the bubbling bed with avoided particle-biomass segregation. A sufficient velocity should be maintained along the riser combustor to induce turbulence, which promotes the char combustion and fluid-to-particle heat transfer. An adequate residence time in the riser guarantees a complete combustion of char and maximum heat transfer. The rate of particle circulation should, therefore, be optimized as both the enthalpy and temperature gain of particles in the riser is vital for the proper functionality of gasification reactor. A detailed literature review on CFB is included in Paper H attached in the annexure.

Table 2: Principle reactions considered during modeling [61, 62]

Enthalpy (kJ/mol)	Reaction	Name	Reaction No:
Homogeneous reactions			
-41	$CO + H_2O \rightarrow CO_2 + H_2$	Water-gas shift	1
-283	$CO + 0.5O_2 \rightarrow CO_2$	CO oxidation	2
-242	$H_2 + 0.5O_2 \rightarrow H_2O$	H ₂ combustion	3
	$CH_4 + 2O_2 \rightarrow CO_2 + 2H_2O$	Methane oxidation	4.1
	$CH_4 + 1.5O_2 \rightarrow CO + 2H_2O$	Methane oxidation	4.2
	$CH_4 + 0.5O_2 \rightarrow CO + 2H_2$	Methane oxidation	4.3
+206	$CH_4 + H_2O \rightarrow CO + 3H_2$	Methane reforming	5
Heterogeneous reaction			
-111	$C + 0.5O_2 \rightarrow CO$	Char Partial oxidation	6.1
-394	$C + O_2 \rightarrow CO_2$	Char combustion	6.2
	$2\left(\frac{\pi + 1}{\pi + 2}\right)C + O_2 \rightarrow \left(\frac{2\pi}{\pi + 2}\right)CO$ $+ \left(\frac{2\pi}{\pi + 2}\right)CO_2$	Char combustion	6.3
	$\pi = 3 \times 10^8 \exp(-30178/T_p)$	[63]	
	$\frac{[CO]}{[CO_2]} = 2400 \left(\exp - 51830/RT \right)$		
	$C_xH_yO_z + (x/2 - z/2)O_2 \rightarrow xCO + y/2H_2$	Char Partial oxidation	6.4
+172	$C + CO_2 \rightarrow 2CO$	Boudouard reaction	7
+131	$2C + H_2O \rightarrow CO + H_2$	Steam gasification	8.1
-75	$C + 2H_2 \rightarrow CH_4$	Methanation	9

2.4 Modeling of biomass gasification

Modeling of biomass gasification is a growing research interest as different modeling concepts are useful from preliminary studies to detailed optimization. Thermodynamic equilibrium models, kinetic models, computational fluid dynamic (CFD) models and artificial neural networks models are the bottom-line approaches found in literature [64]. The properties of biomass such as enthalpy of formation, heating value, proximate analysis and ultimate analysis is needed for any modeling effort. The knowledge pyrolysis composition of char, tar and gases, properties of pyrolysis products such as heating value, heat capacity, thermal conductivity etc., rate of pyrolysis, enthalpy of pyrolysis and chemical kinetic of involved homogeneous and heterogeneous reactions are important in different stages of modeling.

Thermodynamic equilibrium models are the simplest in construction. Stoichiometric and non-stoichiometric modeling are the two main wings of equilibrium modeling used by previous studies. In first approach, the involved compounds, stoichiometric reactions and the equilibrium constants should be defined. In contrast, non-stoichiometric method only needs the feed elemental composition, whereas the equilibrium conditions are predicted using "Gibb's free energy" [60, 65, 66]. The targeted gaseous compounds should be defined and according to J. Prins, et al. [67], the product composition can be accurately modeled considering CO, CO₂, CH₄, H₂, N₂ and H₂O. The assumption of infinite residence time allows the reactor to reach chemical equilibrium at particular operating conditions, whereas the model is free from reactor configuration. Consequently, the equilibrium modeling is a sensible choice to evaluate the maximum reactor performance as a function of the chemical composition of the feed and reactor process parameters. The assumptions of infinite residence time, perfect mixing and homogeneous conditions over the reactor are never achieved. The accuracy of predictions is strongly related to the reaction time scale over gas residence time. As an example, the equilibrium composition is reached faster at high temperatures, whereas at lower temperatures, it is far away from equilibrium [68, 69]. Several studies have suggested to incorporate non-equilibrium factors to the model to improve the predictions [70-72].

Kinetic modeling is the follow up improvement that considers the kinetic rate of the involved reactions. In contrast to the equilibrium modeling, kinetic models are competent in incorporating the residence time and the reactor dimensions. As the model depends on average heat and mass transfer coefficients with assuming of perfect mixing, the localize variations across the reactor are not captured. The kinetics are affected by the limiting process either of chemical kinetics, pore diffusion and external mass transfer, where the later one varies locally.

Artificial neural network (ANN) modeling is based on experimental investigations and relating input-output parameters. Even though the ANN models are, sometimes, good predictors, the model's reproducibility in different contexts are not guaranteed unless all the decisive input parameters are incorporated.

2.4.1 CFD modeling

In contrast to all mentioned modeling approaches, the CFD models try to reach the physical reality by solving mass, momentum, energy and species conservation equations over the entire domain.

Owing to the improvement of computer power and numerical algorithms, CFD predictions of multiphase particle flows are becoming more accurate [73]. Parallelization of processors and Graphical Processing Units (GPU) powered by

Compute United Device Architecture (CUDA) are recent advances in computer technology [74-76]. Particle interactions, momentum and mass transfer between particles and fluid followed by scale differences in time and space, make it more complex to describe the dense phase fluidized beds [77]. The spatial scale difference are present due to the particles in micro scale, local particle structures such as bubbles in meso scale and reactors in macro scale. Accurate modeling of these terms are necessary for the simulation stability and construction of well-posed governing equations [78]. Further, interfacial phenomena such as foaming in gas-liquid systems, particle agglomeration and breakup need added concerns during modeling [79]. The employed constitutive models, such as fluid drag, are empirical and suffers from lack of experimental validations in a wide range of particle and flow properties [80].

The modeling approach can be different based on particle loading as well. If the particle loading is extremely low, considering the influence from fluid flow over particles is sufficient and not vice versa. This is known as one-way coupling. The fluid equations are solved independent of the particles. As the particle concentration increases, the fluid phase starts to get affected by the particle phase demanding gas-to-particle and particle-to-gas two-way coupling. The two way coupling is a source of non-linear behavior in fluid momentum equation [81, 82]. Up to a certain limit, the volume of the particles can be neglected compared to the fluid volume and therefore, the fluid continuity equation can be constructed without considering the particle volume. Above a certain concentration, the particle-particle interactions add significant contribution to the overall flow dynamics and three-way coupling; fluid-to-particle, particle-to-fluid and between particles, is needed [83, 84]. Tsuji [83] has briefed the modeling of dense phase gas-particle flows.

In direct numerical simulations (DNS) and Lattice-Boltzmann method (LBM), the particle motion is tracked solving Newton's equation of motion. DNS fully resolves the fluid flow around individual particles, whereas LBM approximates the flow structure around individual particles. However, in the applied research grounds, discrete particle method (CFD-DPM) provides the highest possible resolution for dense particle systems like fluidized beds [85]. Unlike in DNS and LBM simulations, Navier Stokes equations with a suitable averaging mechanism are used to model the fluid phase, where the fluid properties are averaged in cell scale. Therefore, this approach is identified as Eulerian Lagrangian modeling. A constitutive equation for the fluid-drag is needed whereas the particle collisions are modelled with hard-sphere or soft-sphere approach. As 80% of the computational cost is consumed for detecting the particle contacts and integration, DPM is not efficient for dense phase large-scale reactors [77, 86, 87].

Alternatively, the dispersed models, known as Eulerian models, are more computationally economical. The most primary construction is the diffusion modeling that considers the all phases as a single mixture, which needs a single set of conservation equations. However, two-fluid Eulerian model (TFM) has been the pioneer modeling method used for decades. Disregarding the particle size distribution and differences in density and shape, all the particles are considered as a single phase, continuous and interpenetrating with the fluid phase [86]. Two sets of conservation equations are resolved for fluid and particle phase. The TFM is possible to extent to a multi-fluid model by introducing separate phases for different particle sizes, densities and shapes. Nevertheless, the discrete existence of the particles is lost and further, there can be possible uncaptured meso-scale structures such as bubbles and clusters if the grid is coarse. In the initial stage, the particle phase viscosity and stresses were approximated with empirical correlations. Development of the kinetic theory of granular flows (KTGF) provided a distinctive method to derived the particle phase properties in Eulerian format [85].

The grid resolution and the calculation time step should be decided based on the convergence criteria, resolution of the simulation results and the computational time. Consistent implementation of auxiliary sub-models for heat & mass transfer, reaction kinetics, turbulence, heat capacities etc. plus constitutive equations for the gas-particle and particle-particle interactions is vital for the prediction accuracy [73].

Parallel to the development of computer resources, enormous efforts were made to improve the construction of the modeling to reduce the computational cost of DPM and eliminate the disadvantage of lost information in continuum TFM. Dense discrete phase modeling (DDPM) and multiphase particle-in-cell (MP PIC) are such efforts found in the literature [85, 88]. In DDPM, the particle velocities and volume fractions are calculated in the Lagrangian frame, whereas the particle-particle interactions are calculated based on KTGF. In MP PIC modeling, particles with equal properties of size, velocity and species are grouped into parcels, which are tracked in the Lagrangian frame. Forces resulted from particle interactions are approximated using particle stress function [89].

2.4.2 The MP PIC method

The early evidences of particle-in-cell (PIC) method are found in the works of Harlow during 1960s. The main motivation was high-speed computations of fluid phase systems with minimized numerical diffusion (false diffusion) at the discontinuities related to Eulerian modeling. Further, PIC technique eliminates the instabilities related to Lagrangian modeling at large distortions [90, 91]. The fluid was represented by discrete mass points moving through an Eulerian grid with fixed

coordinates. It was possible to capture the subgrid resolutions not updated on the grid and the history of motion of each fluid species. Besides fluid dynamics, the PIC method was used to simulate ice dynamics, plasma physics application and large material deformation related to soil dynamics [89]. The PIC method was one development of the Eulerian and Lagrangian hybrid methods having the objective of eliminating the difficulties and inefficiencies of each method when applied individually [87, 92].

The methods was extended for multiphase systems by Andrews and O'Rourke [90] and was named as the multiphase particle-in-cell (MP PIC) methods. The fluid is considered as a continuum and modeled with Navier-Stokes equations. Particle distribution in terms of location, size and velocity is derived by solving Liouville equation for the particle distribution function (PDF). The particular equation is similar to the Boltzmann equation for gas dynamics, but with extended capability of capturing the properties as particle size and density distribution. The particles having the same size, density, velocity and location are grouped in to parcels, also known as computational particles or clouds. Similar to DEM simulations, the parcel motion through the Eulerian grid is modeled using the Lagrangian concept. The parcels should be smaller than the grid cells that allows a particular cell to accommodate multiple parcels. Particles per parcel remains constant over the entire simulation time where the value is decided by the solid volume fraction along with the specified number of parcels per cell. The total number of parcels is a function of number of parcels per cell and the number of cells encloses in the initial particle patching. The most attractive feature of the parcel representation is its ability to model commercial reactors with 10^{13} particles using 10^6 parcels [93].

The particle interactions are modeled with the continuum theory and the collision force is calculated by the isotropic solid stress function as a spatial gradient. The particle pressure reaches to infinity as the particle volume fraction reaches the maximum packing, closed pack volume fraction, that prevent the particle volume fraction surpass the maximum. Particle properties derived based on continuum approach are calculated in the advanced time step and mapped to individual particles at the current time using interpolation functions. In brief, the particle properties, which are efficiently calculated on the grid, are derived based on grid (continuum approach) and rest of the properties are calculated at the particle scale. The scalar properties such as pressure and continuity are calculated at the cell centers and the momentum transfer at the cell face using a staggered grid. Further, computational work is concentrated on the particle phase in regions where particles are sited. This boosts the computational efficiency without much increase in numerical error [94, 95].

The assumptions, model reduction terms and governing equations in the initial development of MP PIC method are given by Andrews, O'Rourke and Snider [87, 90]. Barracuda VR incorporated the MP PIC method into Computational Particle Fluid Dynamic (CPFD) commercial software package to simulate multiphase systems, especially for dense phase particle flows. There are number of research articles with the MP PIC method used as directly coded by a programming language or CFD software [93, 96-107]. However, the present thesis is focused on CPFD simulation works done in non-reactive and reactive systems.

2.4.3 The CPFD construction

Governing equations are extensively explained in the work of Andrews and O'Rourke [90], Snider [87] and Snider, et al. [108]. The gas phase mass and momentum conservation are modeled with continuity and time averaged Navier-Stokes equations:

$$\frac{\partial(\alpha_g \rho_g)}{\partial t} + \nabla \cdot (\alpha_g \rho_g u_g) = 0 \quad (\text{E1})$$

$$\frac{\partial(\alpha_g \rho_g u_g)}{\partial t} + \nabla \cdot (\alpha_g \rho_g u_g u_g) = -\nabla P - F + \nabla \cdot (\alpha_g \tau_g) + \alpha_g \rho_g g \quad (\text{E2})$$

where α_g , ρ_g and u_g are gas phase volume fraction, density and velocity respectively. F is the total momentum exchange with particle phase per volume, g is the gravitational acceleration, P is the pressure, and τ_g is the gas phase stress tensor. The stress tensor for the gas phase is given by,

$$\tau_g = \mu_g \left[(\nabla u_g + \nabla u_g^T) - \frac{2}{3} \nabla \cdot u_g I \right] \quad (\text{E3})$$

μ_g refers to the shear viscosity that is the sum of the laminar and turbulent components. The large eddy simulation is used for the large-scale turbulence modeling while the subgrid scale turbulence is captured with the Smagorinsky model:

$$\mu_{g,t} = C_s \rho_g \Delta^2 |\nabla u_g + \nabla u_g^T| \quad (\text{E4})$$

The default value for the model constant C_s is 0.01. Δ is the sub-grid length scale and calculated by:

$$\Delta = (\delta x \delta y \delta z)^{1/3} \quad (\text{E5})$$

The interface momentum transfer is calculated through the viscous drag force:

$$F = \iint f \left\{ m_p \left[D_p(u_g - u_p) - \frac{\nabla P}{\rho_p} \right] \right\} dm_p du_p \quad (\text{E6})$$

The subscript P refers to the particle phase properties where m and u symbolizes the mass and velocity respectively. D_p is the drag function. The particle phase dynamics are derived using the particle distribution function (PDF) calculated from the Liouville equation given as:

$$\frac{\partial f}{\partial t} + \nabla(fu_p) + \nabla u_p(fA_p) = 0 \quad (\text{E7})$$

where A_p , is the particle acceleration and is expressed by:

$$A_p = \frac{\partial(u_p)}{\partial t} = D_p(u_g - u_p) - \frac{\nabla P}{\rho_p} - \frac{\nabla \tau_p}{\rho_p \alpha_p} + g \quad (\text{E8})$$

α_p is the particle volume fraction and τ_p is particle stress function that used to formulate the interphase interactions of particles.

$$\alpha_p = \iint f \frac{m_p}{\rho_p} dm_p du_p \quad (\text{E9})$$

$$\tau_p = \frac{10P_s \alpha_p^\beta}{\max[(\alpha_{cp} - \alpha_p), \varepsilon(1 - \alpha_p)]} \quad (\text{E10})$$

P_s is a constant with the units of pressure, α_{cp} is the particle volume fraction at close packing, β is a constant between 2 and 5 and ε is a very small number in the order of 10^{-7} . Hence, the particle stress merely depend on the packing intensity and independent from the particle size, density, shape and velocity. Particle Reynolds number is given by:

$$Re = \frac{2\rho_f |v_f - v_p|}{\mu_f} \left(\frac{3V_p}{4\pi} \right)^{1/3} \quad (\text{E11})$$

The interpolation functions are explained in detail in the work of Snider [87] and Snider, et al. [109]. The development of the particle collision model for the MP PIC method is discussed in series of publications of O'Rourke and Snider [95, 110-112]. The Liouville equation; the particle distribution function, was firstly modified by adding the Bhatnagar, Gross and Krook (BGK) type equation to the right side of the equation. This represents the ratio of the difference between current distribution and equilibrium Boltzmann distribution to the particle collision time. There are two

collision time scales representing the particle velocity equilibrium and the equilibrium of the fluid film.

Maximum momentum redirection is the main adjustable parameter for particle-particle interactions, whereas the pressure constant of the particle stress function can also give a considerable impact [113]. A blended acceleration model is also included to cope with the particle segregation. Three parameters, normal-to-wall momentum retention, tangent-to-wall momentum retention and the diffuse bounce, govern the particle-wall interactions. As the particle mass is considered unchanged at the collision, these retention coefficients quantify the post-collision particle velocity. A normal-to-wall retention coefficient of 0.3 indicates that the normal component of particle velocity will be 30% of the value before collision. The diffuse bounce is an estimation for the deflection of the reflecting angle of particle after colliding with the wall (surface roughness effect). The momentum retention parameters are primarily decided by the hardness of the particles. The default or mostly used values in literature studies are given in Table 3.

Table 3: Particle modeling parameter

Maximum momentum redirection	40%
Pressure constant	1
Particle-wall normal momentum retention	0.3
Particle-wall tangential momentum retention	0.99
Diffuse bounce	0.1

The Gidaspow drag model, which is also identified as the Wen-Yu-Ergun drag model in CPFD, was used in many studies. The CPFD construction of the drag model, with transition formulation from Wen-Yu to Ergun, is as follows.

$$D_{Wen-Yu} = \frac{3}{8} C_d \frac{\rho_g}{\rho_p} \frac{|u_g - u_p|}{r_p} \alpha^{-2.65} \quad (E12)$$

$$C_d = \begin{cases} \frac{24}{Re} & (Re < 0.5) \\ \frac{24}{Re} (1 + 0.115Re^{0.687}) & (0.5 \leq Re \leq 1000) \\ 0.4 & (Re > 1000) \end{cases} \quad (E13)$$

$$D_{Ergun} = 0.5 \left(\frac{150\alpha_p}{\alpha_g Re} + 1.75 \right) \frac{\rho_g}{\rho_p} \frac{|u_g - u_p|}{r_p} \quad (E14)$$

$$D_{Wen-Yu-Ergun} = D_{Wen-Yu} (\alpha_p < 0.75\alpha_{cp})$$

$$D_{Wen-Yu-Ergun} = \left(\frac{\alpha_p - 0.85\alpha_{cp}}{0.85\alpha_{cp} - 0.75\alpha_{cp}} \right) (D_{Ergun} - D_{Wen-Yu}) + D_{Wen-Yu} \quad (E15)$$

$$(0.75\alpha_{cp} < \alpha_p < 0.85\alpha_{cp})$$

$$D_{Wen-Yu-Ergun} = D_{Ergun} \quad (\alpha_p > 0.85\alpha_{cp})$$

CPFD is included with inbuilt Courant-Friedrichs-Lewy (CFL), which frequently calculates the appropriate time step based on the mesh size and number of parcels. Therefore, the user is free to define a comparatively large time step at the beginning (which will be considered as the upper limit) that will be reduced to an optimum value as the simulation proceeds [114]. Higher parcel resolution in the system improves the accuracy of the results at the expense of CPU time. The user can adjust it by manipulating the resolution based on initial particle patching or at the particle feeding boundaries.

The species conservation equation for gas phase is as follows,

$$\frac{\partial(\alpha_g \rho_g Y_i)}{\partial t} + \nabla \cdot (\alpha_g \rho_g u_g Y_i) = \nabla \cdot (\alpha_g \rho_g D_t \nabla Y_i) + \delta \dot{m}_{i,chem} \quad (E16)$$

$$D_t = \frac{\mu}{\rho_g Sc}$$

Y_i is the mass fraction of gas species, D_t is the turbulent mass diffusivity and $\delta \dot{m}_{i,chem}$ is the chemical production rate of i^{th} species. Sc is the turbulent Schmidt number with a default value of 0.9.

The enthalpy equation for fluid phase is given by,

$$\frac{\partial(\alpha_g \rho_g H_g)}{\partial t} + \nabla \cdot (\alpha_g \rho_g u_g H_g) \quad (E17)$$

$$= \alpha_g \left(\frac{\partial p}{\partial t} + u_g \cdot \nabla p \right) + \Phi - \nabla \cdot \alpha_g \mathbf{q} + \dot{Q} + S_h + \dot{q}_D$$

H_g is the fluid enthalpy, Φ is the viscous energy dissipation and \dot{Q} is the energy source per volume, \mathbf{q} is fluid heat flux, S_h is the energy exchange from particle to fluid phase and \dot{q}_D is the diffusion enthalpy.

$$\mathbf{q} = -\lambda_g \nabla T_f \quad (E18)$$

$$S_h = \left\{ \iiint f m_p \left[D_p (u_p - u_g)^2 - C_v \frac{dT_p}{dt} \right] - \frac{dm_p}{dt} \left[h_p + \frac{1}{2} (u_p - u_g)^2 \right] \right\} dm_p du_p dT_p \quad (E19)$$

$$q_D = \sum_{i=1}^{N_s} \nabla \cdot H_{g,i} \alpha_g \rho_g D \nabla Y_i \quad (\text{E20})$$

The lump heat equation for the particle is given by,

$$C_v \frac{dT_p}{dt} = \frac{1}{m_p} \frac{\lambda_g Nu_{g,p}}{2r_p} A_p (T_g - T_p) \quad (\text{E21})$$

The mixture properties of heat capacity and enthalpy for fluid phase are calculated as the summation of individual values weighted on mass fraction. λ_g and $Nu_{g,p}$ are fluid thermal conductivity and Nusselt number for heat transfer from fluid to particle.

The fluid to wall heat transfer coefficient is given by,

$$h_{fw} = \left[(0.46 Re_L^{0.5} Pr^{0.33} + 3.66) \frac{k_f}{L} \right] + \left(1 - e^{-10(\alpha_p/\alpha_{cp})} \right) 0.525 Re_p^{0.75} \frac{k_f}{d_p} \quad (\text{E22})$$

The fluid-to-particle heat transfer coefficient is as follows,

$$h_{fp} = (0.37 Re_p^{0.6} Pr^{0.33} + 0.1) \frac{k_f}{d_p} \quad (\text{E23})$$

$$Re_L = \frac{\rho_f U_f L}{\mu_f} \quad Pr = \frac{\mu_f C_{p,f}}{k_f} \quad (\text{E24})$$

Where L is the cell length, k_f is the fluid phase thermal conductivity and d_p is the particle diameter. In CPFD, the particle are assumed isothermal, which means that there is not any temperature gradient in any direction. For this assumption, the internal heat conduction of the particles should be much faster compared to external heat transfer (i.e. Biot number $\ll 1$). This can be true for smaller particles such as sand and may not be true for larger particles with low conductivity such as biomass pellets or wood chips [57].

The gas phase reactions rates are modeled as volume average whereas heterogeneous reactions are possible to model as either volume average or discrete rates in particle scale. Chemical kinetic equation in Arrhenius type or polynomial type can be used. The provision for implementation of thermal devolatilization of particles is a special feature in CPFD where the devolatilization product composition, kinetics and formation enthalpy should be defined by the user. The CPFD material library is equipped with large number of components with physical, thermal and

chemical properties. User can define the temperature weighing for heterogeneous reactions accordingly. Whenever the reactions with large enthalpies are implemented such as combustion, user can damp the progress of the reaction at the beginning, which eliminates the simulation interruptions due to extremely high temperatures.

2.4.4 Previous CPFD studies

CPFD simulation have been widely used to analyze the bubbling fluidized bed reactors [114-123]. A two dimensional bubbling fluidized bed was analyzed by Liang, et al. [114] with CPFD simulation and compared against experimental data and TFM simulation results. The standard downward particle motion and high particle volume fractions at the walls were not captured. The absence of lateral bubble movement prevented the formation of large central bubbles. Therefore, the lateral bubble profile was flat. Stroh, et al. [116] compared Lagrangian DEM, TFM and CPFD simulation results. The CPFD method over predicted the drag force and the particles tended to stay in suspension rather than falling down after the bubble irruption. The authors suggested to improve the probability distribution function and the frictional forces in CPFD method. Fotovat, et al. [124] compared the CPFD results with experimental data acquired using fiber optic sensor in a biomass-sand bubbling bed. When the biomass loading was increased, more uniform small bubbles are prevailed across the cross section rather than center bubble rise in a pure sand bed [125]. The mesh size was selected as at least one biomass particle could retain in a cell.

Riser reactor is a part of the circulating fluidized bed configuration. The particle hydrodynamic is different from a bubbling reactor as the particles are in fast fluidization regime. The smaller the particle diameter, the more the probability of particle transport in clusters. Gidaspow drag model uses the cell average particle volume fraction whereas energy minimization multi-scale (EMMS) model incorporates the heterogeneous particle structures, such as particle clusters in riser reactors. The better performance of EMMS model over Gidaspow in modeling riser sections was shown by Chen, et al. [126]. The authors observed that axial and radial particle profiles in the riser from CPFD simulations were agreeable. CPFD models have been used to various analysis of risers including the effect of particle size distribution and the riser exit geometry for particle back mixing [127, 128], visualizing core annulus structure [129], effect of multiple gas injection in the riser for the cyclone efficiency [130] and others [131, 132]. According to the studies of Raheem, et al. [132], the inclusion of particle size distribution influenced more on the results when the Wen-Yu-Ergun drag model was used whereas the influence was negligible for EMMS.

Full loop CFB cold models with loopseal as the particle recycling mechanism have also been analyzed using CPFD. Wang, et al. [133] worked on optimizing the particle modeling parameters such as closed pack volume fraction based on the rate of particle circulation. The developed model was used by the authors to analyze the effects of aeration and particle inventory for the particle circulation in a follow up study [134]. A similar study was performed by Ma, et al. [135] and Jiang, et al. [136] could identify the inefficiencies of a six cyclone CFB with the CPFD simulations. Kraft, et al. [137] studied a dual reactor CFB to identify the best drag model between the EMMS, Ganser, Turton-Levenspiel and the Wen-Yu-Ergun. There are number of other research works devoted to CFB analysis using CPFD [94, 138-142]. The EMMS drag model performed well in pressure prediction in the riser section and however, it resulted in a significant reduction of particle circulation. The Gidaspow and Ganser drag models were better in predicting the particle circulation with slight over prediction of the fluid drag in the riser.

Although a large percentage of the CPFD studies was devoted to analysis of the particle hydrodynamics in cold multiphase flow models, a considerable number of simulation works related to biomass energy conversion systems such as gasification and pyrolysis [143-145], combustion [139, 146-149], co-firing of coal and biomass [150] and chemical looping combustion [151, 152] can also be found. The works of Snider and Banerjee [153] and Snider, et al. [108] can be considered as the first evidence of heterogeneous chemistry in CPFD modeling.

Kraft, et al. [57] simulated the dual fluidized bed gasification system in CHP plant at Güssing, Austria. Drying and devolatilization kinetics were included with homogeneous and heterogeneous gasification reactions. Chemical kinetic were modeled as volume averaged Arrhenius type equations. The gas composition was compatible with the plant data. Further, simulations could explain that the mixing of hot bed material inside the gasification reactor was not optimal. Klimanek and Bigda [154] focused on CO₂ enhanced gasification of coal in a CFB. The authors suggested that the over-predicted gas temperature at the outlet was due to the adiabatic walls used. The prediction of H₂ composition was higher in simulations compared to experiments whereas the CO content was lower. The oxygen-blown bubbling gasifier at ZECOMIX plant was studied by Di Nardo, et al. [155]. A kinetic model for a steam fed gasifier was developed by Thapa, et al. [156]. The product gas composition was compared with the data of CHP plant in Güssing, Austria. A bubbling fluidized bed gasifier with rice husk as the raw material and air/steam mixture as the gasification agent was studied by Loha, et al. [157]. The Simulations were carried out under different temperature with identical pyrolysis gas compositions for each temperature. The results for CO compositions were greatly identical with experimental whereas H₂ was over-predicted. Xie, et al. [158]

analyzed a riser gasification reactor using forestry residue as the biomass feedstock. The change of the gas compositions with equivalence ratio (ER) was in good agreement with the experimental data. However, the simulation could not capture the trends of carbon conversion as a function of temperature. Authors claimed that the incorrect ratio (0.5) for oxygen consumption between carbon and CO could be the possible reason for the deviation. Instead, it could be due to the migration of elutriated char particles at high ER, where the elutriation was not included in the model. Further, prediction of gas composition and carbon conversion efficiency were exactly similar to the experimental values at 900°C, and the deviation increased with decreasing temperatures. At lower temperatures, the inclusion of generation and conversion of tar in the model is important. The same authors published CPFD simulation results for a coal gasification in a similar reactor geometry [159]. Studies of Liu, et al. [160] is among the few studies of full loop dual circulating fluidized bed gasification in the CPFD platform. The pyrolysis gas composition was derived using elemental and proximity analysis of feedstock of almond pruning. The authors adjusted several kinetic rate equations to upgrade the simulation results to be compatible with the experimental data. Publication of Kong, et al. [161] was found to be the latest work on simulating DCFB gasification using CPFD code. Experimental data from a pilot scale reactor located in University of British Columbia was used in the model validation, whereas rice husk was used as the gasifier feed.

2.5 Conclusion-literature

CPFD is comparatively a newer software package, which is continuously being improved. According to the literature findings mentioned in section 2.4.4, users have observed deviations in simulation results in certain areas such as the absence of lateral bubble movement etc. Therefore, the validation of the models against experimental data is still an essential component, especially in multiphase flow simulations. Minimum fluidization velocity is one of the conclusive parameter in bubbling fluidized bed whereas rate of particle circulation is a crucial designing parameter of circulating fluidized beds. CPFD simulations is becoming an interesting tool in analyzing above mentioned parameters and to understand the particle hydrodynamics, which are difficult to capture with experiments.

Biomass gasification in fluidized beds have extensively being analyzed in the literature and however, the operational parameters and equivalent output parameters are not universal. Therefore, each experimental result adds a certain value to the data pool. Use of every possible feedstock in the close proximity is highly counting in improving the exergy of bio-energy systems. Therefore, analyzing the gasification performance of different biomass feedstock under different operational

conditions is important to strengthen its competitiveness. Number of research works are available in the literature related to CPFD simulation of biomass gasification. In first hand, very few studies have used different pyrolysis models at different gasification temperatures. On the other hand, many studies have only compared the gas composition where tar generation was neglected. However, evaluating the carbon conversion along with the gas composition is important to present the overall performance and to have a good comparison against experimental results.

3 Experimental and CFD Methods

Experimental research works have been the key in many technological out breaks and still it owns a major share on the research field. However in many areas, computer aided research activities are overtaking the identity of experimental grounds, especially when it is possible to define the system with fundamental physics. When it comes to physical phenomenon, such as reactive systems, particle or species diffusion, convective flows etc., Computational Fluid Dynamic (CFD) modeling and simulation is the best choice. The accuracy of simulation results is based on the modeling strategy and the simulation set up. The more the system can model with fundamental physics laws, the more the accuracy. As an example, it says “the accuracy of single phase fluid flow modeling is more precise than a modern sensor can capture”.

However, model simplifications such as empirical approximation are practiced to reduce the overloaded computational cost in complex systems such as multiphase flows. Constructing a common platform is hard for multiphase flows as the system behaviors can be extremely different from one to another, especially in gas-fluid flows. Therefore, still, the multiphase simulation results are validated against experimental studies. In contrast to the errors during model simplification, several other numerical errors are possible during simulation set up (i.e. related to computational grid size and time step). Truncation errors during flux approximation, numerical diffusion from cell averaging, and cumulative residual error from iterative calculations are some examples. Out of many possible sensitivity analyses, grid sensitivity analysis or grid convergence test is carried out for any CFD simulation setup. When it comes to gas-particle multiphase systems, the grid should be fine enough to capture the meso-scale structures and at the same time, a single cell should be large enough to accommodate several particles. The effect of particle modeling parameters such as fluid drag and collision models is also significant for the result. Further, implementation of identical boundary conditions can moreover be challenging, where all of these add a considerable uncertainty for the simulation results. Above all, the measurement uncertainty related to experimental works should also be incorporated during the comparison.

3.1 Experimental Studies

The experimental studies were carried out in three different experimental rigs including bubbling fluidized bed, circulating fluidized bed and air blown bubbling fluidized bed gasifier.

3.1.1 Minimum fluidization studies

Fluidization is achieved as a particle bed is subjected to an upward fluid flow. The static particle phase is loosened as the fluid drag force and buoyancy force together overcome the gravitational and other contact forces between particles. This critical point is well known as the minimum fluidization velocity (MFV). The fluid velocity is taken as the superficial velocity. The actual fluid velocity through the particle phase is calculated by,

$$V_{actual} = \frac{\text{superficial velocity}}{(1 - \text{particle volume fraction})}$$

In fluidized beds, the fluid flow needs to regulate accordingly with reaction requirements and at the same time, a healthy fluidization condition should be guaranteed. Therefore, the knowledge of minimum fluidization velocity of the phase is important. During the operation, there is a possibility of breakup or agglomeration of particles. The understanding of the minimum fluidization is, therefore, important as a function of particle size, density and temperature. This study focuses on calculating the change of MFV as a function of size. The test facility, as given in Figure 8, is located at the University of South-Eastern Norway (USN), Porsgrunn.

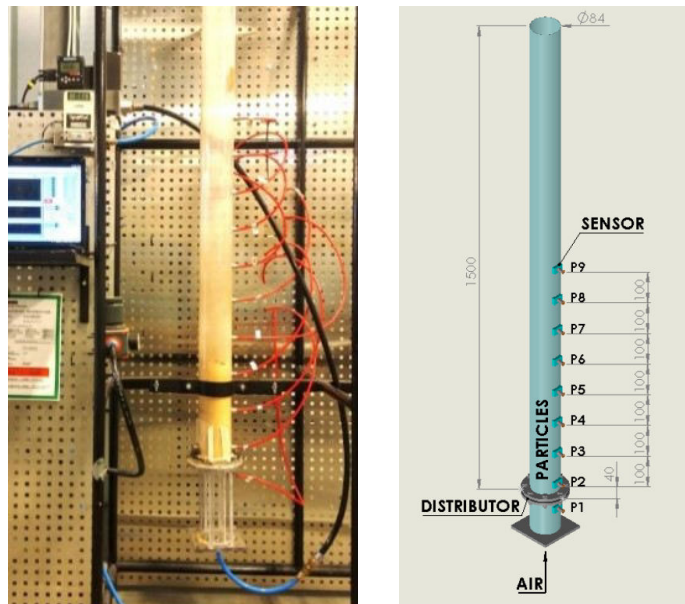


Figure 8: Experimental test rig for evaluate MFV with airflow controller and pressure transducers connected via LabVIEW program.

The reactor is made out of transparent acryl material with a gas distributor at the bottom, which holds the particle bed. The column is 84 mm in diameter and 1000mm in height. Pressure tapping points are placed at equal spacing of 100mm along the height where a separate pressure transducer is connected to each. The pressure signals are linked to a LabVIEW program via National Instruments data

acquisition device. With the program, signals are converted into pressure data using a calibration table, whereas the data logging can be activated at a frequency defined by the user.

Initially, the particles were filled to the reactor, at least up to two or three pressure connectors. Air was taken from a compressor and fed to the reactor with a flow controller in between. The air flowrate was increased stepwise starting from a low value until bed movement was observed and the pressure data was logged at each flowrate. Afterwards, the bed pressure gradient was plotted against the superficial velocity. As given in Figure 9, the MFV is taken as the velocity at sharp turn from the increasing trend to a flat profile. Sand was used as the particle phase. The particles were sieved to get a narrow size distribution (about 100 micron). Eight different particle sizes with narrow size distribution (about 100 micron difference between largest and smallest) was used.

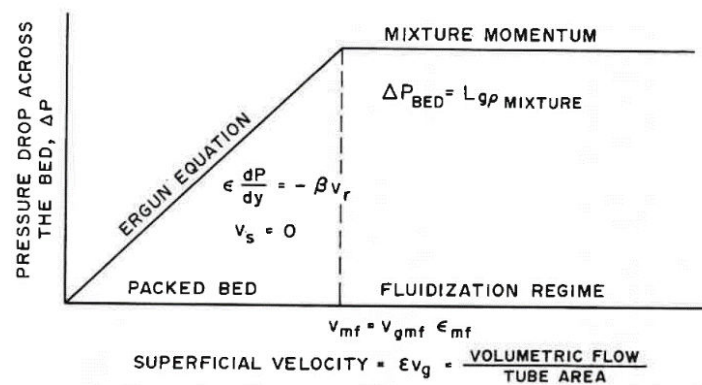


Figure 9: Calculating procedure of minimum fluidization velocity

3.1.2 Construction and experimental studies in circulating fluidized bed (CFB)

The gas-particle resident time, for some cases, is not sufficient in bubbling fluidized bed and therefore, CFB reactor are used instead. Further, as discussed in Chapter 02, dual reactor circulating fluidized bed gasification is an important designing to increase the syngas quality by eliminating nitrogen dilution. In such a system, the rate of circulation of the particle phase decides the thermal energy flow between the reactors. The CFB systems are reviewed in Paper F, where further information can be found. Aeration rates in each reactor, aeration in particle recycling device (i.e. loopseal) and particle properties (i.e. size and density) are the key parameters used in adjusting the rate of circulation. Therefore, in order to understand the particle behavior and as a source for CFD model validation, a CFB reactor was constructed at USN. As illustrated in Figure 10, the CFB unit is equipped with a riser reactor, cyclone separator and a loopseal as the particle recycling mechanism.

$$\text{Rate of circulation} = \frac{A_s \cdot h}{t} \times \text{bulk density} \quad \left(\frac{\text{kg}}{\text{s}}\right)$$

A_s is the cross sectional area of standpipe and h is the accumulated particle height during t seconds. The consistency of the results were verified using principle component analysis plots. Experimental results together with simulations are discussed in Paper I.

3.1.2 Experimental studies of air gasification in bubbling fluidized bed

The bubbling fluidized bed gasifier at USN, designed in collaboration with the University of Natural Resources and Applied Life Sciences in Vienna, Austria, was used for the experimental studies. As illustrated in Figure 11, the unit is consisting of a reactor, biomass feeding screw conveyors, biomass hopper, air preheater, electrical heating at reactor walls, temperature and pressure sensors, gas sampling port and a central PLC control unit. When the reactor configuration is finalized and constructed, the reactor temperature, equivalence ratio and type of biomass are the main adjustable parameters. These parameters were studied using wood pellets, grass pellets and wood chips. Detailed information about the experimental procedure is given in paper H.

Bubbling fluidized bed has the simplest geometrical shape with limited boundaries. Therefore, rather than performing CPFD model validation in a circulating fluidized bed, the convenient method is first to validate the gasification model using a bubbling fluidized bed. The particle hydrodynamics in a CFB can be validated in a non-reactive environment simultaneously. Once the rate of particle circulation is known, the two reactors in a dual circulating fluidized bed can be analyzed separately, which will reduce the computational time. Therefore, the experimental studies and CPFD model validation in air-fed bubbling fluidized bed gasification were necessary for successive simulations in optimization and steam gasification.

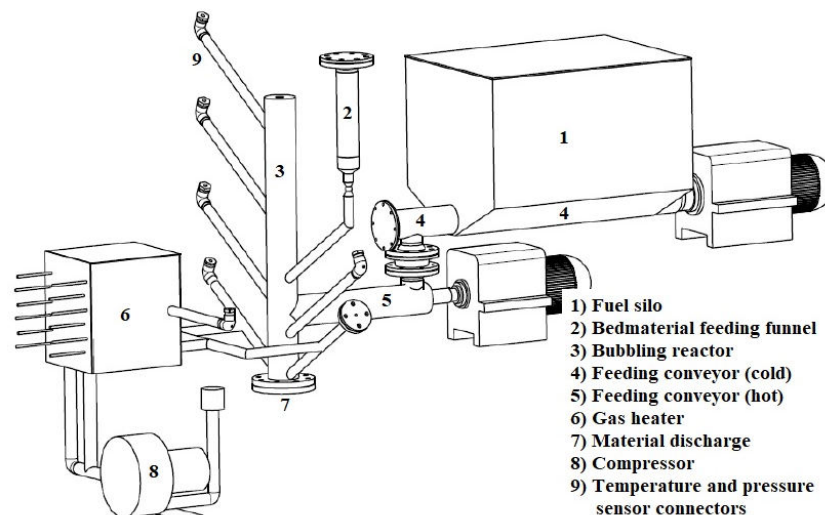


Figure 11: Bubbling fluidized bed gasifier and auxiliary equipment at USN

3.2 CFD simulation studies

Barracuda VR, version 17.3.0 was used with Intel(R) Xeon(R) CPU E (5) 1660 v4 @ 3.20 GHz processor for the simulation works. Simulations were performed for non-reactive bubbling and circulating fluidized bed. The air gasification experiments were used in comparison with CFPD results in biomass gasification.

3.2.1 Bubbling fluidized bed simulations

Initial CFPD studies were performed to calculate the minimum fluidization velocity for different particle sizes, densities and particle size distribution. A similar arrangement as in experimental studies was used. Figure 12 illustrated the computational domain with grid and pressure transient data points. Sand particles were used as the particle phase with air as the fluidizing agent. Further details are included in Paper A.

Simulations to study the effect of grid size and simulation time step on MFV, bed pressure drop and bubble behavior were carried out using the same geometry. The detailed simulations procedures can be found in Paper B. The Gidaspow or Wen-Yu-Ergun hybrid drag model was used in both of the studies.

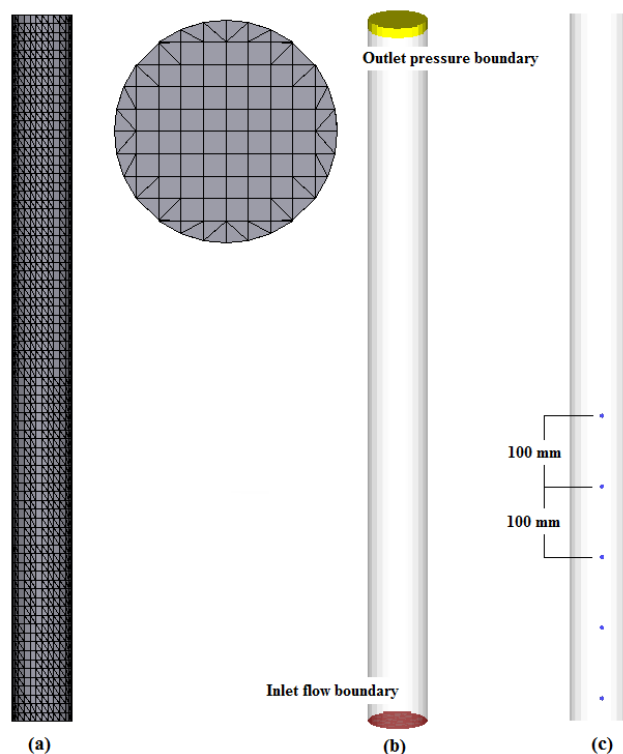


Figure 12: CFPD geometry for calculating MFV (a) grid, (b) boundary conditions and (c) transient data points for pressure.

3.2.2 Circulating fluidized bed analysis

The initial simulations of CFB were carried out using experimental works of Thapa [139]. The authors used a similar experimental rig as explained in the experimental method of CFB in section 3.1.2. The system pressure and rate of particle circulation were considered in the comparison of simulation results and experimental data. Initially, a grid convergence test was carried out. Afterwards, the sensitivity of particle modeling parameters of closed pack volume fraction, pressure constant in particle stress model, normal particle to wall and tangential particle to wall momentum retention coefficients and fluid drag models were analyzed. These parameters were optimized to obtain the experimental value of particle circulation. Detailed information are included in Paper C and the computational model is illustrated in Figure 13. The optimized modeling parameters were re-validated with experimental results from the CFB at USN.

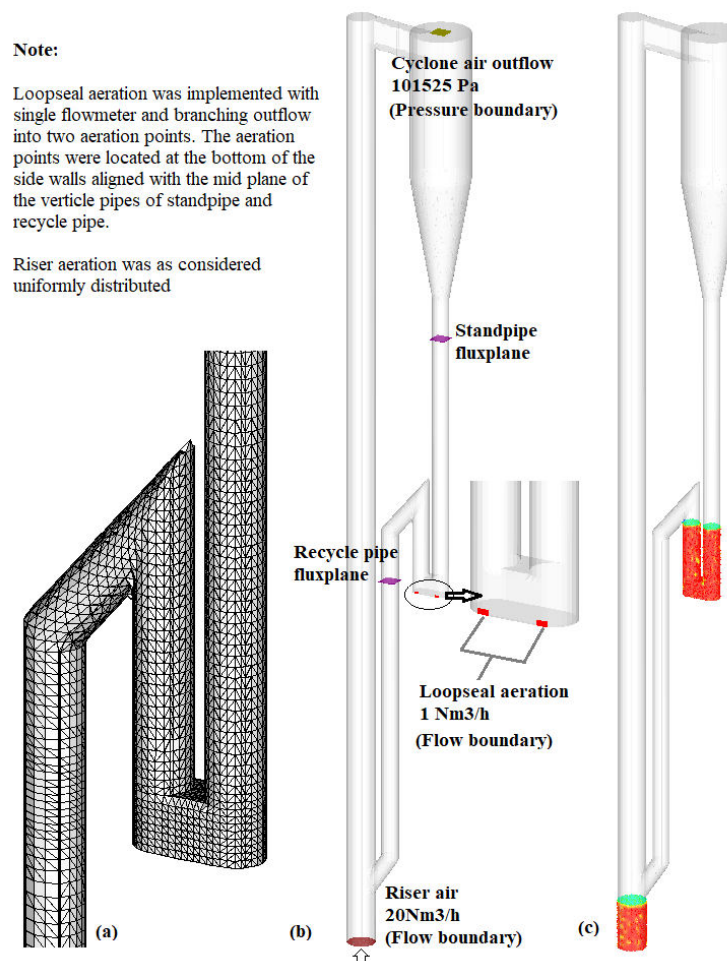


Figure 13: Computational grid, boundary conditions and initial particle filling of CFB simulation setup

The experimental rig was made out of narrow pipes, especially the loopseal section. Therefore, even slight variation in the pipe diameter cause a considerable variation in the system pressure and rate of particle circulation. Further, the particle size

distribution is measured using the sieve analysis method. Particles smaller than the minimum sieve size used can be present. Therefore, an uncertainty analysis based on the loopseal pipe diameter and particle size distribution was carried out for the same geometry as illustrated in Figure 13. Further details are included in Paper D.

Loopseal, or generally particle recycling mechanism, plays an important role as a gas seal between reactors and as a circulation rate control. Therefore, a detailed CPFD analysis was performed to analyze the effects of rate of aeration, aeration location/configuration and dimensions of the loop seal for rate of particle circulation. The inbuilt option of “boundary connection” tool was used to isolate the loopseal section from the complete CFB. Figure 14 depicts the computational domain used in the study where further details can be found in Paper E.

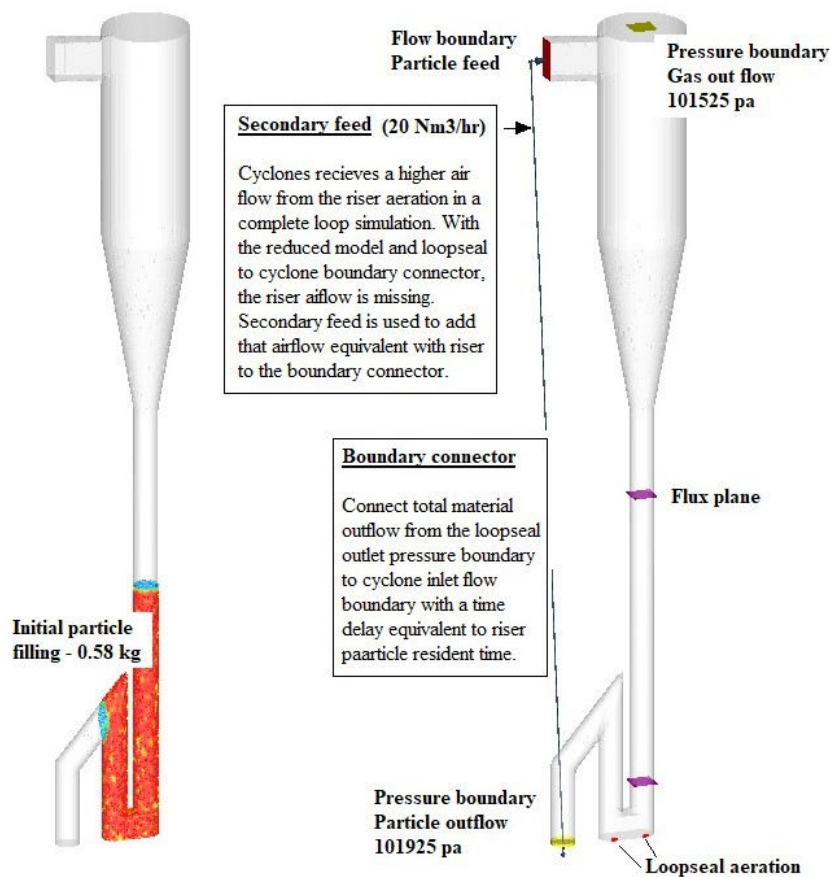


Figure 14: Computational domain use in loopseal analysis

3.2.3 Steam Gasification in bubbling fluidized bed

The steam gasification of biomass became more straight forward and practical with the appearance of the dual reactor CFB system. However, the simulation of a full loop system consumes an extended computational time. A DCFB gasification system has two major concerns. First to optimize the gasification reactor to achieve the required gas composition with a better efficiency. Secondly, to guarantee that the riser combustor could deliver the asked heat demand by the gasification reactor.

Therefore, two reactors were analyzed separately as illustrated in Figure 15. Paper F and Paper G contain the simulation results for a steam gasification reactor (as highlighted in Figure 15) in a simple cylindrical geometry. The simulation setup is given in Figure 16 in which the effects of temperature and steam-to-biomass ratio was analyzed.

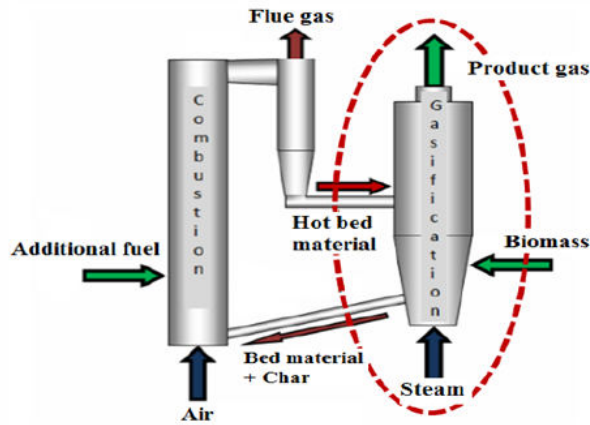


Figure 15: Dual reactor CFB gasification

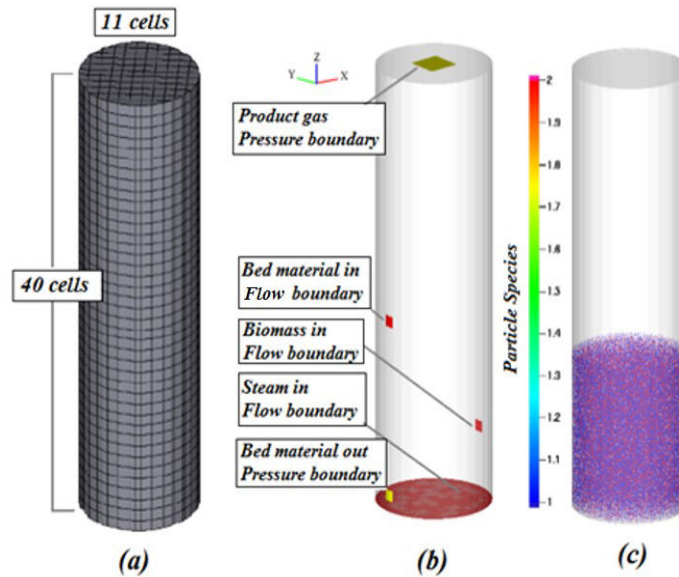


Figure 16: Computational domain and boundary conditions used in steam gasification in a bubbling fluidized bed

3.2.4 Air Gasification in Bubbling fluidized bed

In steam gasification simulations, random values were selected for the biomass size. In contrast, simulation of air gasification in bubbling fluidized bed was based on experimental studies explained in section 3.1.2. Fuel particles are larger compared to the bed material and according to the previous studies, a computational cell should be large enough to accommodate at least one biomass particle. As illustrated in Figure 17, because of the orthogonal gridding available in CPF, small triangular

sectioned cells are formed at the circumference for cylindrical reactors with small diameters. Therefore, in order to comply with the requirement, the cylindrical reactor was replaced with a square-sectioned reactor with twice the identical cross sectional area. Consequently, the air and fuel feed rates were doubled. Further, instead of single feeding location, two feeding boundaries are included at opposite surfaces in order to minimize the possible errors due to use of a large geometry. The final grid consisted with 2695 cells. The boundary conditions, initial particle patching, flux planes and transient data points are illustrated in Figure 18.

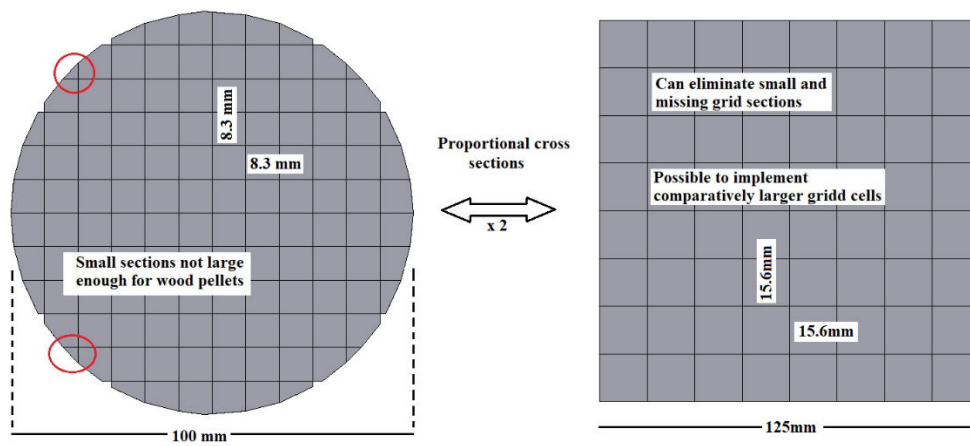


Figure 17: Replacement of circular section with square section

The biomass particles were considered as spherical and 5mm in diameter. The solid phase and volatile phase from pyrolysis were quantified as 20% and 80% where the moisture content was also included in the volatile phase. The enthalpy of devolatilization was taken as 150 kJ/kg with kinetic rate as follows.

$$\text{Rate of release} = 1.49 \times 10^5 \exp\left(\frac{1340}{T}\right) [\text{volatile}] \quad \text{kg/s}$$

The volatile phase included H₂O, H₂, CO₂, CO, CH₄ and benzene as the model tar species with mass fractions 0.095, 0.01, 0.275, 0.42, 0.08 and 0.12 respectively. Particle properties and modeling parameters are given in Table 4.

Thermal boundary condition with steady 700°C were applied to replicate the controlled wall temperature with electrical heaters. In the experiments, biomass injection started after heating the reactor up to 650-700°C temperature. Similarly, the initial fluid and particle temperature for the simulation were taken as 700°C. The transient data points along the reactor height measured the temperature and pressure, where the locations are exactly similar to the sensors during experiments. Transient point at the gas outflow boundary logged the gas mole fractions. Volume average chemistry was used to model both gas phase and gas-solid heterogeneous reactions. The kinetic rates used in the study is given in

Table 5, where a detailed literature study is included in Appendix A. Higher molecular hydrocarbons of ethane, propane etc. were discarded and tar was modeled by a single component taken as benzene.

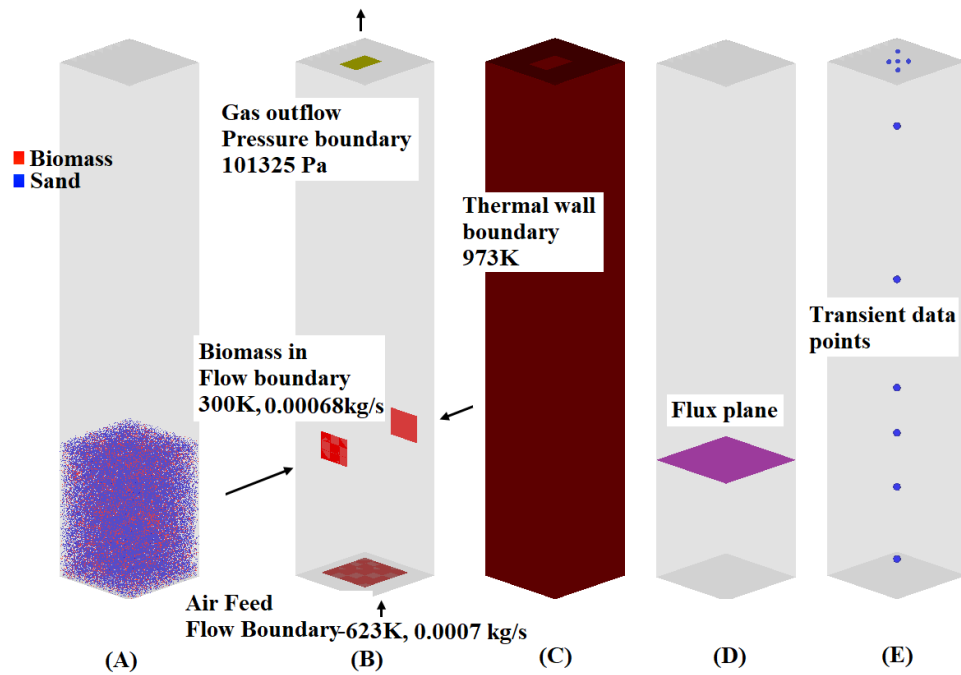


Figure 18: Simulation setup (A) initial particle filling (B, C) boundary conditions (D) flux plane (E) transient data points

Table 4: Particle properties and modeling parameters used in simulation

Particle properties	
Biomass size (spherical)	2mm
Biomass density (pellet)	1000 kg/m ³
Char density (after pyrolysis)	300 kg/m ³
Sand (mean diameter)	300 micron
Boundary flows	
Bottom air flow	5 kg/h
Biomass flow	4.8 kg/h
N ₂ flow with biomass	0.5 L/min
Modeling parameters	
Close pack volume fraction	0.6
Maximum momentum redirection	40%
Particle stress model	default
Normal-to-wall momentum retention	0.3
Tangent-to-wall momentum retention	0.9
Diffuse bounce	3
Blended acceleration model	activated
Drag model	Wen-Yu-Ergun

Table 5: Chemical kinetics

$CO + H_2O \rightarrow CO_2 + H_2$	$6.4 \times 10^9 T \exp\left(-3.926 \times 10^4/T\right)$
$CO + 0.5O_2 \rightarrow CO_2$	$4.78 \times 10^8 \exp\left(-6.69 \times 10^4/RT\right) [CO] [O_2]^{0.3} [H_2O]^{0.5}$
$H_2 + 0.5O_2 \rightarrow H_2O$	$2.2 \times 10^9 \exp\left(-1.09 \times 10^5/RT\right) [H_2] [O_2]$
$CH_4 + 1.5O_2 \rightarrow CO + 2H_2O$	$2.8 \times 10^9 \exp\left(-2.03 \times 10^5/RT\right) [CH_4]^{-0.3} [O_2]^{1.3}$
$CH_4 + 0.5O_2 \rightarrow CO + 2H_2$	$4.4 \times 10^{11} \exp\left(-1.26 \times 10^5/RT\right) [CH_4]^{0.5} [O_2]^{1.25}$
$CH_4 + H_2O \rightarrow CO + 3H_2$	$3.0 \times 10^8 \exp\left(15000/T\right) \left([CH_4] [H_2O] \right. \\ \left. - \frac{[CO][H_2]}{6.14 \times 10^{13} \exp(-28116/T)} \right)$
$C + \frac{1}{2}O_2 \rightarrow CO$	$1.47 \times 10^5 \exp\left(-1.13 \times 10^8/RT\right) [O_2]$
$2C + H_2O \rightarrow CO + H_2$	$1040. T. \exp(-11200/RT) [H_2O]$
$C + CO_2 \rightarrow 2CO$	$3.42 T \exp\left(-15600/T\right) [CO_2]$
$C_6H_6 + 5H_2O \rightarrow 5CO + 6H_2 + CH_4$	$4.4 \times 10^8 \exp\left(-2.2 \times 10^5/RT\right) [C_6H_6]$
$C_6H_6 + 3O_2 \rightarrow 6CO + 3H_2$	$1.58 \times 10^{15} \exp\left(-2.026 \times 10^5/RT\right) [C_6H_6] [O_2]$

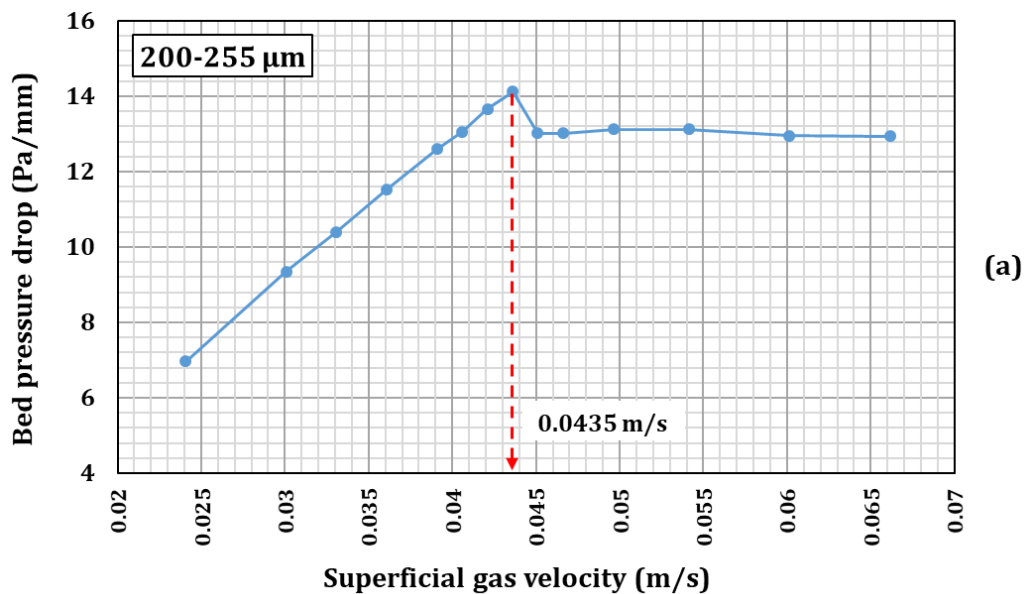
Barracuda settings take the walls as no-slip boundary for the gas phase. The simulation was set up using finite volume method, whereas the subgrid-scale turbulence is captured with large eddy simulation. Partial donor cell differencing scheme, which is a weighted average of central difference and upwind scheme, was selected for flux approximations at the cell face. The residuals for iterations were kept as default values in Barracuda.

4 Results

The thesis is presented as a collection of research publication and therefore, the results are summarized and discussed briefly in this section. The experimental works in bubbling fluidized bed, circulating fluidized bed and air-fed bubbling fluidized bed gasifier were followed by CPFD model comparison for arbitrary selected set of experiments from each. This section is lined up with presenting experimental work and its CPFD model validation. The results and discussion related to subsequent analysis using the validated models are referred to the papers.

4.1 Experimental analysis of minimum fluidization velocity

Fluidization is a temporary state of sufficiently fine solid particles in the presence of an upward fluid flow, which enables the particles to achieve fluid properties. The superficial fluid velocity at the turning point, which is identified as the minimum fluidization velocity (MFV), is therefore one of the fundamental analysis in any fluidized bed research. The sand particles with 2650 kg/m^3 density were sieved for 8 different narrow size ranges of $200\text{-}255 \mu\text{m}$, $255\text{-}300 \mu\text{m}$, $300\text{-}355 \mu\text{m}$, $355\text{-}425 \mu\text{m}$, $600\text{-}710 \mu\text{m}$, $710\text{-}850 \mu\text{m}$, $850\text{-}1000 \mu\text{m}$ and $1000\text{-}1180 \mu\text{m}$. An illustrative graph of calculating the MFV is given in Figure 19 whereas Figure 20 summarize the change of MFV as a function of particle size.



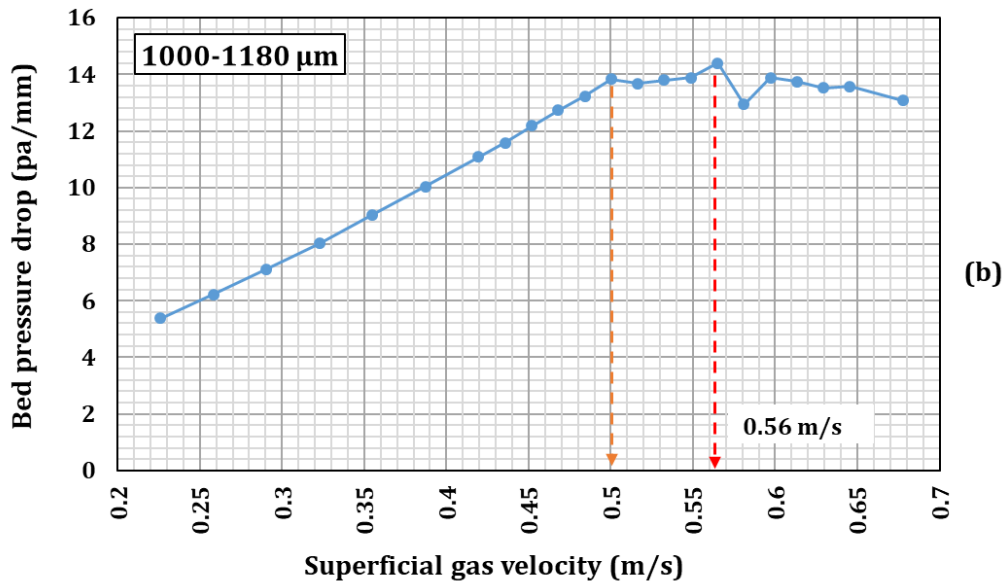


Figure 19: Pressure gradient vs superficial velocity plots for estimating the MFV for 200-255 μm (a) and 1000-1180 μm (b) sized particles

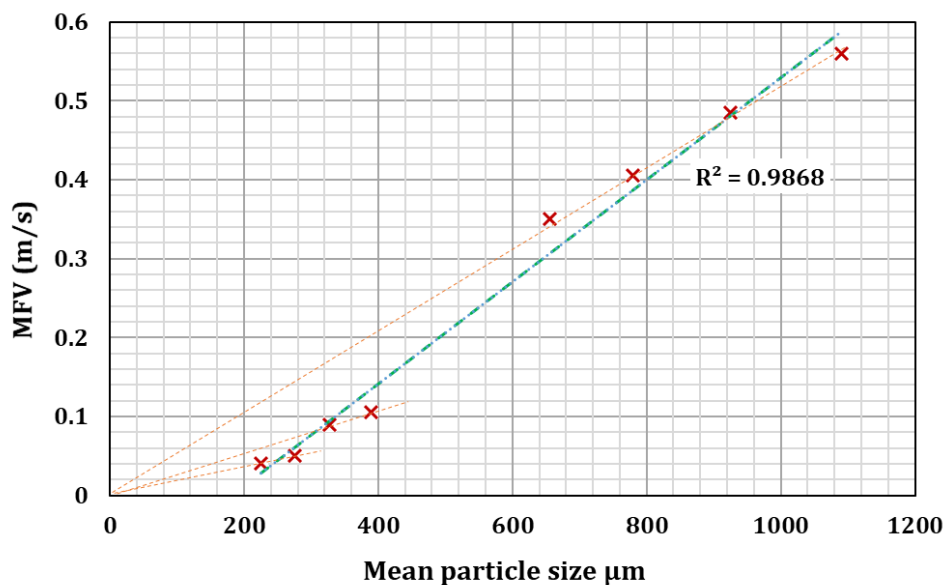


Figure 20: Change of minimum fluidization velocity as a function of particle size.

Each experiment was performed using 2100 ml of sand and the average weight was 2900g. The bed pressure drop gradient vs superficial air velocity plot for 200-255 μm shows the standard behavior for narrow cut particle size distributions. However, in the 1000-1180 μm curve, there are two possible points that can be taken as MFV (Figure 20). The fluidization is partly initiated at 0.5 m/s and however, the complete fluidization is achieved at 0.56 m/s. This type of behavior can be observed whenever the size distribution is wide. The bed pressure drop at fluidization conditions were approximately between 12.5-14.0 Pa/mm. The maximum observed pressure gradient immediately before minimum fluidization was approximately 14 Pa/mm for 200-255 μm , 255-300 μm , 300-355 μm , 600-710

μm and 1000-1180 μm sizes, whereas it reached above 15 Pa/mm for rest of the sizes. The dotted green line in Figure 20 is the linear approximation of the change of MFV against particle size. Theoretically, the particle size vs MFV curve should pass through the origin. Instead, as illustrated with red dotted lines in Figure 20, it was possible to assemble the particles into three different size groups where each group showed a linear behavior independently within the group. The 200-455 μm particles and the 655-1180 μm particles were from two different samples, however from the same geographical origin. The particle shape and the surface roughness can be different depending on the method that the particles are formed. The simple average was used for the particle mean size in the plot, where the size distribution can be skewed towards the lower or upper size. Further, the separating out of smaller size could be incomplete during the sieving. Finally, the MFV may be not exactly linear, especially due to the growing significance of contact forces towards reduced particle sizes. The data could not fit to a realistic higher order polynomial either. In addition, any uncertainty related to flowrate and pressure measurement could be responsible for either negative or positive variation of MFV estimation with experiments.

4.2 CPFD simulations for estimating MFV

There are number of correlations developed for the estimation of MFV where many of them demands the knowledge of bed voidage at the minimum fluidization. On the other hand, correlations are not competent enough in estimating MFV of particles with a wide size distribution. Therefore, it is important that the CPFD simulations can be used to predict the minimum fluidization velocity. As the Ergun correlation has been extensively used, the inbuilt Wen-Yu-Ergun drag model was used for the simulation. The construction of the blended model is given by Equation 12 to 15 in section 2.4.3. Experimental data of 200-250 μm particles was used to compare the simulation results. The bulk density of particles after 1 meter free fall was approximately 1450 kg/m³, which gives 0.55 of particle volume fraction. However, the CPFD counts on closed pack volume fraction parameter, which is the maximum allowable packing and 0.6 is the suggested default. Further, the laminar and turbulent coefficients of the Ergun equation is 150 and 1.75 in the original setting whereas it is 180 and 2 in CPFD default setup. Therefore, simulations were carried out for both combinations and the results are given in Figure 21 with experimental data.

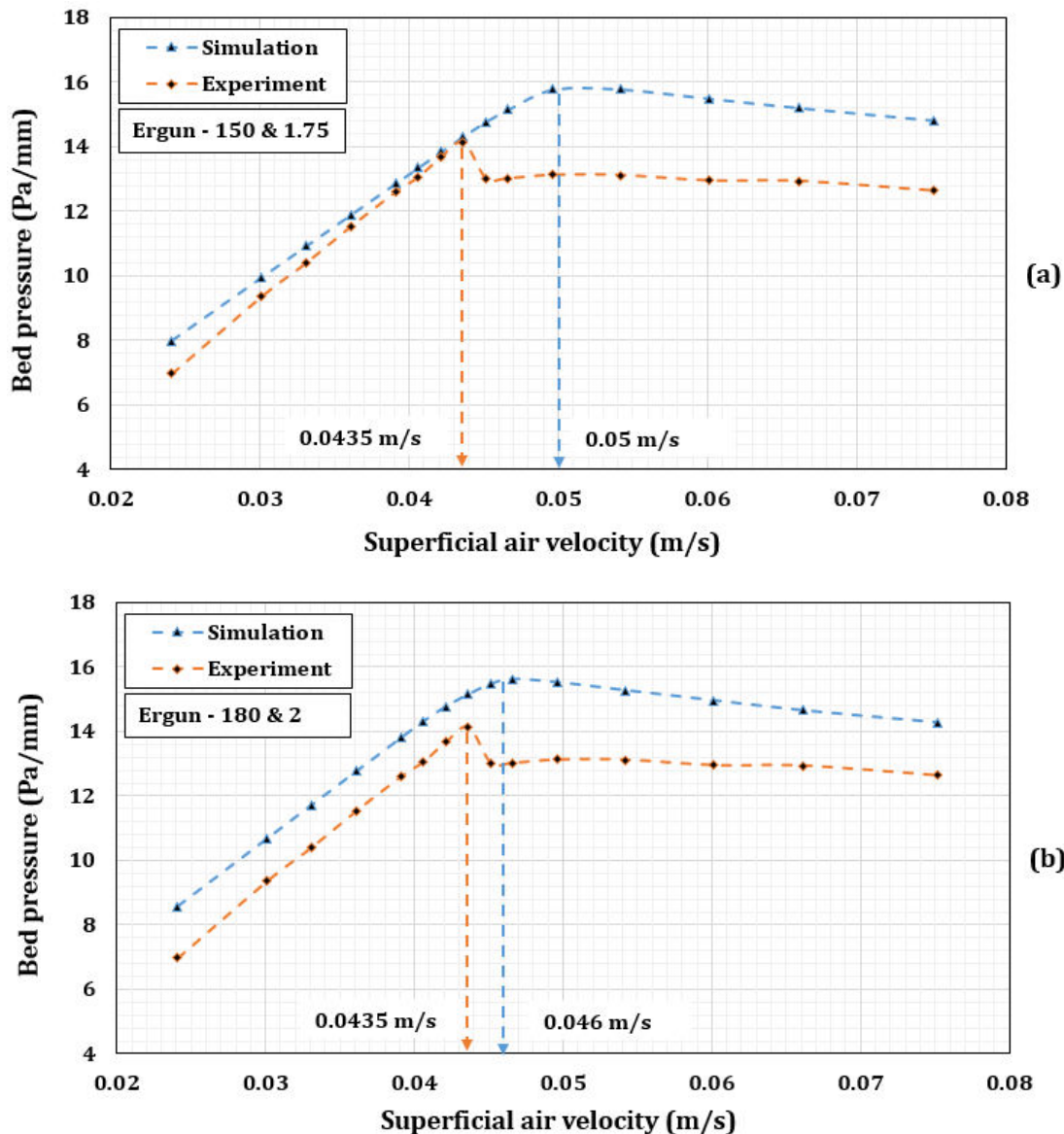


Figure 21: Comparison of experimental data and CPFD simulation results of MFV for different Ergun coefficients (200-250 μm)

According to the Figure 21 (a), the pressure drop prediction for packed bed conditions is precise with original Ergun coefficients of 150 and 1.75. However, the predicted MFV is higher than experiments having 13% error, which suggests that the calculated fluid drag is less than the actual. The particle sphericity is not included in the CPFD Wen-Yu-Ergun default setup and therefore, the particles were considered as spherical. As the Ergun coefficients were changed to 180 and 2, the prediction accuracy of MFV improved and the error is reduced down to 3.5%. The pressure drop during the packed bed conditions is, however, higher compared to experiments. Nevertheless, both cases show a similar pressure drop at the fluidization conditions. By looking into simulation plots, it can be observed that the curve moves horizontally as the Ergun coefficients are changed. Compared to the experiments, the bed pressure at fluidization conditions is higher for the

simulations. At the minimum fluidization, the simulation pressure prediction reaches 160 Pa/cm, which is 14% higher than in the experiments.

The close pack volume fraction (VF_{CP}) was constant at 0.6 for the two cases. However, in a number of simulations, it was observed that the gradient of the curve during packed bed conditions is greatly changed with the VF_{CP} . The lower the VF_{CP} , the lower the pressure gradient at packed bed conditions and the higher the estimated MFV. As the bed pressure drop at fluidized bed conditions is concerned, lower VF_{CP} reduced the error. The term close pack volume fraction is the measurement of maximum allowable packing. Therefore, the observed higher bed pressure at fluidization conditions, which is getting reduced at low VF_{CP} , suggests that the simulation does not capture the bed expansion at fluidization accurately. As the curves in Figure 21 are examined further towards the higher velocities, the pressure gradient curve from the simulation is trending downwards gradually, and it can be assumed that the simulation curve will meet the experimental value. The bubbles appear after the bed achieved maximum expansion. The first bubbles were observed visually approximately at 0.045 m/s air velocity during the experiments. If the assumed conditions of reduced expansion in the simulation is true, the bubbles should not appear until the pressure reaches the experimental value. The graphical files validated the assumption to a certain extent as no bubbling was observed even at the highest velocity of 0.066 m/s.

The MFV analysis for different sizes, densities and size distributions are presented and discussed in Paper A. As many studies represented the particles with weighted average mean size, different size distributions with same mean size of 600 μm was selected. The results are depicted in Figure 22. Even with the same mean size, a 0.125 m/s difference could be observed between maximum and minimum MFVs. The more the finer particles than the mean size, the lower the MFV is. As an example, the mixture of case B in Figure 22 contains 50% of each 800 μm and 400 μm particles. However, due to the presence of 400 μm particles, the resultant MFV is less than 600 μm mono dispersed particles.

Paper B tries to present the interconnections between grid size, time-step and the simulation time for the calculation of MFV. Further to the end of the paper, the importance of a substantially fine grid to capture the local particle structures as bubbles are discussed.

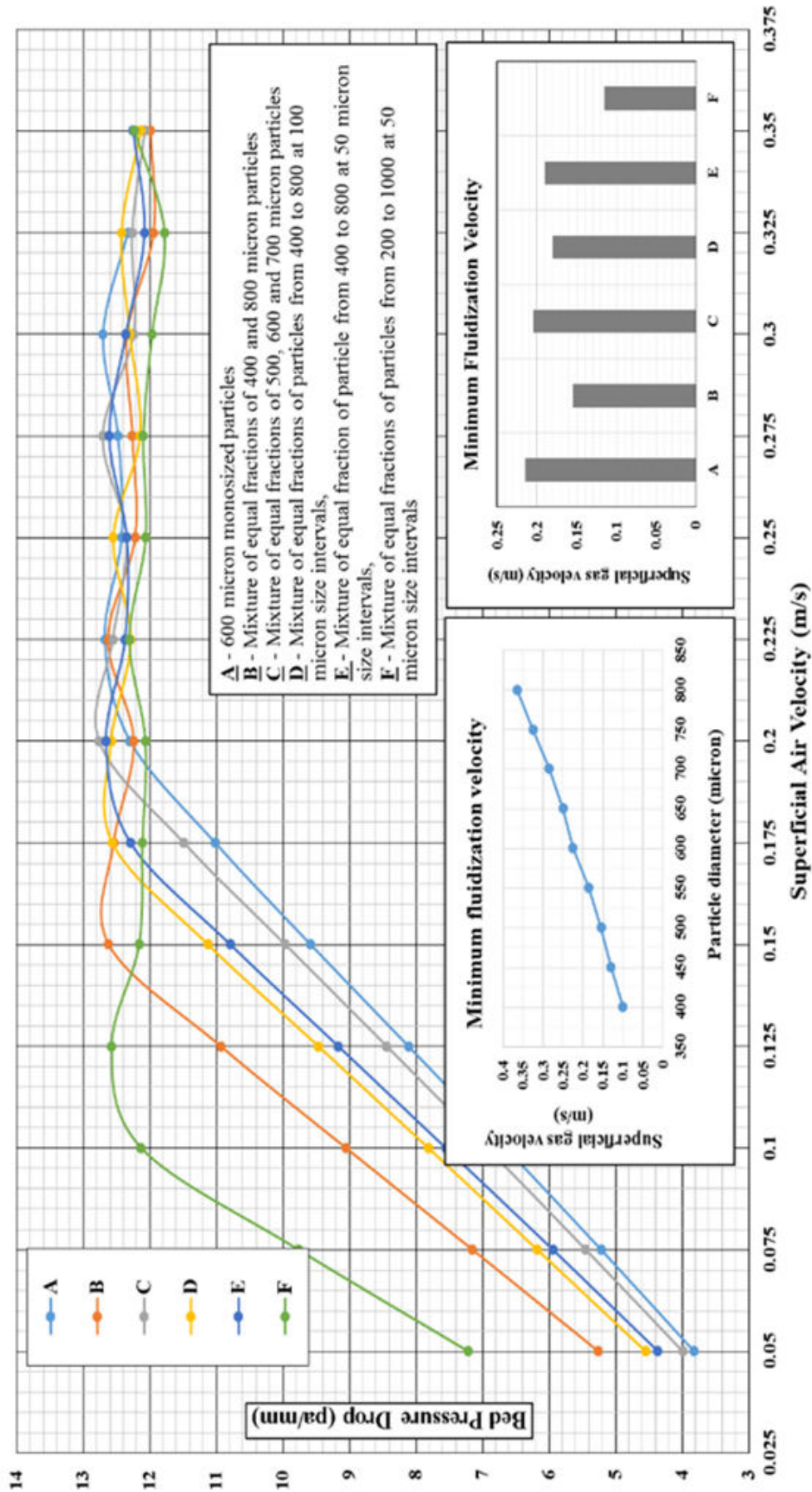


Figure 22: Sensitivity of MFV for different particle size distributions (Paper A)

4.3 Circulating Fluidized bed - Experiment

The sand particle sizes used in experiments were 850-1000 μm and 1000-1180 μm , where the bulk densities were 1377 kg/m^3 and 1390 kg/m^3 respectively. The material density was 2650 kg/m^3 . Due to the static charges, accurate measurement of the particle circulation rate for smaller sizes was not precise. Whenever the recycle pipe aeration is vigorous, the particle overflow was not smooth but happened in clusters. With reduced particle sizes, these clusters tended to rise unbroken in the riser section. The clusters redirected sharply at the riser exit and showed a stratified or dune flow in the horizontal section between the riser exit and the cyclone. As the particles continued to redirect to the dense particle phase at the pipe bottom, it continued to accumulate. The particle accumulation in this section was not countable and could lead to deviated particle holdup in the loopseal and the riser. As this was identified as an extra concern in the model validation, high velocities in the riser were used. The bend at the loopseal overflow showed a certain flow hindrance. As the bend was constructed with pipe segments, a short horizontal section is present at the overflow and as a result, particles tended to stack across it. Consequently, the cross section for the particle flow was reduced where this effect was observed considerable at low loopseal aerations rates. These behaviors are illustrated in Figure 23.

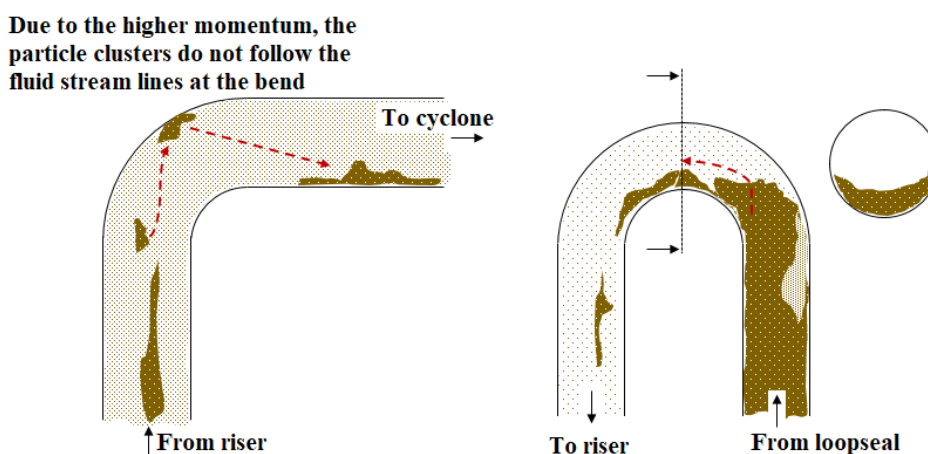


Figure 23: Particle accumulation at riser-to-cyclone connector and flow hindrance across loopseal overflow during experiments

The riser aeration was kept constant for each particle size and the loopseal aerations were varied to identify the contribution of each aerations of loopseal bottom and standpipe for the rate of particle circulation. The principle component analysis (PCA) plots illustrated in Figure 24 were developed using Unscrambler software package, which is useful in understanding the contribution of two loopseal aerations. First Plot in Figure 24 was helpful to demonstrate the data consistency. Both bottom aeration (FR2) and standpipe aeration (FR3) show a considerable

effect on particle circulation. According to the second plot, the effect of the FR3 is 60% while FR2 contributed by 40%.

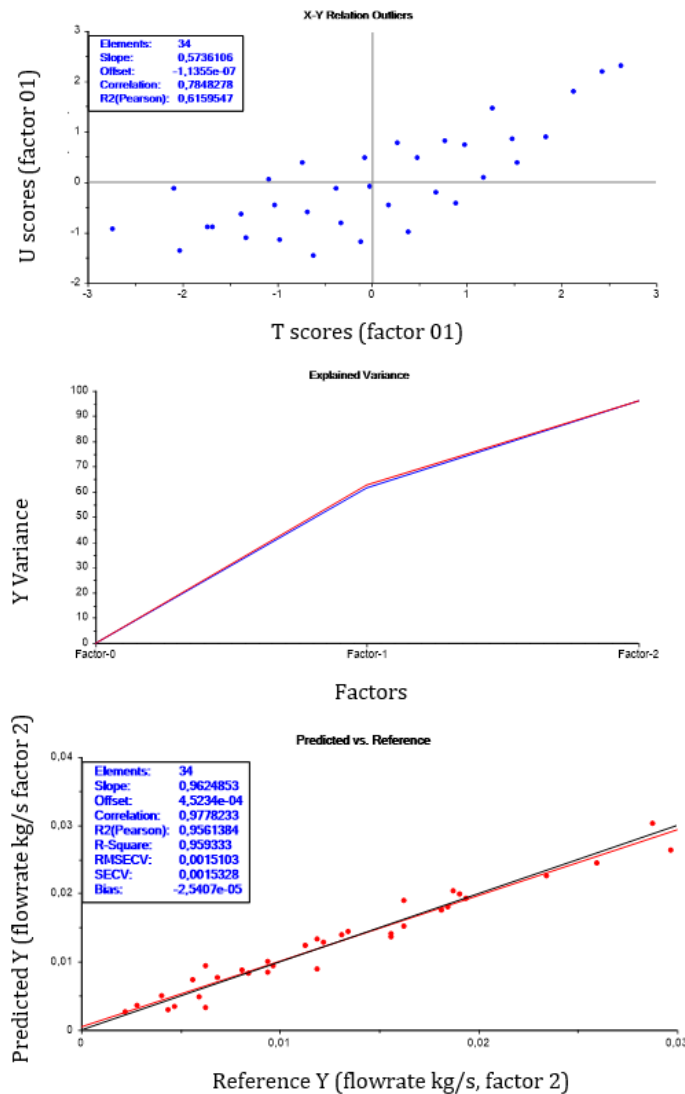


Figure 24: PCA plots for 850-1000 μm particle size (Factor-1 represent the FR3 and Factor-2 is for FR2)

The experimental data of rate of circulation and standpipe particle height for 1000-1180 μm particles are illustrated with different loopseal aerations in Figure 25. The rate of particle circulation was taken as the x-axis (which is actually the dependent variable) as it could be arranged in increasing order. If the x-axis was represented by one of the loopseal aeration, a wiggly plot was observed that was hardly readable. Even with the overall decreasing trend of the standpipe bed height over increased particle circulation, local variations can be seen. The variations are extreme at lower circulation rates and progressively diminished at high circulations. This can be due to non-smooth particle feeding from the loopseal and variations of the bubble existence in the standpipe (i.e. bubbles expand the bed). There can also be height measurement uncertainty due to fluctuating bed surface. Similar to particle

circulation, a PCA test was performed to relate the loopseal aeration with standpipe bed height as well. FR2 contributed nearly 75% in controlling the standpipe bed height.

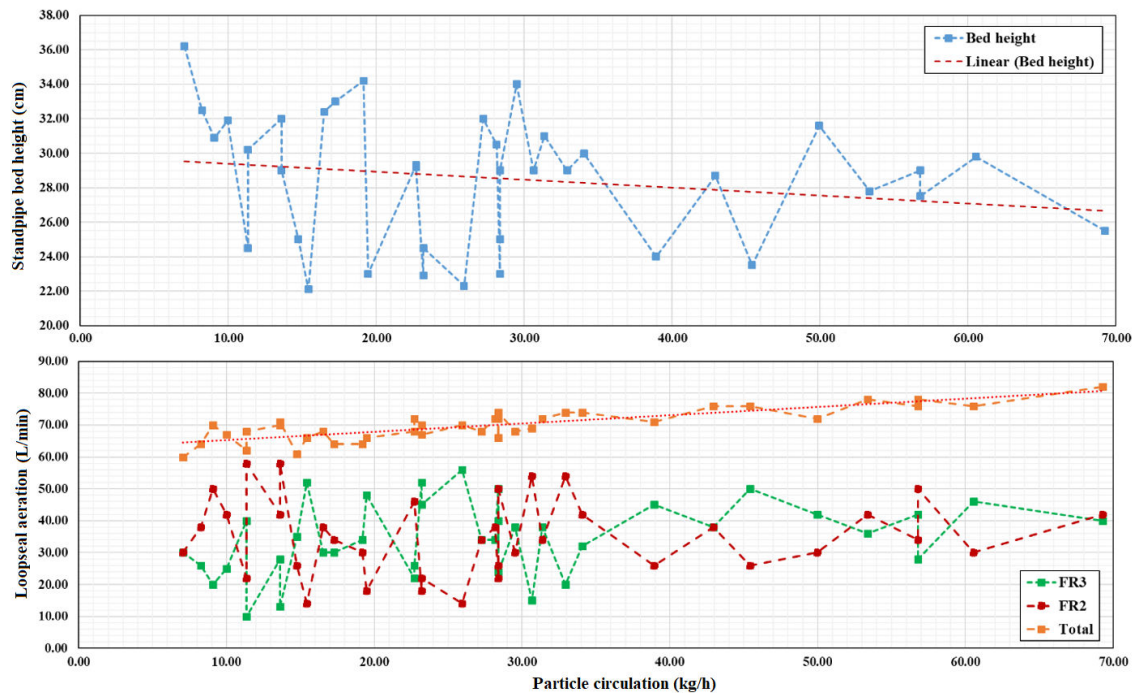


Figure 25: The relationships between particle circulation vs standpipe bed height, and particle circulation vs loopseal aeration for 1000-1180 μm particles

The cumulative (bottom and standpipe) loopseal aeration was changed between 60 L/min and 80 L/min during the experiments, an increase by 23%. Simultaneously, particle circulation improved from 7 kg/h to 69 kg/h, which is an 885% increment. The increment of particle circulation against aeration is low until the total aeration reaches 70 L/min. After 70 L/min, the circulation rate increases rapidly. The circulation can be improved further with loopseal aeration and however, it should be optimized together with the required particle loading in the riser. Moreover, at higher rates of loopseal aerations, the particle dynamics can be rigorous and consequently, there can be more tendency of particle overflow as clusters, rather than uniform overflow, from the loopseal.

A similar graphical representation for 850 μm -1000 μm sized particles is given in Figure 26, which has similar trends as for 1000 μm -1180 μm sized particles. The critical aeration rate is approximately 50 L/min, which is 70 L/min for 1000 μm -1180 μm particles. The rate of circulation could be increased above 100 kg/h with total loopseal aeration of 65 L/min, whereas the circulation was around 10 kg/h for 1000-1180 μm particles for the respective loopseal aeration. Therefore, it can be concluded that the rate of circulation can be improved vastly by slight change in the particle size.

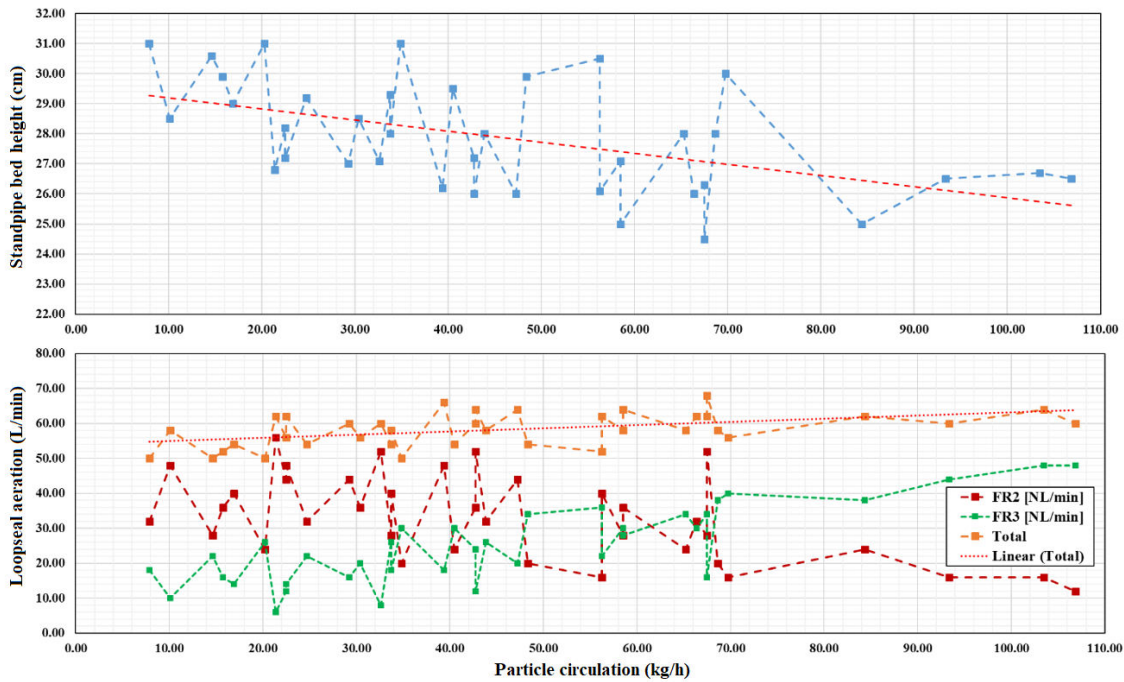


Figure 26: The relationships of particle circulation vs standpipe bed height and particle circulation vs loopseal aeration for 850-1000 μm particles

4.4 CPFD simulation of circulating fluidized bed

An extensive analysis of grid sensitivity and particle modeling parameters are presented in Paper C. The experimental studies of Thapa et al. was used for the model validation as illustrated in section 3.2.2.

The grid construction across the loopseal section showed a high impact for the rate of particle circulation. As the reactor dimensions were comparatively small, the grid refinement at the loopseal encounter restrictions, because the cell size should be several times of the particle diameter. The number computational particles defined by the default software setting was sufficient, where the circulation was not affected by further increase of computational particles. The pressure constant in the particle stress model (E10) showed the highest impact compared to other particle modeling parameters as closed pack volume fraction and particle-wall momentum retention coefficients. Figure 27 illustrates the sensitivity of the pressure constant (P_s) over the rate of particle circulation, whereas the rest of the analysis are included in Paper C. The same geometry was used to analyze the sensitivity of the loopseal pipe diameter and the particle size distribution, which are included in the Paper D.

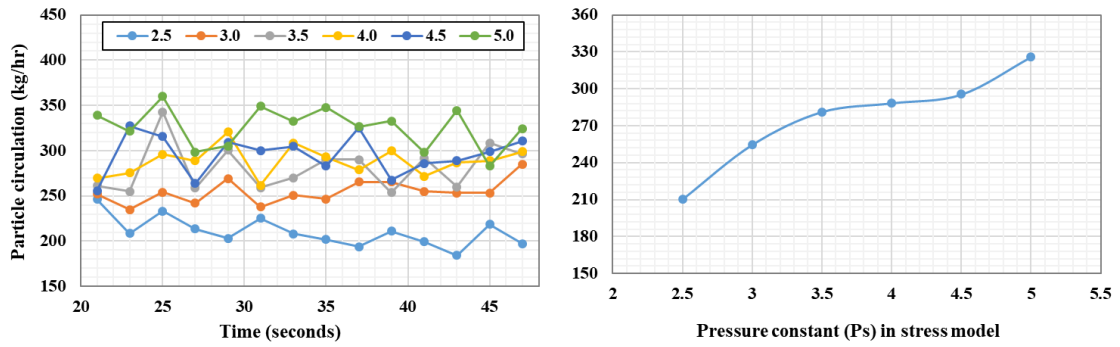


Figure 27: Effect of the pressure constant in particle stress model for the rate of particle circulation. Different colors represent different constants from 2.5 to 5.

The loopseal establishes a great flow restriction, which can be used as a controller for particle circulation. A detailed understanding of particle hydrodynamics across the loopseal is therefore vital in optimization. Paper E presents the CPFD studies of loopseal hydrodynamics and the effects of different aerations in rate and location. The rate of aeration could be optimized and the simulation results are illustrated in Figure 28. The particle height in the standpipe decreased gradually with increased aeration and the optimum rate was identified as 0.9 m³/h.

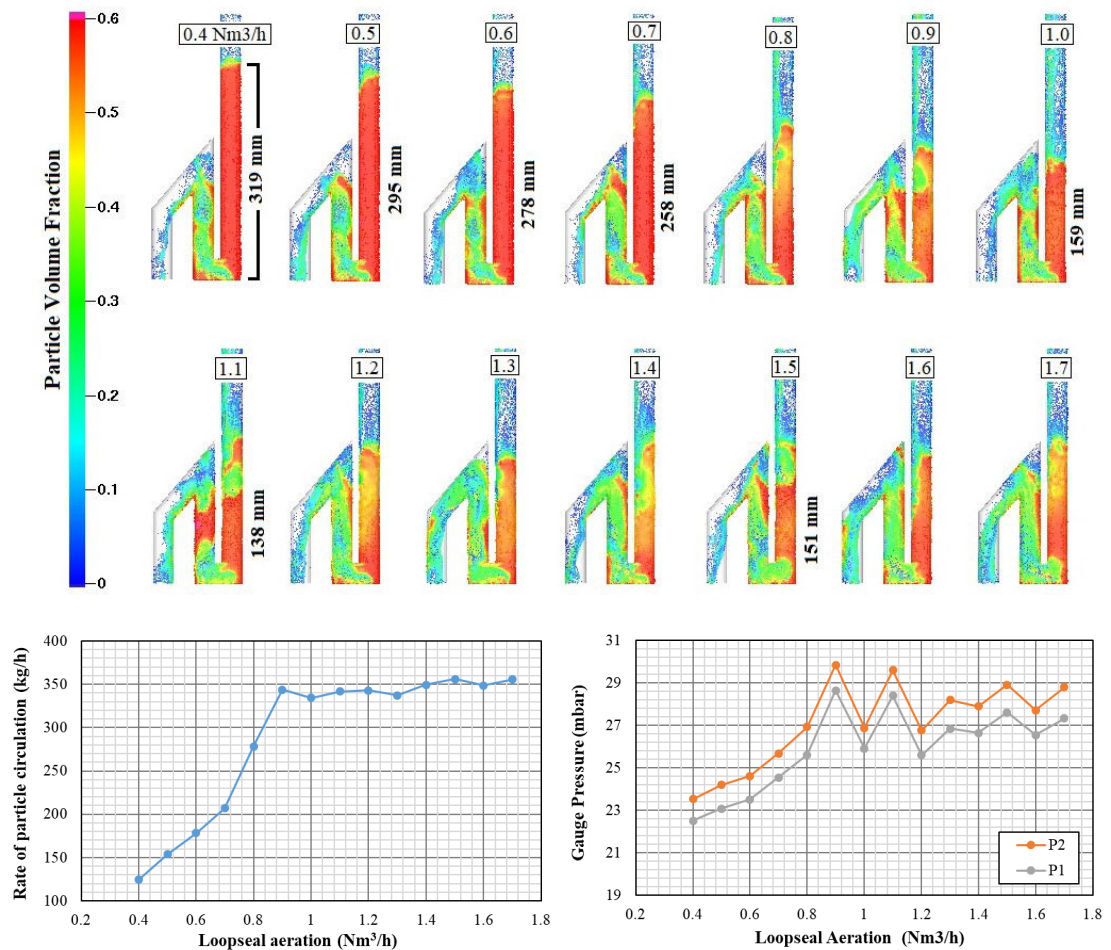


Figure 28: Effect of the loopseal aeration for the rate of particle circulation (P1 and P2 refer to loopseal recycle pipe and standpipe respectively)

Subsequently, the particle behavior in the riser was also analyzed. The riser and the cyclone are at dilute phase with particle volume fractions below 0.1. Therefore, a distinguished variance of particle volume fraction cannot be identified over the cross section of the riser other than few particle clusters at different elevations. The typical particle flow pattern in riser reactors is a core-annulus structure with high particle flow adjacent to the axis of the reactor column. Therefore, the particle speed and vertical velocity were also visualized using GMV graphical files, which is illustrated in Figure 29. More distributed particle speeds can be observed at low elevations of the riser. To the higher elevations, a particle layer of lower speed is formed gradually near the riser walls. This resembles with the core-annulus flow and a complete low speed particle layer could have been formed if the flow had an extra height along the riser reactor. Further, the illustration of the Z-velocity clearly shows the negative velocity near the walls.

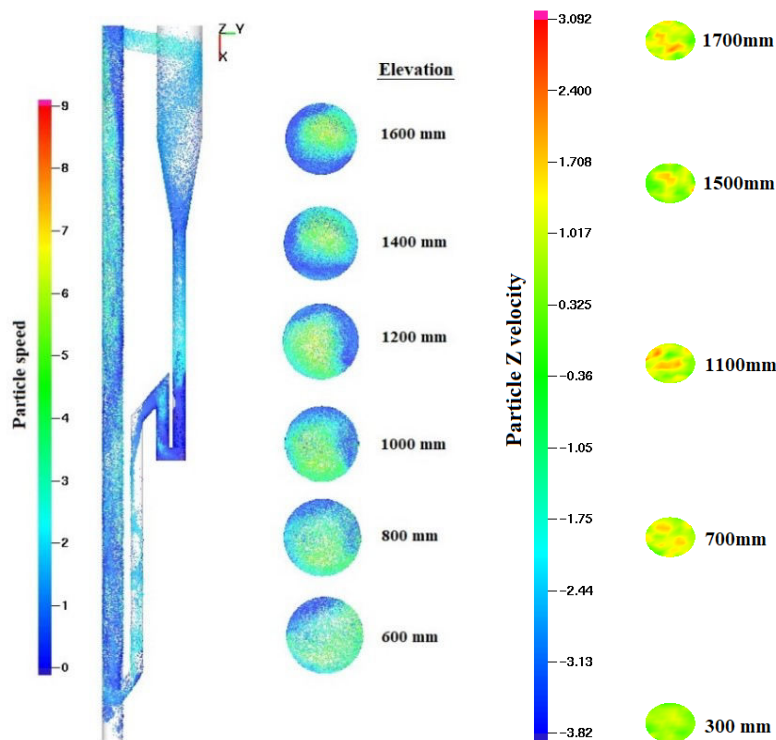


Figure 29: Particle speed over the CFB and sectional views at different heights in the riser (left) and particle vertical velocity (right)

A separate simulation was carried out to identify the particle residence time at each section of cyclone, loopseal and riser. The same geometry, flowrates (riser-20 m³/h and loopseal-1 m³/h) and sand particles (mean diameter 150 micron) were used. As illustrated in Figure 30, a particle injection boundary was used at the entrance of the cyclone and its flow was monitored using different flux planes placed at the riser top and bottom, the cyclone dip and loopseal out.

The residence time in loopseal and riser were calculated as the time difference for the same cumulative particle flow between the respective flux planes. As marked in Figure 30, the residence time in the loopseal is the highest, approximately 4.5 seconds. Due to the high velocities associated in the riser, the residence time is merely 1.0 to 1.5 seconds. The lowest residence time, nearly 0.5 seconds, was observed in the cyclone and between the recycle overflow to the riser bottom. After achieving steady state, the curves are parallel to each other and therefore it can be concluded that there is not any tracer particle accumulation in a particular section. The total resident time is slightly above 6 seconds.

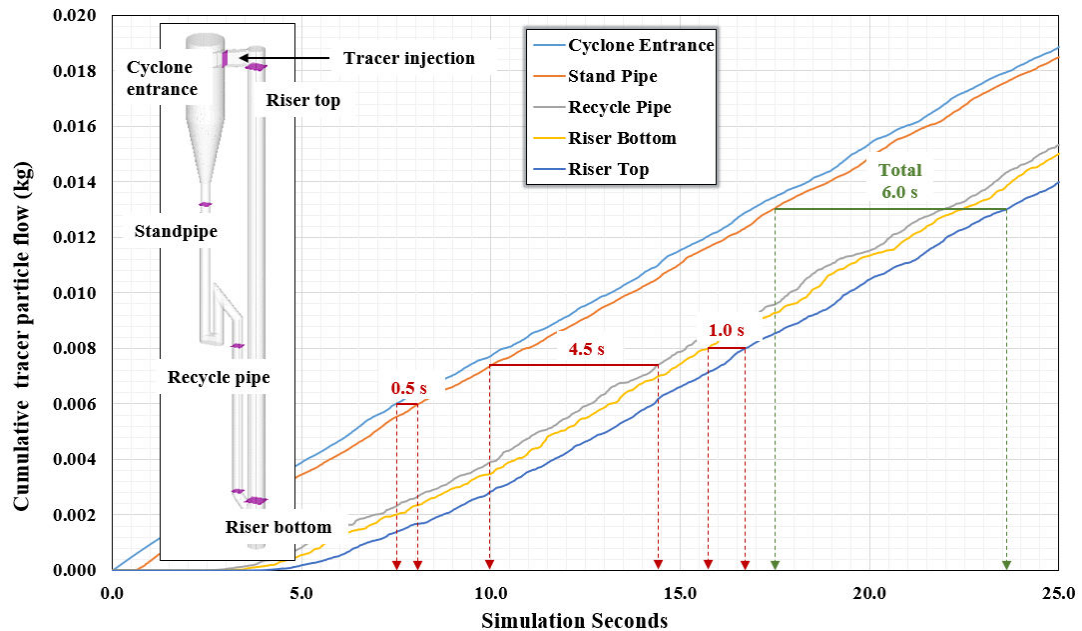


Figure 30: Flux planes used for the calculation of residence time and cumulative flow across flux planes.

4.4.1 Revalidation of the CFPD particle-modeling parameters

As mentioned in section 4.4, the optimization of particle modeling parameters was performed using the experimental work of Thapa et al. In order to increase the reproducibility of the model, subsequent simulations were performed for the CFB geometry at USN explained in section 4.3 and the results were compared with the experimental data. The geometry, boundary conditions and the particle hydrodynamics are depicted in Figure 31.

The pressure constant, normal and tangential particle-wall moment retention coefficients and the drag model were 5, 0.85, 0.85 and Wen-Yu-Ergun respectively. The loopseal bottom aeration was implemented with injection boundary conditions. The porosity of the distributor plate at the loopseal bottom aeration (35%-40%) was considered in calculating the injection velocity. The loopseal bottom and standpipe aerations were $1.3 \text{ m}^3/\text{h}$, $0.016 \text{ m}^3/\text{h}$ and $0.044 \text{ m}^3/\text{h}$ respectively.

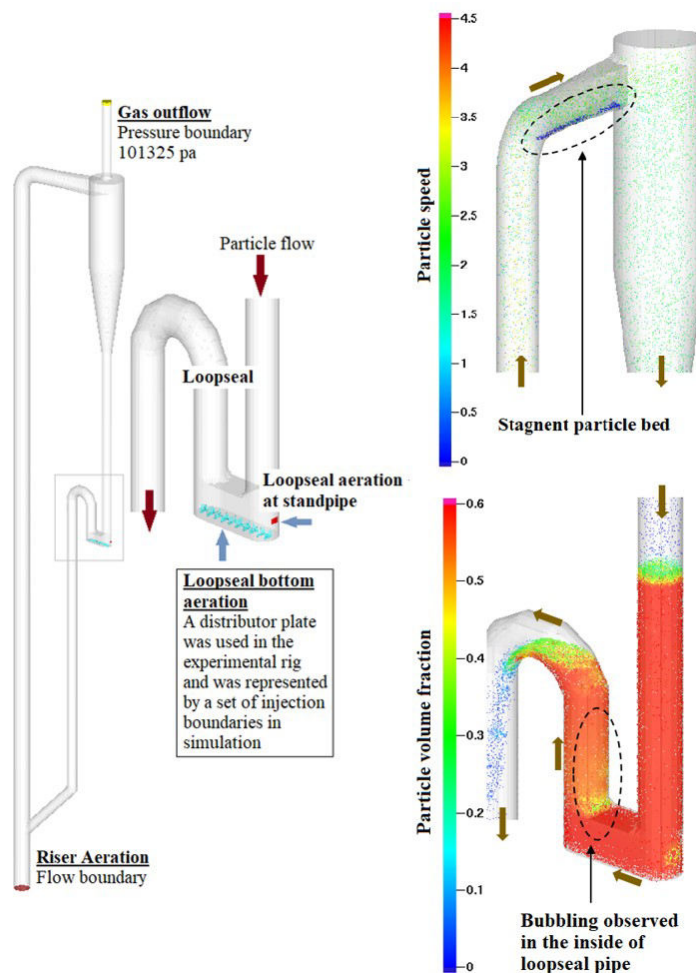


Figure 31: CFB model re-validation. Boundary conditions and particle hydrodynamics

As per the visual observations during experiments, the bubbles emerged and moved up close to the inner side of the recycle pipe. As in Figure 31, this could clearly be observed in the simulation. Further, the stagnant particles along the riser-cyclone connection could also be observed in the simulations. Particle clusters were hardly observed in the riser, especially due to large particle size. The observed rate of particle circulation was 90.1 kg/h, which is merely a 3% deviation from the experimental results.

4.4.2 Effect of the particle inventory for particle circulation

A comprehensive literature review on circulating fluidized beds and loopseals is included in Paper E. Particle inventory is one of the parameters that governs the rate of circulation. The CFB geometry used for initial model validation (Figure 13) was used in CPFD analysis to identify the effect of particle inventory.

The loopseal is designed on pressure balance over the rest of the system and as the particle inventory effects on the systems pressure, the rate of particle circulation

can be varied accordingly. The riser aeration was $20 \text{ m}^3/\text{h}$ where the loopseal aeration was $1.0 \text{ m}^3/\text{h}$, which was kept constant over the entire analysis. Figure 32 carries the rate of particle circulation and standpipe particle height for different particle mass, where Figure 33 graphically illustrates the particle behaviour.

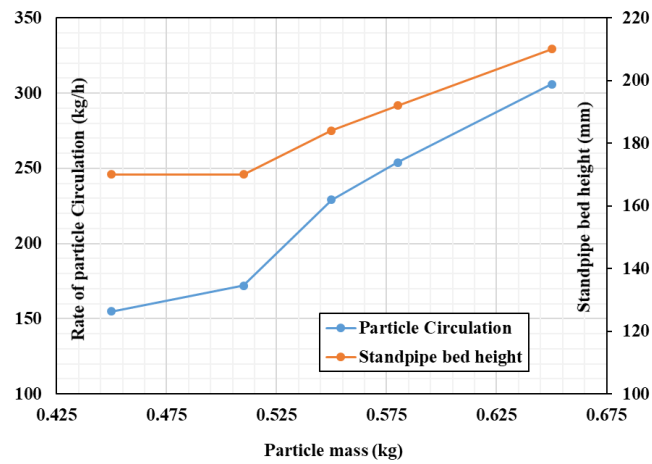


Figure 32: Rate of particle circulation as a function of particle inventory

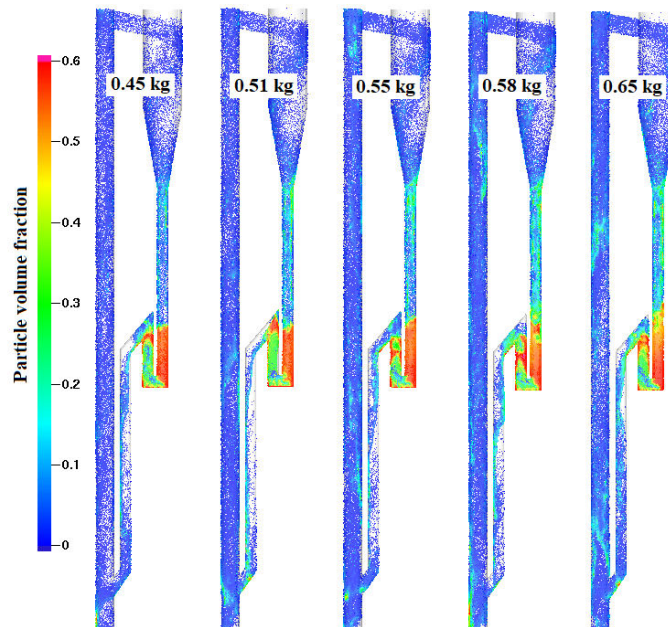


Figure 33: The change of particle circulation against particle inventory and visualization of particle hydrodynamics

The rate of circulation increases gradually with the particle inventory. The change is significant between 0.51 and 0.55 kg of particle inventories. As the particle hydrodynamics given in Figure 33 is carefully examined, the standpipe bed heights during 0.45 and 0.51 kg of particle inventory are almost same, which is further approximately similar with the overflow weir height. As the particle mass is further increased, the standpipe bed height develops above the overflow weir height that boost the circulation. As summarized in Paper E, the pressure developed by the

standpipe greatly effect on the circulation. This can be achieved by either increasing the standpipe bed height or increasing the particle slip velocity along the standpipe. Subsequent to the abrupt increment between 0.51kg to 0.55 kg, the circulation rate increases linearly until 0.65kg. According to the Figure 33, it seems possible to correlate the standpipe bed height to the rate of circulation, which constructs an easy method to predict the circulation. The development of the clusters in the riser can also be observed with increasing circulation rate. As the circulation increases, particles cross the overflow weir as dense clusters where some of these travel along the riser unbroken. Figure 34 illustrates the pressure variation across the CFB for different particle inventories. Increasing standpipe bed height is clearly illustrated by increasing pressure at P2. The riser pressure drop also shows an increasing trend with particle inventory. Rate of aerations were not changed and therefore, the increased pressure is due to high particle loading in the riser.

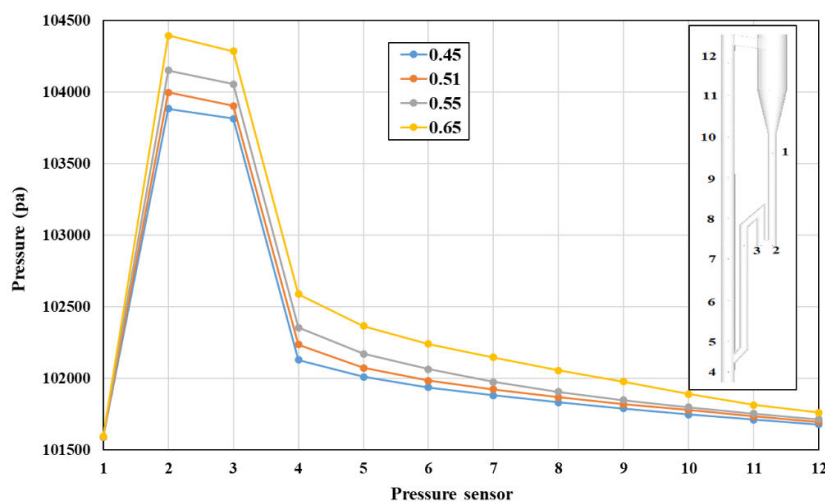


Figure 34: Pressure over the CFB system for different particle inventories.

4.5 Bubbling fluidized bed gasification

Three different biomass feedstock of wood chip, wood pellet and grass pellets, were gasified in an electrically heated bubbling fluidized bed reactor as given Figure 11. A detailed discussion of the experiments and the results are included in Paper H. Four different ERs from 0.075 to 0.16 and three different temperatures of 650 °C, 750 °C and 800 °C were tested.

The feeding was continuously encountered interruptions for wood chips due to particle stuck in feeding screw. Due to the large heterogeneity of the wood chip and discontinuous operation of the feeding screw, the biomass flowrate into the reactor was not steady. As the producer gas is a strong function of volatiles, discontinuous feeding could add uncertainties to the measured gas composition and consequently to the follow up calculations of carbon conversion and LHV. The percentage gas

compositions for wood chips is given in Figure 35, whereas Table 6 summarizes the gasification performances.

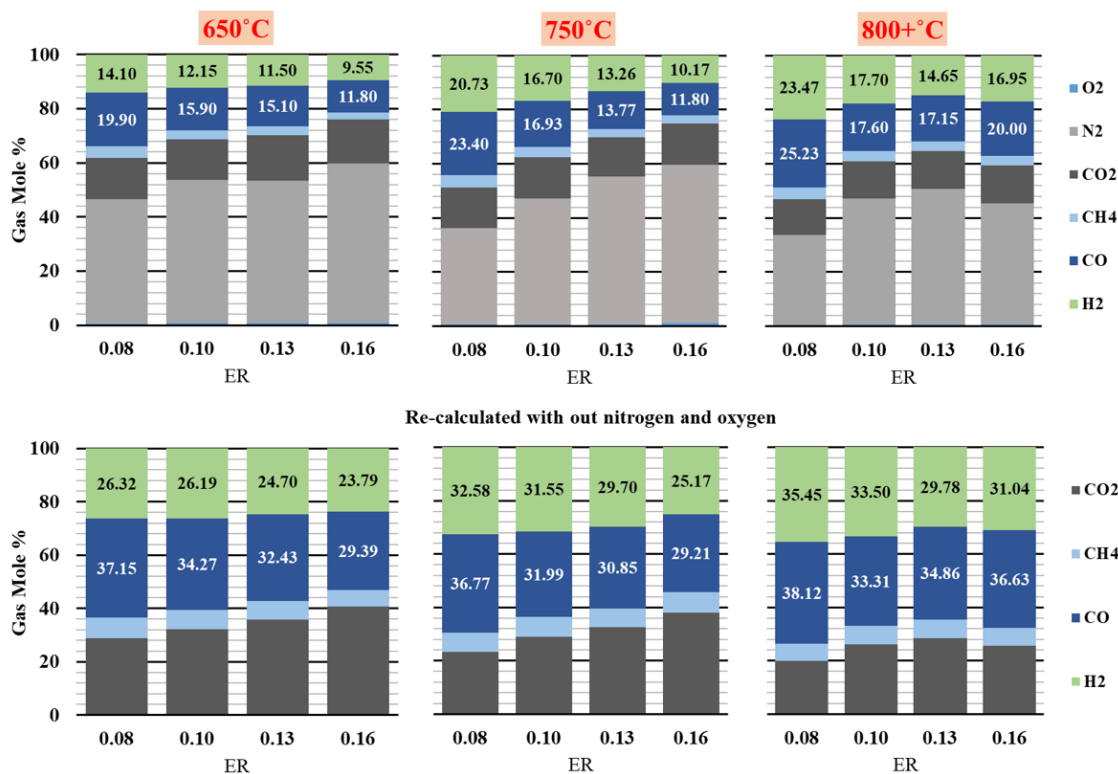


Figure 35: Composition of producer gas with ER and temperature for wood chips.

Gasification of grass pellets were not successful due to agglomerations and low carbon conversion. Wood chips and pellets could deliver product gas with good compositions of CO and H₂. At lower temperatures, increased ER reduced the gas quality as a result of N₂ dilution. In contrast at 800°C, minor reduction of H₂ and CO content with increased ER was outweighed by improved carbon conversion and gas yield. The respective H₂ and CO contents were 16.9% and 20% for wood chips and 17.2% and 18.8% for wood pellets at 800°C and 0.16 ER. Reactor temperature of 650°C was not sufficient to obtain an acceptable gas composition and carbon conversion. Progressively, the gas quality was improved at 750°C and however, the carbon conversion was approximately 50%. The best reactor performance for wood chips happened at 800°C and 0.16 ER with 75% carbon conversion efficiency. For wood pellets, both 0.125 and 0.15 ER at 800°C gave the best overall performance with 70% carbon conversion. The main motivation for using low ERs compared to literature values was to identify the minimum ER that is sufficient to maintain a steady char content without accumulation in the bed. ER around 0.15 can be identified as the minimum value, but it requires supplementary electrical heating to maintain the reactor temperature around 800°C.

Table 6: Gasification performance indicators for wood chips

ER	Gas production rate (Nm ³ /h)	Gas Yield (Nm ³ /kg biomass)	LHV (MJ/Nm ³)	CCE %	CGE %	Energy Rate (MJ/h)
650°C						
0.08	2.11	0.92	5.52	38.80	28.15	11.65
0.1	2.44	1.06	4.53	38.90	26.70	11.05
0.13	3.07	1.33	4.31	50.13	31.98	13.24
0.16	3.27	1.42	3.41	46.62	26.97	11.16
750°C						
0.08	2.71	1.18	6.86	54.10	44.85	18.57
0.1	2.78	1.21	5.35	46.92	35.89	14.86
0.13	2.92	1.27	3.91	41.78	27.59	11.42
0.16	3.31	1.44	3.68	46.66	29.47	12.20
800°C						
0.08	2.90	1.26	7.25	57.83	50.89	21.07
0.1	2.77	1.21	5.48	45.36	36.67	15.18
0.13	3.22	1.40	4.94	51.79	38.42	15.90
0.16	4.32	1.88	5.68	75.83	59.27	24.54

ER – equivalence ratio, LHV – lower heating value, CCE – carbon conversion efficiency, CGE – cold gas efficiency

4.6 CPFD simulation of bubbling fluidized bed gasification

Integrating the chemical kinetics of biomass gasification accurately into the CPFD bubbling fluidized bed model is a challenging task. The main uncertainty arises from the prediction of compositional break down of biomass into gases, tar and char during pyrolysis. There is not any universal model that can be applied as it can be varied depending on type and size of biomass, temperature, heating rate (any limitation of heat transfer from bed to particles) and turbulence (the residence time) etc. Even though the average fluidized bed temperature is known, the local temperature at the biomass feeding can be lower unless a good mixing is not induced. The temperature plots using CPFD simulation in Figure 36 provides evidence for this, where in certain time steps, the temperature at biomass feed drops below 300°C. The drop indicates the biomass particle heating and pyrolysis, where a drop always followed by an abrupt increase that suggests the oxidation of gaseous products. This increasing temperature just above the bed was observed during the experiments as well. The sharp drop of temperature at the startup and just above the feeding location is due to the starting of biomass feeding that could be observed during the experiments. Temperature towards the bottom of the reactor changes in a comparatively narrow range and is hardly pushed above the average. However, during the simulation time of 200 seconds, the bed temperature shows an increasing

trend. The gas temperature to the exit becomes steadier and fluctuates around 700°C.

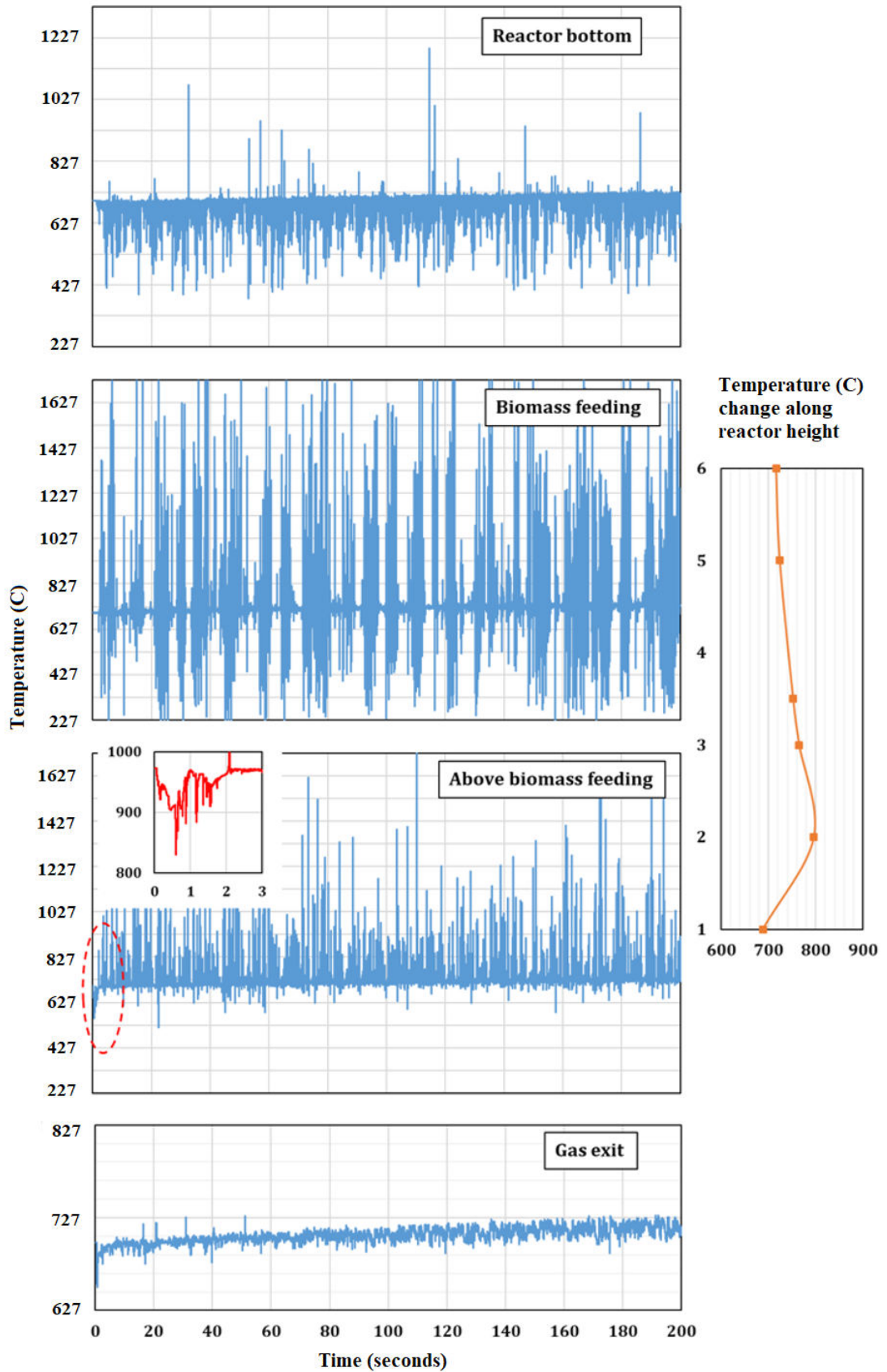


Figure 36: Variation of the temperature along the reactor height

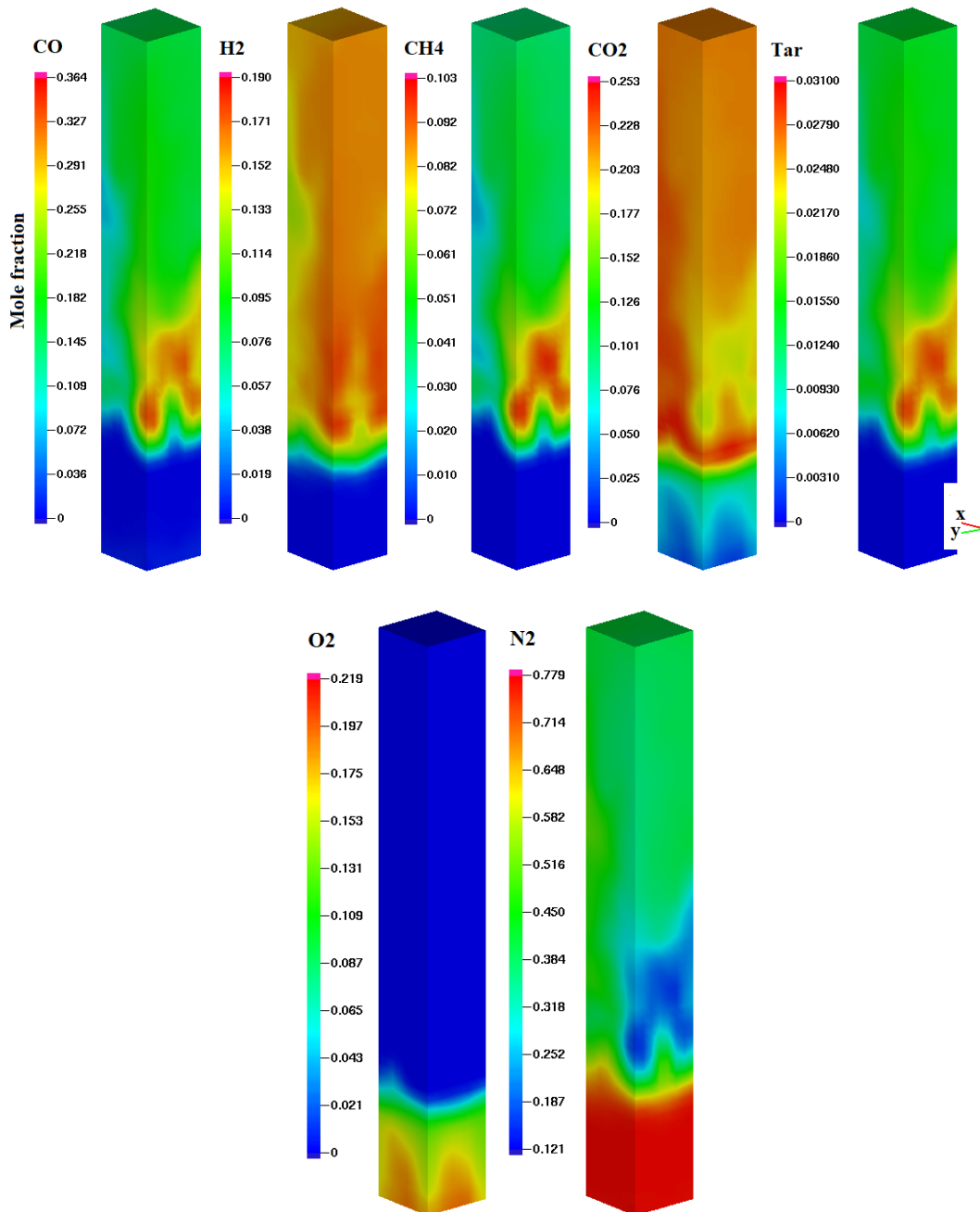


Figure 37: Distribution of the gaseous components across the reactor

According to the graphical illustrations of distribution of the gaseous products over the geometry, Oxygen is fully consumed as it reaches the particle bed surface and only CO₂ shows a noticeable change within the bed. The sudden drop in N₂ composition above the bed is due to high loading of volatile fraction from pyrolysis. The data suggests that the gasses are well mixed at the outlet showing approximately uniform composition. Figure 38 includes the gas compositions from both simulation and experiments for an easy comparison. The prediction of H₂, CO and CH₄ from simulation is very similar with the experimental values. However, prediction of CO₂ is considerably higher compared to the experiment, whereas the concentration of N₂ is lower. Tar was not measured during experiment and it was

observed as 1.5% from the simulations. Increased carbon content from CO₂ in the producer gas suggests that more carbon and O₂ should be included in the tar and char than implemented in the simulation. Variation of gas composition due to periodic biomass feeding and possible errors related to gas chromatography measurements are potential experimental uncertainties. The primary error related to simulation is from the biomass pyrolysis composition. The prediction accuracy can be improved by further tuning of the pyrolysis model and heterogeneous chemistry.

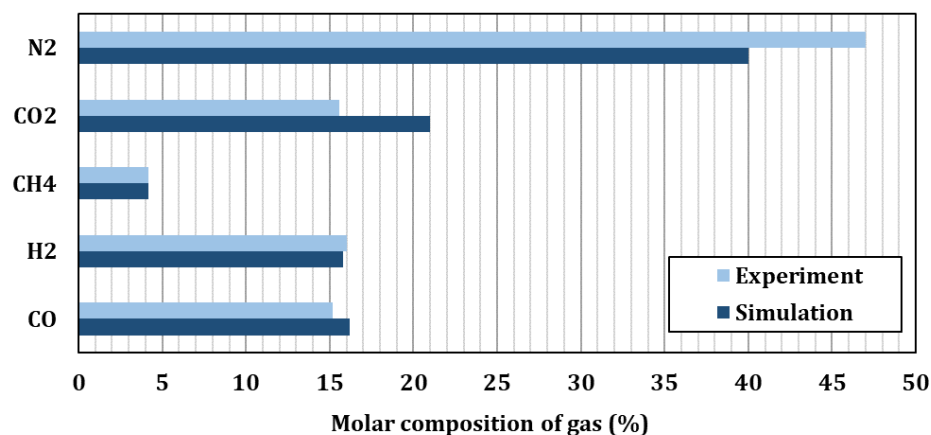


Figure 38: comparison of gas composition from simulation against experiments for wood pellets at 750°C and 0.125 ER

4.7 Summary

Fluidization is an important phenomenon in many different contexts where particles are involved. Observing the reactor interior is difficult unless costly technologies and cumbersome post data analysis are performed. With the competency in solving the conservation equations in 3-D coordinate system, CFD offers an alternative platform to analyze the physical dynamic systems. The challenging constructions of multiphase CFD modeling were extensively discussed and much efforts have been taken to make multiphase CFD simulations realistic for industrial scale. Computational particle fluid dynamic (CPFD) is a tailor-made CFD concept especially for gas-particle systems. CPFD is gathered in to Barracuda VR®, which is a highly user friendly software.

The bubbling and circulating fluidized bed systems were extensively analyzed with CPFD simulations where experimental comparison is also presented. The minimum fluidization velocity (MFV) increases with the particle size and however, the change is not linear. The linear behavior was observed in different particle groups. Wen-Yu-Ergun blended correlation was used for the simulation. Even with precise prediction of bed pressure drop at static conditions, the MFV prediction was slightly higher, which suggested a decreased estimation of the fluid drag. The usefulness of CPFD

simulation is highlighted in estimating the MFV of particle phases with a size distribution. Optimization of Ergun coefficient and multiplier for the drag model should be tested for more precise prediction of MFV.

A circulating fluidized bed was constructed to generate data for model validation. Experiments with smaller particle sizes were interrupted due to particle accumulation at riser-cyclone connection and due to static charges. The experiments were planned to identify the optimum between loopseal bottom aeration and standpipe aeration. Both aerations contributed for an effective operation where standpipe aeration showed an increase effect over 60%. The initial model validation and modeling parameter optimization were carried out using literature experimental data set. The pressure constant in the particle stress function and particle-wall momentum retention parameters were found to be the most influencing, which needed to change to 5 and 0.85 respectively. An in-depth analysis of particle hydrodynamic across the loopseal was performed where emergence of the bubbles at the standpipe can be predicted, to a great extent, by monitoring the recycle pipe pressure drop. Consequently, efforts were made to re-validate the optimized model using experiments conducted in UNS circulating fluidized bed. The model behaved well for the selected set of experimental data. Some parts of the geometry was constructed with narrow pipes (i.e. loopseal) where the wall effect can be extremely influencing. Therefore, the model should be further tested and optimized for a larger scale geometry.

Biomass gasification in bubbling fluidized bed has extensively been analyzed. Many of the previous works used equivalence ratios (ER) above 0.2 up to 0.4. In contrast, reduced ER from 0.1 to 0.16 were used in the experiments. The main supporting idea was to identify the minimum ER that is sufficient to maintain a steady char content in the bed without accumulation. Below 0.16/0.15 ER, the bed pressure was increasing during the experiments, which is an indirect indication of char accumulation. The reactor temperature needed to raise above 800°C for a reasonable carbon conversion over 70%. With the wood chips, the gas production, carbon conversion efficiency and lower heating value were 1.88 Nm³/kg of biomass, 75.83% and 5.68 MJ/Nm³ respectively at 800°C and 0.16 ER. The missing 24% of the carbon is supposed to include in tar and elutriated char particles. The construction of the CFPD model with chemical kinetics was challenging. The predicted gas compositions for CO and CO₂ were higher compared to experiments while N₂ is lower. Apart from the possible uncertainties incorporated with measurements in gas chromatography, the pyrolysis composition of gas, tar and char can greatly effect on the simulation results. Therefore, it is a prime importance to find a reasonably representative pyrolysis model for the gasification geometry used in the simulations. Further, modeling of small scale reactors with CFPD encounters the

challenge of particle-to-grid size ratio. As an example, use of wood chips in the size of 20-30mm in a 100mm diameter reactor only allows to have 3 cells along the diameter. The convergence difficulties are provoked unless the cell size is several times the particle size. For instance, nearly 70-80% of the mass is released to the gas phase during pyrolysis. However, the char volume is merely shrunk by 20-30%. Consequently, the cell pressure should be vastly increased to accommodate the released gases, leading to failed convergence.

5 Conclusion

According to the experimental studies with sand particles, minimum fluidization velocity is not exactly linear with the particle size. In, circulating fluidized bed (CFB) systems, the rate of particle circulation can be manipulated with the loopseal aeration, for a great extent. Contribution from the aeration at the standpipe of the loopseal is higher compared to bottom aeration for the circulation. Further, the rate of circulation is possible to increase greatly by a slight reduction of the particle size. The understanding of this is important, because the particle attrition is highly possible as the process proceeds.

Computational particle fluid dynamic (CPFD) is a robust CFD platform for gas-particle multiphase flow systems. The prediction MFV with CPFD is agreeable and however, the bed expansion at the minimum fluidization is not captured well. It is, therefore, suggested that the particle modeling parameters should further be analyzed and the CFD code should be further improved to capture the bed expansion at minimum fluidization. Adjustment of the particle modeling parameters, especially the pressure constant in particle stress model and the particle-wall momentum retention coefficients, is needed to tune the CPFD model setup for an accurate prediction of particle circulation in CFB. Analysis of the optimized parameters in a different geometry with different aeration configuration can increase the model reproducibility. There is an optimum value for the rate of loopseal aeration where the circulation is difficult to improve further by merely increasing the loopseal aeration beyond this optimum. Likewise, a robust CPFD model is incalculably useful for designing, optimization and scaling up of fluidized bed systems. Further, the "boundary connector" option in CPFD is a useful tool to isolate specific sections from a complex geometry, which consequently reduce the efforts in gridding and simulation time.

The gasification of grass pellets need low superficial velocities to minimize the attrition of carbon particles while feeding of biomass into the bed could also help. Use of catalysts is also suggested to realize improved carbon conversion at reduced temperature. If the external heat energy is assumed to extract from either waste heat or renewable sources instead of electrical heating used in experiments, the understanding of the minimum equivalence ratio (at different reactor temperatures) is vital in maximizing the CO and H₂ content. Development of a CPFD model for air gasification is challenging due to varying pyrolysis product compositions as a function of temperature, particle size, and species. As the CPFD model can capture local temperature variations inside the bed, it is extremely productive if the CPFD is further improved to implement temperature based pyrolysis product compositions. As the dual reactor steam gasification is concerned, the simulation time is extremely high, which allows to simulate merely several

hundreds of seconds. Therefore in first hand, it is important to optimize the particle hydrodynamics in a non-reactive environment, which can deliver useful information such as rate of particle circulation and residence time in each section. Subsequently, the reactors can be simulated separately with reactions (i.e. bubbling reactor and riser combustion reactor separately). Finally, the most optimized conditions should be tested in the complete geometry.

References

- [1] D. H. Meadows, D. L. Meadows, J. Randers, and W. W. Behrens, *The Limits To Growth*. New York: Universe Books, 1972.
- [2] A. Najam and C. J. Cleveland, "Energy and Sustainable Development at Global Environmental Summits: An Evolving Agenda," *Environment, Development and Sustainability*, journal article vol. 5, no. 1, pp. 117-138, 2003.
- [3] S. Meakin, "THE RIO EARTH SUMMIT: SUMMARY OF THE UNITED NATIONS CONFERENCE ON ENVIRONMENT AND DEVELOPMENT," Available: <http://publications.gc.ca/Pilot/LoPBdP/BP/bp317-e.htm>
- [4] Y. Liu *et al.*, "Impacts of 1.5 and 2.0°C global warming on rice production across China," *Agricultural and Forest Meteorology*, vol. 284, p. 107900, 2020.
- [5] E. P. Agency. (2020 May 25). *Global Greenhouse Gas Emissions Data*. Available: <https://www.epa.gov/ghgemissions/global-greenhouse-gas-emissions-data>
- [6] OurWorldData. (2020 May 25). *CO₂ and Greenhouse Gas Emissions*. Available: <https://ourworldindata.org/co2-and-other-greenhouse-gas-emissions>
- [7] N. R. Council, *Verifying Greenhouse Gas Emissions: Methods to Support International Climate Agreements*. Washington, DC: The National Academies Press, 2010, p. 124.
- [8] T. S. Buchholz, T. A. Volk, and V. A. Luzadis, "A participatory systems approach to modeling social, economic, and ecological components of bioenergy," *Energy Policy*, vol. 35, no. 12, pp. 6084-6094, 2007.
- [9] R. Fouquet, "Historical energy transitions: Speed, prices and system transformation," *Energy Research & Social Science*, vol. 22, pp. 7-12, 2016.
- [10] L. Song, Y. Fu, P. Zhou, and K. K. Lai, "Measuring national energy performance via Energy Trilemma Index: A Stochastic Multicriteria Acceptability Analysis," *Energy Economics*, vol. 66, pp. 313-319, 2017.
- [11] REN21, "Renewables 2019 Global Status Report," 2020. Available: www.ren21.net/wp-content/uploads/2019/05/gsr_2019_full_report_en.pdf.
- [12] WorldBioenergyAssociation, "Global Bioenergy Statistics 2019," 2019, Available: https://worldbioenergy.org/uploads/191129%20WBA%20GBS%202019_LQ.pdf.
- [13] S. K. Sansaniwal, M. A. Rosen, and S. K. Tyagi, "Global challenges in the sustainable development of biomass gasification: An overview," *Renewable and Sustainable Energy Reviews*, vol. 80, pp. 23-43, 2017.
- [14] Z. Wang, Q. Bui, B. Zhang, and T. L. H. Pham, "Biomass energy production and its impacts on the ecological footprint: An investigation of the G7 countries," *Science of The Total Environment*, vol. 743, p. 140741, 2020.
- [15] G. Zanchi, N. Pena, and N. Bird, "Is woody bioenergy carbon neutral? A comparative assessment of emissions from consumption of woody bioenergy and fossil fuel," *GCB Bioenergy*, vol. 4, no. 6, pp. 761-772, 2012.

- [16] J. Dewulf, H. Van Langenhove, and B. Van De Velde, "Exergy-Based Efficiency and Renewability Assessment of Biofuel Production," *Environmental Science & Technology*, vol. 39, no. 10, pp. 3878-3882, 2005.
- [17] European Commission. (2020 May 25). *Climate strategies & targets*. Available: https://ec.europa.eu/clima/policies/strategies_en
- [18] P. Moriarty, X. Yan, and S. J. Wang, "Liquid biofuels: not a long-term transport solution," *Energy Procedia*, vol. 158, pp. 3265-3270, 2019.
- [19] B. Cavicchi, "The burden of sustainability: Limits to sustainable bioenergy development in Norway," *Energy Policy*, vol. 119, pp. 585-599, 2018.
- [20] N. Scarlat, J.-F. Dallemand, O. J. Skjelhaugen, D. Asplund, and L. Nesheim, "An overview of the biomass resource potential of Norway for bioenergy use," *Renewable and Sustainable Energy Reviews*, vol. 15, no. 7, pp. 3388-3398, 2011.
- [21] N. H. Afgan, D. A. Gobaisi, M. G. Carvalho, and M. Cumo, "Sustainable energy development," *Renewable and Sustainable Energy Reviews*, vol. 2, no. 3, pp. 235-286, 1998.
- [22] P. McKendry, "Energy production from biomass (part 1): overview of biomass," *Bioresource Technology*, vol. 83, no. 1, pp. 37-46, 5// 2002.
- [23] J. M. Rosúa and M. Pasadas, "Biomass potential in Andalusia, from grapevines, olives, fruit trees and poplar, for providing heating in homes," *Renewable and Sustainable Energy Reviews*, vol. 16, no. 6, pp. 4190-4195, 2012.
- [24] R. Slade, A. Bauen, and R. Gross, "Global bioenergy resources," *Nature Climate Change*, vol. 4, no. 2, pp. 99-105, 2014.
- [25] J. Szczodrak and J. Fiedurek, "Technology for conversion of lignocellulosic biomass to ethanol," *Biomass and Bioenergy*, vol. 10, no. 5, pp. 367-375, 1996.
- [26] W. Hermann, "An Assessment of Biomass Feedstock and Conversion Research Opportunities," Global Climate & Energy Project, Stanford University 2005, Available: https://gcep.stanford.edu/pdfs/assessments/biomass_assessment.pdf.
- [27] M. Hoogwijk, A. Faaij, R. van den Broek, G. Berndes, D. Gielen, and W. Turkenburg, "Exploration of the ranges of the global potential of biomass for energy," *Biomass and Bioenergy*, vol. 25, no. 2, pp. 119-133, 2003.
- [28] M. Hoogwijk, A. Faaij, B. Eickhout, B. de Vries, and W. Turkenburg, "Potential of biomass energy out to 2100, for four IPCC SRES land-use scenarios," *Biomass and Bioenergy*, vol. 29, no. 4, pp. 225-257, 2005.
- [29] A. C. Caputo, M. Palumbo, P. M. Pelagagge, and F. Scacchia, "Economics of biomass energy utilization in combustion and gasification plants: effects of logistic variables," *Biomass and Bioenergy*, vol. 28, no. 1, pp. 35-51, 2005.
- [30] K. Srirangan, L. Akawi, M. Moo-Young, and C. P. Chou, "Towards sustainable production of clean energy carriers from biomass resources," *Applied Energy*, vol. 100, pp. 172-186, 2012.
- [31] S. R. Chia *et al.*, "Sustainable approaches for algae utilisation in bioenergy production," *Renewable Energy*, 2017.

- [32] R. Gusain and S. Suthar, "Potential of aquatic weeds (Lemna gibba, Lemna minor, Pistia stratiotes and Eichhornia sp.) in biofuel production," *Process Safety and Environmental Protection*, vol. 109, pp. 233-241, 2017.
- [33] H. L. Zhu *et al.*, "Co-gasification of beech-wood and polyethylene in a fluidized-bed reactor," *Fuel Processing Technology*, vol. 190, pp. 29-37, 2019.
- [34] G. Wang, B. Fan, H. Chen, and Y. Li, "Understanding the pyrolysis behavior of agriculture, forest and aquatic biomass: Products distribution and characterization," *Journal of the Energy Institute*, 2020.
- [35] Y. B. Yang, H. Yamauchi, V. Nasserzadeh, and J. Swithenbank, "Effects of fuel devolatilisation on the combustion of wood chips and incineration of simulated municipal solid wastes in a packed bed☆," *Fuel*, vol. 82, no. 18, pp. 2205-2221, 2003.
- [36] F. V. Tinaut, A. Melgar, J. F. Pérez, and A. Horrillo, "Effect of biomass particle size and air superficial velocity on the gasification process in a downdraft fixed bed gasifier. An experimental and modelling study," *Fuel Processing Technology*, vol. 89, no. 11, pp. 1076-1089, 2008.
- [37] T. M. Ismail, A. Ramos, M. Abd El-Salam, E. Monteiro, and A. Rouboa, "Plasma fixed bed gasification using an Eulerian model," *International Journal of Hydrogen Energy*, vol. 44, no. 54, pp. 28668-28684, 2019.
- [38] Y. Su, Y. Luo, Y. Chen, W. Wu, and Y. Zhang, "Experimental and numerical investigation of tar destruction under partial oxidation environment," *Fuel Processing Technology*, vol. 92, no. 8, pp. 1513-1524, 2011.
- [39] M. A. Masmoudi, K. Halouani, and M. Sahraoui, "Comprehensive experimental investigation and numerical modeling of the combined partial oxidation-gasification zone in a pilot downdraft air-blown gasifier," *Energy Conversion and Management*, vol. 144, pp. 34-52, 2017.
- [40] A. K. Sharma, "Modeling and simulation of a downdraft biomass gasifier 1. Model development and validation," *Energy Conversion and Management*, vol. 52, no. 2, pp. 1386-1396, 2011.
- [41] T. Imam and S. Capareda, "Characterization of bio-oil, syn-gas and bio-char from switchgrass pyrolysis at various temperatures," *Journal of Analytical and Applied Pyrolysis*, vol. 93, pp. 170-177, 2012.
- [42] G. Bofo-Mensah, K. M. Darkwa, and G. Laryea, "Effect of combustion chamber material on the performance of an improved biomass cookstove," *Case Studies in Thermal Engineering*, vol. 21, p. 100688, 2020.
- [43] C. Yin and S. Li, "Advancing grate-firing for greater environmental impacts and efficiency for decentralized biomass/wastes combustion," *Energy Procedia*, vol. 120, pp. 373-379, 2017.
- [44] J. S. Smith, S. I. Safferman, and C. M. Saffron, "Development and application of a decision support tool for biomass co-firing in existing coal-fired power plants," *Journal of Cleaner Production*, vol. 236, p. 117375, 2019.
- [45] A. A. Bhuiyan, A. S. Blicblau, A. K. M. S. Islam, and J. Naser, "A review on thermo-chemical characteristics of coal/biomass co-firing in industrial furnace," *Journal of the Energy Institute*, vol. 91, no. 1, pp. 1-18, 2018.

- [46] J. J. Chew and V. Doshi, "Recent advances in biomass pretreatment – Torrefaction fundamentals and technology," *Renewable and Sustainable Energy Reviews*, vol. 15, no. 8, pp. 4212-4222, 2011.
- [47] J. Shankar Tumuluru, S. Sokhansanj, J. R. Hess, C. T. Wright, and R. D. Boardman, "REVIEW: A review on biomass torrefaction process and product properties for energy applications," *Industrial Biotechnology*, vol. 7, no. 5, pp. 384-401, 2011.
- [48] R. Janssen, A. F. Turhollow, D. Rutz, and R. Mergner, "Production facilities for second-generation biofuels in the USA and the EU – current status and future perspectives," *Biofuels, Bioproducts and Biorefining*, vol. 7, no. 6, pp. 647-665, 2013.
- [49] M. Costa and D. Piazzullo, "Biofuel Powering of Internal Combustion Engines: Production Routes, Effect on Performance and CFD Modeling of Combustion," (in English), *Frontiers in Mechanical Engineering, Methods* vol. 4, no. 9, 2018.
- [50] S. N. Naik, V. V. Goud, P. K. Rout, and A. K. Dalai, "Production of first and second generation biofuels: A comprehensive review," *Renewable and Sustainable Energy Reviews*, vol. 14, no. 2, pp. 578-597, 2010.
- [51] A. Bauen, G. Berndes, M. Junginger, M. Londo, and F. Vuille, "Bioenergy – a Sustainable and Reliable Energy Source,"
- [52] M. Mohammadi, G. D. Najafpour, H. Younesi, P. Lahijani, M. H. Uzir, and A. R. Mohamed, "Bioconversion of synthesis gas to second generation biofuels: A review," *Renewable and Sustainable Energy Reviews*, vol. 15, no. 9, pp. 4255-4273, 2011.
- [53] A. Kumar, D. D. Jones, and M. A. Hanna, "Thermochemical Biomass Gasification: A Review of the Current Status of the Technology," *Energies*, vol. 2, no. 3, pp. 556-581, 2009.
- [54] S. Wang and Y. Shen, "CFD-DEM study of biomass gasification in a fluidized bed reactor: Effects of key operating parameters," *Renewable Energy*, vol. 159, pp. 1146-1164, 2020.
- [55] S. K. Sansaniwal, K. Pal, M. A. Rosen, and S. K. Tyagi, "Recent advances in the development of biomass gasification technology: A comprehensive review," *Renewable and Sustainable Energy Reviews*, vol. 72, pp. 363-384, 2017.
- [56] X. T. Li, J. R. Grace, C. J. Lim, A. P. Watkinson, H. P. Chen, and J. R. Kim, "Biomass gasification in a circulating fluidized bed," *Biomass and Bioenergy*, vol. 26, no. 2, pp. 171-193, 2004.
- [57] S. Kraft, F. Kirnbauer, and H. Hofbauer, "CPFD simulations of an industrial-sized dual fluidized bed steam gasification system of biomass with 8MW fuel input," *Applied Energy*, vol. 190, pp. 408-420, 2017.
- [58] A. Gómez-Barea and B. Leckner, "Modeling of biomass gasification in fluidized bed," *Progress in Energy and Combustion Science*, vol. 36, no. 4, pp. 444-509, 2010.

- [59] T. Song, J. Wu, L. Shen, and J. Xiao, "Experimental investigation on hydrogen production from biomass gasification in interconnected fluidized beds," *Biomass and Bioenergy*, vol. 36, pp. 258-267, 2012.
- [60] M. Puig-Arnavat, J. C. Bruno, and A. Coronas, "Review and analysis of biomass gasification models," *Renewable and Sustainable Energy Reviews*, vol. 14, no. 9, pp. 2841-2851, 2010.
- [61] M. A. Masmoudi, M. Sahraoui, N. Grioui, and K. Halouani, "2-D Modeling of thermo-kinetics coupled with heat and mass transfer in the reduction zone of a fixed bed downdraft biomass gasifier," *Renewable Energy*, vol. 66, pp. 288-298, 2014.
- [62] R. Yan, H. Yang, T. Chin, D. T. Liang, H. Chen, and C. Zheng, "Influence of temperature on the distribution of gaseous products from pyrolyzing palm oil wastes," *Combustion and Flame*, vol. 142, no. 1, pp. 24-32, 2005.
- [63] E. Desroches-Ducarne, J. C. Dolignier, E. Marty, G. Martin, and L. Delfosse, "Modelling of gaseous pollutants emissions in circulating fluidized bed combustion of municipal refuse," *Fuel*, vol. 77, no. 13, pp. 1399-1410, 1998.
- [64] L. Gerun *et al.*, "Numerical investigation of the partial oxidation in a two-stage downdraft gasifier," *Fuel*, vol. 87, no. 7, pp. 1383-1393, 2008.
- [65] I. P. Silva, R. M. A. Lima, G. F. Silva, D. S. Ruzene, and D. P. Silva, "Thermodynamic equilibrium model based on stoichiometric method for biomass gasification: A review of model modifications," *Renewable and Sustainable Energy Reviews*, vol. 114, p. 109305, 2019.
- [66] S. Jarunghammachote and A. Dutta, "Thermodynamic equilibrium model and second law analysis of a downdraft waste gasifier," *Energy*, vol. 32, no. 9, pp. 1660-1669, 2007.
- [67] M. J. Prins, K. J. Ptasinski, and F. J. J. G. Janssen, "Thermodynamics of gas-char reactions: first and second law analysis," *Chemical Engineering Science*, vol. 58, no. 3, pp. 1003-1011, 2003.
- [68] A. Gagliano, F. Nocera, F. Patania, M. Bruno, and D. G. Castaldo, "A robust numerical model for characterizing the syngas composition in a downdraft gasification process," *Comptes Rendus Chimie*, vol. 19, no. 4, pp. 441-449, 2016.
- [69] C. R. Altafini, P. R. Wander, and R. M. Barreto, "Prediction of the working parameters of a wood waste gasifier through an equilibrium model," *Energy Conversion and Management*, vol. 44, no. 17, pp. 2763-2777, 2003.
- [70] D. A. Rodriguez-Alejandro, H. Nam, A. L. Maglinao, S. C. Capareda, and A. F. Aguilera-Alvarado, "Development of a modified equilibrium model for biomass pilot-scale fluidized bed gasifier performance predictions," *Energy*, vol. 115, pp. 1092-1108, 2016.
- [71] H. Ghassemi and R. Shahsavan-Markadeh, "Effects of various operational parameters on biomass gasification process; a modified equilibrium model," *Energy Conversion and Management*, vol. 79, pp. 18-24, 2014.

- [72] Y.-i. Lim and U.-D. Lee, "Quasi-equilibrium thermodynamic model with empirical equations for air–steam biomass gasification in fluidized-beds," *Fuel Processing Technology*, vol. 128, pp. 199-210, 2014.
- [73] A. Almuttahir and F. Taghipour, "Computational fluid dynamics of high density circulating fluidized bed riser: Study of modeling parameters," *Powder Technology*, vol. 185, no. 1, pp. 11-23, 2008.
- [74] X. Liu, C. Zhu, S. Geng, M. Yao, J. Zhan, and G. Xu, "Two-fluid modeling of Geldart A particles in gas–solid micro-fluidized beds," *Particuology*, vol. 21, pp. 118-127, 2015.
- [75] D. Jajcevic, E. Siegmann, C. Radeke, and J. G. Khinast, "Large-scale CFD–DEM simulations of fluidized granular systems," *Chemical Engineering Science*, vol. 98, pp. 298-310, 2013.
- [76] H. P. Zhu, Z. Y. Zhou, R. Y. Yang, and A. B. Yu, "Discrete particle simulation of particulate systems: Theoretical developments," *Chemical Engineering Science*, vol. 62, no. 13, pp. 3378-3396, 2007.
- [77] P. Sreekanth, S. Madhava, and J. O. B. Thomas, "Computational Gas-Solids Flows and Reacting Systems: Theory, Methods and Practice." Hershey, PA, USA: IGI Global, 2011.
- [78] D. Gidaspow, *Multiphase Flow and Fluidization: Continuum and Kinetic Theory Descriptions*. New York: Academic Press, 1994.
- [79] J. R. Grace and F. Taghipour, "Verification and validation of CFD models and dynamic similarity for fluidized beds," *Powder Technology*, vol. 139, no. 2, pp. 99-110, 2004.
- [80] B. G. M. van Wachem and A. E. Almstedt, "Methods for multiphase computational fluid dynamics," *Chemical Engineering Journal*, vol. 96, no. 1, pp. 81-98, 2003.
- [81] B. H. Xu and A. B. Yu, "Numerical simulation of the gas-solid flow in a fluidized bed by combining discrete particle method with computational fluid dynamics," *Chemical Engineering Science*, vol. 52, no. 16, pp. 2785-2809, 1997.
- [82] S. Subramaniam, "Lagrangian–Eulerian methods for multiphase flows," *Progress in Energy and Combustion Science*, vol. 39, no. 2, pp. 215-245, 2013.
- [83] Y. Tsuji, "Multi-scale modeling of dense phase gas–particle flow," *Chemical Engineering Science*, vol. 62, no. 13, pp. 3410-3418, 2007.
- [84] N. A. Patankar and D. D. Joseph, "Modeling and numerical simulation of particulate flows by the Eulerian–Lagrangian approach," *International Journal of Multiphase Flow*, vol. 27, no. 10, pp. 1659-1684, 2001.
- [85] Z. Qinghong, W. Shuyan, L. Huilin, L. Guodong, W. Shuai, and Z. Guangbo, "A coupled Eulerian fluid phase-Eulerian solids phase-Lagrangian discrete particles hybrid model applied to gas-solids bubbling fluidized beds," *Powder Technology*, vol. 315, pp. 385-397, 2017.
- [86] H. Enwald, E. Peirano, and A. E. Almstedt, "Eulerian two-phase flow theory applied to fluidization," *International Journal of Multiphase Flow*, vol. 22, pp. 21-66, 1996.

- [87] D. M. Snider, "An Incompressible Three-Dimensional Multiphase Particle-in-Cell Model for Dense Particle Flows," *Journal of Computational Physics*, vol. 170, no. 2, pp. 523-549, 2001.
- [88] I. S. Hwang, H. J. Jeong, and J. Hwang, "Numerical simulation of a dense flow cyclone using the kinetic theory of granular flow in a dense discrete phase model," *Powder Technology*, vol. 356, pp. 129-138, 2019.
- [89] S. Benyahia and J. E. Galvin, "Estimation of Numerical Errors Related to Some Basic Assumptions in Discrete Particle Methods," *Industrial & Engineering Chemistry Research*, vol. 49, no. 21, pp. 10588-10605, 2010.
- [90] M. J. Andrews and P. J. O'Rourke, "The multiphase particle-in-cell (MP-PIC) method for dense particulate flows," *International Journal of Multiphase Flow*, vol. 22, no. 2, pp. 379-402, 1996.
- [91] F. H. Harlow, "PIC and its progeny," *Computer Physics Communications*, vol. 48, no. 1, pp. 1-10, 1988.
- [92] F. Harlow, "The Particle-In-Cell Method for Numerical Solution of Problems in Fluid Dynamics," The University of California, New Mexico 1962, Available: <https://permalink.lanl.gov/object/tr?what=info:lanl-repo/lareport/LA-DC-5288>.
- [93] J. Leboreiro, G. G. Joseph, C. M. Hrenya, D. M. Snider, S. S. Banerjee, and J. E. Galvin, "The influence of binary drag laws on simulations of species segregation in gas-fluidized beds," *Powder Technology*, vol. 184, no. 3, pp. 275-290, 2008.
- [94] H. Liu, R. J. Cattolica, and R. Seiser, "Operating parameter effects on the solids circulation rate in the CFD simulation of a dual fluidized-bed gasification system," *Chemical Engineering Science*, vol. 169, pp. 235-245,
- [95] P. J. O'Rourke and D. M. Snider, "An improved collision damping time for MP-PIC calculations of dense particle flows with applications to polydisperse sedimenting beds and colliding particle jets," *Chemical Engineering Science*, vol. 65, no. 22, pp. 6014-6028, 2010.
- [96] S. Wang, K. Luo, C. Hu, L. Sun, and J. Fan, "Impact of operating parameters on biomass gasification in a fluidized bed reactor: An Eulerian-Lagrangian approach," *Powder Technology*, vol. 333, pp. 304-316, 2018.
- [97] D. Hirche, F. Birkholz, and O. Hinrichsen, "A hybrid Eulerian-Eulerian-Lagrangian model for gas-solid simulations," *Chemical Engineering Journal*, 2018.
- [98] L. Yan, C. J. Lim, G. Yue, B. He, and J. R. Grace, "Simulation of biomass-steam gasification in fluidized bed reactors: Model setup, comparisons and preliminary predictions," *Bioresource Technology*, vol. 221, pp. 625-635, 2016.
- [99] J. Xie, W. Zhong, and A. Yu, "MP-PIC modeling of CFB risers with homogeneous and heterogeneous drag models," *Advanced Powder Technology*, vol. 29, no. 11, pp. 2859-2871, 2018.

- [100] M. Feng, F. Li, W. Wang, and J. Li, "Parametric study for MP-PIC simulation of bubbling fluidized beds with Geldart A particles," *Powder Technology*, vol. 328, pp. 215-226, 2018.
- [101] F. Li, F. Song, S. Benyahia, W. Wang, and J. Li, "MP-PIC simulation of CFB riser with EMMS-based drag model," *Chemical Engineering Science*, vol. 82, pp. 104-113, 2012.
- [102] S. F. Sia, X. Zhao, Y. Yu, and Y. Zhang, "Multiphase particle-in-cell simulation in severe internal carotid artery stenosis," *Powder Technology*, 2018.
- [103] A. Ozel, J. Kolehmainen, S. Radl, and S. Sundaresan, "Fluid and particle coarsening of drag force for discrete-parcel approach," *Chemical Engineering Science*, vol. 155, pp. 258-267, 2016.
- [104] J. Zeng, H. Li, and D. Zhang, "Numerical simulation of proppant transport in propagating fractures with the multi-phase particle-in-cell method," *Fuel*, vol. 245, pp. 316-335, 2019.
- [105] F. Song, F. Li, W. Wang, and J. Li, "A sub-grid EMMS drag for multiphase particle-in-cell simulation of fluidization," *Powder Technology*, vol. 327, pp. 420-429, 2018.
- [106] W. Zhang and C. You, "Numerical approach to predict particle breakage in dense flows by coupling multiphase particle-in-cell and Monte Carlo methods," *Powder Technology*, vol. 283, pp. 128-136, 2015.
- [107] S. Benyahia and S. Sundaresan, "Do we need sub-grid scale corrections for both continuum and discrete gas-particle flow models?," *Powder Technology*, vol. 220, pp. 2-6, 2012.
- [108] D. M. Snider, S. M. Clark, and P. J. O'Rourke, "Eulerian-Lagrangian method for three-dimensional thermal reacting flow with application to coal gasifiers," *Chemical Engineering Science*, vol. 66, no. 6, pp. 1285-1295, 2011.
- [109] D. M. Snider, P. J. O'Rourke, and M. J. Andrews, "Sediment flow in inclined vessels calculated using a multiphase particle-in-cell model for dense particle flows," *International Journal of Multiphase Flow*, vol. 24, no. 8, pp. 1359-1382, 1998.
- [110] P. J. O'Rourke, P. Zhao, and D. Snider, "A model for collisional exchange in gas/liquid/solid fluidized beds," *Chemical Engineering Science*, vol. 64, no. 8, pp. 1784-1797, 2009.
- [111] P. J. O'Rourke and D. M. Snider, "Inclusion of collisional return-to-isotropy in the MP-PIC method," *Chemical Engineering Science*, vol. 80, pp. 39-54, 2012.
- [112] P. J. O'Rourke and D. M. Snider, "A new blended acceleration model for the particle contact forces induced by an interstitial fluid in dense particle/fluid flows," *Powder Technology*, vol. 256, pp. 39-51, 2014.
- [113] J. C. Bandara, C. Jayarathna, R. Thapa, H. K. Nielsen, B. M. E. Moldestad, and M. S. Eikeland, "Loop seals in circulating fluidized beds – Review and parametric studies using CPFD simulation," *Chemical Engineering Science*, vol. 227, p. 115917, 2020.

- [114] Y. Liang, Y. Zhang, T. Li, and C. Lu, "A critical validation study on CPFD model in simulating gas–solid bubbling fluidized beds," *Powder Technology*, vol. 263, pp. 121-134, 2014.
- [115] J. M. Weber, K. J. Layfield, D. T. Van Essendelft, and J. S. Mei, "Fluid bed characterization using Electrical Capacitance Volume Tomography (ECVT), compared to CPFD Software's Barracuda," *Powder Technology*, vol. 250, pp. 138-146, 2013.
- [116] A. Stroh, F. Alobaid, M. T. Hasenzahl, J. Hilz, J. Ströhle, and B. Epple, "Comparison of three different CFD methods for dense fluidized beds and validation by a cold flow experiment," *Particuology*, vol. 29, pp. 34-47, 2016.
- [117] J. Parker, K. LaMarche, W. Chen, K. Williams, H. Stamato, and S. Thibault, "CFD simulations for prediction of scaling effects in pharmaceutical fluidized bed processors at three scales," *Powder Technology*, vol. 235, pp. 115-120, 2013.
- [118] S. Vashisth, A. H. Ahmadi Motlagh, S. Tebianian, M. Salcudean, and J. R. Grace, "Comparison of numerical approaches to model FCC particles in gas–solid bubbling fluidized bed," *Chemical Engineering Science*, vol. 134, pp. 269-286, 2015.
- [119] S. Karimipour and T. Pugsley, "Application of the particle in cell approach for the simulation of bubbling fluidized beds of Geldart A particles," *Powder Technology*, vol. 220, pp. 63-69, 2012.
- [120] Janitha Chandimal Bandara, Marianne Eikeland, and B. Moldestad, "Analyzing the effects of particle density, size, size distribution and shape for minimum fluidization velocity with Eulerian-Lagrangian CFD simulation," presented at the Proceedings of the 58th Conference on Simulation and Modelling (SIMS 58), 2017.
- [121] Chameera Jayarathna, Britt Moldestad, and L.-A. Tokheima, "Validation of results from Barracuda® CFD modelling to predict the minimum fluidization velocity and the pressure drop of Geldart A particles," presented at the Proceedings of the 58th Conference on Simulation and Modelling (SIMS 58), 2017.
- [122] Widuramina S. Amarasinghe, Chameera K. Jayarathna, Bovinda S. Ahangama, Britt M. E. Moldestad, and L.-A. Tokheim, "Experimental Study and CFD Modelling of Minimum Fluidization Velocity for Geldart A, B and D Particles," *International Journal of Modeling and Optimization*, vol. 7, no. 3, pp. 152-156, 2017.
- [123] G. Qiu, J. Ye, and H. Wang, "Investigation of gas–solids flow characteristics in a circulating fluidized bed with annular combustion chamber by pressure measurements and CPFD simulation," *Chemical Engineering Science*, vol. 134, pp. 433-447, 2015.
- [124] F. Fotovat, A. Abbasi, R. J. Spiteri, H. de Lasa, and J. Chaouki, "A CPFD model for a bubbly biomass–sand fluidized bed," *Powder Technology*, vol. 275, pp. 39-50, 2015.
- [125] F. Fotovat, J. Chaouki, and J. Bergthorson, "The effect of biomass particles on the gas distribution and dilute phase characteristics of sand–biomass

- mixtures fluidized in the bubbling regime," *Chemical Engineering Science*, vol. 102, pp. 129-138, 2013.
- [126] C. Chen, J. Werther, S. Heinrich, H.-Y. Qi, and E.-U. Hartge, "CPFD simulation of circulating fluidized bed risers," *Powder Technology*, vol. 235, pp. 238-247, 2013.
- [127] X. Shi, X. Lan, F. Liu, Y. Zhang, and J. Gao, "Effect of particle size distribution on hydrodynamics and solids back-mixing in CFB risers using CPFD simulation," *Powder Technology*, vol. 266, pp. 135-143, 2014.
- [128] X. Shi, Y. Wu, X. Lan, F. Liu, and J. Gao, "Effects of the riser exit geometries on the hydrodynamics and solids back-mixing in CFB risers: 3D simulation using CPFD approach," *Powder Technology*, vol. 284, pp. 130-142, 2015.
- [129] Y. Wu, L. Peng, L. Qin, M. Wang, J. Gao, and X. Lan, "Validation and application of CPFD models in simulating hydrodynamics and reactions in riser reactor with Geldart A particles," *Powder Technology*, vol. 323, pp. 269-283, 2018.
- [130] H. Cho, J. Kim, C. Park, K. Lee, M. Kim, and I. Moon, "Uneven distribution of particle flow in RFCC reactor riser," *Powder Technology*, vol. 312, pp. 113-123, 2017.
- [131] S. S. Rodrigues, A. Forret, F. Montjovet, M. Lance, and T. Gauthier, "CFD modeling of riser with Group B particles," *Powder Technology*, vol. 283, pp. 519-529, 2015.
- [132] D. Raheem, B. Zilmaz, and S. Ozdogan, "Cold Flow Simulation of a 30 kWth CFB Riser with CPFD," *Journal of Applied Fluid Mechanics*, vol. 13, pp. 603-614, 2020.
- [133] Q. Wang *et al.*, "Application of CPFD method in the simulation of a circulating fluidized bed with a loop seal, part I—Determination of modeling parameters," *Powder Technology*, vol. 253, pp. 814-821, 2014.
- [134] Q. Wang *et al.*, "Application of CPFD method in the simulation of a circulating fluidized bed with a loop seal Part II—Investigation of solids circulation," *Powder Technology*, vol. 253, pp. 822-828, 2014.
- [135] Q. Ma, F. Lei, and Y. Xiao, "Numerical analysis of operating conditions for establishing high-density circulating fluidized bed by CPFD method," *Powder Technology*, vol. 338, pp. 446-457, 2018.
- [136] Y. Jiang, G. Qiu, and H. Wang, "Modelling and experimental investigation of the full-loop gas–solid flow in a circulating fluidized bed with six cyclone separators," *Chemical Engineering Science*, vol. 109, pp. 85-97, 2014.
- [137] S. Kraft, F. Kirnbauer, and H. Hofbauer, "Influence of drag laws on pressure and bed material recirculation rate in a cold flow model of an 8MW dual fluidized bed system by means of CPFD," *Particuology*, vol. 36, pp. 70-81, 2018.
- [138] M. Upadhyay, H. C. Park, J. G. Hwang, H. S. Choi, H.-N. Jang, and Y.-C. Seo, "Computational particle-fluid dynamics simulation of gas-solid flow in a circulating fluidized bed with air or O₂/CO₂ as fluidizing gas," *Powder Technology*, vol. 318, pp. 350-362, 2017.

- [139] R. K. Thapa, A. Frohner, G. Tondl, C. Pfeifer, and B. M. Halvorsen, "Circulating fluidized bed combustion reactor: Computational Particle Fluid Dynamic model validation and gas feed position optimization," *Computers & Chemical Engineering*, vol. 92, pp. 180-188, 2016.
- [140] Janitha Bandara, Marianne Eikeland, and B. Moldestad, "Analyzing the Effects of Geometrical and Particle Size Uncertainty in Circulating Fluidized Beds using CPFD Simulation," presented at the Proceedings of The 60th SIMS Conference on Simulation and Modelling SIMS, Västerås, Sweden, 2019.
- [141] Q. Tu and H. Wang, "CPFD study of a full-loop three-dimensional pilot-scale circulating fluidized bed based on EMMS drag model," *Powder Technology*, vol. 323, pp. 534-547, 2018.
- [142] X. Zhu, P. Dong, Q. Tu, Z. Zhu, W. Yang, and H. Wang, "Investigation of gas-solid flow characteristics in the cyclone dipleg of a pressurised circulating fluidised bed by ECT measurement and CPFD simulation," *Measurement Science and Technology*, vol. 30, no. 5, p. 054002, 2019.
- [143] Y. Wu, X. Shi, C. Wang, J. Gao, and X. Lan, "CPFD Simulation of Hydrodynamics, Heat Transfer, and Reactions in a Downer Reactor for Coal Pyrolysis with Binary Particles," *Energy & Fuels*, vol. 33, no. 12, pp. 12295-12307, 2019.
- [144] M. Upadhyay, H. C. Park, and H. S. Choi, "Multiphase fluid dynamics coupled fast pyrolysis of biomass in a rectangular bubbling fluidized bed reactor: Process intensification," *Chemical Engineering and Processing - Process Intensification*, vol. 128, pp. 180-187, 2018.
- [145] G. Zhou, W. Zhong, A. Yu, and J. Xie, "Simulation of coal pressurized pyrolysis process in an industrial-scale spout-fluid bed reactor," *Advanced Powder Technology*, vol. 30, no. 12, pp. 3135-3145, 2019.
- [146] C. Jia, J. Li, J. Chen, S. Cui, H. Liu, and Q. Wang, "Simulation and prediction of co-combustion of oil shale retorting solid waste and cornstalk in circulating fluidized bed using CPFD method," *Applied Thermal Engineering*, vol. 165, p. 113574, 2020.
- [147] J. Yan *et al.*, "Validation and application of CPFD model in simulating gas-solid flow and combustion of a supercritical CFB boiler with improved inlet boundary conditions," *Fuel Processing Technology*, vol. 208, p. 106512, 2020.
- [148] Q. Liu, W. Zhong, and A. Yu, "Oxy-fuel combustion behaviors in a fluidized bed: A combined experimental and numerical study," *Powder Technology*, vol. 349, pp. 40-51, 2019.
- [149] S. Kraft, M. Kuba, F. Kirnbauer, K. Bosch, and H. Hofbauer, "Optimization of a 50 MW bubbling fluidized bed biomass combustion chamber by means of computational particle fluid dynamics," *Biomass and Bioenergy*, vol. 89, pp. 31-39, 2016.
- [150] Q. Liu, W. Zhong, J. Gu, and A. Yu, "Three-dimensional simulation of the co-firing of coal and biomass in an oxy-fuel fluidized bed," *Powder Technology*, vol. 373, pp. 522-534, 2020.
- [151] X. Chen, J. Ma, X. Tian, J. Wan, and H. Zhao, "CPFD simulation and optimization of a 50 kWth dual circulating fluidized bed reactor for chemical looping

- combustion of coal," *International Journal of Greenhouse Gas Control*, vol. 90, p. 102800, 2019.
- [152] J. M. Parker, "CFD model for the simulation of chemical looping combustion," *Powder Technology*, vol. 265, pp. 47-53, 2014.
- [153] D. Snider and S. Banerjee, "Heterogeneous gas chemistry in the CPFD Eulerian–Lagrangian numerical scheme (ozone decomposition)," *Powder Technology*, vol. 199, no. 1, pp. 100-106, 2010.
- [154] A. Klimanek and J. Bigda, "CFD modelling of CO₂ enhanced gasification of coal in a pressurized circulating fluidized bed reactor," *Energy*, vol. 160, pp. 710-719, 2018.
- [155] A. Di Nardo, G. Calchetti, and S. Stendardo, "Modeling and Simulation of an Oxygen-Blown Bubbling Fluidized Bed Gasifier using the Computational Particle- Fluid Dynamics (CPFD) Approach," *Journal of Applied Fluid Mechanics*, vol. 11, no. 4, pp. 825-834, 2018.
- [156] R. K. Thapa, C. Pfeifer, and B. M. Halvorsen, "Modeling of reaction kinetics in bubbling fluidized bed biomass gasification reactor," *INTERNATIONAL JOURNAL OF ENERGY AND ENVIRONMENT*, vol. 5, no. 1, pp. 35-44, 2014.
- [157] C. Loha, H. Chattopadhyay, and P. K. Chatterjee, "Three dimensional kinetic modeling of fluidized bed biomass gasification," *Chemical Engineering Science*, vol. 109, pp. 53-64, 2014.
- [158] J. Xie, W. Zhong, B. Jin, Y. Shao, and H. Liu, "Simulation on gasification of forestry residues in fluidized beds by Eulerian–Lagrangian approach," *Bioresource Technology*, vol. 121, pp. 36-46, 2012.
- [159] J. Xie, W. Zhong, B. Jin, Y. Shao, and Y. Huang, "Eulerian–Lagrangian method for three-dimensional simulation of fluidized bed coal gasification," *Advanced Powder Technology*, vol. 24, no. 1, pp. 382-392, 2013.
- [160] H. Liu, R. J. Cattolica, and R. Seiser, "CFD studies on biomass gasification in a pilot-scale dual fluidized-bed system," *International Journal of Hydrogen Energy*, vol. 41, no. 28, pp. 11974-11989, 2016.
- [161] D. Kong, S. Wang, K. Luo, C. Hu, D. Li, and J. Fan, "Three-dimensional simulation of biomass gasification in a full-loop pilot-scale dual fluidized bed with complex geometric structure," *Renewable Energy*, vol. 157, pp. 466-481, 2020.

Annexure A

Literature review:

Compositional analysis of pyrolysis products and reaction kinetics for modeling of Biomass Gasification.

Compositional analysis of pyrolysis products and reaction kinetics for modeling of Biomass Gasification

Formation Enthalpy and Chemical composition of Biomass

Biomass is a complex material in which the composition changes between species, because of age and from one place to another depending on rainfall, soil conditions etc. Therefore, its chemical formulae is not unique. Carbon, hydrogen and oxygen are the primary elements that builds the biomass structure, where there can be minor amounts of nitrogen, sulphur, chlorine and non-reactive ash formed from mineral components including aluminum, silica, calcium, ferrous, magnesium, sodium, phosphorous etc. Moisture is abandoned in fresh biomass and however, a drying process can separate it out. Therefore, in dry and ash-free (daf) basis, the chemical formulae of biomass can be expressed as $CH_aO_bN_cS_d$. The subscripts a, b, c and d are molar composition of relevant elements normalized based on carbon moles [1]. Enthalpy of formation is a key parameter in modeling of biomass gasification that depends on its composition. Rodriguez-Alejandro et al [2] used a formulation that used hydrogen molar value “a” to predict the formation enthalpy of biomass.

$$h_{f,biomass}^{\circ} = (-190.3 - 1407a) \left(\frac{btu}{lb}\right)$$

However, many studies have used the heating value of biomass under complete oxidization to calculate the formation enthalpy [3].

$$h_{f,biomass}^{\circ} = LHV_{biomass} + h_{f,CO_2}^{\circ} + \frac{a}{2} h_{f,H_2O}^{\circ}$$

Higher heating value (HHV) is defined as the heat energy (per unit mass or volume) after complete oxidation and bringing down the product temperature to 25°C. The lower heating value (LHV) is what we get after subtracting the heat of vaporization of water vapor from HHV. The higher heating value can be experimentally determined in a bomb calorimeter or calculated based on elemental composition of biomass. As an example [4],

$$HHV_{biomass}(MJ/kg) = 0.3536\%C + 1.1783\%H + 0.1005\%S - 0.1034\%O - 0.0151\%N - 0.0211\%Ash$$

Or proximity analysis,

$$HHV_{biomass}(MJ/kg) = 0.3491\%FC + 0.1559\%VM - 0.0078\%Ash [5]$$

Table 1: Correlations for HHV estimations

Formula	Reference
Proximity analysis data	
$HHV = 0.196(FC) + 14.119$	[6]
$HHV = 0.312(FC) + 0.1534(VM)$	[6]
$HHV = -10.81408 + 0.3133(VM + FC)$	[7]
$HHV = 0.3543(FC) + 0.1708(VM)$	[8]
$HHV = 19.914 - 0.2324(AC)$	[9]
$HHV = -3.0368 + 0.2218(VM) + 0.2601(FC)$	[9]
$HHV = 0.3536FC + 0.1559VM - 0.0078AC$	[5]
$HHV = 0.1905(FC) + 0.2521(VM)$	[10]
Ultimate analysis data	
$HHV = 0.2949C + 0.8550H$	[10]
$HHV = 0.3259C + 3.4597$	[9]
$HHV = 0.4373C - 1.6701$	[11]
$HHV = 0.335C + 1.423H - 0.154O - 0.0151N$	[6]
$HHV = 0.3491C + 1.1783H + 0.1005S - 0.1034O$	[4]

Table 2: Properties of different biomass feedstock

Species	Ultimate Analysis (%)				Proximity Analysis (%)				LHV/HHV* (MJ/kg)	Ref
	C	H	O	N	VM	FC	M	Ash		
Beech	48.1	5.9	45.4	0.2	74.8	15.7	8.8	0.7	15	[12]
Pine	51.3	5.8	42.3	0.1	78.1	14.7	6.3	0.5	17.4	[13]
pine	47.9	6.2	38.3		79.7	12.7	7.5	0.1	17.6	[14]
Pine bark	55.5	5.6	37.7	0.17	62.5	25.7	10.9	0.85	20	[15]
MSW	48	6.3	43.6	1.39	79.8	20	17.6	0.2	14.4	[16]
Rice straw	35.6	4.63	58.7	0.94	62.8	15.9	13.5	7.8		[17]
Species	Cellulose %			Hemicellulose%		Lignin%		Extractives		Ref
Almond shell	26			30		33		-		[18]
Hardwood	43			35		22				[19]

Pyrolysis

The first process to occur during thermochemical conversion is the moisture evaporation from biomass. However, in fluidized beds, as the biomass particles are fed into a high temperature zone, moisture evaporation can be considered as instant. As the particles are heated over 150°C, the pyrolysis process starts. The solid biomass undergoes thermal decomposition breaking up into three distinguishable products of charcoal, permanent gases and tar which is a condensable gas at lower temperatures. The quantitative and qualitative understanding each of this fractions is crucial in gasification reactor designing [20].

As the product distribution is a complex function of many process parameters and chemical and physical properties of feedstock, researchers find it difficult to formulate a universal pyrolysis model [21]. Therefore, the inclusion of most compatible pyrolysis sub-model is one of the decisive components during the construction of gasification model. As an example, the bed temperature of an auto-thermal bubbling fluidized bed gasifier is maintained by char oxidation reactions. Hence, if the char mass fraction used in the model is lower than the actual, the reactor bed temperature can be lower compared to experiments. On the other hand, over 80% of the initial biomass weight ends up in the volatile phase. The gas residence time in the freeboard of a fluidized bed reactor may be not sufficient to reach the equilibrium and consequently, the pyrolysis gas composition, itself, partially decides the final gas composition. Therefore, inaccurate implementation of pyrolysis gas composition may lead to deviated results [22, 23].

Many pyrolysis studies have been performed using Thermogravimetric analysis (TGA) starting from reduced temperatures followed by heating at known rates. However, in a fluidized bed, biomass particles are directly fed to the high temperature sand bed. Further, biomass particles are prepared at sub-millimeter scale for TGA experiments whereas it can be several centimeters in a reactor. According to the pyrolysis mechanism, these differences are significant and consequently add uncertainties to the gasification model predictions. As illustrated in Figure 1, the relative fraction of the char can be approximated by the fixed carbon content given in proximity analysis. However, some studies found that the char fraction after pyrolysis was higher than the fixed carbon in proximity analysis [24]. Based on chemical composition, fractional char yield from cellulose, hemicellulose and lignin are 0.05, 0.1 and 0.55 respectively [19]. The respective values are 0, 0.075 and 0.3 as stated by Blondeau and Jeanmart [23]. Taking the difference between fixed carbon and elemental carbon given in ultimate analysis, the carbon content transferred to the volatile phase is possible to calculate. Whenever, the temperature rise above 1000°C, the soot formation is also important which force tiny carbon particles into the gaseous phase of the reactor. The soot formation is maximum approximately around 1200°C and less significant below 1000°C [25, 26]. The total hydrogen and oxygen content, available in ultimate analysis, can be assumed to migrate into the volatile phase [26]. Different studies used number of different methods to formulate the composition of the volatile phase. Numerical values from experiments with similar conditions can directly be used.

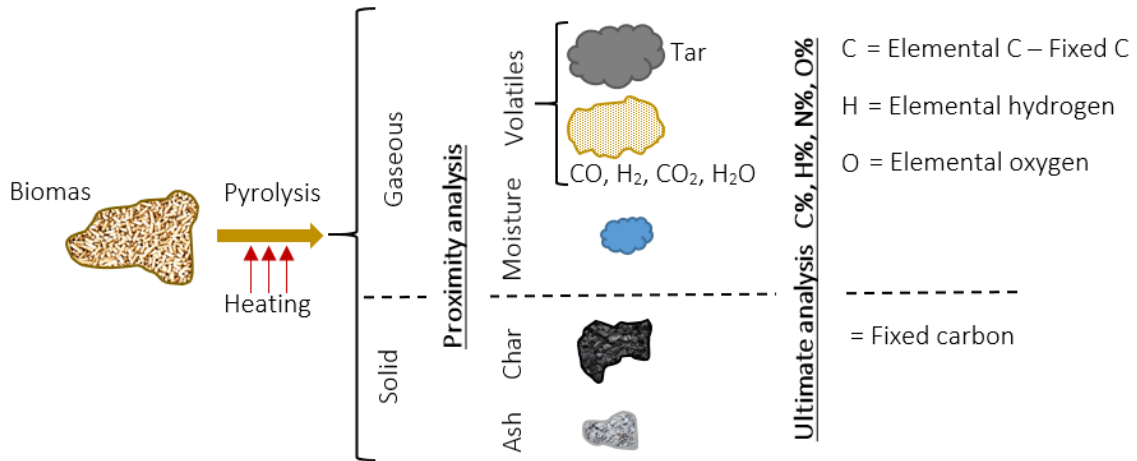


Figure 1: Quantification of biomass pyrolysis products

Gas composition from Pyrolysis

Several studies have tried to present the relative compositions of char, tar and permanent gases using temperature dependent equations. The CO₂, CO, H₂ and CH₄ composition in the gas phase was also tried to present similarly as functions of temperature [27]. In the equations, Y refers to the mas fractions.

$$Y_{char} = 7.97 \times 10^{-5}T^2 - 0.125 \times T + 68.87$$

$$Y_{tar} = -1.38 \times 10^{-4}T^2 + 0.12 \times T + 12.64$$

$$Y_{gas} = 1.12 \times 10^{-4}T^2 - 0.058 \times T + 30.77$$

$$Y_{CO/gas} = -2.65 \times 10^{-4}T^2 + 0.27 \times T - 32.71$$

$$Y_{CO_2/gas} = -2.85 \times 10^{-5}T^2 - 0.029 \times T + 70.89$$

$$Y_{CH_4/gas} = 6.69 \times 10^{-5}T^2 - 0.037 \times T + 4.28$$

$$Y_{H_2O/gas} = 7 \times 10^{-5}T^2 - 0.0371 \times T + 5.1117$$

A similar set of equations were developed for 5mm thick wood chips in fluidized bed conditions. The rate of particle heating was mentioned as 20-40 °Cs⁻¹ where the data can be used between 700°C and 1000°C. The tar generation is included using four chemical components. The temperature is in Kelvin scale [28].

Table 3: Prediction of pyrolysis product composition

Product mass yield	Model equation $aT^2 + bT + c$		
	a	b	c
Permanent gases			
CH ₄	-4.341×10^{-5}	10.12×10^{-2}	-51.08
H ₂	1.362×10^{-5}	-2.517×10^{-2}	12.19
CO	-3.524×10^{-5}	9.770×10^{-2}	-24.93
CO ₂	3.958×10^{-5}	-9.126×10^{-2}	64.02
C ₂ H ₂	-6.873×10^{-5}	14.94×10^{-2}	-76.89
C ₂ H ₆	8.265×10^{-6}	-2.105×10^{-2}	13.38
Tar			
C ₆ H ₆ (benzene)	-3.134×10^{-5}	7.544×10^{-2}	-42.72
C ₇ H ₈ (Toluene)	-4.539×10^{-6}	0.687×10^{-2}	1.462
C ₆ H ₆ O (Phenol)	1.508×10^{-5}	-3.662×10^{-2}	22.19
C ₁₀ H ₈ (Naphthalene)	-8.548×10^{-6}	1.882×10^{-2}	-9.851
H ₂ O	5.157×10^{-5}	11.86×10^{-2}	84.91

A similar work is found which was developed for pyrolysis of wood pellets in a bubbling fluidized bed reactor [29] where a graphical illustration is given in Figure 2.

$$X_i = m_{0,i} \times T^{b_{0,i}} \quad i - CO, H_2, CO_2, CH_4$$

$$\log_{10} X_i = \log_{10} m_{0,i} + b_{0,i} \log_{10} T$$

Species	$m_{0,i}$	$b_{0,i}$
H ₂	1.3353×10^{-16}	5.72682
CO	1.8006×10^7	-1.87095
CO ₂	2.4808×10^3	-0.69559
CH ₄	4.4313×10^5	-1.49449

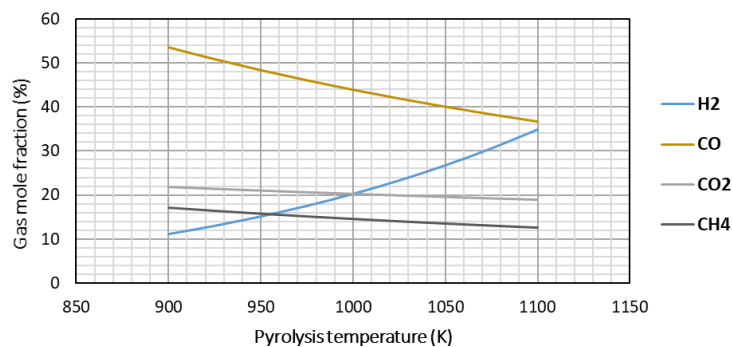


Figure 2: Change of pyrolysis gas composition over temperature [29].

Other studies focused on solving a linear system to obtain the gas phase mole fractions [30].

$$\begin{pmatrix} X_{CO} \\ X_{CO_2} \\ X_{H_2} \\ X_{CH_4} \\ X_{H_2O} \\ X_{C_6H_6} \\ X_{C_{10}H_8} \\ X_{C_6H_6O} \end{pmatrix} = \begin{bmatrix} 1/M_{CO} & 1/M_{CO_2} & 0 & 1/M_{CH_4} & 0 & 6/M_{C_6H_6} & 10/M_{C_{10}H_8} & 6/M_{C_6H_6O} \\ 0 & 0 & 2/M_{H_2} & 4/M_{CH_4} & 2/M_{H_2O} & 6/M_{C_6H_6} & 8/M_{C_{10}H_8} & 6/M_{C_6H_6O} \\ 1/M_{CO} & 2/M_{CO_2} & 0 & 0 & 1/M_{H_2O} & 0 & 0 & 1/M_{C_6H_6O} \\ 1 & -\Omega_1 & 0 & 0 & 0 & 0 & 0 & 0 \\ 0 & -\Omega_2 & 0 & 0 & 0 & 0 & 0 & 0 \\ 0 & -\Omega_3 & 0 & 1 & 0 & 0 & 0 & 0 \\ 0 & 0 & 0 & 0 & 0 & -\Omega_4 & 0 & 1 \\ 0 & 0 & 0 & 0 & 0 & -\Omega_5 & 1 & 0 \end{bmatrix} \times \begin{pmatrix} Y_{C,vol}/M_C \\ Y_{H,vol}/M_H \\ Y_{O,vol}/M_O \\ 0 \\ 0 \\ 0 \\ 0 \\ 0 \end{pmatrix}$$

The tar fraction is modeled with benzene, naphthalene and phenol. “X” refers to the mole fractions of gas phase and “Y_{vol}” refers to the elemental mass fractions of the volatile phase. The information about molar production ratios of Ω_1 , Ω_2 and Ω_3 as a function of temperature is important to proceed with the calculations [31].

$$\begin{aligned}
\Omega_1 &= X_{CO}/X_{CO_2}, \Omega_2 = X_{H_2O}/X_{CO_2}, \Omega_3 = X_{CH_4}/X_{CO_2} \\
Y_{CO}/Y_{CO_2} &= \exp(-1.845 + 7730.3/T - 5019898/T^2) \\
Y_{H_2O}/Y_{CO_2} &= 1 \\
Y_{CH_4}/Y_{CO_2} &= 5 \times 10^{-16} \times T^{5.06}
\end{aligned}$$

Ω_4 and Ω_5 models the relative fractions of tar components which are given by,

$$\Omega_4 = X_{C_6H_6O}/X_{C_6H_6}, \Omega_5 = X_{C_{10}H_8}/X_{C_6H_6}$$

The phenol fraction is equivalent with the lignin content of the biomass whereas the benzene and naphthalene fractions are equivalent with half of the cellulosic content (cellulose + hemicellulose). However, in contrast to pyrolysis process, the gasification is carried out at elevated temperatures and therefore, tar is cracked to form gaseous compounds. As a result, many research works have neglected the tar generation/cracking during the gasification model development. The rate equations have also been used to approximate the volatile composition after pyrolysis [22].

$$VM = (Y_{CO})CO + (Y_{CO_2})CO_2 + (Y_{H_2})H_2 + (Y_{H_2O})H_2O + (Y_{CH_4})CH_4 + (Y_{Tar1})Tar1$$

$$Y_{CO} : Y_{CO_2} : Y_{H_2} : Y_{H_2O} : Y_{CH_4} : Y_{Tar1} = r_{CO} : r_{CO_2} : r_{H_2} : r_{H_2O} : r_{CH_4} : r_{Tar1}$$

$$r_i = K_i e^{\left(\frac{-E_i}{RT}\right)}$$

$$Y_{CO} + Y_{CO_2} + Y_{H_2} + Y_{H_2O} + Y_{CH_4} + Y_{Tar1} = 1$$

Component	K_i (1/s)	E_i (kJ/mol)
CO	9.00×1009	111.0
CO ₂	5.23×1009	105.0
H ₂	4.73×1004	92.5
H ₂ O	3.68×1013	149.5
CH ₄	1.09×1005	71.3
Tar ₁	2.09×1010	112.7

The above methods present a general construction where the volatile composition can be evaluated as a function of temperature. In contrast, many other research publications present directly the numerical values for volatile composition along with process conditions such as temperature, particle size, heating rate and reactor configuration.

Product yields and gas compositions related to flash pyrolysis at high temperatures and N₂ environment are given in Table. The product yields and gas compositions are very much different from each other. The H₂ content of the pyrolysis gas is extremely low at lower temperatures and boosts with temperature. At elevated temperatures, the tar content reached a negligible level in some studies. The liquid or tar fraction is maximized around 500°C temperature and sharply reduced above 700°C [32, 33]. Besides CH₄, ethylene C₂H₄ is the significant hydrocarbon exists in the gaseous product of pyrolysis. The C₂ hydrocarbon content is higher for grass. Above 700°C, the derived char has <3% of volatiles and can be considered as carbon. Further, the CO₂ content of the gaseous fraction is high in almond shell and straw compared to wood. However, CO is the main component in the pyrolysis gas stream at higher temperatures than 600°C whereas CO₂ dominant at lower temperatures [34]. H₂ content also boosts as the pyrolysis temperature is increased whereas the CH₄ content is not likewise sensitive over temperature [35]. Figure 3 illustrates the relative proportions of gaseous, tar and char under varying temperature whereas Figure 4 depicts information about the evolution of the product composition over time.

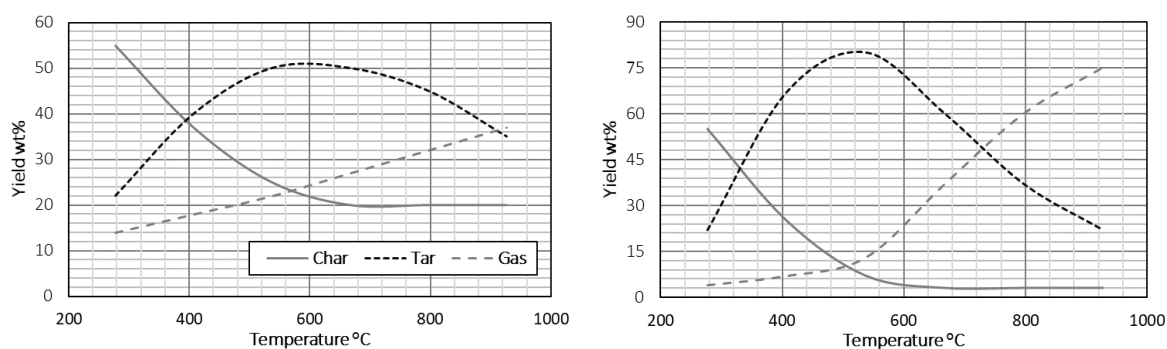


Figure 3: Relative fractions of char, gas and tar from pyrolysis under varying temperature. Left [33], right [36], re-drawn

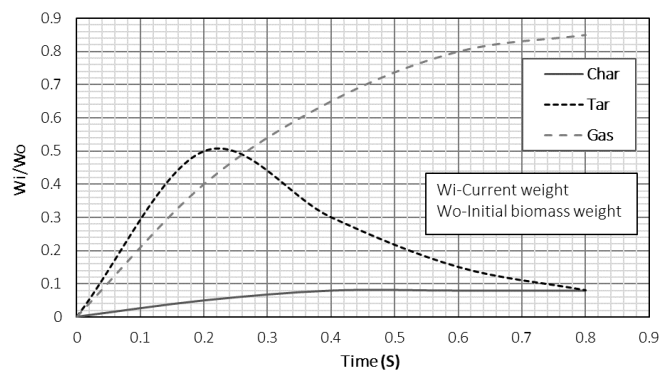


Figure 4: Change in product composition with time [37], re-drawn

Several studies have considered the volatile phase as a single compound with $C_xH_yO_z$ as the chemical formula. The volatiles are then oxidized to form CO and H₂, which continue to break down into CO₂ and H₂O [14, 20].

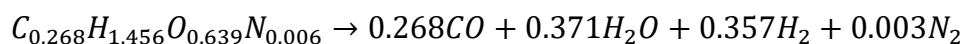


Table 4: Product yield and gas phase composition from fast pyrolysis

Biomass	Temp	P. Size	Char	Tar	Gas	CO	CO ₂	H ₂	C _x H _n	CH ₄	Ref.
	°C										
Almond shell	500	0.6-2.5	26	49.3	24.7	39	39	7		15	[24]
Almond shell	800	0.6-2.5	21.5	31	47.5	34	19	28		19	[24]
Wheat straw	800	0.5-1	13.2	1	75.8	28	24	35	3	10	[38]
Birch wood	800	0.8-1	7.2	1.1	77.7	50.3	8.3	16.2	6.2	16.2	[38]
Birch wood	1000	0.8-1	5.6	0.2	87	45.7	7.5	34	0.5	11.7	[38]
Softwood	800	0.4	15	10	75	55	5.7	21.5	7.8	10	[39]
Softwood	1000	0.4	15	10	75	48.5	5.5	29	7	10	[39]
Switch grass	510	0.25-1	20	45.3	16.5	25.6	16.2	36	13.2	9	[40]
Beech wood	512	0.25-1	14.5	55.5	13	31.5	19.2	46.5	1.2	1.6	[40]

Other studies has given the mass yield of pyrolysis as kg/kg of biomass [41]. Nunn, et al. [42] have stated the percentage migration of carbon, hydrogen and oxygen into char, tar and gases during primary pyrolysis. Further, in their study, the Arrhenius coefficients of chemical kinetics for pyrolysis are given separately for each compound rather than single values. The total volatile was 92% with 41% of gas and 51% tar. Yan, et al. [43] have tested palm oil waste in a TGA coupled with FTIR over a wide range of temperatures. The gas phase was mainly consisted with CO (25% mol) and H₂ (45% mole) above 800°C temperature whereas char yield was 25%. Below 700°C, other gases of H₂O, CH₄ and CO₂

were present in significant amounts. Loha, et al. [44] have considered the weight fractions of pyrolysis gas [H_2 , CO , CO_2 , CH_4 , and H_2O] as [0.026, 0.476, 0.261, 0.085, and 0.152] at $800^\circ C$ and [0.033, 0.465, 0.268, 0.082, 0.0152] at $900^\circ C$.

A gas species prediction scheme (algorithm), as illustrated in Figure xx has also been used in some studies [20].

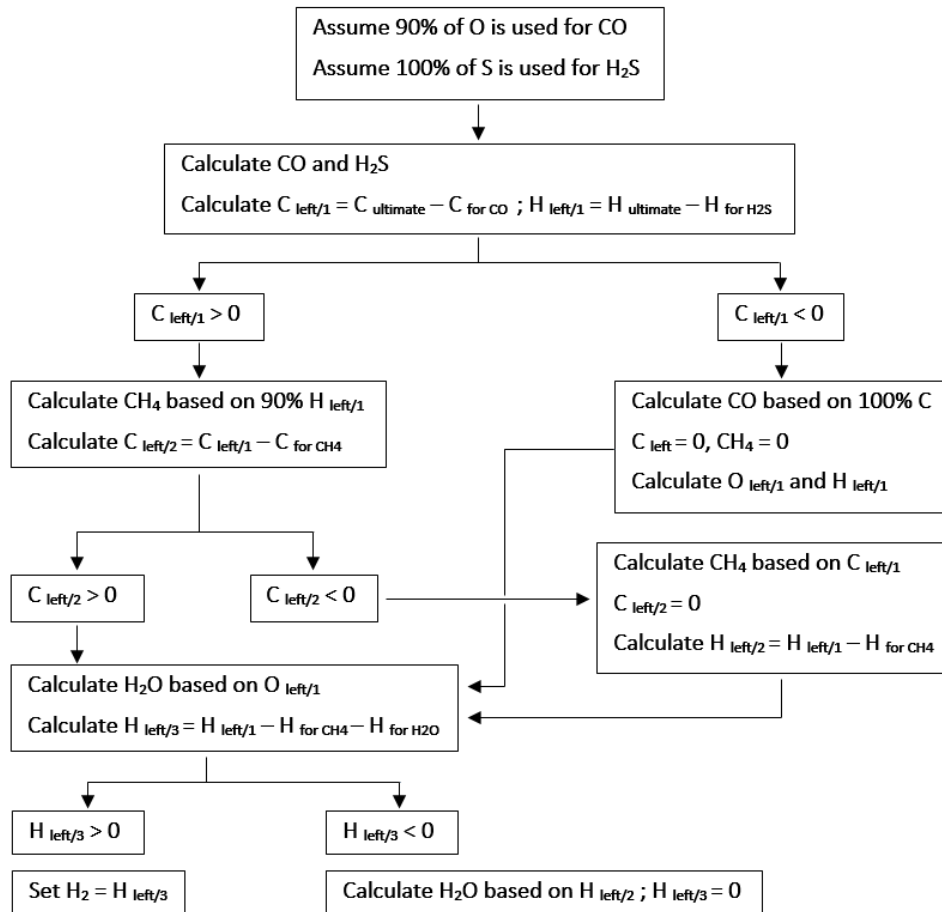


Figure 5: Prediction algorithm for pyrolysis gas composition

The maximum gas yields (mass) of pyrolysis of 1 mm wood particles at a 5 K/min heating rate up to 1173K are given in Figure 6.

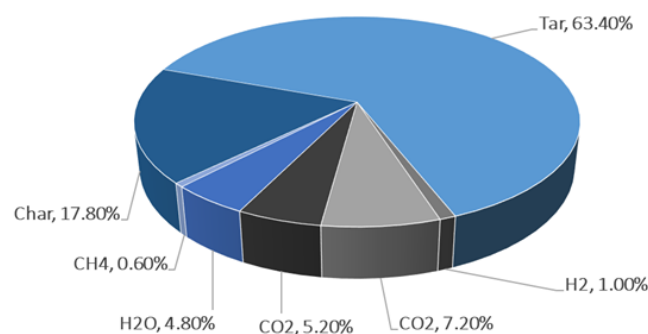


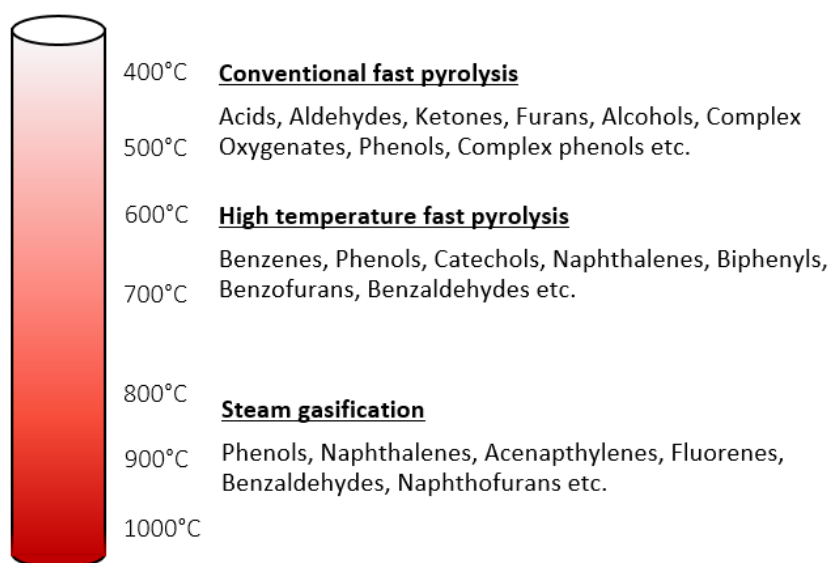
Figure 6: Maximum gas yields of wood pyrolysis [45]

The size of wood particles is another important parameter for the pyrolysis product distribution. Some studies observed that gas yield increases proportionally with size while tar shows a opposite trend [35]. In contrast, gas yield is slightly decreasing and tar is slightly increasing in other studies [46]. In common, both studies observed that the char fraction is increased with the particle size.

Tar Generation and composition

Modeling of tar formation, restructuring, reforming and cracking is a difficult task. There can be hundreds of different chemical components whereas some heavier components are GC undetectable. In general, tar can be defined as a mixture of hydrocarbons with single to 5-ring aromatic compounds, oxygenated hydrocarbons and complex poly-aromatic hydrocarbons (PAH). In general, it has been agreed to define tar as any organic contaminant with a molecular weight larger than benzene [47]. As illustrated in Table, it is reasonable to eliminate the tar production at elevated reactor/pyrolysis temperatures above 800°C. In contrast, the exclusion of tar at reduced temperatures than 800°C could lead to deviated results in the gas composition.

Tars are classified in to three main categories. Primary tars from pyrolysis occur at 400°C-700°C temperature, which is mainly consisted with oxygenated compounds. At elevated temperature, primary tar is restructured to form secondary and tertiary products. Secondary products include phenolic and olefin compounds formed at 700°C-850°C. As the temperature is increased further beyond 850°C, tertiary compounds such as naphthalene and poly aromatic hydrocarbons (PAH) appear [48]. Soot formation also become significant at elevated temperature, mainly originated from tertiary tar cracking.



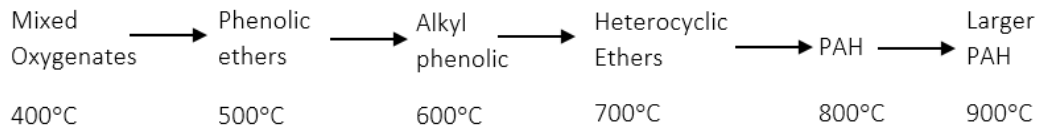


Figure 7: Formulation of tar during pyrolysis and gasification as a function of temperature [49] [50], re-drawn

When it comes to modelling, many authors have excluded the complex formulation of tar and instead, tar was represented by few compounds as benzene (C_6H_6), toluene (C_7H_8), phenol (C_6H_6O) and Naphthalene ($C_{10}H_8$) as it compose 70-95% of the tar [51, 52]. Naphthalene represent the PAHs which is the cause for soot formation [53]. Number of efforts are available where the mass yields (g/kg of biomass) of these compounds are modeled as a function of temperature [52].

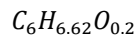
$$Y_{C_7H_8} = -6 \times 10^{-5}T^2 + 0.10701 T - 48$$

$$Y_{C_{10}H_8} = -1 \times 10^{-4}T^2 + 0.218 T - 115.32$$

$$Y_{C_6H_6} = -3 \times 10^{-4}T^2 + 0.7017 T - 387.6$$

$$Y_{C_6H_6O} = -2 \times 10^{-5}T^2 - 0.068 T + 46.42$$

Some other studies has taken the tar as a single compound with a chemical formula [31];



Pyrolysis enthalpy and properties of pyrolysis products

As mentioned previously, the moisture evaporation is fast in a gasification reactor. The related enthalpy can be calculated based on the moisture content (kg/kg of biomass) and latent heat of evaporation, which is approximately 2.2 MJ/kg at atmospheric pressure. The enthalpy of pyrolysis is formulated using the resultant of sensible heat for particle heating and devolatilization enthalpy [54].

The heat capacity (CP) of biomass varies with temperature and moisture content. However, the knowledge of CP on dry basis is enough as the effect of moisture can be integrated with the CP of water up to 60% moisture [55]. The effect of the temperature can only be recorded up to 150°C temperature as the biomass devolatilization starts afterwards. Therefore, CP should be separately considered for raw biomass and char for precise calculations. Further on biomass CP can be highly varied depending on species and pretreatment such as densification (i.e. palletization) whereas the CP of char can further be varied depending on pyrolysis conditions. However, unique values of CP for all biomass types has been used in many designing calculations. The heat capacity measurements are performed either in adiabatic calorimeter or differential scanning calorimetry (DSC). Dupont, et al. [55] experimentally analyzed the CP of 21 different biomass types including beech, pine, poplar, rice husk, miscanthus, wheat straw etc. At

310K, the CP varied between 1300 J/kg/K and 1500 J/kg/K whereas 1400 J/kg/K and 1750 J/kg/K at 350K. Further, CP showed a linear relationship against temperature. In contrast, developing a temperature dependent correlation for char CP is difficult, especially for chars derived at lower temperature. However in general, the CP of char can be taken as 1000 J/kg/K and 1500 J/kg/K between 310K and 550K temperature. Pauner and Bygbjerg [56] used CP as 2200 J/kg/K and thermal conductivity as 0.17 W/m/K in his studies. Thermal conductivity (TC) is also important parameter where lower values result in a temperature gradient for larger particles. Guo, et al. [57] has reported that the TC depend on fiber orientation where it is higher in grain direction compared to perpendicular direction. Therefore, the TC of original wood pieces is higher than the wood pellets of same wood sample as the fibers are ground for pelletizing. The authors has summarized several values and correlations for CP and TC of biomass from literature [58-60]. Singh and Goswami [61] investigated the thermal properties using cumin seed and concluded that the CP and TC can be modeled by a second order polynomial related to temperature and moisture.

Table 5: Thermal properties of biomass species

Species	Thermal conductivity (W/m/K)	Specific heat capacity (kJ/kg/K)
Wood	$0.002(\rho_{dry} + 0.024)$	$0.0046T - 0.113$ [0 – 100C]
Wood	0.55 [Parallel to grain]	1.07 [20 – 150C dry]
	0.11 [perpendicular to grain]	1.38 [9.5% M]
Soft wood	0.098	$0.00546T - 0.524$
Alfalfa pellets	$0.049 + 0.0082M$	$1.083 + 0.089M - 0.0021M^2$
Fir	0.2	1.733
spruce	0.32	1.112
Soft wood	$0.219 + 0.01M$	$1.01 + 0.032M$
Peanut shells	0.12 [3.5% M], 0.16 [28.7% M]	2.7, 4.1

M – moisture content

The CP of biomass accounts for the sensible heat absorption during particle heating. In addition the enthalpy of devolatilization should also be incorporated. Pyrolysis is a complex process with many factors affecting to the final product. As an example, the temperature causes significant changes in the reaction chemistry and thus the enthalpy. Even though the pyrolysis is believed to be endothermic in general, the exothermicity of intermediate reactions such as tar condensation and tar conversion into secondary char, have been discussed in literature. As the pyrolysis moves from atmospheric pressure to high pressures, the HP moves from endothermic to endothermic, which is indirectly represented by higher char yield. [62-64]. A possible reason is the exothermic secondary reactions occurs as the volatile phase migrate through a large biomass particle [65]. According to the literature mentioned by Daugaard and Brown [54], the pyrolysis enthalpy (HP) can be in the range of 0.7 MJ/kg to 3.5 MJ/kg. The authors experimentally

found the HP of oak, oat hulls, pine and corn-stover to be 1.46, 0.78, 1.64 and 1.35 MJ/kg respectively with ± 0.3 MJ/kg deviation. The study of Hosokai, et al. [66] reported that the HP is possible to vary from -0.5 to 1.5 MJ/kg depending on the product yield. Further in their study, the endothermicity and exothermicity were illustrated graphically as in Figure 8.

The heating value and other thermal properties of gaseous mixture can be calculated by summing up weighted average properties of individual gas species, if the gas composition is known. In contrast, the properties of char and liquid/tar/oil fraction can be varied depending on biomass and pyrolysis conditions.

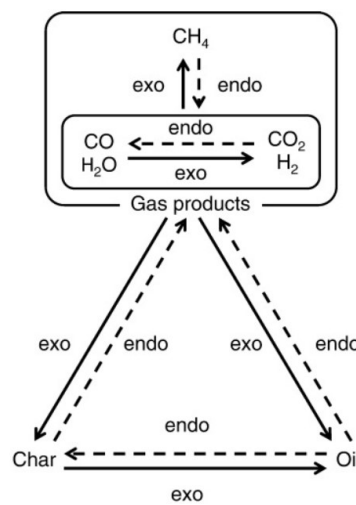


Figure 8: The process trends of biomass pyrolysis towards exothermic or endothermic

Pyrolysis Kinetics

Majority of the pyrolysis kinetics found in literature were developed for discrete phase where the Arrhenius type rate equation is extended with a function of conversion. However, only volume averaged rate equations are mentioned here.

Notes	Rate	Units	Ref.
	$2.119 \times 10^{11} \exp\left(-2.027 \times 10^5 / RT\right) [\text{volatile}]^{1.5}$		[30]
Drying at 400 °C	$5.13 \times 10^6 \exp\left(-8.8 \times 10^4 / RT\right) [\text{moisture}]$	mol/m ³ s	[31]
	$7.0 \times 10^7 \exp\left(-1560 / T\right) [\text{volatile}]$		[19]
Three parallel reaction model	$R_{gas} = 1.44 \times 10^4 \exp\left(-8.86 \times 10^4 / RT\right) [BM]$ $R_{tar} = 4.13 \times 10^6 \exp\left(-1.12 \times 10^5 / RT\right) [BM]$ $R_{char} = 7.38 \times 10^5 \exp\left(-1.065 \times 10^5 / RT\right) [BM]$	mol/m ³ s	[15, 67]
	$3.4 \times 10^4 \exp\left(-6.9 \times 10^4 / RT\right) [Vol]$		[14]

Drying		$5.13 \times 10^{10} \exp(-10585/T)$ [moisture]	[68]
Global reaction without tar		$C_{19.82}H_{24.52}O_{11.86} \rightarrow 5.96CO + 2.95CO_2 + 8.26H_2 + 1.5CH_4 + 0.5C_2H_4 + 8.41C$ Reaction enthalpy - 310 kJ $1.49 \times 10^5 \exp(-1340/T)$ [volatile]	[68]

Ranzi, et al. [69] and Blondeau and Jeanmart [70] have presented a detailed pyrolysis kinetics and secondary cracking based on different biomass constituents of cellulose, hemicellulose and lignin. Modeling of drying has several approaches. The first and simplest method is to work on an energy balance considering infinite thin drying front. The next and mostly used construction in CFD modeling is considering the drying as a chemical reaction, which is modeled with an Arrhenius type expression. A moisture dependent expression for temperature is another approach that describes the equilibrium moisture content in wood. The fourth method is the diffusion models derived based on experimental and numerical modeling [67].

Gasification Reactions

When it comes to gasification reaction after the primary pyrolysis, many of the modelling efforts considered simple reaction mechanism excluding the intermediates. Some research works considered the temperature dependent fractions for CO and CO₂ to model the char oxidation [45]. Oxygen is a limiting component in gasification and therefore in many studies, the oxidation first converts char into CO followed by CO oxidation. The water-gas shift reaction is biased back and forth depending on reaction temperature and therefore, the reverse reaction is considered. Methane reforming is also important and together with water-gas shift, the composition of the gas is strongly influenced. Chemical kinetics of these reactions is also important, especially in kinetic and CFD modeling. It carries the information whether the residence time is enough for complete conversion under process conditions. However, the kinetics used in literature is highly varied.

Table 6: Principle reactions considered during modeling (excluding tar) [43, 71]

Enthalpy	Reaction	Name	Reaction
Homogeneous reactions			
-41	$CO + H_2O \rightarrow CO_2 + H_2$	Water-gas shift	1
-283	$CO + 0.5O_2 \rightarrow CO_2$	CO oxidation	2
-242	$H_2 + 0.5O_2 \rightarrow H_2O$	H ₂ combustion	3
	$CH_4 + 2O_2 \rightarrow CO_2 + 2H_2O$	Methane oxidation	4.1
	$CH_4 + 1.5O_2 \rightarrow CO + 2H_2O$	Methane oxidation	4.2
	$CH_4 + 0.5O_2 \rightarrow CO + 2H_2$	Methane oxidation	4.3
+206	$CH_4 + H_2O \rightarrow CO + 3H_2$	Methane reforming	5

Heterogeneous reaction			
-111	$C + 1/2 O_2 \rightarrow CO$	Char Partial oxidation	6.1
-394	$C + O_2 \rightarrow CO_2$	Char combustion	6.2
	$2 \left(\frac{\pi + 1}{\pi + 2} \right) C + O_2 \rightarrow \left(\frac{2\pi}{\pi + 2} \right) CO$ $+ \left(\frac{2\pi}{\pi + 2} \right) CO_2$ $\pi = 3 \times 10^8 \exp(-30178/T_p)$ $[CO]/[CO_2] = 2400 \left(\exp(-51830/RT) \right)$	Char combustion [72]	6.3
	$C_x H_y O_z + (x/2 - z/2) O_2$ $\rightarrow xCO + y/2 H_2$	Char Partial oxidation	6.4
+172	$C + CO_2 \rightarrow 2CO$	Boudouard reaction	7
+131	$2C + H_2O \rightarrow CO + H_2$ $2C + \beta H_2O \rightarrow (2 - \beta)CO + \beta H_2$ $+ (\beta - 1)CO_2$ $\beta = 1.2$	Steam gasification	8.1 8.2
-75	$C + 2H_2 \rightarrow CH_4$	Methanation	9
The enthalpy is given in (kJ/mol)			

Table 7: Gasification kinetic rate equations and other modeling parameters

Reaction	Units	Eq.	Ref
Water gas shift reaction			
$2.78 \exp(-1.26 \times 10^4/RT) [CO] [H_2O]$	kmol/m ³ /s	1	[30]
$2.78 \times 10^3 \exp(-1.26 \times 10^4/RT) \left([CO][H_2O] - \frac{[CO_2][H_2]}{0.029 \exp(\frac{4094}{T})} \right)$	kmol/m ³ /s	1	[18, 73]
$6.4 \times 10^9 T \exp(-3.926 \times 10^4/T)$	mol/m ³ /s	1	[16, 71]
$2.824 \times 10^{-2} \exp(-3.284 \times 10^4/RT) [CO] [H_2O]$	kmol/m ³ /s	1	[41, 74]
$2.78 \times 10^3 \exp(1510/T) \left([CO][H_2O] - \frac{[CO_2][H_2]}{0.0265 \exp(\frac{3968}{T})} \right)$	kmol/m ³ /s		[75]
$2.978 \times 10^{12} \exp(-3.69 \times 10^5/RT) \left([CO][H_2O] - \frac{[CO_2][H_2]}{\exp(-3.777 + \frac{4118.6}{T})} \right)$			
Forward & backward format			
$2.78 \exp(-1510/T) [CO] [H_2O] \text{ forward}$			[76]
$93.69 \exp(-5604/T) [CO_2] [H_2] \text{ backward}$			

CO oxidation			
$4.4 \times 10^{11} \exp\left(-1.2552 \times 10^5 / RT\right) [CO]^{0.5} [O_2]^{1.25}$	kmol/m ³ /s	2	[77]
$2.32 \times 10^{12} \exp\left(-1.67 \times 10^5 / RT\right) [CO] [O_2]^{0.25} [H_2O]^{0.5}$	kmol/m ³ /s	2	[73]
$4.78 \times 10^8 \exp\left(-6.69 \times 10^4 / RT\right) [CO] [O_2]^{0.3} [H_2O]^{0.5}$	kmol/m ³ /s	2	[73]
$1.28 \times 10^{17} \exp\left(-2.89 \times 10^5 / RT\right) [CO] [O_2]^{0.25} [H_2O]^{0.5}$	kmol/m ³ /s	2	[72]
$7.2 \times 10^{14} \exp\left(-3.4743 \times 10^4 / T\right) [CO] [O_2]^{0.5} [H_2O]^{0.5}$	mol/m ³ /s	2	[41]
$10^{17.6} \exp\left(-2 \times 10^4 / RT\right) [CO]^{0.25} [H_2O]^{0.5}$	kmol/m ³ /s		[78]
$3.98 \times 10^{20} \exp\left(-20129 / T\right) [CO] [O_2]^{0.25} [H_2O]^{0.5}$			
$3.09 \times 10^4 \exp\left(-9.976 \times 10^4 / RT\right) [CO] [O_2]$			
H₂ combustion			
$1 \times 10^{14} \exp\left(-4.2 \times 10^4 / RT\right) [H_2] [O_2]$	kmol/m ³ /s	3	[30]
$5.16 \times 10^{13} T^{-1.5} \exp\left(-2.85 \times 10^4 / RT\right) [H_2]^{1.5} [O_2]$	kmol/m ³ /s	3	[73]
$2.2 \times 10^9 \exp\left(-1.09 \times 10^5 / RT\right) [H_2] [O_2]$	kmol/m ³ /s	3	[72]
$1.63 \times 10^9 T^{1.5} \exp\left(-3.42 \times 10^3 / T\right) [H_2]^{1.5} [O_2]$	mol/m ³ /s	3	[78]
$2.196 \times 10^{18} \exp\left(-13127 / T\right) [H_2] [O_2]$			[75]
$8.83 \times 10^8 \exp\left(-9.976 \times 10^4 / RT\right) [H_2] [O_2]$			
Methane combustion			
$5.012 \times 10^{11} \exp\left(-2 \times 10^5 / RT\right) [CH_4]^{0.5} [O_2]$	kmol/m ³ /s	4.2	[77]
$4.4 \times 10^{11} \exp\left(-1.26 \times 10^5 / RT\right) [CH_4]^{0.5} [O_2]^{1.25}$	kmol/m ³ /s	4.3	[79]
$2.8 \times 10^9 \exp\left(-2.03 \times 10^5 / RT\right) [CH_4]^{-0.3} [O_2]^{1.3}$	kmol/m ³ /s	4.2	[73]
$5.16 \times 10^{13} T^{-1} \exp\left(-1.3 \times 10^5 / RT\right) [CH_4] [O_2]$	kmol/m ³ /s	4.1	[73]
$1.585 \times 10^9 T^{1.5} \exp\left(-2.4157 \times 10^4 / T\right) [CH_4]^{0.7} [O_2]^{0.8}$		4.2	[72]
$4.99 \times 10^{13} \exp\left(-2.03 \times 10^5 / RT\right) [CH_4]^{0.7} [O_2]^{0.8}$		4.3	[18]
Methane reforming			
$3.015 \times 10^8 \exp\left(-1.2552 \times 10^5 / RT\right) [CH_4] [H_2O]$	kmol/m ³ /s	5	[80]
$3.015 \times 10^3 \exp\left(-1.2552 \times 10^5 / RT\right) [CH_4] [H_2O]$	mol/m ³ /s	5	[15, 18]
$7.3 \times 10^{-2} \exp\left(-3.615 \times 10^4 / RT\right) [CH_4] [H_2O]$			[71]
$3.0 \times 10^5 \exp\left(-15042 / T\right) [CH_4] [H_2O]$			[74]
Char Partial oxidation			
$59.8 \times T_g P^{0.3} \exp\left(-1.22 \times 10^4 / T\right) [BM]^{0.5} [O_2]$		6.4	[14]
$0.554 \exp\left(-1.0824 \times 10^4 / T\right) [O_2]$		6.1	[31]
$1.47 \times 10^5 \exp\left(-1.13 \times 10^8 / RT\right) [O_2]$		6.1	[80]
$4.34 \times 10^7 \theta_p T \exp\left(-13590 / T\right) [O_2]$		6.1	[74]
Char combustion			
$0.554 \exp\left(-1.0824 \times 10^4 / T\right) [O_2]$		6.3	[72]

Boudouard reaction			
$1.272 m_s T \exp(-22645/T) [CO_2]$	mol/m ³ /s	7	[16]
$4364 \exp(-29844/T) [CO_2]$	mol/m ² /s	7	[45]
$36.16 \exp(-7.739 \times 10^4/RT) [CO_2]$	mol/m ³ /s	7	[81]
$8.28 \exp(-1.882 \times 10^8/RT) [CO_2]$			[80]
$8.28 \exp(-1.882 \times 10^8/RT) [CO_2]$			[18]
$\left(\frac{1}{1/h_m + CRF \cdot 15170 \exp(1.21 \times 10^5/RT)} \right) A_p ([H_2O] - [H_2][CO_2]/K_{eq})$			[76]
* A_p is the specific surface area, CRF is the char reactivity factor	Kmol/m ³ /s		[41]
$3.42 T \exp(-15600/T) [CO_2]$			
$2 \times 10^{-8} \exp(-360065/T) [CO_2]$			
Boudouard backward reaction			
$1.044 \times 10^{-4} m_s T^2 \exp(-2363/T - 20.92) [CO]^2$			[74]
Steam gasification			
$1.272 m_s T \exp(-22645/T) [H_2O]$	mol/m ³ /s	8	[16]
$3.6 \times 10^{12} \exp(-3.1 \times 10^5/RT) [H_2O]$	kmol/m ³ /s		[53]
$1.517 \times 10^4 \exp(-1.216 \times 10^5/RT) [H_2O]$	mol/m ³ /s	8	[81]
$8.28 \exp(-1.882 \times 10^8/RT) [H_2O]$		8	[80]
$8.28 \exp(-1.882 \times 10^8/RT) [H_2O]$			[18]
$\left(\frac{1}{1/h_m + CRF 36.16 \exp(77390/RT)} \right) A_p ([CO_2] - [CO_2]^2/K_{eq})$			[76]
$3.42 T \exp(-15600/T) [H_2O]$	1/s		[82]
$2 \times 10^5 \exp(-6000/T) [H_2O]$			[41]
$\left[\frac{4.93 \times 10^3 \exp(-18522/T) \cdot P_{H_2O}}{1 + 10.1 \exp(-3548/T) \cdot P_{H_2O} + 1.53 \times 10^{-9} \exp(-25161/T)} \right]$	1/s		[41]
$\left[\frac{2.1 \times 10^7 \exp(-196000/RT)}{1 + \left(2 \times 10^7 / \exp(-37000/RT) \cdot P_{H_2O} \right)} \right]$			[83]
Steam gasification backward reaction			
$1.044 \times 10^{-4} m_s T^2 \exp(-6319/T - 17.29) [H_2O][CO]$			[74]
Methanation			
$1.368 \times 10^{-3} m_s T \exp(-8078/T - 7.087) [H_2]$	mol/m ³ /s	9	[16]
$4.189 \times 10^{-3} m_s T \exp(-1.92 \times 10^4/T - 7.087) [H_2]$			[71]
Methanation reverse reaction			
$0.151 m_s T^{0.5} \exp(-13578/T - 0.372) [CH_4]^{0.5}$			[74]
R - universal gas constant [J/mol/k], Concentrations - Kmol/m ³			
Other Modeling parameters needed			
▪ Char Thermal conductivity (W/m/K)			
$\lambda_s = 0.0013 + 5 \times 10^{-5} T + 6.3 \times 10^{-4} T^2$ [18]			

$$\lambda_s = 1.47 + 0.011T \text{ [84]}$$

$$\lambda_s = 0.105 \text{ [85]}$$

- **Char specific heat (J/kg/K)**

$$C_{p/char} = 0.36T + 1390$$

$$C_{p/char} = 1430 + 0.355T - 7.32 \times 10^7 T^{-2} \text{ [70]}$$

$$C_{p/char} = 2300 \text{ [84]}$$

- **Char lower heating value**

$$LHV_{char} = 31,300 \text{ kJ/kg}$$

- **Biomass specific heat (J/kg/K)**

$$C_{p/biomass} = 3.68T + 103.1 \text{ [67]}$$

$$C_{p/biomass} = 1112 + 4.85(T - 273) \text{ [41]}$$

$$C_{p/biomass} = 2300 - 1150 \exp(-0.0055T) \text{ [70]}$$

- **Tar specific heat**

$$C_{p/tar} = 88.627 + 0.12074T - 0.12735 \times 10^{-4} T^2 - \left(0.36688 \times 10^7 / T^2\right) \text{ [J/mol/K]}$$

$$C_{p/tar} = 1800 - 800 \exp(-0.0055T) \text{ [kJ/kg/K] [70]}$$

- Tar formation enthalpy $h_{f/tar}^\circ = 82.927 \text{ kJ/mol}$

- Tar lower heating value $LHV_{tar} = 40,579 \text{ kJ/kg [15], 22-26 MJ/kg [50]}$

- As the char combustion reactions are really fast, diffusion rate is also added incorporated with kinetic rate in some studies [16],

$$R = \frac{P_{O_2}}{K_{chem} + K_{diff}}, \quad K_{diff} = \frac{5.06 \times 10^{-7}}{d_p} \times \left(\frac{T_s + T_g}{2}\right)^{0.75}$$

- The volume average kinetics are mentioned here whereas a pool of kinetic equations based on particle conversion are available in literature. These are primarily derived using Thermogravimetric analysis.
 - The units are not exactly mentioned in many studies
 - In certain kinetic equations, for the value within the exponential, E_a/R is given instead of E_a .
 - The consistency of units of the kinetic reactions are important, especially whenever the kinetic data are extracted from different sources.
 - The density of char can be calculated, if the biomass density, proximity analysis and particle shrinkage is known.
-

Tar cracking and reforming

Tar undergoes different chemical changes such as cracking (thermal), steam reforming (H₂O), dry reforming (CO₂), partial oxidation, hydrogenation and carbon formation [73]. Primary tar is mainly consisted with oxygenate compounds and following elevated temperatures, water is removed where the secondary tar is formed that is getting gradually free from oxygen. A chemical point of view was illustrated by Li and Suzuki [50]. Due to the complexity of kinetics, the rate coefficients of pre-exponential factor (A_s) and activation energy (E_a) of possible reactions reported in literature are highly varied. Following Table 8 includes the tar reactions and respective kinetic data used by Fourcault, Marias and Michon [53] and Masmoudi, Halouani and Sahraoui [18]. Similar reaction equations with many different kinetic coefficients are available in literature [78].

Table 8: Reaction rate of model tar components

Equation	Rate
$C_{10}H_8 \rightarrow 10C + 4H_2$	$5.56 \times 10^{15} \exp\left(-3.6 \times 10^5/RT\right) [C_{10}H_8]^2 [H_2]^{-0.7}$
$C_{10}H_8 + 4H_2O \rightarrow C_6H_6 + 4CO + 5H_2$	$1.58 \times 10^{12} \exp\left(-3.24 \times 10^5/RT\right) [C_{10}H_8] [H_2O]^{0.4}$
$C_7H_8 + H_2 \rightarrow C_6H_6 + CH_4$	$1.04 \times 10^{12} \exp\left(-2.47 \times 10^5/RT\right) [C_7H_8] [H_2]^{0.5}$
$C_6H_6 + 5H_2O \rightarrow 5CO + 6H_2 + CH_4$	$4.4 \times 10^8 \exp\left(-2.2 \times 10^5/RT\right) [C_6H_6]$
$C_6H_6 + 7.5 O_2 \rightarrow 6CO_2 + 4H_2O$	$1.738 \times 10^1 \exp\left(-1.255 \times 10^5/RT\right) [C_6H_6]^{-0.1} [O_2]^{1.25}$
$C_6H_6 + 3O_2 \rightarrow 6CO + 3H_2$	$1.58 \times 10^{15} \exp\left(-2.026 \times 10^5/RT\right) [C_6H_6] [O_2]$
$C_7H_8 + 9O_2 \rightarrow 7CO_2 + 4H_2O$	$1.426 \times 10^1 \exp\left(-1.255 \times 10^5/RT\right) [C_7H_8]^{-0.1} [O_2]^{1.25}$
Concentration - kmol/m ³ , rate - kmol /m ³ s	
$C_6H_6O + 4O_2 \rightarrow 6CO + 3H_2O$	$2.4 \times 10^{11} \exp\left(-1.255 \times 10^5/RT\right) [C_6H_6O]^{-0.1} [O_2]^{1.85}$
$C_6H_6 + 4.5 O_2 \rightarrow 6CO + 3H_2O$	$3.8 \times 10^7 \exp\left(-5.545 \times 10^3/RT\right) [C_6H_6] [O_2]$
$C_{10}H_8 + 7O_2 \rightarrow 10 CO + 4H_2O$	$9.2 \times 10^6 T \exp\left(-8 \times 10^4/RT\right) [C_{10}H_8]^{0.5} [O_2]$
$C_7H_8 + 3.5O_2 \rightarrow 7CO + H_2$	1.3 $\times 10^{11} \exp\left(-1.256 \times 10^5/RT\right) [C_7H_8] [O_2]^{0.5} [H_2O]^{0.5}$
$C_6H_6O \rightarrow CO + 0.4C_{10}H_8 + 0.15C_6H_6$ $+ 0.1CH_4 + 0.75H_2$	$10^4 \exp\left(-1 \times 10^5/RT\right) [C_6H_6O]$
$C_6H_6O + 3H_2O \rightarrow 2CO + CO_2$ $+ +0.05C + 2.95CH_4$ $+ 0.1H_2$	$10^5 \exp\left(-1 \times 10^5/RT\right) [C_6H_6O]$
$C_7H_8 + 10.5H_2O$ $\rightarrow 3.5CO + 3.5CO_2$	$2.32 \times 10^5 \exp\left(-3.56 \times 10^5/RT\right) [C_7H_8]$
$C_6H_6 + 3H_2O + 3CO_2 \rightarrow 9CO + 6H_2$	$2 \times 10^{11} \exp\left(-1.96 \times 10^5/RT\right) [C_6H_6]$ [mol/(m ³ .S)]
$C_{10}H_8 + H_2O + 5CO_2 \rightarrow 15CO + 9H_2$	$4.3 \times 10^{13} \exp\left(-3.32 \times 10^5/RT\right) [C_{10}H_8]^{0.2} [H_2]^{0.3}$ [mol/(m ³ .S)]

Su, et al. [17] have identified approximately 25% tar during pyrolysis where 2-Propenoic acid ($C_3H_4O_2$) was the main tar component followed by Cresol (C_7H_8O), Benzofurans (C_8H_8O), naphthalene ($C_{10}H_8$) and Propanone ($C_3H_6O_2$).

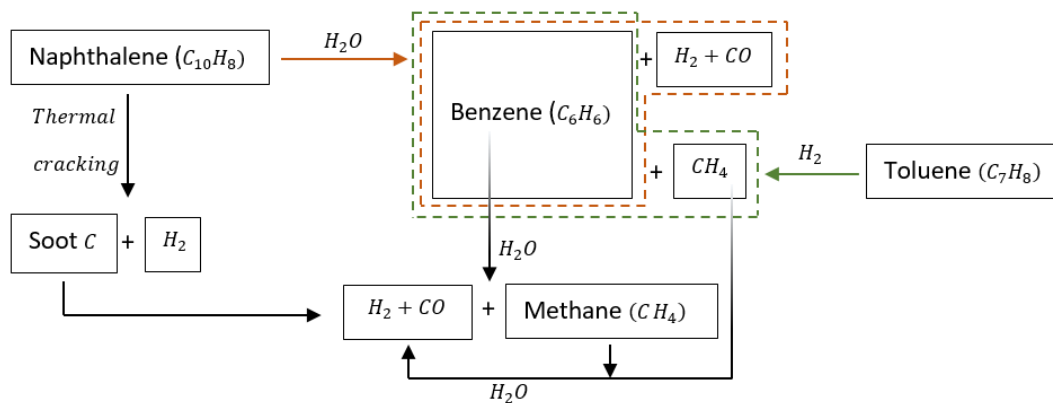


Figure 9: A simple tar cracking sequence [53]

Some studies have mentioned the tar cracking product yields and kinetic rate without regarding any chemical formula for tar. Studies of Wurzenberger et al presented that only 78% (i.e. volatile phase consist with 63.4% of tar) of the tar is cracked where the rest remains as inert tar [45]. CO is the main tar-cracking product, which has been used as an indicator of extent of cracking. During the primary pyrolysis, the H_2 content is very low and however with increased temperature, H_2 content grows exponentially, which can be even better in quantifying the tar cracking. Acetic acid is resistant over thermal cracking whereas other primary tars such as acetol and guaiacol are cracked greatly above 800 °C. Secondary tar compounds such as phenol showed a resistance for thermal cracking whereas naphthalene, a tertiary tar, showed an exponential increase between 800-1000°C [48]. Benzene is the least reactive tar component over other model compounds of toluene and naphthalene where Li and Suzuki [50] has summarized tar conversion mechanisms and kinetics. Liu, et al. [86] studied the tar cracking using toluene as the model compound and observed that the cracking improved from 5.4% without steam to 41.6% with steam. The gas composition of toluene steam reforming under different temperatures are given in Figure 10 where the reaction enthalpy is 869.1 kJ/mol.

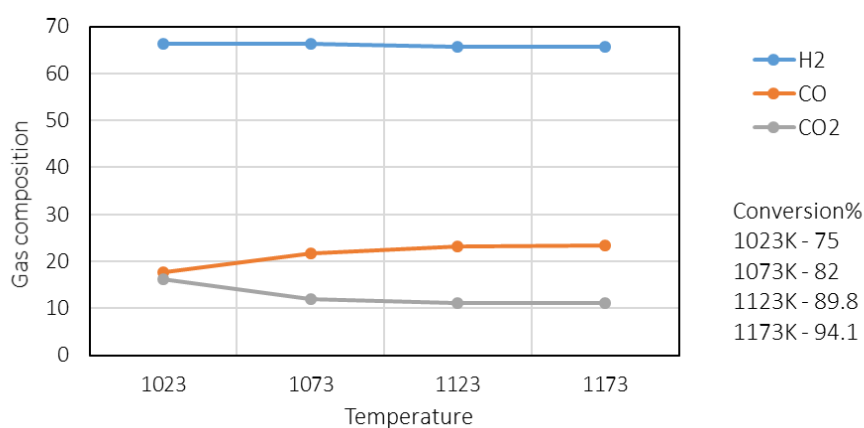


Figure 10: Steam reforming gas composition of toluene [87]

Table 9: Tar cracking and reforming kinetics

Thermal tar Cracking							
Notes	Mass/molar* fractions					Rate	Ref
	CO	CO ₂	H ₂	CH ₄ +C _n H _m	H ₂ O		
22% inert tar/*	0.563	0.11	0.017	0.088	0.22	$10^{4.98} \exp(-93.37/RT_p) W_{tar}$ [kg/(kg.S)]	[41, 45]
Conversion of gravimetric tar	Temperature dependent composition					$4 \times 10^4 \exp(-76.6 \times 10^3/RT)$ [tar] [mol/(m ³ .S)]	[48]
Based on 2 tar species	0.602	0.121	0	0.137	0.14	$3 \times 10^3 \exp(-66.3 \times 10^3/RT)$ [tar1] [mol/(m ³ .S)]	[88]
at 600°C, Spruce wood.	0.534	0.085	0.002	0.209	0.17	1.13 $\times 10^6 \exp(-66.3 \times 10^3/RT)$ [tar2] [mol/(m ³ .S)]	
	Three tar categories tar1 (185mg/g), tar2 (281mg/g) tar3 (99.7 mg/g). Tar 3 is not thermally cracked						
						$tar \rightarrow gas$ $tar \rightarrow char$	$4.28 \times 10^6 \exp(-1.075 \times 10^5/RT)$ [tar] [85] $10^5 \exp(-1.075 \times 10^5/RT)$ [tar]
Tar reforming							
Global reaction	$C_6H_{6.2}O_{0.2} + 5.8H_2O \rightarrow 6CO + 8.9H_2$					$70 \exp(-16736/RT)$ [tar] ^{0.25} [H ₂ O] ^{1.25} [mol/(m ³ .S)]	[15]
Tar oxidation							
Global reaction	$C_6H_{6.2}O_{0.2} + 4.45O_2 \rightarrow 6CO + 3.1H_2O$					2.07 $\times 10^4 \exp(-4.1646 \times 10^4/T)$ [tar] ^{0.5} [O ₂]	[31]
						$2.07 \times 10^4 T P^{0.3}$ $\exp(-4.1646 \times 10^4/T)$ [tar] ^{0.5} [O ₂]	[19]

By looking in to the pyrolysis gas composition and kinetics, selecting of appropriate set of data is complicated. For an example, the order of the pre exponential factor of water-gas shift reaction varies from zeroth to ninth. As a result, the hydrogen content of a steam fed gasification reactor can be varied by a large margin. Therefore, importing the data from a similar system with approximate operational conditions is important.

Particle shrinkage

The particle volume is considerably reduced, especially under high temperature fast pyrolysis, which can be up to 70% of the initial volume. Related to a cylindrical biomass particle, the longitudinal shrinkage can approach 22% whereas radial can be up to 40% [70, 89]. However, shrinkage phenomenon has been considered by limited number of studies. Different types of models are found in literature such as uniform shrinkage,

shrinking shell and shrinking cylinder [85]. The pyrolysis process is speeded up simultaneously with particle shrinkage, which is highly effective in thick particles with a temperature gradient inside. According to [85], the pyrolysis time can reduce down by 5-30% for thermally thick particles. Shrinkage influences the pyrolysis in diverse means. First, the pyrolysis region is thinned with consequent increase in the pyrolysis temperature. The volatile residence time inside the particle is therefore reduced resulting, reduced gas yield, reduced char yield and increased tar yield. In certain studies, the shrinkage factor is given as a function of external radiative heat flux whereas it is described by a temperature dependent function in other studies [89].

References

- [1] I. P. Silva, R. M. A. Lima, G. F. Silva, D. S. Ruzene, and D. P. Silva, "Thermodynamic equilibrium model based on stoichiometric method for biomass gasification: A review of model modifications," *Renewable and Sustainable Energy Reviews*, vol. 114, p. 109305, 2019/10/01/ 2019, doi: <https://doi.org/10.1016/j.rser.2019.109305>.
- [2] D. A. Rodriguez-Alejandro, H. Nam, A. L. Maglinao, S. C. Capareda, and A. F. Aguilera-Alvarado, "Development of a modified equilibrium model for biomass pilot-scale fluidized bed gasifier performance predictions," *Energy*, vol. 115, pp. 1092-1108, 2016/11/15/ 2016, doi: <https://doi.org/10.1016/j.energy.2016.09.079>.
- [3] Y.-i. Lim and U.-D. Lee, "Quasi-equilibrium thermodynamic model with empirical equations for air-steam biomass gasification in fluidized-beds," *Fuel Processing Technology*, vol. 128, pp. 199-210, 2014/12/01/ 2014, doi: <https://doi.org/10.1016/j.fuproc.2014.07.017>.
- [4] S. A. Channiwala and P. P. Parikh, "A unified correlation for estimating HHV of solid, liquid and gaseous fuels," *Fuel*, vol. 81, no. 8, pp. 1051-1063, 2002/05/01/ 2002, doi: [https://doi.org/10.1016/S0016-2361\(01\)00131-4](https://doi.org/10.1016/S0016-2361(01)00131-4).
- [5] J. Parikh, S. A. Channiwala, and G. K. Ghosal, "A correlation for calculating HHV from proximate analysis of solid fuels," *Fuel*, vol. 84, no. 5, pp. 487-494, 2005/03/01/ 2005, doi: <https://doi.org/10.1016/j.fuel.2004.10.010>.
- [6] A. Demirbaş, "Calculation of higher heating values of biomass fuels," *Fuel*, vol. 76, no. 5, pp. 431-434, 4// 1997, doi: [http://dx.doi.org/10.1016/S0016-2361\(97\)85520-2](http://dx.doi.org/10.1016/S0016-2361(97)85520-2).
- [7] L. Jiménez and F. González, "Study of the physical and chemical properties of lignocellulosic residues with a view to the production of fuels," *Fuel*, vol. 70, no. 8, pp. 947-950, 8// 1991, doi: [http://dx.doi.org/10.1016/0016-2361\(91\)90049-G](http://dx.doi.org/10.1016/0016-2361(91)90049-G).
- [8] T. Cordero, F. Marquez, J. Rodriguez-Mirasol, and J. J. Rodriguez, "Predicting heating values of lignocellulosics and carbonaceous materials from proximate analysis," *Fuel*, vol. 80, no. 11, pp. 1567-1571, 9// 2001, doi: [http://dx.doi.org/10.1016/S0016-2361\(01\)00034-5](http://dx.doi.org/10.1016/S0016-2361(01)00034-5).
- [9] C. Sheng and J. L. T. Azevedo, "Estimating the higher heating value of biomass fuels from basic analysis data," *Biomass and Bioenergy*, vol. 28, no. 5, pp. 499-507, 5// 2005, doi: <http://dx.doi.org/10.1016/j.biombioe.2004.11.008>.

- [10] C.-Y. Yin, "Prediction of higher heating values of biomass from proximate and ultimate analyses," *Fuel*, vol. 90, no. 3, pp. 1128-1132, 3// 2011, doi: <http://dx.doi.org/10.1016/j.fuel.2010.11.031>.
- [11] D. A. Tillman, *Wood as an energy resource*. New York: Academic Press, 1978.
- [12] H. L. Zhu *et al.*, "Co-gasification of beech-wood and polyethylene in a fluidized-bed reactor," *Fuel Processing Technology*, vol. 190, pp. 29-37, 2019/07/01/ 2019, doi: <https://doi.org/10.1016/j.fuproc.2019.03.010>.
- [13] G. Wang, B. Fan, H. Chen, and Y. Li, "Understanding the pyrolysis behavior of agriculture, forest and aquatic biomass: Products distribution and characterization," *Journal of the Energy Institute*, 2020/04/25/ 2020, doi: <https://doi.org/10.1016/j.joei.2020.04.004>.
- [14] Y. B. Yang, H. Yamauchi, V. Nasserzadeh, and J. Swithenbank, "Effects of fuel devolatilisation on the combustion of wood chips and incineration of simulated municipal solid wastes in a packed bed☆," *Fuel*, vol. 82, no. 18, pp. 2205-2221, 2003/12/01/ 2003, doi: [https://doi.org/10.1016/S0016-2361\(03\)00145-5](https://doi.org/10.1016/S0016-2361(03)00145-5).
- [15] F. V. Tinaut, A. Melgar, J. F. Pérez, and A. Horrillo, "Effect of biomass particle size and air superficial velocity on the gasification process in a downdraft fixed bed gasifier. An experimental and modelling study," *Fuel Processing Technology*, vol. 89, no. 11, pp. 1076-1089, 2008/11/01/ 2008, doi: <https://doi.org/10.1016/j.fuproc.2008.04.010>.
- [16] T. M. Ismail, A. Ramos, M. Abd El-Salam, E. Monteiro, and A. Rouboa, "Plasma fixed bed gasification using an Eulerian model," *International Journal of Hydrogen Energy*, vol. 44, no. 54, pp. 28668-28684, 2019/11/05/ 2019, doi: <https://doi.org/10.1016/j.ijhydene.2019.08.035>.
- [17] Y. Su, Y. Luo, Y. Chen, W. Wu, and Y. Zhang, "Experimental and numerical investigation of tar destruction under partial oxidation environment," *Fuel Processing Technology*, vol. 92, no. 8, pp. 1513-1524, 2011/08/01/ 2011, doi: <https://doi.org/10.1016/j.fuproc.2011.03.013>.
- [18] M. A. Masmoudi, K. Halouani, and M. Sahraoui, "Comprehensive experimental investigation and numerical modeling of the combined partial oxidation-gasification zone in a pilot downdraft air-blown gasifier," *Energy Conversion and Management*, vol. 144, pp. 34-52, 2017/07/15/ 2017, doi: <https://doi.org/10.1016/j.enconman.2017.04.040>.
- [19] A. K. Sharma, "Modeling and simulation of a downdraft biomass gasifier 1. Model development and validation," *Energy Conversion and Management*, vol. 52, no. 2, pp. 1386-1396, 2011/02/01/ 2011, doi: <https://doi.org/10.1016/j.enconman.2010.10.001>.
- [20] I. Janajreh and M. Al Shrah, "Numerical and experimental investigation of downdraft gasification of wood chips," *Energy Conversion and Management*, vol. 65, pp. 783-792, 2013/01/01/ 2013, doi: <https://doi.org/10.1016/j.enconman.2012.03.009>.
- [21] G. Qi, Z. Wang, S. Zhang, Y. Dong, J. Guan, and P. Dong, "Numerical simulation on biomass-pyrolysis and thermal cracking of condensable volatile component," *International Journal of Hydrogen Energy*, vol. 45, no. 22, pp. 12283-12297, 2020/04/21/ 2020, doi: <https://doi.org/10.1016/j.ijhydene.2020.02.199>.
- [22] P. Kaushal and R. Tyagi, "Advanced simulation of biomass gasification in a fluidized bed reactor using ASPEN PLUS," *Renewable Energy*, vol. 101, pp. 629-636, 2017/02/01/ 2017, doi: <https://doi.org/10.1016/j.renene.2016.09.011>.

- [23] J. Blondeau and H. Jeanmart, "Biomass pyrolysis in pulverized-fuel boilers: Derivation of apparent kinetic parameters for inclusion in CFD codes," *Proceedings of the Combustion Institute*, vol. 33, no. 2, pp. 1787-1794, 2011/01/01/ 2011, doi: <https://doi.org/10.1016/j.proci.2010.06.150>.
- [24] J. F. González *et al.*, "Pyrolysis of Almond Shells. Energy Applications of Fractions," *Industrial & Engineering Chemistry Research*, vol. 44, no. 9, pp. 3003-3012, 2005/04/01 2005, doi: 10.1021/ie0490942.
- [25] X. Wang *et al.*, "Soot formation during biomass pyrolysis: Effects of temperature, water-leaching, and gas-phase residence time," *Journal of Analytical and Applied Pyrolysis*, vol. 134, pp. 484-494, 2018/09/01/ 2018, doi: <https://doi.org/10.1016/j.jaap.2018.07.015>.
- [26] A. Trubetskaya, P. A. Jensen, A. D. Jensen, A. D. Garcia Llamas, K. Umeki, and P. Glarborg, "Effect of fast pyrolysis conditions on biomass solid residues at high temperatures," *Fuel Processing Technology*, vol. 143, pp. 118-129, 2016/03/01/ 2016, doi: <https://doi.org/10.1016/j.fuproc.2015.11.002>.
- [27] M. Trninić, A. Jovović, and D. Stojiljković, "A steady state model of agricultural waste pyrolysis: A mini review," *Waste Management & Research*, vol. 34, no. 9, pp. 851-865, 2016, doi: 10.1177/0734242x16649685.
- [28] L. Abdelouahed, O. Authier, G. Mauviel, J. P. Corriou, G. Verdier, and A. Dufour, "Detailed Modeling of Biomass Gasification in Dual Fluidized Bed Reactors under Aspen Plus," *Energy & Fuels*, vol. 26, no. 6, pp. 3840-3855, 2012/06/21 2012, doi: 10.1021/ef300411k.
- [29] P. Gopalakrishnan, "Modeling of Biomass Steam Gasification in a Bubbling Fluidized Bed Gasifier," Doctor of Philosophy, Chemical and Process Engineering University of Canterbury, 2013.
- [30] N. Ngamsidhiphongs, P. Ponpesh, A. Shotipruk, and A. Arpornwichanop, "Analysis of the Imbert downdraft gasifier using a species-transport CFD model including tar-cracking reactions," *Energy Conversion and Management*, vol. 213, p. 112808, 2020/06/01/ 2020, doi: <https://doi.org/10.1016/j.enconman.2020.112808>.
- [31] A. M. Salem and M. C. Paul, "An integrated kinetic model for downdraft gasifier based on a novel approach that optimises the reduction zone of gasifier," *Biomass and Bioenergy*, vol. 109, pp. 172-181, 2018/02/01/ 2018, doi: <https://doi.org/10.1016/j.biombioe.2017.12.030>.
- [32] K. Smets, P. Adriaensens, G. Reggers, S. Schreurs, R. Carleer, and J. Yperman, "Flash pyrolysis of rapeseed cake: Influence of temperature on the yield and the characteristics of the pyrolysis liquid," *Journal of Analytical and Applied Pyrolysis*, vol. 90, no. 2, pp. 118-125, 2011/03/01/ 2011, doi: <https://doi.org/10.1016/j.jaap.2010.11.002>.
- [33] C. Di Blasi, G. Signorelli, C. Di Russo, and G. Rea, "Product Distribution from Pyrolysis of Wood and Agricultural Residues," *Industrial & Engineering Chemistry Research*, vol. 38, no. 6, pp. 2216-2224, 1999/06/01 1999, doi: 10.1021/ie980711u.
- [34] P. A. Horne and P. T. Williams, "Influence of temperature on the products from the flash pyrolysis of biomass," *Fuel*, vol. 75, no. 9, pp. 1051-1059, 1996/07/01/ 1996, doi: [https://doi.org/10.1016/0016-2361\(96\)00081-6](https://doi.org/10.1016/0016-2361(96)00081-6).
- [35] J. Soria, R. Li, G. Flamant, and G. D. Mazza, "Influence of pellet size on product yields and syngas composition during solar-driven high temperature fast pyrolysis of biomass,"

- Journal of Analytical and Applied Pyrolysis*, vol. 140, pp. 299-311, 2019/06/01/ 2019, doi: <https://doi.org/10.1016/j.jaap.2019.04.007>.
- [36] D. S. Scott, J. Piskorz, M. A. Bergougnou, R. Graham, and R. P. Overend, "The role of temperature in the fast pyrolysis of cellulose and wood," *Industrial & Engineering Chemistry Research*, vol. 27, no. 1, pp. 8-15, 1988/01/01 1988, doi: 10.1021/ie00073a003.
- [37] B. M. Wagenaar, W. Prins, and W. P. M. van Swaaij, "Flash pyrolysis kinetics of pine wood," *Fuel Processing Technology*, vol. 36, no. 1, pp. 291-298, 1993/12/01/ 1993, doi: [https://doi.org/10.1016/0378-3820\(93\)90039-7](https://doi.org/10.1016/0378-3820(93)90039-7).
- [38] R. Zanzi, K. Sjöström, and E. Björnbom, "Rapid pyrolysis of agricultural residues at high temperature," *Biomass and Bioenergy*, vol. 23, no. 5, pp. 357-366, 2002/11/01/ 2002, doi: [https://doi.org/10.1016/S0961-9534\(02\)00061-2](https://doi.org/10.1016/S0961-9534(02)00061-2).
- [39] C. Dupont *et al.*, "Biomass pyrolysis: Kinetic modelling and experimental validation under high temperature and flash heating rate conditions," *Journal of Analytical and Applied Pyrolysis*, vol. 85, no. 1, pp. 260-267, 2009/05/01/ 2009, doi: <https://doi.org/10.1016/j.jaap.2008.11.034>.
- [40] C. E. Greenhalf, D. J. Nowakowski, A. B. Harms, J. O. Titiloye, and A. V. Bridgwater, "A comparative study of straw, perennial grasses and hardwoods in terms of fast pyrolysis products," *Fuel*, vol. 108, pp. 216-230, 2013/06/01/ 2013, doi: <https://doi.org/10.1016/j.fuel.2013.01.075>.
- [41] R. Radmanesh, J. Chaouki, and C. Guy, "Biomass gasification in a bubbling fluidized bed reactor: Experiments and modeling," *AIChE Journal*, vol. 52, no. 12, pp. 4258-4272, 2006/12/01 2006, doi: 10.1002/aic.11020.
- [42] T. R. Nunn, J. B. Howard, J. P. Longwell, and W. A. Peters, "Product compositions and kinetics in the rapid pyrolysis of sweet gum hardwood," *Industrial & Engineering Chemistry Process Design and Development*, vol. 24, no. 3, pp. 836-844, 1985/07/01 1985, doi: 10.1021/i200030a053.
- [43] R. Yan, H. Yang, T. Chin, D. T. Liang, H. Chen, and C. Zheng, "Influence of temperature on the distribution of gaseous products from pyrolyzing palm oil wastes," *Combustion and Flame*, vol. 142, no. 1, pp. 24-32, 2005/07/01/ 2005, doi: <https://doi.org/10.1016/j.combustflame.2005.02.005>.
- [44] C. Loha, H. Chattopadhyay, and P. K. Chatterjee, "Three dimensional kinetic modeling of fluidized bed biomass gasification," *Chemical Engineering Science*, vol. 109, pp. 53-64, 2014/04/19/ 2014, doi: <https://doi.org/10.1016/j.ces.2014.01.017>.
- [45] J. C. Wurzenberger, S. Wallner, H. Raupenstrauch, and J. G. Khinast, "Thermal conversion of biomass: Comprehensive reactor and particle modeling," *AIChE Journal*, vol. 48, no. 10, pp. 2398-2411, 2002, doi: 10.1002/aic.690481029.
- [46] S. Rapagnà and G. Mazziotti di Celso, "Devolatilization of wood particles in a hot fluidized bed: Product yields and conversion rates," *Biomass and Bioenergy*, vol. 32, no. 12, pp. 1123-1129, 2008/12/01/ 2008, doi: <https://doi.org/10.1016/j.biombioe.2008.02.010>.
- [47] L. Devi, K. J. Ptasinski, and F. J. J. G. Janssen, "A review of the primary measures for tar elimination in biomass gasification processes," *Biomass and Bioenergy*, vol. 24, no. 2, pp. 125-140, 2003/02/01/ 2003, doi: [https://doi.org/10.1016/S0961-9534\(02\)00102-2](https://doi.org/10.1016/S0961-9534(02)00102-2).

- [48] P. Morf, P. Hasler, and T. Nussbaumer, "Mechanisms and kinetics of homogeneous secondary reactions of tar from continuous pyrolysis of wood chips," *Fuel*, vol. 81, no. 7, pp. 843-853, 2002/05/01/ 2002, doi: [https://doi.org/10.1016/S0016-2361\(01\)00216-2](https://doi.org/10.1016/S0016-2361(01)00216-2).
- [49] J. Ren, Y.-L. Liu, X.-Y. Zhao, and J.-P. Cao, "Biomass thermochemical conversion: A review on tar elimination from biomass catalytic gasification," *Journal of the Energy Institute*, vol. 93, no. 3, pp. 1083-1098, 2020/06/01/ 2020, doi: <https://doi.org/10.1016/j.joei.2019.10.003>.
- [50] C. Li and K. Suzuki, "Tar property, analysis, reforming mechanism and model for biomass gasification—An overview," *Renewable and Sustainable Energy Reviews*, vol. 13, no. 3, pp. 594-604, 2009/04/01/ 2009, doi: <https://doi.org/10.1016/j.rser.2008.01.009>.
- [51] L. Gerun *et al.*, "Numerical investigation of the partial oxidation in a two-stage downdraft gasifier," *Fuel*, vol. 87, no. 7, pp. 1383-1393, 2008/06/01/ 2008, doi: <https://doi.org/10.1016/j.fuel.2007.07.009>.
- [52] A. M. Salem, I. N. Zaini, M. C. Paul, and W. Yang, "The evolution and formation of tar species in a downdraft gasifier: Numerical modelling and experimental validation," *Biomass and Bioenergy*, vol. 130, p. 105377, 2019/11/01/ 2019, doi: <https://doi.org/10.1016/j.biombioe.2019.105377>.
- [53] A. Fourcault, F. Marias, and U. Michon, "Modelling of thermal removal of tars in a high temperature stage fed by a plasma torch," *Biomass and Bioenergy*, vol. 34, no. 9, pp. 1363-1374, 2010/09/01/ 2010, doi: <https://doi.org/10.1016/j.biombioe.2010.04.018>.
- [54] D. E. Dugaard and R. C. Brown, "Enthalpy for Pyrolysis for Several Types of Biomass," *Energy & Fuels*, vol. 17, no. 4, pp. 934-939, 2003/07/01 2003, doi: 10.1021/ef020260x.
- [55] C. Dupont, R. Chiriac, G. Gauthier, and F. Toche, "Heat capacity measurements of various biomass types and pyrolysis residues," *Fuel*, vol. 115, pp. 644-651, 2014/01/01/ 2014, doi: <https://doi.org/10.1016/j.fuel.2013.07.086>.
- [56] M. A. Pauner and H. Bygbjerg, "Spontaneous ignition in storage and production lines: Investigation on wood pellets and protein powders," *Fire and Materials*, Article vol. 31, no. 8, pp. 477-494, 2007, doi: 10.1002/fam.945.
- [57] W. Guo, C. J. Lim, X. Bi, S. Sokhansanj, and S. Melin, "Determination of effective thermal conductivity and specific heat capacity of wood pellets," *Fuel*, vol. 103, pp. 347-355, 2013/01/01/ 2013, doi: <https://doi.org/10.1016/j.fuel.2012.08.037>.
- [58] M. Gupta, J. Yang, and C. Roy, "Predicting the effective thermal conductivity of polydispersed beds of softwood bark and softwood char☆," *Fuel*, vol. 82, no. 4, pp. 395-404, 2003/03/01/ 2003, doi: [https://doi.org/10.1016/S0016-2361\(02\)00308-3](https://doi.org/10.1016/S0016-2361(02)00308-3).
- [59] B. Peters and C. Bruch, "Drying and pyrolysis of wood particles: experiments and simulation," *Journal of Analytical and Applied Pyrolysis*, vol. 70, no. 2, pp. 233-250, 2003/12/01/ 2003, doi: [https://doi.org/10.1016/S0165-2370\(02\)00134-1](https://doi.org/10.1016/S0165-2370(02)00134-1).
- [60] V. S. P. Bitra, S. Banu, P. Ramakrishna, G. Narender, and A. R. Womac, "Moisture dependent thermal properties of peanut pods, kernels, and shells," *Biosystems Engineering*, vol. 106, no. 4, pp. 503-512, 2010/08/01/ 2010, doi: <https://doi.org/10.1016/j.biosystemseng.2010.05.016>.

- [61] K. K. Singh and T. K. Goswami, "Thermal properties of cumin seed," *Journal of Food Engineering*, vol. 45, no. 4, pp. 181-187, 2000/09/01/ 2000, doi: [https://doi.org/10.1016/S0260-8774\(00\)00049-2](https://doi.org/10.1016/S0260-8774(00)00049-2).
- [62] S. Ciuta, F. Patuzzi, M. Baratieri, and M. J. Castaldi, "Enthalpy changes during pyrolysis of biomass: Interpretation of intraparticle gas sampling," *Applied Energy*, vol. 228, pp. 1985-1993, 2018/10/15/ 2018, doi: <https://doi.org/10.1016/j.apenergy.2018.07.061>.
- [63] C. Di Blasi, C. Branca, and A. Galgano, "On the Experimental Evidence of Exothermicity in Wood and Biomass Pyrolysis," *Energy Technology*, vol. 5, no. 1, pp. 19-29, 2017, doi: 10.1002/ente.201600091.
- [64] L. Basile, A. Tugnoli, C. Stramigioli, and V. Cozzani, "Influence of pressure on the heat of biomass pyrolysis," *Fuel*, vol. 137, pp. 277-284, 2014/12/01/ 2014, doi: <https://doi.org/10.1016/j.fuel.2014.07.071>.
- [65] W.-C. R. Chan, M. Kelbon, and B. B. Krieger, "Modelling and experimental verification of physical and chemical processes during pyrolysis of a large biomass particle," *Fuel*, vol. 64, no. 11, pp. 1505-1513, 1985/11/01/ 1985, doi: [https://doi.org/10.1016/0016-2361\(85\)90364-3](https://doi.org/10.1016/0016-2361(85)90364-3).
- [66] S. Hosokai, K. Matsuoka, K. Kuramoto, and Y. Suzuki, "Practical estimation of reaction heat during the pyrolysis of cedar wood," *Fuel Processing Technology*, vol. 154, pp. 156-162, 2016/12/15/ 2016, doi: <https://doi.org/10.1016/j.fuproc.2016.08.027>.
- [67] K. M. Bryden, K. W. Ragland, and C. J. Rutland, "Modeling thermally thick pyrolysis of wood," *Biomass and Bioenergy*, vol. 22, no. 1, pp. 41-53, 2002/01/01/ 2002, doi: [https://doi.org/10.1016/S0961-9534\(01\)00060-5](https://doi.org/10.1016/S0961-9534(01)00060-5).
- [68] H. Liu, R. J. Cattolica, R. Seiser, and C.-h. Liao, "Three-dimensional full-loop simulation of a dual fluidized-bed biomass gasifier," *Applied Energy*, vol. 160, pp. 489-501, 2015/12/15/ 2015, doi: <https://doi.org/10.1016/j.apenergy.2015.09.065>.
- [69] E. Ranzi *et al.*, "Chemical Kinetics of Biomass Pyrolysis," *Energy & Fuels*, vol. 22, no. 6, pp. 4292-4300, 2008/11/19 2008, doi: 10.1021/ef800551t.
- [70] J. Blondeau and H. Jeanmart, "Biomass pyrolysis at high temperatures: Prediction of gaseous species yields from an anisotropic particle," *Biomass and Bioenergy*, vol. 41, pp. 107-121, 2012/06/01/ 2012, doi: <https://doi.org/10.1016/j.biombioe.2012.02.016>.
- [71] M. A. Masmoudi, M. Sahraoui, N. Grioui, and K. Halouani, "2-D Modeling of thermo-kinetics coupled with heat and mass transfer in the reduction zone of a fixed bed downdraft biomass gasifier," *Renewable Energy*, vol. 66, pp. 288-298, 2014/06/01/ 2014, doi: <https://doi.org/10.1016/j.renene.2013.12.016>.
- [72] E. Desroches-Ducarne, J. C. Dolignier, E. Marty, G. Martin, and L. Delfosse, "Modelling of gaseous pollutants emissions in circulating fluidized bed combustion of municipal refuse," *Fuel*, vol. 77, no. 13, pp. 1399-1410, 1998/10/01/ 1998, doi: [https://doi.org/10.1016/S0016-2361\(98\)00060-X](https://doi.org/10.1016/S0016-2361(98)00060-X).
- [73] A. Gómez-Barea and B. Leckner, "Modeling of biomass gasification in fluidized bed," *Progress in Energy and Combustion Science*, vol. 36, no. 4, pp. 444-509, 2010/08/01/ 2010, doi: <https://doi.org/10.1016/j.peccs.2009.12.002>.

- [74] J. Xie, W. Zhong, B. Jin, Y. Shao, and H. Liu, "Simulation on gasification of forestry residues in fluidized beds by Eulerian–Lagrangian approach," *Bioresource Technology*, vol. 121, pp. 36-46, 2012/10/01/ 2012, doi: <https://doi.org/10.1016/j.biortech.2012.06.080>.
- [75] X. Xiang, G. Gong, Y. Shen, C. Wang, and Y. Shi, "A comprehensive mathematical model of a serial composite process for biomass and coal Co-gasification," *International Journal of Hydrogen Energy*, vol. 44, no. 5, pp. 2603-2619, 2019/01/28/ 2019, doi: <https://doi.org/10.1016/j.ijhydene.2018.12.077>.
- [76] R. Johansson, H. Thunman, and B. Leckner, "Influence of intraparticle gradients in modeling of fixed bed combustion," *Combustion and Flame*, vol. 149, no. 1, pp. 49-62, 2007/04/01/ 2007, doi: <https://doi.org/10.1016/j.combustflame.2006.12.009>.
- [77] P. Nakod, "CFD Modeling and Validation of Oxy-Fired and Air-Fired Entrained Flow Gasifiers," *International Journal of Chemical and Physical Sciences*, vol. 2, no. 6, pp. 28-40, 2013.
- [78] P. Ji, W. Feng, and B. Chen, "Production of ultrapure hydrogen from biomass gasification with air," *Chemical Engineering Science*, vol. 64, no. 3, pp. 582-592, 2009/02/01/ 2009, doi: <https://doi.org/10.1016/j.ces.2008.10.015>.
- [79] W. P. Jones and R. P. Lindstedt, "Global reaction schemes for hydrocarbon combustion," *Combustion and Flame*, vol. 73, no. 3, pp. 233-249, 1988/09/01/ 1988, doi: [https://doi.org/10.1016/0010-2180\(88\)90021-1](https://doi.org/10.1016/0010-2180(88)90021-1).
- [80] U. Kumar and M. C. Paul, "CFD modelling of biomass gasification with a volatile break-up approach," *Chemical Engineering Science*, vol. 195, pp. 413-422, 2019/02/23/ 2019, doi: <https://doi.org/10.1016/j.ces.2018.09.038>.
- [81] Y. Wang and C. M. Kinoshita, "Kinetic model of biomass gasification," *Solar Energy*, vol. 51, no. 1, pp. 19-25, 1993/07/01/ 1993, doi: [https://doi.org/10.1016/0038-092X\(93\)90037-0](https://doi.org/10.1016/0038-092X(93)90037-0).
- [82] J. Ren, J.-P. Cao, X.-Y. Zhao, F.-L. Yang, and X.-Y. Wei, "Recent advances in syngas production from biomass catalytic gasification: A critical review on reactors, catalysts, catalytic mechanisms and mathematical models," *Renewable and Sustainable Energy Reviews*, vol. 116, p. 109426, 2019/12/01/ 2019, doi: <https://doi.org/10.1016/j.rser.2019.109426>.
- [83] M. Morin, S. Pécate, and M. Hémati, "Experimental study and modelling of the kinetic of biomass char gasification in a fluidized bed reactor," *Chemical Engineering Research and Design*, vol. 131, pp. 488-505, 2018/03/01/ 2018, doi: <https://doi.org/10.1016/j.cherd.2017.09.030>.
- [84] S. Hermansson and H. Thunman, "CFD modelling of bed shrinkage and channelling in fixed-bed combustion," *Combustion and Flame*, vol. 158, no. 5, pp. 988-999, 2011/05/01/ 2011, doi: <https://doi.org/10.1016/j.combustflame.2011.01.022>.
- [85] K. M. Bryden and M. J. Hagge, "Modeling the combined impact of moisture and char shrinkage on the pyrolysis of a biomass particle☆," *Fuel*, vol. 82, no. 13, pp. 1633-1644, 2003/09/01/ 2003, doi: [https://doi.org/10.1016/S0016-2361\(03\)00108-X](https://doi.org/10.1016/S0016-2361(03)00108-X).
- [86] S. Liu, D. Mei, L. Wang, and X. Tu, "Steam reforming of toluene as biomass tar model compound in a gliding arc discharge reactor," *Chemical Engineering Journal*, vol. 307, pp. 793-802, 2017/01/01/ 2017, doi: <https://doi.org/10.1016/j.cej.2016.08.005>.

- [87] B. Zhao *et al.*, "Steam reforming of toluene as model compound of biomass pyrolysis tar for hydrogen," *Biomass and Bioenergy*, vol. 34, no. 1, pp. 140-144, 2010/01/01/ 2010, doi: <https://doi.org/10.1016/j.biombioe.2009.10.011>.
- [88] J. Rath and G. Staudinger, "Cracking reactions of tar from pyrolysis of spruce wood," *Fuel*, vol. 80, no. 10, pp. 1379-1389, 2001/08/01/ 2001, doi: [https://doi.org/10.1016/S0016-2361\(01\)00016-3](https://doi.org/10.1016/S0016-2361(01)00016-3).
- [89] M. Bellais, K. O. Davidsson, T. Liliedahl, K. Sjöström, and J. B. C. Pettersson, "Pyrolysis of large wood particles: a study of shrinkage importance in simulations☆," *Fuel*, vol. 82, no. 12, pp. 1541-1548, 2003/08/01/ 2003, doi: [https://doi.org/10.1016/S0016-2361\(03\)00062-0](https://doi.org/10.1016/S0016-2361(03)00062-0).

Annexure B

Scientific Publications

Paper A

Janitha C. Bandara, Marianne S. Eikeland, Britt M.E. Moldestad

Analyzing the Effects of Particle Density, Size and Size Distribution for Minimum Fluidization Velocity with Eulerian-Lagrangian CFD Simulation

Conference: Proceedings of the 58th Conference on Simulation and Modelling (SIMS 58), September 25 – 27, 2017, Reykjavik, Iceland. PP 60-65

DOI: 0.3384/ecp1713860

Analyzing the Effects of Particle Density, Size and Size Distribution for Minimum Fluidization Velocity with Eulerian-Lagrangian CFD Simulation

Janitha C. Bandara¹ Marianne S. Eikeland¹ Britt M. E. Moldestad¹

¹Faculty of Technology, Natural Sciences and Maritime Sciences, University College of Southeast Norway
{Janitha.bandara, Marianne.Eikeland, britt.moldestad}@usn.no

Abstract

Fluidized bed reactor systems are widely used due to excellent heat and mass transfer characteristics followed by uniform temperature distribution throughout the reactor volume. The importance of fluidized beds is further demonstrated in high exothermic reactions such as combustion and gasification where fluidization avoids the hot spot and cold spot generation. A bed material, such as sand or catalyst, is normally involved in fluidized bed combustion and gasification of biomass. Therefore, it is vital to analyze the hydrodynamics of bed material, especially the minimum fluidization velocity, as it governs the fluid flowrate into the reactor system. There are limitations in experimental investigations of fluidized beds such as observing the bed interior hydrodynamics, where CFD simulations has become a meaningful way with the high computer power. However, due to the large differences in scales from the particle to the reactor geometry, complex interface momentum transfer and particle collisions, CFD modeling and simulation of particle systems are rather difficult. Multiphase particle-in-cell method is an efficient version of Eulerian-Lagrangian modeling and Barracuda VR commercial package was used in this work to analyze the minimum fluidization velocity of particles depending on size, density and size distribution.

Wen-YU-Ergun drag model was used to model the interface momentum transfer where default equations and constants were used for other models. The effect of the particle size was analyzed using monodispersed Silica particles with diameters from 400 to 800 microns. Minimum fluidization velocity was increased with particle diameter, where it was 0.225 m/s for the 600 microns particles. The density effect was analyzed for 600 microns particles with seven different density values and the minimum fluidization velocity again showed proportionality to the density. The effect of the particle size distribution was analyzed using Silica. Particles with different diameters were mixed together according to pre-determined proportions as the final mixture gives a mean diameter of 600 microns. The 600 microns monodispersed particle bed showed the highest minimum fluidization velocity. However, some particle mixtures were composed with larger particles up to 1000 micron, but with a fraction of smaller particles down to

200 microns at the same time. This shows the effect of strong drag from early fluidizing smaller particles. The only variability for pressure drop during packed bed is the particle size and it was clearly observed in all three cases.

Keywords: Fluidization, Bioenergy, Particle properties, Minimum fluidization velocity

1 Introduction

Fluidization occurs whenever a collection of particles is subjected to an upward fluid flow at a sufficient flowrate where the gravity and inter-particle forces are in counterbalance with the fluid drag force (Horio 2013). The fluidized bed technology was first introduced in the petroleum industry for catalytic cracking processes, which later penetrated into energy, environmental and processing industry (Horio 2013, Winter and Schratzer 2013, Vollmari, Jasevičius et al. 2016). The technology enhances the gas-solid contact and mixing, which leads to increased heat and mass transfer characteristics. Further, it guarantees the homogeneous temperature and concentrations throughout the reactor, which increases the possibility and reliability of scaled up operation. Good control over solid particles, large thermal inertia of solids (Esmaili and Mahinpey 2011), increased efficiency, reduced emissions and wide range of operating conditions are additional advantages of the fluidized bed systems (Winter and Schratzer 2013). The importance of the fluidized bed technology is highlighted specially in exothermic reactions such as biomass combustion as it avoids hot spot and cold spot generation due to intense mixing and particle collision. Hot spots lead to ash melting followed by agglomeration and clinkering (Behjat, Shahhosseini et al. 2008, Horio 2013) whereas cold spots reduces tar cracking and thus, reduced gas quality.

Bio-energy is the fourth largest energy source, which accounts for 10% to 14% of the world energy profile (REN21 2016). The lignocellulosic fraction of the biomass is the major contributor of bioenergy. In contrast to the simple, inefficient and small-scaled combustion practices, there is a tendency to use advanced technologies such as fluidized bed gasification followed by either heat & power generation or liquid fuel synthesis. However, due to low density, large particle size and extreme shapes of the particles,

biomass is difficult to fluidize alone (Cui and Grace 2007). Therefore, biomass fluidized bed combustors and gasifiers are operated with the assistance of fluidizing materials such as sand, alumina, catalysts etc., which is known as bed material (Fotovat, Ansart et al. 2015). Hence, it is meaningful to study the fluidization behavior of bed materials as it principally governs the bed hydrodynamics. Bubbling fluidization stands slightly above the minimum fluidization. Hence, it is important to manipulate the minimum fluidization velocity in bubbling fluidized bed gasification systems, because it governs the mass flowrate of gasifying agent into the reactor system.

The fluidization properties are governed by both particle properties such as particle size, particle density, particle shape etc. and fluid properties (Fotovat, Ansart et al. 2015). However, there can be additional effects from the bed diameter, geometry, aspect ratio and distributor design as well. The transition superficial gas velocity from fixed bed to fluidized bed is referred to as the minimum fluidization velocity, which is one of the most important parameters in the design of fluidized beds (Coltters and Rivas 2004). Depending on Geldart's powder classification and superficial gas velocity, particles tend to fluidize in homogeneous, bubbling, slugging or sprouting beds (Geldart 1973).

Computational Fluid Dynamics (CFD) simulations are beginning to appear in a meaningful way with the tremendous growth in computer power along with sophisticated mathematical models and efficient algorithms (Cooper and Coronella 2005, Kia and Aminian 2017). The faster and more accurate CFD simulations of fluidization systems, makes it easier to get detailed predictions compared to the expensive and time consuming experiments. On the other hand, CFD is a smart tool in optimizing the geometry, which is difficult or even impossible to achieve with experiments. Further, it provides an insight into the bed interior, which again is difficult to achieve with experiments unless more advanced technologies are used. Extreme operational conditions can also be analyzed in advanced to guarantee the safe operation of experimental setups.

However, modeling of gas-solid flow behavior is challenging due to the complexities arising from the coupling of turbulent gas flow and particle motions together with inter-particle collisions. The differences in scale from particles to geometry is another difficult parameter in the CDF simulations. Lagrangian-Eulerian and Eulerian-Eulerian are the basic modeling approaches in gas-solid multiphase systems. Lagrangian-Eulerian modeling solves the Newtonian equation of motion for each individual particle in the system while the gas phase is modeled as a continuum with Navier-Stokes equations. In contrast, the Eulerian-Eulerian modeling considers both phases as continuous and interpenetrating, which are modeled with the

Navier-Stokes equations (Xie, Zhong et al. 2013). Even though Eulerian-Eulerian modeling consumes less computer power, it is complex in modeling stage, as it needs more closure functions. In contrast, the Lagrangian-Eulerian simulations need high computer power, and it is unrealistic to use for industrial scale reactors. Multiphase particle-in-cell (MP-PIC) was developed as an extension to the Lagrangian-Eulerian simulations, where particle are modeled in both discrete and continuous phase (Snider 2001, Xie, Zhong et al. 2013). Instead of individual particles, it considers groups of particles sharing common characteristics. These groups are referred to as parcels or computational particles. Particle properties that are best calculated on the grid are calculated using continuous modeling in the advanced time step and interpolated back to individual particles. The successive development of the MP-PIC method is illustrated in the works of Snider, O'Rourke and Andrew s (Andrews and O'Rourke 1996, Snider, O'Rourke et al. 1998, Snider 2001, Snider 2007, O'Rourke and Snider 2012). This particular method is embedded in Barracuda VR commercial software package, which is becoming popular in CFD modeling of gas-solid systems and has brought forward the concept of computational particle fluid dynamics (CPFD). Hence, the objective of this work is to analyze the effect of particle properties of density, size and size distribution on the minimum fluidization velocity with CPFD simulation.

2 Methods and Computational Setup

Barracuda VR 17.1.0 was used for the simulations where a simple cylindrical geometry of 1000 mm in height and 84mm in diameter was considered. A uniform grid was applied with 8000 cells in total, which is illustrated in Figure 1. Grid refinements at the wall was not performed as it was assumed that there was no boundary layer formation with the dense phase particle system. Default grid generator settings were used, which removes the cells having less fraction of volume than 0.04 and greater aspect ratio than 15:1.

Isothermal temperature of 300 K was used where sand (SiO_2) was used as the basic bed material. However, other materials as aluminum oxide (Al_2O_3), nickel oxide (NiO), calcium (Ca), ferric oxide (Fe_2O_3), titanium oxide (TiO_2) and zirconium (ZrO_2) were used to analyze the effect of density on the minimum fluidization velocity. Air at atmospheric pressure was used as fluidizing gas in all the cases. Particles were filled up to 350mm of height and the random packing option was used.

The close pack volume fraction, maximum momentum redirection from collisions, normal to wall momentum retention and tangent to wall momentum retention were set to 0.6, 40%, 0.3 and 0.99 respectively. Default values for the parameters in the particle stress model were kept unchanged. Blended acceleration model was activated

for the mixtures of different particle sizes. The column was operated at atmospheric pressure where the air outlet at the top plane was defined as a pressure boundary. Inlet boundary was defined as a flow/velocity boundary with varying air velocities over time. Each velocity was maintained for 4 seconds. Further, uniform air distribution at the inlet and no particle exit from the pressure boundary were assumed. The bed pressure was monitored in the center of the bed at five different heights. The boundary conditions and the pressure monitoring points are depicted in Figure 1.

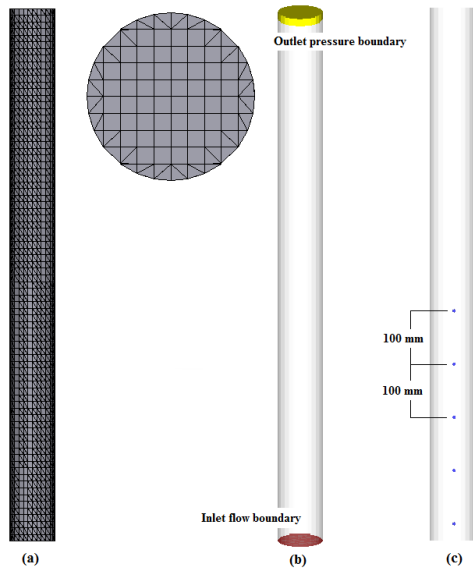


Figure 1. (a) Grid, (b) Boundary conditions, (c) Pressure data points

3 Results and Discussion

The bed materials used in fluidized bed gasification and combustion are usually polydispersed with a wide size distribution. However, monodispersed particle beds were used in this work to demonstrate the effect of particle size for minimum fluidization velocity. Attempts were made to analyze the effect of the particle size mixtures later in this work.

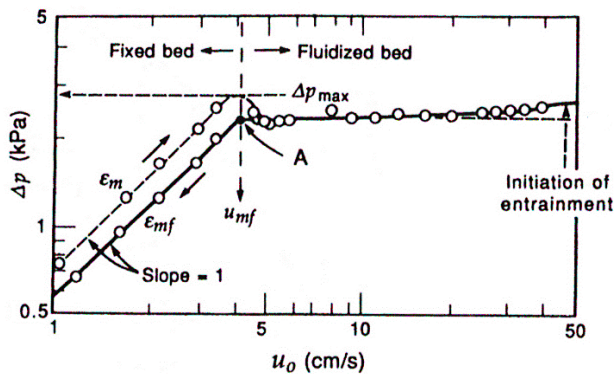


Figure 2. Gas velocity vs pressure drop diagram (Kunii and Levenspiel 1991)

The pressure drop (Δp) versus superficial gas velocity U_0 diagram is useful in determining the transition from fixed bed to fluidized bed. During the fixed bed operation, the bed pressure drop is proportional to the gas velocity. Once the bed reaches the minimum fluidization velocity, the bed pressure drop decreases a little, and stabilizes at the static bed pressure. The bed continues to stay around that pressure until the particle entrainment starts (Kunii and Levenspiel 1991). This behavior and figuring out of the minimum fluidization velocity U_{mf} , is illustrated in Figure 2.

Fluid drag force resulted from the upward fluid flow is one of the most important particle forces in any fluidized bed system. Due to this, many researchers have worked towards the optimization of drag models for particular cases. The author has experimentally validated the good performance of the Wen-Yu-Ergun drag model in a previous work (Bandara, Thapa et al. 2016). Gidaspow proposed a drag model where the interface momentum transfer coefficient, K_{sg} , is selected from either Wen-YU or Ergun correlation depending upon the gas volume fraction (Sobieski 2009). When the gas volume fraction is greater than 0.8, Wen-Yu correlation is applied which is given by:

$$K_{\frac{sg}{WenYu}} = \frac{3}{4} \frac{C_d \rho_g \varepsilon_g (1 - \varepsilon_g) (u_s - u_g)}{d_p} \varepsilon_g^{-2.65} \quad (1)$$

Where C_d is:

$$C_d = \begin{cases} \frac{24}{\varepsilon_g Re_s} [1 + 0.15(\varepsilon_g Re_s)^{0.687}], & Re_s \leq 1000 \\ 0.44, & Re_s > 1000 \end{cases} \quad (2)$$

When the gas volume fraction is less than 0.8, Ergun correlation is used which is given by:

$$K_{\frac{sg}{Ergun}} = 150 \frac{\mu_g (1 - \varepsilon_g)^2}{\varphi^2 d_p^2 \varepsilon_g} + 1.75 \frac{\rho_g (u_g - u_s) (1 - \varepsilon_g)}{\varphi d_p} \quad (3)$$

Where, subscripts g , p and s refer to gas phase, particle and solid phase respectively. U is the velocity, ρ is the density ε is the volume fractions, φ is the sphericity, μ is the viscosity, Re is the Reynold's number and d is the particle diameter.

3.1 Effect of the Particle Size

Geldart has worked towards classifying the particles according to both size and density in the early 1970s (Geldart 1973). Same author has discussed the effect of the particle size distribution in fluidized beds in a separate publication. This work analyses these effects from computational fluid dynamic aspects. To demonstrate the effect of the particle size, sand particles from 400 to 800 microns were used. The particle density was 2200 kg/m³ and it was further assumed that the particles were spherical. As shown in Figure 3, the

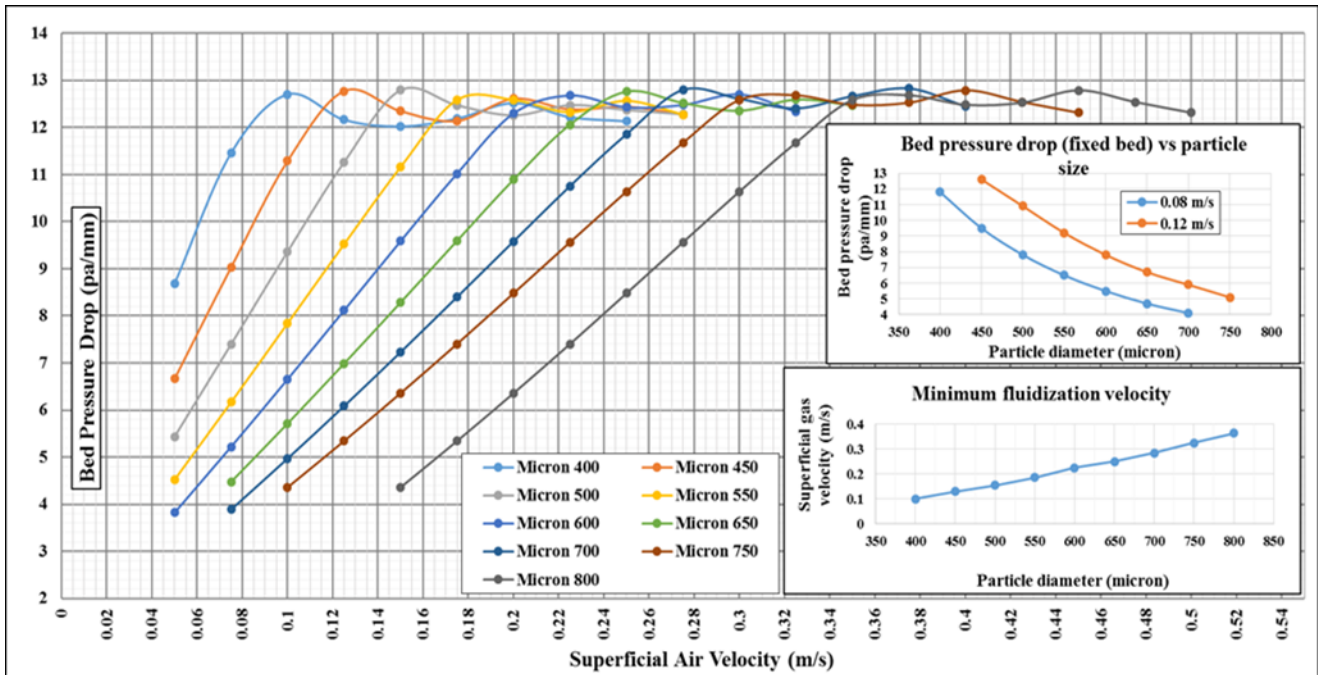


Figure 3. Minimum fluidization velocity plots for different size particles. Right upper corner sub-plot illustrates the pressure drop during fixed bed at two different gas velocities

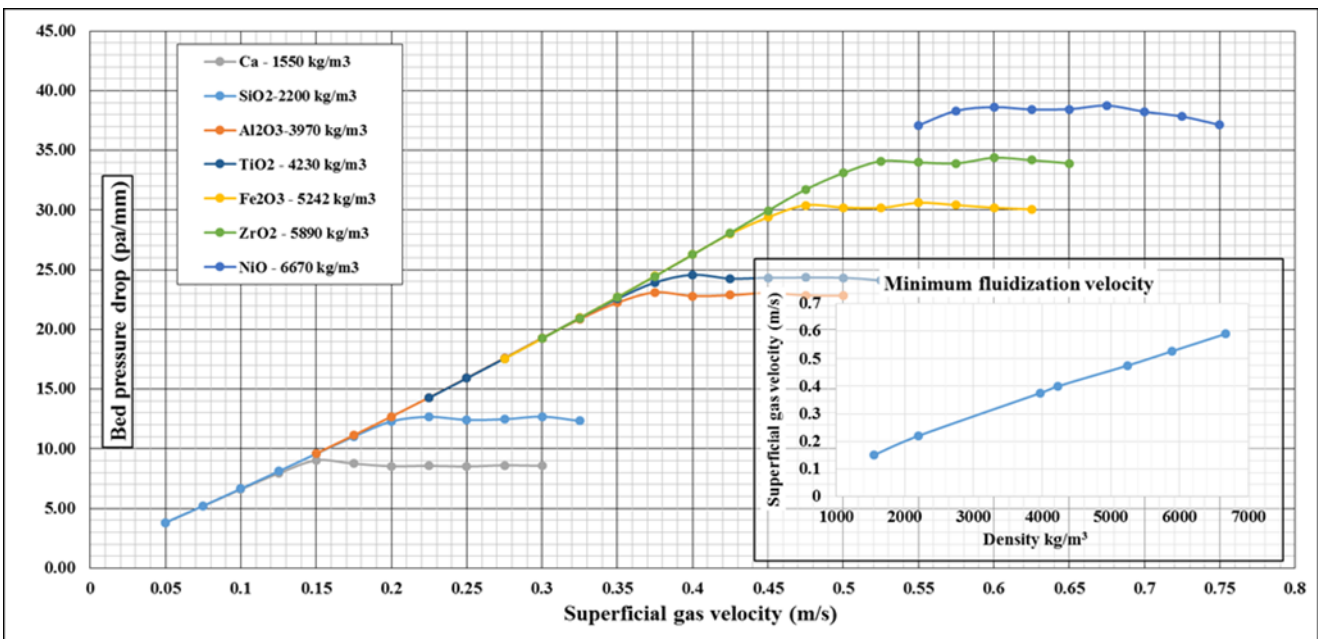


Figure 4: Effect of the particle density for minimum fluidization velocity

minimum fluidization velocity increases linearly with the particle diameter as expected. Bed pressure drop shows a linear relationship with the superficial gas velocity during the packed bed region. Further, it is clear from the figure that the bed pressure drop at the minimum fluidization is almost the same for all the particle sizes. It is also agreeable because, the bed weight is counter balanced by the pressure drop at the fluidization and the bed mass was approximately constant for all the sizes. The fluctuations of the pressure

drop in the fluidizing region is also realistic which can be observed in many experimental results as well.

3.2 Effect of the Particle Density

A 600-micron sand bed was considered as the reference and the effect of different densities were analyzed for 600-micron particles. According to the simulation results depicted in Figure 4, the minimum fluidization velocity is proportional to the particle density. As the particle diameter is similar, all the plots follow the same line during the packed bed operation.

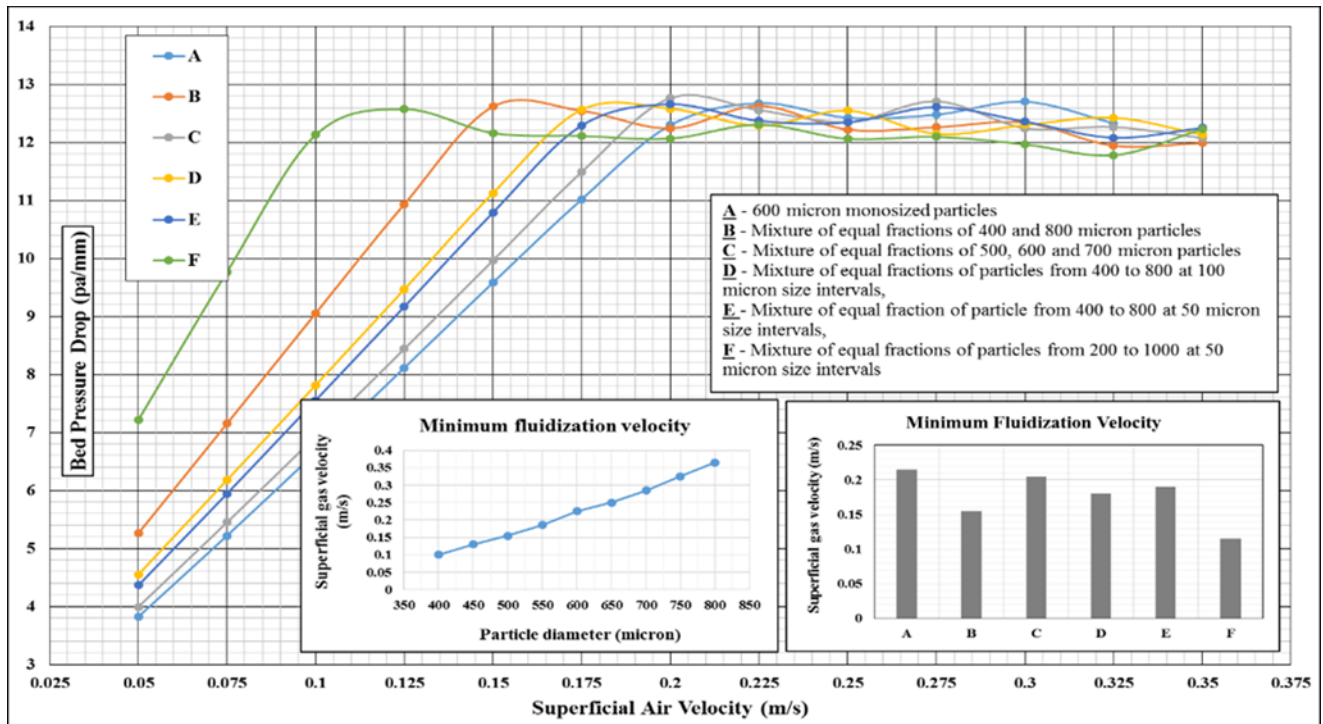


Figure 5. Effect of the particle size distribution on the minimum fluidization velocity

3.3 Effect of the Particle Size Distribution

The final and major task of this work is to see the functioning of CFD technique in predicting the minimum fluidization velocity behavior of particle mixtures of different sizes. Specially, empirical models for the drag force have been developed considering mono size particles. However, the particle drag force in a mixture of different size particles differs compared to that in a mono-size particle bed.

The effect of the particle size distribution was compared with the 600-micron monodispersed silica particles. Different particle mixtures of silica all with a mean particle diameter as 600-micron were simulated. The description of the particle mixtures are given in Figure 5. Particle mixtures were defined by introducing one particle species for each size and filling them randomly with pre-defined volume fractions, which collectively accounts for 0.6 solid/particle volume fraction.

According to the same Figure 5, 600-micron monodispersed particles has the highest minimum fluidization velocity, which is approximately 0.21 m/s. The minimum fluidization velocity of mixture C is close to the value of the 600-micron monodispersed sample. This might be due to the narrow size distribution of mixture C around 600 micron. The minimum fluidization velocity of mixtures D and E is closer to each other, but the values are less than A and C. The particle sizes of D and E mixtures are distributed between 400 and 800 micron in a similar way to a certain extent. The size distribution of pre-mentioned mixtures are in a broad range with oversized and undersized particles than 600 micron. The mixture B,

which is having equal fractions of 400 and 800 micron particles, shows a lower minimum fluidization velocity compared to A, C, D and E. This particular mixture contains half of the fraction with 400 microns, which is comparatively less compared to 600. Finally, the mixture F with the highest size distribution (between 200 to 1000 microns) shows the lowest minimum fluidization velocity among the six different mixtures considered.

It is important to note the possibility of reducing the minimum fluidization velocity by adding a certain fraction of smaller sized particles. As an example, even though the mixture F contains considerable amounts of particles larger than 600 micron, the minimum fluidization velocity still substantially drops below the value of monodispersed 600 microns sample. In this situation, the larger particles are affected both by the fluid drag force and by the momentum from smaller particles (particle drag). According to the simulations carried out for different diameters, smaller particles are prone to fluidized at lower gas velocities. Therefore, the drag force from the fine particles make the larger particles fluidize at lower gas velocities when those are in a mixture. However, the simulation time was increased considerably for particle mixtures than monodispersed particle beds.

4 Conclusion

The effects of particle size, density and size distribution on the minimum fluidization velocity were analyzed using the MP-PIC CFD simulation technique. Barracuda VR commercial software package was used in all the simulations. A previously validated model, which uses

the Wen-YU-Ergun model for the fluid drag, was used. However, the model had not been validated for particles with size distribution for several sizes. It is good to conduct experimental analysis further to guarantee the reproducibility of simulation data.

Minimum fluidization velocity was observed to be linearly proportional to the particle size. On the other hand, the minimum fluidization velocity increases approximately by a factor of two when the particle density is doubled. It is the pressure drop, which is more concerned during packed bed operation. Simulation results for different size and densities prove that it is the particle size, which governs the pressure drop. However, it is not easy to observe a clear relationship between minimum fluidization velocity and particle sizes when it comes to particle mixtures. The smaller particles in a mixture greatly affects and reduces the minimum fluidization velocity. Thus, this phenomenon is useful in operating a bubbling fluidized bed reactor at different gas velocities, simply by adding either larger or smaller particles depending on the requirement. Finally, the Barracuda CPFD simulations can provide precise and quick insight into the bed hydrodynamics.

Acknowledgement

The authors would like to forward their gratitude to University College of Southeast Norway for providing of the Barracuda VR software package and computer facilities.

References

- Andrews, M. J. and P. J. O'Rourke (1996). "The multiphase particle-in-cell (MP-PIC) method for dense particulate flows." *International Journal of Multiphase Flow* **22**(2): 379-402.
- Bandara, J. C., R. K. Thapa, B. M. E. Moldestad and M. S. Eikeland (2016). "Simulation of Particle Segregation in Fluidized Beds" *9th EUROSIM Congress on Modelling and Simulation*, Oulu, Finland, IEEE.
- Behjat, Y., S. Shahhosseini and S. H. Hashemabadi (2008). "CFD modeling of hydrodynamic and heat transfer in fluidized bed reactors." *International Communications in Heat and Mass Transfer* **35**(3): 357-368.
- Coltters, R. and A. L. Rivas (2004). "Minimum fluidation velocity correlations in particulate systems." *Powder Technology* **147**(1-3): 34-48.
- Cooper, S. and C. J. Coronella (2005). "CFD simulations of particle mixing in a binary fluidized bed." *Powder Technology* **151**(1-3): 27-36.
- Cui, H. and J. R. Grace (2007). "Fluidization of biomass particles: A review of experimental multiphase flow aspects." *Chemical Engineering Science* **62**(1-2): 45-55.
- Esmaili, E. and N. Mahinpey (2011). "Adjustment of drag coefficient correlations in three dimensional CFD simulation of gas-solid bubbling fluidized bed." *Advances in Engineering Software* **42**(6): 375-386.
- Fotovat, F., R. Ansart, M. Hemati, O. Simonin and J. Chaouki (2015). "Sand-assisted fluidization of large cylindrical and spherical biomass particles: Experiments and simulation." *Chemical Engineering Science* **126**: 543-559.
- Geldart, D. (1972). "The effect of particle size and size distribution on the behaviour of gas-fluidised beds." *Powder Technology* **6**(4): 201-215.
- Geldart, D. (1973). "Types of gas fluidization." *Powder Technology* **7**(5): 285-292.
- Horio, M. (2013). 1 - Overview of fluidization science and fluidized bed technologies A2 - Scala, Fabrizio. *Fluidized Bed Technologies for Near-Zero Emission Combustion and Gasification*, Woodhead Publishing: 3-41.
- Kia, S. A. and J. Aminian (2017). "Hydrodynamic modeling strategy for dense to dilute gas-solid fluidized beds." *Particuology* **31**: 105-116.
- Kunii, D. and O. Levenspiel (1991). *Fluidization Engineering*. Washington Street, Newton, MA, Butterworth-Heinemann.
- O'Rourke, P. J. and D. M. Snider (2012). "Inclusion of collisional return-to-isotropy in the MP-PIC method." *Chemical Engineering Science* **80**: 39-54.
- REN21 (2016). *Renewables 2016 Global Status Report*.
- Snider, D. M. (2001). "An Incompressible Three-Dimensional Multiphase Particle-in-Cell Model for Dense Particle Flows." *Journal of Computational Physics* **170**(2): 523-549.
- Snider, D. M. (2007). "Three fundamental granular flow experiments and CPFD predictions." *Powder Technology* **176**(1): 36-46.
- Snider, D. M., P. J. O'Rourke and M. J. Andrews (1998). "Sediment flow in inclined vessels calculated using a multiphase particle-in-cell model for dense particle flows." *International Journal of Multiphase Flow* **24**(8): 1359-1382.
- Sobieski, W. (2009). "Switch Function and Sphericity Coefficient in the Gidaspow Drag Model for Modeling Solid-Fluid Systems." *Drying Technology* **27**(2): 267-280.
- Vollmari, K., R. Jasevičius and H. Kruggel-Emden (2016). "Experimental and numerical study of fluidization and pressure drop of spherical and non-spherical particles in a model scale fluidized bed." *Powder Technology* **291**: 506-521.
- Winter, F. and B. Schratzer (2013). 23 - Applications of fluidized bed technology in processes other than combustion and gasification A2 - Scala, Fabrizio. *Fluidized Bed Technologies for Near-Zero Emission Combustion and Gasification*, Woodhead Publishing: 1005-1033.
- Xie, J., W. Zhong, B. Jin, Y. Shao and Y. Huang (2013). "Eulerian-Lagrangian method for three-dimensional simulation of fluidized bed coal gasification." *Advanced Powder Technology* **24**(1): 382-392.

Paper B

Janitha C. Bandara, Henrik K. Nielsen, Britt M.E. Moldestad, Marianne S. Eikeland

Sensitivity Analysis and Effect of Simulation parameters of CPFD Simulation in Fluidized Beds

Conference: Proceedings of the 59th Conference on Simulation and Modelling (SIMS 59), 26-28 September 2018, Oslo Metropolitan University, Norway. PP 334-341

DOI: 10.3384/ecp18153334

Sensitivity Analysis and Effect of Simulation parameters of CFPD Simulation in Fluidized Beds

Janitha C. Bandara¹ Henrik K. Nielsen² Britt M.E. Moldestad¹ Marianne S. Eikeland¹

¹Department of Process, Energy and Environmental Technology, University College of Southeast Norway, Norway, {Janitha.bandara, britt.moldestad, Marianne.Eikeland}@usn.no

²Department of Engineering Sciences, University of Agder, Norway, {henrik.kofoed.nielsen}@uia.no

Abstract

Fluidized bed technology is broadly applied in industry due to its distinct advantages. CFD simulation of fluidized beds is still challenging compared to single-phase systems and needs extensive validation. Multiphase particle-in-cell is a recently developed lagrangian modeling technique and this work is devoted to analyze the sensitivity of grid size, time step, and model parameters, which are the essences of accurate results. Barracuda VR 17.1.0 commercial CFD package was used in this study.

500 μ m sand particles and air was used as the bed material and fluidization gas respectively. Five different grids, having 27378, 22176, 16819, 9000 and 6656 computational cells were analysed, where five different time steps of 0.05, 0.01, 0.005, 0.001 and 0.0005 were used for each grid. One velocity step was maintained for 8 seconds. The bed pressure drop at packed bed operation was high for simulations with reduced time steps while equal pressure drops were observed during fluidization for all time steps. Time steps of 0.0005s and 0.001s and 0.005s produced equal result of 0.15 m/s for minimum fluidization velocity, irrespective of the grid size. The results from time steps of 0.05 and 0.01 are converged to the results from time steps of 0.005 and 0.001 by increasing simulation time per one velocity step.

Keywords: Fluidized bed, Minimum fluidization velocity, CFD simulations, Multiphase particle-in-cell method, Grid size, Time step

1 Introduction

Gas-solid fluidized bed technology is widely utilized in energy generation, chemical, petrochemical, pharmaceutical, environmental, electronic and metallurgical processing industries due its distinct advantages of high heat and mass transfer, controlled material handling, large thermal inertia of solids and isothermal operating conditions (de Souza Braun et al. 2010)(Vejahati et al. 2009)(Esmaili and Mahinpey 2011). Computational fluid dynamic (CFD) modeling has been identified as an excellent tool to produce

missing information during the scaling up of lab/pilot scale fluidized beds to industrial scale. Further, it is a fast and cost effective method for system optimization.

CFD solves the conservation equations for mass, momentum, energy and species where this technique has been critically validated for the accurate performance in gas or liquid single phase flows. However, there are certain challenges related to interface coupling, solid phase modeling and scale differences in gas-solid multiphase flow systems. Eulerian-eulerian and eulerian-lagrangian are the two basic approaches for CFD modeling of multiphase flows.

Multiphase Particle-In-Cell (MP PIC) modeling is a development of eulerian-lagrangian modeling and aims to reduce the computational cost in discrete modeling of particle phase. Instead of tracking individual particles, it considers the parcels containing a certain number of particles with similar properties. The parcels are modeled in the discrete phase while the particle phase interactions are modeled in Eulerian frame. Therefore particle properties are calculated in both Eulerian and Lagrangian frames, which are correlated via interpolation functions. The successive developments of the MP-PIC method is illustrated in the works of Snider, O'Rourke and Andrew (Andrews and O'Rourke 1996)(D M Snider 2001)(D M Snider, O'Rourke, and Andrews 1998)(Dale M Snider 2007)(O'Rourke and Snider 2012).

Validated CFD models can be used to analyze the bubbling fluidized beds in terms of minimum fluidization velocity, bubble rise velocity, bubble diameter and particle mixing and segregation. The conservation equations of mass, species, momentum and energy are in partial differential form. The particular simulation geometry is divided into small cells, which is referred as the computational grid. The conservation equations are then discretized in space and time to get a set of algebraic equations. Finite difference, finite element and finite volume are the main techniques where the finite volume method is mostly used in mass, momentum and energy related 3D systems.

Errors and uncertainties are integrated from the modeling stage to the final computer simulations. Use of empirical equations and model simplification lead to deviations during the model development. The errors

imposed due to the selection of mesh size, time step and discretization method are referred as numerical errors. Truncation and limiting functions at the discontinuities also cause deviations in the result. Iterative algorithms used in simulations provide certain errors while the round off errors are integrated depending upon computer resource (i.e. 32 bit or 64 bit). Finally, improper coding can also lead to certain errors where these are absorbed as discretization errors. Therefore, it is required to identify the possibilities to reduce the errors in the simulations with minimal computational cost.

As the model equations are concerned, it is possible to check the best functioning empirical models. This includes selecting the best drag model in gas-solid multiphase flow systems. Checking different values for the model constants/coefficients in a meaningful way is another approach. Different schemes such as first order upwind, second order upwind and central differencing etc. can be optimized in terms of computer cost and accuracy required. However, many of the mentioned parameters are optimized for general setting in many of the commercial CFD packages. Hence, the most primary parameters to study in first hand are the grid size and the simulation time step. These two parameters are correlated to form Courant-Friedrichs-Lewy (CFL) conditions, which gives the primary indication of the convergence of the simulation. Apart from the convergence, improper implementation of mesh lead to errors and missing information of the systems.

Mesh sensitivity analysis has used to develop a grid independent model. Many of the related works for the mesh sensitivity were carried out for EE simulations and fixed time steps has been adopted based on convergence criteria. In contrast, as solid phase is modeled as discrete particles in EL modeling, the solid phase interactions are directly calculated. Therefore, the effect of the mesh size is comparatively less. Many authors have used the bed pressure drop and the solid volume fraction as the parameters to check the mesh sensitivity. Even though the MP PIC modeling preserves the discrete nature of the particles, it deviates from the original Lagrangian modeling as selected particle properties are calculated in the Eulerian frame.

Barracuda VR is a tailor-made CFD code for multiphase flow systems, which uses MP PIC modeling. Many of the previous studies on sensitivity analysis have been carried out in steady boundary conditions. Instead, this work is focused on studying both changing boundary conditions of inlet flow velocity during the transition of packed bed to fluidized bed and steady boundary conditions in bubbling fluidizing regime. The minimum fluidization velocity, bed pressure drop and bubble characteristics were compared. Barracuda VR 17.1.0 version was used to compare the minimum fluidization velocity, bed pressure drop and bubble characteristics between different configurations of time

step, grid size along with different models and model parameters.

2 MP PIC Model Description

The gas phase mass and momentum conservation are modeled with continuity and time averaged Navier-Stokes equations:

$$\frac{\partial(\alpha_g \rho_g)}{\partial t} + \nabla \cdot (\alpha_g \rho_g u_g) = 0 \quad (1)$$

$$\frac{\partial(\alpha_g \rho_g u_g)}{\partial t} + \nabla \cdot (\alpha_g \rho_g u_g u_g) = -\nabla P + F + \nabla \cdot (\alpha_g \tau_g) + \alpha_g \rho_g g \quad (2)$$

Where α_g , ρ_g , and u_g are gas phase volume fraction, density and velocity respectively. F is total momentum exchange with particle phase per volume, g is gravitational acceleration, P is pressure and τ_g is the gas phase stress tensor, which is given by:

$$\tau_g = \mu_g \left[(\nabla u_g + \Delta u_g^T) - \frac{2}{3} \nabla \cdot u_g I \right] \quad (3)$$

μ_g refers to the shear viscosity that is the sum of the laminar and turbulent components. The large eddy simulation is used for the large-scale turbulence modeling while the subgrid scale turbulence is captured with Smagorinsky model:

$$\mu_{g,t} = C_s \rho_g \Delta^2 |\nabla u_g + \Delta u_g^T| \quad (4)$$

Where Δ is the subgrid length scale and calculated by equation 05. The default value for the model constant C_s is 0.01.

$$\Delta = (\delta x \delta y \delta z)^{1/3} \quad (5)$$

The interface momentum transfer is calculated through the viscous drag force:

$$F = \iint f \left\{ m_p \left[D_p (u_g - u_p) - \frac{\nabla P}{\rho_p} \right] \right\} dm_p du_p \quad (6)$$

Subscript P refers to the particle phase properties where m and u symbolizes the mass and velocity. D_p is the drag function. The particle phase dynamics are derived using particle distribution function (PDF) calculated from the Liouville equation given as:

$$\frac{\partial f}{\partial t} + \nabla (f u_p) + \nabla u_p (f A_p) = 0 \quad (7)$$

Where A_p , is the particle acceleration and is expressed by:

$$A_p = \frac{\partial(u_p)}{\partial t} = D_p (u_g - u_p) - \frac{\nabla P}{\rho_p} - \frac{\nabla \tau_p}{\rho_p \alpha_p} + g \quad (8)$$

α_p is particle volume fraction and τ_p is particle stress function that is used in formulating interphase interactions of particles.

$$\alpha_p = \iint f \frac{m_p}{\rho_p} dm_p du_p \quad (9)$$

$$\tau_p = \frac{10P_s \alpha_p^\beta}{\max[(\alpha_{cp} - \alpha_p), \varepsilon(1 - \alpha_p)]} \quad (10)$$

P_s is a constant with the units of pressure, α_{cp} is the particle volume fraction at close packing, β is a constant between 2 and 5 where ε is a very small number on the order of 10^{-7} .

3 Methods and Computational Model

The minimum fluidization velocity (MFV) was used as the primary measurement for the mesh and time step sensitivity analysis. The simulations were started at the packed bed conditions and the gas velocity was gradually increased from zero to 0.4 m/s with 0.025 increments. Simulations were carried out for 8 seconds at each velocity step. Average pressure drop gradient across the column was plotted against the gas superficial velocity and the minimum fluidization velocity is read (U_{mf}) as illustrated in Figure 1. Five different grid sizes and five different time steps for each grid were used to compare the MFVs. The simulation time for each velocity step was gradually increased in the following simulations gradually up to 20 seconds in selected grids and the results were compared. As the drag model is a function of particle volume fraction, the MFV was analyzed at varied close pack volume fractions.

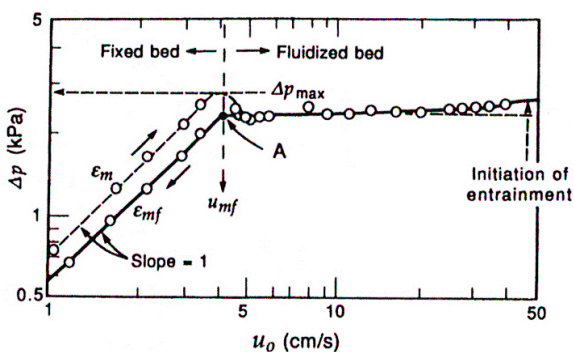


Figure 1. Calculation of minimum fluidization velocity

3.1 Computational model

The dimensions of the geometry were adopted from the experimental rig at the University of Southeast Norway. As shown in Figure 2, a cylindrical column with 84mm in diameter and 1000mm in height with pressure monitoring points in 100mm intervals along the height was created. The gas inlet was set up as a flow boundary while the top gas exit as a pressure boundary at atmospheric pressure with no particle exit. Fluidizing gas was air at 300K with varying superficial velocity.

Further, the velocity inlet was formulated as it homogeneously injects air in axial direction throughout the whole bottom cross section. Each velocity was maintained for 8 seconds. Spherical sand particles with 2200 Kg/m³ in density and 500 micron in diameter was the bed material used. The initial particle bed height was set up to 350mm.

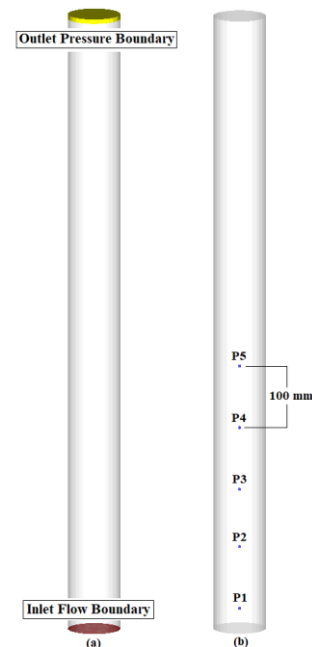


Figure 2. (a) Boundary conditions, (b) Pressure points
Five different meshes with 6656, 9000, 16819, 22176 and 27378 cells were tested and cross sectional views are illustrated in Figure 3.

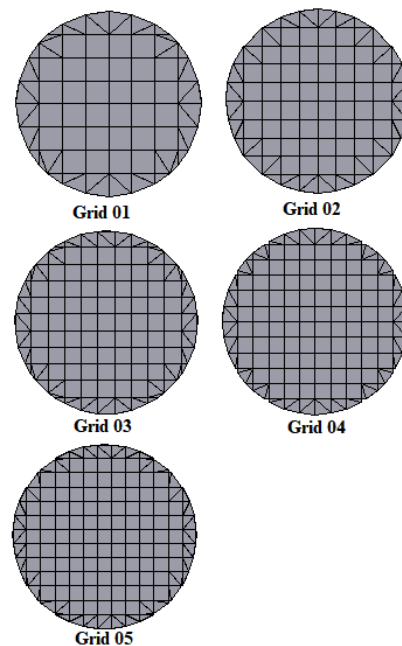


Figure 3. Cross sectional views of different grids
The grid dimensions in x, y and z direction for each mesh are given in Table 1. The normalized grid size in all x, y and z directions were kept below the warning

line in the grid check plot. Grid refinements at the wall was not performed as it was assumed that there was no boundary layer formation with the dense phase particle system. Default grid generator settings were used, which removes the cells having less fraction of volume than 0.04 and greater aspect ratio than 15:1. Four time steps of 0.05, 0.01, 0.005 and 0.001 seconds were checked for each grid.

Table 1. Cell dimensions

No of cells	ΔX (mm)	ΔY (mm)	ΔZ (mm)	Grid No
6656	10.5	10.5	9.6	01
9000	8.40	8.40	11.1	02
16819	7.60	7.60	7.20	03
22176	7.00	7.00	6.5	04
27378	6.46	6.46	6.17	05

Adopting to the previous experience of the author (Bandara, Thapa, Moldestad, & Eikeland, 2016), Wen-Yu-Ergun correlation was used for the initial simulations. It is a combined formulation of Wen-Yu model and Ergun model, which is selected upon the gas volume fraction. When the gas volume fraction is greater than 0.8, Wen-Yu correlation is applied which is given by,

$$K_{\frac{sg}{WenYu}} = \frac{3 C_d \rho_g \varepsilon_g (1 - \varepsilon_g) (u_s - u_g)}{4 d_p} \varepsilon_g^{-2.65} \quad (11)$$

Where C_d is given by,

$$C_d = \begin{cases} \frac{24}{\varepsilon_g Re_s} \left[1 + 0.15 (\varepsilon_g Re_s)^{0.687} \right], & Re_s \leq 1000 \\ 0.44, & Re_s > 1000 \end{cases} \quad (12)$$

When the gas volume fraction is less than 0.8, Ergun correlation is used which is given by,

$$K_{\frac{sg}{Ergun}} = 150 \frac{\mu_g (1 - \varepsilon_g)^2}{\varphi^2 d_p^2 \varepsilon_g} + 1.75 \frac{\rho_g (u_g - u_s) (1 - \varepsilon_g)}{\varphi d_p} \quad (13)$$

Where, subscripts g, p and s refer to gas phase, particle and solid phase respectively. K_{sg} is the interface momentum transfer coefficient, U is the velocity, ρ is the density, ε is the volume fractions, φ is the sphericity, μ is the viscosity, Re is the Reynold's number and d is the particle diameter.

The close pack volume fraction, maximum momentum redirection from collisions, normal to wall momentum retention and tangent to wall momentum retention were set to 0.6, 40%, 0.3 and 0.99 respectively. Default values for the parameters in the particle stress model were kept unchanged. Large eddy simulation was enabled for the turbulence modeling and "partial-donor-cell" was used as the numerical scheme.

4 Results and Discussion

Minimum fluidization is a crucial parameter as it represents the minimum gas required to operate the reactor. It is sensitive to particle properties (size, shape, density etc.) and gas properties (density, humidity, viscosity etc.) along with geometry (aspect ratio). Therefore, it is required to know the minimum fluidization velocity at different contexts. A CFD model can be useful in predicting MFV at various process conditions. This work demonstrates the grid size and time step dependency in calculating the minimum fluidization velocity.

Apart from the 20 simulations mentioned under the methods, time step of 0.0005 was used for grids with high resolutions and one other simulation was carried out at a coarse grid. The plots were generated for each grid at different time steps and each time step for different grids.

According to the force balance at the minimum fluidization condition, the bed pressure drop is proportional to the particle weight and can be expressed as,

$$\frac{\Delta P}{H} = (1 - \varepsilon_{mf}) g (\rho_s - \rho_g) \quad (14)$$

Where, ΔP is bed pressure drop, H is bed height and ε_{mf} is the void fraction at the minimum fluidization.

Equation 14 and many correlations for the MFV need the knowledge of void fraction at minimum fluidization, which is difficult to determine. However, Gidaspo (1994) and Das et al have mentioned about the void fraction at minimum fluidization (ε_{mf}), which varies between 0.44 and 0.476. Implementing the value of 0.45 for the ε_{mf} in equation 14, the pressure drop per unit height of the bed at minimum fluidization is 11.87 Pa/mm.

As approximated by Wen and Yu, the minimum fluidization velocity U_{mf} can be expressed as,

$$U_{mf} = \frac{\mu_g}{\rho_g d_p} \left[\sqrt{1135.7 + 0.048 Ar} - 33.7 \right] \quad (15)$$

Where μ_g is gas viscosity, d_p is particle diameter and Ar is the Archimedes number given by,

$$Ar = \frac{d_p^3 (\rho_s - \rho_g) \rho_g g}{\mu^2} \quad (16)$$

Using Equation 15 and 16, the MFV for the simulated system can be calculated as 0.165 m/s.

Air velocity (u_g) vs pressure drop (ΔP) plots for different grids are illustrated in Figure 4 to 8. Each figure contains plots for different time steps used. Each velocity step was maintained for 8 seconds and the pressure drop was taken as the average value of the 8th second of respective velocity. The averaging was performed to minimize the effect of random pressure fluctuations during fluidization on results. The pressure gradient (Pa/mm) along the column height was

calculated based on P1 and P2 data as illustrated in sketch (b) - **Figure 2**. It was assumed that the P1 and P2 would reach the steady values before the rest of the transient data points (P3, P4 and P5) for pressure.

4.1 Bed Pressure drop

Being a fundamental formulation, pressure drop at onset of fluidization calculated from Equation 14, which is 11.87 Pa/mm, was used as the baseline to compare the results from simulations.

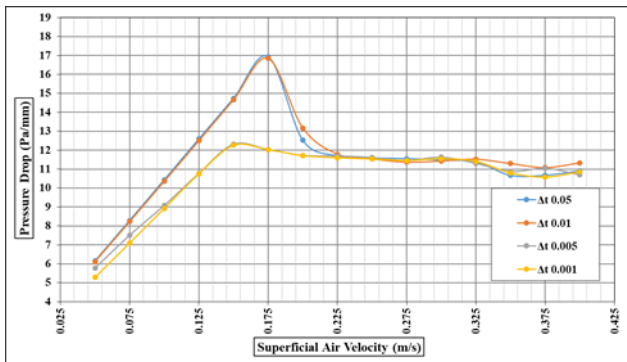


Figure 4. Effect of the time step for MFV at grid 01

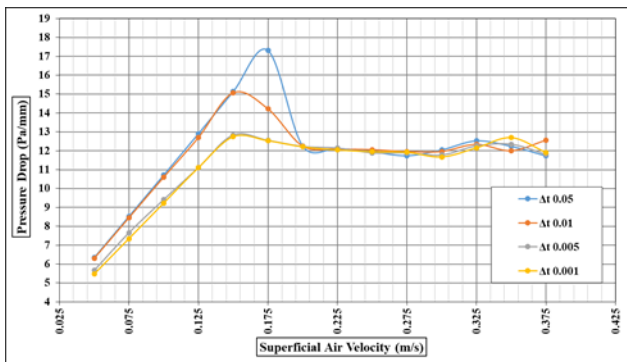


Figure 5. Effect of the time step for MFV at grid 02

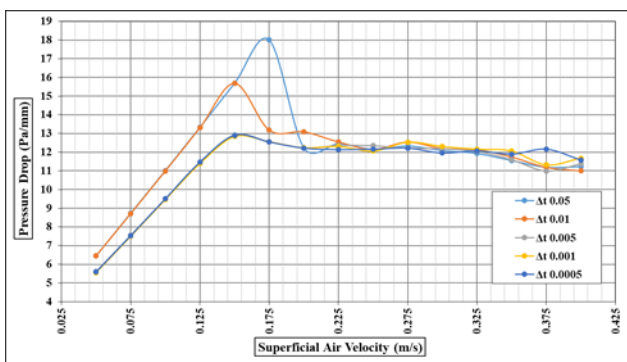


Figure 6. Effect of the time step for MFV at grid 03

4.1.1 Pressure drop at minimum fluidization

The results for the pressure drop at minimum fluidization ($(\Delta P)_{MF}$) using time step 0.05 show the highest variation of 18 Pa/mm in grid 05 and 03. The respective value changes between 17 and 18 Pa/mm at different grids without any distinguishable pattern. At the coarsest grid, grid 01, both time steps of 0.05 and

0.01 give the same of 17 Pa/mm for $(\Delta P)_{MF}$. However, the $(\Delta P)_{MF}$ using time step 0.01 gradually increases from 15 Pa/mm to 16.5 Pa/mm as the grid size is reduced from grid 02 to grid 05. The $(\Delta P)_{MF}$ calculated from time steps of 0.005 and 0.001 are identical for each grid, which gradually increase from 12.5 Pa/mm in grid 01 to 13.5 Pa/mm in grid 05.

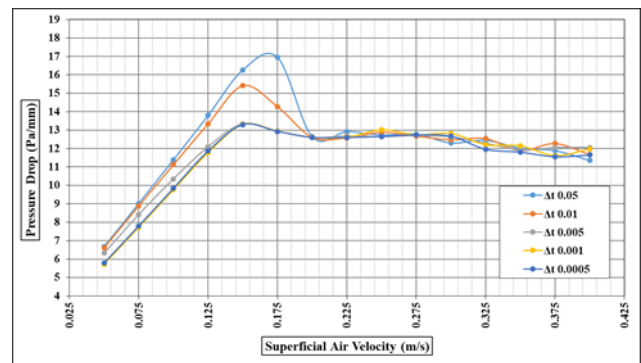


Figure 7. Effect of the time step for MFV at grid 04

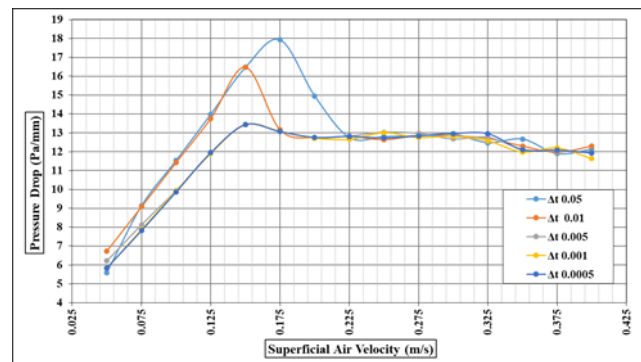


Figure 8. Effect of the time step for MFV at grid 05

4.1.2 Pressure drop during packed bed

Simulation results from time steps of 0.05 and 0.01 behaves almost equally at each grid during packed bed operation. The observed ΔP s are considerably higher compared to time steps of 0.005 and 0.001 at each velocity step. The curves from time steps of 0.001 and 0.0005 are identical throughout the full range of air velocities. The ΔP using time step 0.005 almost follow the time step of 0.001 with slight over prediction in grid 01 and 04. However, the curve converges to that of the time step of 0.001 before the onset of fluidization.

4.1.3 Pressure drop at fluidization regime

The ΔP during fluidization was similar for all the time steps at each grid. However, respective value increases from 11.5 Pa/mm in grid 01 to 13 Pa/mm in grid 02. Almost steady pressure drops can be observed for time steps of 0.0005, 0.001 and 0.005 between 0.2 m/s and 0.325 m/s air velocities. After 0.325 m/s of air velocity, the ΔP starts to fluctuate for all the simulations. The ΔP is dropped down nearly by 1 Pa/mm after 0.325 m/s air velocity except in grid 02, in which the ΔP is slightly increased.

4.2 Minimum Fluidization Velocity

The results for minimum fluidization velocity does not show much variations over the grid sizes. The MFV obtained from time step of 0.05 is 0.175 m/s for all the grids. Time steps of 0.005, 0.001 and 0.0005 produce the same MFV of 0.15 m/s irrespective of the grid size. The time step of 0.01 gives the same MFV velocity of 0.15 m/s for grid 02, 03, 04 and 05 where in grid 01, MFV is increased to 0.175 m/s.

The observed differences in the ΔP and MFV might be related to CFL conditions or not reaching steady state conditions at each velocity steps. The CFL equation is given by:

$$CFL = u \frac{\Delta t}{\Delta x} \quad (17)$$

Where Δt is time step, Δx is cell size (one dimensional modeling) and u is the convective flow velocity.

At lower time steps the air flow is not fully developed. This effect is progressively increased along the column height. Due to that, the air velocity is getting lesser along the height, which force the cells near the inlet flow boundary to store more air according to the step wise increment of air velocity. This leads to increased pressures near the inlet boundary and consequently increased pressure drop gradients. Therefore, the pressure gradients along the height are less linear for higher time steps. Hence, selecting the transient data points of P1, P2...P3 (refer sketch (b) in Figure 2) to calculate the pressure drop gradient was critical for previous simulation results. This variation is clearly illustrated in air velocity vs pressure drop plots in Figure 9. The simulation results from grid 03 was used and the pressure gradients were calculated using different transient data points according to the formulations mentioned at the lower right hand corner of each plot. The time steps of 0.005 and 0.001 produce almost same results irrespective of the transient data points used. Even though the $(\Delta P)_{MF}$ is high with time step of 0.05, all the plots follow a similar trend. In contrast, the curves for time step 0.01 show higher deviations from each other and however, with less $(\Delta P)_{MF}$ compared to time step 0.05. The collective outcome of these results clearly illustrates that the system has not achieved steady state operation completely with the implemented boundary conditions at lower time steps of 0.05 and 0.01.

Therefore, further simulations were carried out for time steps of 0.05 and 0.01 with extended simulation time of 14 seconds and 20 seconds for each velocity step. Grid 03 was used and air velocity vs pressure drop plots are illustrated in Figure 10 and Figure 11 along with the results from 8 seconds simulation time.

When the plots in Figure 11 are compared, results from 14 second and 20 second simulation time are converged to same values in terms of both $(\Delta P)_{MF}$ and

MFV. $(\Delta P)_{MF}$ remains at 13.6 Pa/mm while the MFV is further reduced to 0.13 m/s. This suggests the inability of further improvement of the results merely by increasing the simulation time for time step 0.01. Therefore, it is necessary to carry out additional simulations with increased simulation time for time steps of 0.005 and 0.001 for other grids to see the provisions for the improvements of the results.

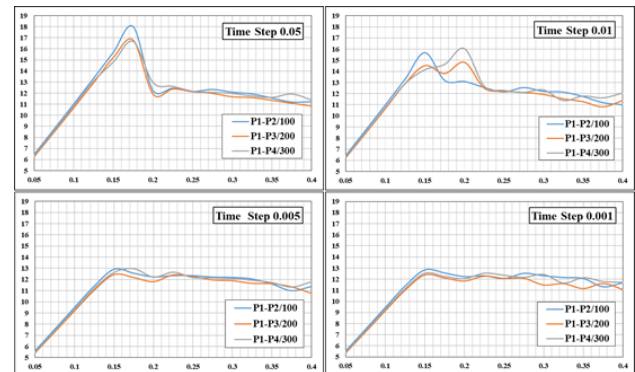


Figure 9. Effect of the time step for MFV at grid 03

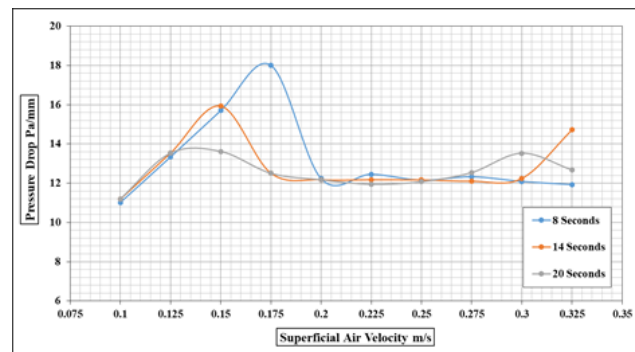


Figure 10. Effect of the simulation time for MFV and pressure drop at time step of 0.05 seconds

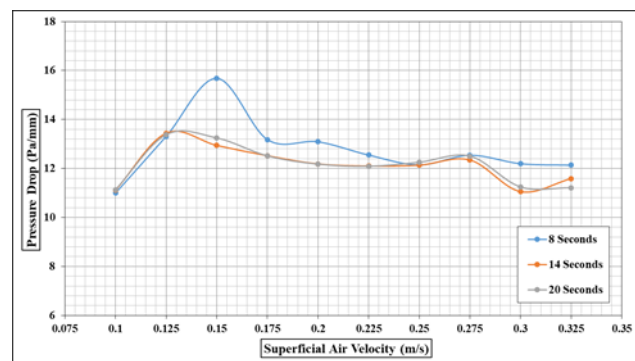


Figure 11. Effect of the simulation time for MFV and pressure drop at time step of 0.01 seconds

4.3 Effect of the close volume fraction for minimum fluidization velocity

Most of the drag models are a function of particle volume fraction (α_p), which is changed depending on particle shape and size distribution. The previously illustrated simulation results were based on close volume fraction of 0.6 and successive simulations are

carried out for 0.55, 0.58 and 0.65. The results are illustrated in Figure 12.

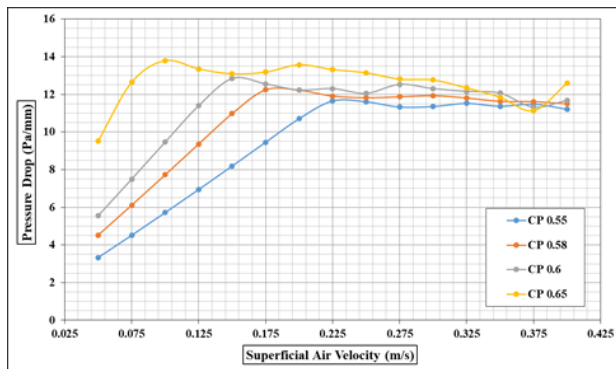


Figure 12. Effect of the close volume fraction for MFV and pressure drop

Grid 03 and time step of 0.001 second were used for the simulations. The pressure drop during packed bed operation is increased with the increased close pack volume fraction. The particles are closely packed that makes it hard for gas to pass through. A slight change in the $(\Delta P)_{MF}$ can also be observed, which is increased proportionally with close volume fraction. There is a significant variation in the MFV, which is reduced down to 0.1 m/s at close volume fraction of 0.65 and as high as 0.225 m/s at 0.55. The drag functions are functions of the particle volume fraction which leads to the difference in MFV. The bed pressure drops are converged together as the air velocity is increased. This is because, the densely packed particles are loosened and attain a more or less common particle volume fraction as the system undergoes rigorous fluidization.

4.4 Effect of the grid size for bubble behavior

The differences in the scales involved is one of the main challenges related to CFD modeling of multiphase systems. Mostly, the particles are in sub-millimeter range while the reactors are in scale of meters. Further, the computational grid can be in the scale of millimeters, centimeters or either in meters depending upon the size of the geometry and computational capacity. Unlike in packed beds, bubbling fluidized beds contain a dense particle phase and a dilute bubble phase. Therefore, the grid should be fine enough to capture the bubble properties as the bubbles play an important role in heat and mass transfer along with particle mixing inside the bed.

Grid 01, 02... 05 and a coarser grid having 2000 cells were simulated for 50 seconds in the bubbling fluidization regime. The time step of 0.001 seconds was used and a constant air velocity of 0,225 m/s was maintained. The behavior of the bubbles in the 40th second of the simulation are illustrated in Figure 13. Smaller and increased number of bubbles appears in the finer grids of grid 05 and 04. The bubble size is becoming larger as the grid size is increased. Finally, the

bubbles are almost disappeared at the coarsest grid with 2000 cells. Therefore, the grid should be fine enough to capture the localized bubble structures. In this case, grid 03 seems to be good enough because, the grid 04 and 05 produce almost the same bubble size.

5 Conclusion

The main objective of the paper was to analyze the effect of time step and grid size for the results in MP PIC modeling. The CPFV commercial package of Barracuda was used in this work. The results give a guidance about the critical parameters to be considered rather than presenting details with model validation.

The minimum fluidization velocity and pressure drop at minimum fluidization were greatly affected by the time step and however, it could be improved by increasing the simulation time. Time steps 0.005s and 0.001s produce the same of minimum fluidization velocity of 0.15 m/s irrespective of the grid resolution. The bed pressure drop at bubbling fluidization regime was not affected considerably by the time step which is 12 pa/mm. However, the minimum fluidization velocity could converge together when the simulation time for a particular air velocity was increased.

The grid size showed a minimal effect on the minimum fluidization velocity. However, the grid size had a great effect on the bubble size and consequently on the bed hydrodynamics. The close volume fraction was also found to be a deciding parameter in simulations for finding the minimum fluidization velocity.

Therefore, the simulation set up should be well optimized depending on the required accuracy of the results and availability of computer power. The physical parameters such as close volume fraction should be accurately measured and implemented in the simulations.

Acknowledgements

The authors like to forward their gratitude to University College of Southeast Norway for providing the Barracuda VR CFD package and computer resources for simulation.

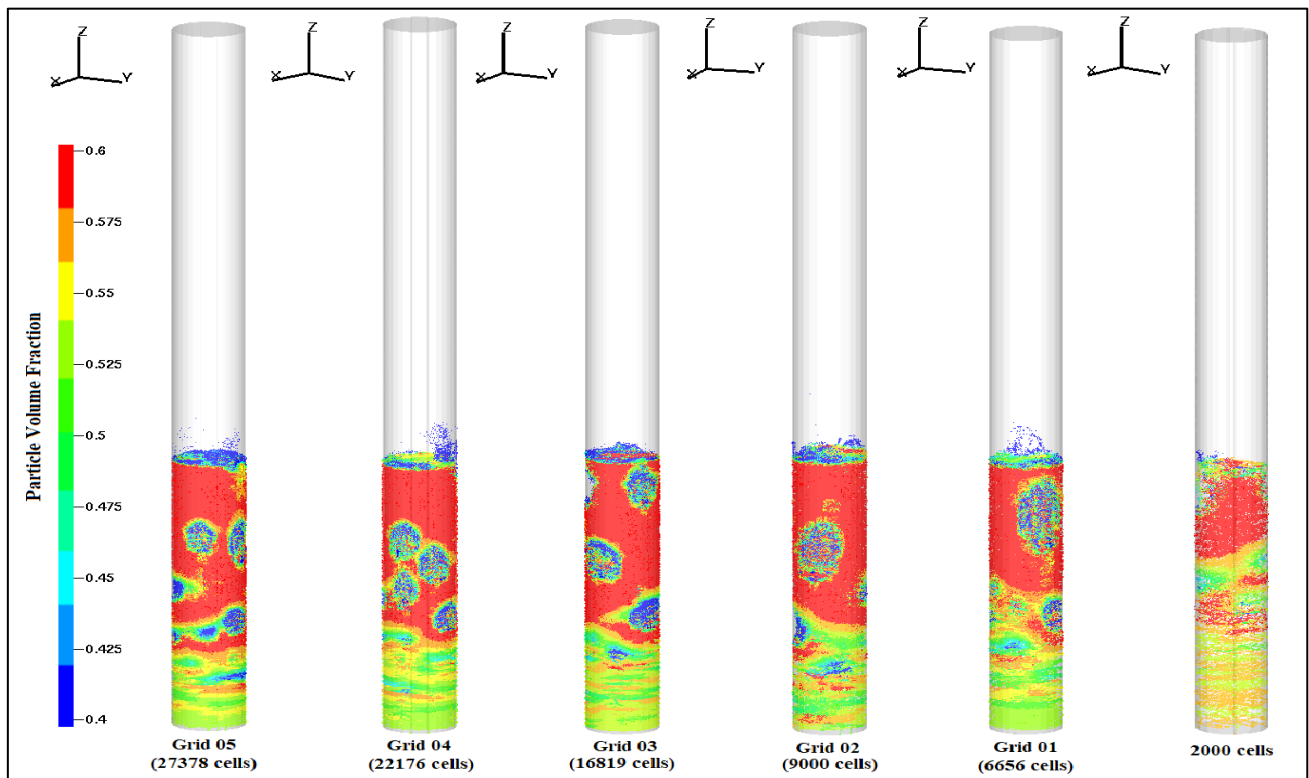


Figure 13. Effect of the computational grid size for the bubble size at 0.225 m/s superficial air velocity

References

- Andrews, M J, and P J O'Rourke. 1996. "The Multiphase Particle-in-Cell (MP-PIC) Method for Dense Particulate Flows." *International Journal of Multiphase Flow* 22 (2): 379–402.
- Gidaspow. 1994, *Multiphase Flow and Fluidization*, Academic press
- Esmaili, Ehsan, and Nader Mahinpey. 2011. "Adjustment of Drag Coefficient Correlations in Three Dimensional CFD Simulation of Gas–solid Bubbling Fluidized Bed." *Advances in Engineering Software* 42 (6): 375–86.
- Geldart, D. 1973. "Types of Gas Fluidization." *Powder Technology* 7 (5): 285–92.
- O'Rourke, Peter J, and Dale M Snider. 2012. "Inclusion of Collisional Return-to-Isotropy in the MP-PIC Method." *Chemical Engineering Science* 80: 39–54.
- Snider, Dale M. 2007. "Three Fundamental Granular Flow Experiments and CPFD Predictions." *Powder Technology* 176 (1): 36–46.
- Snider, D M. 2001. "An Incompressible Three-Dimensional Multiphase Particle-in-Cell Model for Dense Particle Flows." *Journal of Computational Physics* 170 (2): 523–49.
- Snider, D M, P J O'Rourke, and M J Andrews. 1998. "Sediment Flow in Inclined Vessels Calculated Using a Multiphase Particle-in-Cell Model for Dense Particle Flows." *International Journal of Multiphase Flow* 24 (8): 1359–82.
- Souza Braun, Meire Pereira de, Andreza Tangerino Mineto, Hélio Aparecido Navarro, Luben Cabezas-Gómez, and Renato César da Silva. 2010. "The Effect of Numerical Diffusion and the Influence of Computational Grid over Gas–solid Two-Phase Flow in a Bubbling Fluidized Bed." *Mathematical and Computer Modelling* 52 (9): 1390–1402.
- Vejahati, Farshid, Nader Mahinpey, Naoko Ellis, and Mehrdokht B. Nikoo. 2009. "CFD Simulation of Gas-Solid Bubbling Fluidized Bed: A New Method for Adjusting Drag Law." *Canadian Journal of Chemical Engineering* 87 (1): 19–30.
- Bandara, J. C., Thapa, R. K., Moldestad, B. M. E., & Eikeland, M. S. (2016). *Simulation of Particle Segregation in Fluidized Beds* Paper presented at the 9th EUROSIM Congress on Modelling and Simulation, Oulu, Finland.

Paper C

Janitha C. Bandara, Rajan Thapa, Henrik K. Nielsen, Britt M.E. Moldestad, Marianne S. Eikeland

Circulating Fluidized Bed Reactors – Part 01: Analyzing the Effect of Particle Modelling Parameters in Computational Particle Fluid Dynamic (CPFD) Simulation with Experimental Validation

Journal: Taylor and Francis, Particulate Science and Technology (2019)

DOI: 10.1080/02726351.2019.1697773

ISSN: 0272-6351 (Print) 1548-0046 (Online)

Circulating fluidized bed reactors – part 01: analyzing the effect of particle modelling parameters in computational particle fluid dynamic (CPFD) simulation with experimental validation

Janitha C. Bandara^a, Rajan Thapa^a, Henrik K. Nielsen^b, Britt M. E. Moldestad^a, and Marianne S. Eikeland^a

^aDepartment of Process, Energy and Environmental Technology, University of South-Eastern Norway, Porsgrunn, Norway; ^bDepartment of Engineering Sciences, University of Agder, Grimstad, Norway

ABSTRACT

A CPFD hydrodynamic model was developed for a circulating fluidized bed system and the simulation results were validated against experimental data based on particle circulation rate. Sensitivity of the computational mesh was primarily tested and extended grid refinement was needed at the loopseal to match the particle circulation rate with experimental data. The particle circulation rate was independent of the range of number of computational particles used in this study. A 10% reduction of the particle circulation rate was observed as the particle-wall interaction parameter was changed from 0.85 to 0.55 and 17% increment when the close-packed volume fraction was changed from 0.56 to 0.62. The pressure constant in the particle stress model showed the greatest impact for the circulation rate with 57% increment as the constant was changed from 2.5 to 5. The highest absolute variation in the pressure was observed at the loop seal and pressure values were under predicted in all sections.

HIGHLIGHTS

- CPFD simulations are efficient in analyzing fluidized bed systems.
- Manipulating of particle circulation rate is important in circulating fluidized bed.
- Pressure constant in particle stress model is the most influential factor.
- Uncertainties should be minimized prior to optimization of model parameters.

KEYWORDS

Circulating fluidized bed; particle circulation rate; CPFD simulation; sensitivity analysis; model parameters

1. Introduction

Circulating fluidized bed (CFB) is one of the favored technologies in power generation industries due to its distinct advantages of high heat and mass transfer rates, homogeneous reactor temperatures, extended gas-particle contact time, low pollutant emission and fuel flexibility (Li et al. 2004, 2014; Tricomi et al. 2017). Enhanced particle mixing in CFB prevents the generation of hot and cold spots, which is important in gasification and combustion processes as highly exothermic reactions are involved. CFB can be a single/double reactor system as illustrated in Figure 1 or multiple reactor system according to the process requirement. In a single reactor system, the reactor operates at fast fluidization regime in which the particles are carried away with the gas flow, separated with a cyclone and recycled back to the reactor across a proper gas sealing mechanism such as loop seal, L valve, J valve, seal pots, etc. CFB technology is a superior choice to exchange/circulate the same particle phase between different reactors having distinctive reactive environments. Continuous operation, runtime particle

regeneration and controlled material handling some other highlights of CFB. However, efficient and safe design of CFB systems require accurate predictions of the gas-particle behavior in wide range of process conditions, where the rate of particle circulation is one of the most important parameters (Klenov, Noskov, and Parahin 2017).

Experimental studies of fluidized beds are expensive in time and cost. Observation of the interior dynamics of particles demands high-end technologies such as electrical capacitance tomography, particle image velocimetry, and laser Doppler anemometry, etc. Further, the system optimization with a single experimental rig is challenging such as optimization of geometrical shape and dimensions, particle size and feeding positions, etc. Computational fluid dynamic (CFD) modeling and simulation is a remarkable substitution to mitigate aforementioned drawbacks, which have become more realistic and efficient with increased computer power and advanced numerical algorithms (Li et al. 2014). Single-phase CFD simulations produce accurate results more precise than a sensor can capture. In contrast, CFD modeling

CONTACT Janitha C. Bandara  janitha.bandara@usn.no; janithjc@gmail.com  University of South-Eastern Norway, Kjølnes ring 56, P.O. Box 203 N3901, Porsgrunn, Norway.

This article has been republished with minor changes. These changes do not impact the academic content of the article.

© 2019 The Author(s). Published with license by Taylor & Francis Group, LLC.

This is an Open Access article distributed under the terms of the Creative Commons Attribution-NonCommercial-NoDerivatives License (<http://creativecommons.org/licenses/by-nc-nd/4.0/>), which permits non-commercial re-use, distribution, and reproduction in any medium, provided the original work is properly cited, and is not altered, transformed, or built upon in any way.

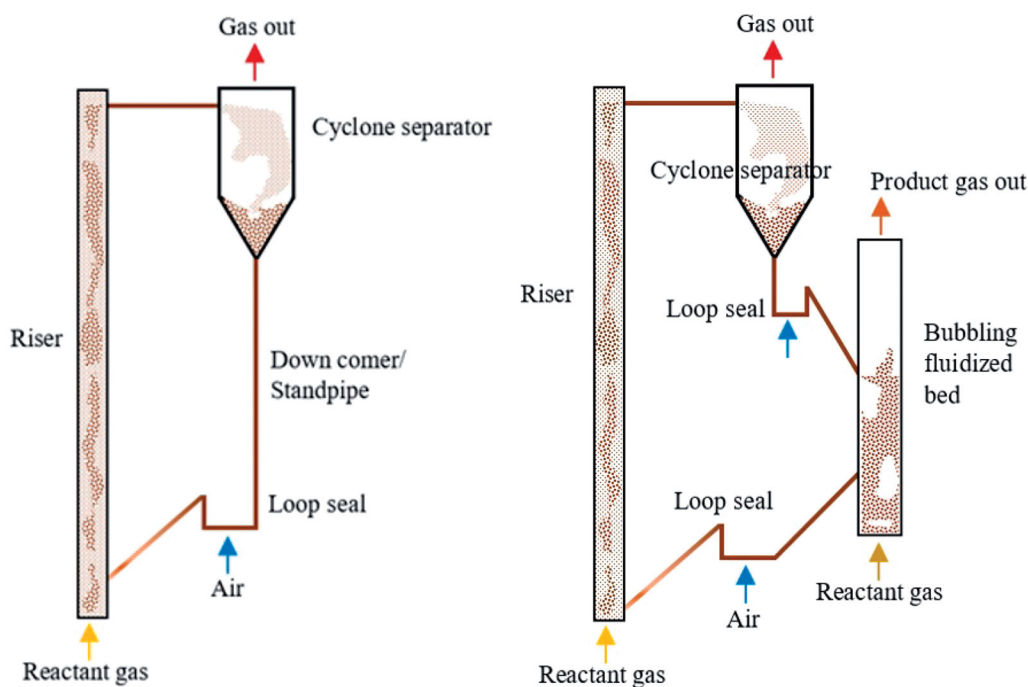


Figure 1. Different configurations of circulating fluidized bed. Circulating fluidized bed (left). Dual reactor circulating fluidized bed (right).

of multiphase flow systems are still challenging. Modeling of phase interactions and inter-particle collision with extended complexities aroused due to scale differences between particles of micron range and large reactors of several meters are the main challenges (Deen et al. 2007).

Eulerian-Eulerian (EE) and Eulerian-Lagrangian (EL) are the two fundamental approaches of multiphase CFD, which can be distinguished based on the treatment method of the dispersed phase. The fluid phase is modeled with Navier-Stokes equations with appropriate averaging method in both cases. Particle phase is mathematically treated as continuous and fully interpenetrating with fluid phase in EE modeling, while the trajectories of each particle are calculated in LE modeling. Kinetic theory of granular flow (KTGF) is used to derive the particle properties in EE method where the LE method uses Newton's second law of motion with hard-sphere or soft-sphere particle contact model. Empirical correlations are necessary at different levels for both EE and LE modeling (Deen et al. 2007). Even though the hydrodynamic predictions from EE simulations are recorded to be satisfactory by many researchers (Snider 2001; Chiesa et al. 2005), the discrete nature of the particles is missing (Chiesa et al. 2005; Jiang, Qiu, and Wang 2014). As the discrete particle method (DPM); LE method for particle systems, is concerned, approximately 80% of the computational cost is used to contact detections of particles and calculating the geometric areas of contact. Hence, increased number of particles in large-scale reactors imposes a substantial computational cost (Klenov, Noskov, and Parahin 2017) where DPM is not viable for industrial reactors in the near future. The computational efficiency of DPM is possible to boost by replacing the individual particle contacts with probabilistic strategy which is used in multiphase particle-in-cell (MP-PIC) method (Pannala, Syamlal, and O'Brien 2011; Ma and Zhao 2018; Moliner et al. 2018).

The multiphase particle-in-cell (MP-PIC) method was developed by Andrews and O'Rourke (1996) and later by Snider (2001), to model dense particle flows. The actual particles are grouped into computational particles (parcels) that contain a number of adjacent particles sharing similar properties of density, size, and velocity. The parcel dynamics are modeled in the Lagrangian frame where the particle forces are calculated in the Eulerian grid considering the continuum approach. This reduces the extensive computational cost related to modeling of inter-particle collisions. Particle stress is calculated in an advanced time step, which is mapped back to individual particles in real-time with interpolation functions. Even with the superior computational efficiency, description of rotation movement and non-spherical shape of the particles are not included, which cause lower prediction accuracy compared to DPM. Detailed governing equations and numerical procedures of the MP-PIC method can be found in the literature. (Andrews and O'Rourke 1996; Snider 2001; Snider and Banerjee 2010; Snider, Clark, and O'Rourke 2011; Chen et al. 2013; Jiang, Qiu, and Wang 2014).

Barracuda VR is a commercial CPFD package that is custom designed for particle systems using MP-PIC modeling. Tu and Wang (2018) have worked on a full loop CFB system to compare the energy minimization multi-scale (EMMS) and the Wen-Yu drag models with experimental validation. Jiang, Qiu, and Wang (2014) have carried out experiments in a six cyclone CFB and monitored the bed hydrodynamics using the electrical capacitance tomography (ECT) technique where the authors have carried out CPFD simulations for the same unit to compare the accuracy of the prediction. Chen et al. (2013) have used the CPFD technique to analyze the performance of a riser section of a CFB and commented on the requirement of drag model optimization. An extended validation of CPFD simulation has

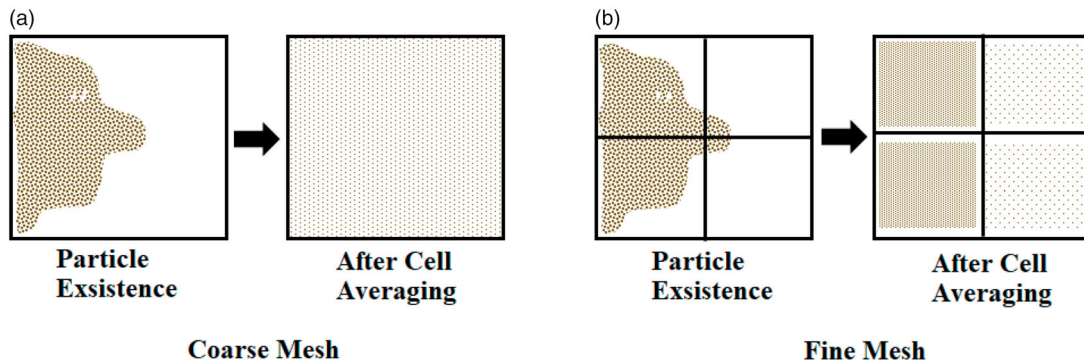


Figure 2. Effect of the mesh size in cell averaged particle volume fraction.

been done by Liang et al. (2014) with the experiments carried out in a bubbling fluidized bed and suggested some required improvements in the simulation setup. CPFD simulations have been used to analyze the nonreactive fluidized bed systems (Snider 2007; Qiu, Ye, and Wang 2015) and reactive systems like combustion and gasification of biomass and coal. (Snider and Banerjee 2010; Abbasi, Ege, and de Lasa 2011; Snider, Clark, and O'Rourke 2011; Xie et al. 2012; Loha, Chattopadhyay, and Chatterjee 2014; Thapa et al. 2016).

Multiphase flows exist in various forms of structures over a wide range of time and length scales (Li and Kwauk 2003). Computational mesh/grid should be sufficiently refined to capture these important mesoscale structures. The effect of the mesh size for cell averaged particle volume fractions is illustrated in Figure 2. Coarse grids destroy the small particle structures while the fine grids lead to high computational cost. In contrast to the DPM, selected particle properties are calculated based on the Eulerian grid in CPFD, which leads to definite effects from the grid size. Local small structures cause large variations in the particle volume fraction over the geometry, which impose a strong influence on interphase momentum and mass transfer by governing the drag force and mass transfer rate (Wang et al. 2010). Therefore, efficient capturing of these structures is crucial in accurate predictions in circulating fluidized bed operation.

The CPFD method further differs from DPM as it models computational particles instead of individual particles in the Lagrangian frame. Therefore, the resolution of the computational particles has an equal importance as the mesh resolution. However, with the implementation of "global cloud resolution" option, the number of computational particles in the system is adjusted accordingly with the cell size and number of cells in the initial particle patch.

Circulating fluidized bed configuration is a widespread technology in combustion and gasification of biomass. Biomass particles are difficult to fluidize due to their low density and irregularity in shape (Cui, and Grace 2007) and therefore, gasification reactors require a supporting particulate phase (bed material) consisting of fine fluidizable particles such as inert sand or catalysts. Despite the fact that the CFD simulation overcomes numerous practical limitations, extensive validation of hydrodynamic models is important for guaranteed data reproducibility. The reactor hydrodynamic is primarily governed by the bed material

and hence, a detailed understanding of the hydrodynamics of bed material in a non-reactive CFB system is important for subsequent CFD analysis in a reactive environment. A similar CFB geometry has been analyzed and presented by Wang et al. using CPFD in two consecutive research articles (Wang et al. 2014a, 2014b). Nevertheless, the effects of the coefficients in particle stress model and particle-wall contact momentum retention are not presented. The particle flow across the loop seal happens in dense phase and as a result, the particle weight is directly applied on the bottom and sidewalls of the loop seal. The pipe cross-section at the loop seal is narrow and therefore, it is expected that the wall friction exert a significant effect over a considerable fraction of the cross-section available for the particle flow. Even though specific values have been defined for hard and soft particles in the technical guidance of Barracuda VR, a sharp shift between soft and hard particles is not real. Hence, the effects of the particle-wall collision parameters are presented, which will be useful for those who need extended tuning. Unlike in bubbling fluidized beds, there exists a resultant particle flow driven by fluid drag and particle collisions against gravity and contact forces (particle-particle and particle-wall). Further, unlike in dilute phase particle flow, the dense phase particle flow across the loop seal is greatly affected by the inter-particle forces. Particle stress model is responsible for calculating the particle-particle forces, which is significant as it reaches the close packing. Therefore, the effects of particle-wall collision and particle stress model parameters are analyzed and presented along with a comprehensive analysis of the effects of grid size, number of computational particles, close pack volume fraction and fluid drag model. The simulation results are compared with experimentally measured rate of particle circulation and system pressure. Barracuda VR 17.3.0 CPFD commercial software was used in this work with Intel(R) Core(TM) i7-5930K CPU 3.50 GHz processor.

2. Experimental and CFD model set up

Model validation is based on experimental studies performed in a full loop CFB unit, which is illustrated in Figure 3. Detailed experimental procedure is given in the work of Thapa et al. (2016). Sand with particle density of 2650 kg/m^3 and mean diameter of $150 \mu\text{m}$ was used as the particle phase and air was used as the fluidizing medium.

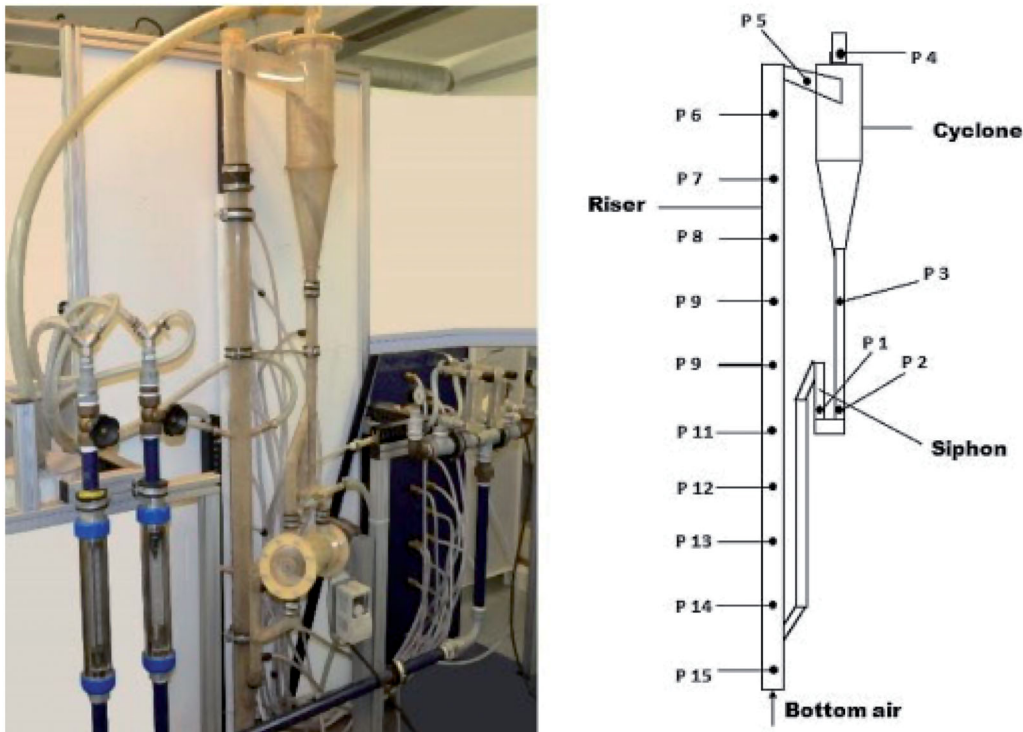


Figure 3. Circulating fluidized bed experimental rig.

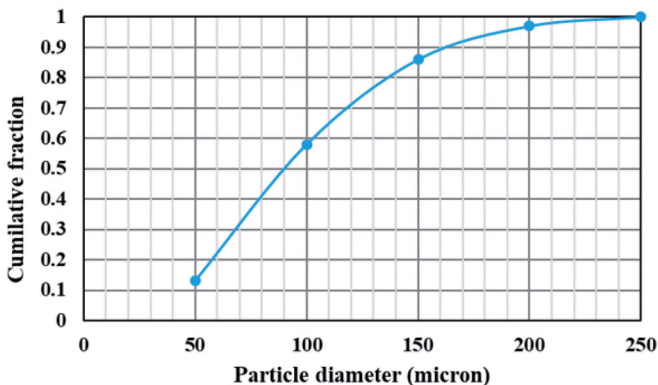


Figure 4. Particle size distribution of the bed material.

The particle size distribution was ranged from 50 to 250 μm and illustrated in Figure 4. The geometrical dimensions were adopted from a scaled drawing. The diameter of the standpipe and the recycle pipe are 30 mm. The horizontal section of the loop seal is 70 mm long and has a cross-section area of 30 mm \times 30 mm. The height of the recycle pipe before the sharp bend is 135 mm. The riser section is 50 mm in diameter and 1700 mm in height. The technical terms related to loopseal sections are defined by Basu and Butler (2009).

A summary of the boundary values, particle properties, and modeling parameters are given in Table 1. The boundary conditions, computational mesh, and initial particle filling are depicted in Figure 5. The fluidizing air to the riser was implemented as a uniform flow boundary throughout the bottom plane of the column and loopseal aeration with

Table 1. Simulation data and model parameters.

Particle mean diameter	130 micron
Aeration gas	Air
Riser fluidized air	20 Nm ³ /h
Loop seal aeration	1 Nm ³ /h
Particle mass	0.58–0.6 kg
Close pack volume fraction	0.6
Collisional momentum redirection	40%
Normal-to-wall momentum retention	0.85
Tangent-to-wall momentum retention	0.85
Initial time step	0.0005 s

injection boundaries as illustrated in Figure 5(b). The initial particle patching was implemented as illustrated in Figure 5(c) and pressure-monitoring points were implemented at P1, P2, P3, P6, and P15 as illustrated in Figure 3. Two flux planes along the standpipe and the recycle pipe were positioned to monitor the particle circulation rate.

Particle stress model was used with default parameters of 1, 3, and 10^{-8} for P_s , β , and ε , respectively. The “blended acceleration model” (BAM) was activated, as the particle phase had a size distribution in the range of 50–250 microns. BAM prevents unrealistic particle segregation by absorbing the sustained particle contacts that is prevalent in dense particle systems. A considerable effect was expected related to particle-wall interaction and hence, the diffuse bounce coefficient (a measure of deviated angle from ideal after collision) was set to 3. Turbulence was modeled with large eddy simulation and the numerical scheme used was Partial Donor Cell (PDC) method, which is a weighted average formulation of central difference and upwind schemes. Courant-Friedrichs-Lewy (CFL) condition is a measurement of the stability of the numerical solver whereas of 0.8 and

Note:

Loopseal aeration was implemented with single flowmeter and branching outflow into two aeration points. The aeration points were located at the bottom of the side walls aligned with the mid plane of the verticle pipes of standpipe and recycle pipe.

Riser aeration was as considered uniformly distributed

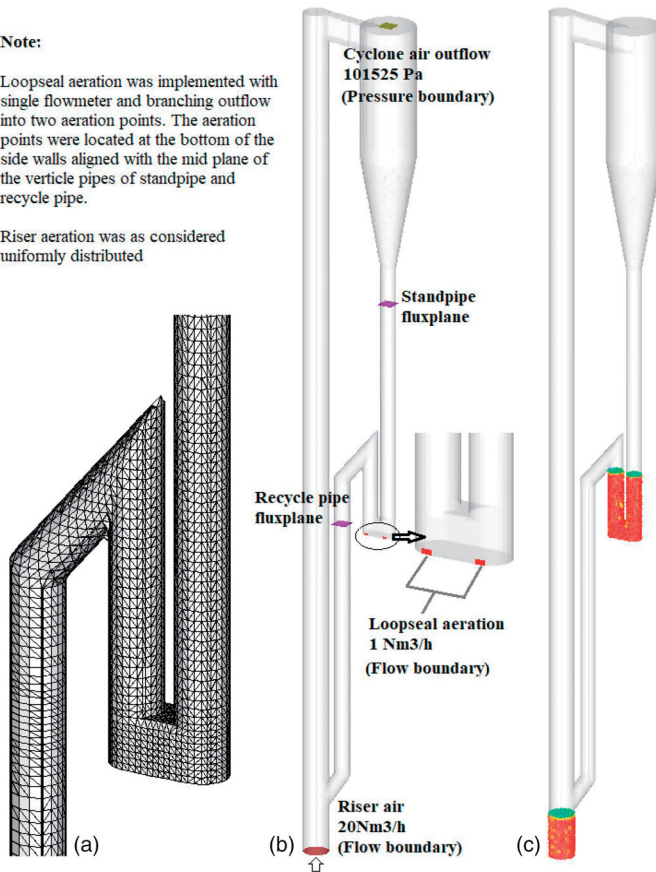


Figure 5. (a)-Computational grid near loopseal, (b)-Boundary conditions and Flux planes, (c)-Initial particle filling.

1.5 were used for minimum and maximum values, respectively. The grid sensitivity analysis was carried out using Wen-Yu-Ergun drag model. The particle-wall interaction coefficients were taken as 0.85 for both normal and tangential collisions as specified by Barracuda VR for hard particles. The closed-pack volume fraction was set as 0.6. The grid convergence (grid sensitivity analysis) test and the effect of computational particles were performed to identify the optimal grid having less computational time with sufficient accuracy. The hydrodynamic model with optimized grid and computational particles was subsequently analyzed for different particle-wall interaction coefficients for perpendicular collisions. The model was subjected to further analysis to identify the effect of the closed-pack volume fraction of particles, pressure constant of particle stress model and four different fluid drag models.

2.1. Governing equations

The drag model is one of the crucial parameters that governs the particle behavior. The riser operates in the dilute phase while the standpipe of the loop seal (dip leg from the cyclone) is supposed to operate in dense phase at either minimum fluidization or packed bed. The Ergun equation has been extensively analyzed and proved for its high accuracy in the dense particle phase and therefore, the Gidaspow

drag model, which is a blended formulation of the Wen-Yu and Ergun drag models, was used for the initial simulation works. The Wen-Yu drag model is used at gas volume fractions higher than 0.8 (Patel, Pericleous, and Cross 1993; Jayarathna et al. 2019).

$$D_{Wen-Yu} = \frac{3}{8} C_d \frac{\rho_g}{\rho_p} \frac{|u_g - u_p|}{r_p} \alpha^{-2.65}$$

$$C_d = \frac{24}{Re}, \quad (Re < 0.5)$$

$$C_d = \frac{24}{Re} (1 + 0.115Re^{0.687}), \quad (0.5 \leq Re \leq 1000)$$

$$C_d = 0.4, \quad (Re > 1000)$$

C_d is the drag coefficient, Re is the particle Reynolds number and r_p is the particle diameter. As the gas volume fraction decreases below 0.8, the Ergun correlation is used (Ergun 1952; Jayarathna et al. 2019),

$$D_{Ergun} = 0.5 \left(\frac{C_1 \alpha_p}{\alpha_g Re} + C_2 \right) \frac{\rho_g}{\rho_p} \frac{|u_g - u_p|}{r_p}$$

The default values for the laminar and turbulent coefficients in the Barracuda VR are 180 (C_1) and 2.0 (C_2) where those are 150 and 1.75 in original Ergun formulation. The particle Reynolds number is given by:

$$Re = \frac{2\rho_p |u_g - u_p|}{\mu_g} \left(\frac{3V_p}{4\pi} \right)^{1/3}$$

The gas phase mass and momentum conservation are modeled with continuity and time-averaged Navier-Stokes equations (Snider 2001):

$$\frac{\partial(\alpha_g \rho_g)}{\partial t} + \nabla \times (\alpha_g \rho_g u_g) = 0$$

$$\frac{\partial(\alpha_g \rho_g u_g)}{\partial t} + \nabla \times (\alpha_g \rho_g u_g u_g) = -\nabla P - F + \nabla \times (\alpha_g \tau_g) + \alpha_g \rho_g g$$

Where α_g , ρ_g , and u_g are gas phase volume fraction, density, and velocity, respectively. F is the total momentum exchange with particle phase per volume, g is the gravitational acceleration, P is the pressure, and τ_g is the gas phase stress tensor. The stress tensor the gas phase is given by,

$$\tau_g = \mu_g \left[\left(\nabla u_g + \Delta u_g^T \right) - \frac{2}{3} \nabla \times u_g I \right]$$

μ_g refers to the shear viscosity that is the sum of the laminar and turbulent components. The large eddy simulation is used for the large-scale turbulence modeling while the subgrid scale turbulence is captured with the Smagorinsky model:

$$\mu_{g,t} = C_s \rho_g \Delta^2 \left| \nabla u_g + \Delta u_g^T \right|$$

Table 2. Properties related to different grid configurations.

Grid	Cells	Cell size ($\Delta x, \Delta y, \Delta z$) (mm)	Computational particles	Computational particles to cell ratio
01	136,000	$7.5 \times 7.5 \times 7.5$	5×10^4	0.367
02	242,592	$6 \times 6 \times 6$	9.2×10^4	0.379
03	338,541	$5 \times 5 \times 5$	1.33×10^5	0.392
Refined grids at loop seal (*the grid sizes at the loop seal)				
04	323,830	$3.75 \times 3.75 \times 3.75^*$	1.86×10^5	0.574
05	401856	$3.75 \times 3.75 \times 3.33^*$	2.35×10^5	0.584

The default value for the model constant C_s is 0.01. Δ is the sub-grid length scale and calculated by,

$$\Delta = (\delta x \delta y \delta z)^{1/3}$$

The interface momentum transfer is calculated through the viscous drag force:

$$F = \iint f \left\{ m_p \left[D_p(u_g - u_p) - \frac{\nabla P}{\rho_p} \right] \right\} dm_p du_p$$

Subscript P refers to the particle phase properties where m and u symbolizes the mass and velocity, respectively. D_p is the drag function. The particle phase dynamics are derived using the particle distribution function (PDF) calculated from the Liouville equation given as (Snider 2001):

$$\frac{\partial f}{\partial t} + \nabla(fu_p) + \nabla u_p(fA_p) = 0$$

Where A_p is the particle acceleration and is expressed by:

$$A_p = \frac{\partial(u_p)}{\partial t} = D_p(u_g - u_p) - \frac{\nabla P}{\rho_p} - \frac{\nabla \tau_p}{\rho_p \alpha_p} + g$$

α_p is the particle volume fraction. τ_p is the particle stress function, which is used to formulate the interphase interactions of particles (Snider 2001; O'Rourke and Snider 2014).

$$\alpha_p = \iint f \frac{m_p}{\rho_p} dm_p du_p$$

$$\tau_p = \frac{10P_s \alpha_p^\beta}{\max[(\alpha_{cp} - \alpha_p), \varepsilon(1 - \alpha_p)]}$$

P_s is a constant with the units of pressure, α_{cp} is the particle volume fraction at close packing, β is a constant between 2 and 5. ε is a very small number in the order of 10^{-7} , which is used to avoid the singularity as particles reach closed pack volume.

Turton–Levenspiel drag model (Turton and Levenspiel 1986):

$$D = \frac{3}{8} C_d \frac{\rho_g}{\rho_p} \frac{|u_g - u_p|}{r_p}$$

$$C_d = \frac{24}{Re} \alpha_p^{-2.65} \left[(1 + 0.173 Re^{0.657}) + \frac{0.413}{1 + 16300 Re^{0.657}} \right]$$

Nonspherical Ganser drag model (Chhabra, Agarwal, and Sinha 1999) where ω is the particle sphericity:

$$C_d = \alpha_p^{-2.65} K_2 \left[\frac{24}{Re K_1 K_2} (1 + c_0 (Re K_1 K_2)^{n_1}) + \frac{24c_1}{1 + \frac{c_2}{Re K_1 K_2}} \right]$$

$$c_0 = 0.1118, \quad c_1 = 0.01794, \quad c_2 = 3305, \quad n_1 = 0.6567, \\ n_2 = 1.8148, \quad n_3 = 0.5743$$

$$K_1 = \frac{3}{1 + 2\omega^{-0.5}}, \quad K_2 = 10^{n_2(-\log \omega)^{n_3}}$$

Nonspherical-Haider-Levenspiel drag model (Chhabra, Agarwal, and Sinha 1999):

$$C_d = \alpha_p^{-2.65} \left[\frac{24}{Re} \left[1 + c_0 \exp(n_1 \omega) (Re)^{(n_2 + n_3 \omega)} \right] + \frac{24c_1 \exp(n_4 \omega) Re}{Re + c_2 \exp(n_5 \omega)} \right]$$

$$c_0 = 8.1716, \quad c_1 = 3.0704, \quad c_2 = 5.378, \quad n_1 = 4.0655, \quad n_2 \\ = 0.0964, \quad n_3 = 0.5565, \quad n_4 = -5.0748, \quad n_5 = 6.2122$$

Richardson–Davidson–Harrison drag model follows the Wen–Yu drag model excluding the functionality of the effect of particle volume fraction.

3. Results and discussion

The particle circulation rate had been experimentally calculated by interrupting the loopseal aeration and measuring the time to build up a certain amount of particles (the bed height) in the standpipe (Thapa et al. 2016). This might substantially influence the particle hydrodynamics in the riser, as the particles are not fed to the riser from the loopseal. A precise measurement of the particle height in the standpipe is challenging during fluidization conditions. The particle circulation rate is highly fluctuating and local measurements might not represent the long-standing average of the system. Further, the system needed to be operated for a certain time to achieve the steady-state conditions prior to taking the measurements where a slight fraction of the particle mass can be escaped. Hence, there can be a discrepancy in system mass between experiments and simulations.

Moreover, uncertainties related to the CPFD model set up might lead to deviations from the actual settings. CPFD requires to feed the envelope density¹ and however, the apparent density of 2650 kg/m³ was used due to insufficient data of particles. Assumption of spherical particles and uncertainty of the particle size distribution might lead to

¹Absolute density is excluding volume of open and close pores of the grain (absolute volume of the particle material) while apparent density is excluding only close pores. Envelope density is calculated by taking average shape of the particle (i.e. including narrow open pores) whereas, inter particle voids are also included in bulk density measurements.

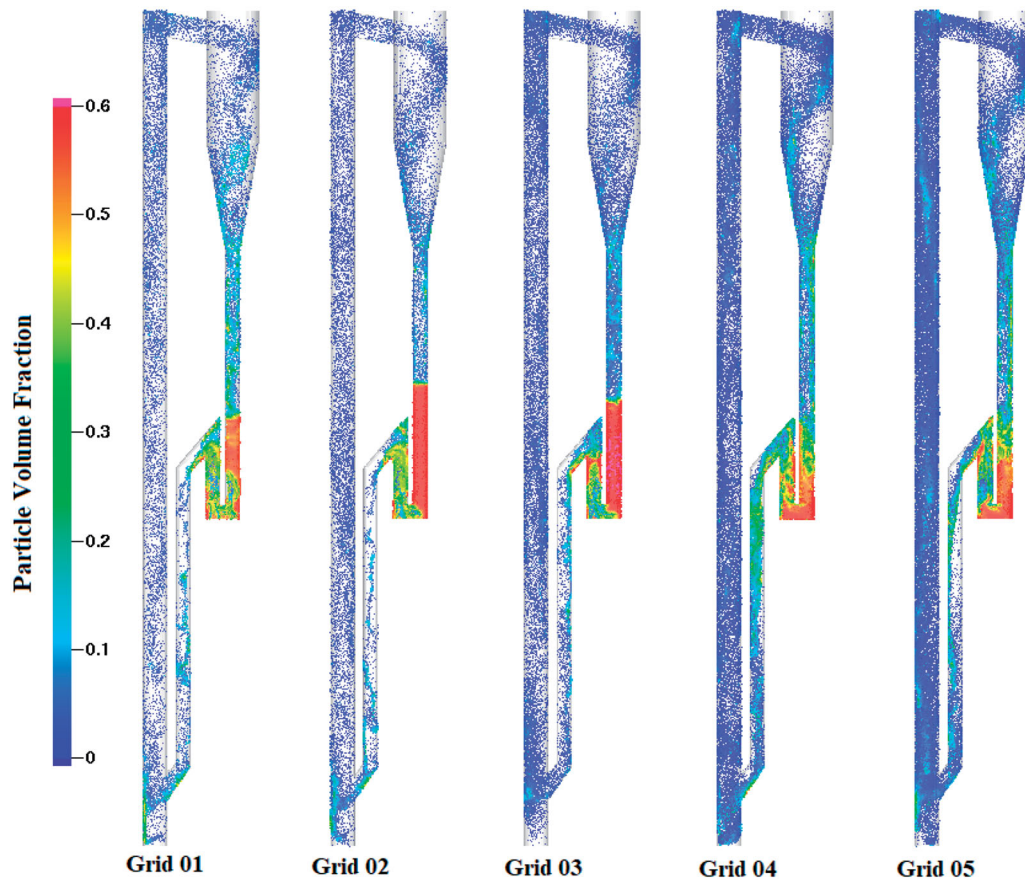


Figure 6. Particle volume fractions at 30th second of the simulation for different grid configurations.

deviations in hydrodynamics of fluidization followed by particle circulation rate.

3.1. Grid sensitivity

The solid circulation rate and the system pressure were analyzed with five different grid configurations. Grid 01, 02, and 03 were constructed using uniform grid option. Grids 04 and 05 were constructed by refining the cell structure simply at the loopseal of Grid 01 and 02, respectively. Table 2 summarizes the number of cells, grid size, and number of computational particles of each grid configuration.

As the number of computational cells is increased, a simultaneous increment of computational particles can be observed. The graphical representation in Figure 6 illustrates the computational particles (i.e. not the real particles). A gradual increment of computational particles towards fine mesh grids is clearly visible from Grid 01 to 05. The ratio between the computational particles to the number of cells is nearly equal in Grid 01, 02, and 03 while Grid 04 and 05 show considerably higher values. As the number of cells is high at the loopseal in Grid 04 and 05, more computational particles are included by the model setup.

Particles tend to accumulate along the standpipe in the coarse grids 02 and 03. Bubbles cannot be observed and hence, the particle bed is either at the packed bed regime or at minimum fluidization conditions. This results in less particle concentration in the other sections of the system,

especially in riser. In contrast, Grid 04 and 05 show rigorous fluidization at the loopseal. The gas jet penetration length at the loopseal aeration was also observed. In the coarse grid simulations, the gas jet dissolves near the injection and does not move much in the direction of the injection. In contrast, the penetration length is high in the refined grids, which might lead to different hydrodynamics at the loopseal and consequently affect the particle circulation rate. Whenever the grid structure changes, the number of parcels, parcel size, and consequently, the number of parcels per cell are changed.

3.1.1. Particle circulation rate

The particle circulation rate is analyzed across the flux plain defined at the recycle pipe (Figure 5). The averaged values over 30th second for different grid configurations and the experimental value are illustrated in the right upper chart of Figure 7. The circulation rates, averaged over two-second intervals of the simulation, are depicted in the right middle plot of Figure 7. Grid 01 shows extremely low circulation rate of 30 kg/h and the grid resolution is insufficient to capture the particle hydrodynamics. A significant improvement of the particle circulation up to 220 kg/h was achieved by a uniform grid refinement towards Grid 02 and 03. However, a substantial difference between Grid 02 and 03 could not be observed even with 100,000 more cells in Grid 03 than in Grid 02. With the observed particle accumulation at the standpipe, successive grid refinements at the loopseal were performed for detailed analysis. Grid 04 and 05 are the

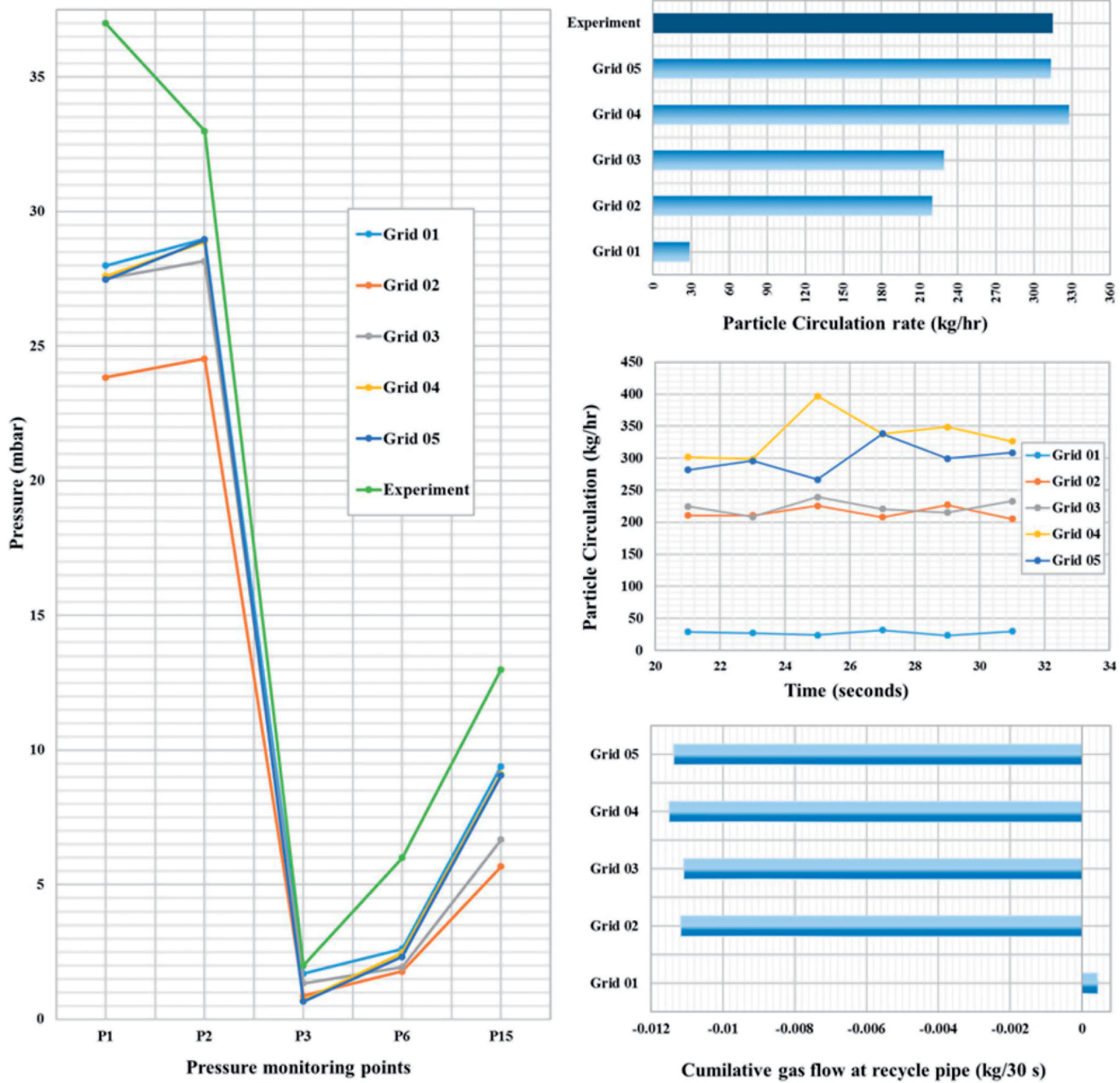


Figure 7. Particle circulation rate and pressure profiles for different grid configurations.

restructured meshes at the loopseal of Grid 02 and 03, respectively. A sensible improvement can be observed in both of the grids 04 and 05 having average circulation rates of 325 kg/h and 315 kg/h, respectively, which is approximately equal to the experimental results. Apart from the extreme deviation at the 25th second, Grid 04 and 05 follow a similar behavior and finally reach a near steady value around 320 kg/h. The circulation rate at the recycle pipe was compared with the additional flux plane defined at the standpipe to verify the steady-state operation. A slight difference between the two flux planes was observed in Grid 01 and 02 whereas Grid 03, 04, and 05 had equal values.

The instant variations of the solid circulation rates between Grid 04 and 05 can be due to different grid structures in the riser, loopseal and cyclone followed by a different number of computational particles at each setup. Large

variations in the cell sizes over the domain are not recommended and further, the lengths in X, Y, and Z directions of a certain cell should be uniform if possible. Further, a sharp change in the cell size should be prevented by implementing a gradient in the direction of change. The number of computational particles is defined based on initial particle patching and the cell sizes in the patching volume. The number and volume of computational particles remain constant in time (for a closed loop system). Whenever computational particles of different sizes exist in the system, the largest should be fine enough to enclose in the finest cells in the domain. The difference in the cell sizes between the loop seal and the rest of the domain is higher in Grid 04 compared to Grid 05. Especially, the meshing near the walls of the cyclone cylindrical section is relatively coarse in Grid 04. This might lead to a slight excess

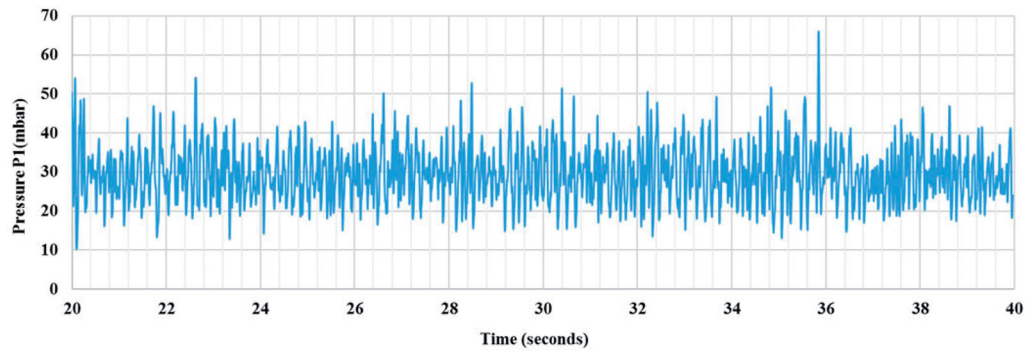


Figure 8. Instantaneous pressure values at P1 from simulation of Grid 04.

prediction of particle circulation when using Grid 04. Grid 05 delivers exactly the same particle circulation rate as that in experiments.

The loopseal aeration had been achieved by two injection points and however, measured by a single flowmeter (during experiments). A slight difference in the pressure at two particular locations could be observed and hence, the related flowrates could be different from each other. Implementing narrow injection pipes in the computational setup requires very fine meshing at the loopseal. Therefore, each aeration point was implemented using injection boundary conditions (in contrast to the standard flow boundaries) with half of the total measured loopseal airflow. The CFB setup has narrow pipes and passages and therefore, minor errors/uncertainties related to lengths might lead to considerable deviations in the simulations results. Due to these uncertainties and simplified implementations in the CFPD setup, the hydrodynamic behavior in the simulations can deviate from the experimental results.

The gas flow behavior across the recycle pipe was also monitored at the same flux plane used to monitor the particle circulation. The results are illustrated to the right at the bottom of Figure 7. The cumulative gas flow after 30 seconds of simulation was compared between the different grids. According to the proper functionality, gas is not expected to pass from the riser through the loopseal to the cyclone. Instead, part of the loopseal-air flows towards the riser, which gives a negative flux in Z direction. Grid 01 displays a positive flux, which is not the expected flow behavior. The rest of the grid tests show an approximately equal negative flow of 0.0115 kg during 30 seconds. The calculated cumulative airflow at the loop seal from the injection boundary conditions is 0.01122 kg, which is nearly equal to 0.0115 kg. However, a slightly higher airflow can be observed in Grid 04 and 05 compared to Grid 02 and 03. The particle circulation is substantially high for these grids and therefore, an additional amount of gas is carried along with the particles. The particle flow in the loopseal is mainly driven by the gas drag and not by the pressure exerted by the standpipe particle inventory.

3.1.2. System pressure

The system pressure at selected locations is plotted in Figure 7 and the simulation results represent the averaged values

between 25 and 30 seconds. The numbering of pressure locations is referred to Figure 3. Grid 2 shows the highest deviation of the pressure compared to the experimental results whereas P_1 shows the highest local variation when all the grid configurations are considered. The pressure data obtained from the simulations follows the same trend as experimental values except for P_1 . P_1 is higher than P_2 during the experiments, whereas P_1 is lower than P_2 in all the simulations. This deviation might be related to the uncertainty of the geometrical dimensions; especially the height of the recycle pipe and pipe diameter of the loopseal. The instantaneous pressures values at P_1 for Grid 04 are illustrated in Figure 8 and high fluctuations between 15 and 45 mbar can be observed. The simulation results reach the experimental value at certain times and therefore, it is recommended to average the pressure data over an extended time (in experiments and simulations).

Assumption of spherical particles, uncertainty related to particle size distribution and implemented closed packed volume fraction followed by deviations in the particle inventory and geometrical dimensions can be the root cause for the pressure deviation between simulation results and experimental data. Further, the particle volume fraction of the riser varies between 0 and 0.1 (Figure 6). The Wen-Yu correlation is used to calculate the fluid drag force at lower particle volume fractions according to the model definition. The drag model for dilute phase flows has not been extensively validated as for the dense phase systems such as packed beds or bubbling fluidized beds. Hence, the low pressures in the riser can be due to reduced particle loading where this particular variation effects on the other sections as well. On the other hand, the Ergun correlation has been developed using Geldart B particles. However, the used particle mixture was at the margin of the Geldart A and B particles, where a fraction of the mixture is classified as Geldart A particles. Therefore, the linear coefficient of the laminar component of the Ergun correlation can be deviated from the original value of 150, which can exert a considerable effect on the pressure profile, especially at the loopseal.

3.2. Effect of the number of computational particles

Even with the analogous pressure profiles, Grid 01 results in reduced particle circulation with unrealistic gas flow behavior and therefore, further analysis was discarded. A

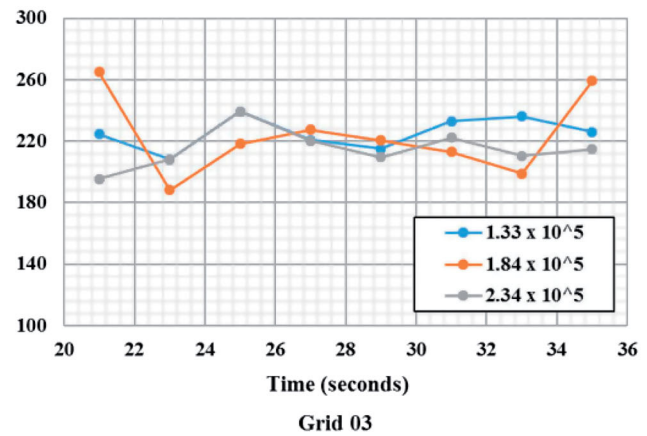
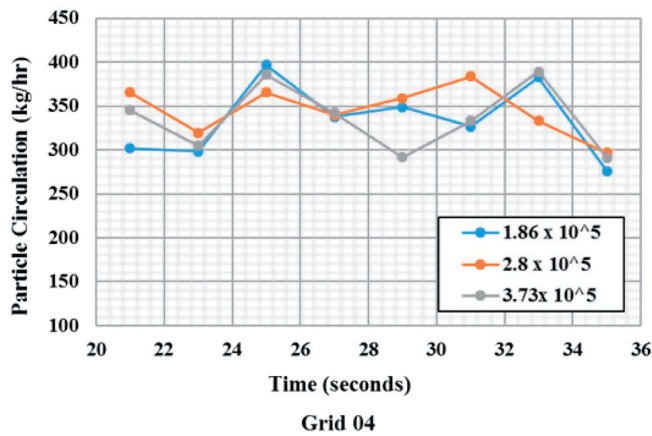


Figure 9. Particle circulation rate with increased computational particle.

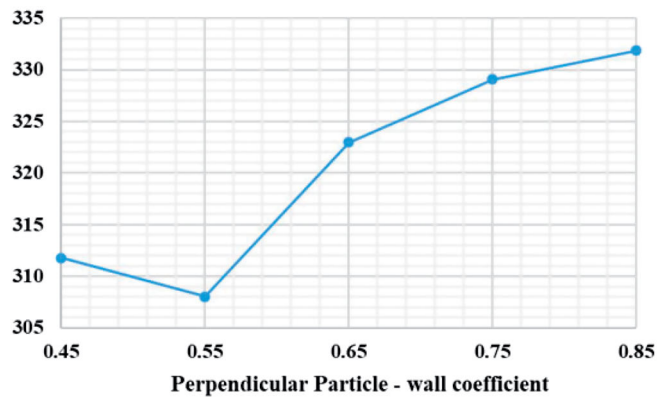
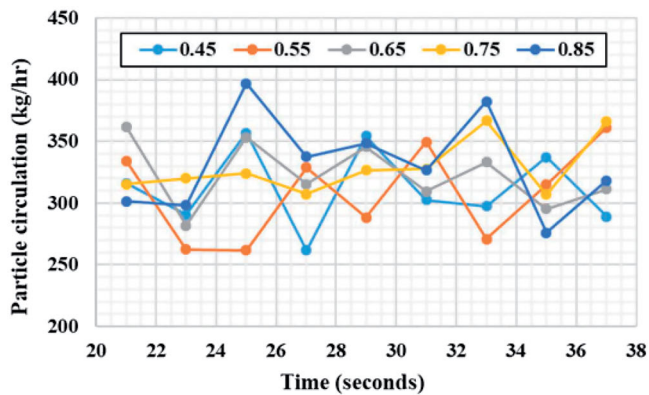


Figure 10. Sensitivity of particle-wall interaction for particle circulation rate.

substantial growth in the particle circulation (approximately 40%) was observed when the grid was refined from Grid 03 to 04. The number of computational particles is a function of the grid that encloses the initial particle patching and it remains unchanged during the simulation unless the system mass is changed. The successive grid refinements from 01 to 05 caused increasing number of computational particles and therefore, supplementary analyses were necessary to verify whether the increased circulation was achieved due to the grid refinement or the increased number of computational particles. Two additional simulations were performed for Grid 03 with 1.84×10^5 and 2.34×10^5 computational particles, which are the same number of particles used in the original Grid 04 and 05, respectively (Table 2). Computational particle convergence analysis was carried out for Grid 04 with two subsequent simulations having 2.8×10^5 and 3.73×10^5 particles.

The simulation results are depicted in Figure 9 and there was not observed any considerable change in the average particle circulation with increased number of computational particles. However, local differences of the circulation rates can be observed for both grids. Therefore, it can be concluded that the bed hydrodynamics has not been affected by changing the number of computational particles. Further, the pressure profiles follow similar characteristics

irrespective of the computational particles. Therefore, Grid 04 with 1.86×10^5 computational particles was used for further analysis.

3.3. Effect of the particle-wall interaction coefficient

The particle-wall interaction is modeled with three parameters of perpendicular collision, tangential collision, and diffuse bounce. The default recommended values for the perpendicular and tangential collision are 0.3 and 0.99, which have been used by many researchers. The effect of these parameters are minimal for vertical fluidized beds. The pipe diameter at the loopseal is narrow and the horizontal passage operates at dense phase where the particle weight directly applies on the pipe walls. Hence, loopseal operation can be considerably affected by particle wall interactions and consequently, the particle circulation rate. Hard particles can be modeled using 0.85 for both coefficients as recommended by Barracuda VR. The perpendicular coefficient was changed from 0.45 to 0.85 (keeping tangential coefficient constant at 0.85) and the particle circulation rate was monitored. The diffuse bounce was set to 3 for all simulations, which carries the information of scattering angle related to particle-wall collisions.

The plots in Figure 10 reflects the instantaneous and 30 second averaged particle circulation rates. The circulation

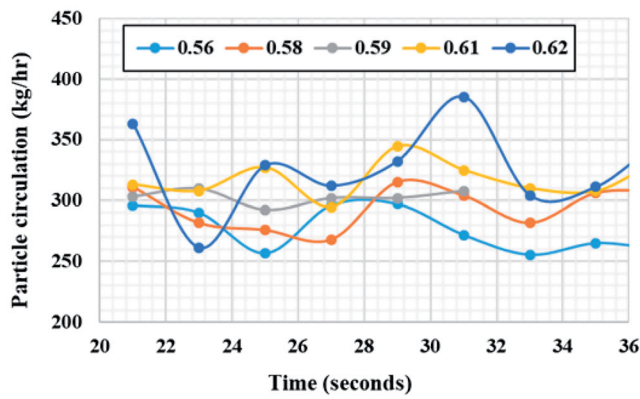


Figure 11. Particle circulation as a function of closed pack volume fraction.

rate increases proportionally with the particle-wall interaction coefficient in the range of 0.55–0.85. The circulation rate is more sensitive to the coefficient at low values and becoming less sensitive at higher values.

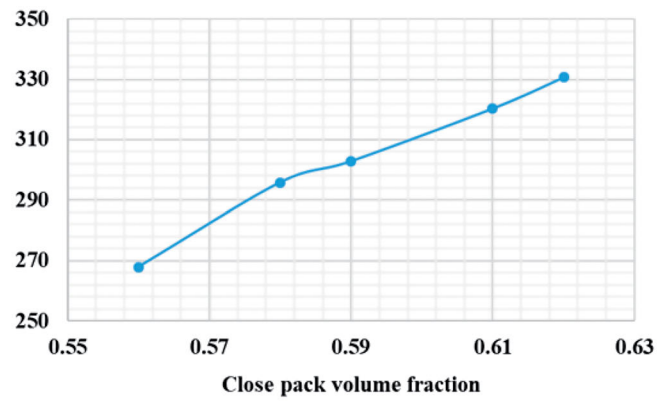
3.4. Effect of the closed pack volume fraction

Closed pack volume fraction carries the information about the degree of maximum packing. The higher the value, the more the resistance for the fluid to penetrate through and hence, the pressure drop is increased. In contrast, the fluid drag correlation is a function of particle volume fraction. Further, the particle stress model uses the closed pack volume fraction in calculating the force exerted from particle collisions. These factors influence the particle hydrodynamics and hence, the closed pack volume fraction is one of the most important parameters in MP PIC modeling. The close pack volume fraction is simply calculated by bulk density to particle density ratio and however, only particle size distribution and absolute density were available. Therefore, the particle circulation rates for different values of closed pack volume fraction were analyzed and the results are given in Figure 11.

A proportional increment in circulation rate can be observed. Referring to the time dependent rate, higher fluctuations can be observed as the closed pack volume fraction is increased and however, the fluctuations are minimum at 0.59. The loopseal pressure readings slightly increased with high close pack volume fractions. As the close pack volume fraction is involved in both drag model and stress model, the observed effect of increasing circulation has two roots. Therefore, extended simulations were conducted changing the pressure constant in stress model equation.

3.5. Effect of pressure constant in particle stress model

The modeling of particle-particle interactions is crucial in dense particle systems, which requires a strong four-way coupling. The loopseal section is at dense phase in standard operating conditions and hence, the particle stress model can have a greater impact on hydrodynamics. As the particles reach close pack volume fraction, the denominator of the stress function reduces to a low number and consequently, the stress is increased generating high forces. The



pressure constant itself contribute to increase the particle stress. As the loopseal operates at dense phase flow regime, this increased force can improve the circulation.

As mentioned in the section “Experimental and CFD model set up”, loopseal aeration was implemented as injection boundary conditions where the mass flowrate and the injection velocity should be defined. The injection velocity showed a considerable impact on particle circulation rate and it was adjusted during grid sensitivity analysis. The optimized value was used for the following simulations in sections of “Effect of the particle-wall interaction coefficient” and “Effect of the closed pack volume fraction”. However, as the pressure constant was changed from 1 to 5, the particle circulation rate increased unrealistically. As the main uncertainty appeared in loopseal aeration, the injection boundary was changed into flow boundary having an identical value to the inner area of 6 mm pneumatic pipe connection. The pressure constant was needed to increase beyond 4.5 to fix the circulation rate with experimental data as depicted in Figure 12. The pressure constant vs. particle circulation curve becomes flat between 3.5 and 4.5, however, the circulation increases proportionally with the pressure constant. The system pressure remained nearly similar irrespective of the different pressure constant values.

3.6. Effect of the fluid drag correlation

The Wen-Yu-Ergun drag model was used for all the prior simulations. The main drive to select this particular model was due to the existence of both dilute and dense phase in the system. Several inbuilt drag functions are available in Barracuda VR, where few models are equipped to model non-spherical particles. The Turton-Levenspiel, Nonspherical-Ganser, Nonspherical-Haider-Levenspiel, and Richardson-Davidson-Harrison drag models were compared with the Wen-Yu-Ergun model based on particle circulation rate. An additional simulation using the Wen-Yu-Ergun model with modified laminar and turbulent coefficients of 180 and 2, respectively (Barracuda default values), were carried out. The results are presented in Figure 13. The Richardson-Davidson-Harrison model showed extremely low circulation of nearly 150 kg/hr where more particles accumulated in the standpipe section of the loop seal. The

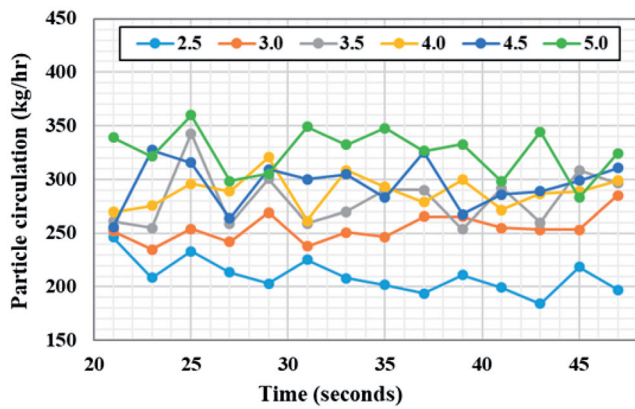


Figure 12. Effect of the pressure constant in the particle stress model.

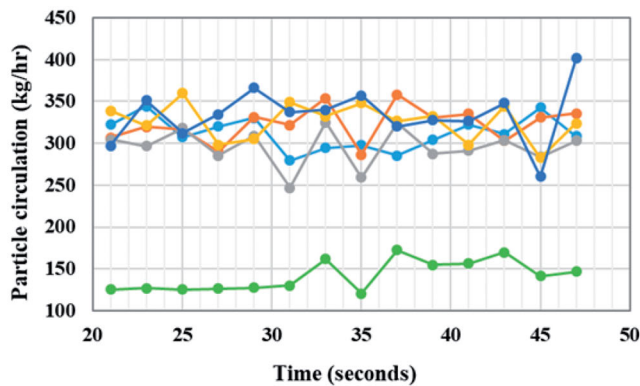
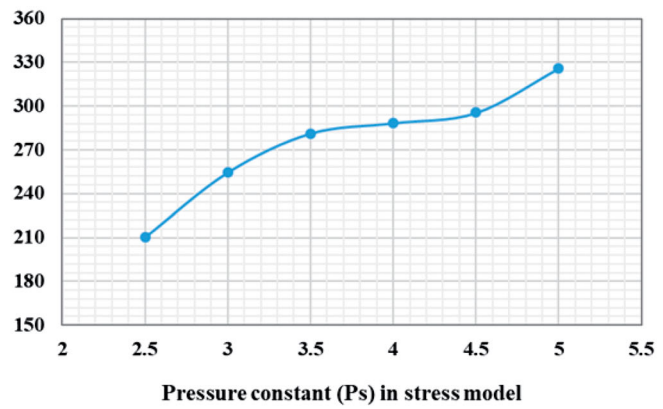
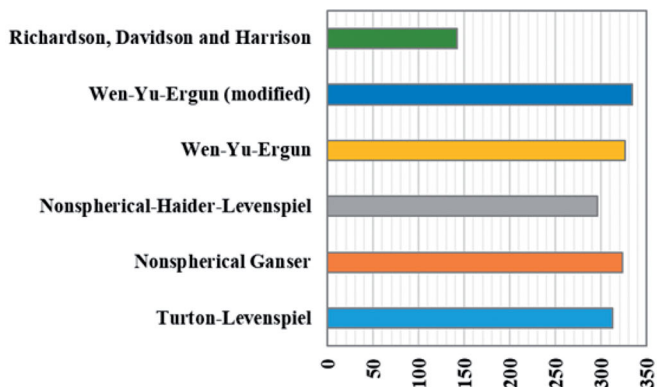


Figure 13. Effect of the drag model for particle circulation rate.



nonspherical Haider-Levenspiel model showed 300 kg/hr where all other drag models resulted in increased circulation above 300 kg/hr reaching the experimental data. Particle volume fractions and particle Reynolds number (Re) are greatly varied over the reactor. High Re and low particle volume fractions can be observed in the riser whereas low Re and high particle volume fractions in the loop seal section. The Richardson-Davidson-Harrison drag model is not a function of both parameters at high Reynolds number where the particle volume fraction is excluded in the full range of Re , which can be the reason for the large deviation. The particle sphericity was taken as 0.9 for models with sphericity as a parameter (Rorato et al. 2019); Nonspherical-Ganser and Nonspherical-Haider-Levenspiel. Both of the models are a function of Re in the full range of Re , which is not the case for Wen-Yu model as the drag turns into a constant at high Re . These differences might lead to varied results for particle circulation. The laminar and turbulent coefficients of the Ergun model have been subjected to continuous modifications depending on particle properties (i.e. Geldart's classification, particle shape, etc.) (Olatunde and Fasina 2019; Ozahi, Gundogdu, and Carpinlioglu 2008). As the coefficients are increased, both bed pressure drop and fluid drag change proportionally, which is clearly illustrative with increased particle circulation with modified coefficients. The system pressure followed the same trend and approximately same results as depicted in Figure 7.

4. Conclusion

The main objective of the research work was to develop a hydrodynamic model for a circulating fluidized bed system using the Barracuda VR CFPD package, which uses the MP-PIC modeling. Effect of the grid resolution and selected simulation parameters were compared with experimental results and the rate of particle circulation was considered as the primary parameter. The system pressure was also monitored.

The grid resolution near the loopseal showed a great influence over the particle circulation rate and grid refinements at the particular section was needed to capture the particle hydrodynamics. Nearly, 40% increment of particle circulation rate was achieved analogous with loopseal grid refinement. Computational Grid 04 and 05 were successful in achieving the particle circulation similar to the experimental data. The system pressure predictions from the simulations were lower than the experimental data, which could be due to associated uncertainties of geometry and particle properties. The number of computational particles defined by the default software settings was observed to be adequate and further increment did not make considerable changes in the circulation rate. The particle circulation rate increased proportionally by 17% as the closed pack volume fraction was changed from 0.56 to 0.6. The effect of the particle-wall interaction coefficient was less significant compared to closed pack volume fraction where approximately 10%

difference was observed from 0.55 to 0.85. Pressure constant in the particle stress model showed the greatest impact on the particle circulation rate with an increment of 57% as the pressure constant changed from 2.5 to 5. The Wen-Yu-Ergun and Nonspherical Ganser drag models resulted in the highest particle circulation rate where Richardson-Davidson-Harrison model under predicted the circulation.

Precise information about the particle properties will be useful in further analysis and concrete validation of the hydrodynamic model. Model validation for different materials with different size and density will improve the reproducibility of the simulation data. If the experimental unit is equipped to measure the particle loading over different sections, it will be useful for further comparison. Whenever the Ergun equation is used, it is a good practice to optimize the linear coefficient experimentally, especially for the particles not grouped within Geldart B. The uncertainties and measurement errors should be minimized to optimize the model parameters. The developed hydrodynamic model is possible to analyze system behaviors against different operational conditions.

Acknowledgement

The authors like to forward their gratitude to University College of Southeast Norway for providing the Barracuda VR CFD package and computer resources for simulation.

References

- Abbasi, A., P. E. Ege, and H. I. de Lasa. 2011. CPFD simulation of a fast fluidized bed steam coal gasifier feeding section. *Chemical Engineering Journal* 174 (1):341–50. doi: [10.1016/j.cej.2011.07.085](https://doi.org/10.1016/j.cej.2011.07.085).
- Andrews, M. J., and P. J. O'Rourke. 1996. The multiphase particle-in-cell (MP-PIC) method for dense particulate flows. *International Journal of Multiphase Flow* 22 (2):379–402. doi: [10.1016/0301-9322\(95\)00072-0](https://doi.org/10.1016/0301-9322(95)00072-0).
- Basu, P., and J. Butler. 2009. Studies on the operation of loop-seal in circulating fluidized bed boilers. *Applied Energy* 86 (9):1723–31. doi: [10.1016/j.apenergy.2008.11.024](https://doi.org/10.1016/j.apenergy.2008.11.024).
- Chen, C., J. Werther, S. Heinrich, H.-Y. Qi, and E.-U. Hartge. 2013. CPFD simulation of circulating fluidized bed risers. *Powder Technology* 235:238–47. doi: [10.1016/j.powtec.2012.10.014](https://doi.org/10.1016/j.powtec.2012.10.014).
- Chhabra, R. P., L. Agarwal, and N. K. Sinha. 1999. Drag on non-spherical particles: An evaluation of available methods. *Powder Technology* 101 (3):288–95. doi: [10.1016/S0032-5910\(98\)00178-8](https://doi.org/10.1016/S0032-5910(98)00178-8).
- Chiesa, M., V. Mathiesen, J. A. Melheim, and B. Halvorsen. 2005. Numerical simulation of particulate flow by the Eulerian-Lagrangian and the Eulerian-Eulerian approach with application to a fluidized bed. *Computers and Chemical Engineering* 29 (2):291–304. doi: [10.1016/j.compchemeng.2004.09.002](https://doi.org/10.1016/j.compchemeng.2004.09.002).
- Cui, H., and J. R. Grace. 2007. Fluidization of biomass particles: A review of experimental multiphase flow aspects. *Chemical Engineering Science* 62 (1–2):45–55. doi: [10.1016/j.ces.2006.08.006](https://doi.org/10.1016/j.ces.2006.08.006).
- Deen, N. G., M. Van Sint Annaland, M. A. Van der Hoef, and J. A. M. Kuipers. 2007. Review of discrete particle modeling of fluidized beds. *Chemical Engineering Science* 62 (1–2):28–44. doi: [10.1016/j.ces.2006.08.014](https://doi.org/10.1016/j.ces.2006.08.014).
- Ergun, S. 1952. Fluid flow through packed columns. *Chemical Engineering Progress* 48:89–94.
- Jayarathna, C. K., M. Balfe, B. M. E. Moldestad, and L.-A. Tokheim. 2019. Improved multi-stage cross-flow fluidized bed classifier. *Powder Technology* 342:621–9. doi: [10.1016/j.powtec.2018.10.026](https://doi.org/10.1016/j.powtec.2018.10.026).
- Jiang, Y., G. Qiu, and H. Wang. 2014. Modelling and experimental investigation of the full-loop gas–solid flow in a circulating fluidized bed with six cyclone separators. *Chemical Engineering Science* 109: 85–97. doi: [10.1016/j.ces.2014.01.029](https://doi.org/10.1016/j.ces.2014.01.029).
- Klenov, O. P., A. S. Noskov, and O. A. Parahin. 2017. Investigation of behaviors of the circulating fluidized bed. *Chemical Engineering Journal* 329:66–76. doi: [10.1016/j.cej.2017.06.092](https://doi.org/10.1016/j.cej.2017.06.092).
- Li, J., and M. Kwauk. 2003. Exploring complex systems in chemical engineering—the multi-scale methodology. *Chemical Engineering Science* 58 (3–6):521–35. doi: [10.1016/S0009-2509\(02\)00577-8](https://doi.org/10.1016/S0009-2509(02)00577-8).
- Li, T., A. Gel, S. Pannala, M. Shahnam, and M. Syamlal. 2014. CFD simulations of circulating fluidized bed risers, part I: Grid study. *Powder Technology* 254:170–80. doi: [10.1016/j.powtec.2014.01.021](https://doi.org/10.1016/j.powtec.2014.01.021).
- Li, X. T., J. R. Grace, C. J. Lim, A. P. Watkinson, H. P. Chen, and J. R. Kim. 2004. Biomass gasification in a circulating fluidized bed. *Biomass and Bioenergy* 26 (2):171–93. doi: [10.1016/S0961-9534\(03\)00084-9](https://doi.org/10.1016/S0961-9534(03)00084-9).
- Liang, Y., Y. Zhang, T. Li, and C. Lu. 2014. A critical validation study on CPFD model in simulating gas–solid bubbling fluidized beds. *Powder Technology* 263:121–34. doi: [10.1016/j.powtec.2014.05.003](https://doi.org/10.1016/j.powtec.2014.05.003).
- Loha, C., H. Chattopadhyay, and P. K. Chatterjee. 2014. Three dimensional kinetic modeling of fluidized bed biomass gasification. *Chemical Engineering Science* 109:53–64. doi: [10.1016/j.ces.2014.01.017](https://doi.org/10.1016/j.ces.2014.01.017).
- Ma, H., and Y. Zhao. 2018. Investigating the fluidization of disk-like particles in a fluidized bed using CFD-DEM simulation. *Advanced Powder Technology* 29 (10):2380–93. doi: [10.1016/j.apt.2018.06.017](https://doi.org/10.1016/j.apt.2018.06.017).
- Moliner, C., F. Marchelli, N. Spanachi, A. Martinez-Felipe, B. Bosio, and E. Arato. 2018. CFD simulation of a spouted bed: Comparison between the Discrete Element Method (DEM) and the Two Fluid Model (TFM). *Chemical Engineering Journal* 377:120446. doi: [10.1016/j.cej.2018.11.164](https://doi.org/10.1016/j.cej.2018.11.164).
- O'Rourke, P. J., and D. M. Snider. 2014. A new blended acceleration model for the particle contact forces induced by an interstitial fluid in dense particle/fluid flows. *Powder Technology* 256:39–51. doi: [10.1016/j.powtec.2014.01.084](https://doi.org/10.1016/j.powtec.2014.01.084).
- Olatunde, G., and O. Fasina. 2019. Modified Ergun equation for airflow through packed bed of loblolly pine grinds. *KONA Powder and Particle Journal Advpub* 36 (0):232. doi: [10.14356/kona.2019003](https://doi.org/10.14356/kona.2019003).
- Ozahi, E., M. Y. Gundogdu, and M. Ö. Carpinlioglu. 2008. A modification on Ergun's correlation for use in cylindrical packed beds with non-spherical particles. *Advanced Powder Technology* 19 (4):369–81. doi: [10.1163/156855208X314985](https://doi.org/10.1163/156855208X314985).
- Pannala, S., M. Syamlal, and T. J. O'Brien. 2011. *Computational gas-solids flows and reacting systems: Theory, methods and practice*. Hershey, USA: Engineering Science Reference.
- Patel, M. K., K. Pericleous, and M. Cross. 1993. Numerical modelling of circulating fluidized beds. *International Journal of Computational Fluid Dynamics* 1 (2):161–76. doi: [10.1080/10618569308904470](https://doi.org/10.1080/10618569308904470).
- Qiu, G., J. Ye, and H. Wang. 2015. Investigation of gas–solids flow characteristics in a circulating fluidized bed with annular combustion chamber by pressure measurements and CPFD simulation. *Chemical Engineering Science* 134:433–47. doi: [10.1016/j.ces.2015.05.036](https://doi.org/10.1016/j.ces.2015.05.036).
- Rorato, R., M. Arroyo, E. Andò, and A. Gens. 2019. Sphericity measures of sand grains. *Engineering Geology* 254:43. doi: [10.1016/j.eng-geo.2019.04.006](https://doi.org/10.1016/j.eng-geo.2019.04.006).
- Snider, D. M. 2001. An Incompressible Three-Dimensional Multiphase Particle-in-Cell Model for Dense Particle Flows. *Journal of Computational Physics* 170 (2):523–49. doi: [10.1006/jcph.2001.6747](https://doi.org/10.1006/jcph.2001.6747).
- Snider, D. M. 2007. Three fundamental granular flow experiments and CPFD predictions. *Powder Technology* 176 (1):36–46. doi: [10.1016/j.powtec.2007.01.032](https://doi.org/10.1016/j.powtec.2007.01.032).
- Snider, D. M., and S. Banerjee. 2010. Heterogeneous gas chemistry in the CPFD Eulerian-Lagrangian numerical scheme (ozone decomposition). *Powder Technology* 199 (1):100–6. doi: [10.1016/j.powtec.2009.04.023](https://doi.org/10.1016/j.powtec.2009.04.023).
- Snider, D. M., S. M. Clark, and P. J. O'Rourke. 2011. Eulerian-Lagrangian method for three-dimensional thermal reacting

- flow with application to coal gasifiers. *Chemical Engineering Science* 66 (6):1285–95. doi: [10.1016/j.ces.2010.12.042](https://doi.org/10.1016/j.ces.2010.12.042).
- Thapa, R. K., A. Frohner, G. Tondl, C. Pfeifer, and B. M. Halvorsen. 2016. Circulating fluidized bed combustion reactor: Computational particle fluid dynamic model validation and gas feed position optimization. *Computers and Chemical Engineering* 92:180–8. doi: [10.1016/j.compchemeng.2016.05.008](https://doi.org/10.1016/j.compchemeng.2016.05.008).
- Tricomi, L., T. Melchiori, D. Chiaramonti, M. Boulet, and J. M. Lavoie. 2017. Sensitivity analysis and accuracy of a CFD-TFM approach to bubbling bed using pressure drop fluctuations. *Frontiers in Bioengineering and Biotechnology* 5 (38): doi: [10.3389/fbioe.2017.00038](https://doi.org/10.3389/fbioe.2017.00038).
- Tu, Q., and H. Wang. 2018. CPFDF study of a full-loop three-dimensional pilot-scale circulating fluidized bed based on EMMS drag model. *Powder Technology* 323:534–47. doi: [10.1016/j.powtec.2017.09.045](https://doi.org/10.1016/j.powtec.2017.09.045).
- Turton, R., and O. Levenspiel. 1986. A short note on the drag correlation for spheres. *Powder Technology* 47 (1):83–6. doi: [10.1016/0032-5910\(86\)80012-2](https://doi.org/10.1016/0032-5910(86)80012-2).
- Wang, Q., H. Yang, P. Wang, J. Lu, Q. Liu, H. Zhang, L. Wei, and M. Zhang. 2014a. Application of CPFDF method in the simulation of a circulating fluidized bed with a loop seal Part II—Investigation of solids circulation. *Powder Technology* 253:822–8. doi: [10.1016/j.powtec.2013.11.040](https://doi.org/10.1016/j.powtec.2013.11.040).
- Wang, Q., H. Yang, P. Wang, J. Lu, Q. Liu, H. Zhang, L. Wei, and M. Zhang. 2014b. Application of CPFDF method in the simulation of a circulating fluidized bed with a loop seal, part I—Determination of modeling parameters. *Powder Technology* 253:814–21. doi: [10.1016/j.powtec.2013.11.041](https://doi.org/10.1016/j.powtec.2013.11.041).
- Wang, W., B. Lu, N. Zhang, Z. Shi, and J. Li. 2010. A review of multi-scale CFD for gas–solid CFB modeling. *International Journal of Multiphase Flow* 36 (2):109–18. doi: [10.1016/j.ijmultiphaseflow.2009.01.008](https://doi.org/10.1016/j.ijmultiphaseflow.2009.01.008).
- Xie, J., W. Zhong, B. Jin, Y. Shao, and H. Liu. 2012. Simulation on gasification of forestry residues in fluidized beds by Eulerian–Lagrangian approach. *Bioresource Technology* 121:36–46. doi: [10.1016/j.biortech.2012.06.080](https://doi.org/10.1016/j.biortech.2012.06.080).

Paper D

Janitha C. Bandara, Britt M.E. Moldestad, Marianne S. Eikeland

Analyzing the Effects of Geometrical and Particle Size Uncertainty in Circulating Fluidized Beds using CPFD Simulation

Conference: Proceedings of the 60th SIMS Conference on Simulation and Modelling (SIMS 60), September 25 – 27, 2019, Västerås, Sweden. PP 182-189

DOI: 10.3384/ecp20170182

Analyzing the Effects of Geometrical and Particle Size Uncertainty in Circulating Fluidized Beds using CPFD Simulation

Janitha C. Bandara¹ Britt M.E. Moldestad¹ Marianne S. Eikeland¹

¹Department of Process, Energy and Environmental Technology, University of South-eastern Norway,
Norway

{janitha.bandara, britt.moldestad, Marianne.Eikeland}@usn.no

Abstract

Computational fluid dynamic modeling and simulation is becoming a useful tool in the detailed analysis of multiphase flow systems. The level of uncertainty is different depending on selected modeling concept and numerical schemes. Physical uncertainties originated from geometrical dimensions and particle properties are important aspects. In this work, CPFD method was used to analyze the effect of dimensional uncertainty of loopseal pipe diameter and particle size distribution in a circulating fluidized bed. Five different pipe diameters were studied and 20% growth in particle circulation rate was observed as the diameter reduced from 30mm to 26mm. The effect of small changes in the particle size distribution was negligible and the particle circulation rate decreased by 32% with monodisperse particles of mean size.

Keywords: CPFD simulation, uncertainty, circulating fluidized bed, particle circulation rate

1 Introduction

Computational fluid dynamic (CFD) modeling and simulation is extensively used in designing and optimizing of reactive and non-reactive systems. The flow predictions for single phase systems with CFD is very much precise and however, multiphase systems are still encountering number of theoretical and numerical challenges, such as wide range of spatio-temporal scales (length scales between single particles, particle clusters, computational grid and geometry), collision, shear and interact of particles, mass and momentum exchange between phases (Pannala et al., 2011).

Different techniques have been developed to model the multiphase systems. Direct numerical simulation (DNS) requires the least modeling effort. However, the computational time is high as it resolves the complete flow field around each particle of the system and the particle movement is modeled with Newton's equation of motion (Bale et al. 2019; Tang et al. 2016). Lattice-Boltzmann method (LBM) uses less computational power as the flow field around the particle is approximated by lattice-Boltzmann equation (Qi, Kuang, and Yu 2019). The simulation time can further be reduced by discrete element method (DEM)

which averages the fluid flow in the scale of computational grid. The particle collisions are modeled using the soft-sphere or hard-sphere approach. Even with increasing computer power, DEM simulations are predicted to be not viable in the coming decade for commercial scale reactors. The contact detection of particles and calculating geometric areas of contact consume more than 80% of the computational time in DEM. The Eulerian-Eulerian modeling which is also identified as the two-fluid (TFM) or multi-fluid modeling has been the main interest over decades due to its capacity of modeling large-scale systems. TFM requires high modeling effort as the particle phase is also considered as a fluid and the properties are derived using the kinetic theory of granular flow (KTGF). Difficulties and complexities of including the particle size distribution, loss of discrete nature of the particles, numerical (false) diffusion are the major disadvantages related to TFM. The computer efficiency of the DEM can be improved by using probabilistic strategy for the particle contact modelling such as the multiphase particle in cell (MP PIC) method where the collisional forces are derived as a stress gradient in the Eulerian grid (Ma & Zhao, 2018; Moliner et al., 2018; Pannala et al., 2011). The model complexity increases progressively from DNS to TFM and simultaneously, the uncertainty also increases due to excess use of empirical correlations, assumptions, approximations and averaging.

The sensitivity, uncertainty and errors are three aspects of the CFD predictions. The sensitivity is primarily involved with the computational grid and convergence test should be performed in first hand for the CFD simulations. The time step and number of computational particles (MP PIC method) are other sensitivity tests. Sensitivity of different coefficients, models and model constants used have equal importance, which can also be addressed as uncertainties (Ostermeier et al., 2019). The uncertainties have different dimensions related to (Mathelin et al., 2005; Walters & Huyse, 2002):

- Assumptions in the main model (i.e. incompressible, inviscid, linearization, neglecting temperature dependences of coefficients)

- Deficiency of information related to phenomenological or auxiliary models (i.e. turbulence model, reaction kinetics)
- Discretization and computational errors (i.e. flux approximation scheme, round off, iterative)
- Describing the physical reality (the geometry, initial and boundary conditions, particle properties such as size distribution, density and shape)

The fundamental structure of the conservation equation are fixed in many CFD codes. The suitability of different numerical schemes and optimization of involved auxiliary models and model parameters are possible. However, uncertainties originated from physical reality should be minimized in first hand. Some experimental data suffers from lack of supporting information (i.e. reporting of mean size of particles over size distribution, the pipe diameters without mentioning internal or external etc.).

Circulating fluidized bed (CFB) technology is a widely applied industrial process. Robust control over the particles, high heat and mass transfer rates are the basic advantages of the CFB technology. The simplest arrangement of a CFB system is illustrated in **Figure 1** and certain CFB systems can be consisted with two or multiple reactors. A typical system contains a bedding material that circulates in a closed loop without being removed out from the system. Riser operates in the fast fluidization regime and the particles are carried away with high gas flowrates, which are separated by a cyclone and fed back to the riser via a flow control valve. Mechanical valves suffer from wearing in high temperature applications where non-mechanical devices such as loopseal are highly preferred in the industry. Rate of particle circulation is one of the important parameters in CFB. The dimensions and aeration of the loopseal should be designed and optimized to fit the targeted flow and avoid gas bypass from the riser.

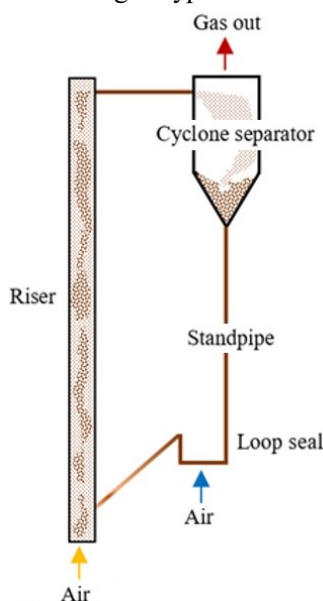


Figure 1: Circulating fluidized bed

The rate of particle circulation is governed by number of parameters such as loopseal aeration, riser gas flow, loopseal dimensions and the particle properties. As discussed prior, deviations in the simulation geometry and particle properties are a subset of the overall uncertainty. This work includes the uncertainty analysis related to pipe dimensions of the loopseal and particle size distribution for MP PIC simulated results. Barracuda VR is a commercial software package built on the MP PIC platform, which brought forward the concept of computational particle fluid dynamics (CPFD). The simulations were performed using Barracuda 17.3.0 and Intel(R) Core(TM) 3.50 GHz processor.

2 CPFD modeling

Andrews & O'Rourke (1996) extended the MP PIC method to particle flow systems, which was developed into CPFD. Later, Snider developed the scheme into three dimensional dense particle flows (Snider, 2001). The subsequent improvements of the particle collision modeling are discussed in several subsequent publications (O'Rourke & Snider, 2012, 2014; O'Rourke & Snider, 2010; O'Rourke et al., 2009). The fluid phase is modeled with Navier-Stokes equations, similar to DEM and TFM. The modeling of the particle phase has hybrid characteristics of discrete and continuum modeling. The real particles are grouped into parcels (computational particles) such that the billions of particles can be represented by millions of parcels. A certain parcel contains a number of real particles having same size, density and velocity. The parcel movement through the fluid domain is modeled similar to DEM. The particle collision force is calculated as a stress gradient on Eulerian grid in the advanced time step and mapped back to real time with interpolation functions. Unlike the TFM, the discrete nature of the particles is preserved and the implementation of the particle size distribution is straightforward.

2.1 Governing equations

The governing equations are referred from Snider (Snider, 2001). Gas phase mass and momentum conservation are modeled with continuity and time averaged Navier-Stokes equations:

$$\frac{\partial(\alpha_g \rho_g)}{\partial t} + \nabla \cdot (\alpha_g \rho_g u_g) = 0 \quad (1)$$

$$\frac{\partial(\alpha_g \rho_g u_g)}{\partial t} + \nabla \cdot (\alpha_g \rho_g u_g u_g) = -\nabla P - F + \nabla \cdot (\alpha_g \tau_g) + \alpha_g \rho_g g \quad (2)$$

Where α_g , ρ_g and u_g are gas phase volume fraction, density and velocity respectively. F is the total momentum exchange with particle phase per volume, g is the gravitational acceleration, P is the pressure, and τ_g

is the gas phase stress tensor. The stress tensor of the gas phase is given by:

$$\tau_g = \mu_g \left[(\nabla u_g + \Delta u_g^T) - \frac{2}{3} \nabla \cdot u_g I \right] \quad (3)$$

μ_g refers to the shear viscosity that is the sum of the laminar and turbulent components. The large eddy simulation is used for the large-scale turbulence modeling while the subgrid scale turbulence is captured with the Smagorinsky model:

$$\mu_{g,t} = C_s \rho_g \Delta^2 |\nabla u_g + \Delta u_g^T| \quad (4)$$

The default value for the model constant C_s is 0.01. Δ is the sub-grid length scale and calculated by:

$$\Delta = (\delta x \delta y \delta z)^{1/3} \quad (5)$$

The interface momentum transfer is calculated through the viscous drag force:

$$F = \iint f \left\{ m_p \left[D_p (u_g - u_p) - \frac{\nabla P}{\rho_p} \right] \right\} dm_p du_p \quad (6)$$

Subscript P refers to the particle phase properties where m and u symbolizes the mass and velocity respectively. D_p is the drag function. The particle phase dynamics are derived using the particle distribution function (PDF) calculated from the Liouville equation given as:

$$\frac{\partial f}{\partial t} + \nabla (f u_p) + \nabla u_p (f A_p) = 0 \quad (7)$$

Where A_p , is the particle acceleration and is expressed by:

$$A_p = \frac{\partial (u_p)}{\partial t} = D_p (u_g - u_p) - \frac{\nabla P}{\rho_p} - \frac{\nabla \tau_p}{\rho_p \alpha_p} + g \quad (8)$$

α_p is particle volume fraction and τ_p is particle stress function used to formulate the interphase interactions of particles.

$$\alpha_p = \iint f \frac{m_p}{\rho_p} dm_p du_p \quad (9)$$

$$\tau_p = \frac{10 P_s \alpha_p^\beta}{\max[(\alpha_{cp} - \alpha_p), \varepsilon(1 - \alpha_p)]} \quad (10)$$

P_s is a constant with the units of pressure, α_{cp} is the particle volume fraction at close packing, β is a constant between 2 and 5 and ε is a very small number on the order of 10^{-7} .

3 Computational method

The experimental data of Thapa et al (2016) was used for the comparison of simulation results. The loopseal and riser pipe diameters were 30mm and 50 mm respectively. The system pressure and rate of particle circulation were available where the circulation rate had been measured by interrupting (stopping) the loopseal aeration followed by measuring the time to accumulate a certain volume of particles at the standpipe. Sand with of 2650 kg/m³ in density and 130 mm in mean diameter (size distribution from 50mm to 250 mm) was the particle phase. Air at atmospheric pressure and temperature was the loopseal and riser aeration fluid

The fluid volume was developed using SOLIDWORKS 2018 and imported to Barracuda VR 17.3.0. Uniform grid option was used and the grid refinement at narrow sections was needed to capture the geometry domain accurately. The total number of cells in the domain was 467376. The turbulence was modelled with large eddy simulation and the partial donor cell method (a weighted average method of central difference and upwind schemes) was used as the advection numerical scheme. The default values were used for the number of iterations, residuals and the minimum and maximum values of Courant-Friedrichs-Lewy (CFL) parameter (which satisfy the convergence criteria). Values of the model constants and other simulation parameters are given in **Table 1**.

Table 1: Simulation parameters

	Parameter	Value
[1]	Closed pack volume fraction	0.6
[2]	Maximum momentum redirection	40%
[3]	Particle-wall collision (Normal & tangential)	0.85
[4]	Diffuse bounce	3
[5]	Pressure constant in particle stress model (P_s in Pascal)	5
[6]	Initial time step (seconds)	0.0003

As the particle flow pattern of a circulating fluidized bed with loopseal is analysed, the riser operates at dilute phase while the loopseal at dense phase. Further, the fluid drag is a function of the particle volume fraction. Therefore, the Wen-Yu-Ergun drag model (Gidaspow) was used as the Ergun correlation has been extensively validated for dense systems. The Wen-Yu model is used at higher gas volume fractions than 0.8, which is given by (Gidaspow, 1994):

$$D_{Wen-Yu} = \frac{3}{8} C_d \frac{\rho_g}{\rho_p} \frac{|u_g - u_p|}{r_p} \alpha^{-2.65} \quad (11)$$

$$C_d = \frac{24}{Re}, \quad (Re < 0.5)$$

$$C_d = \frac{24}{Re} (1 + 0.115 Re^{0.687}), \quad (0.5 \leq Re \leq 1000)$$

$$C_d = 0.4, \quad (Re > 1000)$$

As the gas volume fraction decreases below 0.8, the Ergun correlation is used,

$$D_{Ergun} = 0.5 \left(\frac{C_1 \alpha_p}{\alpha_g Re} + C_2 \right) \frac{\rho_g}{\rho_p} \frac{|u_g - u_p|}{r_p} \quad (12)$$

The default values for the laminar and turbulent coefficients in the Barracuda VR are 180 (C_1) and 2.0 (C_2) where those are 150 and 1.75 in original Ergun formulation. The particle Reynolds number is given by:

$$Re = \frac{2\rho_p |u_g - u_p|}{\mu_g} \left(\frac{3V_p}{4\pi} \right)^{1/3} \quad (13)$$

The rate of particle circulation was measured by the flux plane implemented at the overflow pipe. A flux plane stores the data of the amount of particles by species and fluid pass across a defined area. Two additional flux planes were positioned at standpipe and riser to recognize the steady state conditions. The computational domain was initially occupied exclusively with air where a particle feed flow boundary was used to introduce the particles into the system. The “particle feed control” option was linked to the particle flow boundary to maintain the particle mass in the system between 0.58 kg and 0.60 kg throughout the entire simulation time. The number density manual at the particle feed was set to 200, which decides the resolution of computational particles in the domain. The boundary conditions, flux planes and the pressure monitoring locations are illustrated in **Figure 2**.

The loop seal exerts the highest resistance for the particle flow. Therefore, the pipe diameter of the loop seal was gradually reduced from 30 mm, which is the measured value from a scaled drawing, to 27 mm in successive simulations. The pipe diameters given in the sketch can be the outside diameter and hence the actual diameter for the fluid volume should be equal or less than 30 mm.

Further, the particle size distribution can have uncertainties. Therefore, results from the reported distribution was compared with two other size distributions. The first two alternatives were taken from the arbitrary assumption that the exact size distribution can bias more towards smaller sizes than the reported value (if the sieving had not been done sufficiently). The other set up considered the mono sized particles with mean diameter of 125 microns. The size distributions are plotted in **Figure 3**.

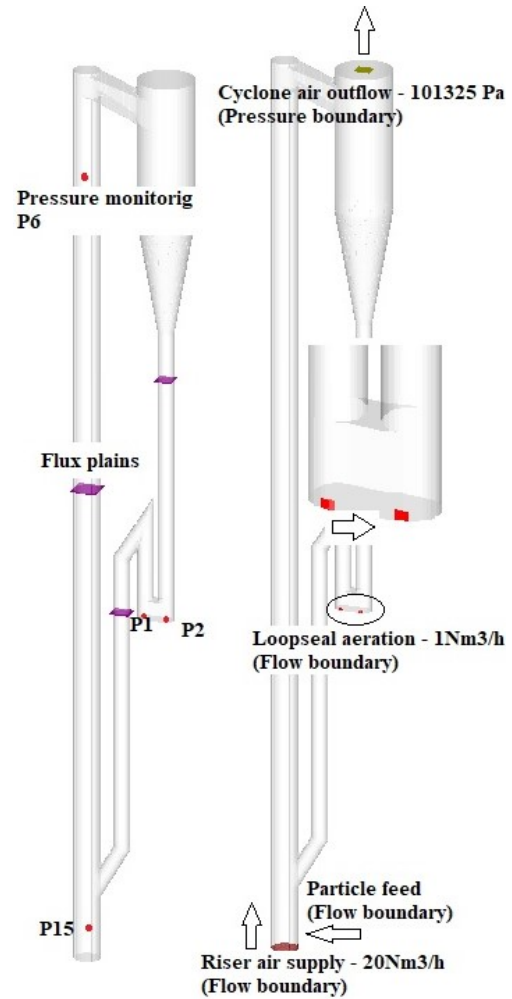


Figure 2: Computational domain; boundary conditions, flux plane and pressure transient data points

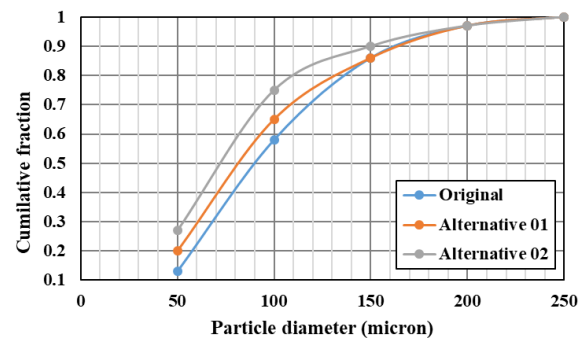


Figure 3: Particle size distribution

4 Results and Discussion

The simulation results for the original geometry was compared with the experimental data of Thapa et al, based on the rate of particle circulation and the system pressure. The particle distribution over the circulating fluidized bed at steady state operation (pseudo) is depicted in **Figure 5**. The enlarged sections in **Figure 5** shows the particle flow behavior in the loop seal.

The particle volume fractions over the riser and the cyclone sections are below 0.1 where a dense particle region can be observed at the bottom of the cyclone conical section. The particle volume fraction in the standpipe is approximately 0.5, which reduces in the horizontal section and recycle pipe. With the observed bubbles, the standpipe seems to operate at bubbling fluidization regime. A rigorous fluidization is prevailed at the horizontal section and the recycle pipe, which indicates that a large fraction of the loopseal aeration passes through the recycle pipe and ends up in the riser. In the loopseal, air tends to flow near the walls of the side of aeration and further, the airflow does not penetrate much within particle bed (in the direction of injection). Extended grid refining at the air injection may improve the length of penetration and however, large differences in the grid sizes (in all X, Y and Z directions) are not preferred in CFPD. Further, a grid cell should be sufficient to place several parcels.

The particle circulation rate was averaged over 30 seconds during steady state operation and calculated to be 315 kg/h, which is approximately equal to the experimental data. However, the rate was highly dynamic and large fluctuations between 100 kg/h to 1000 kg/h could be observed. The airflow rate across the flux plane was -0.00037 kg/s and the loopseal aeration was 0.00036 kg/s. This guarantee the proper operation of the loopseal that does not allow gas to bypass from riser via loopseal. Further, small amount of riser gas is recycled back across loopseal without escaping from the cyclone top. This is possible at high particle circulation rate, where the air is carried along with the voidage of the particle phase. The gas flow across the loopseal had not been monitored during experimental studies and the simulation results are useful in further optimizing the loopseal dimensions. The system pressure was also monitored at different locations (given in Figure 2) and the results are given in Figure 4 together with experimental data. Pressure prediction from the simulation is lower than the experimental data over the entire system. The cyclone exhaust pipe was replaced with a pressure boundary with 101325pa (atmospheric pressure) boundary value and the downstream pressure drop was excluded. Geometrical lengths, pressure monitoring locations, particle size distribution and the assumption of spherical particles can be other physical uncertainties for the deviated pressure readings.

Olatunde, and Fasina (2019) have mentioned the observed deviations related to coefficients of Ergun equation for different particles. The laminar viscous coefficient has reported to as high as 267 while the turbulent coefficient up to 4.02. The barracuda default values of 180 and 2 were used in this study. Further, the competency of the Wen & Yu model for the dilute phase systems is not concretely validated as Ergun model. The particle hold up in the riser depends on the drag force exerted by the gas flow. In this case, the Wen & Yu

model might over predict the drag force and consequently caused a reduced particle, which could lead for a lower pressure drop in the riser. This has a direct effect on the reduced pressure reading from the simulation at the recycle chamber. The effect of the particle phase modelling parameter of closed pack volume fraction is also significant for the pressure drop in dense particle regions. Due to the lack of data related to particle phase, the default value of 0.6 was used. The prediction error of the system pressure can be originated from one or many of these uncertainties and lack of data.

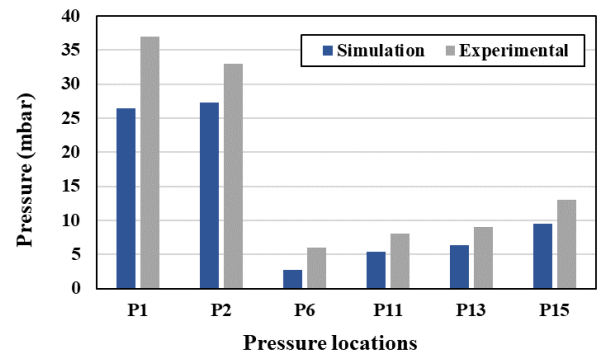


Figure 4: System pressure: experimental vs simulation

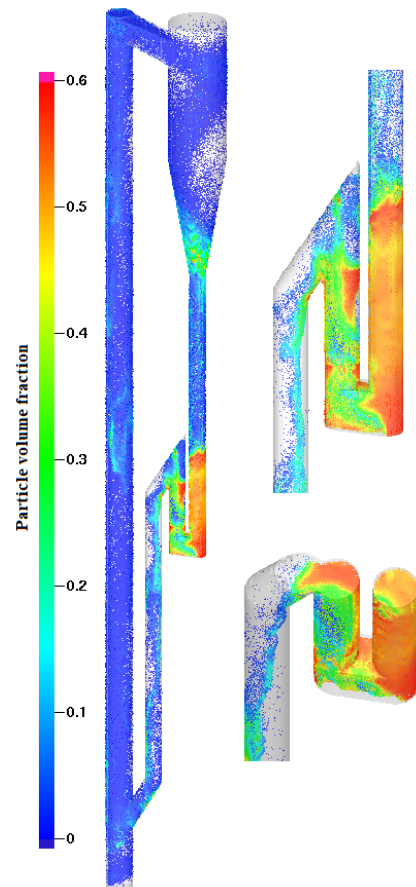


Figure 5: Particle volume fractions over CFB at steady state

4.1 Effect of the loopseal pipe diameter

Successive updates of the simulation parameters related to particle properties were needed to achieve the particle circulation rate similar to experimental values and the optimized values used are given in Table 1. However, the system pressure was not considerably sensitive for the analyzed parameters, where the observed deviations might originate from errors and uncertainties. The highest deviation of the pressure was recorded at the loopseal, which was lower than experimental data. Hence, simulations were performed for different diameters of the loopseal piping.

As illustrated in Figure 6, the particle bed height at the standpipe is slightly increasing towards reduced diameters. The loopseal balances the cumulative pressure drop of the remaining sections of the CFB system and the bed height at the standpipe is automatically adjusted following the system variations.

The rate of particle circulation and the system pressure are illustrated in Figure 7 and Figure 8 respectively. The particle circulation rate is greatly influenced by the pipe diameter, which showed a 20% increment when the diameter was reduced from 30 mm to 27 mm. The variation shows second order polynomial characteristics against pipe diameter. The gas velocity across the loopseal increases as the diameter is reduced and consequently, the fluid drag force on the particle increases. Similarly, the air bypass from cyclone to riser across loopseal has also increased.

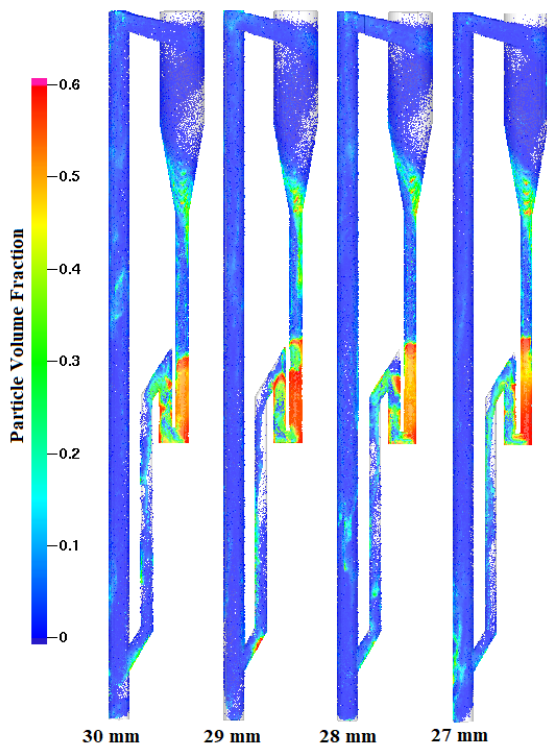


Figure 6: Particle flow hydrodynamics at different loopseal pipe diameters

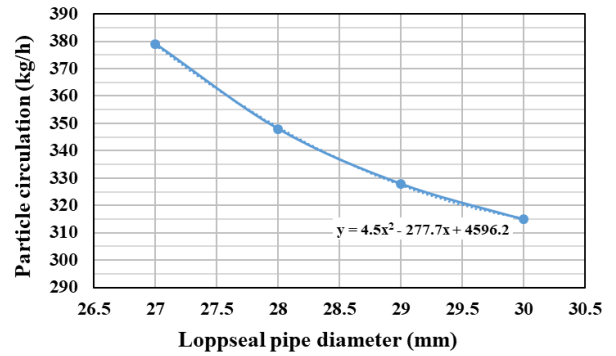


Figure 7: Change of particle circulation rate over different loopseal pipe diameters

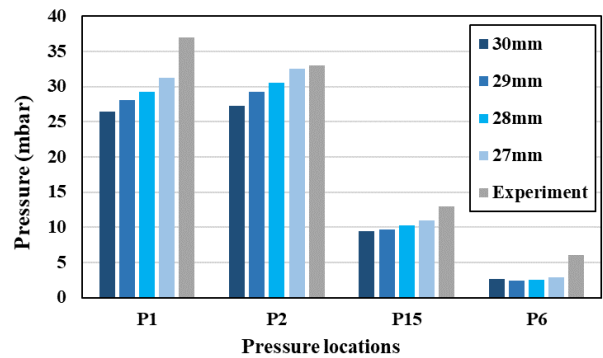


Figure 8: Change of system pressure over different loopseal pipe diameters

An improvement in the pressure prediction can be observed and the results reach the experimental values at P2 and P15. The particle holdup within the riser compartment can be high at increased particle circulation, which contribute for increased pressure at the riser bottom, P15. Prediction error of pressure at P1 may be originated from incorrect height of the recycle pipe, where the height effect can be further analyzed.

4.2 Effect of the particle size distribution

Particle size distribution is measured using sieving analysis equipment. Inadequate sieving time may avoid sufficient separation of particles. Further, with the difficulties of implementing the particle size distribution, monodisperse particles have been widely used (i.e. two-fluid modelling). Therefore, the simulation results from different size distributions as given in Figure 3 and 125 micron monodisperse particles were compared using original geometry. The rate of particle circulation is given in Figure 9.

Significant changes of particle circulation was not observed between different size distributions used. Specially, merely the weight fractions were changed keeping the smallest and largest particle size similar to original. However, a considerable reduction of particle circulation, about 32%, was observed with monodisperse particles. This is a clear illustration of the force exerted by smaller particles on larger particles and

highlights the percentage error related to using mean size rather than size distribution. The geometry and the particle mass were equal for all cases and further, the loopseal operates at fluidizing regime (i.e. size distribution can affect the pressure drop at packed bed conditions), which can be the reason behind the similar pressure results for different size distributions.

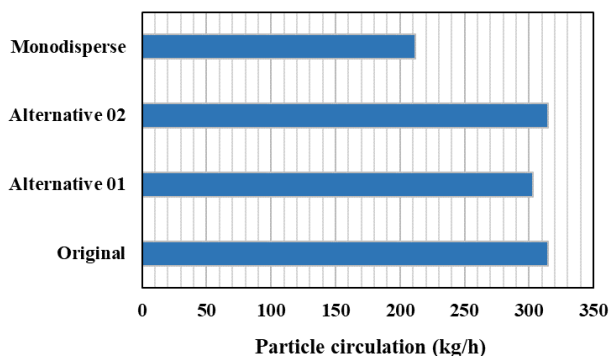


Figure 9: Change of particle circulation with size distribution

5 Conclusion

This work was carried out to analyze the effect of selected uncertainties related to geometrical lengths and particle size distribution in a circulating fluidized bed system. If the experiments are deliberately designed to generate data for CFD model validation, all the necessary parameters are available. However, whenever the existing experimental data from the literature are used in validation, certain uncertainties can be existed and therefore, adequate illustrations should be presented to compensate. The uncertainties related to physical reality and all accurately measurable parameters should be minimized (avoided) prior to the sensitivity analysis of models and model constants.

The loopseal pipe diameter displayed a great influence over particle circulation rate. The system pressure prediction was lower than experimental data in all the sections of the domain. Prediction error of the pressure at the recycle pipe was comparatively high, which might originate from incorrect height of computational geometry used or deviated pressure at the riser bottom due to inaccurate particle holdup in the riser. Small changes in the particle size distribution within the same smallest and largest sizes did not cause much change in particle circulation rate. However, monodisperse particles with mean particle size gave a substantially reduced circulation rate, which was 32% lower.

More uncertainties can be prevailed related to geometrical lengths of other sections, particle mass in the system, particle properties such as sphericity and closed pack volume fraction, loopseal aeration velocity and location. Therefore, further analysis will be supportive to demonstrate the effect of mentioned

uncertainties and it is highly recommended to perform specially designed experiments for CFD model validation with all the required data.

Acknowledgements

The authors like to forward their gratitude to Rajan Thapa for sharing his experimental data and University of South-eastern Norway for facilitating with computer resources and Barracuda VR CPFD software package.

References

- M. J. Andrews and P. J. O'Rourke. The multiphase particle-in-cell (MP-PIC) method for dense particulate flows. *International Journal of Multiphase Flow*, 22: 379-402, 1996.
- S. Bale, S. S. Tiwari, K. Nandakumar, and J. B. Joshi. Effect of Schmidt number and D/d ratio on mass transfer through gas-solid and liquid-solid packed beds: Direct numerical simulations. *Powder Technology*, 354: 529-39, 2019.
- D. Gidapow. *Multiphase Flow and Fluidization: Continuum and Kinetic Theory Descriptions*. Boston: Americal Press, 1994.
- H. Ma and Y. Zhao. Investigating the fluidization of disk-like particles in a fluidized bed using CFD-DEM simulation. *Advanced Powder Technology*, 29:2380-2393, 2018.
- L. Mathelin, M. Y. Hussaini, and T. A. Zang. Stochastic approaches to uncertainty quantification in CFD simulations. *Numerical Algorithms*, 38: 209-236, 2005.
- C. Moliner, F. Marchelli, N. Spanachi, A. Martinez-Felipe, B. Bosio, and E. Arato. CFD simulation of a spouted bed: Comparison between the Discrete Element Method (DEM) and the Two Fluid Model (TFM). *Chemical Engineering Journal*, 2018.
- G. Olatunde and O. Fasina. Modified Ergun Equation for Airflow through Packed Bed of Loblolly Pine Grinds. *KONA Powder and Particle Journal*, advpub, 2019.
- P. J. O'Rourke and D. M. Snider. Inclusion of collisional return-to-isotropy in the MP-PIC method. *Chemical Engineering Science*, 80: 39-54, 2012.
- P. J. O'Rourke and D. M. Snider. A new blended acceleration model for the particle contact forces induced by an interstitial fluid in dense particle/fluid flows. *Powder Technology*, 256: 39-51, 2014.
- P. J. O'Rourke and D. M. Snider. An improved collision damping time for MP-PIC calculations of dense particle flows with applications to polydisperse sedimenting beds and colliding particle jets. *Chemical Engineering Science*, 65: 6014-6028, 2010.
- P. J. O'Rourke, P. Zhao, and D. M. Snider. A model for collisional exchange in gas/liquid/solid fluidized beds. *Chemical Engineering Science*, 64: 1784-1797, 2009.
- P. Ostermeier, S. DeYoung, A. Vandersickel, S. Gleis, and H. Spliethoff, H. (2019). Comprehensive investigation and comparison of TFM, DenseDPM and CFD-DEM for dense fluidized beds. *Chemical Engineering Science*, 196: 291-309, 2019.

- Pannala, S., Syamlal, M., & O'Brien, T. J. (2011). *Computational Gas-Solids Flows and Reacting Systems: Theory, Methods and Practice*. Hershey, USA: Engineering Science Reference.
- Qi, Z., S. Kuang, and A. Yu. 2019. Lattice Boltzmann investigation of non-Newtonian fluid flow through a packed bed of uniform spheres. *Powder Technology* 343; 225-36.
- Snider, D. M. (2001). An Incompressible Three-Dimensional Multiphase Particle-in-Cell Model for Dense Particle Flows. *Journal of Computational Physics*, 170, 523-549.
- Tang, Y., Y. M. Lau, N. G. Deen, E. A. J. F. Peters, and J. A. M. Kuipers. 2016. Direct numerical simulations and experiments of a pseudo-2D gas-fluidized bed. *Chemical Engineering Science* 143; 166-80.
- Thapa, R. K., Frohner, A., Tondl, G., Pfeifer, C., & Halvorsen, B. M. (2016). Circulating fluidized bed combustion reactor: Computational Particle Fluid Dynamic model validation and gas feed position optimization. *Computers & Chemical Engineering*, 92, 180-188.
- Walters, R. W., & Huyse, L. (2002). *Uncertainty Analysis for Fluid Mechanics with Applications*. In. Hanover: NASA Center for AeroSpace Information (CASI).

Paper E

Janitha C. Bandara, Chameera Jayarathna, Rajan Thapa, Henrik K. Nielsen, Britt M.E. Moldestad, Marianne S. Eikeland

Loop seals in circulating fluidized beds – Review and parametric studies using CPFD

Journal: Chemical Engineering Science, Volume 227, 14 December 2020, 115917

DOI: 10.1016/j.ces.2020.115917



Loop seals in circulating fluidized beds – Review and parametric studies using CPFD simulation



Janitha C. Bandara^{a,*}, Chameera Jayarathna^b, Rajan Thapa^a, Henrik K. Nielsen^c, Britt M.E. Moldestad^a, Marianne S. Eikeland^a

^a University of South-Eastern Norway, Faculty of Technology, Kjølnes Ring 56, 3918 Porsgrunn, Norway

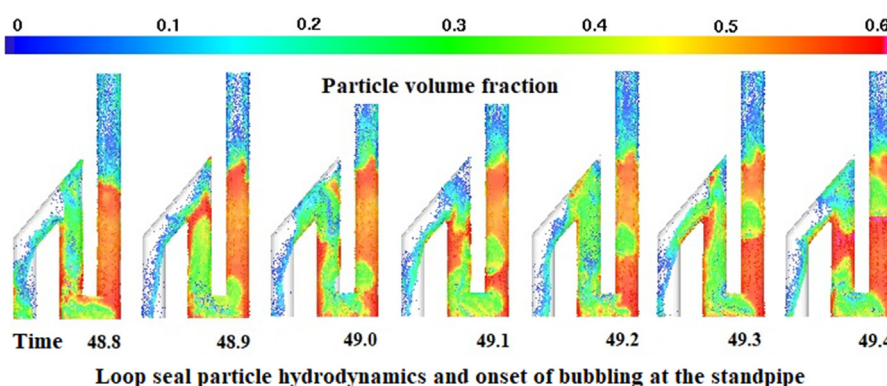
^b SINTEF Tel-Tek, SINTEF Industry, Kjølnes Ring 30, 3918 Porsgrunn, Norway

^c University of Agder, Jon Lilletuns vei 9, 4879 Grimstad, Norway

HIGHLIGHTS

- Loopseal aeration rate and injection configuration exert a great influence over particle circulation in CFB reactors.
- “BC connector” is an interesting CPFD tool to extract a selected section from a complex geometry.
- Optimum loop seal aeration was 0.9 Nm³/h resulting in approximate threshold of particle circulation.
- Uniform bottom aeration of the loop seal resulted in highest rate of particle circulation.

GRAPHICAL ABSTRACT



ARTICLE INFO

Article history:

Received 21 February 2020

Received in revised form 15 May 2020

Accepted 16 June 2020

Available online 20 June 2020

Keywords:

Circulating fluidized bed
Loop seal
Rate of particle circulation
CPFD

ABSTRACT

Loop seal is a robust particle recycling technique used in circulating fluidized bed (CFB) reactors. The rate and the location of the loop seal aeration exert a significant impact on the rate of particle circulation (G_s). The standpipe balances the cumulative pressure drop across the rest of the CFB by adjusting its particle height or gas-particle slip velocity. Higher fraction of the loop seal aeration naturally flows down to riser. Increased pressure drop in the standpipe results in high rate of particle circulation.

Computational-particle-fluid-dynamic (CPFD) code is customized for multiphase flow modelling. The inbuilt tool of “BC connectors” was incorporated to downsize a CFB into a loop seal. The simulation results of G_s and system pressures for loop seal showed a perfect match with experimentally validated CFB model. A parametric study for the effects of aeration rate, aeration position and length of the horizontal section was performed using the developed CPFD model of the loop seal. G_s increased proportionally with the loop seal aeration, reaching an approximate threshold at 0.9 Nm³/h and beyond that G_s did not improve significantly. Uniform aeration from the loop seal bottom realized the highest particle circulation with a 71% increment. The length of the horizontal section of the loop seal exhibited an inverse relationship on the particle circulation.

© 2020 Elsevier Ltd. All rights reserved.

* Corresponding author at: 64A, Vallermyrvegen, 3917 Porsgrunn, Norway.

E-mail address: janitha.bandara@usn.no (J.C. Bandara).

1. Introduction

Circulating fluidized bed (CFB) reactors are attractive in combustion and gasification processes. Intense turbulence and prolonged gas-particle contact time enhance the heat and mass transfer process and consequently, ensure a higher carbon conversion with minimum existence hot-spots and cold-spots (Hai-guang et al., 2011; Xueyao et al., 2013). Fuel flexibility and low emission of pollutant gases further highlight the importance of CFB in energy industry (Wang et al., 2014d).

As illustrated in Fig. 1, a simple CFB consists of a fast fluidization column referred as a riser, a cyclone and a particle recycle valve. The cyclone separates the carried away particles from the riser whereas the particle recycle valve supports the particles to transfer from a lower pressure at the cyclone dip to a higher pressure at the riser bottom with a proper flow control (Basu and Butler, 2009; Basu and Cheng, 2000; Kim et al., 1999; Li et al., 2014; Namkung and Cho, 2002). Dual reactor circulating fluidized bed (DCFB) technology is an excellent choice to cater the processes that need distinct reactive environments. As depicted in Fig. 1 (right), the two reactors share a common circulating particle phase, which acts as a catalyst, reactant or a thermal energy carrier. Depending on relative pressures, a DCFB can have an additional solid recycle valve between two reactors (Bareschino et al., 2014; Pfeifer et al., 2009; Seo et al., 2011). Coal power plants with CO₂ capture, biomass gasification & pyrolysis, catalytic reactors such as FCC and chemical looping combustion are some of the industrial applications of DCFB technology (Bareschino et al., 2014; Bischi et al., 2011; Kim et al., 2002).

Solid recycle valves are designed to prevent or minimize the gas leakage between reactors creating preferred reactive environments while retarding unwanted reactions (Adanez et al., 2012; Bareschino et al., 2014). Further, it should support the differential pressure between two reactors and allow adequate particle circulation (Kim et al., 2002). Mechanical valves such as screw feeders, rotary feeders and slide valves are not reliable with high temperatures, pressures and scaling, sealing & erosion problems associated with combustion or gasification systems, (Namkung and Cho, 2002; Yang et al., 2009). On the contrary, non-mechanical valves are robust due to the absence of moving parts, inexpensiveness

in construction and simplicity in operation (Basu and Cheng, 2000; Cheng and Basu, 1999). L-valve, J-valve, V-valve, N-valve, seal pot and loop seal (LS) are some of the successfully operated non-mechanical valves in the industry. Simply, the particles are circulated without any mechanical pump (Cheng and Basu, 1999; Li et al., 2014; Seo et al., 2011). G_s governs the solid-fluid contact time and the heat transfer across reactors, which are significant parameters in reaction kinetics. Consequently, the overall reactor performance is affected by the G_s (Roy et al., 2001). A substantial resistance to the particle flow (G_s) is exerted by recycle valves and hence, their hydrodynamic study has an equal importance as the reactor hydrodynamics (Shrestha et al., 2016). Loop seals are highly interested in atmospheric CFB combustion and gasification systems over other recycle valve designs (Li et al., 2014). However, interruptions to the particle flow across these valves challenges the safe and stable operation of CFBs and DCFBs. Many shutdowns related with solid processing systems have been reported due to failures of solid recycle system (Namkung and Cho, 2002). Therefore, optimization of geometrical dimensioning and operational parameters of loop seal should be a fundamental concern during any CFB design.

Computational fluid dynamic (CFD) simulation of three-dimensional geometries has become an important tool in designing and optimizing as it generates a detailed picture of interior dynamics, which cannot directly be observed in experiments. Further, optimization of the system geometries such as material feeding position, are difficult or impossible to be achieved solitary with experiments. Therefore, CFD studies are effective in terms of cost, time and safety. With the continuous development of computer power and efficient numerical schemes, CFD has become realistic to be applied in industrial scale reactor systems.

Eulerian-Eulerian (EE) and Eulerian-Lagrangian (EL) are the two main approaches in modeling of multiphase systems. EE modeling considers both fluid and particle phases as fully interpenetrating continua where the conservation equations are modeled with Navier-Stokes equations. Particle phase properties are derived using kinetic theory of granular flow. EE modeling has been the pioneer in multiphase modeling of large scale systems due to its reduced simulation time and has also been proved for its accuracy of prediction by many studies. However, the discrete nature of the

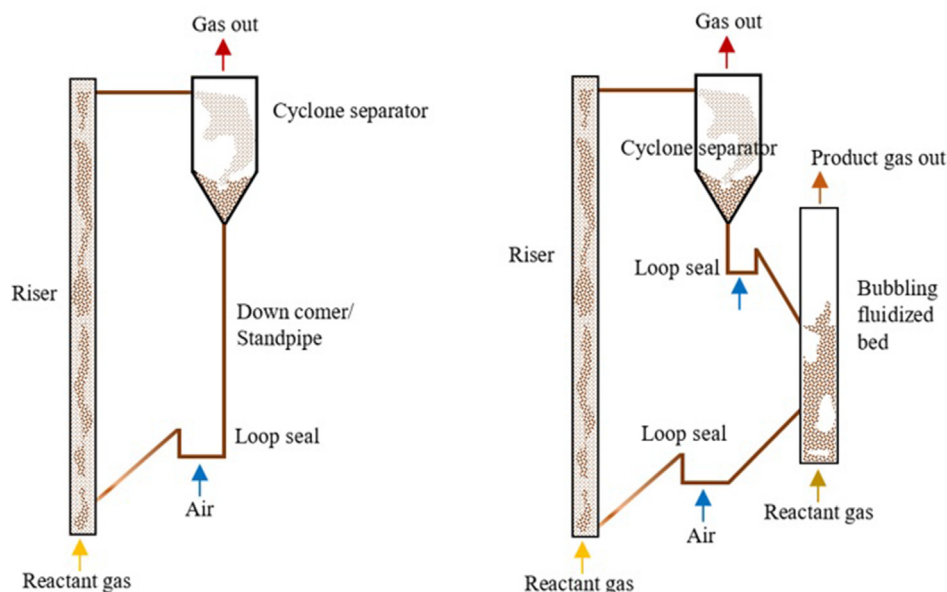


Fig. 1. Circulating fluidized bed system (left) and dual reactor circulating fluidized bed system (right).

particles is not represented in which, the integration of particle size distribution, different densities and shapes are not straight forward (Chiesa et al., 2005; Snider, 2001). In contrast to EE modeling, EL considers the particles as discrete matter which is modeled by Newton's second law of motion. Particle trajectories are calculated for individual particles avoiding the necessity of closure terms in particle phase modeling. Therefore, the discreteness of the particles is preserved whereas the integration of size distribution is straight. Nevertheless, the larger the number of particles, the higher the computer power required, which makes EL simulation unrealistic for systems with high particle loading than 2×10^5 (Chiesa et al., 2005; Jiang et al., 2014).

Computational particle fluid dynamic (CPFD) is a hybrid construction of EE and EL modeling, which overcomes certain limitations of EL approach while preserving the discrete nature of particles. The CPFD is built on multiphase particle-in-cell (MP PIC) concept developed by Andrews and O'Rourke for model dense particle flows (Andrews and O'Rourke, 1996). Real particles, in the neighborhood, having identical properties such as size, density, species, velocity etc. are grouped in to parcels, which are also known as computational particles. The parcel dynamics are modeled in the Lagrangian frame whereas the particle collision forces are calculated in the Eulerian grid using an isotropic stress function. The particle stresses are calculated in an advance time step and mapped to individual particles in the real time using interpolation functions. Snider extended the elementary MP PIC construction into three-dimensional coordinates whereas the governing equations and numerical procedures can be found in literature (Andrews and O'Rourke, 1996; Chen et al., 2013; Jiang et al., 2014; Snider and Banerjee, 2010; Snider, 2001; Snider et al., 2011).

Barracuda VR[®] developed the CPFD platform, which is a commercial package specific for simulation of multiphase systems. CPFD has recently been used in many research areas due to faster simulations and enhanced graphical data illustration. Tu and Wang (2018) analyzed the effect of different drag models for particle hydrodynamics in a CFB with an experimental validation. Jiang et al. (2014) used graphical data developed by electrical capacitance tomography (ECT) in a six cyclone CFB experimental rig to compare the accuracy of simulation prediction. Chen et al. (2013) analyzed a riser section of a CFB and commented on the requirement of drag model optimization for a better prediction. An experimental validation of the CPFD method was presented by Liang et al. (2014) using a bubbling fluidized bed and the required improvements of the model setup were critically discussed. Wang

et al have extensively analyzed the effects of CPFD modeling parameters in a CFB system (Wang et al., 2014c, 2014d). Various other researchers have used the CPFD tool to analyze nonreactive fluidized bed systems (Qiu et al., 2015; Snider, 2007) and reactive systems like combustion and gasification (Abbasi et al., 2011; Loha et al., 2014; Snider and Banerjee, 2010; Snider et al., 2011; Thapa et al., 2016; Xie et al., 2012).

The studies of loop seal hydrodynamics are relatively rare and therefore, authors found that it would be beneficial to review the existing literature. Further, CPFD studies of multiphase systems are significantly less compared to Eulerian (i.e. two fluid model) or Lagrangian modeling (i.e. discrete particle method - DPM). Further, many of the published CFD studies have focused on full loop CFB simulation, instead of explicit analysis loop seal performances. Related to experiments, the importance of the optimization of loop seal aeration has been highlighted (Stollhof et al., 2019). This work was focused in extracting out the loop seal section from an experimentally validated CFB model using "boundary connections" tool in CPFD. Subsequently, loop seal performances were analyzed against different geometrical and operational parameters of loop seal aeration, aeration position and length of the horizontal section of the loop seal. CPFD is an emerging package for simulating particle systems where the content of this work tries to invent the applicability of different inbuilt tools in reducing the geometrical complexity and simulation time. Intel(R) Xeon(R) CPU E (5) 1660 v4 @ 3.20 GHz processor and Barracuda VR[®] 17.3.0 version were used for the simulation of the model.

2. Loop seal - operations and literature review

Number of different loop seal (LS) designing are found where some of them are illustrated in Fig. 2. The structure is closely similar to a downscaled version of a seal pot and advantageously, a LS can be put into operation with a less amount of air. It consists of a stand pipe (SP), supply chamber (SC), recycle chamber (RC), air distributor, overflow weir and a recycle pipe (Hai-guang et al., 2011; Yazdanpanah et al., 2013). As illustrated in Fig. 2, the supply chamber can be connected to the recycle chamber with a simple slit opening and however with the practical restrictions such as refractories and flange connections, the typical connection is a horizontal or an inclined passage. In larger CFB systems, two recycle chambers with two recycle pipes can be used to realize the required G_5 . Further, possibilities of mounting a heat exchanger across the LS have

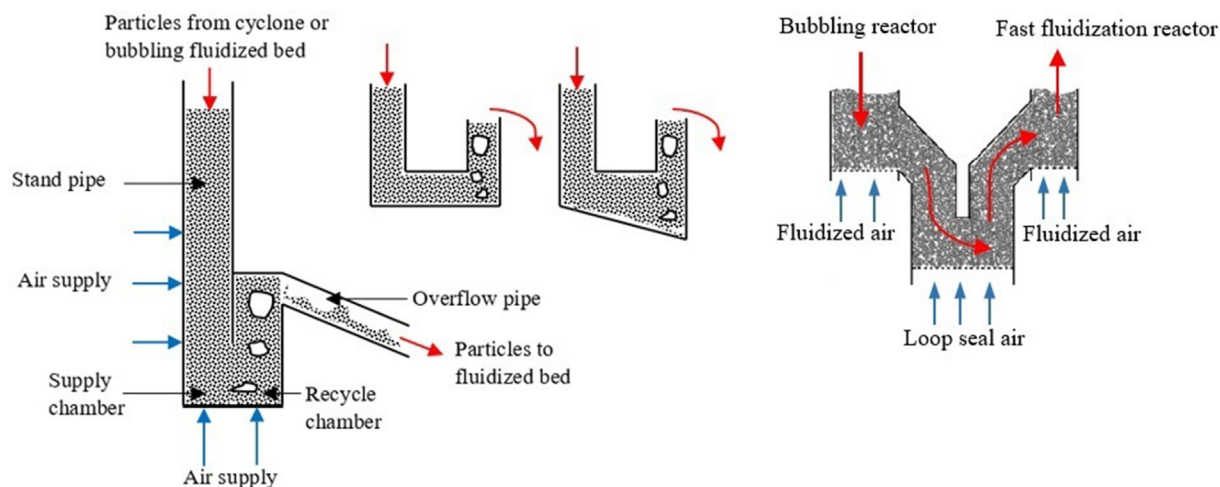


Fig. 2. Different constructions of loop seals.

also been analysed (Basu and Butler, 2009; Basu et al., 2009; Johansson et al., 2006; Stollhof et al., 2019; Yazdanpanah et al., 2013).

LS should be aerated to start its functioning and force the particles to escape out from the overflow weir. At least, the recycle chamber (RC) should be operated above the minimum fluidization velocity (U_{mf}) of the particle phase. However for a smooth operation, the aeration in the recycle chamber (U_{RC}) should surpass the minimum fluidization velocity (U_{mf}) of the largest size in the particle phase (Cheng and Basu, 1999; Cheng et al., 1998). In the absence of supply chamber (SC) aeration (U_{SC}), the distance of particle distribution from the supply chamber to the horizontal section is restricted, which is a function of angle of repose of the particles being used. If the particle distribution does not reach the recycle chamber aeration, the LS functionality is hindered. Therefore in general, both chambers are aerated until the recycle chamber and the horizontal section reach fluidizing conditions and consequently, the hydrostatic pressure and the fluid drag exceed all the associated flow resistances. The supply chamber is directly connected to the standpipe (SP) where the particle dynamics in the stand pipe can be at minimum fluidization, bubbling fluidization or transient packed bed conditions. (Wang et al., 2014b; Yang et al., 2009). Geometrical lengths and aeration positions of the LS are the primary governing factors of G_S , which are needed to optimize at the construction phase. Therefore, particle phase properties, U_{SC} , U_{RC} and SP particle bed height are the runtime parameters on G_S , which are directly involved with the LS section. In addition, gas velocity in the riser (U_G), system pressure drop (ΔP) and system particle inventory (M) also contribute in governing the G_S (Kim et al., 1999; Monazam et al., 2007).

A CFB system reaches a pressure equilibrium at the steady state operation whereas the higher pressure in the standpipe drives the particles through the LS into the riser. The ΔP in the standpipe is equal to the cumulative ΔP over the rest of the CFB system (Cheng et al., 1998; Horio et al., 1989; Kim et al., 2002) and can be given as:

$$\Delta P_{SP} = \Delta P_{Riser} + \Delta P_{LS} + \Delta P_{Cyclone}$$

The standpipe adjusts its ΔP_{SP} accordingly against any pressure variation in the rest of the system and moreover, G_S and ΔP_{SP} show a direct proportionality with each other. Changing the particle bed height at the SP is one of the options in changing the ΔP_{SP} . Secondly, the ΔP across a particle bed is a function of gas-particle slip velocity and consequently, the ΔP_{SP} is possible to adjust by changing the upward gas velocity or the downward particle velocity along the SP. A proper control of the SP gas flow is therefore crucial and many researchers have explored different aeration configurations and flowrates. The recycle chamber aeration is generally fixed at the bottom of the chamber where the injected gas entirely flows down to the riser. Further, a higher fraction of the supply chamber aeration gas are driven to the recycle chamber and finally ends up in the riser. Therefore instead of supply chamber bottom aeration, many studies have focused on aerating at the bottom of the SP, slightly above the horizontal section (as illustrated in Fig. 2). This is identified as vertical aeration (U_V) and supports more gas to escape along the SP. "Moving bed" particle hydrodynamics in the SP supports steadier and a stable particle flow. The elevation from the bottom of the LS to the vertical aeration is another influential parameter, which controls the relative fractions of gas flow down to either sides of SP or recycle chamber. In contrast, some studies have recommended to operate the SP at bubbling fluidization regime, especially in CFB combustion due to clinked formation triggered from heated particle circulation mixed with ash (Kim et al., 2002; Kim et al., 1999).

Yang et al. (2009) have carried out experiments for LS operation in a CFB with quartz sand of 157 μm as the particle phase. Both

recycle chamber and supply chamber were aerated at the bottom of the loop seal. The G_S and system ΔP was measured over varied U_{SC} , U_{RC} , M and U_G . The G_S was found more sensitive to U_{SC} compared to U_{RC} , which was similar to the observation made by Basu and Cheng (2000).

A similar study was performed by Kim et al. (1999) using 65 μm FCC particles. In contrast to the bottom aeration alone, the LS was additionally coupled with vertical aeration. The ΔP_{LS} increased proportionally with the U_G as a result of increased G_S . At a constant U_V of 4 times the U_{mf} of particles, the G_S increased with the bottom aeration up to 1.5 U_{mf} . Moreover, increased U_V than 5.5 U_{mf} created a stagnant bubble at the point of injection and consequently, the narrowed cross section for the particle flow reduced the G_S . The optimum height for the vertical aeration was found to be 2.5 times the SP diameters from the bottom of the LS. In general, particular value has recorded to be two or above for L and J valves (Kim et al., 1999). The same experimental unit was used by the authors to analyse the effects of particle properties (Kim and Kim, 2002). Three different sizes of sand were used to compare the size effect while the effect of the density difference was analysed by FCC against sand particles. The maximum G_S achieved was approximately similar regardless of the size whereas the maximum G_S was higher for high density sand particles. Increased of U_V was the most effective way to reach the identical G_S as the particle size was increased. However, the fluidization number (U_V / U_{mf}) was needed to increase with decrease particle size. According to the author's observation, the vertical aeration showed a higher tendency to flow towards recycle chamber at increased G_S . The effect of the U_V has also been analyzed by Namkung and Cho (2002). Elevated U_V above 1–1.2 U_{mf} resulted in unstable G_S and pressure fluctuations in riser. Continuous bubbling in the SP and a stagnant bubble at the point of U_V injection reduced the cross section for the descending particles. Solid circulation was hindered in the absence of vertical aeration whereas the bottom aeration at the supply chamber resulted in an unstable G_S . In contrast to the finding of Kim and Kim (2002), the maximum G_S achieved was higher for larger particles.

Yazdanpanah et al. (2013) have carried out experiments in an interconnected CFB to analyze the functionality of LS in which, the recycle pipe was connected with a bubbling fluidized reactor. As the particles are fed into the dense bed of bubbling reactor, LS was greatly affected by the particle height in the reactor above the recycle pipe connection point. For instance, the solid buildup in the bubbling reactor reflected as a high particle bed in the SP followed by a high ΔP_{SP} . Injection of helium in tracer amounts was used to analyse the gas flow behaviour inside the LS. Vertical aeration was needed to maintain at an optimum level to prevent the downward gas flow from cyclone towards recycle chamber and finally to the reactor.

Wang et al. (2014b) have analyzed the possibilities of reducing the resistance exerted by the horizontal section of the LS and consequently, to reduce the requirement of LS aeration. A standard U-shaped loop seal was compared with a modified N-shaped design. The horizontal passage was inclined until the tilt angle was larger than the angle of repose of the particles and therefore, a gravity flow from the SP to the recycle chamber prevailed. In addition to the reduction in LS aeration, the proposed designing gave a smooth transition over increasing LS aeration. The studies of Basu and Butler (2009) discussed the effect of particle angle of repose and LS aeration for the onset of its operation. The experiments showed the spread angle of particles becomes zero at minimum fluidization, which is equal to the angle of repose before. In further analysis for the effects of the horizontal passage, increased length resulted a higher resistance for the particle flow and reflected as high aeration requirement followed by a reduction of maximum G_S .

Bareschino et al. (2014) studied a LS with a slit opening instead of horizontal section, between the supply chamber and the recycle

chamber. LS aeration was changed between U_{mf} and $2U_{mf}$ whereas tracer particles and gas species were used to understand the particle hydrodynamics (i.e. residence time) and gas bypass. G_s was not affected considerably as the LS aeration was changed from $1U_{mf}$ to $2U_{mf}$. The LS was fully effective when both supply chamber and recycle chamber were at complete fluidization. The supply chamber started to fluidize at $1.5U_{mf}$. At $1U_{mf}$ of LS aeration, only a fraction of the slit opening was effective and the SP particle flow was highly streamlined. A substantial fraction of the supply chamber aeration bypassed towards the recycle chamber, which caused defluidization of SP. A similar observation has been experienced by many researchers.

Stollhof et al. (2019) worked with a dual reactor CFB system with copper particles of 57 μm . There were two LSs in place whereas in lower LS, the supply chamber and the recycle chamber were directly connected between two reactors. The LSs were aerated with different flowmeters with tracer gas injection to follow up the gas migration paths. Hydrodynamics of the lower LS dominated the reactor operational conditions while the influence of upper LS was minimum. The reactor pressures changed accordingly with the lower LS aeration, which caused in varying particle hold ups between two reactors. Increased share of total LS aeration into the supply chamber helped to prevent the gas leakage between reactors. Lim et al. (2012) have carried out experiments in a DCFB systems and developed an operational map that set limits for the stable operation. The LS aeration was found to be a key component where both too high and too low values lead to malfunctions of gas bypassing and LS overload respectively.

In the study of Bischi et al. (2011), a single supply chamber was connected to two recycle chambers dividing the particle flow into two separate reactors. Percentage particle flow into each reactor was manipulated by different aeration rates at the recycle chamber. Wang et al. (2003) managed to develop an external heat exchanger across the LS of a CFB. Basu and Butler (2009) critically analyzed the LS parameters to be used in CFB boilers. As the length of the horizontal passage was increased, the maximum G_s decreased and a segregated flow along the horizontal passage was observed. Further at higher G_s , entire supply chamber aeration bypassed towards the recycle chamber. The studies of Cheng and Basu (1999) concluded that the system pressure and LS aeration are directly proportional to the G_s and inversely proportional to the particle size. Same authors worked on analyzing the effects of SP diameter and area of slit opening. Smaller pipe diameters resulted in higher G_s whereas G_s was independent above a certain size of the slit opening (Basu and Cheng, 2000). Hai-guang et al. (2011) observed that the particle height in the SP alone cannot fully decide the G_s where they operated the recycle chamber in packed bed, bubbling fluidized bed and fast fluidized bed regimes. According to the observations of Monazam et al. (2007) the LS performance was significantly affected by the riser hydrodynamics and particle inventory in the system. A modeling effort was presented using dimensionless parameters, which concluded the higher sensitivity of SP aeration over recycle chamber aeration for G_s . Li et al developed a mathematical model with experimental validation to predict the loop seal hydrodynamics in two successive publications (Li et al., 2014; Li et al., 2018).

Experimental measurements of G_s have been achieved by various methods. Thapa et al. (2016) used the interruption of LS aeration and subsequent measurement of particle accumulation in the standpipe over a certain period. A spiral vane made with twisted fiberglass was used by Monazam et al. (2007). Kim et al. (2001) measured the G_s by diverting the particle flow from cyclone into an external pipe and taking the rate of accumulation. Electrical capacitance tomography (ECT) technique was used by Wang et al. (2014a) to observe the solid flow behaviour across a LS.

2.1. Developed correlations

Pressure balance over the CFB loop is the key parameter considered in LS designing whereas G_s is directly proportional to system pressure. On the other hand, pressure measurements can easily be implemented, especially at high temperature operation. Further, the aeration flowrates and material inventory inside the CFB are readily available (Namkung and Cho, 2002). Therefore, many researchers have tried to develop prediction models for G_s using aforementioned measurements. Namkung et al. (2001) used the ΔP over the riser to predict the G_s while Cheng and Basu (1999) incorporated the pressure drop across recycle chamber. In contrast, theory based prediction models can also be found. The SP mostly operates at moving packed bed conditions in which the ΔP can be calculated using the Ergun equation. For the recycle pipe, pneumatic conveying principles can be applied (Ergun, 1952). Botsio and Basu (2005) used the sharp crested weir theory to correlate the particle overflow correlated from the weir in the recycle chamber, which is given by,

$$G_s = \frac{2}{3 \times A_{riser}} (1 - \epsilon) \rho_s C W \sqrt{2gH^{3/2}}$$

C is the weir coefficient, W is the width of the weir and H is the particle height above the weir. Yang et al. (2009) has developed a correlation for G_s considering whole CFB system including solid inventory (M), riser gas velocity and supply chamber aeration velocity of the loop seal.

$$G_s = 9.6877(U_G)^{0.575}(U_{SC})^{1.020}(M)^{0.543}$$

Kim et al. (1999) have developed a correlation for circulation rate by modifying the mechanical valve equation with dimensionless variables.

$$G_s = 0.130 \left[\frac{U_{BA}}{U_{mf}} \right]^{0.200} \left[\frac{U_V}{U_{mf}} \right]^{0.372} \left[\frac{L_h}{D_d} \right]^{-0.458} \left[\frac{U_G}{U_t} \right]^{-1.102} \times \sqrt{2\rho_s(1 - \epsilon_{mf})\Delta P_{ls}}$$

Where U_{BA} is the LS bottom aeration, U_V is SP vertical aeration, L_h is the height of the U_V from the bottom of the LS and D_{Sp} refers to the standpipe diameter. U_t and ϵ_{mf} stand for terminal velocity and voidage at minimum fluidization respectively.

Kim et al. (2001) have used the vertical aeration and Archimedes number (Ar) to formulate a correlation for the G_s .

$$G_s = 3.96 \left(\frac{U_V}{U_{mf}} \right)^{0.7} Ar^{0.36}$$

for

$$L_h/D_{Sp} = 2.5, \quad 0 \leq \frac{U_V}{U_{mf}} \leq 6 \quad \text{and} \quad 16.2 \leq Ar \leq 1460$$

$$G_s = 0.1 \left(\frac{U_V}{U_{mf}} \right)^{2.23} Ar^{0.90}$$

for

$$L_h/D_{Sp} = 3.5, \quad 0 \leq \frac{U_V}{U_{mf}} \leq 9 \quad \text{and} \quad 16.2 \leq Ar \leq 205$$

$$Ar = \frac{\rho_g(\rho_p - \rho_g)d_p^3 g}{\mu_g^2}$$

Monazam et al. (2007) modified the L-valve and V-valve equations to predict G_s across a LS using minimum fluidization velocity, vertical aeration at the standpipe bottom, loop seal aeration velocity and particle terminal velocity.

$$G_s = 17.4 \left(\frac{U_V}{U_{mf}} \right)^{1.26} \left(\frac{U_{ls}}{U_t} \right)^{0.17}$$

Bareschino et al. (2014) developed a correlation for the minimum effective superficial gas velocity ($U_{g,ls}^{eff}$) required to operate the supply chamber at fluidizing conditions and minimize the gas leakage from supply chamber towards recycle chamber.

$$U_{g,ls}^{eff} \geq U_{mf} - \frac{G_s A_r \varepsilon_{mf}}{A_{ls} \rho_s (1 - \varepsilon_{mf})}$$

A_r and A_{ls} represent cross sections of the riser and supply chamber cross sections where ε_{mf} stands for bed voidage at minimum fluidization.

3. Experimental and simulation setup

The experimental studies were performed in a full loop CFB rig using sand and air as the particle phase and fluidizing gas respectively. Fig. 3 illustrates the experimental apparatus and the locations of pressure sensors used to monitor the system behaviour. Plexiglas piping and cyclone are useful in visual observation of particle hydrodynamics and to notice process interruptions such as particle accumulation. The connecting pipes from cyclone dip back to the riser, including LS, are 30 mm in diameter. The length of the horizontal section of the LS is 70 mm with a square cross section of 30 mm × 30 mm where the recycle pipe is 135 mm in height. Average diameter of the particle phase was 150 μm with a size distribution between 50 and 200 μm as given in Fig. 4. The absolute particle density of sand was 2650 kg/m³ whereas 0.58 to 0.6 kg of material was used inside for the experiments. Riser and LS aeration were maintained at 20 Nm³/h and 1.1 Nm³/h respectively. The riser aeration was designed with a distributor plate at the bottom of the column. A single flow controller was used for LS aeration where the supply line was divided into two and connected to the bottom of the side walls of recycle and supply chambers. The G_s was measured with interruption of LS aeration where the measured particle volume was converted into mass using particle bulk density.



Fig. 3. Circulating fluidized bed experimental rig (Thapa et al., 2016).

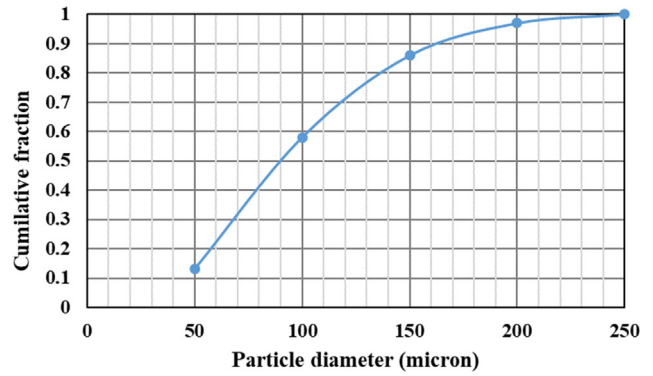
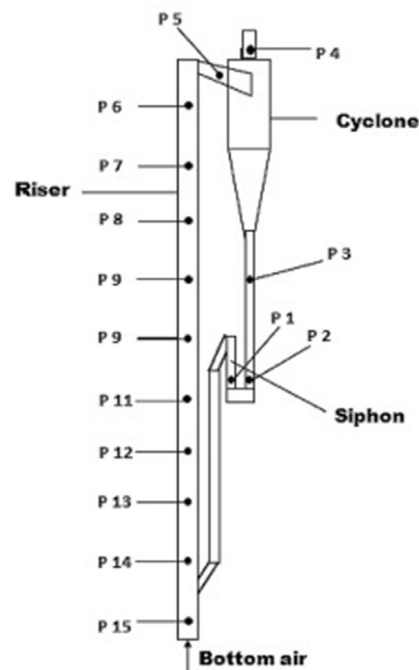


Fig. 4. Particle size distribution.

The initial simulations were performed with the complete CFB loop including riser, cyclone and loop seal with connecting pipes. Grid assembly is the primary element of any CFD model and especially in Barracuda VR[®], the grid refinement is crucial in capturing the exact computational domain of complex sections such as pipe connections. The bulk flow region can be modelled with a coarse grid whereas a finer grid is important to cope with regions having high gradients of pressure, temperature, concentration etc. In Barracuda VR[®], uniform grid sizes are recommended whenever possible. Therefore in general, grid independence check is performed by gradually refining the grid until the simulation results are converged. The computational grid consisted 435,232 cells and the cell structure at different sections are illustrated in Fig. 5. The most refined grid was needed at the LS with 3.75 × 3.75 × 3.75 mm in size. The particle modelling parameters used in this study are given in Table 1.

Boundary conditions, flux planes and initial particle filling are depicted in Fig. 6. The cumulative aeration rate at recycle chamber and supply chamber was 1.1 Nm³/h, which was implemented with two flow boundaries at the bottom of the side walls. The riser aeration was uniformly distributed 20 Nm³/h at the bottom of the reactor. The cyclone exhaust was replaced with a pressure boundary of 101,525 Pa, assuming its effect on the particle circulation



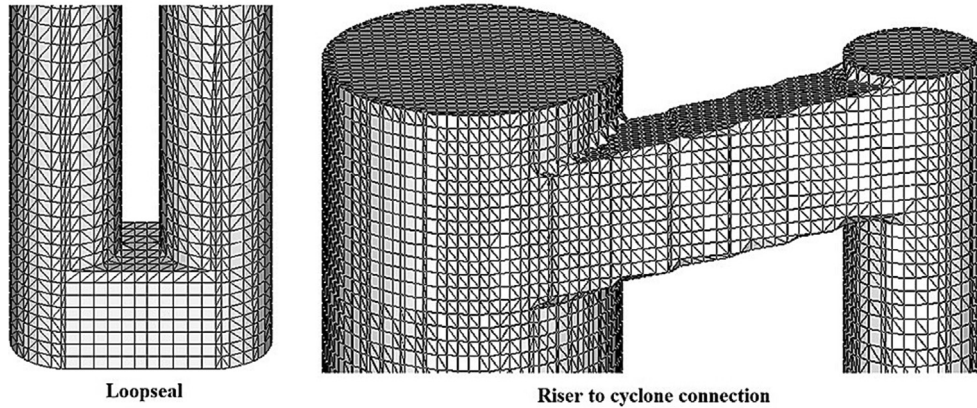


Fig. 5. Computational grid at loop seal and riser cyclone connection.

Table 1
Particle phase model parameters and values.

Fluid drag model	Wen-Yu-Ergun
Close pack volume fraction	0.6
Collisional momentum redirection	40%
Normal-to-wall momentum retention	0.85
Tangent-to-wall momentum retention	0.85
Pressure constant in particle stress model	5
Initial time step	0.0005 s

was negligible. Initial particle mass in the system was between 0.58 and 0.60 kg. Pressure monitoring points were implemented at P1, P2, P3, P6 and P15 as illustrated in Fig. 3. An additional pressure monitoring point was implemented in the loop seal overflow pipe at an identical elevation correspond to P11. Two flux planes in the standpipe and recycle pipe were located to monitor the particle circulation rate.

After CFPD model validation for the CFB complete loop, the LS section was extracted out by removing the riser reactor from the computational mesh. The cyclone was required to be in place for particle feeding and realistic particle entrance into the SP. Further, the presence of cyclone was supposed eliminate the occurrence of particle blowout at higher LS aeration. The disconnected pipe at the cyclone feed was updated as a flow boundary. For the air and particle flowrates at the boundary, average values from full loop simulations were used. Likewise, the disconnection at the overflow pipe was updated as a pressure boundary. The restructured computational domain with two new boundary conditions are depicted in Fig. 6 (c). The computational mesh and other simulation parameters were kept similar to those of the full loop simulation. Later, the reduced model was used to analyse different LS parameters of aeration rate, aeration position and length of the horizontal section.

3.1. MP PIC governing equations

The governing equations are adapted from the work of Snider (Snider, 2001). The gas phase mass and momentum conservation are modeled with continuity and time averaged Navier-Stokes equations:

$$\frac{\partial(\alpha_g \rho_g)}{\partial t} + \nabla \cdot (\alpha_g \rho_g \mathbf{u}_g) = 0$$

$$\frac{\partial(\alpha_g \rho_g \mathbf{u}_g)}{\partial t} + \nabla \cdot (\alpha_g \rho_g \mathbf{u}_g \mathbf{u}_g) = -\nabla P - F + \nabla \cdot (\alpha_g \boldsymbol{\tau}_g) + \alpha_g \rho_g \mathbf{g}$$

Where α_g, ρ_g and \mathbf{u}_g are gas phase volume fraction, density and velocity respectively. F is the total momentum exchange with particle phase per volume, \mathbf{g} is the gravitational acceleration, P is the pressure and $\boldsymbol{\tau}_g$ is the gas phase stress tensor, which is given by:

$$\boldsymbol{\tau}_g = \mu_g \left[(\nabla \mathbf{u}_g + \Delta \mathbf{u}_g^T) - \frac{2}{3} \nabla \cdot \mathbf{u}_g \mathbf{I} \right]$$

μ_g refers to the shear viscosity (sum of the laminar and turbulent components). The large eddy simulation is used for the large-scale turbulence modeling while the sub-grid scale turbulence is captured with the Smagorinsky model:

$$\mu_{g,t} = C_s \rho_g \Delta^2 |\nabla \mathbf{u}_g + \Delta \mathbf{u}_g^T|$$

Where Δ is the sub-grid length scale and calculated by equation 05. The default value for the model constant C_s is 0.01:

$$\Delta = (\delta x \delta y \delta z)^{1/3}$$

The interface momentum transfer is calculated through the viscous drag force:

$$F = \iint f \left\{ m_p \left[D_p (\mathbf{u}_g - \mathbf{u}_p) - \frac{\nabla P}{\rho_p} \right] \right\} dm_p d\mathbf{u}_p$$

Subscript P refers to the particle phase properties where m and \mathbf{u} symbolizes the mass and velocity. D_p is the drag function. The particle phase dynamics are derived using the particle distribution function (PDF) calculated from the Liouville equation given as:

$$\frac{\partial f}{\partial t} + \nabla \cdot (f \mathbf{u}_p) + \nabla \cdot \mathbf{u}_p (f A_p) = 0$$

Where A_p , is the particle acceleration and is expressed by:

$$A_p = \frac{\partial(\mathbf{u}_p)}{\partial t} = D_p (\mathbf{u}_g - \mathbf{u}_p) - \frac{\nabla P}{\rho_p} - \frac{\nabla \boldsymbol{\tau}_p}{\rho_p \alpha_p} + \mathbf{g}$$

α_p is particle volume fraction and $\boldsymbol{\tau}_p$ is particle stress function that is used in formulate the interphase interactions of particles.

$$\alpha_p = \iint f \frac{m_p}{\rho_p} dm_p d\mathbf{u}_p$$

$$\boldsymbol{\tau}_p = \frac{10 P_s \alpha_p^\beta}{\max[(\alpha_{cp} - \alpha_p), \varepsilon(1 - \alpha_p)]}$$

P_s is a constant with the units of pressure, α_{cp} is the particle volume fraction at close packing, β is a constant between 2 and 5 where ε is a very small number on the order of 10^{-7} .

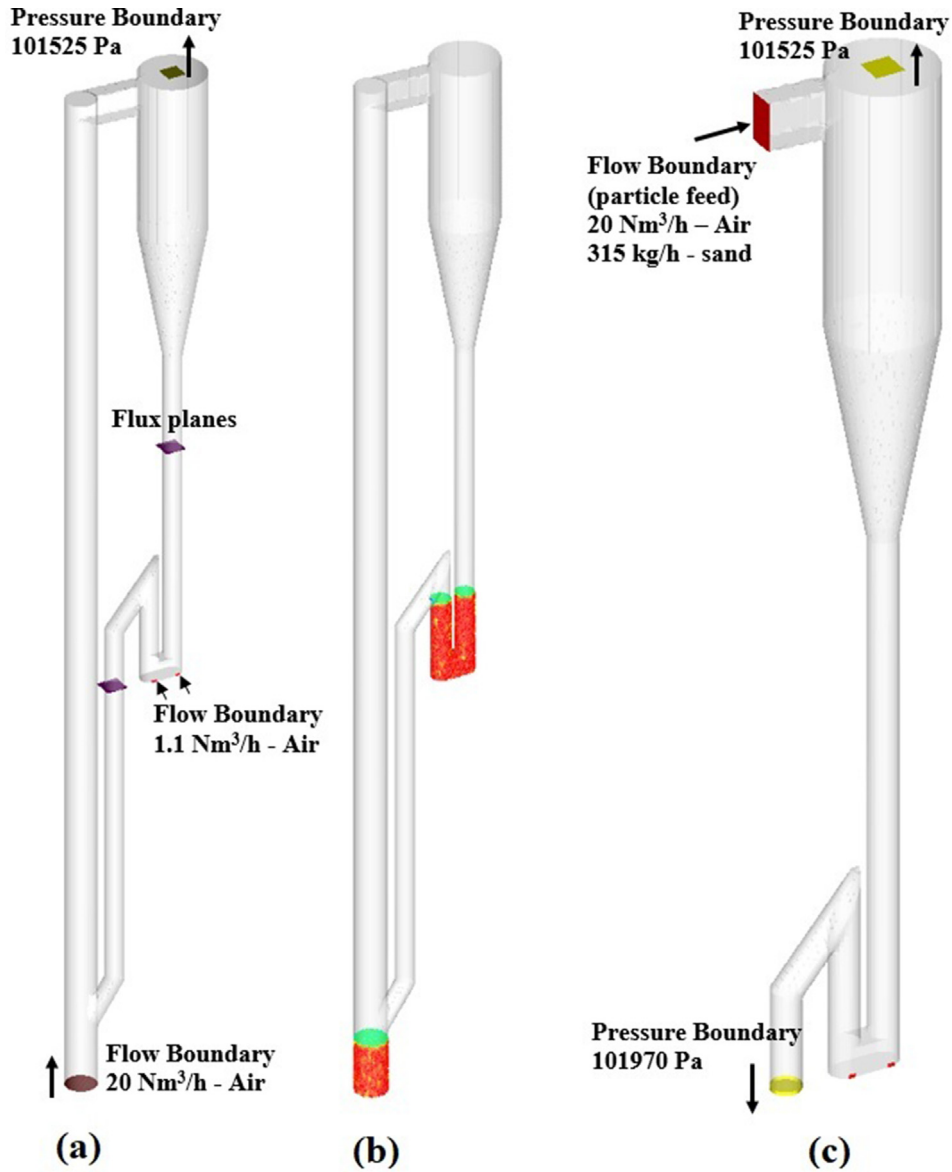


Fig. 6. Computational domain with (a)-boundary conditions and flux planes, (b)-initial particle filling, (c)-restructured computational domain for loop seal.

The riser section is operated in fast fluidization regime and the particles are carried away with gas flow, while the standpipe of the loop seal is in packed, minimum or bubbling fluidization regime. This leads to a broad variation in the particle volume fraction over different sections of the CFB system. Ergun equation has extensively been analysed and its high accuracy has been proved, especially for packed and dense phase. Therefore, Wen-Yu-Ergun drag model; Gidaspow model, in Barracuda VR[®] was used, which uses Wen-Yu drag model at higher gas volume fractions than 0.8,

$$D_{Wen-Yu} = \frac{3}{8} C_d \frac{\rho_g}{\rho_p} \frac{|u_g - u_p|}{r_p} \alpha^{-2.65}$$

$$C_d = \frac{24}{Re}, \quad (Re < 0.5)$$

$$C_d = \frac{24}{Re} (1 + 0.115 Re^{0.687}), \quad (0.5 \leq Re \leq 1000)$$

$$C_d = 0.4, \quad (Re > 1000)$$

C_d is the drag coefficient. Re_s is the particle Reynolds number and r_p is the particle diameter. When the gas volume fraction is less than 0.8, the Ergun correlation is used. As the gas volume fraction decreases below 0.8, the Ergun correlation is used,

$$D_{Ergun} = 0.5 \left(\frac{C_1 \alpha_p}{\alpha_g Re} + C_2 \right) \frac{\rho_g}{\rho_p} \frac{|u_g - u_p|}{r_p}$$

The default values for the laminar and turbulent coefficients in the Barracuda VR[®] are 180 (C_1) and 2.0 (C_2) where those are 150 and 1.75 in original Ergun formulation. The particle Reynolds number is given by:

$$Re = \frac{2\rho_p |u_g - u_p|}{\mu_g} \left(\frac{3V_p}{4\pi} \right)^{1/3}$$

4. Results and discussion

Direct numerical simulation (DNS) solves the complete flow structure over each particle in the system and therefore, empirical

correlations and constitutive equations are not required in the modelling stage. As the number of particles in the system is increasing, DNS becomes computationally costly, which demands model simplification with empirical approximations as in EE or EL approach. Therefore, CFD model validation against experimental data improves the reproducibility of the results.

4.1. Model validation

The authors have discussed the sensitivity of the grid and the effect of parcel resolution in a previous publication (Bandara et al., 2019). System pressures and the rate of particle circulation (G_s) were the available parameters to compare the simulation results over experiments. The particle volume fractions (ϵ_p) over the CFB riser and the LS is depicted in Fig. 7. A dilute flow below 0.1 of ϵ_p prevails in the riser section and a distinguishable variance in particle volume fraction cannot be identified over the cross section of the riser except, for a few particle clusters at different elevations. Therefore according to the drag model setup, Wen-Yu correlation is used to calculate the drag force in the riser. Nevertheless, Wen-Yu correlation is not extensively studied for pneumatic conveying compared to Ergun model in dense phase particle systems. The particle holdup in the riser is reflected by ΔP and as illustrated in Fig. 8, the riser pressure drop is slightly low than experiments. The calculated drag force with Wen-Yu model can be higher than the actual and consequently, the riser particle holdup is possible to decrease in simulations. This suggests that the understanding of particle hold up in the riser could have been

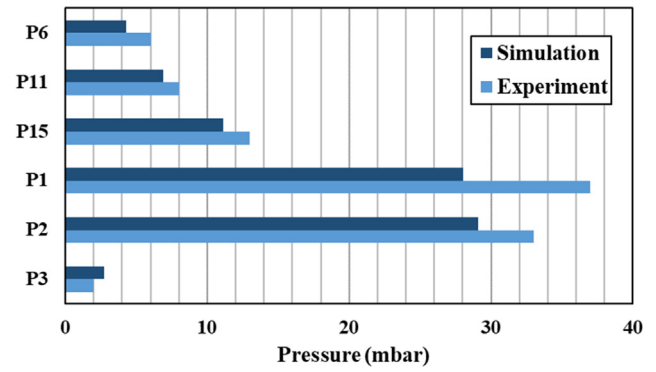


Fig. 8. Pressure (gauge) over the circulating fluidized bed with experiments and simulation.

a significant parameter for the comparison and however, the experimental measurement needs auxiliary attachments to the rig.

An enlarged views of the LS particle hydrodynamics are illustrated in Fig. 7. The aeration gas does not penetrate throughout the width of the loop seal and instead, gas tends to flow adjacent to the walls of the injection where the opposite side stays near to the close pack ϵ_p . This can possibly lead to narrow down the efficient functionality of the LS and consequently a reduced G_s . Average particle bed height at the SP is 170 mm, which is approximately equal with the height of recycle pipe. This is a decent indication that the particle phase trapped inside the

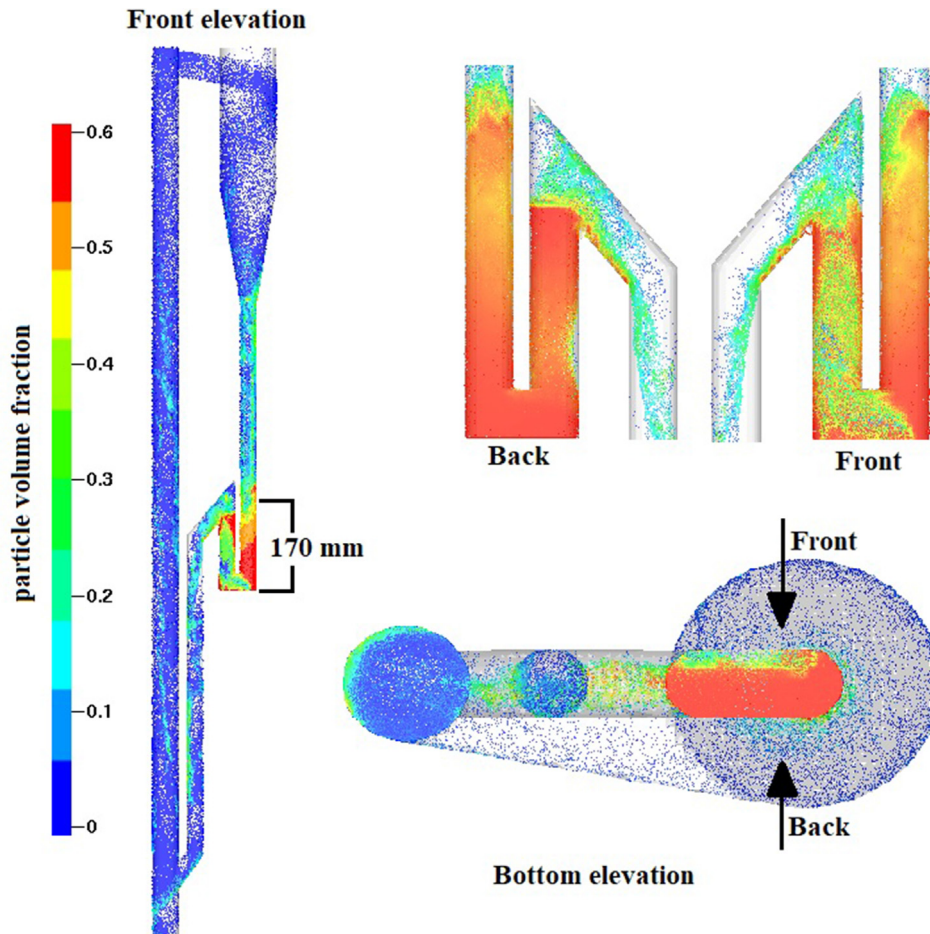


Fig. 7. Hydrodynamic behaviour across circulating fluidized bed and at the loop seal.

loopseal is at complete fluidization state where the particles are driven from SP towards LS overflow by the pressure difference. The dense particle bed in the SP is mostly at the close pack volume fraction of 0.6, which gets diluted up to 0.5 as it reaches the bed surface. The bubble formation, rise and eruption at the SP are not regular and hard to predict. A large fraction of the recycle pipe volume consists with a lower ε_p ranging from 0.3 to 0.45. According to Fig. 8, the simulation under predicts the system pressure and LS shows the highest deviation. There exists a significant pressure difference between supply chamber and recycle chamber related to experiments. However being at the same elevation, a significant difference is not expected between P1 and P2 during a healthy fluidizing state. In contrast, P1 and P2 are approximately similar with each other in simulations, even though the local values are less compared to experiments. In first place, the implemented values of closed pack volume fraction and particle size distribution can be deviated from the actual. Secondly, the particle attrition is possible during a long run of experiments and the size distribution is possible to shift towards lower diameters resulting increased ΔP . As the experimental pressure measurement at the LS is higher, the attrition is a possible reason. Experimental studies have revealed that the linear coefficient of the Ergun equation is a function of the particle's group in the Geldart's classification. Relative to the direction of the particle flow, the pressure gradient is negative in the SP while positive in the recycle pipe. The particle flow along a negative fluid pressure gradient might also lead to deviated pressure calculations. Finally, the primary dimensions of uncertainty incident from nonconformity in geometrical lengths, pressure sensor measurements and physical reality of implementing the boundary conditions could also lead to imperfect pressure prediction.

The experimentally measured average G_S at 20 Nm³/h of riser and 1.1 Nm³/h of LS aerations was 320 kg/h. The particle modelling parameters in the CPFDF model were optimized to match with the experimental G_S . Fig. 9 and Fig. 10 illustrate the instantaneous particle flowrates across the overflow pipe and SP respectively. The flow variation is extreme across the LS overflow, which rises up over 1000 kg/h in certain time steps. The particles are fed as clusters to the overflow pipe due to bubble eruption at the bed surface of Recycle pipe. Nevertheless, the clusters are dispersed along the riser and across the cyclone giving a comparatively less flow variation at the immediate upstream of the LS. As a result of particle escape from the cyclone exhaust, the mass in the system reduced by 0.7% at a rate of 0.3 kg/h over the 50 s of simulation time.

The G_S was experimentally measured by interrupting the LS. As the LS aeration gas is naturally forced towards the riser, the riser hydrodynamics is possible to affect by the absence of LS aeration. Further, the initial measurement of the particle height at the SP could be imprecise due to the unevenness of the bed surface. In

the final conversion of particle volume to mass, the bulk density was assumed to be similar with the experimentally value measured for static conditions. These uncertainties related with the experimental measurements can be included as a positive or negative offset to the actual G_S . Likewise, Simulation results is also possible to affect by number of uncertainties, where some are mentioned previously. Additionally, Barracuda VR[®] requires the envelop density for particle phases that is calculated based on envelop volume as illustrated in Fig. 11. Experimental work reported the absolute density and the envelop density can be deviated considerably depending on the particle irregularities.

Real piping arrangement of the LS aeration was not included as a highly refined mesh was required to capture the small piping into the computational grid. LS aeration was regulated by a single controller and therefore specific flow rates at each of the two aeration locations were not known separately. Consequently, half of the total flow was implemented at each aeration flow boundary in simulation setup.

The CPFDF is equipped with Courant-Friedrichs-Lewy (CFL) manager where initial time step of 0.0005 s was adjusted accordingly to meet up the convergence criteria. During the steady state operation, the average time step was found to be between 0.0003 and 0.0005 s. Even the minimum CFL value of the simulation setup was 0.8, the runtime value was slightly above 1.0 in the majority of the time steps. The computational time for 50 s of simulation was 12.8 h.

4.2. Simulation of downsized computational domain to loop seal

The computational domain was rearranged as in Fig. 6 (c), by deleting the grid occupied over the riser section. The grid structure of the new domain was identical with the corresponding section of complete CFB domain whereas the number of cells were cut down to 168,324 from 435,232. As the cyclone inlet was disconnected from the riser, the material flow from the riser was modelled as a particle flow boundary at the disconnected plane. In contrast to the highly fluctuating particle flow in full loop, time averaged values were used for particle and gas flowrates. The resolution of the computational particles at a particle feed flow boundary is governed by "Number Density Manual". A sensitivity check for the resolution of computational particles was performed and 2.35×10^5 was sufficient, which was resulted from 125 as the number density manual. The particle feed started after 1.4 s adopted from the full loop simulation. The pressure for the particle outflow boundary at the overflow pipe was likewise adopted from the full loop CFB simulations.

As the rate of particle feed was forced at steady 320 kg/h, the performances of full loop CFB and LS simulations were compared using the pressure, particle bed height at the SP and particle hydro-

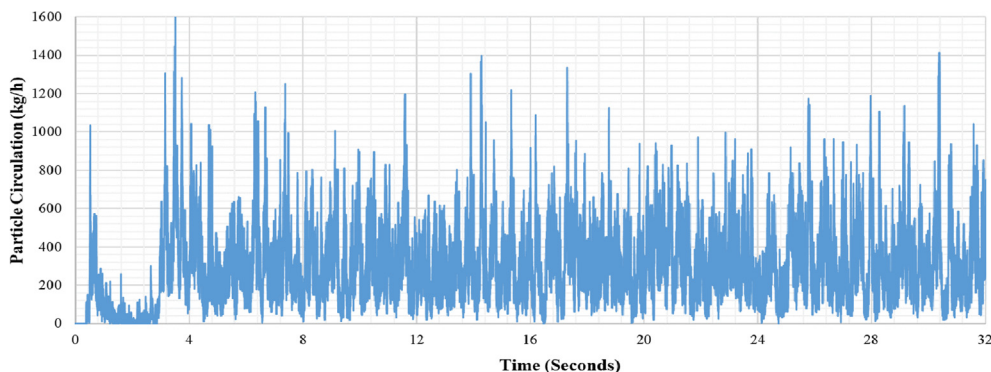


Fig. 9. Simulated Particle flowrate after the loop seal (overflow pipe).

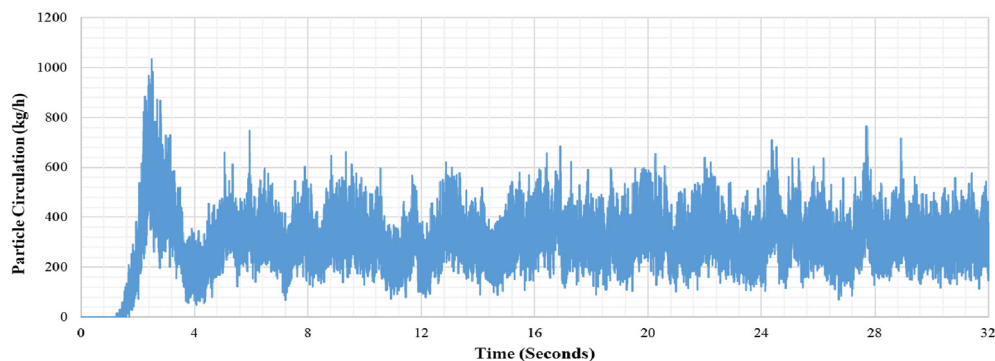


Fig. 10. Particle flowrate before the loop seal (standpipe).

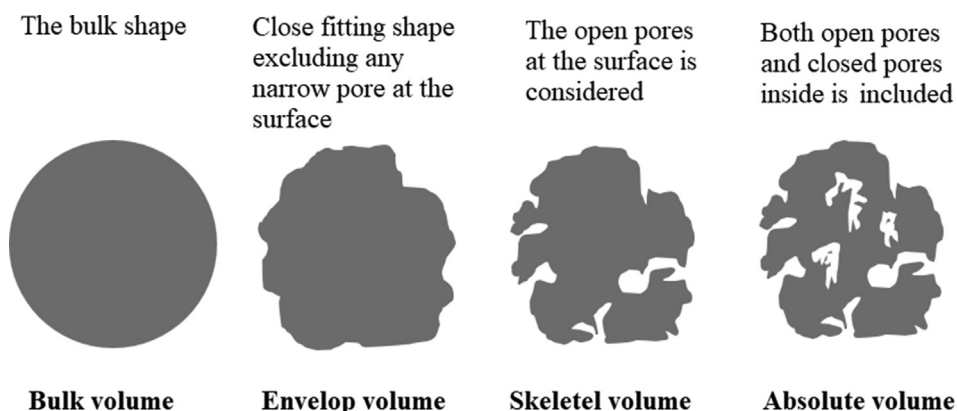


Fig. 11. Definition of particle volumes.

dynamics across the LS. The graphical illustrations of the full loop and the downsized model hydrodynamics in Fig. 12, suggests that both the models have strong similarities. Further, the LS pressure readings were identical in both cases. Therefore, even with implemented steady boundary conditions at the cyclone inlet and LS outlet, the downsized model is functioning accordingly with the full loop CFB. The developed downsized model was therefore used (with slight modifications) to analyse LS performances at varying aeration flowrates, aeration position and the length of loop seal horizontal section.

4.3. Effect of the rate loop seal aeration

The rate of particle and air feed at the cyclone inlet was known from the full loop simulation results. In contrast, the underline ideology of the development of the downsized model was to study the change of particle circulation against different LS parameters. Therefore, it was required to restructure the new model to improve its similarity with the functionality of full loop where the LS out flow boundary was connected with cyclone inlet boundary using “Boundary connector manager” option. A graphical illustration is given in Fig. 12. A time delay of 1.4 s was incorporated in the boundary connector to represent the resident time of particles over the riser reactor. The riser aeration gas flowrate was added to the boundary connector using “secondary feed” option. The initial particle mass was 0.58 kg, which was identical with the full loop CFB simulation.

Loopseal aeration is an auxiliary functionality that adds extra energy footprint. Therefore, it is beneficial to identify the ideal flow conditions. In certain systems with a circulating particle phase, two or more reactors are connected using multiple LS where the

LS performances directly effect on the particle inventory of each reactor. In most of the situations, the LS aeration gas flows down to one of the reactors. Hence, LSs are normally aerated with one of the gas species used in the reactor. The quantification of LS gas bypass to the reactor is therefore important in designing the reactor gas flowrates. The computational model depicted in Fig. 13 was used to analyze the rate of particle circulation at different LS aeration rates from 0.6 Nm³/h to 1.7 Nm³/h at interval of 0.1 Nm³/h.

Particle dynamics over the LS at different aeration rates are illustrated in Fig. 14 and the dense bed heights in the standpipe (SP) are stated at each profile. The dense bed height at the SP was attempted to be measured during the absence of bubbles and with a steady bed surface. The G_s , LS pressure and the overflow pipe air flowrate were plotted against the LS aeration and illustrated in Fig. 15, Fig. 16 and Fig. 17. The height of the dense bed at the SP decreases proportionally with increased aeration up to 0.8 Nm³/h. The SP is at packed bed conditions up to 0.7 Nm³/h of LS aeration, which results a reduced particle circulation. The particles descend as a packed bed along the SP, which are afterwards, dragged along the horizontal section due to the SP pressure and lubrication effect exerted from the aeration. According to the plot in Fig. 17, it is evident that there is not any upward air flow at the SP up to 0.9 Nm³/h, where the total air passes towards the recycle pipe. As the rate of aeration is increased to 0.8 Nm³/h, the bed height drops sharply with a simultaneous boost in G_s from 210 kg/h to 280 kg/h. It can be assumed that the SP starts to fluidize between 0.7 and 0.8 Nm³/h of aeration. The G_s continues to increase up to 343 kg/h as the aeration is increased till 0.9 Nm³/h. According to the Fig. 15, the G_s shows a linear proportionality towards the aeration rate up to 0.9 Nm³/h with a sharp change

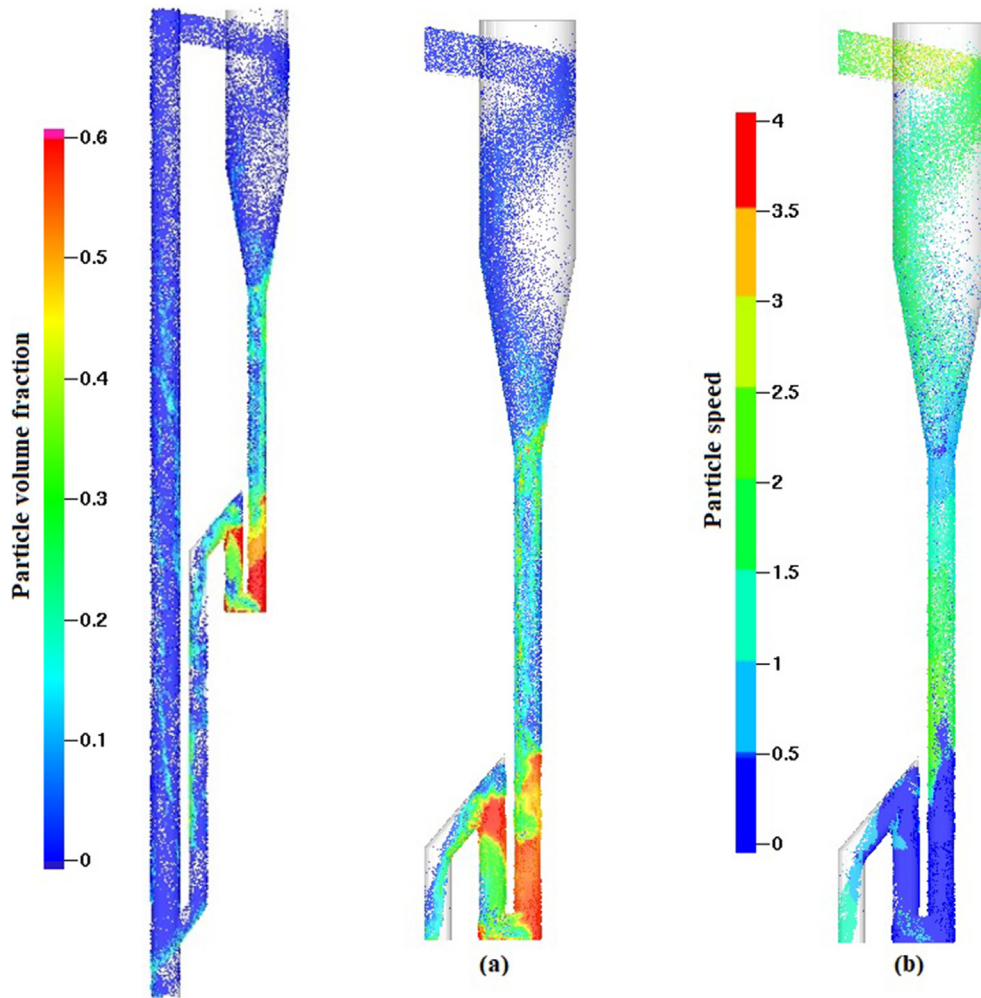


Fig. 12. Particle hydrodynamics of the loop seal, (a)-particle volume fraction, (b)-particle speed.

in the gradient after $0.7 \text{ Nm}^3/\text{h}$. As the aeration is further increased than $0.9 \text{ Nm}^3/\text{h}$, the G_S remains approximately steady with a slight increase up to 355 kg/h , which is merely a 3.5% growth compared to the $0.9 \text{ Nm}^3/\text{h}$ result. Hence according to the observations, the optimum aeration rate is $0.9 \text{ Nm}^3/\text{h}$ approximately, which is a close match with the experimental finding of $1 \text{ Nm}^3/\text{h}$ for a stable LS operation. Analog to the boost in circulation, it can be argued that the SP particle bed starts fluidizing at $0.8 \text{ Nm}^3/\text{h}$ aeration. However, due to the absence of an upward flow as illustrated in Fig. 17, it can be assumed that the bed is at minimum fluidization. A flux plane records the resultant gas flow across the entire cross section where the air carrying in downward direction with the descending particle bed counter-weights the upward fluidization gas flow. After $0.9 \text{ Nm}^3/\text{h}$, a consistent upward air flow is evident according to Fig. 17. This is due to the bubble rise that carries a large amount of air in it. Nevertheless, the downward airflow inside the particle phase is higher than upward, which gives a resultant downward flow. This is further demonstrated by the curves in Fig. 16, which shows the airflow due to LS aeration, total airflow out from the overflow pipe and the difference between those two. The curve profile of the difference follows the “loopseal aeration vs particle circulation” curve in Fig. 15 until $1.2 \text{ Nm}^3/\text{h}$. Increasing difference results from the increasing particle circulation, which carries more air with particles. After this threshold, the bubbling becomes more frequent and therefore, the difference starts to drop even with minor improvement of the particle circu-

lation. The “LS aeration vs the pressure” curve in Fig. 15 also follows the same trend as in particle circulation which is approximately similar with a pressure plot developed to find the minimum fluidization velocity. Pressure difference between P1 and P2 becomes narrow at $0.9 \text{ Nm}^3/\text{h}$ of LS aeration and continues until $1.2 \text{ Nm}^3/\text{h}$, which afterwards starts to increase. The particular trend is possible to explain with the plot in Fig. 16. As explained above, more and more gas starts to rise in the SP after $1.2 \text{ Nm}^3/\text{h}$ and consequently, the relative velocity between particle and gas phases is increased. According to the construction of the Ergun equation, the bed pressure drop is proportional to the relative velocity, which is the reason for increasing pressure at P2 compared to P1 after $1.2 \text{ Nm}^3/\text{h}$ aeration. As discussed in literature review in section 02, the G_S is proportional with the pressure drop of the SP. P2 increases steadily up to $0.9 \text{ m}^3/\text{h}$ and simultaneously, the G_S also increases. Botsio and Basu (2005) reasoned the increased of G_S with LS aeration using the “weir theory” as well. At higher LS aeration, the particle bed inside the recycle chamber expands proportionally reducing its bulk density. Therefore in order to balance the recycle chamber pressure against supply chamber, the particle height above the overflow weir increases, which in turn resulted in increased particle overflow. Further, increased aeration improves the lubrication effect followed by reducing the wall friction. This is highly advantageous, especially the wall effect can be significant in narrow passages compared to larger scale.

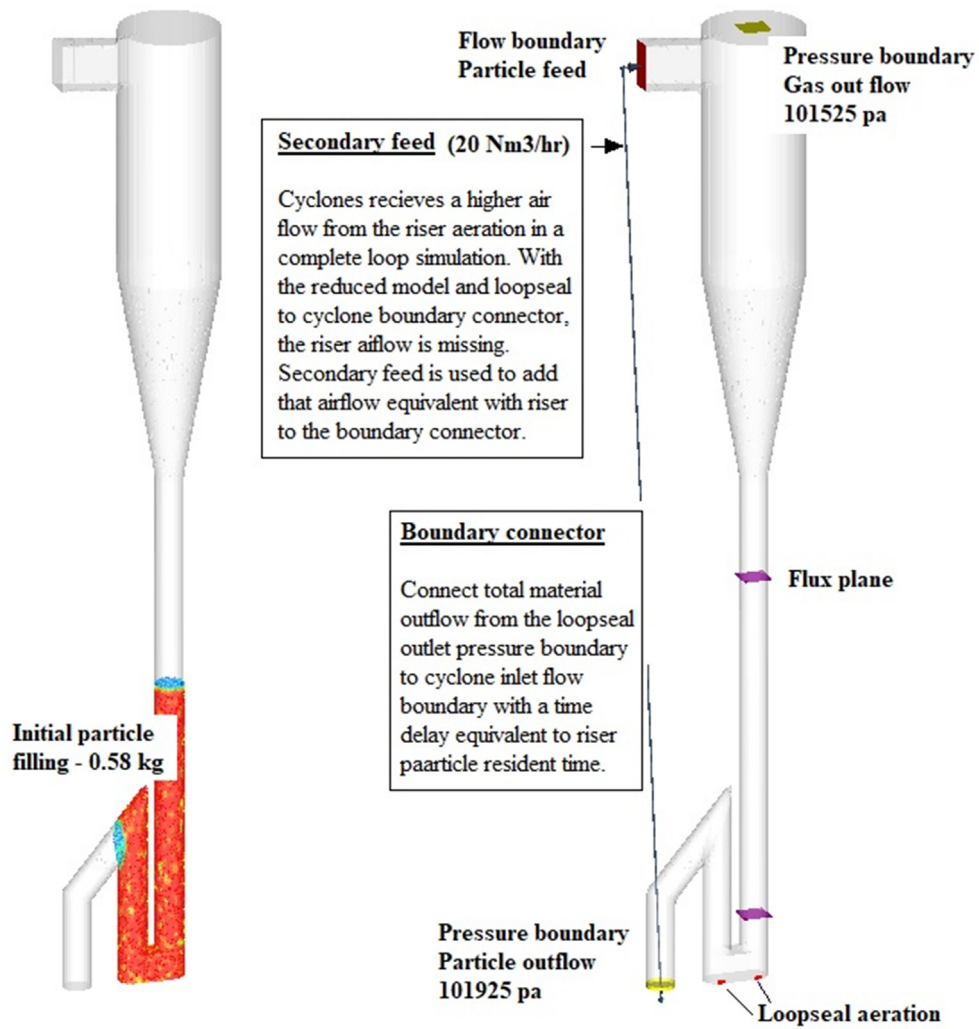


Fig. 13. Initial particle filling and the boundary conditions used to analyze the loopseal performance.

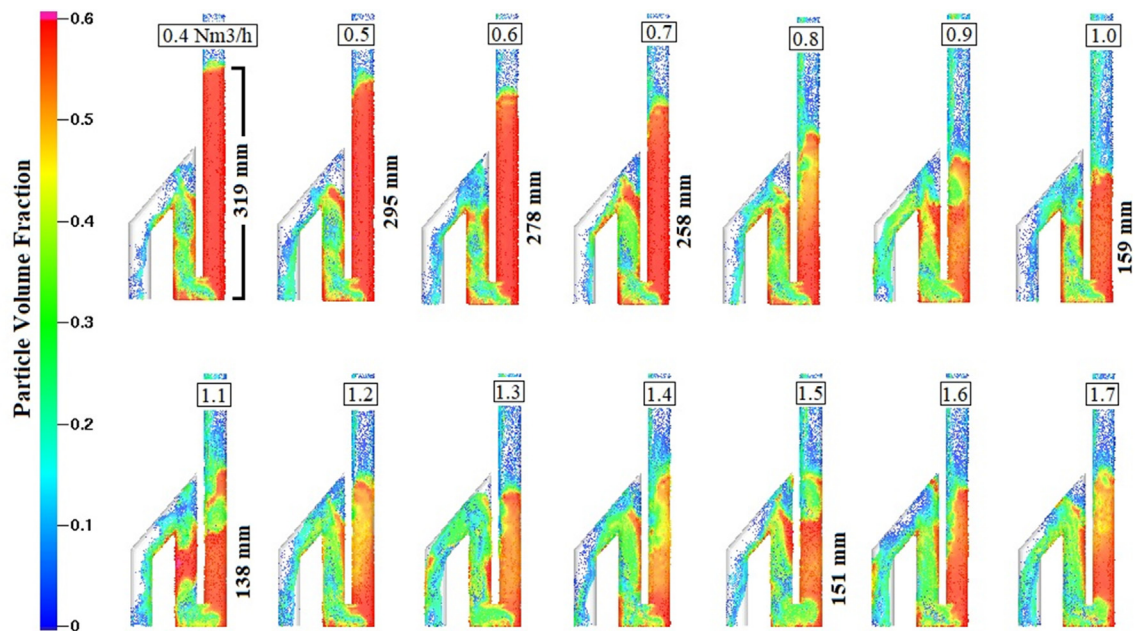


Fig. 14. Particle hydrodynamics over loopseal at different loopseal aeration.

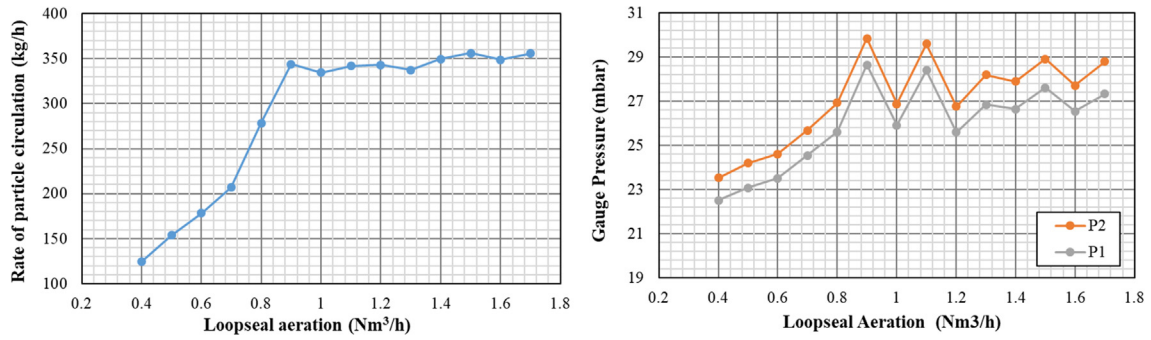


Fig. 15. Change of rate of particle circulation and system pressure as a function of loopseal aeration.

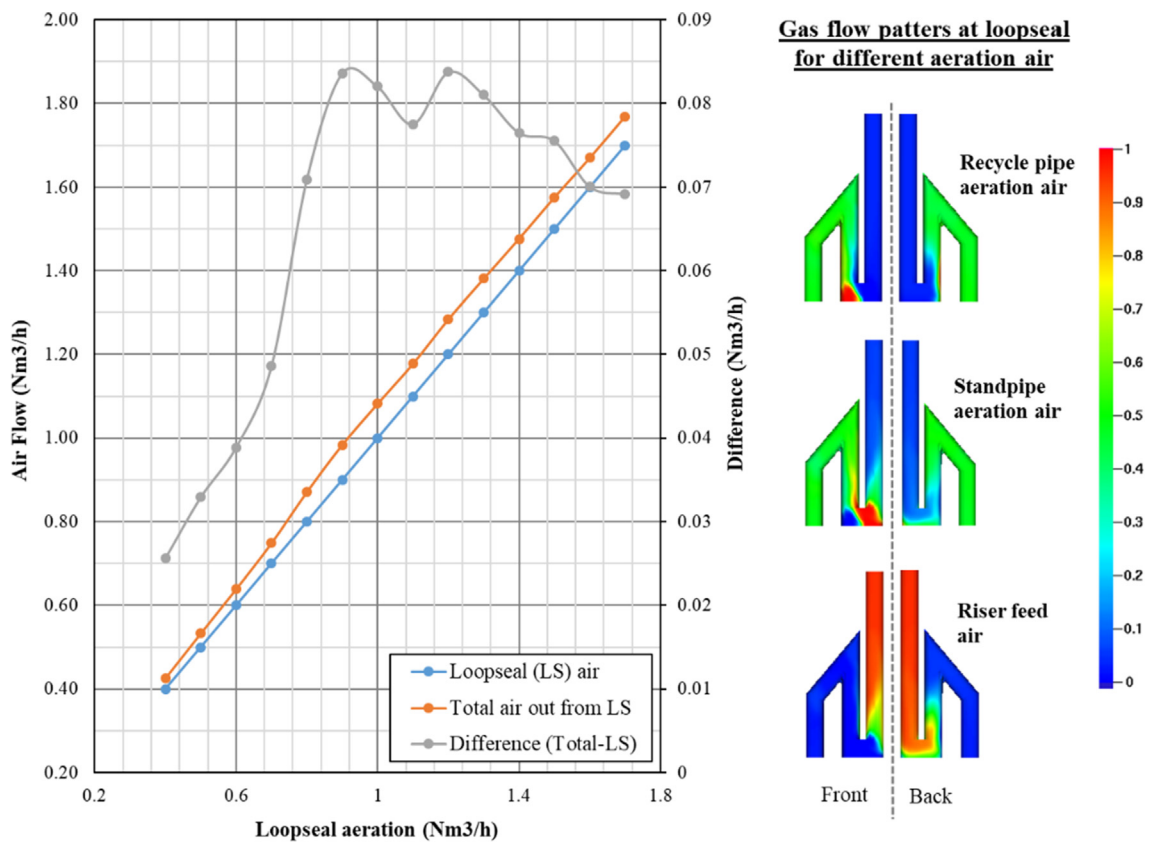


Fig. 16. Comparison of airflow rate at loopseal and total across overflow pipe.

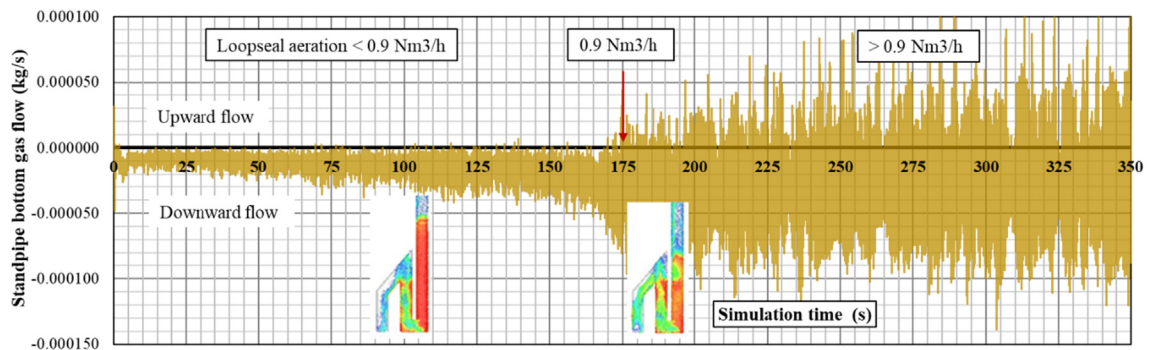


Fig. 17. Rate of airflow at the bottom of the standpipe and transition of standpipe from packed bed to bubbling bed.

The average particle mass in the system is 0.45 kg which fluctuates between 0.41 kg and 0.46 kg. The simulation initiated with 0.59 kg of particle mass in the loopseal. A part of the particles stands outside due to the time delay introduced into the boundary connector which was calculated to be the particle residence time in the riser. Hence, it can be assumed that nearly 0.15 kg of particles resides in the riser during steady operation.

The graphical illustrations in Fig. 16 visualize how the different aeration gases are occupied over the loop seal section at 1.6 Nm³/h loop seal aeration. The recycle pipe aeration gas is completely driven towards the overflow pipe along the direction of injection (front side as mentioned in the Fig. 16). The supply chamber aeration air shows slight upward flow along the SP in the side of injection up to 95 mm from the bottom. However, the concentration dissolves in the higher flow of the riser aeration gas carried with the particle flow. The cyclone and most of the SP volume are occupied by the riser aeration gas. There is a noticeable concentration of riser aeration gas up to the sharp bend between the recycle pipe and the overflow pipe. The riser air crosses the loopseal at the opposite side (back) to the loopseal air injection where the dense particle phase exists, which is clearly illustrated in Fig. 7. Hence, the riser air is mostly carried with the moving particle phase.

In a standard bubbling fluidized bed, the gas rises through the voids in the dense particle phase and is trapped inside the bubbles. Even with occasionally observed bubbles, the particle hydrodynamics in a SP is fairly different from a regular bubbling fluidized bed. In contrast to a bubbling bed, the resultant gas flow is in downward direction due to the gas trapped within the voidage of moving particle phase. Hence, an upward gas flow through the voids in the dense particle phase is restricted where the bubbles alone are mainly responsible for the upward gas transport. As a bubble emerges at the standpipe bottom and penetrates up, the particles around the bubble flow down towards the empty space created by upward

motion of the bubble, which are then dragged towards recycle pipe. As the bubble rises, it collects more fluid from the dispersed phase and as a result of that, the disperse phase gets denser which is depicted in Fig. 19. In a bubbling bed, the bubbles are formed after the maximum expansion of the bed is achieved where the excess gas is collected to form a bubble. Hence, with a uniform bottom gas distribution, bubbles appear at a certain elevation and grow in diameter as it moves up through the dense particle phase. In contrast, a complete bubble initiates at the bottom of the SP which is clearly illustrative in Fig. 18 and Fig. 19. The SP aeration has a high tendency to bypass towards the recycle pipe and however occasionally, a bubble emerges in the SP whenever the recycle pipe pressure develops higher and sustains for a longer time than regular pressure peaks. According to the graphical illustrations in Fig. 18 and Fig. 19, high and long lasting peaks are observed whenever particles slugs are formed at the outflow weir of the recycle pipe. However, bubbles are not observed during every appearance of a slug and hence, the bubble frequency and the diameter is not possible to predict accurately. The pressure at the bottom of the recycle pipe was plotted against the time to make an attempt in understanding the bubble formation, which is illustrated in Fig. 18.

As illustrated in the first plot of Fig. 18, the only bubble observed between 84.5 and 89.0 of simulation seconds is at 85.6th second. A high pressure peak followed by a wide peak can be observed at the onset of bubble formation. Afterwards until 88.4 s, only narrow peaks are observed with no bubbles. A possible bubbling occurrence exists at 88.5th second as highlighted in the plot and however, a bubble did not emerge at the SP. The bubble formation at the standpipe between 104 s and 110 s are also illustrated in the second plot of Fig. 18. In certain instances, the initiated bubbles at the bottom of the SP were dragged back towards the recycle pipe, which can be due to high resistance exerted from the downward particle flow.

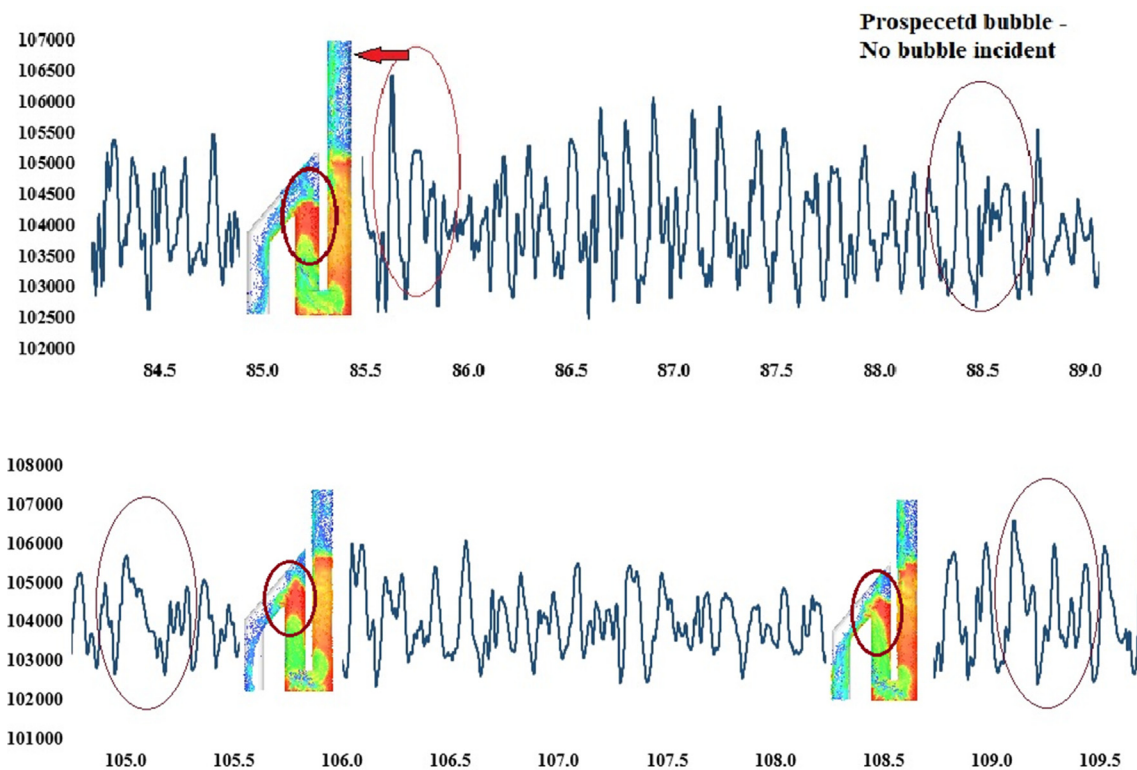


Fig. 18. Time vs pressure plot in recycle pipe to identify the bubble formation.

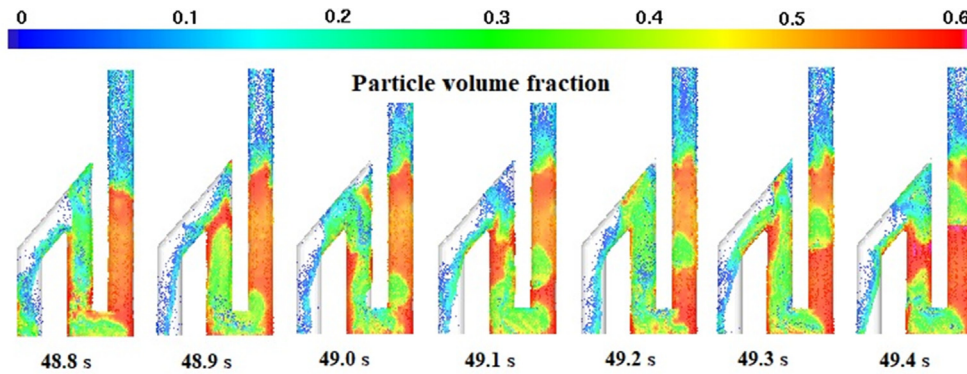


Fig. 19. Bubble rise and following dense phase (below the bubble) in the standpipe.

4.4. Effect of the position of loop seal aeration

A similar model setup as in Fig. 13 was used with different aeration configurations as pictured in Fig. 20. The total LS aeration rate was maintained at $1.1 \text{ Nm}^3/\text{h}$ similar to the primary case where flow was divided equally between the aeration flow boundaries. The aeration locations as shown in 2, 3 and 4 in Fig. 20 were implemented to investigate the trends of particle circulation as a function of height of the vertical aeration (U_v) at the SP. Configuration 1 pictures the original setting similar to experiments. Further, it was observed that the aeration gas did not penetrate greatly into the particle bed beyond the point of injection in the original configuration. Therefore, the effect of aeration with four injection points from both walls of the LS, as in configuration 5, was analyzed. Instead of aeration from the side walls, the rate of circulation was investigated against homogeneous aeration from the bottom of the LS. The average G_s along with percentage of change for respective cases (based on original case) are given in Fig. 21.

According to the experimental works in the scientific literature, the rate of circulation is supposed to improve as the elevation of the standpipe aeration is increased from the bottom up to 2.5

times the SP diameter. However, the data in Fig. 21 indicates that the G_s gradually decreases as the aeration location is successively changed from configuration 2 to 4. Referring to the findings for original aeration configuration, the standpipe particle bed is not always bubbling whereas most of the loopseal aeration gas pass towards the overflow pipe. The graph to the right in Fig. 21 depicts the change of overflow pipe airflow against different configurations. It is evident that the value sharply drops as the SP aeration is moved from configuration 1 to 2, which continues to drop slightly towards configuration 4. It is a clear indication that the SP aeration rises along itself without bypassing to the overflow pipe. The graphical illustrations in Fig. 21 shows that the SP is occupied by large bubbles in 2, 3 and 4th configurations, which limits the available cross sectional area for the particles to descend. Further, the deviated results from literature findings can be due to number of incompatibilities in between particular experimental units and the simulation geometry used in this study. Firstly, recycle pipe and standpipe aerations were different from each other in literature experimental studies whereas particular values were identical in this study. The velocity of LS gas injection can be significant as it decides the length of penetration to the particle bed, which were not mentioned in the literature. The bubbles tend to

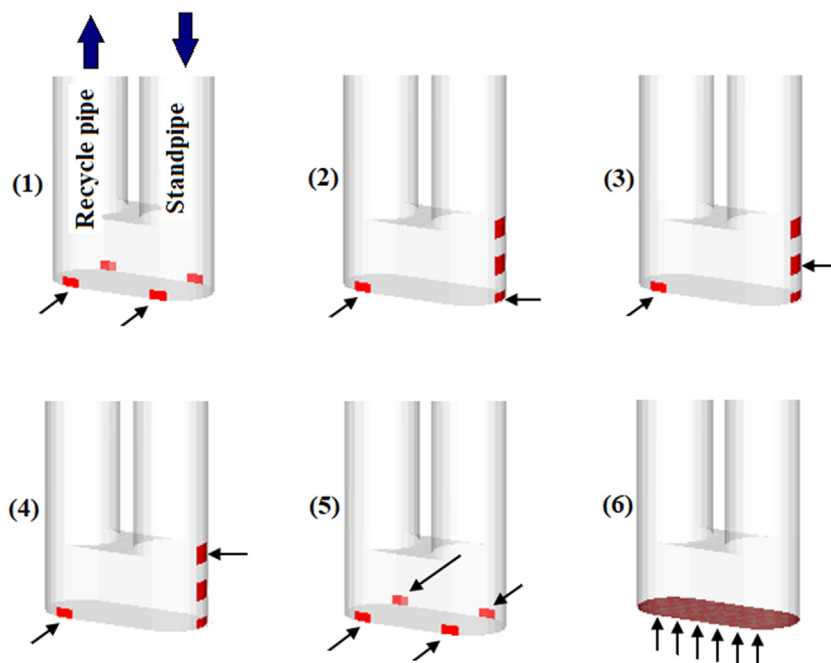


Fig. 20. Different aeration positions used to analyze the circulation rate.

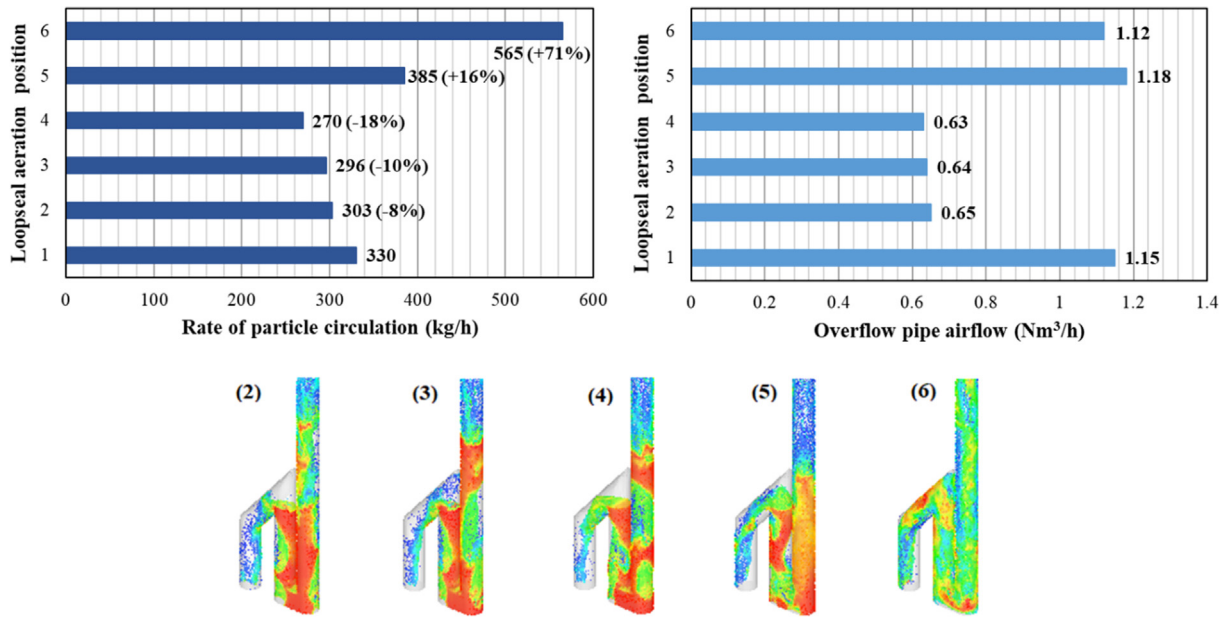


Fig. 21. Change of rate of particle circulation with loopseal aeration position (left), Change of overflow pipe airflow (right) and particle hydrodynamics across loopseal.

rise attached to the walls in the side of the injection. As the bubble rises up, it catches up air trapped in the particle phase and finally turns into slugs, which is clearly visible in 3rd and 4th images in Fig. 21. However, a fraction of the SP aeration is possible to flow towards the recycle pipe at higher injection velocities, which will in turn prevent the slug formation at the SP.

Aeration from both side walls as in configuration 05, improves the circulation by 16% compared to single sided aeration as in the primary setup. When the LS is fed with uniform bottom aeration as in configuration 6, the fluidization and lubrication effects are enhanced in the horizontal passage of the loopseal, which boosts the circulation by 71% up to 565 kg/h. However, the rate of particle circulation is highly fluctuating compared to rest of the configurations. Uniform bottom aeration has its limitations in implementing to large scale industrial units with uninterrupted operation. Instead of uniform aeration, it is possible to mount increased number of injection ports (i.e. bubble caps) at the bottom plane. However, configuration 5 is the simplest to implement whereas increasing number of injection ports will have dual benefits. The more the injection ports, the more the rate of particle circulation becomes and the less the operational hindrance due to malfunctioning of one or two injection ports.

The bubbles rise attached to the walls of the SP, which is one of the identified deviation related to Barracuda VR[®] simulations. The

grid generation tool has a limited competency and the radial grid refinement at the wall boundary is impossible for circular cross sections. A coarse grid structure near the walls hinders the formation of the fluid boundary layer. This makes an easy passage for the bubble to rise. However, the effects of near wall and center bubble rise can be varied with different SP diameters. For instance, being a reduced diameter SP, the bubble migration attached to wall is equally affected to the entire cross section in this study. In contrast, the effects from a center rising bubble over a wall attached bubble can be different in a larger diameter SP.

4.5. Effect of the length of the horizontal section

The length of the horizontal section in a loopseal is possible to vary depending on system requirement such as connecting flanges, insulation and requirement of maintenance space. Further, several attempts have been made to mount heat exchangers across the horizontal section of the LS. Therefore, it is important to understand the variation of the rate of particle circulation as a function of length of the horizontal passage. The different lengths used in the simulation studies and respective circulation rates are illustrated in Fig. 22. The loop seal aeration was maintained at 1.1Nm³/h that was equal with the primary case. The injection ports were placed at similar locations relative to recycle pipe and stand-

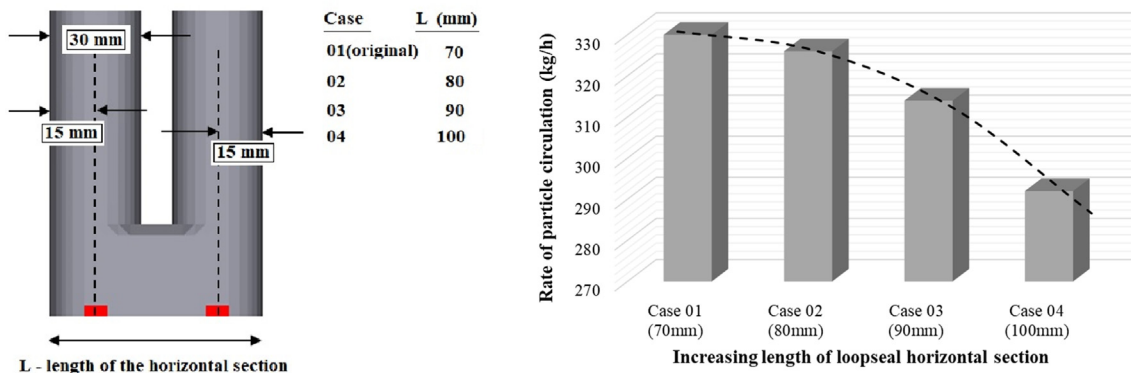


Fig. 22. Different lengths of the loopseal horizontal section and respective rates of particle circulation.

pipe. The rate of circulation decreases in a polynomial way with the increment of the horizontal length. Particles find it difficult to flow in the horizontal direction compared to gravity assisted flow in the SP. The wall resistance is increased and as the aerations ports are moved apart, it is possible to exist a stationary particle phase in between.

5. Conclusion

Loop seal is a robust mechanism for particle recycling in circulating fluidized bed reactor. It is powered by aeration where the rate of aeration is a key parameter that governs the particle circulation. Experimental optimization of geometrical parameters such as shape, dimensions and aeration position of a loop seals is difficult. The main drive of this work was hence, to develop a CFD model for parametric analysis of loop seals.

CPFD is an emerging package having extended functionality to model particle systems with or without chemical reactions. The “boundary connector” function was used in the study to separate the loop seal from a CFB in which the subsequent analysis were performed. It was necessary to include the cyclone section to implement a realistic particle feed into the standpipe. The full loop CFB system was validated against experimental data prior to the model reduction. A time delay of 1.4 s was included in the boundary connector to compensate the residence time of particles in the riser reactor. The value was adopted from the full loop simulation and used for all the following simulations included in this work. During the model downsizing, highly dynamic particle flow in to the cyclone was replaced by a constant flow boundary with the average rate of particle circulation.

Loopseal aeration was found to be crucial for the rate of particle circulation where $0.9 \text{ Nm}^3/\text{s}$ was found to be the optimum flowrate for the studied geometry. Increasing of the aeration from $0.9 \text{ Nm}^3/\text{h}$ to $1.8 \text{ Nm}^3/\text{h}$, could improve the circulation rate merely by 3.5% whereas a 16% improvement could be achieved by keeping the aeration at $0.9 \text{ Nm}^3/\text{h}$ and increasing the number of injections to 4 at both walls of the loopseal. The uniform bottom aeration was the most effective way to improve the particle circulation, which resulted in 71% increment compared to original configuration. In contrast to the increasing trend mentioned in the literature findings, the circulation rate decreased as the height of air injection at the standpipe was increased. This could be due to differences in the injection velocity which has not been mentioned in the literature. Further, equal flowrates were used for both air injections, which is also not compatible with previous studies. Hence, it is recommended to analyse the system with these variables too in prior to comment on literature findings. More uncertainties can be incorporated with particle size distribution, especially particle attrition is possible during the long run of experiments.

The simulation geometry consists of narrow pipes and hence, it is interesting to analyse how the particle hydrodynamics responds for progressively larger dimensions with similar number of aeration points. It is recommended to measure the particle size distribution immediately after a particular experimental measurement. The “boundary connector” option is very useful in simulating a section of a complex system with a close loop of material circulation. The Developed model is capable of further analysis and optimization of loop seal construction and operation.

CRedit authorship contribution statement

Janitha C. Bandara: Conceptualization, Writing - original draft, Validation. **Chameera Jayarathna:** Software. **Rajan Thapa:** Investigation. **Henrik K. Nielsen:** . **Britt M.E. Moldestad:** Supervision. **Marianne S. Eikeland:** Supervision.

Declaration of Competing Interest

The authors declare that they have no known competing financial interests or personal relationships that could have appeared to influence the work reported in this paper.

Acknowledgement

The authors like to forward their gratitude to University of South-eastern Norway for providing the Barracuda VR[®] CFD package and computer resources for simulation.

References

- Abbasi, A., Ege, P.E., de Lasa, H.I., 2011. CPFD simulation of a fast fluidized bed steam coal gasifier feeding section. *Chem. Eng. J.* 174 (1), 341–350.
- Adanez, J., Abad, A., Garcia-Labiano, F., Gayan, P., de Diego, L.F., 2012. Progress in chemical-looping combustion and reforming technologies. *Prog. Energy Combust. Sci.* 38 (2), 215–282.
- Andrews, M.J., O'Rourke, P.J., 1996. The multiphase particle-in-cell (MP-PIC) method for dense particulate flows. *Int. J. Multiph. Flow* 22 (2), 379–402.
- Bandara, J.C., Thapa, R., Nielsen, H.K., Moldestad, B.M.E., Eikeland, M.S., 2019. Circulating fluidized bed reactors – part 01: analyzing the effect of particle modelling parameters in computational particle fluid dynamic (CPFD) simulation with experimental validation. *Particulate Sci. Technol.*, 1–14
- Bareschino, P., Solimene, R., Chirone, R., Salatino, P., 2014. Gas and solid flow patterns in the loop-seal of a circulating fluidized bed. *Powder Technol.* 264 (Supplement C), 197–202.
- Basu, P., Butler, J., 2009. Studies on the operation of loop-seal in circulating fluidized bed boilers. *Appl. Energy* 86 (9), 1723–1731.
- Basu, P., Chandel, M., Butler, J., Dutta, A., 2009. An investigation into the operation of the twin-exit loop-seal of a circulating fluidized bed boiler in a thermal power plant and its design implication. *J. Energy Res. Technol.* 131 (4), 041401–01–8.
- Basu, P., Cheng, L., 2000. An analysis of loop seal operations in a circulating fluidized bed. *Chem. Eng. Res. Des.* 78 (7), 991–998.
- Bischi, A., Langørgen, Ø., Saanum, I., Bakken, J., Seljeskog, M., Bysveen, M., et al., 2011. Design study of a 150kWth double loop circulating fluidized bed reactor system for chemical looping combustion with focus on industrial applicability and pressurization. *Int. J. Greenhouse Gas Control* 5 (3), 467–474.
- Botsio, E., Basu, P., 2005. Experimental investigation into the hydrodynamics of flow of solids through a loop seal recycle chamber. *Can. J. Chem. Eng.* 83 (3), 554–558.
- Chen, C., Werther, J., Heinrich, S., Qi, H.-Y., Hartge, E.-U., 2013. CPFD simulation of circulating fluidized bed risers. *Powder Technol.* 235 (Supplement C), 238–247.
- Cheng, L., Basu, P., 1999. Effect of pressure on loop seal operation for a pressurized circulating fluidized bed. *Powder Technol.* 103 (3), 203–211.
- Cheng, L., Basu, P., Cen, K., 1998. Solids circulation rate prediction in a pressurized loop-seal. *Chem. Eng. Res. Des.* 76 (6), 761–763.
- Chiesa, M., Mathiesen, V., Melheim, J.A., Halvorsen, B., 2005. Numerical simulation of particulate flow by the Eulerian-Lagrangian and the Eulerian-Eulerian approach with application to a fluidized bed. *Comput. Chem. Eng.* 29 (2), 291–304.
- Ergun, S., 1952. Fluid flow through packed columns. *Chem. Eng. Prog.* 48 (2), 89–94.
- Hai-guang, L., Zeng-wu, Z., Zhong-yi, Y., Bao-wei, L., Wen-fei, W., 2011. 6–7 Jan. 2011. Experimental investigation of the loop seal operation status and its judgment in circulating fluidized bed. Paper presented at the 2011 Third International Conference on Measuring Technology and Mechatronics Automation.
- Horio, M., Ishii, H., Kobukai, Y., Yamanishi, N., 1989. A scaling law for circulating fluidized beds. *J. Chem. Eng. Jpn.* 22 (6), 587–592.
- Jiang, Y., Qiu, G., Wang, H., 2014. Modelling and experimental investigation of the full-loop gas–solid flow in a circulating fluidized bed with six cyclone separators. *Chem. Eng. Sci.* 109 (Supplement C), 85–97.
- Johansson, A., Johnsson, F., Andersson, B.-Å., 2006. The performance of a loop seal in a CFB boiler. *J. Energy Res. Technol.* 128 (2), 135–142.
- Kim, S.W., Kim, S.D., 2002. Effects of particle properties on solids recycle in loop-seal of a circulating fluidized bed. *Powder Technol.* 124 (1), 76–84.
- Kim, S.W., Kim, S.D., Lee, D.H., 2002. Pressure balance model for circulating fluidized beds with a loop-seal. *Ind. Eng. Chem. Res.* 41 (20), 4949–4956.
- Kim, S.W., Namkung, W., Kim, S.D., 1999. Solids flow characteristics in loop-seal of a circulating fluidized bed. *Korean J. Chem. Eng.* 16 (1), 82–88.
- Kim, S.W., Namkung, W., Kim, S.D., 2001. Solid recycle characteristics of loop-seals in a circulating fluidized bed. *Chem. Eng. Technol.* 24 (8), 843–849.
- Li, C., Li, H., Zhu, Q., 2014. A hydrodynamic model of loop-seal for a circulating fluidized bed. *Powder Technol.* 252 (Supplement C), 14–19.
- Li, C., Zou, Z., Li, H., Zhu, Q., 2018. A hydrodynamic model of loop seal with a fluidized standpipe for a circulating fluidized bed. *Particuology* 36, 50–58.
- Liang, Y., Zhang, Y., Li, T., Lu, C., 2014. A critical validation study on CPFD model in simulating gas–solid bubbling fluidized beds. *Powder Technol.* 263 (Supplement C), 121–134.

- Lim, M.T., Pang, S., Nijdam, J., 2012. Investigation of solids circulation in a cold model of a circulating fluidized bed. *Powder Technol.* 226 (Supplement C), 57–67.
- Loha, C., Chattopadhyay, H., Chatterjee, P.K., 2014. Three dimensional kinetic modeling of fluidized bed biomass gasification. *Chem. Eng. Sci.* 109 (Supplement C), 53–64.
- Monazam, E.R., Shadle, L.J., Mei, J.S., 2007. Impact of the circulating fluidized bed riser on the performance of a loopseal nonmechanical valve. *Ind. Eng. Chem. Res.* 46 (6), 1843–1850.
- Namkung, W., Cho, M., 2002. Loopseal operation of iron ore particles in pneumatic conveying. *Korean J. Chem. Eng.* 19 (6), 1066–1071.
- Namkung, W.O.N., Guy, C., Legros, R., 2001. Prediction of solids circulation rate in the riser of an internally circulating fluidized bed (ICFB). *Chem. Eng. Commun.* 188 (1), 47–58.
- Pfeifer, C., Puchner, B., Hofbauer, H., 2009. Comparison of dual fluidized bed steam gasification of biomass with and without selective transport of CO₂. *Chem. Eng. Sci.* 64 (23), 5073–5083.
- Qiu, G., Ye, J., Wang, H., 2015. Investigation of gas–solids flow characteristics in a circulating fluidized bed with annular combustion chamber by pressure measurements and CPFD simulation. *Chem. Eng. Sci.* 134 (Supplement C), 433–447.
- Roy, S., Kemoun, A., Al-Dahhan, M., Dudukovic, M.P., 2001. A method for estimating the solids circulation rate in a closed-loop circulating fluidized bed. *Powder Technol.* 121 (2), 213–222.
- Seo, M.W., Nguyen, T.D.B., Lim, Y.I., Kim, S.D., Park, S., Song, B.H., Kim, Y.J., 2011. Solid circulation and loop-seal characteristics of a dual circulating fluidized bed: Experiments and CFD simulation. *Chem. Eng. J.* 168 (2), 803–811.
- Shrestha, S., Si Ali, B., Jan, B.M., Lim, M., El Sheikh, K., 2016. Hydrodynamic properties of a cold model of dual fluidized bed gasifier: A modeling and experimental investigation. *Chem. Eng. Res. Des.* 109 (Supplement C), 791–805.
- Snider, D., Banerjee, S., 2010. Heterogeneous gas chemistry in the CPFD Eulerian-Lagrangian numerical scheme (ozone decomposition). *Powder Technol.* 199 (1), 100–106.
- Snider, D.M., 2001. An incompressible three-dimensional multiphase particle-in-cell model for dense particle flows. *J. Comput. Phys.* 170 (2), 523–549.
- Snider, D.M., 2007. Three fundamental granular flow experiments and CPFD predictions. *Powder Technol.* 176 (1), 36–46.
- Snider, D.M., Clark, S.M., O'Rourke, P.J., 2011. Eulerian-Lagrangian method for three-dimensional thermal reacting flow with application to coal gasifiers. *Chem. Eng. Sci.* 66 (6), 1285–1295.
- Stollhof, M., Penthor, S., Mayer, K., Hofbauer, H., 2019. Influence of the loop seal fluidization on the operation of a fluidized bed reactor system. *Powder Technol.* 352, 422–435.
- Thapa, R.K., Frohner, A., Tondl, G., Pfeifer, C., Halvorsen, B.M., 2016. Circulating fluidized bed combustion reactor: Computational Particle Fluid Dynamic model validation and gas feed position optimization. *Comput. Chem. Eng.* 92 (Supplement C), 180–188.
- Tu, Q., Wang, H., 2018. CPFD study of a full-loop three-dimensional pilot-scale circulating fluidized bed based on EMMS drag model. *Powder Technol.* 323 (Supplement C), 534–547.
- Wang, H., Li, Y., Qiu, G., Song, G., Yang, W., 2014a. Measurement of gas–solids flow in loop seal and external heat exchanger in a circulating fluidized bed. *Powder Technol.* 266, 249–261.
- Wang, P., Lu, J., Xing, W., Yang, H., Zhang, M., 2014b. Impact of loop seal structure on gas solid flow in a CFB system. *Powder Technol.* 264 (Supplement C), 177–183.
- Wang, Q., Luo, Z., Fang, M., Ni, M., Cen, K., 2003. Development of a new external heat exchanger for a circulating fluidized bed boiler. *Chem. Eng. Process. Process Intensif.* 42 (4), 327–335.
- Wang, Q., Yang, H., Wang, P., Lu, J., Liu, Q., Zhang, H., et al., 2014c. Application of CPFD method in the simulation of a circulating fluidized bed with a loop seal Part II—Investigation of solids circulation. *Powder Technol.* 253, 822–828.
- Wang, Q., Yang, H., Wang, P., Lu, J., Liu, Q., Zhang, H., et al., 2014d. Application of CPFD method in the simulation of a circulating fluidized bed with a loop seal, part I—Determination of modeling parameters. *Powder Technol.* 253 (Supplement C), 814–821.
- Xie, J., Zhong, W., Jin, B., Shao, Y., Liu, H., 2012. Simulation on gasification of forestry residues in fluidized beds by Eulerian-Lagrangian approach. *Bioresour. Technol.* 121 (Supplement C), 36–46.
- Xueyao, W., Zhengzhong, M., Jing, L., Xiang, X., Yunhan, X., 2013. Numerical simulation for the loop seal in the circulating fluidized bed and experimental validation. *Appl. Therm. Eng.* 52 (1), 141–149.
- Yang, S., Yang, H., Zhang, H., Li, J., Yue, G., 2009. Impact of operating conditions on the performance of the external loop in a CFB reactor. *Chem. Eng. Process. Process Intensif.* 48 (4), 921–926.
- Yazdanpanah, M.M., Forret, A., Gauthier, T., Delebarre, A., 2013. An experimental investigation of loop-seal operation in an interconnected circulating fluidized bed system. *Powder Technol.* 237 (Supplement C), 266–275.

Paper F

Janitha C. Bandara, Britt M.E. Moldestad, Marianne S. Eikeland

Analysis of the Effect of Steam-to-Biomass Ratio in Fluidized Bed Gasification with Multiphase Particle-in-cell CFD Simulation

Conference: Proceedings of the 58th Conference on Simulation and Modelling (SIMS 58), September 25 – 27, 2017, Reykjavik, Iceland. PP 54-59

DOI: 10.3384/ecp1713854

Analysis of the Effect of Steam-to-Biomass Ratio in Fluidized Bed Gasification with Multiphase Particle-in-cell CFD Simulation

Janitha C. Bandara¹ Marianne S. Eikeland¹ Britt M. E. Moldestad¹

¹Faculty of Technology, Natural Sciences and Maritime Sciences, University College of Southeast Norway
{Janitha.bandara, Marianne.Eikeland, britt.moldestad}@usn.no

Abstract

Biomass has been identified as a key renewable energy source to cope with upcoming environmental challenges. Gasification of biomass is becoming interested in large scale operation, especially in synthesis of liquid fuels. Bubbling and circulating fluidized bed gasification technology has overrun the interest over fixed bed systems. CFD studies of such reactor systems have become realistic and reliable with the modern computer power. Gasifying agent, temperature and steam or air to biomass ratio are the key parameters, which are responsible for the synthesis gas composition. Therefore, multiphase particle-in-cell CFD modeling was used in this study to analyze the steam to biomass, S/B, ratio in fluidized bed gasification.

Due to the complexity of the full loop simulation of dual circulating fluidized bed reactor system, only the gasification reactor was considered in this study. Predicted boundary conditions were implemented for the particle flow from the combustion reactor. The fluidization model was validated against experimental data in beforehand where Wen-Yu-Ergun drag model was found to be the best. The effect of the S/B ratio was analyzed at a constant steam temperature of 1073K and a steam velocity of 0.47 m/s. Four different S/B of 0.45, 0.38, 0.28 and 0.20 were analyzed. The biomass was considered to be in complete dry condition where single step pyrolysis reaction kinetics was used. Each gasification simulation was carried out for 100 seconds. 8% reduction of hydrogen content from 57% to 49% and 17% increment of carbon monoxide from 13% to 30% were observed when the S/B was reduced from 0.45 to 0.20. Countable amounts of methane were observed at S/B of 0.28 and 0.20. The lower heating value of the product gas increased from 10.1 MJ/kg to 12.37 MJ/kg and the cold gas efficiency decreased from 73.2% to 64.6% when the S/B was changed from 0.45 to 0.20. The specific gas production rate varied between 1.64 and 1.04 Nm³/kg of biomass.

Keywords: Biomass gasification, fluidized beds, gasifying agent, multiphase particle-in-cell

1 Introduction

Biomass was one of the key energy sources until the invention of cheap refined petroleum fuels in the 1940s. Since then, biomass energy technologies were not impressively developed until the oil crisis in the 1970s. Since then, biomass-to-energy conversion technologies were subjected to enormous research and developments. Biomass is further outdoing among other renewable energy systems, as it demands to be the sole alternative to replace all use of fossil fuels (Demirbas 2008). Bioenergy is also a key component in setting up the EU energy target of 20-20-20¹ where 10% of the transport related energy is supposed to be achieved via renewables (Scarlat, Dallemand et al. 2011).

Approximately 125 billion liters of biofuels were produced in 2015 where 75% is bio-ethanol and 25% is bio-diesel (Century 2015). The main feedstocks for bio-ethanol have been sugarcane and corn. However, there has been a long term debate of utilizing food commodities for energy production (Naik, Goud et al. 2010). On the other hand, annual terrestrial biomass production by green plants is approximately 100 billion tons of dry organic matter where only a 1.25% is derived as food (Naik, Goud et al. 2010). In other words, 90% of the world accessible biomass stocks are lignocellulosic (Szczo drak and Fiedurek 1996). Therefore, liquid biofuels from lignocellulosic materials, referred as second-generation biofuels, will provide more aspects to the future transportation industry.

Combustion, pyrolysis and gasification are the three main thermo-chemical technologies for conversion of biomass to energy, which eliminate most of the drawbacks related to bio-chemical conversion. Gasification converts solid biomass into a gaseous mixture of carbon monoxide (CO), hydrogen (H₂), methane (CH₄), carbon dioxide (CO₂) and minor fractions of higher molecular hydrocarbons such as tars. The product gas, which is referred as synthesis gas, could be processed into biofuels either by biological fermentation or Fisher-Tropsch (Munasinghe and Khanal 2010). In contrast, the producer gas could be directly combusted in furnaces, boilers, turbines and IC engines or used in solid oxide fuel cells.

¹ 20% reduction of CO₂ emissions, 20% increase of energy efficiency and 20% renewable energy share by 2020

Carbon to Hydrogen (C:H) ratio is the most important parameter in downstream processing of synthesis gas into liquid fuels. It is therefore important to optimize both the syngas composition and flowrates. In this picture, steam is much more desired as the gasification agent compared to air. Steam is further useful in tar cracking via reforming reactions as well. Dual circulating fluidized bed (DCFB) gasification is the best technology, compared to fixed bed and single bubbling fluidized bed reactor, to achieve a high H₂ content in synthesis gas.

This particular DCFB system separates the gasification and combustion reactions into two reactors as illustrated in Figure 1. Drying, pyrolysis and gasification (gas reactions and part of the char reduction) reactions are carried out in the gasification reactor, which normally operates with steam in the bubbling fluidization regime. Temperature and steam-to-biomass ratio (S/B) are the most important parameters for the gas composition. The remaining char from the gasifier is oxidized in the combustion chamber, which provides the heat demand of the gasification via circulation of bed material. Computational fluid dynamic (CFD) simulations integrated with reactions are more convenient, cost effective and efficient in optimization compared to experimental investigations.

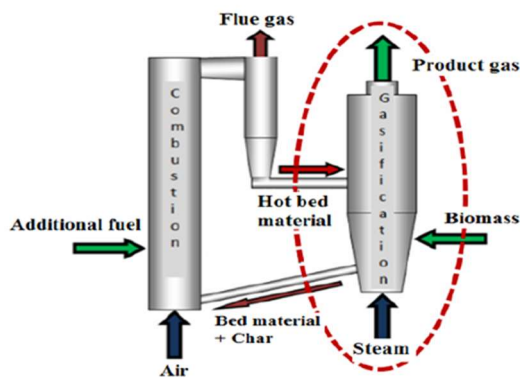


Figure 1. Dual circulating fluidized bed reactor

However, CFD modeling of particle systems are rather complex, and fluidized bed gasification is especially challenging due to the introduction of heterogeneous reactions together with heat and mass transfer. Eulerian-Eulerian (EE) and Eulerian-Lagrangian (EL) are the two basic approaches in modeling particle systems. The multiphase particle-in-cell (MP PIC) technique is an extended version of EL modeling which overcome certain limitations of conventional EL simulations such as modeling of dense particle systems with a large number of particles.

In the MP-PIC approach, the fluid phase is modeled in the Eulerian grid with Navier Stokes equations. Particles having similar characteristics such as size, density, etc. are parceled into units, which are referred as computational particles. Hence, billions of particles could be encapsulated into millions of computational

particles and modelled in the Lagrangian frame of reference (Andrews and O'Rourke 1996). Inter particle stresses are calculated in the Eulerian grid considering the particles as a continuum phase and those values are mapped back to the individual particles, using interpolation functions (Snider 2001). It has found that the required quantity of parcels to model the particle phase accurately is acceptable which realizes the simulation of large-scale particle systems.

The Barracuda VR commercial package is specially developed for multiphase CFD simulations, which uses the MP-PIC approach. This novel approach is referred to as computational particle fluid dynamics (CPFD). Solnordal, Kenche et al. 2015 and Liang, Zhang et al. 2014 have carried out MP PIC simulations for bubbling fluidized beds. Snider, Clark et al. 2011 has presented the integration of heat and reaction chemistry in MP PIC simulations whereas Loha, Chattopadhyay et al. 2014 and Xie et al Xie, Zhong et al. 2012 have carried out gasification simulations in a bubbling fluidized bed reactor. Liu, Cattolica et al. 2015, and Liu, Cattolica et al. 2016 have performed MP PIC simulations in a complete circulating dual fluidized bed system. The ability of defining multi-component particles is a distinctive feature of Barracuda, and facilitates the integration of volatilization reactions involved in gasification and combustion.

A complete loop CFD simulation of the circulating fluidized bed gasification is complex in terms of generating the computational grid and expensive regarding simulation time. On the other hand, the underlying objective of this work is to analyze the effect of S/B in the gasification reactor. Hence, the CFD simulation was narrowed down to the gasification reactor as highlighted in Figure 1.

2 Barracuda CFD setup

The fluidization model was validated with cold bed fluidization experiments and the data has been published by the same author (Bandara, Thapa et al. 2016).

A simple cylindrical geometry of 2000 mm in height and 550 mm in diameter was used. The uniform grid option was applied with 4840 cells in total. The computational grid, boundary conditions and filling of the initial particle species in the bed are illustrated in Figure 2 where other operational and physical parameters are tabulated in Table 1. Uniform steam distribution was used while the steam velocity was maintained slightly above the minimum fluidization velocity. The hot bed material inlet was set as it guides the particle trajectory into the center of the reactor. Particle should driven into the system with a fluid flow where the fluid volume can be manipulated with “slip velocity” option. The bed material outflow was adjusted by changing the pressure at that particular cell where it was connected to the bed material inflow with “particle feed control” option.

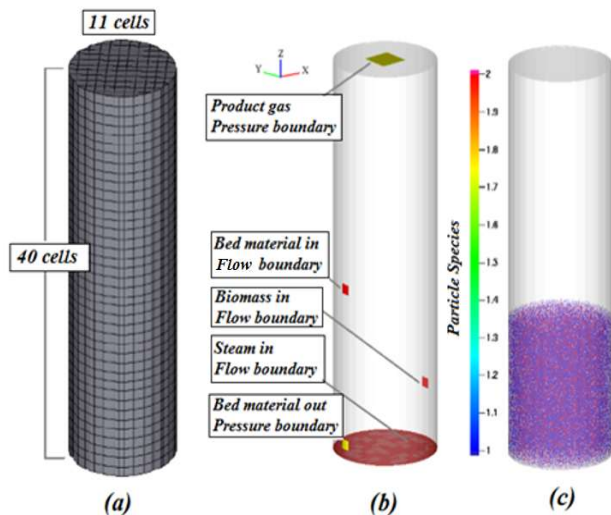


Figure 2. (a) Computational grid, (b) boundary conditions, (c) initial particle species

Table 1. Initial and boundary conditions

Flow boundary parameters			
Stream	Boundary	Parameters	Particle
Steam	Flow	1073 K, 101325 pa, 0.47 m/s	Nil
Gas out	Pressure	101325 pa	Nil
Biomass in	Flow	400 K, 101325 pa, 0.5 m/s,	0.05 kg/s
Bed Material in	Flow	1273 K, 101325 pa, 0.25 m/s	95% of bed material out
Bed Material out	pressure	101325 pa	Particle out flow
Initial conditions			
Fluid	1073 K, 101325 pa, steam, total volume		
Silica	1073 K, 101325 pa, 1000 μm , spherical, 0.48 volume fraction, density 2200 kg/m^3 , 600 mm height initial fill		
Char	1073 K, 101325 pa, 500 μm , spherical, 0.12 volume fraction, density 300 kg/m^3 , 600 mm height initial fill		

Steam pressure and the temperature of the incoming bed material were kept constant throughout all the simulations. It was intended to keep the fluidization behavior and residence time as similar as possible for all the simulations. Therefore, the steam flow boundary was maintained at 0.47 m/s. The S/B ratio was adjusted by changing the biomass flow. Four different S/B ratios of 0.45, 0.38, 0.28 and 0.2, were considered. As particle heating consumes high simulation time, initial particle temperature was set up same as that of the steam. It was further assumed that the initial bed composed with a fraction of char as well.

The Arrhenius reaction rates were used in the homogeneous and heterogeneous reactions. The constants in the reaction models were adapted from Thapa et al (R.K. Thapa, C. Pfeifer et al. 2014) and are tabulated in Table 2. The pyrolysis was modelled as a single step reaction, where the rate is given by,

$$264000 m_s \theta_f \exp \left[\frac{-1262}{T} \right] \quad (1)$$

Following the literature data, the composition of biomass was assumed to be 25% char and 75% volatiles

with no moisture and ash. Formation of tar and higher molecular hydrocarbons was neglected, and only H_2 , CO , CO_2 , CH_4 and H_2O were considered. Weight fractions of CH_4 , CO , CO_2 and H_2 in the pyrolysis gas were taken as 0.1213, 0.6856, 0.1764 and 0.0167 respectively (R.K. Thapa, C. Pfeifer et al. 2014). Simulations were carried out for 100s and the gas composition, gas temperature and particle mass flow rates were analyzed.

Table 2. Reaction kinetics

Steam Reforming $C + \text{H}_2\text{O} \leftrightarrow \text{H}_2 + \text{CO}$	Forward	$1.272 m_s T \exp \left[\frac{-22645}{T} \right] [\text{H}_2\text{O}]$
	Reverse	$1.044 \times 10^{-4} m_s T^2 \exp \left[\frac{-6319}{T} - 17.29 \right] [\text{H}_2][\text{CO}]$
CO_2 gasification $C + \text{CO}_2 \leftrightarrow 2\text{CO}$	Forward	$1.272 m_s T \exp \left[\frac{-22645}{T} \right] [\text{CO}_2]$
	Reverse	$1.044 \times 10^{-4} m_s T^2 \exp \left[\frac{-2363}{T} - 20.92 \right] [\text{CO}]^2$
Methanation $0.5C + \text{H}_2 \leftrightarrow 0.5\text{CH}_4$	Forward	$1.368 \times 10^{-3} m_s T \exp \left[\frac{-8078}{T} - 7.087 \right] [\text{H}_2]$
	Reverse	$0.151 m_s T^{0.5} \exp \left[\frac{-13578}{T} - 0.372 \right] [\text{CH}_4]^{0.5}$
Water-Gas shift $\text{H}_2\text{O} + \text{CO} \leftrightarrow \text{H}_2 + \text{CO}_2$	Forward	$7.68 \times 10^{10} m_s T \exp \left[\frac{-36640}{T} \right] [\text{CO}]^{0.5} [\text{H}_2\text{O}]$
	Reverse	$6.4 \times 10^9 m_s T \exp \left[\frac{-39260}{T} \right] [\text{H}_2]^{0.5} [\text{CO}_2]$
Methane reforming $\text{CH}_4 + \text{H}_2\text{O} \leftrightarrow \text{CO} + 3\text{H}_2$	Forward	$3.0 \times 10^5 T \exp \left[\frac{-15042}{T} \right] [\text{CH}_4][\text{H}_2\text{O}]$
	Reverse	$0.0265 T \exp \left[\frac{-32900}{T} \right] [\text{CO}][\text{H}_2]^3$

3 Results and discussion

A number of researchers have analyzed the effect of steam to biomass ratio and carried out CFD simulations related to biomass gasification. Wei, Xu et al. 2007 has carried out experiments in a free fall reactor and used S/B ratios from 0 to 1.00 in the same temperature ranges adopted in this work. Rapagnà, Jand et al. 2000 has looked into steam gasification in a bubbling fluidized bed reactor with olivine catalysts where S/B ratio between 0.4 to 1.00 had been analyzed. Campoy, Gómez-Barea et al. 2009 has used a mixture of oxygen and steam as the gasifying agent and carried out experiments in a fluidized bed reactor without external heating of the bed. The S/B ratio was between 0 and 0.58. The simulations in this work was initiated with S/B ratio of 0.45 and bed temperature of 1023 K.

3.1 Simulation with S/B ratio of 0.45

A reduction of bed mass from 178.3 kg to 177.1 kg and char fraction of the bed outflow from 3.25% to 0.6% were observed during the simulation time of 100s. However, bed particle outflow and bed particle inflow were connected with 95% mass efficiency (assuming 5% of char availability in the bed particle outflow). The incorrect match of mass flowrate of particle flows might

lead to reduction of the bed mass. On the other hand, there is a considerable reduction of char in the bed outflow. This might be due to insufficient biomass supply compared to char outflow.

Bed hydrodynamics, temperature distribution of particles in the bed and distribution of different particle species are illustrated respectively in (a), (b) and (c) of Figure 3. Referring to the same figure, the bubbling fluidization of the reactor is clearly depicted. However, the particle temperature shows uneven characteristics, especially along the cross section. Heated particles from the combustion reactor seem to be accumulated in the opposite half to the particle inlet of the reactor. Homogeneous distribution of three particle species is illustrated Figure 3 (c) where 1, 2 and 3 in the figure are referred to sand, char and biomass respectively.

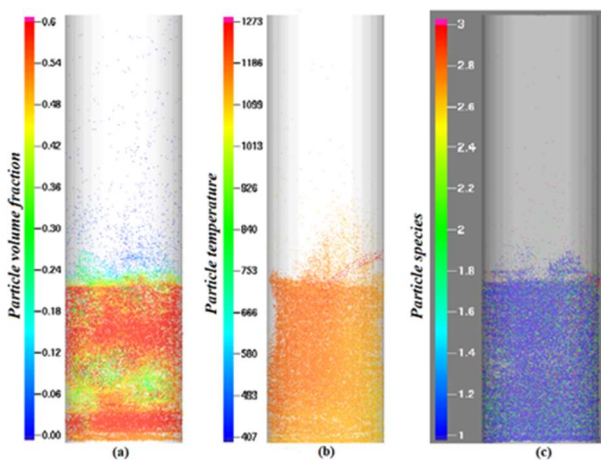


Figure 3. (a) Bubbling fluidization, (b) temperature of bed particles, (c) distribution of particle species

Product gas composition was observed in both axial and radial directions of the reactor, which are illustrated in Figure 4 and Figure 5. The final gas composition from the reactor was read from the center cell of the outflow pressure boundary, which actually acts as a sensor installed.

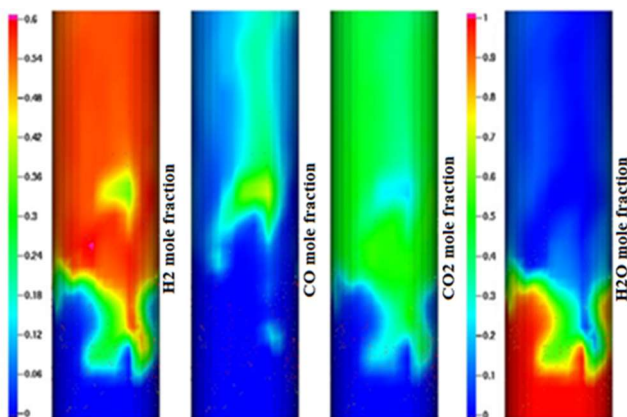


Figure 4. Product gas composition along the reactor height

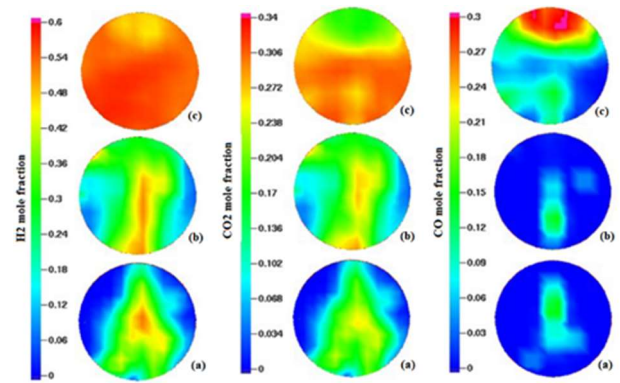


Figure 5. Gas composition at different cross sections along reactor height. (a), (b) and (c) refers to 0.3, 0.6 and 0.9m heights from the bottom of the reactor

No significant change in the gas composition is observed up to the biomass feeding point. This depicts the slow reaction kinetics of the char-steam heterogeneous reactions. The gas phase composition starts to change from the biomass feeding point, which is mainly due to pyrolysis reactions. Even though pyrolysis gas contains nearly 68% of CO, higher concentration cannot be observed even at the biomass feeding point. This is mainly due to high reaction rate of the water-gas shift reaction compared to the pyrolysis reaction, which consumes CO immediately to produce CO₂ and H₂. Therefore, H₂ and CO₂ increase along the reactor height with simultaneous decrease of CO and H₂O.

The gas production rate is also monitored, and the volumetric and mass gas production rates were approximately 0.33m³/s and 0.055kg/s respectively. The flow rates as function of time are plotted in Figure 6. Following the ideal gas law (high temperature and low pressure), the gas production rate was calculated as 1.64 Nm³/kg of biomass, which is well within the data published in literature. The area specific gas production rate, which is one of the useful parameters in reactor sizing, was observed as 0.34Nm³/s·m².

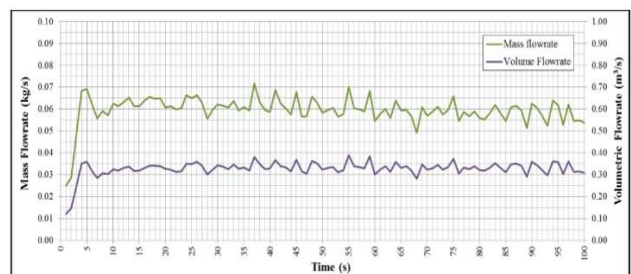


Figure 6. Time evolution product gas flowrates

The average molar gas composition during the final 25s was observed as 0.128-CO, 0.273-CO₂, 0.574-H₂ and 0.025-H₂O. The product gas heating value was calculated to be 10.1 MJ/kg where the lower heating values (LHV) of wood, CO and H₂ were taken as 16 MJ/kg (dry basis), 10 MJ/kg and 120 MJ/kg

respectively. The cold gas efficiency (CGE) was calculated as 73.3% using the equation:

$$CGE = \frac{mass_{gas}(kg)}{mass_{fuel}(kg)} \frac{LHV_{gas}(J/kg)}{LHV_{fuel}(J/kg)} \quad (2)$$

There is an uncertainty related to the calculation of cold gas efficiency because the actual operating conditions of the combustion reactor is not known. A guessed value of 200°C was taken for the temperature increment in the combustion reactor. However, there can be additional fuel supply into the combustion reactor to achieve the desired temperature rise, which indirectly affects for the cold gas efficiency.

3.2 Effect of Steam-to-Biomass ratio

The biomass flowrate was increased from 0.05kg/s to 0.06kg/s, 0.08kg/s and 0.11kg/s to adjust the S/B ratio from 0.45 to 0.38, 0.28 and 0.2 respectively. Temperatures and steam inlet flow velocity were kept unchanged. Similar characteristics of bed hydrodynamics, temperature and particle species distribution were observed as in the case with of S/B of 0.45. Figure 7 illustrates the final gas composition for the respective cases.

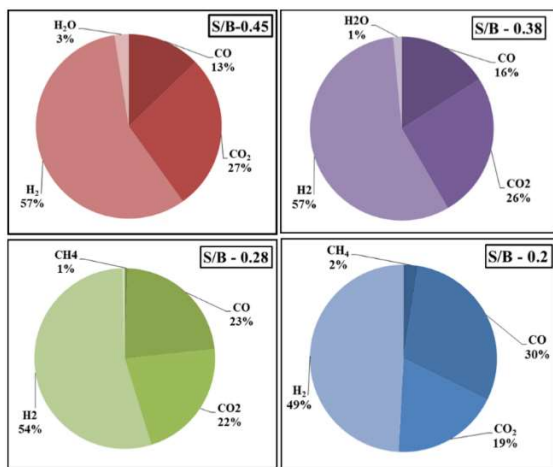


Figure 7. Molar composition of product gas

The molar concentration of H₂ is dramatically reduced from 57% at S/B of 0.45 to 49% at S/B of 0.2 showing a reduction of 8%. In contrast, the concentration of CO has increased by 17% within the respective range. According to the data presented in Figure 3-5, steam is almost totally consumed even for S/B of 0.45. However, the pyrolysis gas volumes in the successive cases of low S/B ratios is increased due to increasing biomass flowrates. As a result, low S/B operation experiences a deficiency of steam to perform the water-gas-shift reaction. Therefore, Product gas is consisted with a substantial share of raw pyrolysis gas. The unreacted fraction of the pyrolysis gas is the root cause for increasing CO concentrations in the product

gas at low S/B. This phenomenon is illustrated Figure 8. Steam reforming reaction adds mass to the pyrolysis gas, which is clear from the figure as product gas mass flowrate always runs above the pyrolysis gas curve. However, the gap between two curves gets narrowed at lower S/B. Further, two curves stand almost parallel to each other at lower S/B than approximately 0.3. The total consumption of steam at S/B of 0.3 is the reason for this behavior.

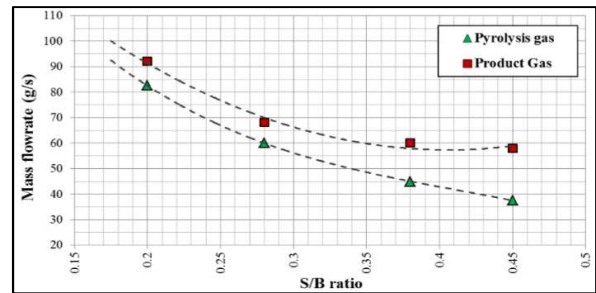


Figure 8. Pyrolysis and product gas mass flowrates

Further, noticeable amount of CH₄ is available in the product gas in both the case of 0.28 and 0.2 S/B. It is evident from the reaction kinetic data in Table 2 that the reaction rate of the water-gas-shift reaction is much higher than the methane reforming. Therefore, steam is initially consumed by CO and when it comes to the respective cases, no steam is left for methane reforming reactions.

As illustrated in Figure 9, the product gas temperature has dropped down by 50K at reduced S/B of 0.28 and 0.2. This happens as more energy is extracted for the pyrolysis reactions with increased biomass feed rate at lower S/B ratios.

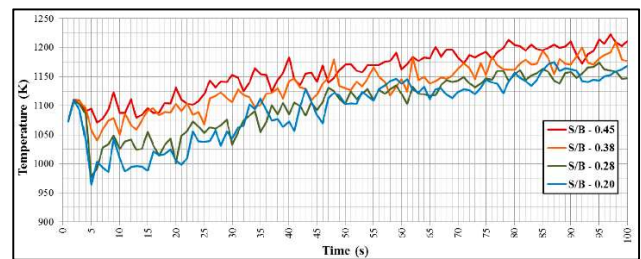


Figure 9. Time evolution product gas temperature at different S/B

The summary of other parameters at different S/B is given in Table 3. The volumetric gas production rate at S/B 0.2 has increased by 33% compared to S/B 0.45. Therefore, the gas production capacity can be increased in the same reactor, simply by changing the S/B ratio. The increase of the molar percentage of the total combustible gases (H₂+CO) in the product gas from 70% to 79% is the reason behind the increased calorific value by 22% from 10.1 MJ/kg to 12.37 MJ/kg in the respective cases. The reduction of the volumetric gas production per kg of biomass is because of the inadequate steam availability to react with the additional released pyrolysis gas at lower S/B.

Table 3. Simulation results for different S/B

	S/B-0.45	S/B-0.38	S/B-0.28	S/B-0.2
Steam flow (kg/s)	22.8	22.8	22.8	22.8
Biomass flow (g/s)	50	60	80	110
Product gas				
Mass flowrate (g/s)	58	60	68	92
Volume flowrate (m ³ /s)	0.331	0.34	0.36	0.44
Mole flowrate (mol/s)	3.36	3.5	3.9	5.1
LHV (MJ/kg)	10.1	10.54	11.5	12.37
Cold gas efficiency	73.2	65.8	61.1	64.6

4 Conclusion

Barracuda VR commercial package with the MP-PIC CFD principle, was used in this work. The product gas quality was observed at different steam-to-biomass ratios. The product gas composition, gas flowrates, heating value and cold gas efficiency showed a significant sensitivity regarding the S/B ratio and following conclusions could be made. As the steam-to-biomass ratio is reduced,

- H₂ content is decreased while CO is increased
- LHV is increased while cold gas efficiency is decreased
- Gas production rate per kg of biomass is reduced

Simulating complete dual fluidized bed reactor system together with a detailed characterization of biomass such as composition and pyrolysis kinetics, will overcome the uncertainties related to this work for a certain extent. Barracuda VR is a sophisticated tool for optimization of the effect of different parameters on the biomass gasification.

Acknowledgements

The authors would like to forward their gratitude to University College of Southeast Norway for providing of the Barracuda VR software package and computer facilities.

References

Andrews, M. J. and P. J. O'Rourke (1996). "The multiphase particle-in-cell (MP-PIC) method for dense particulate flows." *International Journal of Multiphase Flow* **22**(2): 379-402.

Bandara, J. C., R. K. Thapa, B. M. E. Moldestad and M. S. Eikeland (2016). "Simulation of Particle Segregation in Fluidized Beds." *9th EUROSIM Congress on Modelling and Simulation*, Oulu, Finland, IEEE.

Campoy, M., A. Gómez-Barea, F. B. Vidal and P. Ollero (2009). "Air-steam gasification of biomass in a fluidised bed: Process optimisation by enriched air." *Fuel Processing Technology* **90**(5): 677-685.

Century, R. E. P. N. f. t. s. (2015). "RENEWABLES 2015 - Global Status Report", Paris: REN21 Secretariat.

Demirbas, A. (2008). "Biofuels sources, biofuel policy, biofuel economy and global biofuel projections." *Energy Conversion and Management* **49**(8): 2106-2116.

Liang, Y., Y. Zhang, T. Li and C. Lu (2014). "A critical validation study on CPFD model in simulating gas-solid bubbling fluidized beds." *Powder Technology* **263**: 121-134.

Liu, H., R. J. Cattolica and R. Seiser (2016). "CFD studies on biomass gasification in a pilot-scale dual fluidized-bed system." *International Journal of Hydrogen Energy* **41**(28): 11974-11989.

Liu, H., R. J. Cattolica, R. Seiser and C.-h. Liao (2015). "Three-dimensional full-loop simulation of a dual fluidized-bed biomass gasifier." *Applied Energy* **160**: 489-501.

Loha, C., H. Chattopadhyay and P. K. Chatterjee (2014). "Three dimensional kinetic modeling of fluidized bed biomass gasification." *Chemical Engineering Science* **109**: 53-64.

Munasinghe, P. C. and S. K. Khanal (2010). "Biomass-derived syngas fermentation into biofuels: Opportunities and challenges." *Bioresource Technology* **101**(13): 5013-5022.

Naik, S. N., V. V. Goud, P. K. Rout and A. K. Dalai (2010). "Production of first and second generation biofuels: A comprehensive review." *Renewable and Sustainable Energy Reviews* **14**(2): 578-597.

R.K. Thapa, C. Pfeifer and B. M. Halvorsen (2014). "Modeling of reaction kinetics in bubbling fluidized bed biomass gasification reactor" *INTERNATIONAL JOURNAL OF ENERGY AND ENVIRONMENT* **5**(1): 10.

Rapagnà, S., N. Jand, A. Kiennemann and P. U. Foscolo (2000). "Steam-gasification of biomass in a fluidised-bed of olivine particles." *Biomass and Bioenergy* **19**(3): 187-197.

Scarlat, N., J.-F. Dallemand, O. J. Skjelhaugen, D. Asplund and L. Nesheim (2011). "An overview of the biomass resource potential of Norway for bioenergy use." *Renewable and Sustainable Energy Reviews* **15**(7): 3388-3398.

Snider, D. M. (2001). "An Incompressible Three-Dimensional Multiphase Particle-in-Cell Model for Dense Particle Flows." *Journal of Computational Physics* **170**(2): 523-549.

Snider, D. M., S. M. Clark and P. J. O'Rourke (2011). "Eulerian-Lagrangian method for three-dimensional thermal reacting flow with application to coal gasifiers." *Chemical Engineering Science* **66**(6): 1285-1295.

Solnordal, C. B., V. Kenche, T. D. Hadley, Y. Feng, P. J. Witt and K. S. Lim (2015). "Simulation of an internally circulating fluidized bed using a multiphase particle-in-cell method." *Powder Technology* **274**: 123-134.

Szczodrak, J. and J. Fiedurek (1996). "Technology for conversion of lignocellulosic biomass to ethanol." *Biomass and Bioenergy* **10**(5): 367-375.

Wei, L., S. Xu, L. Zhang, C. Liu, H. Zhu and S. Liu (2007). "Steam gasification of biomass for hydrogen-rich gas in a free-fall reactor." *International Journal of Hydrogen Energy* **32**(1): 24-31.

Xie, J., W. Zhong, B. Jin, Y. Shao and H. Liu (2012). "Simulation on gasification of forestry residues in fluidized beds by Eulerian-Lagrangian approach." *Bioresource Technology* **121**: 36-46.

Paper G

Janitha C. Bandara, Britt M.E. Moldestad, Marianne S. Eikeland

Analysing the effect of temperature for steam fluidized-bed gasification of biomass with MP-PIC simulation

Journal: International Journal of Energy and Environment, 2018, Volume 9, Issue 6, PP 529-542



Analysing the effect of temperature for steam fluidized-bed gasification of biomass with MP-PIC simulation

Janitha C. Bandara, Britt M. E. Moldestad, Marianne S. Eikeland

Faculty of Technology, Department of Natural Sciences and Maritime Sciences, University College of South-Eastern Norway, Kjølnes Ring 56, 3901, Porsgrunn, Norway.

Received 3 Sep. 2018; Received in revised form 28 Sep. 2018; Accepted 6 Oct. 2018; Available online 1 Nov. 2018

Abstract

Gasification in fluidized beds is an outstanding technology in biomass to energy conversion. The multiphase particle-in-cell modelling has reduced the computational time related to CFD simulations of dense gas-solid systems like fluidized bed gasification. Barracuda VR commercial CFD package was used to analyse the effect of reactor temperature in steam gasification of biomass.

The product gas composition, lower heating value and the cold gas efficiency were compared for steam at 873K, 973K and 1073K. The steam-to-biomass ratio was maintained at a constant value of 0.45. The hydrogen content of the product gas changed from 36% to 57% as the temperature was increased from 873K to 1073K whereas the carbon monoxide content changed from 33% to 13%. The lower heating value and the cold gas efficiency changed from 10.4 MJ/kg to 10.1 MJ/kg and 76.6% to 73.2% respectively within the same temperature range. The formation of tar was not modelled and the gas composition showed high sensitivity towards the reactor temperature.

Copyright © 2018 International Energy and Environment Foundation - All rights reserved.

Keywords: Biomass; Gasification; Fluidized beds; Temperature; CPFD.

1. Introduction

Energy has been a key drive in human development where excessive consumption of fossil fuels have had negative impacts on the environment. Increased emissions of anthropogenic carbon dioxide from fossil fuel combustion has been identified as the root cause for the global warming and many of the subsequent phenomena. Renewable energy is important in replacing fossil fuels where biomass is the dominating source having 10% to 14% share of the global energy profile [1]. Lignocellulose is the leading bioenergy source, which is about 90% of the accessible biomass feedstock on earth [2]. Biochemical conversion of lignocellulosic materials into secondary fuels and chemicals is less interesting compared to thermochemical conversion, due to low carbon conversion and slow conversion rates. Combustion and co-combustion produce direct heat that can be used in heating applications or power generation. Pyrolysis and gasification products are used in either direct combustion or secondary fuel and chemical synthesis. Fluidized bed combustion and gasification are interested over fixed bed designing due to many inherent advantages. Enhanced gas-solid contact and intense mixing establish efficient heat and mass transfer that guarantees the homogeneous reactor temperature. This increases the possibility and reliability of scaled up operation. Proper control over solid particles, large thermal inertia of solids, increased efficiency, reduced

emissions and wide range of operating conditions are additional advantages of fluidized bed systems [3, 4]. Further, high mixing avoids the hot spot and cold spot generation in highly exothermic reactors. This feature is extremely important in biomass gasification as high temperatures leads to ash melting/agglomeration where reduced tar cracking and char conversion are resulted from low temperatures [5, 6].

1.1 Fluidized bed gasification of biomass

Gasification is an interesting process due to the versatility of the produced gas. Carbon monoxide (CO), hydrogen (H₂), carbon dioxide (CO₂), methane (CH₄), high molecular hydrocarbons (ethane etc.), condensable hydrocarbons (tar) and nitrogen (N₂) are the main components in the product gas where the unconverted char and ash are left in the solid residue [7]. Air is the most common gasifying agent and the lower heating value (LHV) of the product gas is low (4-7 MJ/Nm³) with relatively low H₂ content of 8-14%. As the gas is diluted with N₂, it can only be used in heating applications or power generation industry. In contrast, the product gas from oxygen (O₂) or steam (H₂O) gasification has high LHV up to 18 MJ/Nm³ with H₂ yield up to 60% [8, 9]. The product gas is then referred as “*synthesis gas*” which is possible to use in both power generation and as a feedstock for synthesis of secondary fuels or chemicals (bio-ethanol, synthesis diesel, methanol, bio-methane and H₂ etc.). The LHV is the crucial parameter for heat and power industries, while it is the carbon-to-hydrogen ratio for the synthesis of fuels and chemicals. Apart from many operational difficulties, tar in the product gas has been the major challenge of biomass gasification, which leads to clogging of pipes and catalyst poisoning. In many situations, the heating value and the tar content of the gas decides the product gas quality [7]. A simple pictorial representation of successive steps of biomass gasification is given in Figure 1. Drying and pyrolysis are the first steps where combustion and gasification reactions are responsible for the char and tar conversion into light gases. The total process is more complex with hundreds of reactions and most influencing reactions are listed in Table 2.

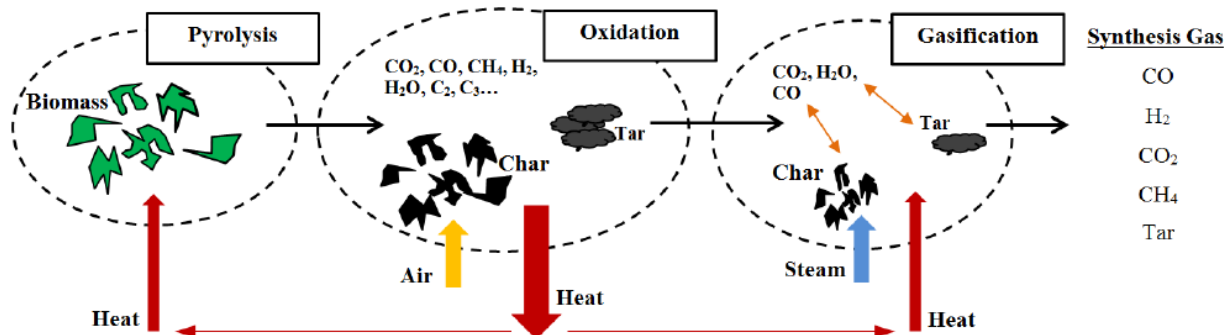


Figure 1. Biomass gasification process.

The complete gasification reaction is endothermic. Hence, it is necessary to supply that energy demand by combusting a fraction of the biomass internally or by external heating, which are distinguished as auto-thermal and allo-thermal gasification respectively. O₂ driven gasification is expensive and therefore, it is necessary to optimize the system between air and steam. As described above, N₂ dilution is the major drawback of the air gasification. Dual circulating fluidized bed (DCFB) gasification, as illustrated in Figure 2, is a better design in overcoming this challenge. A supporting bedding material such as sand particles is used, as the wood chips/pellets are hard to fluidize [10]. DCFB system separates the combustion reactions from the gasification and pyrolysis reactions. Biomass (chips or pellets) is fed into the gasification reactor, which is operated with steam. The biomass go through pyrolysis and gasification reactions to produce synthesis gas. The unreacted char flows down to the combustion reactor along with bed material. The combustion reactor is operated with air in which the bed material absorbs the heat generated from char combustion. The heated bed material is recycled back into the gasification reactor across a cyclone followed by a proper gas seal such as a loopseal. Hence, this combination of exothermal (combustion) and endothermal (gasification) reactors make the whole system an auto-thermal process [11]. Gasification reactor is typically operated in the bubbling fluidization regime, while the combustion reactor is in fast fluidization regime as a riser combustor [12]. This configuration eliminates the N₂ dilution of the product gas with additional advantages as discussed above [13]. Fluidized catalytic cracking (FCC) makes the early

remarks of this configuration where Corella et al [11] have discussed different configurations of dual fluidized bed systems.

Lv et al [9] has carried out experimental studies of steam gasification in a fluidized bed reactor and observed increased carbon conversion, gas yield and H₂ content at elevated temperatures. In contrast, the LHV was observed to become lower at higher temperature. Xiao et al [14] has also done experimental studies in a DCFB gasification system and observed similar results of higher H₂ content with increased temperature. Pfeifer, Koppatz and Hofbauer [15, 16] have carried out detailed experiments of biomass gasification in a DCFB system where the product gas composition was analysed as a function of temperature, bed material and fuel moisture.

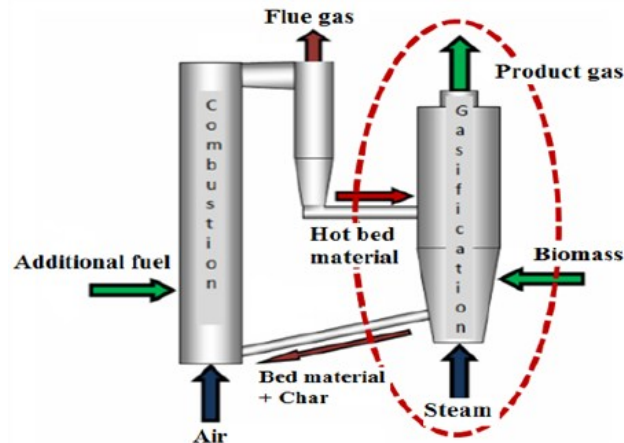


Figure 2. Schematic diagram of dual circulating fluidized bed gasification.

1.2 CFD simulation of fluidized bed gasification

Experimental optimization of fluidized bed gasification is rather challenging and difficult (i.e. optimization of geometry, biomass-feeding location etc.). Computational fluid dynamic (CFD) simulations of three-dimensional geometries in real scale have become realistic with the improved computer power and efficient numerical algorithms. Hence, CFD simulation is a useful tool to analyse the effects of operational conditions such as temperature, pressure, steam-to-biomass ratio (S/B), equivalence ratio (ER) etc. in fluidized bed gasification [17]. The behaviour of different biomass feedstock, particle sizes, flow patterns, geometry etc. can also be analysed with respect to the product gas quality including gas composition and lower heating value (LHV).

CFD is a highly proven technique for single-phase systems where the predictions agree well against the most accurate measurement apparatus [18]. However, CFD modelling and simulation of multiphase systems is challenging due to the additional weights imposed from the dispersed phase (solid particles, liquid droplets etc.) properties. Modelling of momentum exchange between phases, inter particle forces such as electrostatic, van der Waals forces, inter-particle collision and variation in size, shape and density in solid phase are some of the challenges [18]. Additional terms for particle heating, pyrolysis, gas combustion and heterogeneous reactions are involved in fluidized bed gasification. Above all, the dimensional scale differences between the reactor and the particles make the CFD modelling even more challenging [19].

Multiphase CFD models can be broadly distinguished as Eulerian-Eulerian or Eulerian-Lagrangian. In Eulerian-Eulerian modelling, both phases are modelled with Navier Stokes equations considering interpenetrating continua. This approach is referred as two-fluid model, which has been dominating in modelling of dense phase systems over many years due to its less demand of computer power. The discrete nature of particles is not captured in Eulerian modelling while the particle phase properties are approximated with kinetic theory of granular flow (KTGF). Modelling of particle mixtures is difficult, as it is necessary to define a separate phase for each size, shape or density in the mixture. In contrast, Lagrangian modelling of particle phase preserves the discrete nature where each particle is modelled by equations of Newton's law of motion [19]. However, this approach is computationally expensive and limited to 2×10^5 number of particles [20]. The multiphase particle-in-cell (MP PIC) technique is an extended version of the Lagrangian modeling which overcome certain limitations of conventional implementation.

In MP-PIC modeling, the fluid phase is modeled in the Eulerian grid with Navier Stokes equations. Particles having similar characteristics, such as size, shape and density are grouped, which are referred as either parcels or computational particles. Hence, billions of particles could be encapsulated into millions of computational particles and modelled in the Lagrangian approach [21]. Inter particle stresses are calculated in the Eulerian grid considering the particles as a continuum and these values are mapped back to the individual particles, using interpolation functions [22]. It has been found that the required quantity of parcels to model the particle phase accurately is acceptable and makes it possible to simulate large-scale particle systems.

The Barracuda VR commercial package is specially developed for multiphase CFD simulations, which uses the MP-PIC approach. This novel approach is named as computational particle fluid dynamics (CPFD). Solnordal et al [23] and Liang & Zhang [24] have carried out MP-PIC simulations for bubbling fluidized beds. Snider et al [25] have presented the integration of heat and reaction chemistry in MP-PIC simulations whereas Loha et al [26] and Xie et al [27] have published simulations of bubbling fluidized bed gasification. Liu, Cattolica & Seiser [28, 29] have performed MP-PIC simulations for a complete DCFB gasifier system. The ability of defining multi-component particles is a distinctive feature of Barracuda, which facilitates the integration of devolatilization reactions involved in gasification and combustion.

CPFD simulation of a complete DCFB gasification system is complex in generating the computational grid and expensive in simulation time. The main objective of this work was to analyse the effect of the temperature in steam gasification. Therefore, only the gasification reactor of a DCFB system (as highlighted in Figure 2) was simulated with Barracuda VR 17.0.3 version where the particle temperature from the combustion reactor was assumed.

2. MP PIC model equations

The subscripts “g”, “p” and “i” represent the gas phase, particle phase and species respectively. The gas phase mass and momentum conservation is given by continuity and time averaged Navier-Stokes equations those are respectively represented in equation 1 and 2.

$$\frac{\partial(\alpha_g \rho_g)}{\partial t} + \nabla \cdot (\alpha_g \rho_g u_g) = \delta \dot{m}_p \quad (1)$$

$$\frac{\partial(\alpha_g \rho_g u_g)}{\partial t} + \nabla \cdot (\alpha_g \rho_g u_g u_g) = -\nabla P + F + \nabla \cdot (\alpha_g \tau_g) + \alpha_g \rho_g g \quad (2)$$

α , ρ and u represent volume fraction, density and velocity respectively. $\delta \dot{m}_p$ in equation 1 is the mass production from gas-solid reactions. P stands for pressure and F represents the interface momentum transfer. The gas phase stress tensor τ_g is given by equation 3,

$$\tau_g = \mu_g \left[(\nabla u_g + \Delta u_g^T) - \frac{2}{3} \nabla \cdot u_g I \right] \quad (3)$$

μ_g refers to the shear viscosity that is the sum of the laminar and turbulent components. The large eddy simulation is used for the large-scale turbulence modeling while the subgrid scale turbulence is captured with Smagorinsky model as given in equation 4,

$$\mu_{g,t} = C_s \rho_g \Delta^2 |\nabla u_g + \Delta u_g^T| \quad (4)$$

Where Δ is the subgrid length scale and calculated by equation 5. The default value for the model constant C_s is 0.01.

$$\Delta = (\delta x \delta y \delta z)^{1/3} \quad (5)$$

The energy conservation of gas phase is given by,

$$\frac{\partial(\alpha_g \rho_g h_g)}{\partial t} + \nabla \cdot (\alpha_g \rho_g h_g u_g) = \alpha_g \left(\frac{\partial P}{\partial t} + u_g \cdot \nabla P \right) + \phi - \nabla \cdot (\alpha_g q) + \dot{Q} + S_h + \dot{q}_D \quad (6)$$

The enthalpy is represented by h . The viscous dissipation Φ and the energy source per volume \dot{Q} were ignored in this work. S_h is the conservative energy exchange from particle phase to gas phase. \dot{q}_D is the enthalpy diffusion term and q is the gas heat flux.

$$q = \lambda_g \nabla T_g \quad (7)$$

$$\dot{q}_D = \sum_{i=1}^N \nabla \cdot (h_i \alpha_g \rho_g D \nabla Y_{g,i}) \quad (8)$$

Where, λ is the thermal conductivity calculated by molecular conductivity (λ_m) and eddy conductivity λ_t from Reynolds stress mixing theory. The Prandtl (Pr) number, which is calculated from $c_p \mu_t / \lambda_t$ was set as 0.9. D denotes the turbulent mass diffusivity, which is correlated to the viscosity by Schmidt number (Sc) and given by $Sc = \mu / \rho_g D$. The value of the Sc was taken as 0.9. Y represents the species mass fraction. The gas and species enthalpies are calculated from,

$$h_g = \sum_{i=1}^N Y_{g,i} h_i \quad (9)$$

$$h_i = \int_{T_0}^{T_g} C_{p,i} dT + \Delta h_{f,i} \quad (10)$$

$\Delta h_{f,i}$ is the formation enthalpy of species “i” at reference temperature of T_0 . C_p is the specific heat capacity. The pressure is calculated from the equation of state for the ideal gas,

$$P = \rho_g R T_g \sum_{i=1}^N \frac{Y_{g,i}}{MW_i} \quad (11)$$

R is the universal gas constant and the MW refers to the molecular weight of the species. As the gas phase is composed with mixture of gases, transport equation is solved for each species. The transport equation for the each species in the gas phase is given by,

$$\frac{\partial(\alpha_g \rho_g Y_{g,i})}{\partial t} + \nabla \cdot (\alpha_g \rho_g Y_{g,i} u_g) = \nabla \cdot (\rho_g D \alpha_g \nabla Y_{g,i}) + \delta m_{i,chem} \quad (12)$$

D denotes the turbulent mass diffusivity where $\delta m_{i,chem}$ represents the net production of species due to gas phase chemical reactions.

The interface momentum transfer is calculated by the viscous drag force as given in equation 06,

$$F = \iint f \left\{ m_p \left[D_p (u_g - u_p) - \frac{\nabla P}{\rho_p} \right] \right\} dm_p du_p \quad (13)$$

The particle dynamics are formulated with particle distribution function (PSD), which is calculated from Liouville equation.

$$\frac{\partial f_p}{\partial t} + \nabla \cdot (f_p u_p) + \nabla u_p \cdot (f_p A_p) = \frac{f_D - f_p}{\tau_D} \quad (14)$$

f_p is a function of spatial location, velocity, mass and temperature of particles and the time. Therefore $\iiint (f_p) du_p dm_p dT_p$ is the average number of particles per unit volume with velocities, mass and temperatures in the intervals of $(u_p, u_p + du_p)$, $(m_p, m_p + dm_p)$ and $(T_p, T_p + dT_p)$. f_D is the particle distribution function for the local mass averaged particle velocity and τ_D is the particle collision damping time.

Where the particle trajectory and acceleration are given by,

$$u_p = \frac{\partial(x_p)}{\partial t} \quad \text{and} \quad A_p = \frac{\partial(u_p)}{\partial t} = D_p (u_g - u_p) - \frac{\nabla P}{\rho_p} - \frac{\nabla \tau_p}{\rho_p \alpha_p} + g + F_p \quad (15)$$

The particle volume fraction of the above equation is given by,

$$\alpha_p = \iint f \frac{m_p}{\rho_p} dm_p du_p \quad (16)$$

Particle interactions are modeled with the particle stress function developed by Harris and Crighton,

$$\tau_p = \frac{10P_s\alpha_p^\beta}{\max[(\alpha_{cp}-\alpha_p),\varepsilon(1-\alpha_p)]} \quad (17)$$

3. Barracuda CFD setup

A previously validated CDFD hydrodynamic model developed by the authors was used in this work [30]. The Wen-Yu-Ergun drag correlation was used with 40% momentum retention for particle collision. It was necessary to activate the blended acceleration model as the particle mixture was composed with different densities and sizes. The restitution coefficients for the particle-wall collision were 0.3 and 0.99 for normal and tangential directions respectively. Default values of 1, 3 and 10^{-8} were used for P_s , β and ε respectively in particle stress function (equation 17).

The reactor was a 2000 mm high cylindrical column with a diameter of 550 mm in. The computational grid, boundary conditions and the initial particle filling are illustrated in Figure 3.

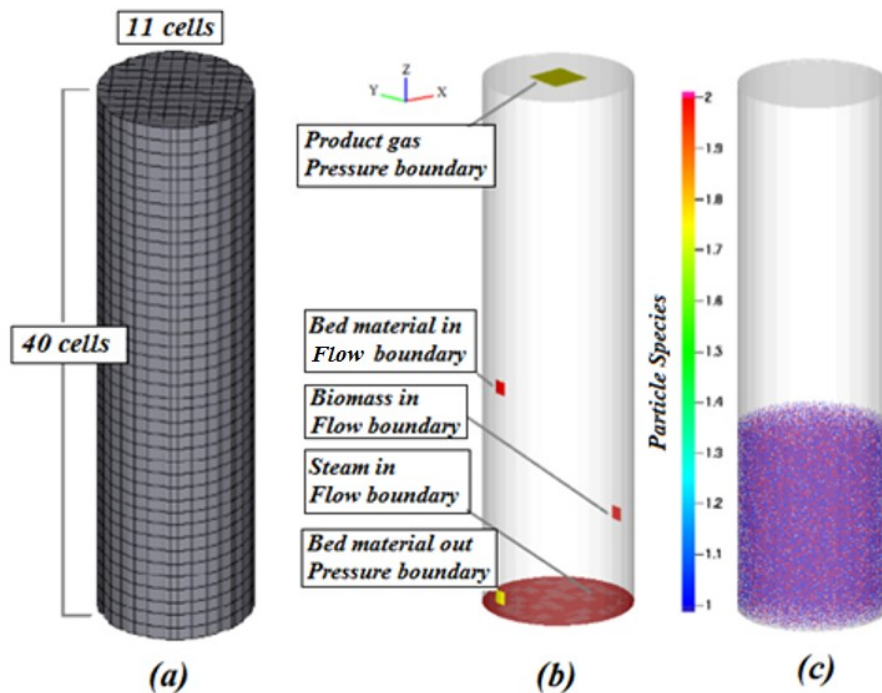


Figure 3. (a) Computational grid, (b) Boundary conditions, (c) Initial particle filling of sand, char and biomass.

Table 1 contains the rest of the operational and physical parameters used in the simulation. Uniform grid option was used and there were 4840 computational cells in the geometry. Uniform steam distribution was assumed without a distributor plate at the bottom flow boundary. Hot bed material from the combustion reactor was assumed free of char and 200K higher than the steam temperature. In Barracuda, particle inflows should be assisted by a fluid stream and the fluid inflow volume can be adjusted by manipulating the “slip velocity” option. The bed material outflow from the reactor bottom was implemented as a pressure boundary where the flowrate was adjusted by changing the pressure of that particular cell. The bed material outflow and hot bed material inflow was connected via “particle feed control” option. A pressure boundary at the reactor top was defined for the produced gas to escape and “no particle exit” option was applied to inhibit the particle outflow. Thermal wall option was not used and therefore, the system was consisted with adiabatic walls.

Steam at 1073 K, 973 and 873 K were used to analyze the system behavior. The initial reactor temperature was set to the respective steam temperature as it takes a substantial time for particle heating from the room

temperature. It was intended to keep the steam-to-biomass ratio at a constant value of 0.45 for all the simulations. Similarly, the steam velocity was also intended to keep at a constant value as it affects the gas residence time and the bed hydrodynamics. However, even with the constant steam velocity of 0.47 m/s, the steam mass flowrates in to the reactor changed due to the varying density resulted from the temperature change. Therefore, it was necessary to change the biomass flowrates accordingly to keep the constant S/B ratio of 0.45. Detailed information about boundary conditions and initial conditions for 1073 K steam temperature are given in Table 01. The biomass flowrates were changed to 0.055 kg/s and 0.06 kg/s at 973 K and 873 K respectively. The Arrhenius reaction rate models were used in the homogeneous and heterogeneous reactions. The constants of the reaction models were adapted from Thapa et al [31] and are tabulated in Table 2.

Table 1. Initial and boundary conditions.

Boundary Conditions			
Stream	Boundary	Parameters	Particle
Steam	Flow	1073K, 101325Pa, 0.47m/s	Nil
Product gas	Pressure	101325pa	Nil
Biomass in	Flow	400K, 101325Pa, 0.5m/s	0.05 kg/s
Bed material in	Flow	1273K, 101325Pa, 0.25m/s	95% bed material out
Bed material out	Pressure	100000pa	Particle outflow
Initial Conditions			
Fluid	1073 K, 101325 Pa, steam, total volume		
Silica	1073 K, 101325 Pa, 1000 μm , spherical, 0.48 volume fraction, density 2200 kg/m^3 , 600 mm height initial fill		
Char	1073 K, 101325 Pa, 500 μm , spherical, 0.12 volume fraction, density 300 kg/m^3 , 600 mm height initial fill		

Table 2. Reaction Kinetics.

Reaction		Reaction Rate Kinetics	Enthalpy
$C + H_2O \leftrightarrow H_2 + CO$ (steam Gasification)	Forward	$1.272m_s T \exp\left[\frac{-22645}{T}\right] [H_2O]$	+131 kJ/mole
	Reverse	$1.044 * 10^{-4} m_s T^2 \exp\left[\frac{-6319}{T} - 17.29\right] [H_2][CO]$	
$C + CO_2 \leftrightarrow 2CO$ (Boudouard reaction)	Forward	$1.272m_s T \exp\left[\frac{-22645}{T}\right] [CO_2]$	+172 kJ/mole
	Reverse	$1.044 * 10^{-4} m_s T^2 \exp\left[\frac{-2363}{T} - 20.92\right] [CO]^2$	
$0.5C + H_2 \leftrightarrow 0.5CH_4$ (Methanation)	Forward	$1.368 * 10^{-3} m_s T \exp\left[\frac{-8078}{T} - 7.087\right] [H_2]$	-75 kJ/mole
	Reverse	$0.151 m_s T^{0.5} \exp\left[\frac{-13578}{T} - 0.372\right] [CH_4]^{0.5}$	
$H_2O + CO \leftrightarrow H_2 + CO_2$ (Water-gas-shift)	Forward	$7.68 * 10^{10} m_s T \exp\left[\frac{-36640}{T}\right] [CO]^{0.5} [H_2O]$	-41 kJ/mole
	Reverse	$6.4 * 10^9 m_s T \exp\left[\frac{-39260}{T}\right] [H_2]^{0.5} [CO_2]$	
$CH_4 + H_2O \leftrightarrow 3H_2 + CO$ (Methane reforming)	Forward	$3.0 * 10^5 T \exp\left[\frac{-15042}{T}\right] [CH_4][H_2O]$	+206 kJ/mole
	Reverse	$0.0265 T \exp\left[\frac{-32900}{T}\right] [CO][H_2]^2$	
Pyrolysis	Forward	$264000 m_s \theta_f \exp\left[\frac{-12629}{T}\right]$	

Following the literature data, the char and volatile fractions of biomass were assumed as 25% and 75% respectively with no moisture and ash. Formation of tar and higher molecular hydrocarbons were neglected where only H_2 , CO , CO_2 , CH_4 and H_2O were assumed to evolve from pyrolysis. Weight fractions of CH_4 , CO , CO_2 and H_2 in the pyrolysis gas were taken as 0.1213, 0.6856, 0.1764 and 0.0167 respectively [31].

4. Results and discussion

Simulations were carried out for 100 seconds and the gas composition, the gas temperature and the particle mass flow rates were monitored. As mentioned in the introduction, the combustion reactor was not modelled in this work. Instead, temperature of the bed material flowing from the combustion reactor was assumed as 200 K higher than that of the respective reactor temperature. Then, the bed material inlet temperatures were 1273, 1173 and 1073 K for 1073, 973 and 873 K reactor temperatures respectively. Average gas composition was read as the time average over final 25 seconds of the simulation. A detailed description of the simulation results for 1073K steam temperature is presented in section 3.1 while the rest of the content elaborates the comparison of results between different temperatures.

4.1 Simulation results of 1073 K steam temperature

Being a continuous reactor system, the bed mass was supposed to be constant over time. However, a slight reduction of bed mass from 178.3 kg to 177.1 kg was observed over 100s of simulation time. Bed particle outflow was also monitored and the plots in Figure 4 depict the variation of total solid and char flowrates.

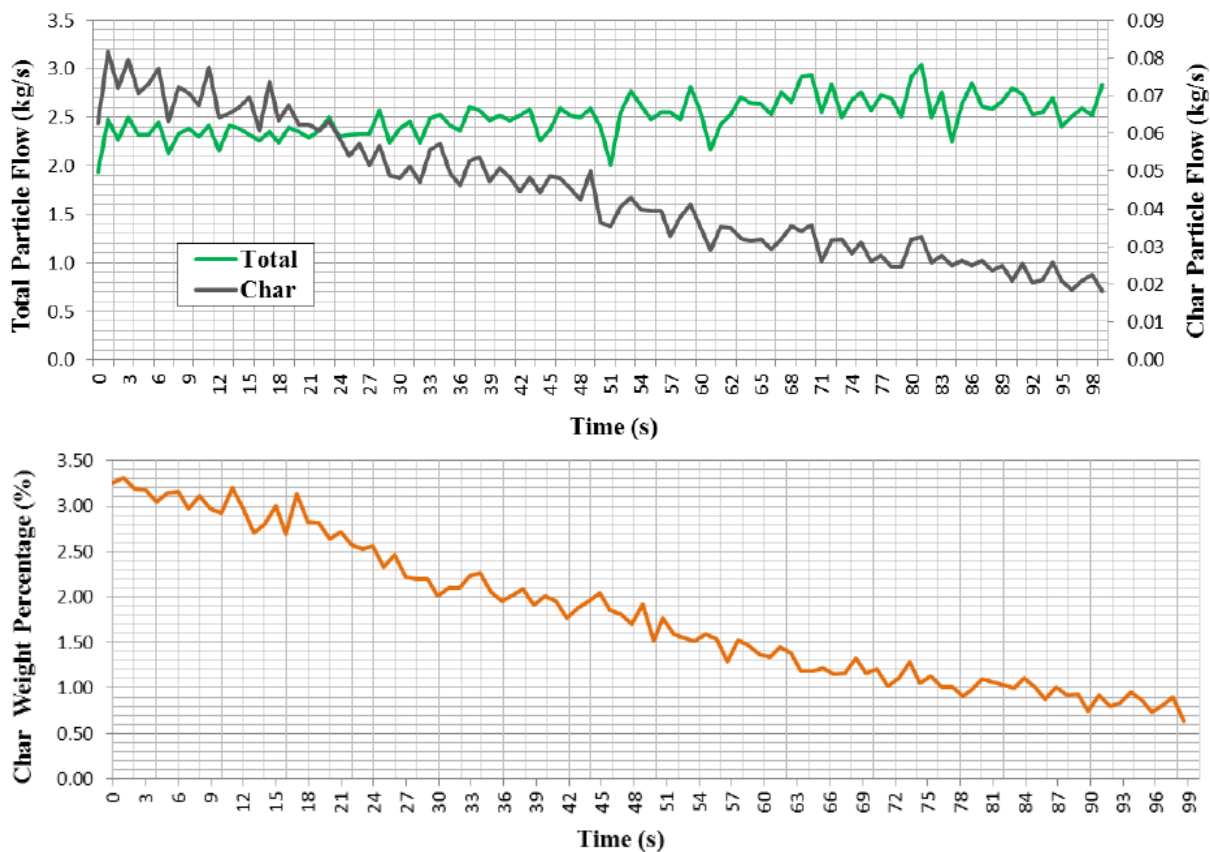


Figure 4. Total solid & char flowrate (up) and char percentage of particle outflow (down).

According to the Figure 4, the char percentage in the particle outflow has got reduced from 3.25% to 0.5%. If the perfect mixing conditions are assumed, char percentage inside the reactor and in the particle outflow should be identical. Therefore, char inventory in the reactor has got reduced simultaneously. Further, the particle outflow was connected to the bed material inlet with 99% efficiency (assuming 1% of char in the particle outflow which undergoes oxidation in the combustion reactor). Hence, the reduction of char inventory in the reactor and inefficient implementation of the boundary connection might lead to the reduction of total material inventory in the reactor. It can be further concluded that the initial char

percentage in the reactor is much higher than the equilibrium char content with the implemented biomass flow of 0.05 kg/s.

As the bed hydrodynamics are concerned, it was desired the column to operate in the bubbling fluidization regime with homogeneous temperature and particle species distribution. Particular parameters are illustrated in Figure 5. Sketch (c) in Figure 5 refers to the distribution of different particle species in the reactor where 1, 2, and 3 represents silica, char and biomass respectively. Sketch (a) clearly depicts that the reactor is operated in the bubbling fluidization regime with a slight particle entrainment in the freeboard. When the sketch (a) and (c) are analysed together, it is clearly illustrated that the entrained fraction consists of biomass particles. The bed temperature shows a slight uneven distribution as shown in sketch (b). However, the particle bed has reached higher temperatures than 1073 K, which was the steam inlet temperature and desired reactor temperature. The pyrolysis reactions and char conversion reactions are endothermic, which absorb the heat from the bed material. The plot (b) in Figure 7 shows that the gas temperature has increased continuously over the simulation time, which suggests the possibility of reducing either the particle circulation rate or the temperature from the combustion reactor. Temperature rise of bed material in the combustion reactor was assumed and it would have been more realistic if the complete reactor system (with both reactors) was simulated. According to the Figure 5 (c), the particle species of silica, char and biomass are finely distributed over the reactor, which is a proper indication of good mixing with less segregation.

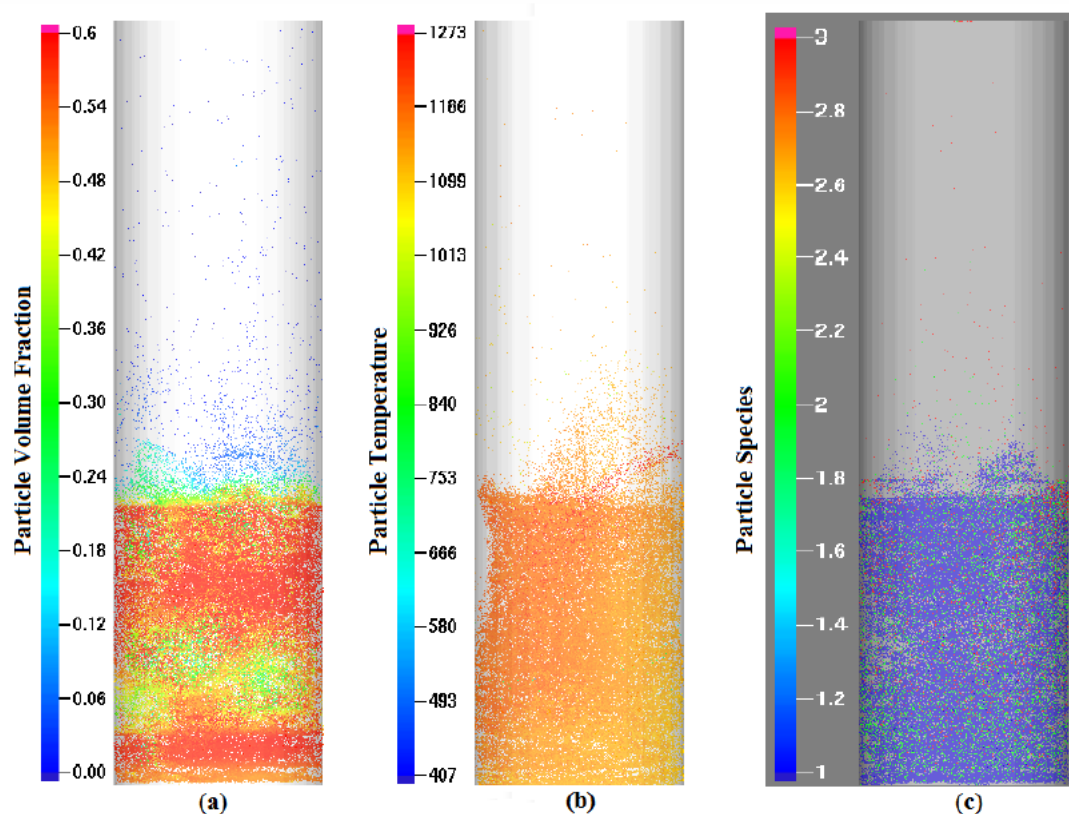


Figure 5. Bed hydrodynamics at 100 s simulation time, (a) Particle volume fractions, (b) Particle temperature distribution, and (c) Particle species distribution (1- sand, 2-char and 3-biomass).

The product gas composition was monitored over the reactor height and the simulation time as illustrated in Figure 6 and Figure 7(a) respectively. Temperature and flowrate of the product gas against the time are plotted in Figure 7(b) and (c). Gas composition does not show noticeable variations up to biomass feeding height of 300mm from the bottom of the reactor. This suggests slow reaction kinetics of the steam-char heterogeneous reaction at reactor temperature. Carbon monoxide is the main constituent in the biomass pyrolysis gas, which is approximately 68%. However, due to the fast kinetics of water-gas-shift reaction, CO is immediately consumed and concentrations drop sharply. The increasing H₂ and CO₂ concentration along the reactor height with simultaneous reduction of CO describes the dominance of the water-gas-shift reaction.

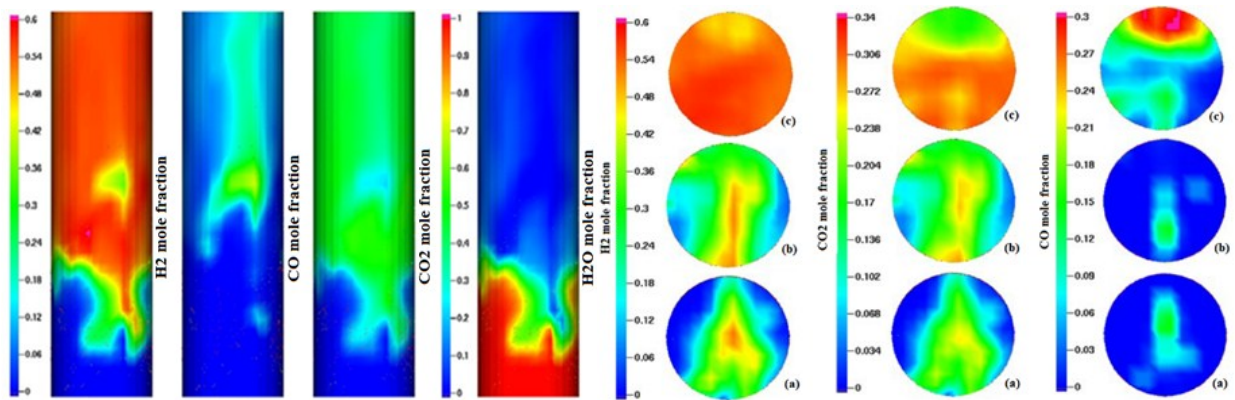


Figure 6. Gas composition along reactor height (left), different cross sections (right), (a) 0.3m, (b) 0.6m and (c), 0.9m.

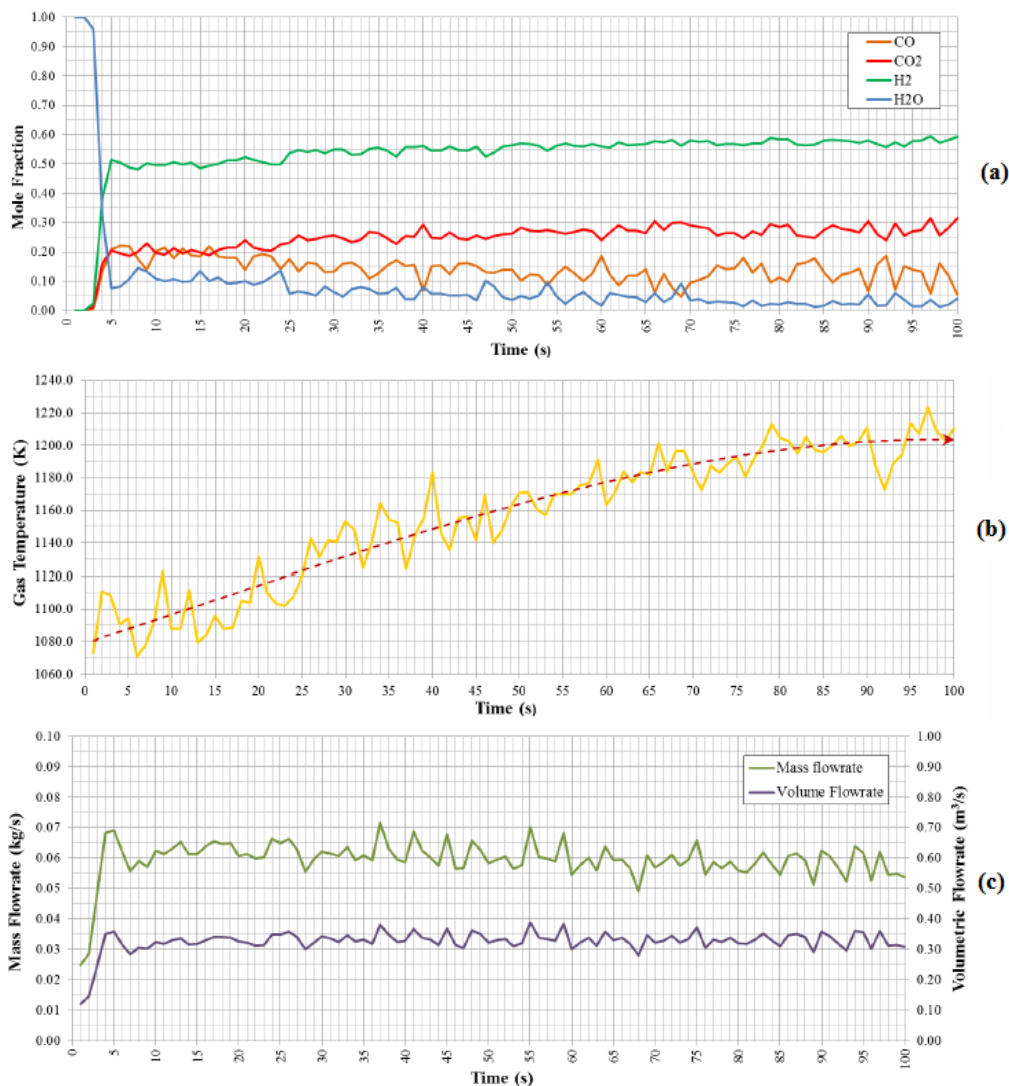


Figure 7. Product gas properties over simulation time, (a) Composition, (b) Temperature (c) Flowrate.

According to Figure 7(a), the system has reached nearly steady state operation in 5 seconds. However, there is a gradual change in the gas compositions with the time. H_2 mole fraction has changed from 0.5 to 0.6 between 5s and 100s, which analogues to the increasing gas temperature. At elevated temperatures, the reaction kinetics are increased and the system reaches the equilibrium state rapidly.

The mass and area specific mass production rates of gas were 0.055 kg/s and 0.23 kg/s/m² respectively. As the produced gas was at high temperatures and atmospheric pressure, the ideal gas law was applied to

reproduce the data at normal temperature and pressure (25 °C and 1 atm). The product gas flowrate was 1.64 Nm³/kg of biomass, which is within the range found in literature. Further, area specific gas production was calculated as 0.34 Nm³/s/m². The average molar gas composition during final 25s simulation was 0.128 of CO, 0.273 of CO₂, 0.574 of H₂ and 0.025 of H₂O. The LHV of the gas was calculated as 10.1 MJ/kg taking LHV of wood, CO and H₂ as 16 MJ/kg (dry basis), 10 MJ/kg and 120 MJ/kg respectively. The cold gas efficiency (CGE) was calculated as 73.3% using following equation,

$$CGE = \frac{mass_{gas}(kg) \cdot LHV_{gas}(J/kg)}{mass_{fuel}(kg) \cdot LHV_{fuel}(J/kg)} \quad (18)$$

There is a certain level of uncertainty related to calculation of cold gas efficiency because, the actual operating conditions of the combustion reactor was not known. Instead, the temperature increase of the bed material in the combustion reactor was assumed as 200K. However, there can be additional fuel supply into the combustion to achieve the aforementioned temperature rise, which indirectly affects the cold gas efficiency.

4.2 Effect of the temperature

The effect of the steam temperature on the product gas was analysed by simulating the same reactor at 973K and 873K temperatures. The temperature increment in the combustion reactor was assumed as 200K, similar to previous case. The time taken to achieve the near steady state conditions got increased as the steam temperature was reduced. The respective times were 7s and 10s to achieve the steady state conditions at 973K and 873K. Further, as illustrated in Figure 3(b), the outlet pressure boundary was defined as a small fraction of the top face of the reactor cylinder. Consequently, it was assumed that the cross sectional variation of the gas composition is averaged out and it is agreeable to represent the gas composition by the centre cell of the outlet pressure boundary. It simply works as a sensor installed at the place of that particular cell. Figures 8, 9 depict the average gas composition at three different temperatures considered.

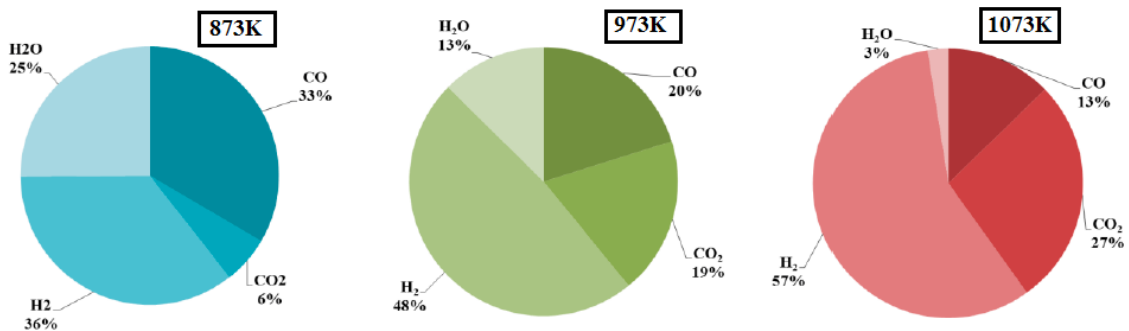


Figure 8. Product gas composition (molar basis) at different temperatures.

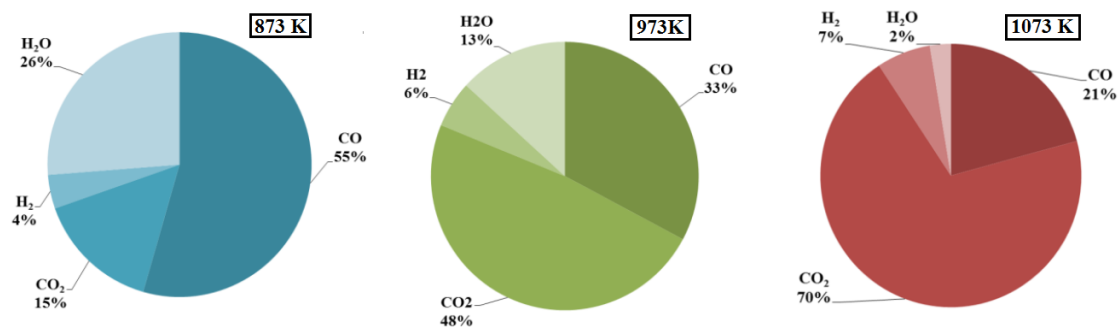


Figure 9. Product gas composition (weight basis) at different temperatures.

Even though the S/B was constant at 0.45 for all the simulations, it was required to change the biomass flowrate accordingly with the varied steam flow due to the temperature change. Therefore, the comparison of the effect of temperature is not 100% representative. However, it is clear that the water-gas-shift reaction dominates over the gas composition. At the temperature of 873K, 25 mole% of the gas is composed of unreacted steam. The steam content reduced to 13 mole% and 3 mole% when the temperature was increased to 973K and 1073K respectively. Simultaneous increment of H₂ and CO₂ along with reduction of H₂O and

CO analogue to increased temperature is a clear indication of triggered chemical kinetics at high temperatures. Therefore, when it comes to 873K and 973K reactor temperature, the gas composition can be improved by providing higher residence time by increasing the reactor height. However, the simulation results from the reactor operation at 1073K show that almost all the steam has been consumed. Hence, it is necessary to increase the gas-solid contact and trigger the heterogeneous reaction between char and CO₂ to improve the gas quality. Reducing the biomass particle size and upgrading the reactor into fast fluidization regime are two possible methods in achieving increased gas-solid contact. Reduced particle size increases the contact surface area where, fast fluidization drives more particles into the freeboard increasing the contact time, which can finally be operated as a circulating fluidized bed. The plots in Figure 10 illustrate the change of gas composition in the reactor freeboard at 1073K and the summary of the simulation results at different temperatures are given in Table 3.

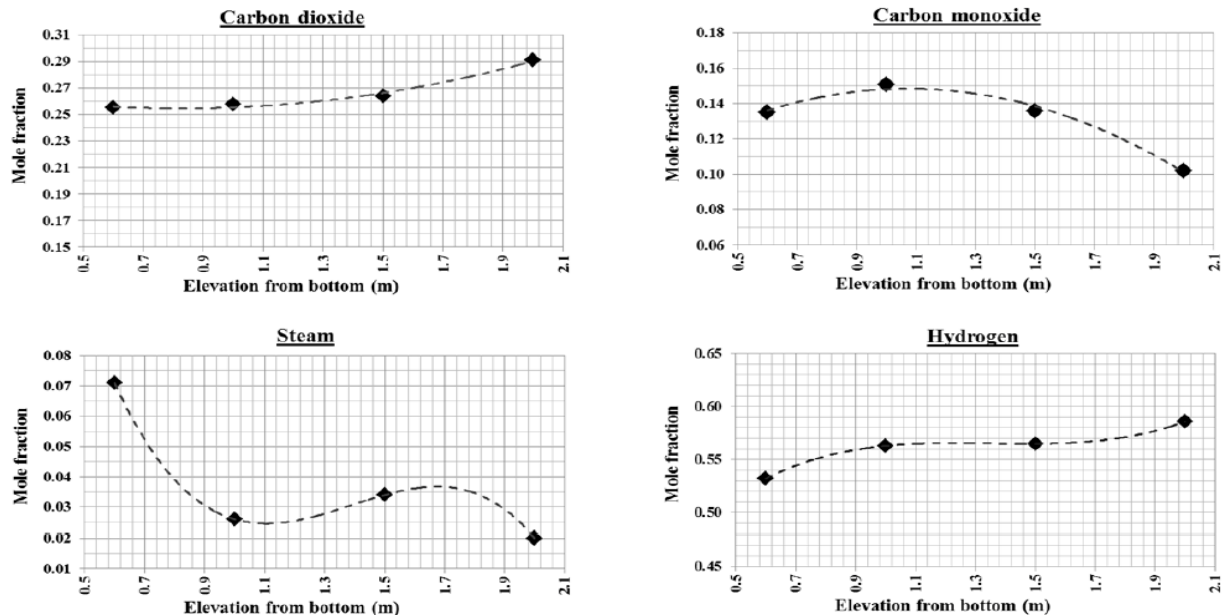


Figure 10. Change of gas composition along reactor freeboard at 1073 K.

Table 3. Simulation derived results at different temperatures.

Parameter	1073K	973K	873K
Steam flow (kg/s)	0.0228	0.0251	0.028
Gas temperature (K)	1200	1100	970
Volumetric gas Production (Nm ³ /s)	0.082	0.091	0.1
Mass gas production (kg/s)	0.055	0.064	0.074
Volumetric gas production (Nm ³ /kg biomass)	1.64	1.65	1.66
LHV (MJ/kg)	10.1	10.0	10.4
Cold gas efficiency (%)	73.2	73.4	76.6

The increased volumetric gas production at reduced temperature is due to the increased steam and biomass flowrates into the system. Further, gas production rate per unit mass of biomass has also increased. Both LHV and CGE have increased slightly with decreased temperature. In order to verify the facts further, an additional simulation was performed at 973K steam temperature with identical steam and biomass flowrates at 1073K. The steam velocity was reduced to 0.45 m/s to maintain the S/B ratio at 0.45. The LHV dropped from 10.1 MJ/kg at 1073K to 9.97 MJ/kg at 973K. In contrast, CGE increased from 73.2% to 76.52% within same temperature range. No significant variation in the gas composition was observed. The gas residence time increases with the reduced gas velocities and consequently, the system has additional time to reach the equilibrium.

5. Conclusion

Barracuda VR commercial CFD package was used in this work where MP-PIC implementation delivered fast results. This suggests its suitability in optimizing the reactor systems. The effect of steam and reactor temperature was analysed regard to gas composition, lower heating value of gas, gas flow rates and cold gas efficiency.

The hydrogen content in the product gas was directly proportional to the reactor temperature. The reaction kinetics are triggered because of the increased temperature that drives the system towards the equilibrium state faster. The carbon monoxide content showed a simultaneous reduction with increased temperature and hydrogen content, which is a clear illustration of the water-gas-shift reaction. Considerable amount of excess steam existed at operational temperatures of 973K and 873K. The underlying reasons can be due to either the changed equilibrium compositions or inadequate residence time, which should be further analysed by increasing the reactor height. The lower heating value of the product gas was not strongly correlated to temperature, which changed from 10.1 MJ/kg to 10.4 MJ/kg as the temperature was changed from 1073K to 873K. There was a slight increment in the cold gas efficiency at reduced temperature from 73.2% at 1073K to 76.6% at 873K. In brief, the gas composition was a strong function of the system temperature while the lower heating value and cold gas efficiency showed only little variations.

The effect of the temperature difference was not 100% illustrative with the applied implementation of boundary conditions. Therefore, it is recommended to keep all other parameters constant except temperature, in order to picture the exact effect of temperature for product gas quality. Simulating the complete dual fluidized bed reactor system together with a detailed characterization of biomass such as composition and pyrolysis kinetics, will overcome the uncertainties related to this work for a certain extent.

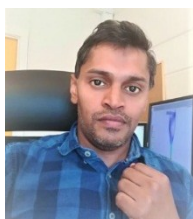
Acknowledgements

The authors would like to forward their gratitude to the University College of Southeast Norway for providing the Barracuda VR software package and computer facilities.

References

- [1] REN21, "Renewables 2016 Global Status Report," 2016.
- [2] J. Szczodrak and J. Fiedurek, "Technology for conversion of lignocellulosic biomass to ethanol," *Biomass and Bioenergy*, vol. 10, no. 5, pp. 367-375, 1996.
- [3] E. Esmaili and N. Mahinpey, "Adjustment of drag coefficient correlations in three dimensional CFD simulation of gas–solid bubbling fluidized bed," *Advances in Engineering Software*, vol. 42, no. 6, pp. 375-386, 2011.
- [4] F. Winter and B. Schratzer, "23 - Applications of fluidized bed technology in processes other than combustion and gasification A2 - Scala, Fabrizio," in *Fluidized Bed Technologies for Near-Zero Emission Combustion and Gasification*: Woodhead Publishing, 2013, pp. 1005-1033.
- [5] Y. Behjat, S. Shahhosseini, and S. H. Hashemabadi, "CFD modeling of hydrodynamic and heat transfer in fluidized bed reactors" *Int. Comm. in Heat and Mass Transfer*, 35(3), 357-368, 2008.
- [6] M. Horio, "1 - Overview of fluidization science and fluidized bed technologies A2 - Scala, Fabrizio," in *Fluidized Bed Technologies for Near-Zero Emission Combustion and Gasification*: Woodhead Publishing, 2013, pp. 3-41.
- [7] A. A. P. Susastriawan, H. Saptoadi, and Purnomo, "Small-scale downdraft gasifiers for biomass gasification: A review," *Renewable and Sustainable Energy Reviews*, vol. 76, pp. 989-1003, 2017.
- [8] X. T. Li, J. R. Grace, C. J. Lim, A. P. Watkinson, H. P. Chen, and J. R. Kim, "Biomass gasification in a circulating fluidized bed," *Biomass and Bioenergy*, vol. 26, no. 2, pp. 171-193, 2004.
- [9] P. M. Lv, Z. H. Xiong, J. Chang, C. Z. Wu, Y. Chen, and J. X. Zhu, "An experimental study on biomass air–steam gasification in a fluidized bed" *Bioresource Technology*, 95 (1), 95-101, 2004.
- [10] H. Cui and J. R. Grace, "Fluidization of biomass particles: A review of experimental multiphase flow aspects," *Chemical Engineering Science*, vol. 62, no. 1, pp. 45-55, 2007.
- [11] J. Corella, J. M. Toledo, and G. Molina, "A Review on Dual Fluidized-Bed Biomass Gasifiers," *Industrial & Engineering Chemistry Research*, vol. 46, no. 21, pp. 6831-6839, 2007.
- [12] G. Xu, T. Murakami, T. Suda, Y. Matsuzaw, and H. Tani, "Two-stage dual fluidized bed gasification: Its conception and application to biomass" *Fuel Processing Tech.* 90(1), 137-144, 2009.
- [13] T. Murakami, G. Xu, T. Suda, Y. Matsuzawa, H. Tani, and T. Fujimori, "Some process fundamentals of biomass gasification in dual fluidized bed," *Fuel*, vol. 86, no. 1, pp. 244-255, 2007.
- [14] Y. Xiao, S. Xu, Y. Song, Y. Shan, C. Wang, and G. Wang, "Biomass steam gasification for hydrogen-rich gas production in a decoupled dual loop gasification system," *Fuel Processing Technology*, vol. 165, pp. 54-61, 2017.
- [15] C. Pfeifer, S. Koppatz, and H. Hofbauer, "Steam gasification of various feedstocks at a dual fluidised bed gasifier: Impacts of operation conditions and bed materials," *Biomass Conversion and Biorefinery*, journal article vol. 1, no. 1, pp. 39-53, 2011.

- [16] S. Koppatz, C. Pfeifer, and H. Hofbauer, "Comparison of the performance behaviour of silica sand and olivine in a dual fluidised bed reactor system for steam gasification of biomass at pilot plant scale," *Chemical Engineering Journal*, vol. 175, pp. 468-483, 2011.
- [17] M. Chiesa, V. Mathiesen, J. A. Melheim, and B. Halvorsen, "Numerical simulation of particulate flow by the Eulerian–Lagrangian and the Eulerian–Eulerian approach with application to a fluidized bed," *Computers & Chemical Engineering*, vol. 29, no. 2, pp. 291-304, 2005.
- [18] J. R. Grace and F. Taghipour, "Verification and validation of CFD models and dynamic similarity for fluidized beds," *Powder Technology*, vol. 139, no. 2, pp. 99-110, 2004.
- [19] X. Ku, T. Li, and T. Løvås, "CFD–DEM simulation of biomass gasification with steam in a fluidized bed reactor," *Chemical Engineering Science*, vol. 122, pp. 270-283, 2015.
- [20] D. Gidaspow, J. Jung, and R. K. Singh, "Hydrodynamics of fluidization using kinetic theory: an emerging paradigm," *Powder Technology*, vol. 148, no. 2, pp. 123-141, 2004.
- [21] M. J. Andrews and P. J. O'Rourke, "The multiphase particle-in-cell (MP-PIC) method for dense particulate flows," *International Journal of Multiphase Flow*, vol. 22, no. 2, pp. 379-402, 1996.
- [22] D. M. Snider, "An Incompressible Three-Dimensional Multiphase Particle-in-Cell Model for Dense Particle Flows," *Journal of Computational Physics*, vol. 170, no. 2, pp. 523-549, 2001.
- [23] C. B. Solnordal, V. Kenche, T. D. Hadley, Y. Feng, P. J. Witt, and K. S. Lim, "Simulation of an internally circulating fluidized bed using a multiphase particle-in-cell method," *Powder Tech.* 274, 123-134, 2015.
- [24] Y. Liang, Y. Zhang, T. Li, and C. Lu, "A critical validation study on CPFD model in simulating gas–solid bubbling fluidized beds," *Powder Technology*, vol. 263, pp. 121-134, 2014.
- [25] D. M. Snider, S. M. Clark, and P. J. O'Rourke, "Eulerian–Lagrangian method for three-dimensional thermal reacting flow with application to coal gasifiers," *Chem. Eng. Sc.*, 66 (6), 1285-1295, 2011.
- [26] C. Loha, H. Chattopadhyay, and P. K. Chatterjee, "Three dimensional kinetic modeling of fluidized bed biomass gasification," *Chemical Engineering Science*, vol. 109, pp. 53-64, 2014.
- [27] J. Xie, W. Zhong, B. Jin, Y. Shao, and H. Liu, "Simulation on gasification of forestry residues in fluidized beds by Eulerian–Lagrangian approach," *Bioresource Technology*, 121, pp. 36-46, 2012.
- [28] H. Liu, R. J. Cattolica, and R. Seiser, "CFD studies on biomass gasification in a pilot-scale dual fluidized-bed system," *Int. Journal of Hydrogen Energy*, vol. 41, no. 28, pp. 11974-11989, 2016.
- [29] H. Liu, R. J. Cattolica, R. Seiser, and C.-h. Liao, "Three-dimensional full-loop simulation of a dual fluidized-bed biomass gasifier," *Applied Energy*, vol. 160, pp. 489-501, 2015.
- [30] J. C. Bandara, R. K. Thapa, B. M. E. Moldestad, and M. S. Eikeland, "Simulation of Particle Segregation in Fluidized Beds" in 9th EUROSIM Congress on Modelling and Simulation, Oulu, Finland, 2016.
- [31] R.K. Thapa, C. Pfeifer, and B. M. Halvorsen, "Modeling of reaction kinetics in bubbling fluidized bed biomass gasification reactor" *Int. Journal of Energy and Environment*, vol. 5, no. 1, p. 10, 2014.



Janitha C. Bandara has completed B.Sc. degree in Chemical and Process Engineering from University of Moratuwa, Sri Lanka in 2007 and Master's degree in Process Technology from University of South-Eastern Norway in 2016. He has industrial and research experience related to biomass gasification in fixed bed and fluidized beds. At present, he is pursuing his PhD degree in experimental studies and CFD simulations of fluidized bed gasification of biomass at University of South-Eastern Norway.
E-mail address: Janitha.bandara@usn.no, janithjc@gmail.com



B.M. E. Moldestad has her Master in Process Technology from Telemark University College. The PhD degree is from Norwegian University of Science and Technology and is in the field flow behaviour in fluidized bed. Her research work includes both experimental and computational multiphase studies. She has worked within the field of fluidization since 2000. She is employed as professor at the University of South-Eastern Norway in the field Process Technology.
E-mail address: britt.moldestad@usn.no



M.S. Eikeland has her Master in Industrial Environmental Technology from Telemark University College. The PhD degree is from Norwegian University of Science and Technology and is in the field of membrane technology with focus on durability of polymer membranes exposed to aggressive gases. She has worked within the field of biomass gasification since 2014. Her research work includes both experimental and process simulation studies. She is employed as Associated Professor at University of South-Eastern Norway.
E-mail address: marianne.eikeland@usn.no

Paper H

Janitha C. Bandara, Rajan Jaiswal, Henrik K. Nielsen, Britt M.E. Moldestad,
Marianne S. Eikeland

Air gasification of biomass in bubbling fluidized bed – short review and
experimental studies

Journal: Chemical Engineering Science (2020 – Submitted)

Air gasification of biomass in bubbling fluidized bed – short review and experimental studies

Janitha C. Bandara*¹, Rajan Jaiswal¹, Henrik K. Nielsen², Britt. M.E. Moldestad¹, Marianne S. Eikeland¹

¹University of South-Eastern Norway, Faculty of Technology, Kjølnes ring 56, 3918, Porsgrunn, Norway

²University of Agder, Jon Lilletuns vei 9, 4879 Grimstad, Norway

*Corresponding Author

Email: janithjc@gmail.com/ Janitha.bandara@usn.no

T.P. +47 40580343

64A, Vallermyrvegen, 3917, Porsgrunn, Norway

Abstract

Gasification is an attractive method for biomass-to-energy conversion and fluidized bed design is one of the best options for large scale operation. A bubbling fluidized bed reactor of 0.1m in diameter was used to analyze three fundamental process parameters of biomass type, equivalence ratio (ER) and temperature. Wood chips, wood pellets and grass pellets were gasified between 650°C and 800°C temperature. The ER was varied between 0.08 and 0.1. Gasification of grass pellets was difficult at 800°C due to agglomeration. The gas composition and carbon conversion of wood chips and wood pellets were better compared to grass pellets. The reactor performances were greatly improved with the temperature where 650°C was not sufficient to achieve a reasonable carbon conversion. At lower temperatures, the gas quality was reduced with ER due to nitrogen dilution and in contrast, the extended carbon conversion at high temperatures counterweighted the nitrogen dilution. The highest carbon conversion was achieved at 800 °C and 0.16 ER which were 75.8% and 70.6% for wood chips and wood pellets.

Key words: Biomass gasification; bubbling fluidized bed; temperature; equivalence ratio

1 Introduction

Biomass is supposed to take the foremost contribution in achieving zero-emission targets, as it is competent to deliver much of the spectrum of petroleum-based products (Ahrenfeldt, Thomsen, Henriksen, & Clausen, 2013; Ferreira et al., 2017). Energy from biomass is more dispatchable compared to the intermittent nature of other renewable energy sources of solar, wind, run-of-river hydropower etc. Energy, economy and environment are strongly related. Therefore, reduction of the greenhouse gas (GHG) emissions with simultaneous industrialization, population growth and increasing living quality is the utmost global challenge (Danish & Wang, 2019; Pio, Tarelho, Tavares, Matos, & Silva, 2020; X. Zhang et al., 2020).

Biomass refers to any primary hydrocarbon material generated by photosynthesis in green plants that did not undergo any geological formation. As the photosynthesis process absorbs back the released carbon dioxide (CO₂) during the combustion for energy, bioenergy, in broad sense, can be considered as a carbon neutral source (Hoogwijk et al., 2003; Nunes, Causer, & Ciolkosz, 2020). Bioenergy has contributed by approximately 12.5% to the global energy profile in 2019 in which, 7.5% is coming from traditional biomass usage¹. Lignocellulosic material such as wood, grass or straws compose 90% of the available biomass (Afgan, Gobaisi, Carvalho, & Cumo, 1998; Kaur-Sidhu, Ravindra, Mor, & John, 2020; Kirch, Medwell, Birzer, & van Eyk, 2020; Szczodrak & Fiedurek, 1996). Second-generation liquid biofuels from lignocellulosic is a trending technology as the first-generation biofuels have been in a vast

¹ REN21 – Global status report - https://www.ren21.net/wp-content/uploads/2019/05/gsr_2019_full_report_en.pdf

dispute due to increased food prices and forest clearing. The further mentioning of the term “biomass” in this work is related to lignocellulosic materials. Due to the inconsistency in chemical and physical properties and the low energy density, biomass is less competitive in its raw form. Fuel pre-processing such as drying, size reduction, palletisation etc. and upgrading into gaseous or liquid fuels are, therefore, emerged as a massive research interest (Asadullah, 2014a).

Heat production from direct combustion of biomass has been the long lasted tradition. However, pyrolysis and gasification are striking technologies owe to the growing demand for liquid and gaseous fuels. Bio-chemical conversion of lignocellulosic is a slow process compared to pyrolysis and gasification with additional drawbacks of high water footprint and energy intensity in final separation of alcohols (Sikarwar et al., 2016; Singh Siwal et al., 2020). Bio-oil is the desired product after pyrolysis, which is a complex mixture of different oxygenated chemicals. Extensive downstream processing such as catalytic hydrogenation, separation techniques etc. are needed to upgrade the bio-oil to stand in line with the petroleum products. In contrast, gasification has a high carbon conversion efficiency, whereas the product gas is more versatile and economical as a feedstock for downstream processing into fuels (Heidenreich & Foscolo, 2015; Safarian, Unnþórsson, & Richter, 2019; Sansaniwal, Pal, Rosen, & Tyagi, 2017).

Air gasification of biomass in bubbling fluidized beds is the simplest form of fluidized bed technology that can be implemented from medium to large scale whereas fixed bed downdraft reactors are popular in small scale applications. Biomass gasification in bubbling fluidized beds has been studied by many research personal where many reactors were auto-thermal, in which the reactions enthalpies were generated by in situ combustion of char. The equivalence ratio (ER) used in many studies were in the range of 0.2 and 0.4. The nitrogen dilution is increased proportionally with the ER and at the same time, and adequate ER is important to maintain the required reactor temperature. Lower ERs than 0.2 has not been widely analyzed as the rule of thumb ER is typically 0.2 or more. Therefore, the main objective of the study was to operate the reactor at lower ERs and use external electrical heating, if required, to sustain the target reactor temperature. The performances of wood chips, wood pellets and grass pellets were studied under varying temperatures and ERs. Authors attached a short review at the beginning, related to general concept biomass with detailed previous studies in bubbling fluidized bed reactors, to make the article more readable.

2 Literature review

The gasification has a long history, which was discovered independently in England and France in the late 18th century. During the mid of 19th century, the gasification process was practiced to produce town gas for street lighting in England and by 1920, it was established in many of the American cities as well. The process was rewarded yet again during the World War II as a substitute for the shortage of petroleum. The declining attractiveness of gasification over the cheap petroleum was redeemed after the oil crisis in 1970s and continued to guarantee its

position as a biomass-to-energy conversion process. Concerns towards the environmental protection, sky rocketing of oil prize, depletion of fossil reserves and energy security concerns added piles of essence for the continuous development of the gasification process since the 1990s (Sansaniwal et al., 2017; Sulaiman, Abdul-Rahim, & Ofozor, 2020). A detailed historical milestones can be found in the publication of Sikarwar et al. (2016).

2.1 Gasification process

Heidenreich and Foscolo (2015) have briefed the key information relevant to biomass gasification. Unlike in pyrolysis, the gasification converts solid biomass, except ash, completely into a gaseous mixture. Biomass carrying oxygen and hydrogen are not sufficient to bring all the carbon into the gas phase (Anis & Zainal, 2011; Belgiorno, De Feo, Della Rocca, & Napoli, 2003; Ghassemi & Shahsavan-Markadeh, 2014). Therefore, a gasifying agent such as air, oxygen, steam or a mixture of these, is used in sub-stoichiometric quantities to convert the remaining carbon. The desired gaseous products are carbon monoxide (CO), hydrogen (H₂), methane (CH₄), other light gases (i.e. ethane and propane) etc. In addition, a considerable amount of CO₂ can present due to the combustion reactions and unconverted long chain hydrocarbons from pyrolysis, which are commonly known as tar². As air is the common gasifying agent in use, nitrogen (N₂) is also present in big quantities. The designing reactor temperature is possible to vary between 600°C and 1100°C. The presence of the particulate matter, soot and coke in the product gas stream is inevitable as well (Fukutome, Kawamoto, & Saka, 2014). Regardless of the gasification designing, biomass particles undergo four major reaction steps of drying, pyrolysis, reduction and oxidation. A simple schematic diagram of the gasification process is illustrated in Figure 1 and the enthalpies for basic reactions are listed in Table 1 (Ongen, Ozcan, & Ozbas, 2016; Sansaniwal et al., 2017). The initial drying and pyrolysis reactions and tar conversion reactions are not included in Table 1 as the particular reactions are highly dependent on biomass properties.

² High molecular weight cyclic/polycyclic hydrocarbon that is condensable at lower temperatures to form black and high viscous liquid.

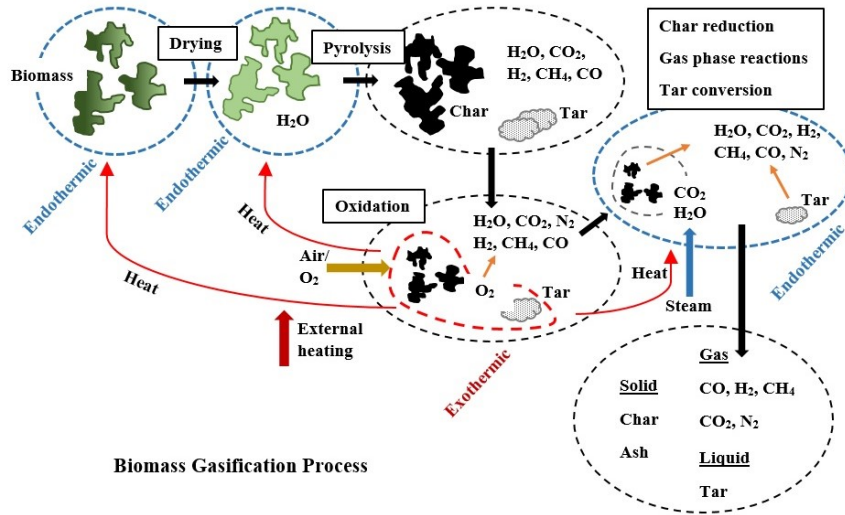


Figure 1: Successive steps of biomass gasification process

Table 1: Basic homogeneous and heterogeneous reactions of gasification

Stoichiometric equation	Reaction name	Enthalpy (kJ/mol)	No:
Oxidative reactions			
$C + O_2 \rightleftharpoons CO_2$	Char combustion	-394	R2
$C + 0.5O_2 \rightleftharpoons CO$	Partial oxidation	-111	R3
$CO + 0.5O_2 \rightleftharpoons CO_2$	CO oxidation	-283	R4
$H_2 + 0.5O_2 \rightleftharpoons H_2O$	Hydrogen combustion	-242	R5
Gasification/Reduction reactions			
$C + H_2O \rightleftharpoons H_2 + CO$	Steam gasification	+131	R6
$C + CO_2 \rightleftharpoons 2CO$	Boudouard reaction	+172	R7
$0.5C + H_2 \rightleftharpoons 0.5CH_4$	Methanation	-75	R8
$H_2O + CO \rightleftharpoons H_2 + CO_2$	Water-gas shift reaction	-41	R9
$CH_4 + H_2O \rightleftharpoons CO + 3H_2$	Methane reforming	+206	R10

Drying is the first step, which occurs below 200°C and the biomass particles are not heated beyond this until much of the water is evaporated. Water evaporation at atmospheric pressure consumes nearly 2300 kJ/kg that is extracted from the system. High content of biomass moisture results in dragging down the reactor temperature causing degradation of the product quality. Oppositely in a steam rich environment, the water-gas-shift forward reaction is favored resulting high H₂ content in the product gas. In general, 10%-20% of moisture is believed to be the optimum for gasification (Ren, Cao, Zhao, Yang, & Wei, 2019).

With the progressive moisture removal, the biomass particles are heated and the volatiles start to escape as the temperature go pass 260°C, which is known as pyrolysis or primary cracking. The evolved gas consists of permanent gases, light tars and heavy tars, in which, the

composition is highly susceptible to the chemical composition and size of the biomass³, rate of particle heating, reactor pressure and external turbulence etc. (Ren, Cao, et al., 2019; Soria, Li, Flamant, & Mazza, 2019). Fast pyrolysis at elevated temperatures yields a large fraction of volatiles with a reduced amount of char, which is the desired behavior for gasification process. High heating rate, intermediate temperature (450-500°C) with low residence time maximize the tar production while slow pyrolysis produces high char quantity (Cheng, Bayat, Jena, & Brewer, 2020; Sattar, Leeke, Hornung, & Wood, 2014). Besides, the chemical structure, inorganic compounds and the pore structure of char are a sensitive function of pyrolysis conditions. Therefore, a detailed account on the pyrolysis process with respect to reactor conditions is important (Di Blasi, 2009; Mani, Mahinpey, & Murugan, 2011; Neves, Thunman, Matos, Tarelho, & Gómez-Barea, 2011; Tong et al., 2019; White, Catallo, & Legendre, 2011). The freeboard length and temperature is crucial for the gas phase reactions, especially to complete the tar cracking or reforming reactions. Heterogeneous char reactions with the steam and CO₂ are the rate limiting reactions in the gasification process, which improves the carbon conversion efficiency. The carbon to hydrogen ratio in the produced gas is a major concern if the gasification process is attached with a downstream process to produce chemicals and fuels. Steam gasification, steam reforming of tar and water-gas-shift reactions are important as those boost the H₂ content (Ferreira et al., 2017). Apart from the steam reforming, tar undergoes cracking at high temperatures and the presence of catalysts improves the produced gas quality and the gasification efficiency. Drying, pyrolysis and reduction reactions are endothermic where cumulative enthalpy with added heat losses calculate the heat energy requirement for a steady process. Fractional char combustion and external heating are two possibilities of integrating the process enthalpy. A successful gasifier designing is, therefore, challenged by the competency of available information of all involved processes (Sansaniwal et al., 2017).

Equation 01, 02, 03 and 04 show the procedures to calculate the lower heating value of synthesis gas (LHV), the gas yield (GY), the carbon conversion efficiency (CCE %) and the cold gas efficiency (CGE %) respectively, which are the main parameters used in quantifying the gasifier performance (Meng, Ma, Wang, Liu, & Wang, 2019; Serrano, Kwapinska, Horvat, Sánchez-Delgado, & Leahy, 2016).

$$LHV (MJ/m^3) = \{[H_2] * 107.98 + [CO] * 126.36 + [CH_4] * 358.18\}/1000 \quad \text{Equation 1}$$

Contribution from other hydrocarbons of C₂ and C₃ is possible to incorporate to the Equation 1 with volumetric heat value.

$$GY \left(\frac{Nm^3}{kg \text{ biomass}} \right) = \frac{\text{Volume rate of producer gas} \left(\frac{Nm^3}{h} \right)}{\text{Biomass feed rate} \left(\frac{kg}{h} \right)} \quad \text{Equation 2}$$

³ Cellulose (40-50%), hemi-cellulose (25-35%) and lignin (15-35%) are the main organic constituents of biomass whereas ash and extractives are possible minor contributors (Hameed, Sharma, Pareek, Wu, & Yu, 2019)

$$CCE \% = \frac{12(CO\%+CO_2\%+CH_4\%+2*C_2H_4\%)*GY}{22.4*fuel\ C\%*100} 100\% \quad \text{Equation 3}$$

$$CGE = \frac{GY * LHV_{syngas}}{LHV_{biomass}} 100\% \quad \text{Equation 4}$$

2.2 Types of gasifiers

A considerable number of review studies covering different wings of gasification can be found in the scientific literature. (Karl & Pröll, 2018; Motta, Miranda, Maciel Filho, & Wolf Maciel, 2018; Parthasarathy & Narayanan, 2014; Ren, Cao, et al., 2019; Ren, Liu, Zhao, & Cao, 2019; Shahbaz, yusup, Inayat, Patrick, & Ammar, 2017; Singh Siwal et al., 2020; Susastriawan, Saptoadi, & Purnomo, 2017; Valderrama Rios, González, Lora, & Almazán del Olmo, 2018; Widjaya, Chen, Bowtell, & Hills, 2018; Y. Zhang et al., 2019). The major classification of gasification is based on the particle hydrodynamic inside the reactor. Fixed bed, fluidized bed and entrained flow are the three main types of reactors in operation. Reactors that generate required reaction enthalpy inside is identified as auto-thermal while reactors that extracts heat from an outside source as allo-thermal. Further, reactors can be distinguished based on gasifying agents as well.

2.2.1 Fixed bed gasifiers

Updraft, downdraft and crossdraft are three different configurations of fixed bed reactors and the selection between these are based on operational simplicity, available form of biomass and required producer gas quality (Couto, Rouboa, Silva, Monteiro, & Bouziane, 2013). Schematic diagrams of updraft and downdraft configurations are illustrated in Figure 2. The major highlight of the fixed bed modes is the existence of distinct reaction zones of drying, pyrolysis, reduction and oxidation. The downward biomass flow is assisted by the gravity in all three formats. The existence of different reaction zones along the reactor height varies accordingly with the point of injection and flow direction of the gasifying agent. The oxidized products of CO₂ and H₂O are regenerated into energy potential gases of CO and H₂ during the passage across char reduction zone. Channeling and arching are major problems within the reactor top, which act as a biomass hopper (Dai, Cui, & Grace, 2012). Non homogeneity of the biomass particle size is the main cause for channeling and as a results, easy bypass tunnels are opened for the gas stream. Tunneling reduces the particle-gas contact, which can interrupt the updraft gasifier. Arching hinders the expected gravity flow of biomass, which is, in some reactors, overcome by mechanical stirrers or vibrators. Feedstock with low bulk densities such as straw is therefore not suitable to be used in the fixed bed gasifiers unless densified into briquettes or pellets.

The combusted gas stream is in direct contact with the pyrolysis and drying feedstock in the updraft configuration. The thermally efficiency of the process is increased as the sensible heat loss with the outflow gas is minimized. Further, particulates generated in the combustion and reduction zones are filtered during the gas passage through the raw biomass at the reactor top. High moisture tolerance up to 60% is an interesting feature and however, the product gas

versatility is narrowed down due to extremely high content of tar. Updraft gasification is mostly suitable for immediate combustion of the produced gas for heat production, which has been tested in small scale cooking stoves (Njenga et al., 2016; Ren, Cao, et al., 2019; Varunkumar, Rajan, & Mukunda, 2012).

Instead, downdraft gasification requires low moisture feed than 20% for an uninterrupted operation. “Stratified” and “Imbert” are the two main downdraft gasifier designs. Tar generation is minimized in downdraft gasification as the pyrolysis gas seeks its path through the combustion zone and the hot char bed before leaving the reactor. The concept behind the throat design is to increase the combustion zone temperature and induce high turbulence that guarantee the complete cracking of tars. The combustion zone temperature is a key parameter as it governs the zone reaction kinetics and heat transfer to other zones. In achieving this, a steady fuel flow should be maintained across the combustion zone, which is realized by removing a fraction of unconverted char (7%-8%) from the bottom of a downdraft reactor. Further according to different char gasification models, the char reactivity reduces at higher degree of conversion (Wang et al., 2016). As the char moves down along the reduction zone, the particle size is reduced as a result of the conversion and breakup due to high pressure applied from the standing reactor content. Consequently, the pressure drop increases with simultaneous decrease in the air flow followed by reduced combustion zone temperature.

Commercial fixed bed units are, in general, auto-thermal systems powered by air as the gasifying agent (Reed & Das, 1988). Char oxidation increases the CO₂ content in the product gas whereas air fed reactors suffer from N₂ dilution over 50%. External heat integration is difficult and inefficient to implement in fixed bed systems. According to the detailed comparison published by Warnecke (2000), many advantages are incorporated with the fluidized bed reactors compared to the fixed bed, except the limited turndown ratio in fluidized beds.

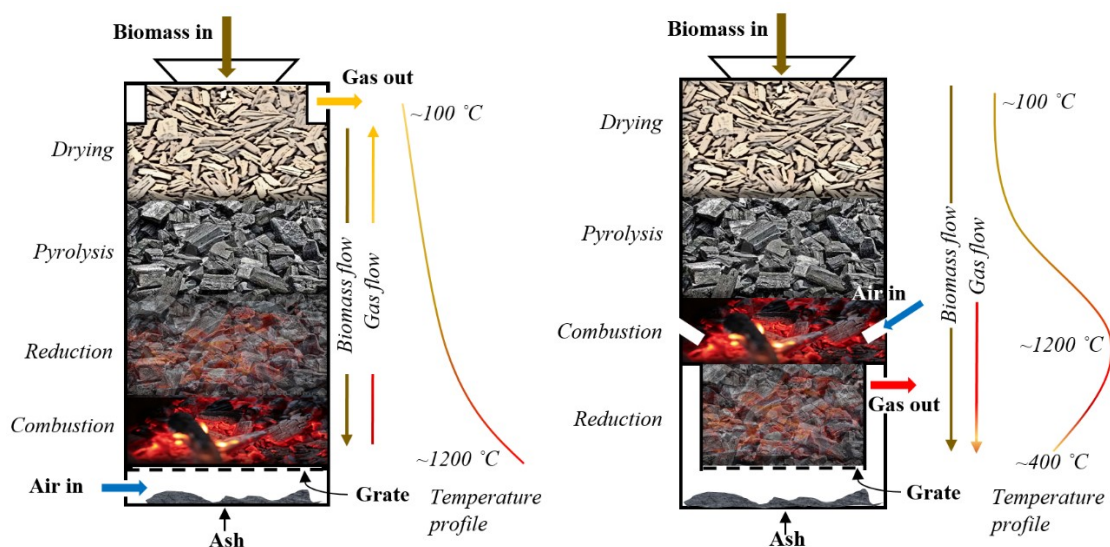


Figure 2: Existence of different reaction zones and temperature profiles of updraft (left) and downdraft (right) fixed bed gasification

2.2.2 Fluidized bed gasification

Standalone fluidization of biomass particles is difficult due to their irregularity in shape, size and density, which is therefore, assisted by a denser and finer particle phase known as bed material (Cui & Grace, 2007). Due to the intense mixing of particles, high temperature gradients are diminished inside the reactor, which is the main difficulty in scaled up operation of the fixed bed gasifiers. Fuel flexibility with high heat and mass transfer are some other highlights. Particle mixing is triggered by bubble movement in a bubbling fluidized bed (BFB) and particles are not supposed to escape out from the reactor (González-Vázquez, García, Gil, Pevida, & Rubiera, 2018; Ku, Jin, & Lin, 2017). The external heat integration is more reliable in bubbling fluidized beds compared to fixed bed reactors. An illustrative sketch of a bubbling fluidized bed is given in Figure 3. High degree of mixing diminishes the distinguished reaction zones of drying, pyrolysis, reduction and oxidation in the fluidized beds. Avoiding the segregation of different particle phases inside the bubbling reactor is challenging and therefore, system optimization is crucial to identify the correct particle size for the bed material.

A circulating fluidized bed (CFB) gives an increased gas-particle contact time in a high turbulent environment, which enhances the heat and mass transfer operations. CFB reactors are tall installations with auxiliary attachments of cyclone for gas-particle separation and particle recycle mechanisms such as loop seals. The size of the fuel particle is more selective compared to a bubbling bed as the reactor should be operated beyond the terminal velocity. The impact of particles with high momentum against bends, cyclone walls etc., increases the particle attrition, which also cause erosion problems (Couto et al., 2013). External heat integration is more practical as the particle phase flows in and out from the main reactor. Oxygen fed gasification is not economical in operation. Steam fed reactors need an external heating source to maintain the reactor temperature above 800°C for an efficient conversion. Dual reactor circulating fluidized bed (DCFB) gasification system has proved to be one of the effective ways of producing high quality gas that is not diluted with N₂. The presence of N₂ is extremely undesired for the downstream processing of syngas into chemicals. As illustrated in Figure 3, the char combustion is isolated into a separate reactor from the devolatilization and gasification reactions. The gasifier is fluidized by steam that triggers the carbon conversion via steam gasification, tar reforming and water-gas shift reactions. The flowing out bed material particles from the gasification reactor carry the unreacted char particles into the combustion reactor, which operates with air at fast fluidization regime. As particles flow up concurrently with the air flow, the reactor is named as riser combustor. The liberated energy from char combustion is absorbed by the bed material, which are recycled back to the gasification reactor providing the gasification enthalpies. A cyclone and a proper gas seal mechanism such as loop seals should be installed across the reactor connecting pipes (Karl & Pröll, 2018; Mauerhofer et al., 2019). If the gasification reactor is considered alone, the process is allo-thermal and however as a single unit, DCFB is auto-thermal in principle. Chemical looping gasification (CLG) with in situ CO₂ capture is another development using DCFB method. A CO₂ absorption compound such as CaO particles are mixed with the bedding material, which traps the CO₂ molecules

generated in the gasification reactor and CaCO_3 is formed. CLC can, therefore, be used to produce H_2 rich syngas with high loading of steam. CaCO_3 particles are regenerated back to CaO in the combustion reactor releasing CO_2 . CaO also has catalytic effect that improves the carbon conversion and tar cracking (Acharya, Dutta, & Basu, 2009; Xu, Chen, Soomro, Sun, & Xiang, 2018). The utmost challenge of DCGB is whether the char combustion in riser is sufficient to heat up the particles to the requirement of the gasification reactor. The combustion gas stream is at a higher temperature, equal or higher than particle temperature, where heat recovery is important in improving the thermal efficiency.

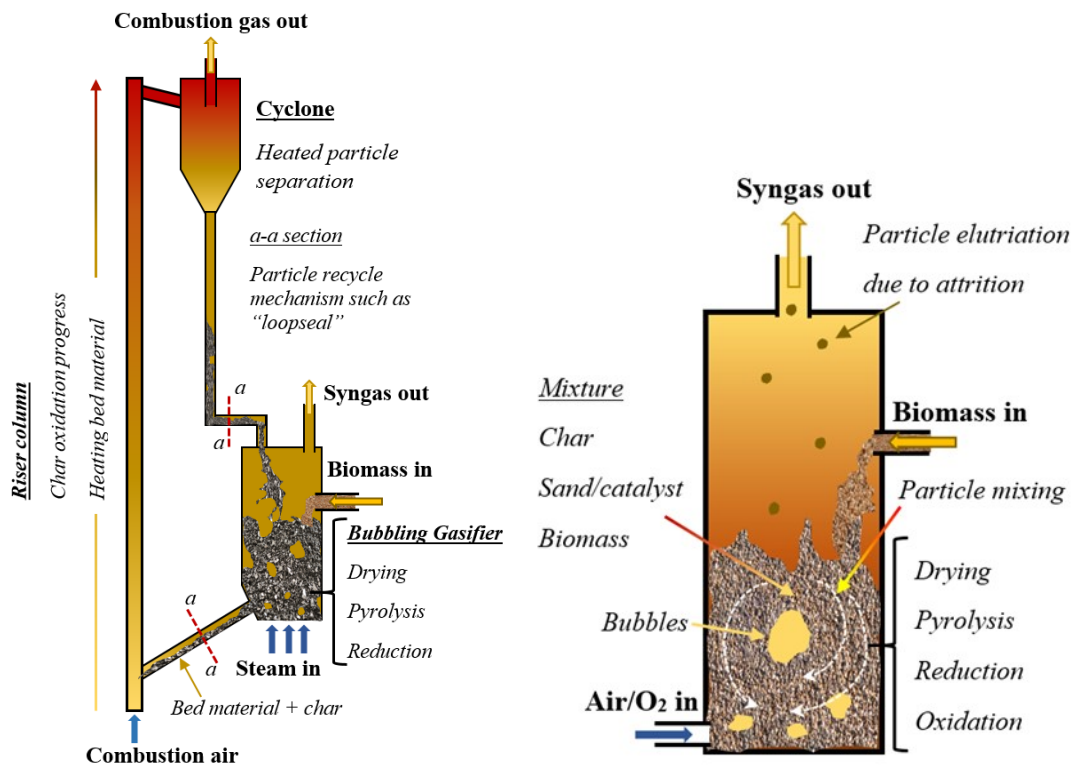


Figure 3: Fluidized bed gasification, duel-reactor circulating fluidized bed (left) and bubbling fluidized bed (right)

2.2.3 Other reactor types

Entrained flow gasifiers operate at extremely high temperatures up to 1500°C with extended carbon conversion and tar cracking. Finely ground biomass ($<1\text{mm}$) and gasifying agent are injected from the reactor top and flow down co-currently where the particle residence time is between 1-5 seconds. Commercial scale entrained flow gasifiers are, in many cases, operated with coal and oxygen (Dhanavath et al., 2018; Fleck et al., 2018; W. M. S. W. Ismail, Mohd Thaim, & Abdul Rasid, 2019; Schneider, Grube, Herrmann, & Rönsch, 2016). Rotary kiln and plasma reactors are two other prospected designing for gasification whereas supercritical water gasification was developed for high moisture biomass (Sikarwar et al., 2016).

2.3 Syngas composition and effect of the operational parameters

The gaseous product from the gasification process is distinguished as either producer gas or synthesis gas respectively depending on whether the gas is diluted with N₂ or not. Undoubtedly, the gasifying agent primarily counts on the gas quality. The gasifier designing, physical and chemical properties of biomass feedstock, the reactor temperature and pressure, the residence time, the equivalence ratio (ER), steam-to-biomass ratio (SBR) and the catalysts are the succeeding parameters for the gas composition (Abdoulmoumine, Kulkarni, & Adhikari, 2014; Aydin, Yucel, & Sadikoglu, 2018; González-Vázquez et al., 2018; Lapuerta, Hernández, Pazo, & López, 2008; Narváez, Orío, Aznar, & Corella, 1996; Pereira, da Silva, de Oliveira, & Machado, 2012; Sheth & Babu, 2009). Carbon conversion is triggered by increased temperature, and consequently, the gasifier efficiency is increased. Further, steam reforming and thermal cracking of tars are favored at elevated temperatures, which improves the gas heating value with higher H₂ and CH₄ contents. Temperature limitations are applied for feedstock with low ash melting temperature. In fluidized bed gasification, molten ash could bind the bed material together to form agglomerates or clinkers that interrupts the fluidization. Bed material endorsed with catalysts play a vital role in improving the gas quality by assisting tar cracking at reduced temperatures. Dolomite, olivine, nickel based catalysts and olivine impregnated with Ni and iron (Fe) have been extensively studied (Islam, 2020; Sikarwar et al., 2016). The ER for air gasification is between 0.2 and 0.4 where the gas heating value is decreased as the ER is increased. The steam-to-biomass ratio (SBR) is reported between 0.3 and 0.6 (Nam et al., 2018). However in an auto-thermal air gasifier, ER may be required to adjust beyond the optimum calculated value to reach the designed reactor temperature. Pressure is not significantly affecting the gas composition and heating value, which can be useful whenever the downstream application needs a higher pressure (i.e. gas turbine). Hanaoka, Inoue, Uno, Ogi, and Minowa (2005) have studied the effect of the major components of biomass; cellulose, hemi-cellulose and lignin, on gas production and concluded that the cellulose-to-gas conversion is extremely high with 97.9% whereas 52.8% for lignin. The relative compositions of CO, H₂ and CO₂ are also sensitive to the biomass constituents. Heating value of the product gas is possible to upgrade from 5 MJ/Nm³ to 18 MJ/Nm³ as the gasifying agent is shifted from air to oxygen or steam in a DCFB (Gómez-Barea & Leckner, 2010). The H₂ content is maximized up to 60% with steam whereas, CO reaches the maximum of 40%-45% with oxygen as the gasifying agent. The H₂ and CO content from air gasification varies between 10%-25% (Pio, Tarelho, & Matos, 2017; Sansaniwal et al., 2017).

The presence of detrimental components/contaminants such as alkali metals, particulates, sulfur and chlorine compounds, cause corrosion and erosion of the reactor and piping. Tar is identified as one of the major barriers in commercialization of gasification because of the process hindrance in clogging pipes, engines (< 100 mg/Nm³), turbine (< 5 mg/Nm³) fouling and catalyst poisoning in Fischer–Tropsch (FT) synthesis (< 0.1 mg/Nm³) and solid oxide fuel cells (< 1 mg/Nm³) (Asadullah, 2014a, 2014b; Sikarwar et al., 2016). Tar conversion into permanent gases improves the syngas quality; specially the heating value. Therefore, in addition to the

main reactor, particle filtering and tar reduction accessories are key components. Tar generation, properties and cracking; thermal cracking, catalytic cracking, steam reforming during biomass gasification are studied and reviewed by many research personal (Abdoulmoumine, Adhikari, Kulkarni, & Chattanathan, 2015; Anis & Zainal, 2011; Devi, Ptasinski, & Janssen, 2003; Han & Kim, 2008; Shen & Yoshikawa, 2013; Surjosatyo, Anggriawan, Hermawan, & Dafiqurrohman, 2019; Valderrama Rios et al., 2018). Downdraft fixed bed gasification is superior in low tar content (0.01-6 g/Nm³) whereas updraft gasification produces the highest tar content (10-150 g/Nm³). The tar content from CFB gasification is in the range of 2 to 30 g/Nm³ (Couto et al., 2013). The exhaust gas carries out a considerable enthalpy in which, a heat recovery system can improve the gasifier efficiency (Belgiorno et al., 2003). By using bed catalytic particles, the reactor temperature can be reduced and consequently the sensible heat loss with the leaving gas. Syngas fermentation is also becoming popular in producing alcohol and carboxylic acids (Sun, Atiyeh, Huhnke, & Tanner, 2019).

2.4 Bubbling fluidized bed gasification-previous studies

Bubbling fluidized bed technology was discussed in section 2.2.2 and the following content within this section discuss the previous studies.

Meng et al. (2019) carried out bubbling fluidized bed experiments in a cylindrical reactor with 3.5 m in height and 207 mm in diameter. The feedstock sawdust was 150-350 micron in size and bed material silica sand was 180-250 micron. Gasifying agents of air, oxygen enriched air, air/steam mix and oxygen/steam mix were studied for different equivalent ratios between 0.20 and 0.3. Increasing the oxygen content from 21% to 99% resulted a significant improvement in H₂, CO and CH₄ content in the syngas. As a result of less N₂ content, the LHV upgraded from 6.16 to 12.17 MJ/m³. Over the entire tested ERs, the oxygen content in the product gas remained steady, which guarantees a sufficient resident time. The H₂ content increased proportionally with SBR between 0.8 and 3.0. A successive drop of LHV was observed with SBR for air/steam mix whereas it showed a maximum at 1.4 for oxygen/steam mix. As the ER was increased from 0.2 to 0.3, the LHV continuously dropped, the H₂ content increased, the gas yield increased and the CO content decreased for all the mixtures. The relative amounts of steam, air and oxygen in the blends and variation of the reactor temperature were not mentioned. The size range of sand and sawdust could definitely lead to segregation in the fluidized bed.

An auto-thermal bubbling fluidized bed was used by Pio et al. (2017) to gasify pine wood pellets and forest residual chips using air as the gasifying agent. The reactor was 250 mm in diameter and the static bed height was 230 mm filled with 355-1000 micron sand particles. The effects of ER was studied from 0.17 to 0.36 with an average biomass feed of 9-12 kg/h. At the lowest ER of 0.17, the reactor temperature could bring up to 700°C. The H₂ and CO contents were inversely proportional with ER and varied between 2.0%-12.7% and 14.2%-17.5% respectively. The authors claimed that the variation in gas composition was due to different biomass species and char behavior inside the bed such as segregation. The LHV was also inversely proportional to ER, which changed between 4.4 and 6.9 MJ/Nm³ in higher and lower

ends of ER. Higher temperature favored the H₂ and CO production with increased LHV. The gas yield was in between 1.2 to 2.2 Nm³/kg and the highest CGE was observed at an intermediate ER of 0.25. The efficiency was poor at lower and higher ERs respectively due to high contents of tars and extended oxidation of gasses.

Campoy, Gómez-Barea, Villanueva, and Ollero (2008) studied the gasification behavior in a bubbling fluidized bed using wood pellets with air and air/steam mixtures as the gasifying agents. Reactive zone diameter was 250mm where 290 micron size ofite particles was used as the bed material. Auto-thermal conditions were maintained during all the combinations of gasifying agents. In air gasification, the CO, H₂, CH₄ contents and the gas yield varied between 18.2-15.8%, 13.2-8.7%, 6%-4.6% and 0.6-1.2 Nm³/kg biomass respectively as the ER was changed from 0.19 to 0.35. Intermediate ER and SBR resulted in highest H₂ content whereas the gasification efficiency increased proportionally with ER while the LHV decreased. Increased tar yield could be observed at higher ERs, which was in contrast to the numerous literature findings. SBR was adjusted by the biomass flowrate from 11.5 kg/h to 20.5 kg/h, which could be the reason for deviated result for tar content. Therefore, analyzing the interrelations between different parameters using multivariate data analysis is vital in result interpretation. The experimental unit was modified with auxiliary electrical heating and used by the authors (Campoy, Gómez-Barea, Vidal, & Ollero, 2009) biomass gasification in O₂ enriched air-steam mixtures. The H₂ and CO contents could be increased over 27% and 25% respectively with a maximum LHV of 8 MJ/Nm³.

Experimental work of González-Vázquez et al. (2018) covered a wide range of operational variables such as temperature (700, 800 and 900°C), ER (0.13 and 0.25), SBR (0.04 to 1.85) and steam-to-air ratio (S/A) (10/90 to 70/30) with eight different feedstock including pine and chestnut sawdust, almond shells, cocoa shells etc. A cylindrical reactor of 77mm in diameter and 1000 mm in height was used with coal ash particles in the size range of 212 micron to 710 micron as the bed material. Due to the electrical heating, the reactor can be considered as partly auto-thermal. The H₂ content showed a direct proportionality against the temperature and S/A. Steam reforming and water gas shift reactions compete for the steam and therefore, the required reaction can be promoted by shifting the reactor environment as favorable for that particular reaction. As the reactor temperature increases, the forward reaction of water gas shift is retarded due to its exothermic characteristics and oppositely, the chemical kinetic rate is improved. H₂ production was more sensitive to the reactor temperature than the S/A. The maximum contents H₂ and CO recorded were 36% (900°C, ER-0.13 and S/A-70/30) and 38% (700C, ER-0.13 and S/A-70/30) respectively. The gas yield was between 0.8 and 1.5 Nm³/kg biomass whereas the HHV was nearly constant over the entire set of experiments. The CGE and energy yield increased from 50% to 80% and 7.5 to 16 MJ/kg biomass as the temperature was changed from 700 to 900°C (S/A – 70/30). The H₂ content showed a narrow range irrespective of the biomass species while the CO yield exhibited a considerable variation between 14% (cocoa shells) and 38% (almond shells).

A considerable number of literature publications are available discussing different aspects related to the bubbling fluidized beds (Arena & Di Gregorio, 2014; Behainne & Martinez, 2014; Fremaux, Beheshti, Ghassemi, & Shahsavan-Markadeh, 2015; Hervy, Remy, Dufour, & Mauviel, 2019; T. M. Ismail, Ramos, Monteiro, El-Salam, & Rouboa, 2020; Karatas, Olgun, & Akgun, 2013; Kim et al., 2013; Makwana, Pandey, & Mishra, 2019; Nam et al., 2018; Pio et al., 2020; Sarker, Bimbela, Sánchez, & Nielsen, 2015; Serrano et al., 2016; Subramanian, Sampathrajan, & Venkatachalam, 2011; Yu et al., 2015). However, a direct comparison between different researches and even between different sessions within same research work is difficult. As an example, changing of airflow to manipulate the ER will alter the fluidization conditions. In contrast, adjusting the biomass flow in manipulating ER will reduce the temperature at the feeding point inside the bed, which will lead to altered pyrolysis conditions. The composition and morphology of biomass can be considerably different even within same species due to variation in the geography, age, rainfall, different tree sections such as branches etc. Further, migration of biomass particles throughout the reactor can exert a significant impact where the distribution efficiency is affected by the reactor diameter and number of biomass injection points. Segregation of biomass particles from the bed material is also possible, which was rarely addressed in the literature. The Gas residence time along the reactor freeboard is significant as the reforming and water gas shift reactions are progressed improving the gas quality. Finally, some experiments were recorded as auto-thermal while some were partly allo-thermal making it difficult to compare.

3 Materials and experimental methods

3.1 Biomass Feedstock

Wood pellets and grass pellets were commercially available and the wood chips were extracted from locally grown pine trees in Telemark, Norway. Compared to standard cylindrical 6 mm diameter of pellets, woodchips come in different shapes and sizes. Average length of the raw pellets were 30-40 mm and however, the pellets are broken in the feeding conveyors. As illustrated in Figure 4, the real size of the pellets at the reactor entrance was 10 mm or less. The chips were sieved using 30 mm sieve and visually observed for any remaining larger chips. Biomass were tested for ultimate and proximate analysis at Eurofins testing facility and the results are given in Table 2.



Figure 4: Gasifier feed material and size scales, wood pellets, grass pellets and wood chips (from left to right)

Table 2: Fuel biomass properties

Biomass type	Ultimate analysis (%)				Proximate analysis (%)				LHV (dry) MJ/kg
	C	H	O	N	Fixed C	Volatile	Moisture	Ash	
Wood pellets	50.9	6.0	42.6		14.0	77.8	7.90	0.30	18.94
Grass pellets	46.9	5.7	33.7	3.19	12.61	69.5	8.40	9.49	16.7
Wood chips	51.0	6.1	42.2		13.5	74.8	11.1	0.58	18.8

3.2 Experimental system description

The experimental facility at University of South-Eastern Norway is a collaborative development with BOKU, Austria. The reactor is 100mm in diameter and 1000mm in height designed to operate at bubbling fluidization and atmospheric pressure. Three electrical heaters of 3kW are attached to the reactor outer walls with insulation. Gasifying air is supplied by a compressor, which is preheated and manipulated with a mass flowmeter. An isometric sketch of the experimental unit is given in Figure 5. Fuel is stored in a silo and conveyed to the reactor using two screw feeders. The feeding screw is disconnected into two units with a non-conductive flange connection in between to avoid conductive heat flow from the reactor to the silo. Biomass is fed 250mm above the reactor bottom.

Four temperature and pressure sensors are mounted along the reactor height with several additional sensors at silo, screw conveyor, air pre-heater, air inlet, gas outlet and reactor heating coil. Sensor data acquisition and parameter controlling is achieved by a PLC controller, which is also connected to a computer with a LabVIEW platform. The hot conveyor is directly connected to the reactor and operates continuously at a constant speed. The main purpose is to avoid any formation of “*Biomass Bridge*” between two screws, which interrupts any backward propagation of fire and reaches the silo. The rate of biomass feed is adjusted either by changing the cold conveyor operating time (< 17% of full conveyor capacity) or speed (>17% full capacity). The default cut off limits for reactor heater and air-preheater are 1000°C and 600°C respectively. A constant 0.5 L/min nitrogen flow is maintained across the silo to avoid any gas leakage from reactor to silo. A nitrogen supply line is in place to flush the reactor at any emergency shutdown. Gas detection sensors for H₂, CO and N₂ are fixed above the reactor to identify any gas leakage. The produced gas is burnt with propane in a ventilated chimney.

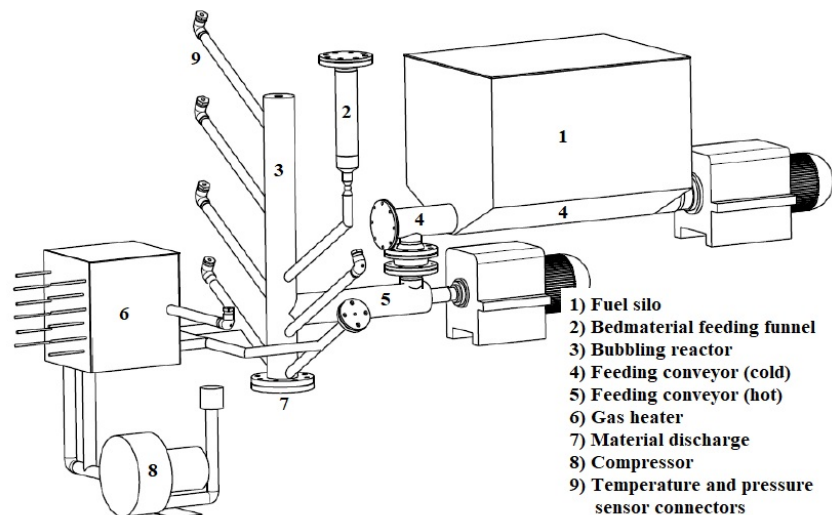


Figure 5: Bubbling fluidized bed experimental rig with auxiliary attachments

The produced gas analysis were carried out using a robust SRI gas chromatography (GC) with a thermal conductivity detector (TCD) located in the experimental facility. A silica gel packed column was used for CO₂ detection with a molecular sieve 13X packed column for N₂, O₂, CH₄, and CO. The GC was operated with helium as the carrier gas and the H₂ composition was calculated by the difference. Helium does not support detecting H₂ accurately at lower concentrations. The accuracy of calculating the H₂ composition by difference was validated with several samples using N₂ as the carrier gas. Gas sampling tube is fixed at the top of the reactor and syringes with airtight valves were used for sampling.

3.2.1 Experimental procedure

Prior to the gasification experiments, the screw conveyor was calibrated for feed rate at different speeds for wood chips, wood pellets and grass pellet. Two liters of sand with 2650 kg/m³ in density and 200-400 μm in size (292 μm mean size), was introduced into the reactor. The reactor heaters and the air preheater were switched on while maintaining a sufficient air flow to keep the bed fluidizing. Once the bed material temperature reached 650°C, the fuel feeding was started. For the primary analysis of the effects of temperature and equivalence ratio, the fuel feeding rate was maintained at a constant value. The reactor heaters were needed to switch on occasionally to maintain the desired reactor temperature. Manipulation of air preheater was also useful in setting up the reactor temperature. The bed pressure was constantly monitored to identify any formation of agglomerates inside. Three gas samples were checked for each combination of biomass type, temperature and ER. The samples were extracted at 10 minutes intervals and kept for cooling down in order to let the tar condense. Precautionary measures were always taken to remove the gas volume collected inside the tube during previous sampling.

4 Results and Discussion

Successful running of a biomass system is many times more challenging than a fossil fuel system, which are standard in physical and chemical properties. Instead, wood chips are highly diverse, especially in size whereas the pellets are more regular. The screw conveyor functionality was uninterrupted with the pellets and however, frequent blockages of wood chips could be observed. The free falling of longer woodchips in horizontal orientation from the cold conveyor to the hot caused the particle blockage in the narrow connecting pipe. The presence of dusty-moist particles also caused particles to get stuck between the screw and the surrounding pipe of the conveyor. Interrupted fuel flow was possible to identify either by increasing reactor temperature due to char combustion and decreasing bed pressure drop in the absence of biomass feeding.

A manual valve with a mass-flow meter was used to adjust the airflow, where the flowrate could vary during the operation as a result of frequent pressure fluctuations inside the reactor. The grass pellet feed calibration plot is given in Figure 6 where the wood pellets and wood chips showed a similar behaviour. The feed rate was not constant over time and changed, in positive and negative directions, from the average. Due to the periodic operation of cold conveyor at lower biomass feed rates, the reactor experienced zero biomass inflow frequently. Composition of the produced gas is principally formulated by the volatile composition from pyrolysis and therefore, periodic and varied biomass feeding could exert a certain uncertainty to the measured gas composition. It is suggested to modify the hot screw with a variable pitch that is wider at the connection with cold screw and gradually decreasing towards the reactor. Even with periodic operation of the cold conveyor, the wider pitch supports in collecting a certain amount of biomass while the narrow pitch near the reactor guarantees a steady inflow to the reactor. A schematic representation comparing the original and varying pitch is given in Figure 7. As sand particles migrate into the conveyor, the bubbling sand bed surface is not possible to maintain higher than the hot conveyor-reactor connection. With the involved high temperature and abrasion of sand between the screw and the pipe wall, the conveyor pipe suffers from possible erosion. Partly filled cross section and horizontal orientation of the conveyor pipe makes an easy passage for the sand to flow in. An inclined conveyor with varying pitch, converging cross section and N₂ flushing is suggested as in Figure 7. The biomass fills the entire cross section at the connection with reactor due to converging effect and further with N₂ flushing, the incoming sand particles can be directed back to the reactor.

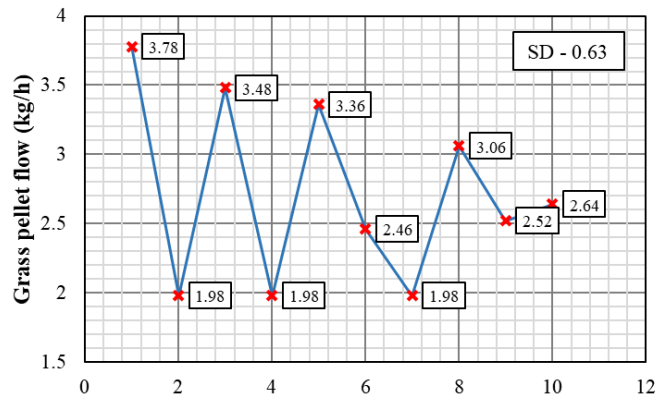


Figure 6: Variation of fuel feed rate for grass pellets measured in 2 minutes time periods

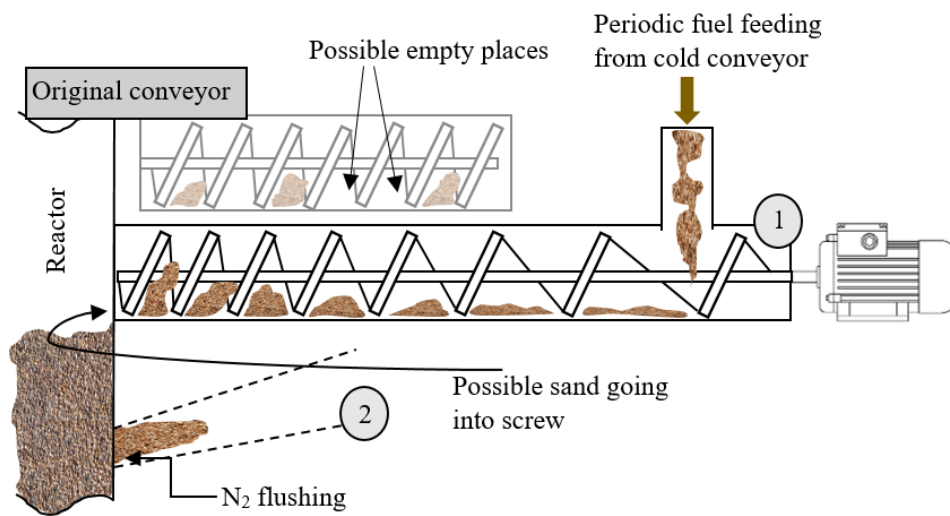


Figure 7: Suggested modifications to the reactor; 1- changing pitch of the conveyor, 2 – changing pitch with narrowing pipe cross section

4.1 Experimental results

Tuning of the conveyor system exactly to get the desired biomass flow was impossible due to the particle size heterogeneity. Therefore, the cold conveyor was operated at 2% of the maximum capacity, which resulted in 2.3 kg/h, 2.42 kg/h and 2.7 kg/h flowrates for woodchips, wood pellets and grass pellets respectively. The minimum air flowrate of 1.5 kg/h was selected based on the minimum fluidization velocity of used particle phase. Because of uniform cross section over the entire height, migrating of fine carbon particles and sand particles by attrition was expected. Therefore, higher air flowrates were not applicable with the used sand particle size. The ER values based on flowrates and the ultimate analysis data are given Table 3. The changed air flowrate could alter the fluidization conditions and being a small diameter reactor, changing the biomass feed rate could have worse effects. Drying and pyrolysis processes extract energy from the bed, which reduce the reactor temperature at the location of biomass injection. The more the biomass inflow, the more the temperature reduction, which will in turn, change the pyrolysis conditions. Further, the studies of Agu, Tokheim, Pfeifer, and Moldestad (2019)

have identified that the fluidization velocity greatly decide whether the biomass particles are in mix with the sand or segregate. Therefore, the proper selection of bed material properties and fluidization velocity is vital. As a separate flowmeter was not installed, the gas production rate was approximated using inlet-outlet N₂ balance. The following experimental results can, therefore, be infected with aforementioned uncertainties.

The ERs above 0.2 was used in many studies following literature values. This threshold was setup mainly to reach a manageable tar level in the product gas. Any remaining oxygen above the bed surface leads to oxidation reactions. CO, H₂, and CH₄ oxidation decrease the product gas quality whereas partial oxidation of tar improves the gas quality. In contrast, tars can be thermally or catalytically cracked as a downstream process. According to the author's viewpoint, the best context on this reactor configuration is to maximize the pyrolysis gas fraction as the biomass is fed to the bed surface. Subsequently, the air flowrate should be calculated that is sharply adequate to oxidize the char inside the bed, in which all of the oxygen is consumed before leaving the particle bed. The bed pressure drop was used to understand this limit, because if the char is fully consumed, the bed pressure drop should remain constant and if not, pressure drop should develop over time. Therefore, the ER was increased gradually from a lower value until the bed pressure drop reached steady over time. For illustration, the bed pressure drop plots for wood pellets are given in Figure 8.

The first plot in Figure 8 represent the wood pellets gasification at 0.08 ER and 600/700°C temperature range. The initial jump of pressure from 15.5 mbar to 19 mbar was due to the start of biomass feeding. The red colored trend line in the plot illustrates that the bed pressure increased gradually. Char accumulation inside the bed is the reason behind. A similar trend could be observed for increased ER of 0.125 at the same temperature. However, the gradient of the trend line was comparatively less. The third plot in Figure 8 represents higher temperatures over 800°C with 0.16 ER. The pressure drop remained approximately at a steady value. Consequently, it can be concluded that the 0.16 ER is marginally sufficient to oxidize the char fraction generated at +800°C.

Table 3: Equivalence ratios calculated based on ultimate analysis and air flowrates for different fuel types

Biomass	Feed (kg/h)	Rate	Stoichiometric Air (kg/h)	Actual air flowrate (kg/h)			
				1.5	2	2.5	3.0
Equivalence Ratio (ER)							
Wood pellet	2.42		19.6	0.075	0.100	0.125	0.150
Grass pellet	2.72		21.3	0.070	0.090	0.120	0.140
Wood chips	2.30		18.9	0.080	0.100	0.130	0.160

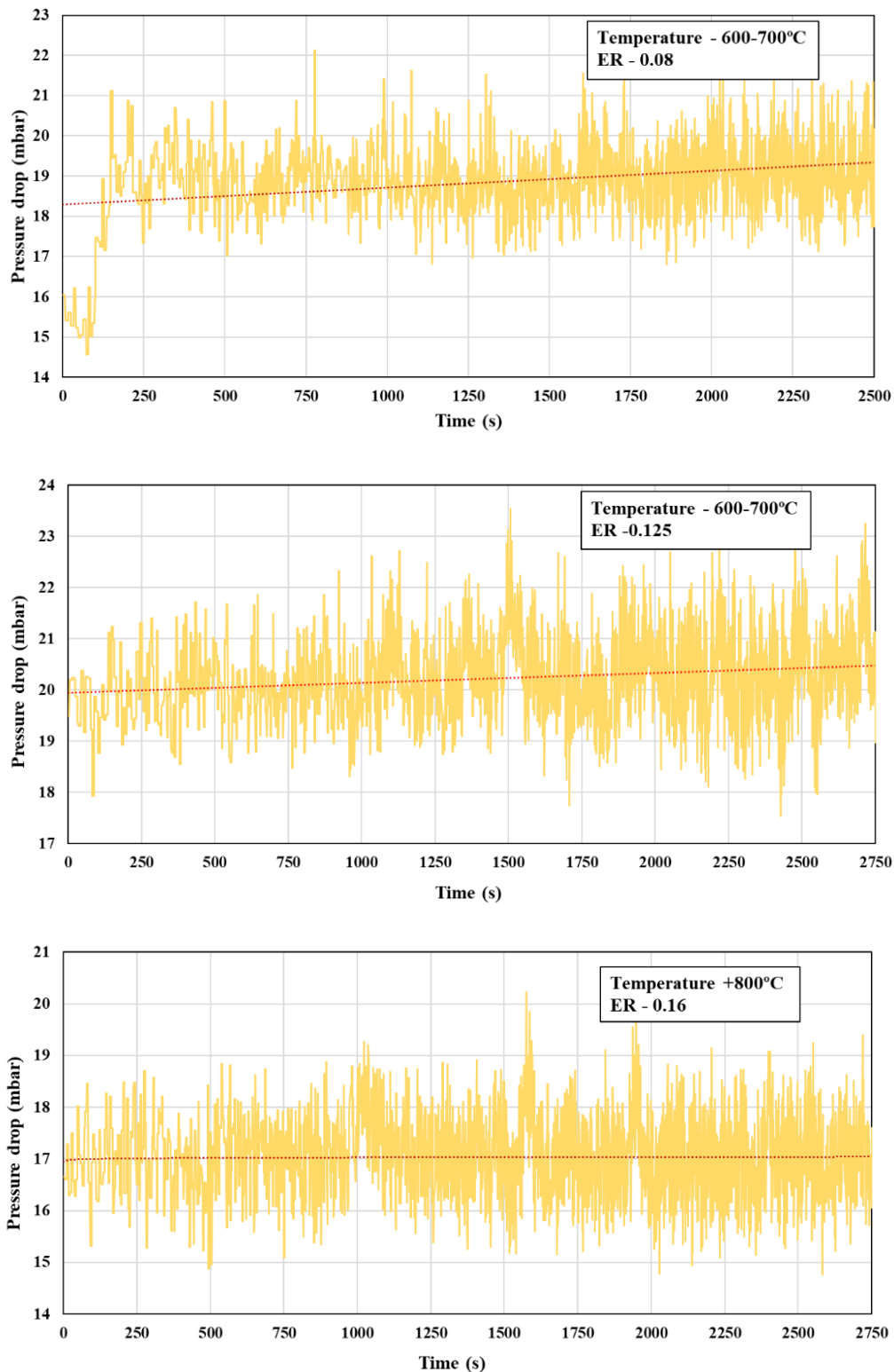


Figure 8: The change of bed pressure with time for different ER and temperature

The electrical heaters could only increase the bed temperature up to 675°C within a reasonable time. Therefore, some biomass is combusted in the bed to accelerate the heating for elevated temperatures of 750°C and above 800°C. At lower ERs below 0.1, the reactor temperature could not maintain above 650°C without the electrical heaters. At higher ERs, it was possible to take

up the temperature to 750°C range being the electrical heaters switched off and however, the heaters were continuously operated for higher temperatures than 800°C range.

4.1.1 Gasification of wood chips

Figure 9 summarizes the product gas composition obtained with wood chips. The presence of oxygen is less than 1% for all the temperatures and ER ranges, which is hardly noticeable at the bottom of the bar chart. The gas sampling was carried out manually with airtight syringes and therefore, some air contamination was expected. However with the observed low O₂ concentrations, it can be concluded that the air contamination was minimum during the sampling and further, the gas resident time was sufficient to oxidative reactions to complete.

The temperature profile along the reactor at 650°C and for different ERs are illustrated in Figure 10. The temperature sensors T8, T3 and T4 are located at air inlet, inside to the bed and just above the bed respectively. Electrical heaters were in operation for lower ERs of 0.08 and 0.1 where the average temperature of reactor wall was 750°C. Therefore, the product gas was continuously heated from the bed surface to the exit. The temperature gain in 0.08 ER is higher than 0.1 because of the low gas flow. In contrast, the gas temperatures at ERs of 0.13 and 0.16 were approximately constant from above the bed to exit. The electrical heaters were not used and the reactor wall temperature was same as the reactor bed. The endothermic characteristics of progressing pyrolysis reaction is the main reason for observed temperature drop just above the bed (T4). Even though the bed temperature was nearly constant around 650°C, the comparison for different ERs has slight uncertainty because of the temperature variation at the gas exit.

In general, for air gasification in auto-thermal conditions, the most suitable position for biomass feeding is above the bed surface. If the biomass is fed to the bottom of the bed, the O₂ can easily react with the evolved gases instead of char particles degrading the gas composition. Consequently, there is possible accumulation of char particles inside the reactor. However as the biomass is fed above the bed, the bed material and fluidization velocities should be selected carefully so that the generated char is well mixed with the bed material without segregating towards the bed surface.

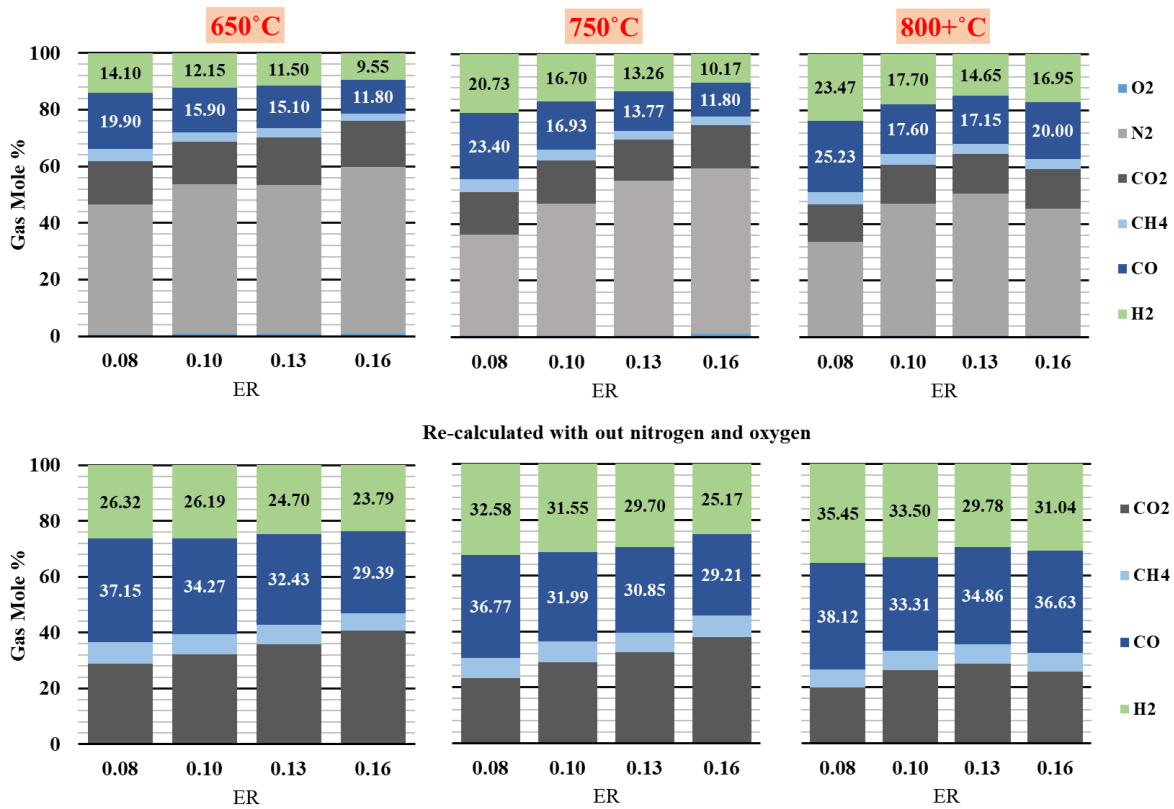


Figure 9: Product gas composition of wood chips at different equivalence ratio and reactor temperatures

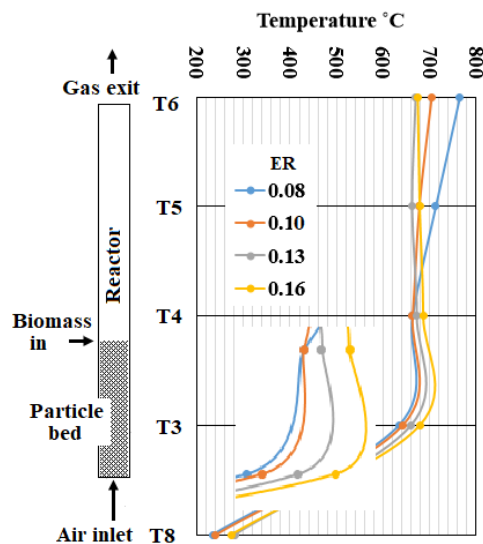


Figure 10: Temperature profile along the reactor height at 650°C operation for different ERs of woodchips

According to Figure 9, a significant effect from temperature and ER on the gas composition can be observed. In the temperature range of 650°C and 750°C, the H₂ and the CO molar compositions gradually decrease with increasing ER. The collective effect of amplified N₂ content in the product gas and possible gas phase oxidation reactions can be the reasons. In

contrast at 800°C temperature, H₂ and CO compositions drop initially and improve from 0.13 to 0.16. The increased O₂ supply and high reaction rates at increased temperature could accelerate the tar cracking reactions. Figure 11 carries the same information in Figure 10 and however, the gas compositions (included N₂ and O₂) are plotted as a function of temperature for different ERs. Variation of the gas compositions between 650°C and 750°C at 0.16 ER is very little. At 800°C temperature and 0.16 ER, the H₂ and CO compositions improve by 66% and 69% respectively showing an exponential trend. The CH₄ composition increases slightly from 650°C to 800°C in linearly. The reforming and tar cracking reactions are accelerated at higher temperatures resulting higher H₂ and CO. At 0.13 ER, H₂ linearly increases from 650°C to 800°C without a sharp change at 450°C as observed at 0.16 ER. The decreasing profile and the compositions of CO₂ are similar for both ERs. The CH₄ composition is nearly constant over the entire temperature range. The reduction of CO content from 650°C to 750°C is hard to explain, which can be a result of measurement uncertainty. Furthermore, the reactor temperature exerts a significant impact on the pyrolysis product yield and gas phase compositions. The higher the temperature, the higher the gas yield and the lower the tar yield. Consequently, a less gas residence time is sufficient to complete the tar conversion reactions. With the absence of external heating, the freeboard temperature may not be higher in a regular auto-thermal reactor and consequently, the tar cracking reactions may retard.

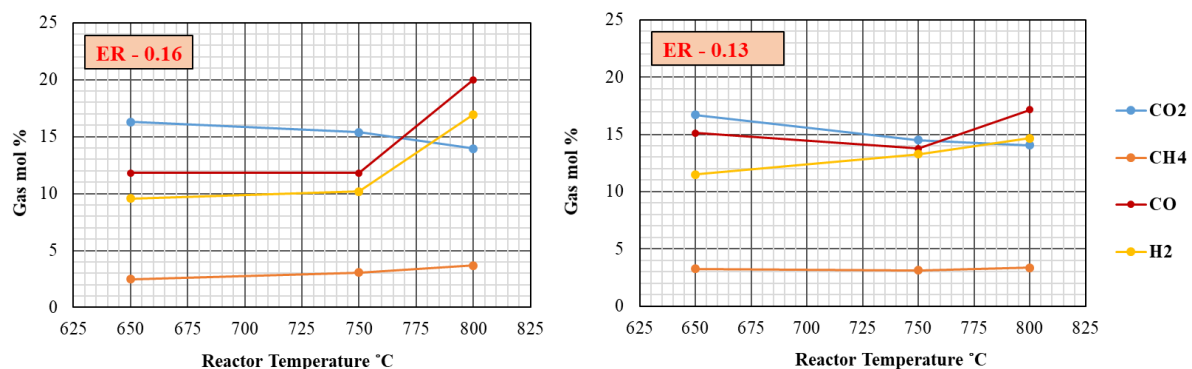


Figure 11: Gas composition of CH₄, H₂, CO₂ and CO as a function of reactor temperature for woodchips.

The total energy yield, which is a function of the gas heating value and the gas yield, has an equal importance as the gas composition, especially when the product gas is used for thermal energy generation. The performance indicators of the product gas flow, gas yield, LHV, carbon conversion efficiency (CCE %), cold gas efficiency (CGE %) and energy production rate for woodchips at different temperatures and ERs are given in Table 4. The product gas flow was calculated using N₂ balance where the accuracy mainly depends on precise measurement of the inlet air flowrate and the GC measurements. As the calculating steps of LHV, CCE% and CGE% are incorporated with the gas yield, any uncertainty involved with the product gas flowrate can appear in those parameters too.

Table 4: Gasification performance indicators for wood chips

ER	Product Gas (Nm ³ /h)	Gas Yield (Nm ³ /kg biomass)	LHV (MJ/Nm ³)	CCE %	CGE %	Energy Rate (MJ/h)
650°C						
0.08	2.11	0.92	5.52	38.80	28.15	11.65
0.1	2.44	1.06	4.53	38.90	26.70	11.05
0.13	3.07	1.33	4.31	50.13	31.98	13.24
0.16	3.27	1.42	3.41	46.62	26.97	11.16
750°C						
0.08	2.71	1.18	6.86	54.10	44.85	18.57
0.1	2.78	1.21	5.35	46.92	35.89	14.86
0.13	2.92	1.27	3.91	41.78	27.59	11.42
0.16	3.31	1.44	3.68	46.66	29.47	12.20
800°C						
0.08	2.90	1.26	7.25	57.83	50.89	21.07
0.1	2.77	1.21	5.48	45.36	36.67	15.18
0.13	3.22	1.40	4.94	51.79	38.42	15.90
0.16	4.32	1.88	5.68	75.83	59.27	24.54

The sharp change of the gasification temperature from 750°C and 800°C is clearly reflected by the data in Table 4 as well. Similar to the gas composition, a significant difference cannot be observed in the gas yield between 650°C and 750°C for the entire ER range. However, as the values compared for 0.16 ER, the gas yield has improved by 30% at 800°C compared to 750°C. The increasing trend and numerical values of gas yield are similar to literature data. LHV is mainly a function of the relative compositions of H₂, CO and CH₄, which therefore decreases with the ER and increases with the temperature. In spite of some minor deviation, the CCE% and CGE% are improved with both ER and temperature. The energy flow was calculated as a multiplication of gas flowrate and the LHV, which is considerably low at 650°C and gradually improves for higher temperatures. According to the authors, the better operating conditions are highlighted in the Table 4. The combination of temperature 800°C and 0.08 ER gives the highest LHV. Nevertheless the CCE% and CGE% are relatively low. Similarly, respective values are even lower at 750°C and 0.08 ER. Despite the fact of slightly lower LHV of 5.68 MJ/Nm³, the temperature of 800°C with 0.16 ER gives the best values for other parameters where the CCE% and CGE% have reasonable values of 76% and 60% respectively. Therefore, any prospected experiments at higher ERs should be carried out above 800°C reactor temperature. Char accumulation was not observed in the bed at 800°C temperature and 0.16 ER. Therefore,

remaining 24% of the carbon is included in the tar, elutriated fine char and soot carbon.

4.1.2 Gasification of Wood pellets and grass pellets.

The gas compositions for wood pellets are given in Figure 12 and Figure 13, whereas Figure 14 presents the information related to grass pellet gasification. Equivalent information as in Table 4 for wood pellets and grass pellets are given in Table A1 and Table A2 respectively in appendix. The gas compositions related to all the experimental runs are given in Table A3. The ERs of wood pellets and grass pellets are slightly different from wood chips as it was difficult to fine tune the screw feeder. Grass pellets contain significantly higher ash content compared wood and moreover, the ash melting temperature is lower. This fact was reflected with the failed attempts of operating the reactor over 800°C where large agglomerates formed covering the total reactor cross section. A picture of an agglomerate formed during the experiments is given in Figure 15. Successful experiments could perform for 0.07 and 0.1 ER at 800°C temperature. However, the oxygen loading is above 0.1 ER, which leads to local hotspots that initiate agglomerates.

Wood chips and wood pellets show approximately similar results. However, a clear difference can be observed in gas compositions of grass pellets gasification compared to the wood chips and wood pellets. The H₂ and CO fractions are lower for grass pellets in all the experiments, whereas the CO₂ fraction is higher. At 650°C, the gas composition from wood chip is richer in H₂ and CO than for wood pellets. In contrast at 750°C, the wood pellets gas composition is richer in H₂ and CO. At elevated temperature, a clear trend cannot be observed for wood chips and wood pellets. Wood chips are higher in moisture than wood pellets whereas wood pellets might lose a fraction of volatiles during pelletizing process.

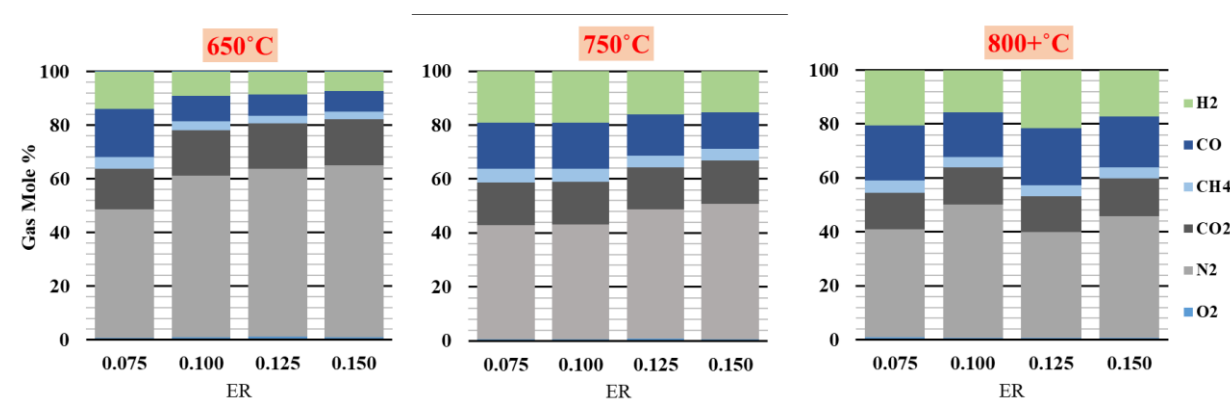


Figure 12: Product gas composition for wood pellets at different equivalence ratio and reactor temperatures

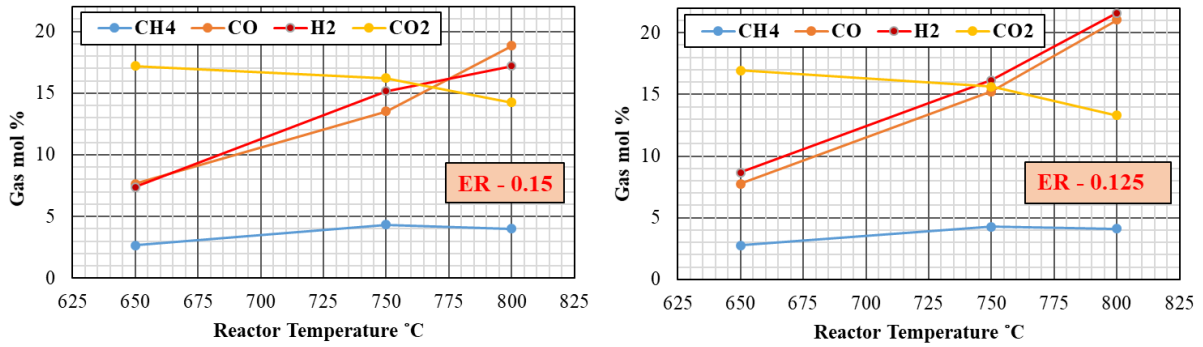


Figure 13: Gas composition of CH₄, H₂, CO and CO₂ as a function of reactor temperature for wood pellets

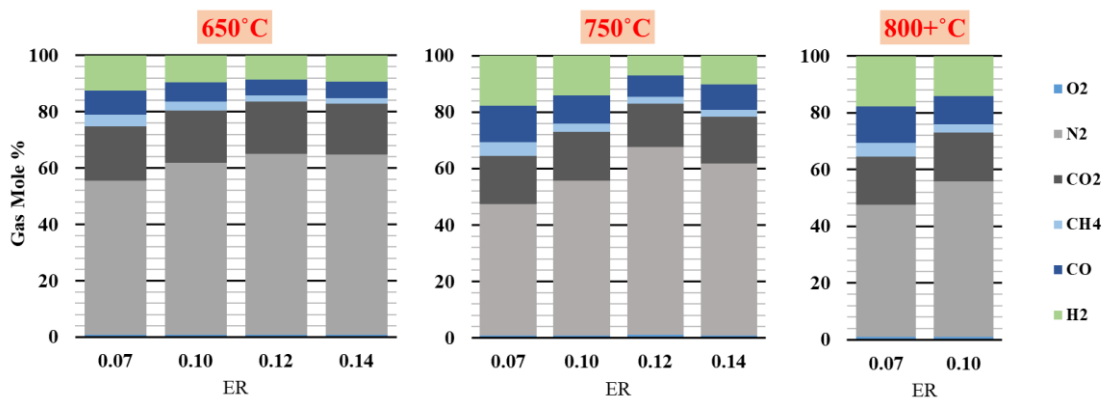


Figure 14: Product gas composition for grass pellets at different equivalence ratio and reactor temperatures



Figure 15: Formation of agglomerates during grass pellet gasification

The CCE% and the CGE% improve with temperature and ER. A significant difference of the gas yield (+34%), LHV (+15%), CCE (+46%) and CGE (+54%) can be observed between 0.13 and 0.16 ERs at the 800°C temperature for wood chips. In contrast, the particular parameters are approximately similar for wood pellets between 0.125 and 0.15 ERs. In general, the gasification performance parameters for wood pellets are better in 750°C temperature range

whereas wood chips have the best gasifier performance at 800°C. In the temperature ranges of 750 °C and 800 °C, the temperature variation was $\pm 20^\circ\text{C}$, which could be a decisive factor for the comparison of gas compositions and other parameters of CGE% and CCE%.

As the wood chips and pellets are concerned, the reduced CCE% is mainly due to unaccounted tar and char particle migration with the exhaust gas stream. Further, a char accumulation was observed at reduced ERs and temperatures. If the char particle migration is assumed to be similar at specific ERs, the improved carbon conversion at elevated temperature is mainly due to triggered tar cracking reactions. Further, according to the literature, tar yield from pyrolysis is maximized between 500°C and 600°C, and is sharply reduced above 700°C (Di Blasi, Signorelli, Di Russo, & Rea, 1999). However, the CCE is not significantly improved with temperature for the grass pellets. Therefore, it can be concluded that the migration of char particles with the exhaust gas is the dominant factor for the reduced CCE related to grass pellets.

5 Conclusion

Gasification is a proven technology in converting solid biomass into a gaseous mixture of H_2 , CO and CH_4 as the main components with an energy potential. The product gas is versatile as a feedstock for liquid fuel synthesis and for direct energy applications. Fluidized bed gasification is attractive over fixed bed designing, especially due to its ability of large scale operation.

Three different biomass feedstock of wood chip, wood pellet and grass pellets, were gasified in an electrically heated bubbling fluidized bed reactor. Four different ERs from 0.075 to 0.16 and three different temperatures of 650 °C, 750 °C and 800 °C were tested. Discontinuous biomass feed and $\pm 20^\circ\text{C}$ temperature variation could add uncertainty during the comparison between different feedstock. Authors suggest a modification to the biomass feeding conveyor which could avoid discontinuous feeding.

Gasification of grass pellets were not successful due to agglomerations and reduced carbon conversion. Further experimental efforts with different bed material sizes are suggested for the grass pellets. Both wood chips and pellets gave extremely good gas compositions. At lower temperatures, increased ER reduced the gas quality as a result of N_2 dilution. In contrast at 800°C temperature, minor reduction in the H_2 and CO content with increased ER was outweighed by improved carbon conversion and gas yield. The respective H_2 and CO contents were 16.9% and 20% for wood chips and 17.2% and 18.8% for wood pellets at 800 °C temperature and 0.16 ER. Reactor temperature of 650 °C was not sufficient to obtain an acceptable gas composition and carbon conversion. Progressively, the gas quality was improved at 750 °C and however, the carbon conversion was approximately 50%. The best reactor performance for wood chips happened at 800 °C and 0.16 ER with 75% carbon conversion efficiency. For wood pellets, both 0.125 and 0.15 ER at 800 °C gave the best overall performance with 70% carbon conversion. The main motivation for using low ERs compared to literature values was to identify the minimum ER that is sufficient to maintain a steady char

content without accumulation in the bed. ER around 0.15 can be identified as the minimum value.

Acknowledgement

The authors would like to extend their sincere thanks to the workshop and members of the gasification research group at the University of South-eastern Norway.

Appendix

Table A1: Gasification performance indicators for wood pellets

ER	Product Gas (Nm3/h)	Gas Yield (Nm3/kg biomass)	LHV (MJ/Nm3)	CCE %	CGE %	Energy Rate (MJ/h)
650°C						
0.075	2.02	0.84	5.38	33.64	25.00	10.89
0.1	2.14	0.88	3.36	28.19	16.54	7.20
0.125	2.57	1.06	2.91	31.25	17.14	7.47
0.15	3.01	1.25	2.71	36.69	18.76	8.17
750°C						
0.075	2.29	0.94	6.05	38.28	31.72	13.82
0.1	3.03	1.25	6.00	50.60	41.77	18.19
0.125	3.37	1.39	5.19	52.36	40.12	17.48
0.15	3.86	1.60	4.89	58.28	43.42	18.91
800°C						
0.075	2.41	1.00	6.40	41.23	35.42	15.43
0.1	2.61	1.08	5.13	39.42	30.73	13.39
0.125	4.11	1.70	6.45	69.93	60.85	26.51
0.15	4.30	1.78	5.66	70.62	55.91	24.35

Table A2: Gasification performance indicators for grass pellets

ER	Product Gas (Nm3/h)	Gas Yield (Nm3/kg biomass)	LHV (MJ/Nm3)	CCE %	CGE %	Energy Rate (MJ/h)
650°C						
0.07	1.77	0.65	3.96	22.43	14.33	7.01
0.1	2.11	0.78	3.02	23.71	13.03	6.38
0.12	2.51	0.92	2.41	26.06	12.36	6.05
0.14	3.03	1.11	2.43	30.95	15.04	7.36
750°C						
0.07	2.08	0.76	5.26	28.50	22.33	10.93
0.1	2.35	0.86	3.85	27.81	18.48	9.05
0.12	2.42	0.89	2.60	24.38	12.89	6.31
0.14	3.18	1.17	3.14	34.94	20.34	9.96
800°C						
0.07	2.08	0.76	5.26	28.50	22.33	10.93
0.1	2.35	0.86	3.85	27.81	18.48	9.05

Table A3: Gas molar composition for all experimental runs with different ERs, temperatures and feedstock

Wood Chips												
T (°C)	650.00				750.00				800+			
ER	0.080	0.100	0.130	0.160	0.080	0.100	0.130	0.160	0.080	0.100	0.130	0.160
O2	0.60	0.70	0.90	0.70	0.63	0.67	0.93	1.20	0.50	0.63	0.70	0.65
N2	45.83	52.90	52.53	59.15	35.73	46.40	55.13	58.40	33.30	46.53	50.10	44.75
CO2	15.40	14.95	16.70	16.30	14.83	15.37	17.23	15.37	13.20	13.77	14.05	13.95
CH4	4.17	3.40	3.27	2.50	4.67	3.93	3.37	3.07	4.30	3.77	3.35	3.70
CO	19.90	15.90	15.10	11.80	23.40	16.93	10.07	11.80	25.23	17.60	17.15	20.00
H2	14.10	12.15	11.50	9.55	20.73	16.70	13.27	10.17	23.47	17.70	14.65	16.95
CH4+H2+CO	38.17	31.45	29.87	23.85	48.80	37.57	26.70	25.03	53.00	39.07	35.15	40.65
Wood Pellets												
T (°C)	650.00				750.00				800+			
ER	0.075	0.100	0.125	0.150	0.075	0.100	0.125	0.150	0.075	0.100	0.125	0.150
O2	0.73	0.90	1.13	0.90	0.67	0.70	0.80	0.70	0.83	0.77	0.70	0.70
N2	47.83	60.23	62.73	64.20	42.33	42.55	47.90	50.07	40.10	49.40	39.25	45.00
CO2	15.07	17.00	16.93	17.20	15.67	15.60	15.63	16.20	13.67	13.83	13.30	14.25
CH4	4.53	3.33	2.77	2.65	5.10	5.00	4.27	4.33	4.50	3.77	4.10	4.00
CO	17.97	9.40	7.77	7.65	17.07	17.10	15.23	13.53	20.43	16.50	21.05	18.85
H2	13.87	9.13	8.67	7.40	19.17	19.05	16.17	15.17	20.47	15.73	21.60	17.20
CH4+H2+CO	36.37	21.87	19.20	17.70	41.33	41.15	35.67	33.03	45.40	36.00	46.75	40.05
Grass Pellets												
T (°C)	650.00				750.00				800+			
ER	0.070	0.100	0.120	0.140	0.070	0.100	0.120	0.140	0.070	0.100	0.120	0.140
O2	0.80	0.93	0.87	0.90	0.93	0.93	1.03	0.87	0.93	0.93		
N2	54.63	61.07	64.27	63.93	46.53	54.87	66.50	60.93	46.53	54.87		
CO2	19.33	18.50	18.43	18.10	17.10	17.10	15.37	16.50	17.10	17.10		
CH4	4.33	3.17	2.13	1.93	4.80	2.97	2.47	2.53	4.80	2.97		
CO	8.50	6.83	5.80	5.93	12.90	9.97	7.70	8.90	12.90	9.97		
H2	12.40	9.50	8.50	9.20	17.73	14.17	6.93	10.27	17.73	14.17		
CH4+H2+CO	25.23	19.50	16.43	17.07	35.43	27.10	17.10	21.70	35.43	27.10	0.00	0.00

Reference

- Abdoulmoumine, N., Adhikari, S., Kulkarni, A., & Chattanathan, S. (2015). A review on biomass gasification syngas cleanup. *Applied Energy*, *155*, 294-307. doi:<https://doi.org/10.1016/j.apenergy.2015.05.095>
- Abdoulmoumine, N., Kulkarni, A., & Adhikari, S. (2014). Effects of Temperature and Equivalence Ratio on Pine Syngas Primary Gases and Contaminants in a Bench-Scale Fluidized Bed Gasifier. *Industrial & Engineering Chemistry Research*, *53*(14), 5767-5777. doi:10.1021/ie404401n
- Acharya, B., Dutta, A., & Basu, P. (2009). Chemical-Looping Gasification of Biomass for Hydrogen-Enriched Gas Production with In-Process Carbon Dioxide Capture. *Energy & Fuels*, *23*(10), 5077-5083. doi:10.1021/ef9003889
- Afgan, N. H., Gobaisi, D. A., Carvalho, M. G., & Cumo, M. (1998). Sustainable energy development. *Renewable and Sustainable Energy Reviews*, *2*(3), 235-286. doi:[http://dx.doi.org/10.1016/S1364-0321\(98\)00002-1](http://dx.doi.org/10.1016/S1364-0321(98)00002-1)
- Agu, C. E., Tokheim, L.-A., Pfeifer, C., & Moldestad, B. M. E. (2019). Behaviour of biomass particles in a bubbling fluidized bed: A comparison between wood pellets and wood chips. *Chemical Engineering Journal*, *363*, 84-98. doi:<https://doi.org/10.1016/j.cej.2019.01.120>
- Ahrenfeldt, J., Thomsen, T. P., Henriksen, U., & Clausen, L. R. (2013). Biomass gasification cogeneration – A review of state of the art technology and near future perspectives. *Applied Thermal Engineering*, *50*(2), 1407-1417. doi:<https://doi.org/10.1016/j.applthermaleng.2011.12.040>
- Anis, S., & Zainal, Z. A. (2011). Tar reduction in biomass producer gas via mechanical, catalytic and thermal methods: A review. *Renewable and Sustainable Energy Reviews*, *15*(5), 2355-2377. doi:<https://doi.org/10.1016/j.rser.2011.02.018>
- Arena, U., & Di Gregorio, F. (2014). Gasification of a solid recovered fuel in a pilot scale fluidized bed reactor. *Fuel*, *117*, 528-536. doi:<https://doi.org/10.1016/j.fuel.2013.09.044>
- Asadullah, M. (2014a). Barriers of commercial power generation using biomass gasification gas: A review. *Renewable and Sustainable Energy Reviews*, *29*, 201-215. doi:<https://doi.org/10.1016/j.rser.2013.08.074>
- Asadullah, M. (2014b). Biomass gasification gas cleaning for downstream applications: A comparative critical review. *Renewable and Sustainable Energy Reviews*, *40*, 118-132. doi:<https://doi.org/10.1016/j.rser.2014.07.132>
- Aydin, E. S., Yucel, O., & Sadikoglu, H. (2018). Numerical and experimental investigation of hydrogen-rich syngas production via biomass gasification. *International Journal of Hydrogen Energy*, *43*(2), 1105-1115. doi:<https://doi.org/10.1016/j.ijhydene.2017.11.013>

- Behainne, J. J. R., & Martinez, J. D. (2014). Performance analysis of an air-blown pilot fluidized bed gasifier for rice husk. *Energy for Sustainable Development*, 18, 75-82. doi:<https://doi.org/10.1016/j.esd.2013.11.008>
- Belgiorno, V., De Feo, G., Della Rocca, C., & Napoli, R. M. A. (2003). Energy from gasification of solid wastes. *Waste Management*, 23(1), 1-15. doi:[https://doi.org/10.1016/S0956-053X\(02\)00149-6](https://doi.org/10.1016/S0956-053X(02)00149-6)
- Campoy, M., Gómez-Barea, A., Vidal, F. B., & Ollero, P. (2009). Air–steam gasification of biomass in a fluidised bed: Process optimisation by enriched air. *Fuel Processing Technology*, 90(5), 677-685. doi:<https://doi.org/10.1016/j.fuproc.2008.12.007>
- Campoy, M., Gómez-Barea, A., Villanueva, A. L., & Ollero, P. (2008). Air–Steam Gasification of Biomass in a Fluidized Bed under Simulated Autothermal and Adiabatic Conditions. *Industrial & Engineering Chemistry Research*, 47(16), 5957-5965. doi:10.1021/ie800220t
- Cheng, F., Bayat, H., Jena, U., & Brewer, C. E. (2020). Impact of feedstock composition on pyrolysis of low-cost, protein- and lignin-rich biomass: A review. *Journal of Analytical and Applied Pyrolysis*, 104780. doi:<https://doi.org/10.1016/j.jaap.2020.104780>
- Couto, N., Rouboa, A., Silva, V., Monteiro, E., & Bouziane, K. (2013). Influence of the Biomass Gasification Processes on the Final Composition of Syngas. *Energy Procedia*, 36, 596-606. doi:<https://doi.org/10.1016/j.egypro.2013.07.068>
- Cui, H., & Grace, J. R. (2007). Fluidization of biomass particles: A review of experimental multiphase flow aspects. *Chemical Engineering Science*, 62(1), 45-55. doi:<https://doi.org/10.1016/j.ces.2006.08.006>
- Dai, J., Cui, H., & Grace, J. R. (2012). Biomass feeding for thermochemical reactors. *Progress in Energy and Combustion Science*, 38(5), 716-736. doi:<https://doi.org/10.1016/j.pecs.2012.04.002>
- Danish, & Wang, Z. (2019). Does biomass energy consumption help to control environmental pollution? Evidence from BRICS countries. *Science of The Total Environment*, 670, 1075-1083. doi:<https://doi.org/10.1016/j.scitotenv.2019.03.268>
- Devi, L., Ptasiński, K. J., & Janssen, F. J. J. G. (2003). A review of the primary measures for tar elimination in biomass gasification processes. *Biomass and Bioenergy*, 24(2), 125-140. doi:[https://doi.org/10.1016/S0961-9534\(02\)00102-2](https://doi.org/10.1016/S0961-9534(02)00102-2)
- Dhanavath, K. N., Shah, K., Islam, M. S., Ronte, A., Parthasarathy, R., Bhargava, S. K., & Bankupalli, S. (2018). Experimental investigations on entrained flow gasification of Torrefied Karanja Press Seed Cake. *Journal of Environmental Chemical Engineering*, 6(1), 1242-1249. doi:<https://doi.org/10.1016/j.jece.2017.12.061>
- Di Blasi, C. (2009). Combustion and gasification rates of lignocellulosic chars. *Progress in Energy and Combustion Science*, 35(2), 121-140. doi:<https://doi.org/10.1016/j.pecs.2008.08.001>

- Di Blasi, C., Signorelli, G., Di Russo, C., & Rea, G. (1999). Product Distribution from Pyrolysis of Wood and Agricultural Residues. *Industrial & Engineering Chemistry Research*, 38(6), 2216-2224. doi:[10.1021/ie980711u](https://doi.org/10.1021/ie980711u)
- Ferreira, S. D., Lazzarotto, I. P., Junges, J., Manera, C., Godinho, M., & Osório, E. (2017). Steam gasification of biochar derived from elephant grass pyrolysis in a screw reactor. *Energy Conversion and Management*, 153, 163-174. doi:<https://doi.org/10.1016/j.enconman.2017.10.006>
- Fleck, S., Santo, U., Hotz, C., Jakobs, T., Eckel, G., Mancini, M., . . . Kolb, T. (2018). Entrained flow gasification Part 1: Gasification of glycol in an atmospheric-pressure experimental rig. *Fuel*, 217, 306-319. doi:<https://doi.org/10.1016/j.fuel.2017.12.077>
- Fremaux, S., Beheshti, S.-M., Ghassemi, H., & Shahsavan-Markadeh, R. (2015). An experimental study on hydrogen-rich gas production via steam gasification of biomass in a research-scale fluidized bed. *Energy Conversion and Management*, 91, 427-432. doi:<https://doi.org/10.1016/j.enconman.2014.12.048>
- Fukutome, A., Kawamoto, H., & Saka, S. (2014). Gas- and coke/soot-forming reactivities of cellulose-derived tar components under nitrogen and oxygen/nitrogen. *Journal of Analytical and Applied Pyrolysis*, 108, 98-108. doi:<https://doi.org/10.1016/j.jaap.2014.05.012>
- Ghassemi, H., & Shahsavan-Markadeh, R. (2014). Effects of various operational parameters on biomass gasification process; a modified equilibrium model. *Energy Conversion and Management*, 79, 18-24. doi:<https://doi.org/10.1016/j.enconman.2013.12.007>
- Gómez-Barea, A., & Leckner, B. (2010). Modeling of biomass gasification in fluidized bed. *Progress in Energy and Combustion Science*, 36(4), 444-509. doi:<https://doi.org/10.1016/j.pecs.2009.12.002>
- González-Vázquez, M. P., García, R., Gil, M. V., Pevida, C., & Rubiera, F. (2018). Comparison of the gasification performance of multiple biomass types in a bubbling fluidized bed. *Energy Conversion and Management*, 176, 309-323. doi:<https://doi.org/10.1016/j.enconman.2018.09.020>
- Hameed, S., Sharma, A., Pareek, V., Wu, H., & Yu, Y. (2019). A review on biomass pyrolysis models: Kinetic, network and mechanistic models. *Biomass and Bioenergy*, 123, 104-122. doi:<https://doi.org/10.1016/j.biombioe.2019.02.008>
- Han, J., & Kim, H. (2008). The reduction and control technology of tar during biomass gasification/pyrolysis: An overview. *Renewable and Sustainable Energy Reviews*, 12(2), 397-416. doi:<https://doi.org/10.1016/j.rser.2006.07.015>
- Hanaoka, T., Inoue, S., Uno, S., Ogi, T., & Minowa, T. (2005). Effect of woody biomass components on air-steam gasification. *Biomass and Bioenergy*, 28(1), 69-76. doi:<https://doi.org/10.1016/j.biombioe.2004.03.008>
- Heidenreich, S., & Foscolo, P. U. (2015). New concepts in biomass gasification. *Progress in Energy and Combustion Science*, 46, 72-95. doi:<https://doi.org/10.1016/j.pecs.2014.06.002>

- Hervy, M., Remy, D., Dufour, A., & Mauviel, G. (2019). Air-blown gasification of Solid Recovered Fuels (SRFs) in lab-scale bubbling fluidized-bed: Influence of the operating conditions and of the SRF composition. *Energy Conversion and Management*, 181, 584-592. doi:<https://doi.org/10.1016/j.enconman.2018.12.052>
- Hoogwijk, M., Faaij, A., van den Broek, R., Berndes, G., Gielen, D., & Turkenburg, W. (2003). Exploration of the ranges of the global potential of biomass for energy. *Biomass and Bioenergy*, 25(2), 119-133. doi:[http://dx.doi.org/10.1016/S0961-9534\(02\)00191-5](http://dx.doi.org/10.1016/S0961-9534(02)00191-5)
- Islam, M. W. (2020). A review of dolomite catalyst for biomass gasification tar removal. *Fuel*, 267, 117095. doi:<https://doi.org/10.1016/j.fuel.2020.117095>
- Ismail, T. M., Ramos, A., Monteiro, E., El-Salam, M. A., & Rouboa, A. (2020). Parametric studies in the gasification agent and fluidization velocity during oxygen-enriched gasification of biomass in a pilot-scale fluidized bed: Experimental and numerical assessment. *Renewable Energy*, 147, 2429-2439. doi:<https://doi.org/10.1016/j.renene.2019.10.029>
- Ismail, W. M. S. W., Mohd Thaim, T., & Abdul Rasid, R. (2019). Biomass gasification of oil palm fronds (OPF) and *Koompassia malaccensis* (Kempas) in an entrained flow gasifier: A performance study. *Biomass and Bioenergy*, 124, 83-87. doi:<https://doi.org/10.1016/j.biombioe.2019.03.012>
- Karatas, H., Olgun, H., & Akgun, F. (2013). Experimental results of gasification of cotton stalk and hazelnut shell in a bubbling fluidized bed gasifier under air and steam atmospheres. *Fuel*, 112, 494-501. doi:<https://doi.org/10.1016/j.fuel.2013.04.025>
- Karl, J., & Pröll, T. (2018). Steam gasification of biomass in dual fluidized bed gasifiers: A review. *Renewable and Sustainable Energy Reviews*, 98, 64-78. doi:<https://doi.org/10.1016/j.rser.2018.09.010>
- Kaur-Sidhu, M., Ravindra, K., Mor, S., & John, S. (2020). Emission factors and global warming potential of various solid biomass fuel-cook stove combinations. *Atmospheric Pollution Research*, 11(2), 252-260. doi:<https://doi.org/10.1016/j.apr.2019.10.009>
- Kim, Y. D., Yang, C. W., Kim, B. J., Kim, K. S., Lee, J. W., Moon, J. H., . . . Lee, U. D. (2013). Air-blown gasification of woody biomass in a bubbling fluidized bed gasifier. *Applied Energy*, 112, 414-420. doi:<https://doi.org/10.1016/j.apenergy.2013.03.072>
- Kirch, T., Medwell, P. R., Birzer, C. H., & van Eyk, P. J. (2020). Small-scale autothermal thermochemical conversion of multiple solid biomass feedstock. *Renewable Energy*, 149, 1261-1270. doi:10.1016/j.renene.2019.10.120
- Ku, X., Jin, H., & Lin, J. (2017). Comparison of gasification performances between raw and torrefied biomasses in an air-blown fluidized-bed gasifier. *Chemical Engineering Science*, 168, 235-249. doi:<https://doi.org/10.1016/j.ces.2017.04.050>
- Lapuerta, M., Hernández, J. J., Pazo, A., & López, J. (2008). Gasification and co-gasification of biomass wastes: Effect of the biomass origin and the gasifier operating conditions. *Fuel Processing Technology*, 89(9), 828-837. doi:<https://doi.org/10.1016/j.fuproc.2008.02.001>

- Makwana, J. P., Pandey, J., & Mishra, G. (2019). Improving the properties of producer gas using high temperature gasification of rice husk in a pilot scale fluidized bed gasifier (FBG). *Renewable Energy*, *130*, 943-951. doi:<https://doi.org/10.1016/j.renene.2018.07.011>
- Mani, T., Mahinpey, N., & Murugan, P. (2011). Reaction kinetics and mass transfer studies of biomass char gasification with CO₂. *Chemical Engineering Science*, *66*(1), 36-41. doi:<https://doi.org/10.1016/j.ces.2010.09.033>
- Mauerhofer, A. M., Schmid, J. C., Benedikt, F., Fuchs, J., Müller, S., & Hofbauer, H. (2019). Dual fluidized bed steam gasification: Change of product gas quality along the reactor height. *Energy*, *173*, 1256-1272. doi:<https://doi.org/10.1016/j.energy.2019.02.025>
- Meng, F., Ma, Q., Wang, H., Liu, Y., & Wang, D. (2019). Effect of gasifying agents on sawdust gasification in a novel pilot scale bubbling fluidized bed system. *Fuel*, *249*, 112-118. doi:<https://doi.org/10.1016/j.fuel.2019.03.107>
- Motta, I. L., Miranda, N. T., Maciel Filho, R., & Wolf Maciel, M. R. (2018). Biomass gasification in fluidized beds: A review of biomass moisture content and operating pressure effects. *Renewable and Sustainable Energy Reviews*, *94*, 998-1023. doi:<https://doi.org/10.1016/j.rser.2018.06.042>
- Nam, H., Rodriguez-Alejandro, D. A., Adhikari, S., Brodbeck, C., Taylor, S., & Johnson, J. (2018). Experimental investigation of hardwood air gasification in a pilot scale bubbling fluidized bed reactor and CFD simulation of jet/grid and pressure conditions. *Energy Conversion and Management*, *168*, 599-610. doi:<https://doi.org/10.1016/j.enconman.2018.05.003>
- Narváez, I., Orío, A., Aznar, M. P., & Corella, J. (1996). Biomass Gasification with Air in an Atmospheric Bubbling Fluidized Bed. Effect of Six Operational Variables on the Quality of the Produced Raw Gas. *Industrial & Engineering Chemistry Research*, *35*(7), 2110-2120. doi:10.1021/ie9507540
- Neves, D., Thunman, H., Matos, A., Tarelho, L., & Gómez-Barea, A. (2011). Characterization and prediction of biomass pyrolysis products. *Progress in Energy and Combustion Science*, *37*(5), 611-630. doi:<https://doi.org/10.1016/j.peccs.2011.01.001>
- Njenga, M., Iiyama, M., Jamnadass, R., Helander, H., Larsson, L., de Leeuw, J., . . . Sundberg, C. (2016). Gasifier as a cleaner cooking system in rural Kenya. *Journal of Cleaner Production*, *121*, 208-217. doi:<https://doi.org/10.1016/j.jclepro.2016.01.039>
- Nunes, L. J. R., Causer, T. P., & Ciolkosz, D. (2020). Biomass for energy: A review on supply chain management models. *Renewable and Sustainable Energy Reviews*, *120*, 109658. doi:<https://doi.org/10.1016/j.rser.2019.109658>
- Ongen, A., Ozcan, H. K., & Ozbas, E. E. (2016). Gasification of biomass and treatment sludge in a fixed bed gasifier. *International Journal of Hydrogen Energy*, *41*(19), 8146-8153. doi:<https://doi.org/10.1016/j.ijhydene.2015.11.159>

- Parthasarathy, P., & Narayanan, K. S. (2014). Hydrogen production from steam gasification of biomass: Influence of process parameters on hydrogen yield – A review. *Renewable Energy*, 66, 570-579. doi:<https://doi.org/10.1016/j.renene.2013.12.025>
- Pereira, E. G., da Silva, J. N., de Oliveira, J. L., & Machado, C. S. (2012). Sustainable energy: A review of gasification technologies. *Renewable and Sustainable Energy Reviews*, 16(7), 4753-4762. doi:<https://doi.org/10.1016/j.rser.2012.04.023>
- Pio, D. T., Tarelho, L. A. C., & Matos, M. A. A. (2017). Characteristics of the gas produced during biomass direct gasification in an autothermal pilot-scale bubbling fluidized bed reactor. *Energy*, 120, 915-928. doi:<https://doi.org/10.1016/j.energy.2016.11.145>
- Pio, D. T., Tarelho, L. A. C., Tavares, A. M. A., Matos, M. A. A., & Silva, V. (2020). Co-gasification of refused derived fuel and biomass in a pilot-scale bubbling fluidized bed reactor. *Energy Conversion and Management*, 206, 112476. doi:<https://doi.org/10.1016/j.enconman.2020.112476>
- Reed, T. B., & Das, A. (1988). *Handbook of biomass downdraft gasifier engine systems*. Retrieved from United States: <https://www.osti.gov/servlets/purl/5206099>
- Ren, J., Cao, J.-P., Zhao, X.-Y., Yang, F.-L., & Wei, X.-Y. (2019). Recent advances in syngas production from biomass catalytic gasification: A critical review on reactors, catalysts, catalytic mechanisms and mathematical models. *Renewable and Sustainable Energy Reviews*, 116, 109426. doi:<https://doi.org/10.1016/j.rser.2019.109426>
- Ren, J., Liu, Y.-L., Zhao, X.-Y., & Cao, J.-P. (2019). Biomass thermochemical conversion: A review on tar elimination from biomass catalytic gasification. *Journal of the Energy Institute*. doi:<https://doi.org/10.1016/j.joei.2019.10.003>
- Safarian, S., Unnpórsson, R., & Richter, C. (2019). A review of biomass gasification modelling. *Renewable and Sustainable Energy Reviews*, 110, 378-391. doi:<https://doi.org/10.1016/j.rser.2019.05.003>
- Sansaniwal, S. K., Pal, K., Rosen, M. A., & Tyagi, S. K. (2017). Recent advances in the development of biomass gasification technology: A comprehensive review. *Renewable and Sustainable Energy Reviews*, 72, 363-384. doi:<https://doi.org/10.1016/j.rser.2017.01.038>
- Sarker, S., Bimbela, F., Sánchez, J. L., & Nielsen, H. K. (2015). Characterization and pilot scale fluidized bed gasification of herbaceous biomass: A case study on alfalfa pellets. *Energy Conversion and Management*, 91, 451-458. doi:<https://doi.org/10.1016/j.enconman.2014.12.034>
- Sattar, A., Leeke, G. A., Hornung, A., & Wood, J. (2014). Steam gasification of rapeseed, wood, sewage sludge and miscanthus biochars for the production of a hydrogen-rich syngas. *Biomass and Bioenergy*, 69, 276-286. doi:<https://doi.org/10.1016/j.biombioe.2014.07.025>
- Schneider, J., Grube, C., Herrmann, A., & Rönsch, S. (2016). Atmospheric entrained-flow gasification of biomass and lignite for decentralized applications. *Fuel Processing Technology*, 152, 72-82. doi:<https://doi.org/10.1016/j.fuproc.2016.05.047>

- Serrano, D., Kwapinska, M., Horvat, A., Sánchez-Delgado, S., & Leahy, J. J. (2016). Cynara cardunculus L. gasification in a bubbling fluidized bed: The effect of magnesite and olivine on product gas, tar and gasification performance. *Fuel*, 173, 247-259. doi:<https://doi.org/10.1016/j.fuel.2016.01.051>
- Shahbaz, M., Yusup, S., Inayat, A., Patrick, D. O., & Ammar, M. (2017). The influence of catalysts in biomass steam gasification and catalytic potential of coal bottom ash in biomass steam gasification: A review. *Renewable and Sustainable Energy Reviews*, 73, 468-476. doi:<https://doi.org/10.1016/j.rser.2017.01.153>
- Shen, Y., & Yoshikawa, K. (2013). Recent progresses in catalytic tar elimination during biomass gasification or pyrolysis—A review. *Renewable and Sustainable Energy Reviews*, 21, 371-392. doi:<https://doi.org/10.1016/j.rser.2012.12.062>
- Sheth, P. N., & Babu, B. V. (2009). Experimental studies on producer gas generation from wood waste in a downdraft biomass gasifier. *Bioresource Technology*, 100(12), 3127-3133. doi:<https://doi.org/10.1016/j.biortech.2009.01.024>
- Sikarwar, V. S., Zhao, M., Clough, P., Yao, J., Zhong, X., Memon, M. Z., . . . Fennell, P. S. (2016). An overview of advances in biomass gasification. *Energy & Environmental Science*, 9(10), 2939-2977. doi:10.1039/C6EE00935B
- Singh Siwal, S., Zhang, Q., Sun, C., Thakur, S., Kumar Gupta, V., & Kumar Thakur, V. (2020). Energy production from steam gasification processes and parameters that contemplate in biomass gasifier – A review. *Bioresource Technology*, 297, 122481. doi:<https://doi.org/10.1016/j.biortech.2019.122481>
- Soria, J., Li, R., Flamant, G., & Mazza, G. D. (2019). Influence of pellet size on product yields and syngas composition during solar-driven high temperature fast pyrolysis of biomass. *Journal of Analytical and Applied Pyrolysis*, 140, 299-311. doi:<https://doi.org/10.1016/j.jaap.2019.04.007>
- Subramanian, P., Sampathrajan, A., & Venkatachalam, P. (2011). Fluidized bed gasification of select granular biomaterials. *Bioresource Technology*, 102(2), 1914-1920. doi:<https://doi.org/10.1016/j.biortech.2010.08.022>
- Sulaiman, C., Abdul-Rahim, A. S., & Ofor, C. A. (2020). Does wood biomass energy use reduce CO2 emissions in European Union member countries? Evidence from 27 members. *Journal of Cleaner Production*, 253, 119996. doi:<https://doi.org/10.1016/j.jclepro.2020.119996>
- Sun, X., Atiyeh, H. K., Huhnke, R. L., & Tanner, R. S. (2019). Syngas fermentation process development for production of biofuels and chemicals: A review. *Bioresource Technology Reports*, 7, 100279. doi:<https://doi.org/10.1016/j.biteb.2019.100279>
- Surjosatyo, A., Anggriawan, M. B., Hermawan, A. A., & Dafiqurrohman, H. (2019). Comparison between secondary thermal cracking methods and venturi scrubber filtering in order to reduce tar in biomass gasification. *Energy Procedia*, 158, 749-754. doi:<https://doi.org/10.1016/j.egypro.2019.01.200>

- Susastriawan, A. A. P., Saptoadi, H., & Purnomo. (2017). Small-scale downdraft gasifiers for biomass gasification: A review. *Renewable and Sustainable Energy Reviews*, 76, 989-1003. doi:<https://doi.org/10.1016/j.rser.2017.03.112>
- Szczodrak, J., & Fiedurek, J. (1996). Technology for conversion of lignocellulosic biomass to ethanol. *Biomass and Bioenergy*, 10(5), 367-375. doi:[http://dx.doi.org/10.1016/0961-9534\(95\)00114-X](http://dx.doi.org/10.1016/0961-9534(95)00114-X)
- Tong, W., Liu, Q., Yang, C., Cai, Z., Wu, H., & Ren, S. (2019). Effect of pore structure on CO₂ gasification reactivity of biomass chars under high-temperature pyrolysis. *Journal of the Energy Institute*. doi:<https://doi.org/10.1016/j.joei.2019.08.007>
- Valderrama Rios, M. L., González, A. M., Lora, E. E. S., & Almazán del Olmo, O. A. (2018). Reduction of tar generated during biomass gasification: A review. *Biomass and Bioenergy*, 108, 345-370. doi:<https://doi.org/10.1016/j.biombioe.2017.12.002>
- Varunkumar, S., Rajan, N. K. S., & Mukunda, H. S. (2012). Experimental and computational studies on a gasifier based stove. *Energy Conversion and Management*, 53(1), 135-141. doi:<https://doi.org/10.1016/j.enconman.2011.08.022>
- Wang, G., Zhang, J., Shao, J., Liu, Z., Wang, H., Li, X., . . . Zhang, G. (2016). Experimental and modeling studies on CO₂ gasification of biomass chars. *Energy*, 114, 143-154. doi:<https://doi.org/10.1016/j.energy.2016.08.002>
- Warnecke, R. (2000). Gasification of biomass: comparison of fixed bed and fluidized bed gasifier. *Biomass and Bioenergy*, 18(6), 489-497. doi:[https://doi.org/10.1016/S0961-9534\(00\)00009-X](https://doi.org/10.1016/S0961-9534(00)00009-X)
- White, J. E., Catallo, W. J., & Legendre, B. L. (2011). Biomass pyrolysis kinetics: A comparative critical review with relevant agricultural residue case studies. *Journal of Analytical and Applied Pyrolysis*, 91(1), 1-33. doi:<https://doi.org/10.1016/j.jaap.2011.01.004>
- Widjaya, E. R., Chen, G., Bowtell, L., & Hills, C. (2018). Gasification of non-woody biomass: A literature review. *Renewable and Sustainable Energy Reviews*, 89, 184-193. doi:<https://doi.org/10.1016/j.rser.2018.03.023>
- Xu, C., Chen, S., Soomro, A., Sun, Z., & Xiang, W. (2018). Hydrogen rich syngas production from biomass gasification using synthesized Fe/CaO active catalysts. *Journal of the Energy Institute*, 91(6), 805-816. doi:<https://doi.org/10.1016/j.joei.2017.10.014>
- Yu, M. M., Masnadi, M. S., Grace, J. R., Bi, X. T., Lim, C. J., & Li, Y. (2015). Co-gasification of biosolids with biomass: Thermogravimetric analysis and pilot scale study in a bubbling fluidized bed reactor. *Bioresource Technology*, 175, 51-58. doi:<https://doi.org/10.1016/j.biortech.2014.10.045>
- Zhang, X., Zhang, M., Zhang, H., Jiang, Z., Liu, C., & Cai, W. (2020). A review on energy, environment and economic assessment in remanufacturing based on life cycle assessment method. *Journal of Cleaner Production*, 255, 120160. doi:<https://doi.org/10.1016/j.jclepro.2020.120160>

Zhang, Y., Xu, P., Liang, S., Liu, B., Shuai, Y., & Li, B. (2019). Exergy analysis of hydrogen production from steam gasification of biomass: A review. *International Journal of Hydrogen Energy*, 44(28), 14290-14302.
doi:<https://doi.org/10.1016/j.ijhydene.2019.02.064>

Paper I

Ali Moradi, Nastaran Ahmadpour Samani, Masih Mojarrad, Mohammad Sharfuddin,
Janitha C. Bandara, Britt M. E. Moldestad

Experimental and Computational studies of circulating fluidized bed

Journal: International Journal of Energy Production and Management, 2020, Volume
05, PP 302-313 16-18 June 2020 (online)

EXPERIMENTAL AND COMPUTATIONAL STUDIES OF CIRCULATING FLUIDIZED BED

ALI MORADI, NASTARAN AHMADPOUR SAMANI, MASIH MOJARRAD, MOHAMMAD SHARFUDDIN, JANITHA C. BANDARA & BRITT M. E. MOLDESTAD
University of South-Eastern Norway, Norway.

ABSTRACT

Biomass gasification represents an efficient process for the production of power, heat and biofuels. Different technologies are used for gasification and this article focuses on a circulating fluidized bed (CFB) system. Understanding the behaviour of particles is of primary importance and a cold flow CFB experimental unit was constructed and tested. The particle circulation rate is greatly affected by the loop seal performance, and therefore the loop seal should be properly optimized to maintain an uninterrupted operation. Smooth flow regimes were obtained for the CFB by varying the loop seal aeration rates. Particles with size 850–1000 μm and 1000–1180 μm were chosen for the experiments. The minimum flow rates of air into the riser for the two particle sizes were found to be 1.3 and 1.5 Sm^3/min , respectively. To obtain a smooth flow regime, a velocity range for aeration in the loop seal was found for the two particle sizes. Based on the experimental results, combinations of flow rates were suggested for the simulations. A Computational Particle Fluid Dynamic (CPFD) model was developed using Barracuda VR, and the model was validated against experimental results. The simulated results for the system regarding the pressure and the height of the bed material in the standpipe agreed well with the experimental results. The deviation between the experimental and computational pressure was less than 0.5% at all the locations for both the particle sizes. The deviation in particle level was about 6% for the 850–1000 μm particles and 17% for the 1000–1150 μm particles. Both the experiments and the simulations predicted that a small fraction of the circulating sands are emitted from the top of the rig. The validated CPFD model was further used to predict the flow behaviour and the particle circulation rate in the CFB.

Keywords: Baracuda, circulating fluidized bed, CPFD, gasification, loop seal, multiphase flow.

1 INTRODUCTION

Consumption of energy is increasing rapidly worldwide and the expansion of renewable energy sources is needed. Scientists are working on the development of technologies and logistics related to energy extraction from renewable sources. Fluidized bed is a promising technology in biomass gasification and combustion due to good mixing capacity, which gives a high mass and energy transfer with uniform temperature over the gasifier. There are several potential configurations of fluidized bed reactors applicable for industrial operations. Circulating fluidized bed (CFB) is one of the technologies, which has come into the limelight during the previous two decades due to its extensive applications. CFB has been recently used in the combustion process, fluid catalytic cracking in petroleum refineries, gasification of coal and biomass, chemical synthesis, removal of pollutants, etc. [1]. The advantages of CFB gasification is that it has relatively low tar production, high degree of conversion, reduced residence time and good ability to scale-up.

A typical setup for a CFB reactor is presented schematically in Fig. 1. The CFB operates at the fast fluidization regime and consists of a riser, a cyclone, a downcomer and a gas-sealing mechanism such as a loop seal. The loop seal is a type of particle flow control valves designed for recycling of the particles back to the riser with a proper control. In the riser, the particles are fluidized by introduction of a fluid with a higher velocity than the particle terminal velocity. The fluid is fed from the bottom of the reactor. The loop seal is also needed to

aerate to keep the particle phase in fluidized conditions (i.e. over minimum fluidization). An efficient and safe design of CFB systems requires accurate predictions of the gas-particle behaviour at different process conditions. The rate of particle circulation is one of the most important parameters in any CFB system [2]. The application of the CPFDF numerical method to simulate a CFB with a loop seal has been previously studied by Wang *et al.* [3] and Bandara *et al.* [4]. The aim of their studies was to investigate the influence of the rate of loop seal aeration, fluidized air velocity in the riser and the total bed inventory on the particle circulation properties.

In this work, experimental studies of a CFB are performed to obtain a better understanding of the particle behaviour under varying loop seal and riser aeration conditions. The results will help to find smooth operational regimes for the CFB. The experiments were performed using sand particles as the bed material and air as the fluidizing fluid. Sand is often used as bed material in fluidized bed reactors. The bed material is used to ensure good mixing of the fuel and the fluidizing gas in the reactor, and to enhance the mass and energy transfer. In a biomass CFB reactor, the biomass reacts very fast with the gas, producing a synthesis gas and char. Unreacted char will follow the sand particles through the cyclone, the standpipe, the loop seal and back to the riser. The circulation behaviour will mainly be controlled by the sand particles and very little by the char, and using sand in the experiments and simulations will give a good indication of the flow behaviour in the CFB. This article includes both experimental results and development of a Computational Particle Fluid Dynamic (CPFDF) model to predict particle distribution at different positions in the CFB system, circulation

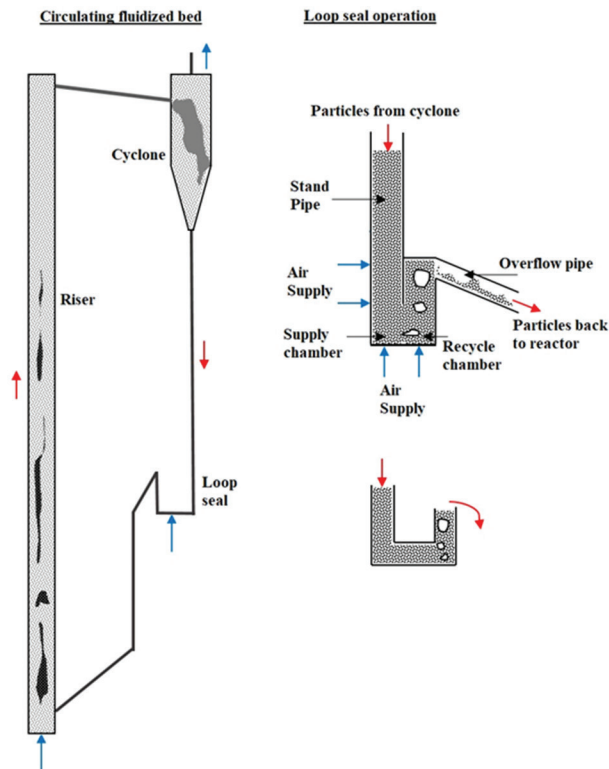


Figure 1: CFB system.

rates and pressure profiles. The CPFD simulation results were compared against experimental data.

2 MATERIALS AND METHODS

2.1 Experimental setup

The schematic of the CFB used for experiments is shown in Fig. 2. The inside diameter of the riser is 54 mm whereas the cyclone riser connections are constructed with 34 mm Plexiglas pipes. The riser stands 2300 mm high from the bottom gas-distributor plate. The horizontal section of the loop seal is a 34×34 mm section box with 100 mm in length. There are three fluid inlets to the CFB: the first in the bottom of the riser (FR1), the second in the bottom of the loop seal (FR2) and the third in the right-hand side of the loop seal standpipe (FR3).

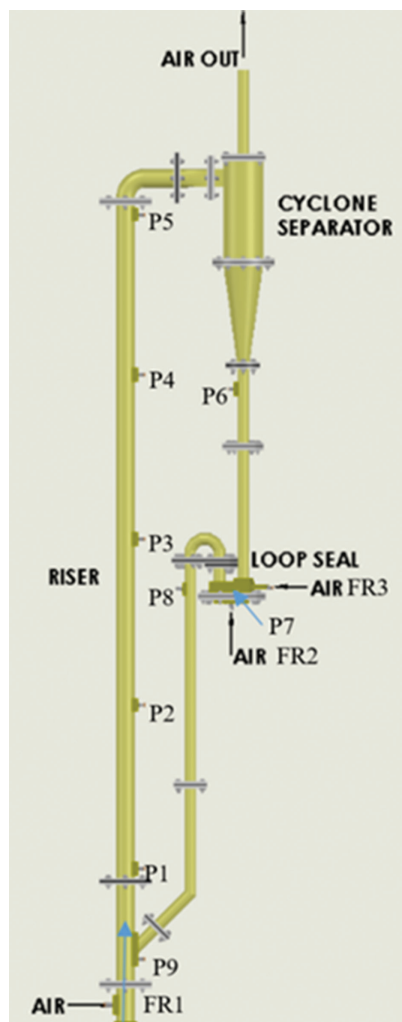


Figure 2: CAD drawing from SolidWorks of the experimental setup of CFB.

Sand with density 2650 kg/m^3 was used as the particle phase while the fluidizing gas was air. Initially, 520 mm of sand was filled into the loop seal and led to the riser by aerating FR2 and FR3. The flow rate of FR1 was gradually increased until the particles are conveyed to achieve a steady circulation of particles.

The aim of this study is to find the range of flow rates that can be used for FR2 and FR3, and the minimum flow rate of FR1. The minimum flow of FR1 is referred to as the velocity that maintains a steady flow in the riser, whereas the maximum flow is decided by the increasing amount of particles escaping with the cyclone gas outflow. Above the maximum velocity, the level of the sand in the standpipe became unstable and fluctuated considerably. For this purpose, FR3 was fixed at a very high flow rate (about $0.06 \text{ Sm}^3/\text{min}$) and FR2 was increased smoothly from zero until the sands started entering the riser. At that velocity, the minimum velocity for FR2 was observed and recorded. In the next step, FR2 was set at the recorded minimum value and FR3 was increased gradually from zero until the sand started to circulate. Then FR3 was increased by a step of $0.004 \text{ Sm}^3/\text{min}$ until the level of sand in the standpipe started to fluctuate. During the steady-state operation at each velocity, the system pressure and the flow rates of the sand inside the standpipe were recorded. To determine the flow rate of sand, FR2 and FR3 were closed and immediately the increasing sand level in the standpipe during a known time was observed and recorded. The sand flow rate was calculated from:

$$FR_p = \frac{A_s \cdot h}{t} \times \text{bulk density} \left(\frac{\text{kg}}{\text{s}} \right) \quad (1)$$

where FR_p is the flow rate of the sand inside the standpipe, A_s is the surface area of the pipe (9.0746 cm^2), h is the height of the accumulated particles in the standpipe and t is the time.

2.2 Development of a CPFDF model

The CPFDF model was developed in the Barracuda VR 17.3.0 commercial CFD code. The fluid domain is crucial for the calculations, and therefore the interior dimensions of the experimental unit were measured carefully. The model for the fluid domain was developed in the SolidWorks platform and was imported into CPFDF in STL file format. Subsequently, the fluid domain was captured into the computational grid using the grid generation tool. The grid resolution is a key parameter for the accuracy and meets the convergence of numerical calculation. Moreover, the wall boundaries, internal solid features, such as parcel resolution, and the boundary surfaces are also affected by the grid configuration in CPFDF. Figure 3 illustrates the generated grid over different sections of the CFB system. The grid resolution should be

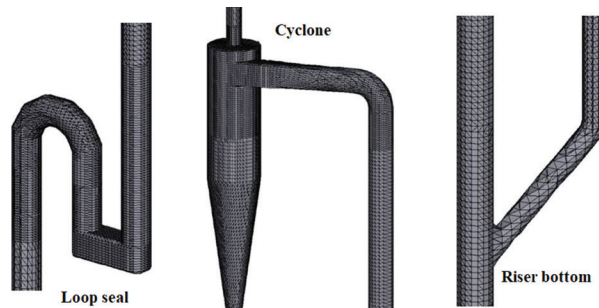


Figure 3: Grid generation for CPFDF modelling.

optimized with respect to accuracy and computational time, and the higher the number of cells the longer the computational time. For particle systems, there are limitations to the grid resolution, where the cell size should be several times larger than the size of the largest particles in the system. According to the studies of Bandara *et al.* [4], the grid resolution at the loop seal is the most crucial. Therefore, the loop seal grid was refined to the maximum extent, keeping an acceptable cell size to particle size ratio.

Fluid drag is the main force acting on the particles, and the general format of the drag force is expressed as:

$$F_p = m_p D (u_f - u_p) \quad (2)$$

where m_p is the mass of particles, u_f is the fluid velocity, u_p is the particle velocity and D is the drag coefficient. Several in-built drag models are available in the Barracuda package, and detailed information about different drag models with references are discussed in the Barracuda manual [5]. Previous results from CPFDF simulations of bubbling fluidized bed gasifiers have shown a good agreement with experimental data when the Wen–Yu drag model was used [6–8]. Furthermore, simulations of CFB systems [4, 9] have also shown better results with Wen–Yu/Ergun drag model, and therefore it was used in this study. The Wen–Yu/Ergun drag model covers the whole range of particle volume fractions where the Ergun drag model is proved excellent for dense phase systems and the Wen–Yu model is appropriate for dilute systems. Chen *et al.* tested different drag models in a CPFDF scheme and the results indicated that the drag force is overestimated, although the cumulative method used to compute drag force is more accurate than the proportional method in the two-fluid model [10]. The Wen–Yu/Ergun drag coefficient is used when the gas volume fraction is higher than 0.8 and it is given by:

$$D_{Wen-Yu} = \frac{3}{8} C_d \frac{\rho_g}{\rho_p} \frac{|u_g - u_p|}{r_p} a^{-2.65} \quad (3)$$

with

$$C_d = \frac{24}{R_e}, \quad (R_e < 0.5) \quad (4)$$

$$C_d = \frac{24}{R_e} (1 + 0.115 R_e^{0.687}), \quad (0.5 \leq R_e \leq 1000) \quad (5)$$

$$C_d = 0.4, \quad (R_e > 1000) \quad (6)$$

where C_d is the drag coefficient, R_e is the Reynolds number and r_p is the particle diameter. As the gas volume fraction decreases below 0.8, the Ergun correlation is used:

$$D_{Ergun} = 0.5 \left(\frac{C_1 \alpha_p}{\alpha_g R_e} + C_2 \right) \frac{\rho_g}{\rho_p} \frac{|u_g - u_p|}{r_p} \quad (7)$$

The default values for the laminar and turbulent coefficients in the Barracuda VR[®] are $C_1 = 180$ and $C_2 = 2.0$. The particle modelling parameter values were adopted from the work of Bandara *et al.* [4].

Establishment of boundary conditions is the succeeding step after the grid generation. The gas out from the cyclone was defined as a pressure boundary with provisions for particle escaping. The riser and the loop seal aerations were implemented as flow boundaries. Figure 4 illustrates the boundary conditions and the initial particle filling in the standpipe, which is identical with the experimental procedure. The rate of particle circulation and the rate of

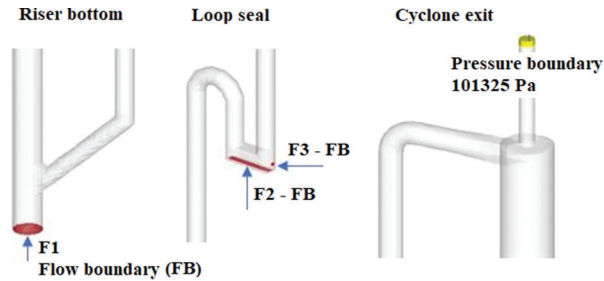


Figure 4: Boundary conditions.

particle escape from the cyclone are monitored using flux planes. Transient data points were used to log the system pressure at identical locations as in the experimental rig.

In addition to the grid resolution, the numerical scheme and the calculation time step are important to obtain accurate simulation results. Smaller time steps give more accurate solutions, but require a longer simulation time. Consequently, there is a trade-off between accuracy and calculation time. As a result, the time steps have to be defined so that the accuracy is sufficient and the calculation time is reasonable. Based on the experience, the time steps were set to 0.005 s. The time duration of the simulation was chosen as 45 s, which was sufficient to ensure that the system reaches steady-state conditions. The partial donor cell numerical scheme was used, which is a weighted average hybrid of central difference and upwind schemes. The large eddy simulation (LES) was used to model the turbulence prevailing at higher length scales, whereas the Smagorinsky model guarantees the capturing of subgrid scale turbulences.

3 RESULTS AND DISCUSSION

The results from the simulations and comparison between simulations and experiments are presented in this section. The rate of particle circulation, system pressure and particle bed height at the standpipe were used for the comparison. Gas velocities practiced in the riser section were well above the particle terminal velocity. The particle overflow from the loop seal is not uniform, and instead it delivers particle clusters. Therefore, at lower velocities, these clusters travel along the riser unbroken, impact at the bend of the riser exit and partly accumulate at the riser–cyclone connecting section. Smaller particles have a high tendency to travel as clusters along the riser. In the experimental tests with the smaller particles, interruptions occurred due to static charges. On the other hand, higher velocities inside the riser increase the turbulence, and consequently the clusters are dispersed, which was an advantageous dimension of the used high velocities in the riser.

3.1 Experimental results

Several particle sizes were tested, but due to the problem with electrostatic charge, particles with size 850–1000 μm and 1000–1180 μm were chosen for the experiments. The minimum flow rates of air into the riser (FR1) for these two particle sizes were found to be 1.3 and 1.5 Sm^3/min , respectively. The ranges of flow rates of gas injection from the bottom of the loop seal (FR2) were found to be 0.012–0.056 Sm^3/min for the smallest particles and 0.014–0.058 Sm^3/min for the largest particles. The respective flow rate ranges for FR3 in the loop seal were found to be 0.006–0.048 Sm^3/min and 0.01–0.056 Sm^3/min . Based on the experimental results, combinations of flow rates were suggested for the simulations. The properties for the

Table 1: Particle density, particle size range and air flow rates suggested for the simulations.

Simulation cases	Particle size [μm]	Bulk density [kg/m^3]	FR1 [Sm^3/min]	FR2 [Sm^3/min]	FR3 [Sm^3/min]
Simulation 1	850–1000	1377	1.3 (9.5 m/s)	0.016	0.044
Simulation 2	850–1000	1377	1.3 (9.5 m/s)	0.028	0.030
Simulation 3	850–1000	1377	1.3 (9.5 m/s)	0.052	0.016
Simulation 4	1000–1180	1390	1.5 (11 m/s)	0.018	0.048
Simulation 5	1000–1180	1390	1.5 (11 m/s)	0.032	0.030
Simulation 6	1000–1180	1390	1.5 (11 m/s)	0.054	0.020

particles used in the experiments and the selected combinations of the flow rates suggested for the simulations are given in Table 1.

In the experimental tests, the only results that could be measured with high accuracy were particle level in the standpipe and the pressure profile over the CFB. These results are presented in Section 3.2 together with the simulation results, and they are used to validate the CFPD model. Predicting the flow rate of particle circulation by stopping the circulation and observing the increase of particles in the standpipe over a certain time was also tried. However, due to uncertainties in the measurements, these experimental results are not used for validation of the CFPD model. One reason is that the gas distributor plate does not function in a manner exactly similar to the uniform gas distribution implemented in the simulations. Another reason is that an occasional particle layer is created at the inside surface of the standpipe bottom due to static charges. This narrows down the cross-sectional area for the particles to descend. Finally, the measurements of particle circulation rate in the simulations are performed during the steady-state operation without interrupting the process. It was observed that a fraction of the circulating sand particles was transferred with the gas out of the CFB via the cyclone.

3.2 Validation of CFPD model

Figure 5 shows a comparison between experimental and simulation results regarding the particle level in the standpipe for Simulations 3 and 6. Simulation 3 was performed with

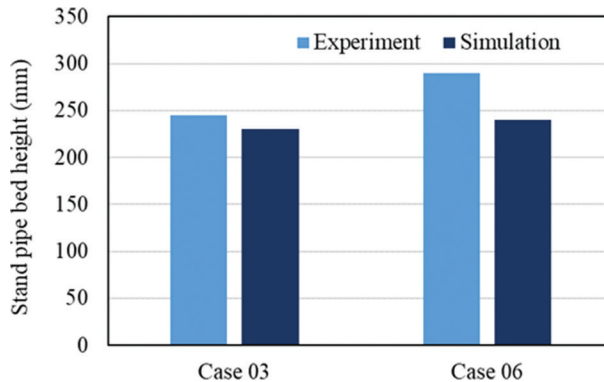


Figure 5: Comparison between experimental and simulation results.

850–1000 μm particles, and the flow rates FR2 and FR3 were 0.052 and 0.016 Nm^3/min , respectively. Simulation 6 was carried out using 1000–1150 μm particles, and the flow rates FR2 and FR3 were set to 0.054 and 0.020 Nm^3/min , respectively. The simulations give slightly higher particle levels than the experiment. The deviations between the experimental and computational levels are about 6% for the 850–1000 μm particles and 17% for the 1000–1150 μm particles. A wire was installed inside the experimental standpipe to prevent particles from sticking to the wall due to electrostatic forces. The wire reduces the volume of the pipe slightly and thereby increases the level of the particles. Furthermore, there may be a slight difference in the bubbling behaviour between experiments and simulations, which consequently may cause the deviated results for the bed height. However, the level of agreement between the results from the experiments and the simulations is acceptable.

In Figs. 6 and 7, the pressure profiles along the CFB are presented for particles with size 850–1000 and 1000–1150 μm , respectively. The comparison shows good agreement between the computational and the experimental results for both types of particles. The deviation is $<0.5\%$ at all the locations. The particle attrition is a common problem, and therefore the particle size distribution may change with time. As a result, the system pressure and rate of particle circulation can change with time, which is not captured by the simulations.

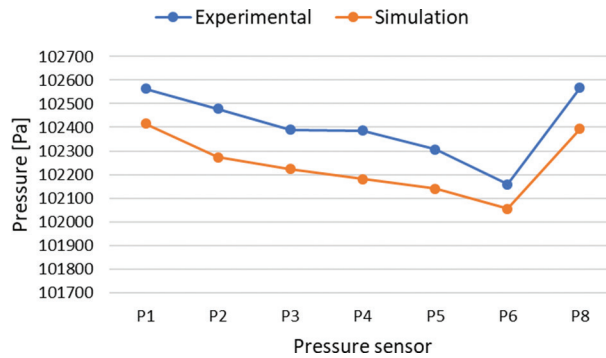


Figure 6: Comparison of computational and experimental pressures along the CFB for 850–1000 μm particles.

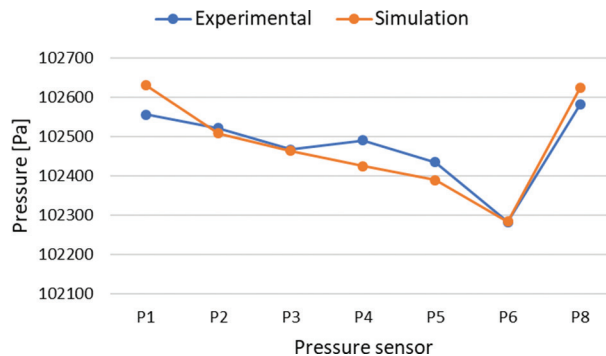


Figure 7: Comparison of computational and experimental pressures along the CFB for 1000–1150 μm particles.

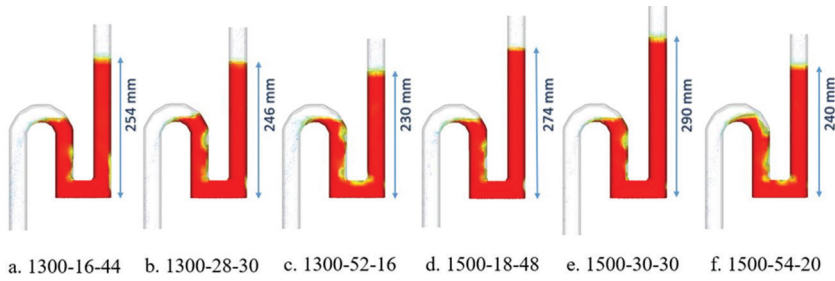


Figure 8: Level of particles in the downcomer.

3.3 CPFD simulation results

The validated CPFD model was further used to study the hydrodynamics, the pressure profiles and fluctuations, the circulation rates and the loss of particles from the CFB rig via the exit of the cyclone. The simulations were performed for six different cases.

3.3.1 Particle hydrodynamics and height in standpipe

Figure 8 illustrates the level of sand particles in the downcomer at steady-state conditions for different air flow rates. The level of the particle gives a rough understanding about the particle distribution across the system. Reduced heights in the standpipe represent high particle loading in the riser and vice versa.

Figure 9 shows the volume fraction of sand particles in the CFB at steady-state condition for the different cases. Although particle volume fractions could not be measured accurately in the experiments, a slightly high concentration of particles at the cyclone bottom and the riser bottom as shown in Fig. 9 was observed in the experiments as well. Furthermore, the figure illustrates that the bubble rise occurs close to the recycle pipe at the inner wall of the loop seal. The same bubble location was observed in the experiments.

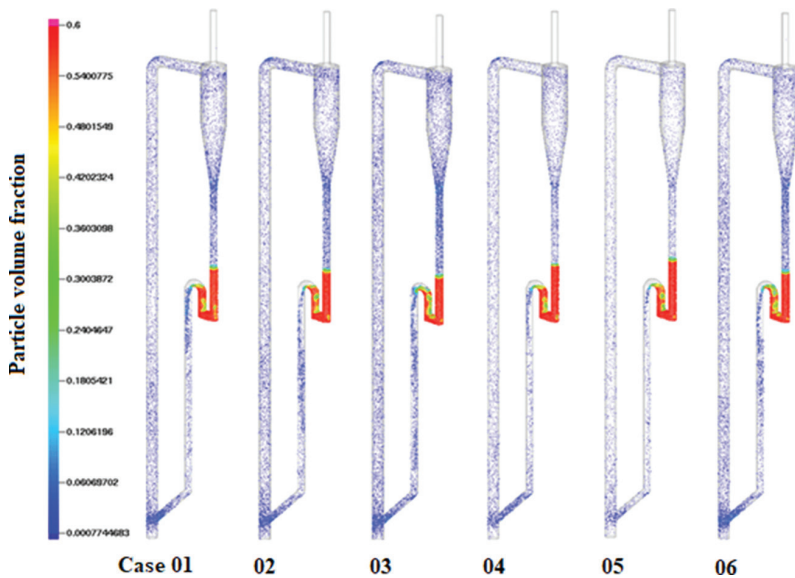


Figure 9: Volume fraction of sand particles at steady-state condition.

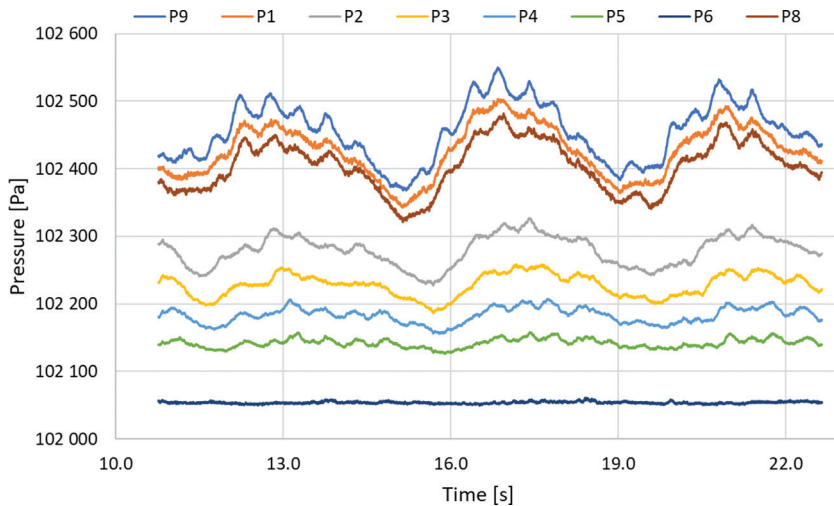


Figure 10: Pressure variation versus time at different positions in the CFB.

3.3.2 System pressure

Figure 10 shows the pressure and pressure variations during the simulations at different positions in the rig as a function of time for Case 1. The observation is done for the time interval 10–25 s, when the CFB system was running at steady-state conditions. According to the figure, the time-evolved pressure variation is high for P8, P9 and P1, which represent the loop seal outflow, the loop seal–riser connection and the loop seal bottom, respectively. As particle clusters are fed out of the loop seal and as the clusters continue towards the riser bottom, the flow rate of the particle is highly varied. This may be the most likely cause of the high fluctuations in pressure. However, the clusters are broken as they travel along the riser and the flow is becoming more homogeneous. Therefore, the pressure, P2–P5, is getting uniform towards the top of the riser.

The average pressure drop along the riser of the rig is illustrated in Fig. 11. The pressure decreases gradually with a uniform gradient from P2 to P5.

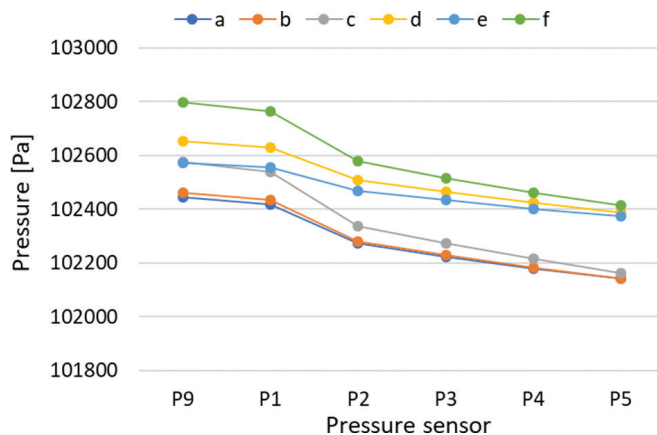


Figure 11: Average pressure drop along the riser of the rig.

Table 2: Particle circulation and particle loss: results from CPFDF simulations.

Simulation case	Mass flow rate of particle circulation [kg/s]	Particle loss [kg/s]
Simulation 1	0.031	7.76E-05
Simulation 2	0.034	9.83E-05
Simulation 3	0.047	1.34E-04
Simulation 4	0.023	1.00E-04
Simulation 5	0.015	6.06E-05
Simulation 6	0.041	1.59E-04

3.3.3 Rate of particle circulation

To investigate the mass flow rate of particle circulation and particle loss, the average values for these variables have been calculated by using the flux plane data files in Barracuda. Table 2 presents the mass flow rates of particles for all the six simulation cases. It was observed that the FR3 had a greater effect in improving the rate of particle circulation FR2. Simulations 3 and 6 have the highest air flow rates for FR3, which owned the highest rate of circulation. However, the rate of particle circulation from the simulation showed accountable variations from the experiments. Some improvements of the experimental rig are needed to enable accurate measurements regarding particle circulation and particle ejection.

4 CONCLUSION

A CFB is studied to find the gas velocities that give smooth operational conditions. Experiments and CPFDF simulations were carried out for this purpose. For the experiments, silica sand was selected as the particle phase. Several particle sizes were tested, but due to the problem with electrostatic charge, particles with size 850–1000 μm and 1000–1180 μm were chosen for further experiments and simulations. The minimum flow rates of air into the riser (FR1) for these two particle sizes were found to be 1.3 and 1.5 Sm^3/min , respectively. The ranges of flow rates of gas injected from the bottom of the loop seal (FR2) were found to be 0.012–0.056 Sm^3/min for the smallest particles and 0.014–0.058 Sm^3/min for the largest particles. The respective flow rate ranges for FR3 in the loop seal were found to be 0.006–0.048 Sm^3/min and 0.01–0.056 Sm^3/min . The pressure in the riser decreased with the increasing flow rate. The level of sand in the standpipe decreased with increasing flow rate.

A CPFDF model was established using the commercial simulation software Barracuda VR. The simulations were carried out for some selected experiments. Comparison between the simulations and the experimental results showed good consistency regarding pressures along the riser and the level of the sand particles in the standpipe. The deviation between the experimental and computational pressure was <0.5% at all the locations for both particle sizes. The deviation in particle level was about 6% for the 850–1000 μm particles and 17% for the 1000–1150 μm particles. The accuracy in the experimental results regarding circulating rate of particles was considered to be low, and the results were therefore not used to validate the CPFDF model. Both the experiments and the simulations predicted a small loss of the circulating sand particles via the outflow from the cyclone. The validated CPFDF model was used to predict the particle circulation rates and the flow behaviour in the CFB at different operational conditions.

REFERENCES

- [1] Grace, J.R. & Bi, H., Introduction to circulating fluidized beds. *Circulating Fluidized Beds*, Springer, pp. 1–20, 1997.
- [2] Klenov, O.P., Noskov, A.S. & Parahin, O.A., Investigation of behaviors in circulating fluidized bed. *Chemical Engineering Science*, **329**, pp. 66–76, 2017. <https://doi.org/10.1016/j.ces.2017.06.092>
- [3] Wang, Q., Wang, P., Yang, H., Lu, J., Liu, Q., Zhang, H., Wei, L. & Zhang, M., Application of CPFD method in the simulation of a circulating fluidized bed with a loop seal Part II—Investigation of solids circulation. *Powder Technology*, **253**, pp. 822–828, 2014. <https://doi.org/10.1016/j.powtec.2013.11.040>
- [4] Bandara, J.C., Thapa, R., Nielsen, H.K., Moldestad, B.M.E. & Eikeland, M.S., Circulating fluidized bed reactors – Part 01: Analyzing the effect of particle modelling parameters in Computational Particle Fluid Dynamic (CPFD) simulation with experimental validation. *Particulate Science and Technology*, 2019, doi:10.1080/02726351.2019.1697773
- [5] CPFD Software. LLC, “Barracuda VR Series 15,” User Manual.
- [6] Jaiswal, R., Furuvi, N.C.I.S., Thapa, R.K. & Moldestad, B.M.E., Method of identifying an operating regime in a bubbling fluidized bed gasification reactor. *International Journal of Energy Production & Management*, **5(1)**, pp. 24–34, 2020. <https://doi.org/10.2495/eq-v5-n1-24-34>
- [7] Furuvi, N.C.I.S., Jaiswal, R., Thapa R.K. & Moldestad, B.M.E., CPFD model for prediction of flow behavior in an agglomerated fluidized bed gasifier. *International Journal of Energy Production and Management*, **4(2)**, pp. 105–114, 2019. <https://doi.org/10.2495/eq-v4-n2-105-114>
- [8] Furuvi, N.C.I., Jaiswal, R., Thapa, R.K. & Moldestad, B.M.E., Study of agglomeration in fluidized bed gasification of biomass using CPFD simulations. *Linköping Electronic Conference Proceedings*, **170**, pp. 176–181, 2019.
- [9] Thapa, R.K., Frohner, A., Tondl, G., Pfeifer, C. & Halvorsen, B.M., Circulating fluidized bed combustion reactor: Computational Particle Fluid Dynamic model validation and gas feed position optimization. *Computers & Chemical Engineering*, **92**, pp. 180–188, 2016. <https://doi.org/10.1016/j.compchemeng.2016.05.008>
- [10] Chen, C., Werther, J., Heinrich, S., Qi, H.-Y. & Ulrich, E., CPFD simulation of circulating fluidized bed risers. *Powder Technology*, **235**, pp. 238–247, 2013. <https://doi.org/10.1016/j.powtec.2012.10.014>

Doctoral dissertation no. 92

2021

**Simulation and parameter optimization of
fluidized-bed and biomass gasification**

Dissertation for the degree of Ph.D

Janitha Bandara

ISBN: 978-82-7206-590-3 (print)

ISBN: 978-82-7206-591-0 (online)

usn.no

